University of Southampton

Faculty of Medicine

Clinical & Experimental Sciences

The Role of Tetraspanin-10 in the Retinal Pigment Epithelium and its Influence in Age-Related Macular Degeneration.

by

Rebecca Anne Kaye, BMBCh, MA (Oxon)

ORCID ID 0000-0002-1504-3201

Thesis for the degree of Doctor of Philosophy

December 2024

University of Southampton

Abstract

Faculty of Medicine

Clinical and Experimental Sciences

Thesis for the degree of Doctor of Philosophy

The Role of Tetraspanin-10 in the Retinal Pigment Epithelium and its Influence in Age-Related Macular Degeneration.

by

Rebecca Anne Kaye, BMBCh, MA (Oxon)

Age related macular degeneration (AMD) is the leading cause of vision loss in the Western World [1], accounting for 5.6% of global blindness [1][2, 3]. Irreversible visual impairment arises due to the gradual loss of photoreceptors and their supportive cells: the retinal pigment epithelium (RPE). Currently therapeutics are only available to treat 50% of patients with AMD and in the long-term are ineffective. This is due to an incomplete understanding of the pathophysiology. Genetic risk is a key element of AMD susceptibility and multiple risk loci have been identified including a novel single nucleotide polymorphism (SNP) at Tetraspanin 10 (TSPAN10) [4-7]. The purpose of this work was to elucidate the role of TSPAN10 within the RPE and subsequently understand how it contributes to AMD.

CRISPR/Cas-9 gene editing was utilised to produce two TSPAN10 knock-out (k.o) clones in human embryonic stem cells (hESCs) that were then differentiated into RPE. Three separate differentiations for both TSPAN10 k.o and WT cells were produced for robustness, and their genomic DNA, transcripts and protein characterised. TSPAN10 has a significant influence on hESC-RPE pigmentation. TSPAN10 k.o cells were less pigmented than WT hESC-RPE, evidenced both macroscopically in culture, microscopically using transmission electron microscopy (TEM), and through measurement of tyrosinase production and function.

Transcriptomics suggested TSPAN10 k.o has a significant influence on oxidative stress in the RPE. Catalase (*CAT*) is a key enzyme protecting the cell from oxidative stress, *CAT* mRNA expression was significantly reduced in TSPAN10 k.o clones (p_{adj}= 1.39 x 10^{-20}). Functional correlation revealed increased oxidative stress in k.o cells at baseline and reduced catalase production. A functional assay also assessed the effect of TSPAN10 k.o on RPE phagocytic function, revealing a similar response to oxidatively stressed WT RPE.

Finally, a cohort study in human beings analysing the impact of AMD genetic risk loci on outer retinal thickness, revealed the AMD risk SNP at *TSPAN10* to be significantly associated with thinning of the RPE-Bruch's membrane and photoreceptor complexes.

The work presented within this thesis demonstrates the multiple plausible roles that TSPAN10 may have in the RPE and gives insight into its role in AMD. Aligning this with further functional work is a key next step.

Achievements throughout PhD

Peer-reviewed papers

- **Kaye RA**, Patasova K, Patel PJ, Hysi P, Lotery AJ; UK Biobank Eye and Vision Consortium. Macular thickness varies with age-related macular degeneration genetic risk variants in the UK Biobank cohort. Sci Rep. 2021 Dec 1;11(1):23255. doi: 10.1038/s41598-021-02631-2. PMID: 34853365; PMCID: PMC8636487.
- Menten MJ, Holland R, Leingang O, Bogunović H, Hagag AM, **Kaye R**, Riedl S, Traber GL, Hassan ON, Pawlowski N, Glocker B, Fritsche LG, Scholl HPN, Sivaprasad S, Schmidt-Erfurth U, Rueckert D, Lotery AJ. Exploring Healthy Retinal Aging with Deep Learning. Ophthalmol Sci. 2023 Mar 1;3(3):100294. doi: 10.1016/j.xops.2023.100294. PMID: 37113474; PMCID: PMC10127123.
- Anders P, Traber GL, Pfau M, Riedl S, Hagag AM, Camenzind H, Mai J, **Kaye R**, Bogunovic H, Fritsche LG, Rueckert D, Schmidt-Erfurth U, Sivaprasad S, Lotery AJ, Scholl HPN. Comparison of Novel Volumetric Microperimetry Metrics in Intermediate Age-Related Macular Degeneration: PINNACLE Study Report 3. Transl Vis Sci Technol. 2023 Aug 1;12(8):21. doi: 10.1167/tvst.12.8.21. PMID: 37624605
- **Joint first author**. Hagag AM, **Kaye R**, Hoang V, Riedl S, Anders P, Stuart B, Traber G, Appenzeller-Herzog C, Schmidt-Erfurth U, Bogunovic H, Scholl HP, Prevost T, Fritsche L, Rueckert D, Sivaprasad S, Lotery AJ. Systematic review of prognostic factors associated with progression to late age-related macular degeneration: Pinnacle study report 2. Surv Ophthalmol. 2023 Oct 25:S0039-6257(23)00140-6. doi: 10.1016/j.survophthal.2023.10.010. PMID: 37890677.

Awards

- Tim Millar Prize for Best Oral Presentation by an Early Career Researcher, Faculty of Medicine Conference, University of Southampton, 2023
- Michael Arthur Clinical Academic Trainee Research Prize, University of Southampton, 2022
- Association for Research in Vision & Ophthalmology Travel Grant, 2021

Oral Presentations

Faculty of Medicine Conference, Southampton, June 2022 “Macular thickness varies with age-related macular degeneration genetic risk variants in the UK Biobank cohort.”

The Macular Society Gene Editing meeting, Oxford, September 2022, “Using CRISPR-Cas9 to investigate the role of Tetraspanin-10 in the retinal pigment epithelium and age-related macular degeneration.”

Interdisciplinary Dementia and Ageing Centre (IDeAC), Southampton, November 2022, “Tetraspanin 10 in the retinal pigment epithelium and its role in age-related macular degeneration.”

Centre for Human Development, Stem Cells and Regeneration (CHDSCR) Symposium, Southampton, May 2023, “Tetraspanin-10 a novel AMD risk variant and its role in the retinal pigment epithelium.”

Faculty of Medicine Conference, Southampton, June 2023 “CRISPR/Cas9 mutagenesis of Tetraspanin-10, a novel AMD risk variant, impacts human retinal pigment epithelial cell pigmentation and oxidative stress.”

Poster Presentations

Association of Research in Vision and Ophthalmology, San Francisco (Virtual), April 2021, “Choroidal Vascularity in Chronic Central Serous Chorioretinopathy.”

> Rebecca Kaye, Tunde Peto, Andrew J Lotery; Choroidal Vascularity in Chronic Central Serous Chorioretinopathy. Invest. Ophthalmol. Vis. Sci. 2021;62(8):1902.

Doctoral Research Poster Showcase, Southampton, December 2022, “The Role of Tetraspanin-10 in the Retinal Pigment Epithelium and its relevance to Age Related Macular Degeneration.”

Association of Research in Vision and Ophthalmology, New Orleans, April 2023, CRISPR/Cas9 mutagenesis of Tetraspanin-10, a novel AMD risk variant, impacts human retinal pigment epithelial cell pigmentation and oxidative stress

Rebecca Kaye, Jorn Lakowski, Andrew J Lotery; CRISPR/Cas9 mutagenesis of Tetraspanin-10, a novel AMD risk variant, impacts human retinal pigment epithelial cell pigmentation and oxidative stress. Invest. Ophthalmol. Vis. Sci. 2023;64(8):3197.

Patient Group Presentations

Retina UK, Southampton, March 2023, “Inherited retinal diseases and prospects for therapy.”

Declaration of Authorships

Academic Thesis: Declaration of Authorship

I, Rebecca Kaye, declare that this thesis and the work presented in it are my own and has been generated by me as the result of my own original research.

The Role of Tetraspanin-10 in the Retinal Pigment Epithelium and its Influence in Age-Related Macular Degeneration.

I confirm that:

1. This work was done wholly or mainly while in candidature for a research degree at this University;

2. Where any part of this thesis has previously been submitted for a degree or any other qualification at this University or any other institution, this has been clearly stated;

3. Where I have consulted the published work of others, this is always clearly attributed;

4. Where I have quoted from the work of others, the source is always given. With the exception of such quotations, this thesis is entirely my own work;

5. I have acknowledged all main sources of help;

6. Where the thesis is based on work done by myself jointly with others, I have made clear exactly what was done by others and what I have contributed myself;

7. Parts of this work have been published as:

> **Kaye RA**, Patasova K, Patel PJ, Hysi P, Lotery AJ; UK Biobank Eye and Vision Consortium. Macular thickness varies with age-related macular degeneration genetic risk variants in the UK Biobank cohort. Sci Rep. 2021 Dec 1;11(1):23255. doi: 10.1038/s41598-021-02631-2. PMID: 34853365; PMCID: PMC8636487.

Signed: .....Rebecca Kaye.....

Date: .....08/07/2024.....

Acknowledgements

I would like to thank both my supervisors Professor Andrew Lotery and Dr. Jorn Lakowski for all their help, support, and guidance.

Liliya Nazlamova for all her help with stem cell culture and training in molecular techniques.

Thank you to all the staff in the Biological Imaging Unit, specifically Catherine Griffiths for training me in transmission electron microscopy, Dave Johnston for his limitless knowledge of confocal microscopy and David Chatelet for his advice with image analysis.

Thank you to the Clegg laboratory in San Diego California for responding to all my email queries.

Thank you to the Vision Research Group & the post-doctoral researchers, Dr Savannah Lynn, Dr Jennifer Dewing & Dr Eloise Keeling for all their informal advice and helpful suggestions.

Thank you to my husband Alex for all your support and our two wonderful children Florence and Sophie.

Finally thank you to the Gift of Sight Charity and the Wellcome Trust for funding this PhD.

All data collected within this thesis was conducted by me, with the exception of several instances. Here, help was given by colleagues or outsourced and is formally acknowledged below:

- The Wessex Medical Institute for karyotyping both mutant cell clones (Appendix A).
- NovoGene Europe for the RNA sequencing and the differential gene and gene set analysis (Chapter 5).
- All Sanger sequencing was outsourced to Source Bioscience.
- Retinal organoid cDNA was provided by my supervisor Dr Jorn Lakowski (Chapter 3)
- The modified px459 plasmid was provided by my supervisor Dr Jorn Lakowski (Chapter 3)
- Dr Carolann Mcguire trained and assisted me with the flouresence activated cell sorting (FACS) (Chapter 6)
- Grace Patterson cut several of the Transwell® membranes for transmission electron microscopy presented in Chapter 6
- My supervisor Dr Jorn Lakowski performed cryo-sectioning of human foetal eyes (Chapter 7)
- Magdalena Martinez downloaded and processed the bulk RNA sequencing data from human foetal eyes in Chapter 7.

- Karina Patasova at Kings College London for statistical analysis of the data presented in Chapter 8

Table of Contents

List of Tables

List of Figures

List of Abbreviations

A2E	Bis-retinoid N-retinyl-N-retinylidene ethanolamine
ACTB	Beta Actin
ADAM10	ADAM Metallopeptidase Domain 10
AMD	Age-related Macular Degeneration
ApoE	Apolipoprotein E
ATP	Adenosine triphosphate
BEST1	Bestrophin – 1
BCA	Bicinchoninic Acid
BLOC1S1	Biogenesis of lysosome-related organelles complex 1 subunit 1
BrM	Bruch's Membrane
BMP	Bone morphogenic protein
BRB	Blood-Retinal Barrier
BSA	Bovine Serum Albumin
CAGE	Cap Analysis of Gene Expression
C3	Complement Factor 3
CFB	Complement Factor B
CFH	Complement Factor H
CFI	Complement Factor I
CFTR	Cystic fibrosis transmembrane conductance regulator
Cq	Quantification cycle
crRNA	Customized guide RNA
CRALBP	Retinaldehyde-binding protein
CRISPR/Cas9	Clustered regularly interspaced short palindromic repeats with Cas9 endonuclease
DAPI	4', 6'-diamino-2-phenylindole
ddH2O	Double distilled Water
DHICA	5,6,-dihydroxyindole-2-carboxylic acid
DHI	5,6-dihydroxyindole.
DKK-1	Dickkopf-related protein 1
DMEM	Dulbecco's Modified Eagle's Medium
DNA	Deoxyribonucleic acid
dsDNA	Double strand DNA
EDTA	Ethylenediaminetetraacetic acid
ELISA	Enzyme Linked Immunosorbent Assay
ER	Endoplasmic reticulum
EFPC	Eye field progenitor cells
eQTL	Expression quantitative trait loci
FANTOM5	Functional annotation of the mammalian genome
FGF	Fibroblast growth factor
FHR-4	Factor H Regulator 4
GA	Geographic Atrophy
GAPDH	Glyceraldehyde-3-phosphate Dehydrogenase
gDNA	Genomic DNA
GFR	Growth-factor reduced
GTeX	Genotype-Tissue Expression Project
GSK3β	Glycogen synthase kinase 3 beta
GWAS	Genome Wide Association Study
HDR	Homology directed repair
Hes1	Hes Family BHLH Transcription Factor 1
Hey2	Hairy/enhancer-of-split related with YRPW motif protein 1
hESC	Human embryonic stem cell
hiPSC	Human induced pluripotent stem cell
HTRA1	Serine protease HTRA1
IGF-1	insulin-like growth factor 1
ILM	Inner limiting membrane
INL	Inner nuclear layer
Indel	Insertions or deletions
IPL	Inner plexiform layer
KO	Knock out
LAMP-1	Lysosome Associated Membrane Protein 1
L-Dopa	Dihydroxyphenalanine
MAK	Male germ cell-associated kinase
MerTK	Tyrosine Kinase c-mer
MITF	Melanocyte Inducing Transcription Factor
mRNA	Messenger RNA

NHEJ	Non-homologous end joining
NF-kB	Nuclear Factor kappa-light-chain-enhancer of activated B cells
NGS	Next Generation Sequencing
NMD	Nonsense-mediated decay
NPLOC4	NPL4 Homolog, Ubiquitin Recognition Factor
ONL	Outer nuclear layer
OPL	Outer plexiform layer
ORF	Open reading frame
OTX2	Orthodenticle Homeobox 2
PAM	Protospacer adjacent motif
PBS	Phosphate-buffered saline
PBST	Phosphate-buffered saline with Tween-20
PCR	Polymerase Chain Reaction
PEDF	Pigment epithelium-derived factor
PFA	Paraformaldehyde
POS	Photoreceptor outer segments
PTC	Premature termination codon
Rab5	Ras-related protein Rab-5A
RB	Retinoblastoma
RDS	Retinal Degeneration Gene
RD3L	Retinal degeneration protein-3 like
RDM	Retinal differentiation media
ROS	Reactive oxygen species
RNA	Ribonucleic acid
RNAi	RNA interference
RNP	Ribonucleoprotein complex
ROM1	Rod outer segment membrane protein 1
RPE	Retinal Pigmented Epithelium
RPE-65	Retinal pigment epithelium-specific 65 kDa protein
RT	Room temperature
RT-qPCR	Quantitative Real-Time Polymerase Chain Reaction
SEM	Standard Error of the Mean
shRNA	Short hairpin RNAs
sgRNA	Single-guide RNA
SNP	Single nucleotide polymorphism
STRING	Search Tool for the Retrieval of Interacting Genes/Proteins
SOC	Super Optimal broth with Catabolite repression
SOD2	Superoxide Dismutase 2
SV40	Simian virus 40
Ta	Annealing temperature
TABS	Topcon Advanced Boundary Segmentation
TALENs	Transcription activator-like effector nucleases
TEER	Transepithelial Electrical Resistance
TEM	Transmission Electron Microscopy
TGFβ	Transforming growth factor beta
Tm	Melting temperature
TMEM199	Transmembrane protein 199
TRPM1	Transient receptor potential cation channel subfamily M member 1
tracrRNA	Scaffold RNA
TspanC8	C8 Tetraspanins
TSPAN10	Tetraspanin 10
TSPAN17	Tetraspanin 17
TSPAN18	Tetraspanin 18
TWAS	Transcriptome-wide association studies
TYR	Tyrosinase
TYRP1	Tyrosinase-Related Protein 1
UVB	Type B ultraviolet
VEGF	Vascular Endothelial Growth Factor
WT	Wild type
ZFNs	Zinc finger nucleases
ZO-1	Zonula occludens-1

1 Introduction

Vision is the dominant sense [2]. The importance of sight is reflected in the language we use daily. "Seeing is believing", establishing sight as the paradigm of belief. A new idea ‘in the light of day’ can ‘open our eyes’, while ignorance can ‘blind us to the truth’ and ‘leave us in the dark’.

We live in a visual age. Our reliance on sight and therefore our eyes is evident from the moment we wake and reach for our mobile phones, drive our cars, work at our computers, and finally return home to watch our televisions. Subsequently, sight bears great importance for both human physical and psychological wellbeing. In fact, blindness and visual impairment are amongst the most feared medical conditions after cancer and cardiovascular disease [3, 4]. It is therefore not surprising that there is great clinical interest in understanding the intricacies and pathologies of the eye.

This introduction will discuss a cell type of particular importance to the healthy functioning of the retina: the retinal pigmented epithelium (RPE). The RPE will be initially viewed within the context of a healthy functioning retina, followed by its role in retinal pathology, with a focus on age-related macular degeneration (AMD). The pathophysiology of AMD will be addressed in relation to genetic influences, in particular the role of a poorly understood gene, *tetraspanin-10*.

1.1 The Retina & the RPE

1.1.1 Development of the retina

The retina, including the RPE, forms from the diencephalon, the neuroepithelium of the posterior forebrain. Following neural induction the eye field is specified, bisected, and evaginates to form the two optic vesicles. On contact with the overlying surface ectoderm each optic vesicle is patterned into regions that give rise to the optic stalk, neural retina, and RPE. From there, the optic vesicle invaginates to form the concave eye cup. Due to the invagination of the optic cup, the apical aspect of the primitive neural retina comes to lie adjacent to the apical surface of the RPE, thereby removing the intraretinal space.

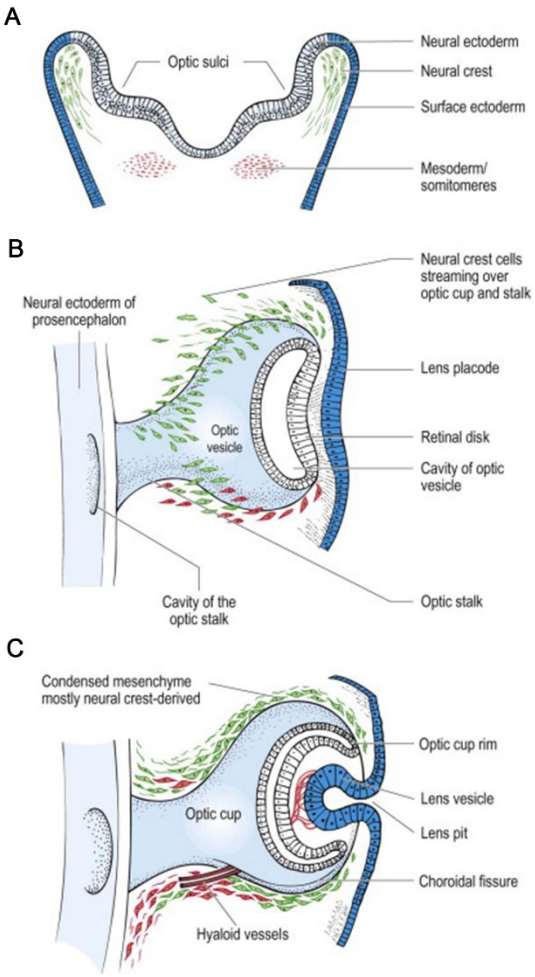

Figure 1-1 Schematic of ocular embryonic development
Diagrammatic representation of embryonic development from day 22 to week 8.
A Formation of the optic sulci which evaginate to form the optic vesicles
B The optic vesicles are formed and patterned into regions
C Invagination of the optic cup. Mesenchyme forms from neural crest.
Diagram taken from John V. Forrester, Andrew D. Dick, Paul G. McMenamin, Fiona Roberts, Eric Pearlman, Chapter 2 - Embryology and early development of the eye and adnexa, The Eye (Fourth Edition), Available from https://doi.org/10.1016/B978-0-7020-5554-6.00002-2 [5]

1.1.2 Anatomy of the Retina

The human retina is an intricate structure comprised of the neuroretina and the underlying RPE. The neuroretina can be divided into nine layers: the outer and inner segments of photoreceptors (rods and cones), the external limiting membrane, the outer nuclear layer, outer plexiform layer, inner nuclear layer, inner plexiform layer, ganglion cell layer, nerve fibre layer and internal limiting membrane, depicted in Figure 1 – 2.

The cell types of the neuroretina include six types of neuronal cells including photoreceptors, horizontal cells, bipolar cells, amacrine cells and ganglion cells, and three main types of glial cell including Muller glial cells, astrocytes and microglia.

Below the photoreceptor layer is the RPE. The RPE provides nutrients and removes waste material from photoreceptors. Initially it was thought one RPE cell serviced up-to 45

photoreceptors [6], however, recent evidence in the mouse suggests this number can be greater than 200 [7]. Interestingly the ratio of RPE to photoreceptors differs in various species. For example, in the mouse this ratio is much greater than that seen in humans [8, 9]. The basement membrane of the RPE is formed from Bruch's membrane (BrM). BrM, the innermost layer of the choroid, is a pentalaminar structure, the innermost layer is composed of the RPE basement membrane followed by two collagenous layers divided by a middle elastic zone and finally the choriocapillaris basement membrane [10, 11].

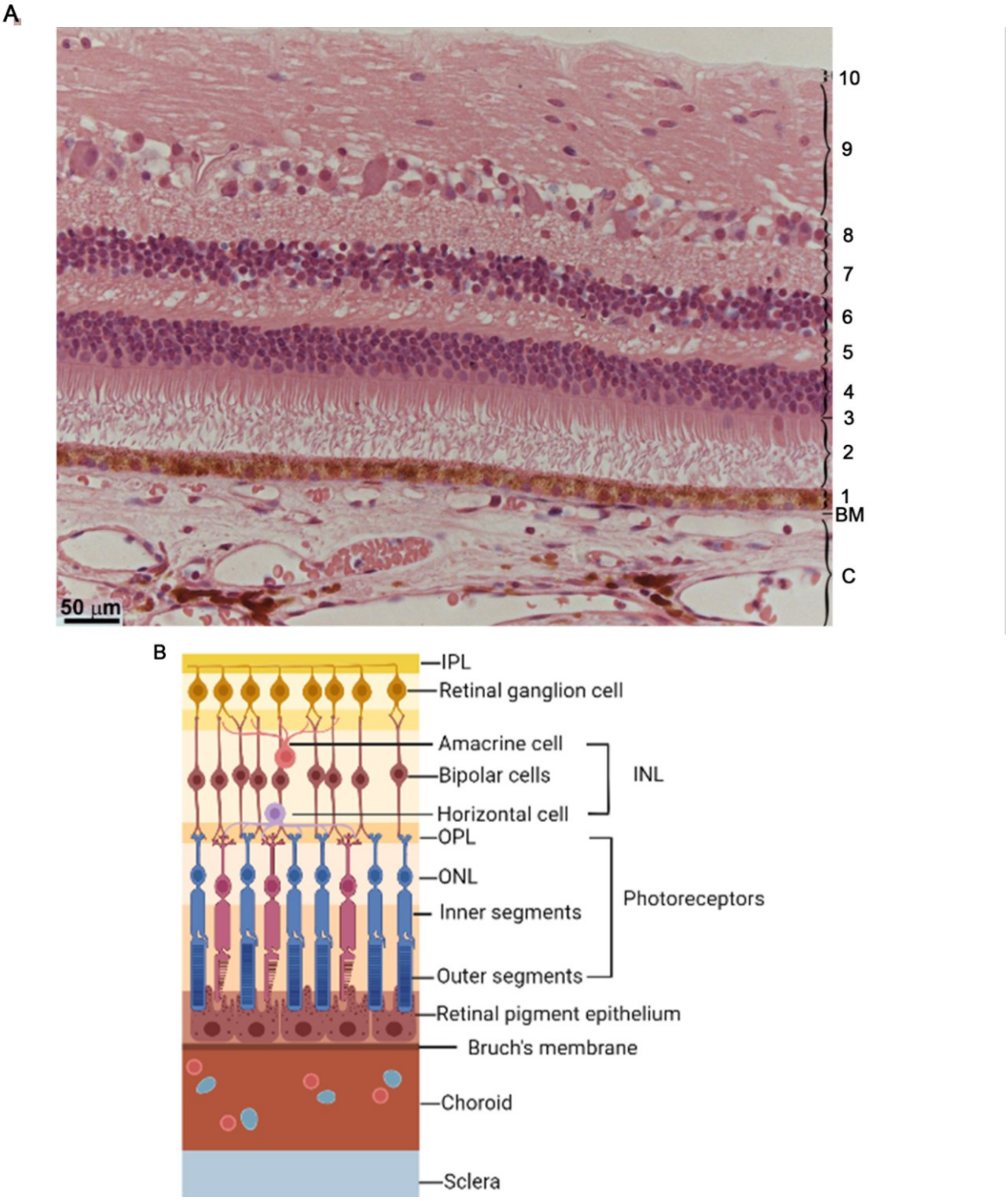

Figure 1-2 The human retina
A: Histological section of the human retina stained with haematoxylin/eosin.
1: Retinal pigment epithelium; 2: Photoreceptor layer; 3: Outer limiting membrane; 4: Outer nuclear layer; 5: Outer plexiform layer; 6: Inner nuclear layer; 7: Inner plexiform layer; 8: Ganglion-cell layer; 9: Nerve-fibre layer; 10: Inner limiting membrane; BM: Bruch's membrane; C: Choroidal vascular layer. Image adapted from (©2012 Triviño A,De Hoz R, Rojas B, Gallego BI, Ramírez AI, Salazar JJ, Ramírez JM.[12] Available from: http://dx.doi.org/10.5772/48359)
B: Schematic of the human retina displaying the various layers and cell types.
Abbreviations: IPL, inner plexiform layer; INL, inner nuclear layer; OPL, outer plexiform layer; ONL, outer nuclear layer.
Image created using Biorender.com

1.2 The RPE

The RPE consists of a monolayer of largely cuboidal-shaped pigmented cells found beneath the neuroretina and overlying the vascular blood supply of the choriocapillaris. Occupying this strategic position in the outer retina the RPE performs multiple functions which are essential for retinal homeostasis, photoreceptor survival and thereby maintenance of life-long vision. The RPE also forms the outer blood-retinal barrier (BRB) which confers an immune privileged state within the ocular environment [13, 14]. The inner BRB, similarly to the blood-brain barrier is formed by endothelial cells in the inner retinal microvasculature [13], whose tight junctions are modulated by glial cells, such as astrocytes [15]. A non-inclusive list of RPE functions includes the absorption of light, the daily phagocytosis and processing of shed photoreceptor outer segments (POS), re-isomerization of all-trans-retinal to 11-cis-retinal in the visual cycle, trans-epithelial transport, polarised secretion of molecules towards the overlying neuroretina and the underlying choroid, and paracrine cellular communication [16] [17]. Figure 1 – 3 highlights the many functions of the RPE. The absorption of light by the RPE, specifically its energy, helps to protect the oxygen-rich retina from photo-oxidation. Light absorption occurs through melanin within melanosomes and other RPE pigments that filter distinct wavelengths of light, protecting the macula from oxidative stress [18]. The hexagonal RPE forms tight junctions, classified as a tight epithelium, forming a diffusion-impermeable layer. As such, the RPE must actively transport biological materials between the apically abutting photoreceptors and the basolateral choroidal vasculature. This transport is critical to the balance of water, ions, and pH within the subretinal space. The RPE is a high cuboidal epithelium in the fovea, but transitions to a lower cuboidal type at the equatorial regions of the human retina [19]. These regional morphological variations are due to its specialised functions in different parts of the retina, for example at the fovea the high cuboidal RPE provides a larger surface area for interactions with densely packed photoreceptors in addition to more space for intracellular organelles and a greater metabolic capacity supporting the photoreceptors high energy requirements [17].

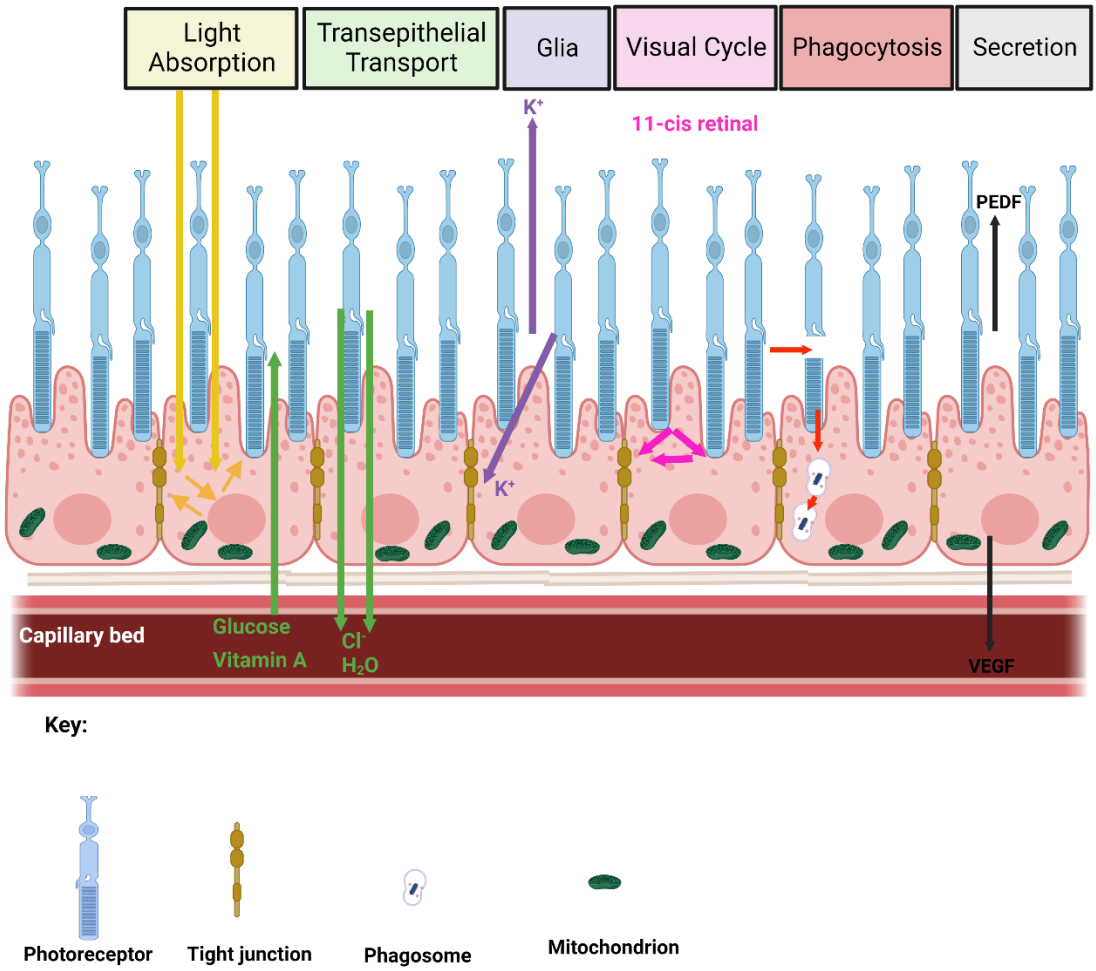

Figure 1-3 Main functions of the Retinal Pigment Epithelium
The Retinal Pigment Epithelium (RPE) is critical for normal vision function and maintenance of retinal homeostasis. There are many physical characteristics and functions key to this crucial role of the RPE including, the absorption of scattered light, transepithelial transport to and from the choroid, formation of a blood retinal barrier, spatial buffering of ions (aided by Muller glia cells) and a role in phototransduction via the recycling of 11-cis retinal. Furthermore, the RPE secretes various cytokines and growth factors and phagocytoses shed photoreceptor outer segments (POS).
Abbreviations: PEDF, pigment epithelium derived factor; VEGF, vascular endothelial growth factor
Image created using Biorender.com. Image adapted from [17].

1.2.1 RPE polarity

Cellular polarity refers to the asymmetric distribution of proteins, mRNA and/or organelles between the apical and basolateral membranes of a cell. Epithelial cells are typified by their polarisation. Generally, simple epithelia are monolayers with an apical pole that faces a lumen and a basolateral pole that faces a solid tissue. Interactions between the basolateral membrane and the underlying tissue thus induce epithelial polarity. The RPE differs to typical epithelia, given that its apical surface borders tissue as opposed to lumen, with apical microvilli protruding into the subretinal space. Two types of microvilli exist in the RPE:

1. Long thin microvilli, which increase the surface area of the RPE for transepithelial transport [17, 20].
2. Specialised photoreceptor sheaths, extensions of the RPE which ensheath the outer segments of photoreceptors, facilitating phagocytosis [17].

The polarity of the RPE is crucial for both RPE structure and function. Structurally the apical portion contains microvilli, whilst the basal membrane displays numerous invaginations known as basal infolds which act to increase the surface area for metabolite and nutrient exchange between the retina and the systemic circulation [17].

Functionally, both the apical and basal membranes of the RPE contain various pumps, transporters, receptors, and passive ion channels. Notably, the apical membrane features the electrogenic Na^+/K^+ ATPase, whilst the basal membrane includes a Cl^- / HCO_3^- exchange transporter. This transepithelial movement of Cl^- and K^+ ions allows water to move across the RPE [21], a crucial function to help maintain an adhesive force between the RPE and the retina [17]. The transport of other ions, such as Na^+ and HCO_3^- is essential for pH regulation and the polarization/hyperpolarization of cell membranes [22].

An essential function of the RPE is the phagocytosis of POS. This function necessitates the apical distribution of the receptors α5β5 integrin and tyrosine kinase c-mer (MerTK) [17]. Furthermore, organelles distributed within the RPE are localised as a result of polarity with mitochondria towards the basal surface along the same axial plane as the nucleus [22]. Conversely, melanosomes localise towards the RPE apical surface in the presence of light.

The polarity of the RPE is essential for its multifaceted roles in supporting photoreceptors, maintaining retinal homeostasis, and protecting the retina from damage.

1.2.2 Blood Retinal Barrier (BRB) Function

The BRB can be divided into inner and outer layers. The outer BRB is formed by a circumferential belt of apical tight junctions laterally between neighbouring RPE cells [1]. Collectively this creates a seal that isolates the retina from the systemic circulation. There is an intimate relationship between RPE cell polarity and tight junctions, controlling paracellular permeability across the epithelium, and acting as a physical barrier to maintain distinct apical and basolateral membrane compositions [23].

The permeability, selectivity and ‘tightness’ of this outer BRB is determined by tight junction proteins, including claudins, occludins and zonula-occludens (ZO) [13, 14, 24, 25]. Claudins are largely considered to be the main proteins important for tight junction strand formation [23]. Claudins form pores facilitating the passive diffusion of molecules through the paracellular space [26]. Each claudin is thought to have a unique effect on selectivity and

permeability with the specific paracellular properties of different epithelia resulting from their individual pattern of claudin expression [25]. Claudin-19, claudin-3 and claudin-10 have all been reported in the tight-junction complex of human RPE. However, claudin-19 is by far the predominant claudin [27], determining permeability and semi-selectivity of tight junctions.

Another crucial protein in RPE tight junction formation is the 60 kDa membrane protein occludin [28]. Occludin further regulates tight-junction permeability, and its presence is often indicative of enhanced barrier function in *in vitro* RPE cultures where claudin expression is absent [29]. ZO are early tight-junction proteins that create a scaffold by interacting with both the actin cytoskeleton and the occludin and claudin proteins. ZO-1 is exclusively located at tight junctions in epithelial cells [30], however, when tight junctions are not formed ZO-1 are concentrated in adherens junctions [31-34], indicating its role in maintaining cell-cell adhesion.

1.2.3 RPE phagocytic activity

The RPE are the most actively phagocytic cells in the human body. Each RPE cell is capable of the diurnal removal of approximately 30-50 POS tips daily [35]. The phagocytic process comprises three distinct phases, recognition/binding, internalisation, and digestion, each of which is separately regulated. Three receptors are crucial for the internalisation and digestion of POS; MerTK, αvβ5 integrin and the macrophage phagocytosis receptor CD36 [36]. It is widely accepted that MerTK is involved in the activation of phagocytosis [37], CD36 is essential for POS internalisation [38] and αvβ5 integrin is required for the binding of POS to the RPE and the circadian regulation of phagocytosis [39, 40]. Once internalized, POS are transported to the basal region of the RPE in phagosomes for processing through the endo-lysosomal pathway. The continuous phagocytosis of POS places a significant proteolytic burden on the RPE monolayer, especially considering its post-mitotic nature. The RPE endures one of the highest proteolytic demands in the human body, with a single macula RPE cell engulfing over one billion outer segment discs throughout an individual's lifetime [6]. To manage this high volume of phagocytic material and to clear damaged organelles and misfolded proteins, the RPE has evolved multiple efficient clearance mechanisms [41]. Three of which, phagocytosis, endocytosis and autophagy, are interrelated and culminate in the proteolytic degradation of components within lysosomes. The fourth, the Ubiquitin Proteasome, is the primary mechanism for the degradation of damaged, misfolded or aggregated proteins [42]. Whilst organelle associated or membrane-bound proteins are targeted to lysosomes via endocytic or autophagy pathways [41].

1.2.4 RPE secretory functions

The RPE produces a variety of secretory molecules which are essential for the function and survival of the overlying photoreceptors. The two most significant of which are Pigment Epithelium Derived Growth Factor (PEDF) and Vascular Endothelial Growth Factor (VEGF) [43]. In the healthy eye, PEDF acts a neuroprotective and antiangiogenic factor to help maintain the retinal and choriocapillaris structure [43-45]. VEGF is required for the prevention of endothelial cell apoptosis and is vital for maintaining a healthy vasculature [46]. Secretion of these two opposing proteins is tightly regulated within the RPE, where perturbations in the relative amounts of VEGF and PEDF can lead to retinal disease including choroidal neovascularisation (CNV) [47].

1.2.5 Melanin production in the RPE

Melanins are synthesized by a small population of pigment cells, including melanocytes and the RPE [48]. Melanocytes of the skin, hair and uveal tract derive from the neural crest [49, 50], in contrast those in the RPE, ciliary body and iris, derive from the neuroectoderm [51].

Melanogenesis occurs early in the RPE and is evident by approximately the fifth week of foetal life [51, 52]. Unlike neural crest derived melanocytes, those of neuroectodermal origin in the eye do not transfer their pigment to neighbouring cells [50] and are not capable of resuming melanogenesis after birth [49, 51]. Despite these differences, both types of melanocytes produce melanin pigments within specialised subcellular organelles called melanosomes [53].

Melanosomes mature through several stages (Figure 1 – 4A). Initially they lack pigment (stages I and II), however, they are progressively filled with enzymes and membranous structures (stage III) until eventually the internal structure of the mature organelle becomes completely melanised (stage IV) [50, 52, 53]. Melanogenesis occurs within these matured organelles. Here, tyrosine is converted to either eumelanin (black-brown pigment) or pheomelanin (yellow-red pigment). Tyrosinase is the key enzyme involved and catalyses the rate limiting step – the hydroxylation of tyrosine to dopaquinone [53, 54] (Figure 1 – 4B). Melanin formation is not possible without tyrosinase [55] which is only synthesized in postnatal RPE [52], and not in the adult RPE [56].

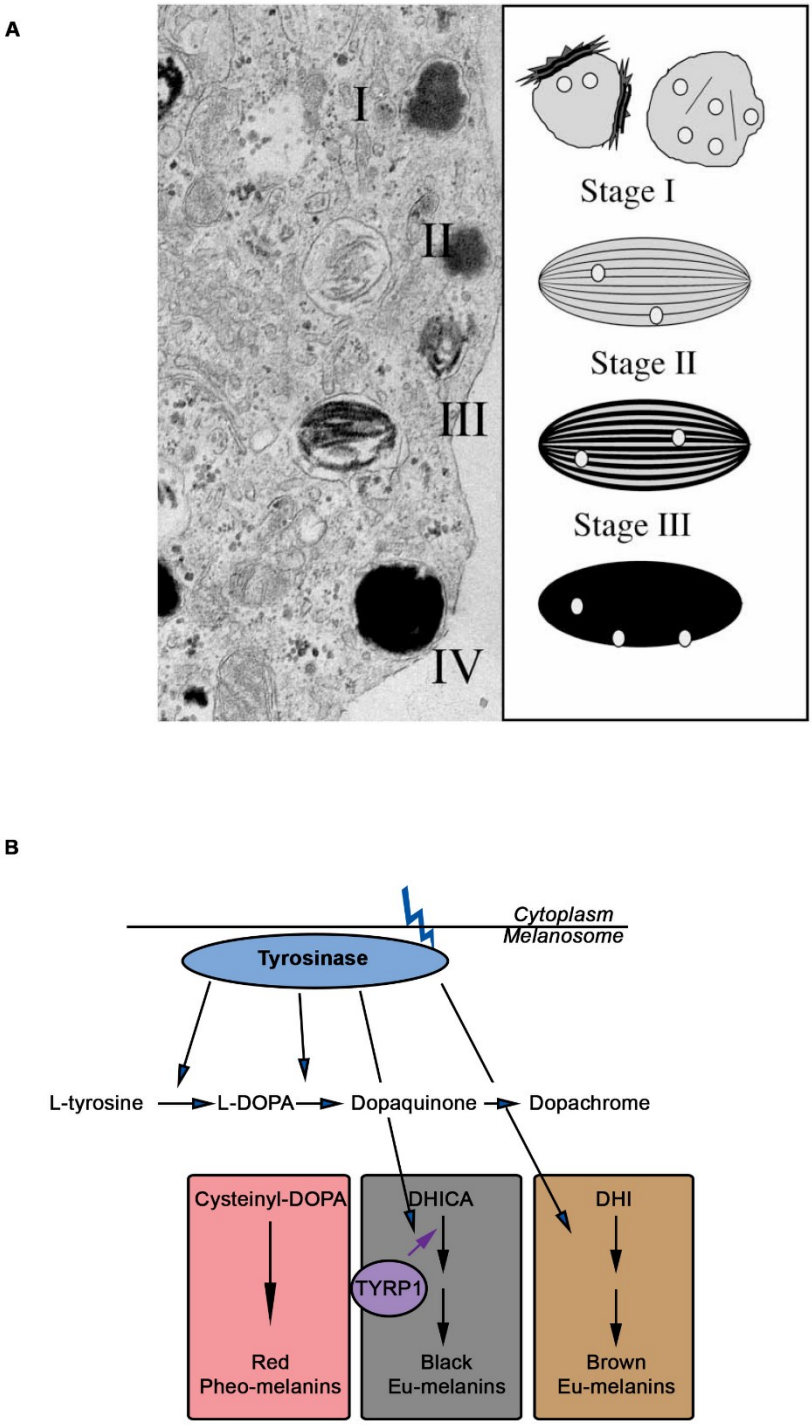

Figure 1-4 Melanosome stages and melanin formation
A: (Left) An electron micrograph of melanoma cells, illustrating the four stages of melanosome development. (Right) A schematic diagram of each of the four stages of melanosome development and their morphological features.
Image adapted from (2002, Raposo, G. and M.S. Marks, The dark side of lysosome-related organelles: specialization of the endocytic pathway for melanosome biogenesis. [57]
Available at: doi: 10.1034/j.1600-0854.2002.030401.
B: A schematic depicting melanin synthesis. Initially tyrosinase converts L-tyrosine to L-DOPA, before catalysing the hydroxylation of L-DOPA to Dopaquinone. It is also specifically involved in the formation of eumelanin.
L-DOPA, Dihydroxyphenalanine; TYRP1, Tyrosinase-Related Protein 1; DHICA, 5,6,-dihydroxyindole-2-carboxylic acid; DHI, 5,6-dihydroxyindole.

1.2.6 Protection against light and free radicals

The retina is constantly exposed to visible light placing it under continuous stress. The RPE is located at the outermost retinal layer and acts to absorb and filter natural light, through melanin, thereby protecting the cells of the neural retina, the photoreceptors. At the macula, where light is focused there are specific pigments known as carotenoids, which are critical for protecting the retina from blue light and oxidative damage [58]. Since the eyes are exposed to various light stimuli, they exist in a physiological state of photooxidation, accumulating high levels of oxygen free radicals that threaten oxidative damage. As a result, RPE cells contain antioxidants such as superoxide dismutase (SOD2) and catalase [59]

Dysfunction or abnormalities of the RPE monolayer are correlated with early stages of pathology linked to a range of ocular conditions, such as AMD. In AMD the RPE degenerates; this is most pronounced at the macula, the central portion of the retina that is responsible for high acuity and colour vision [17]. Consequently, most *in vitro* studies investigating AMD focus on the RPE.

A bottleneck in the study of RPE function has traditionally been the lack of source material, leading investigators to use spontaneously immortalised cell lines, which in some ways mimic the function of primary RPE cells. Recent advances in the field of stem cell differentiation have led to the establishment of protocols for both spontaneous and targeted differentiation toward RPE fate [60, 61]. Combined with gene-editing techniques such as CRISPR/Cas9, this provides an excellent platform for studying the effect of specific protein variants in RPE cells, defining a strategy that we will also use in this study.

1.3 Age Related Macular Degeneration

AMD is the leading cause of vision loss in the Western World [62], affecting more than 180 million people globally [63, 64]. AMD is a complex, progressive, chorioretinal degenerative disease that affects the central region of the retina known as the macula. AMD is typically classified into early and late forms, with late AMD known as either ‘wet’ or ‘dry’. The wet form, also known as choroidal neovascularisation (CNV), can be treated with intra-vitreal injections of anti-vascular endothelial growth factor (anti-VEGF) [65, 66]. For the dry form, also known in its advanced stages as geographic atrophy (GA), two treatments targeting the complement system were very recently approved by the Food and Drug Administration (FDA) to slow disease progression [67] [68]. Three major factors contribute to AMD: advanced age, environmental and genetic risk factors [69-72]

1.3.1 Pathophysiology of AMD

AMD is a multifactorial disorder, with dysregulation in the complement, lipid, angiogenic, inflammatory, and extracellular matrix pathways implicated in its pathogenesis. Many risk

factors have been identified for AMD; age is by far the strongest risk factor, with nearly all late AMD cases occurring in people older than 60 years [73]. AMD risk is also influenced by environmental factors, such as smoking and diet [73]. Smoking is the strongest (and only agreed upon) modifiable risk factor for AMD. It has been consistently associated with a two-times increased risk for developing late AMD (odds ratios 1·7–3·0) [73], and around a 10-year-younger age at onset [74].

The characteristic lesions of AMD are drusen, which can be identified in the macula. Both histological examination and electron microscopy demonstrate that drusen correspond to basal linear deposits containing membranous material located between the RPE and BrM [75]. Drusen consist of several components, more than 40% of their volume is composed from neutral lipids with esterified and unesterified cholesterol [76]. Over 129 different proteins [77] have been identified in drusen, including TIMP3, vitronectin, β-amyloid, apolipoproteins, and proteins involved in complement regulation [78]. Drusen and atrophic changes are the hallmark of dry AMD, where GA is the late manifestation of disease. GA is characterised by loss of RPE cells, overlying photoreceptors and the underlying choriocapillaris. Atrophy of the RPE was thought to be the initiating event in GA [79], however, recent work suggests that degeneration of the choriocapillaris is observed in GA even in areas of intact RPE [80].

1.3.2 Genetics in AMD

Genes are the functional unit of heredity. The genomes of individual humans are 99.6% identical. The remaining 0.4%, or the genetic variation, partially determines the difference in phenotype between people. Single nucleotide polymorphisms (SNP) are the most common form of human genetic variation [81]. A SNP is a change of a single nucleotide at a specific position in the human genome. SNPs found in a coding region of the genome can be categorised into two types: synonymous, those which do not lead to a change in protein sequence and non-synonymous, those affecting the protein sequence.

The term trait in genetics refers to a phenotype that varies between individuals but shows a certain level of stability across time. Mendelian (or monogenic) traits are inherited in concordance with Mendelian principles, i.e., a dominant or recessive mode of inheritance. Complex (or quantitative) traits result from the actions of (or interaction between) multiple genetic variants and environmental factors. Height, refractive error, diabetes and many common diseases, including AMD, are examples of complex traits.

Genetic studies have provided valuable insights into the mechanisms underlying AMD. An increased susceptibility to AMD has been linked to polymorphisms in genes involved in the complement immune response. The genes implicated include *Complement factor H* (*CFH*),

Complement 3 (C3), *Complement factor I* (*CFI*), and *Complement Factor B* (*CFB*), suggesting that a disrupted and/or dysregulated immune response may contribute to pathology. Interestingly, the presence of at least one *CFH* risk allele is estimated to account for a population attributable risk fraction for early and late AMD of 10% and 53%, respectively [82].

To further understand the genetic influences in AMD a Genome-Wide Association Study (GWAS) was undertaken by the International AMD Genomics Consortium in 2016 [71]. Including 16,144 patients with advanced AMD, 6657 with intermediate AMD and 20,765 controls. Over 12 million variants were examined, of which 52 reached genome-wide significance. Polymorphisms in the afore-mentioned complement genes were included, along with several other novel and known mutations such as the Age-Related Maculopathy Susceptibility-2 (ARMS2) gene [83], although the function of this protein in disease pathophysiology remains undetermined.

Over the past two decades the role of the complement system, ARMS2 and lipoprotein homeostasis have been investigated in AMD, amongst other plausible disease-causing candidates. Genetic variants in these diverse biological systems are highly associated with an increased risk of AMD, with polymorphisms in *CFH* and *ARMS2* considered to be responsible for nearly 80% of the genetic risk [84] [85]. The aforementioned GWAS, however, identified 34 loci that account for 46% of the genetic variance in AMD, amongst them many novel variants [71]. The role of such novel variants identified to be associated with AMD have not, as of yet been investigated. Indeed, of the 16 de novo variants described, only three have to date been further investigated, PILRB/PILRA [86], MMP9 [87] and ABCA1 [88] [89].

The aim of this thesis was to investigate and further understand the role of previously un-investigated loci in AMD using an *in vitro* cellular model.

1.3.3 Selecting a target SNP for investigation

The majority of SNPs highly associated with AMD are within introns, therefore, they are non-coding DNA variants. Determining the pathogenicity of DNA variants that would not be expected to alter protein structure directly can be challenging. Variants can often have downstream effects that are not inherently obvious from examining the DNA code alone. The pathogenic mechanism can therefore only be revealed after RNA analysis of the target tissue. This scenario was exactly depicted in the discovery of male germ cell-associated kinase (*MAK)*, a recently described retinitis pigmentosa gene, where an insertion at exon 9 disrupts splicing [90]. The authors investigated the expression of *MAK* by generating induced pluripotent stem cell (iPSC)-derived retinal tissue from donors with the described mutation.

As in many common diseases [91-94] the majority of AMD loci have strongly associated variants in non-coding regions of the genome, suggesting that they may act through gene regulation. Regulatory variants that affect human disease can have strong effects, but it can be challenging to identify causal distal regulatory variants and link them with their target genes.

The abundance and nucleotide sequence (due to splicing variants) of RNA for any particular gene varies greatly amongst different tissues. Therefore, for the majority of Mendelian retinal diseases, easily accessible tissue such as blood and skin are not suitable for RNA analysis. Interestingly, whilst most diseases display a phenotype only in one tissue, a large proportion of disease genes are in fact expressed at the RNA level in numerous unaffected tissues. This suggests that the cellular context in which a gene is expressed can help to predict the impact of variants. This is epitomised by *retinoblastoma (RB)* mutations which can cause retinoblastoma, a malignancy of the retina, due to inactivation of the retinoblastoma gene. However, *RB* inactivation is also seen in several human malignancies including osteosarcoma and small cell lung cancer, with the cellular context of gene expression critical to the type of malignancy [95].

Transcriptomic analysis of the retina in living patients is not possible. Stem cell culture and differentiation protocols developed over the past decades have made *in vitro* derivation of retinal cells possible [61, 96-98]. Stem cell derived retinal cells have been shown to accurately recapitulate a patient's retina to such a degree that they can be used as a model system for transcriptome analysis [99].

Synthetic introduction of variants into wildtype cells is a powerful means of providing convincing evidence of a variant's pathogenicity. Especially for non-coding variants whose function is not immediately evident, the ability to demonstrate that an artificially introduced variant causes sufficient cellular dysfunction to cause disease can be extremely helpful in supporting their pathogenicity.

1.3.3.1 Expression quantitative trait loci

GWAS studies are incredibly useful to identify potential disease-causing variants, however, a significant disparity exists between the identification of susceptibility variants and comprehending the specific roles those respective loci play in disease development. The association between DNA polymorphisms, typically SNPs, and variable transcript levels, coupled with the growing recognition of the impact of regulatory variation in shaping phenotypic variations, highlighted gene expression as a crucial mechanism underlying complex traits, such as AMD.

Over the last decade there has been a considerable effort in the research community for the analysis of genome function, especially regarding genome variation. One of the most noticeable advances are the extensive studies on expression quantitative trait loci (eQTLs), namely, the discovery of genetic variants that explain variation in gene expression levels. eQTL studies hold potential not only for analysing functional sequence variation but also for comprehending fundamental gene regulation processes and interpretating GWAS studies.

eQTLs are generated by statistically associating genetic variants with gene expression levels using genomic and transcriptomic data from large sets of biological samples, followed by rigorous quality control and multiple testing corrections to identify significant associations. [100]. The primary objective of eQTL studies is to reveal the direct mechanisms governing gene expression regulation, and their findings are likely to propose potential candidate genes implicated in disease pathology. Progress in machine learning techniques could enable a broader examination of gene expression regulation at a global level. This alternative methodology goes beyond the study of individual genetic variants and instead combines GWAS and gene expression datasets to identify associations between genes and traits in transcriptome-wide association studies (TWAS) [101].

The generation of eQTL data for the human eye in conjunction with GWAS has allowed further identification of possible causal genes for AMD [102]. Ratnapriya *et al*., identified potential causal genes in 6 AMD GWAS loci in human retinal samples [103]. However, their analysis did not include RPE/choroid transcriptomic data, nor did it examine the differences between macula and peripheral tissues, both of which are highly relevant to AMD pathology. The RPE is highly regarded as a key tissue in AMD pathophysiology, with clinical and histological signs often seen first in the RPE and BrM [104-107], making it an extremely important tissue to isolate for transcriptomic analysis.

A more recent study by Orozco et al., generated both eQTL and transcriptomic data in the human RPE and choroid from 129 donor eyes [102]. Authors identified 15 putative causal genes for AMD on the basis of co-localisation of genetic association signals for AMD risk and eye eQTL. These included novel genes highly expressed in the RPE, such as tetraspanin 10 (TSPAN10) and transient receptor potential cation channel subfamily M member 1 (TRPM1), as well as previously identified genes such as transmembrane protein 199 (TMEM199) and biogenesis of lysosome-related organelles complex 1 subunit 1 (BLOC1S1). Furthermore, they performed both bulk RNA-seq and nuclear-seq, which is a single-cell technique in the human retina and RPE. The use of a single-cell approach rather than bulk analysis in heterogenous tissue is crucial since this approach avoids Simpson's paradox [108]. Simpson's paradox is a phenomenon by which a trend will appear in several

different groups of data but will disappear or reverse when groups are combined. This means that bulk analysis in heterogenous tissue may mask effects as if a gene is found in a rare cell type, the contributions of transcripts from more abundant cell types may mask effects. The same principle applies to perturbations that might plausibly affect either expression or cell type number. For example, if a patient has a mutation that results in loss of a certain cell type, genes expressed selectively by that cell will appear down regulated in bulk analysis. Whereas single-cell sequencing would reveal complete loss of a cell population. The use of single-cell sequencing and cell type specific eQTL in the Orozco *et al*., study therefore reduces the detection of false positive SNP disease associations increasing our confidence in their results [102].

The identification of putative causal genes for AMD, highly expressed in the RPE helped form our candidate gene approach. TSPAN10 was identified as a plausible candidate and taken forwards, interestingly the aforementioned study by Orozco *et al*., saw reduced expression of TSPAN10 in individuals carrying the risk AMD SNP rs6565597. It was therefore hypothesised, that genetic variation driving the decreased expression of TSPAN10 is also responsible for the increase in AMD risk. The reasons for TSPAN10 selection will be outlined in the following section.

1.4 Tetraspanin 10 (TSPAN10)

Tetraspanins are a large group of integral membrane proteins with four transmembrane α-helices. Tetraspanins are typically located at the plasma membrane and are involved in cell adhesion, migration, fusion processes, cellular activation & signalling. The distribution of tetraspanins is cell specific, with their location dependent on the cell type and its specific functions. Tetraspanins are highly conserved in evolution, with expression seen in all multi-cellular organisms [109].

TSPAN10 belongs to the tetraspanin family, which also includes RDS/peripherin and ROM1, both of which are known loci of inherited eye disease [110, 111]. Specifically, TSPAN10 belongs to the C8 tetraspanins, also known as TspanC8. This subgroup of tetraspanins all contain eight cysteines in their extracellular domain and includes TSPAN5, TSPAN10, TSPAN14, TSPAN15, TSPAN17 and TSPAN33. All members of the TspanC8 subgroup regulate the exit of the transmembrane matrix metalloprotease ADAM10 from the endoplasmic reticulum (ER), and the majority its' maturation [112] [113] (Figure 1 – 5). Over-expression of any of the six TspanC8s *in vitro* in cell lines promotes ADAM10 exit from the ER [112-114]. The interaction of TspanC8s with ADAM10 has been shown through co-immunoprecipitation experiments, however, comparatively to the other family members, TSPAN10 interacts with ADAM10 relatively poorly [112, 113]. Furthermore, the TspanC8s

have differing downstream effects, TSPAN10 & TSPAN17 for example, do not affect ADAM10 surface expression in HeLa cells, in contrast to the other TspanC8 family members [113]. This was demonstrated using transient transfection of GFP-tagged TspanC8s in HeLa cells. Whilst the majority of tetraspanins are located at the cell surface, TSPAN10 appears to be restricted to intracellular vesicles, such as the ER and late endosomes [113] (Figure 1 – 5). Unfortunately, further understanding of TSPAN10's role in the ER or endosome is unknown.

TSPAN10 has been shown to bind ADAM10 via its cysteine-rich domain and regulates ADAM10 dependent Notch signalling [115]. This has been demonstrated during osteoclastogenesis [115]. Short hairpin RNAs (shRNA) targeting murine *TSPAN10* were introduced into osteoclasts using a lentiviral vector and mRNA expression of Notch target genes *Hes1* & *Hey1* was reduced in TSPAN10 k.o. osteoclasts, suggesting attenuation of the transcriptional activities of Notch. Furthermore, there were reduced cell surface levels of ADAM10 and attenuation of Notch receptor processing and activation in TSPAN10 k.o osteoclasts [115]. This influence on ADAM10 cell surface levels is not consistent across cell types. These differing results are most likely related to the expression levels of *TSPAN10*, which differ significantly based on cell type [116, 117].

TSPAN10 is a relatively poorly characterised member of the TspanC8 group. Data from the human protein atlas reports weak expression of *TSPAN10* at the mRNA level in many cell types, Figure 1 – 6A [116]. Interestingly, this dataset uses genotype tissue expression (GTeX) retinal data from Ratnapriya *et al*., [103], which did not include the RPE nor choroid in their analysis. FANTOM5 (functional annotation of the mammalian genome) analysis provides comprehensive expression profiles and functional annotation of mammalian cell-type specific transcriptomes using Cap Analysis of Gene Expression (CAGE) [118]. FANTOM5 reports *TSPAN10* expression to be highest in the retina, at 367.1 scaled tags per million [116, 117], Figure 1 – 6B.

TSPAN10 is also known as Oculospanin given that it was originally discovered in the eye in 2002 [119]. It was initially detected via immunofluorescence and western blotting in the RPE, iris, ciliary body and retinal ganglion cells [119]. Single-cell RNA sequencing data from the retina and choroid has further isolated *TSPAN10* to the RPE and melanocytes within the choroid [120], depicted in Figure 1 – 6C. TSPAN10 has been detected in non-ocular tissues, such as the skin, where it appears to have preferential expression in pigmented cell types [116]. Interestingly, TSPAN10 has been shown to reduce the migration of melanoma cells [121]. Recently, *TSPAN10* expression was found to reduce as oesophageal squamous cell carcinoma worsens [122].

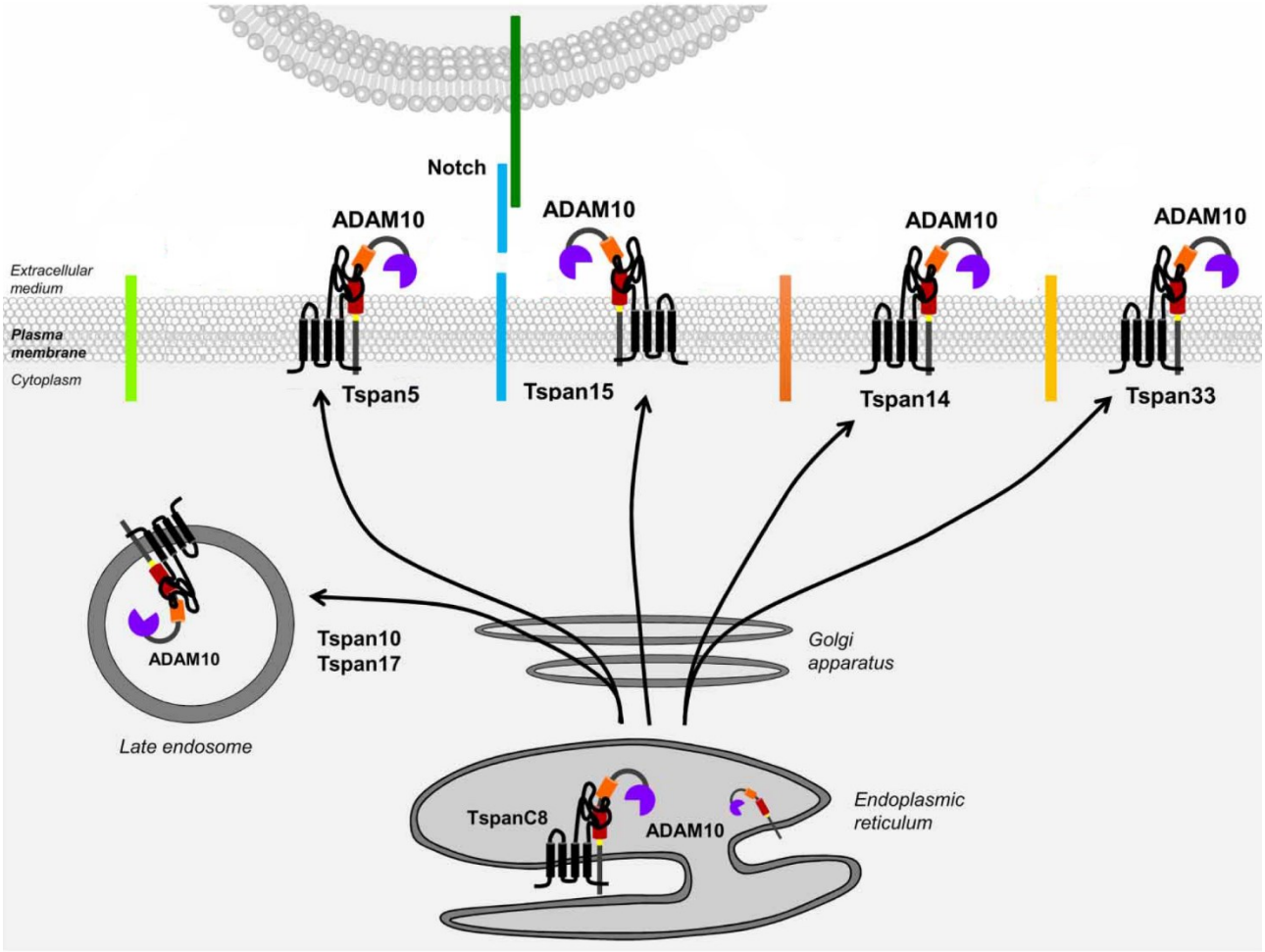

Figure 1-5 TspanC8s differentially regulate ADAM10 subcellular localisation and membrane compartmentalisation.
The interaction of TspanC8 with ADAM10 allows its exit from the endoplasmic reticulum and its accumulation in either late endosomes (Tspan10 and Tspan17) or at the plasma membrane (Tspan5, Tspan14, Tspan15 and Tspan33).
Image adapted from [123]

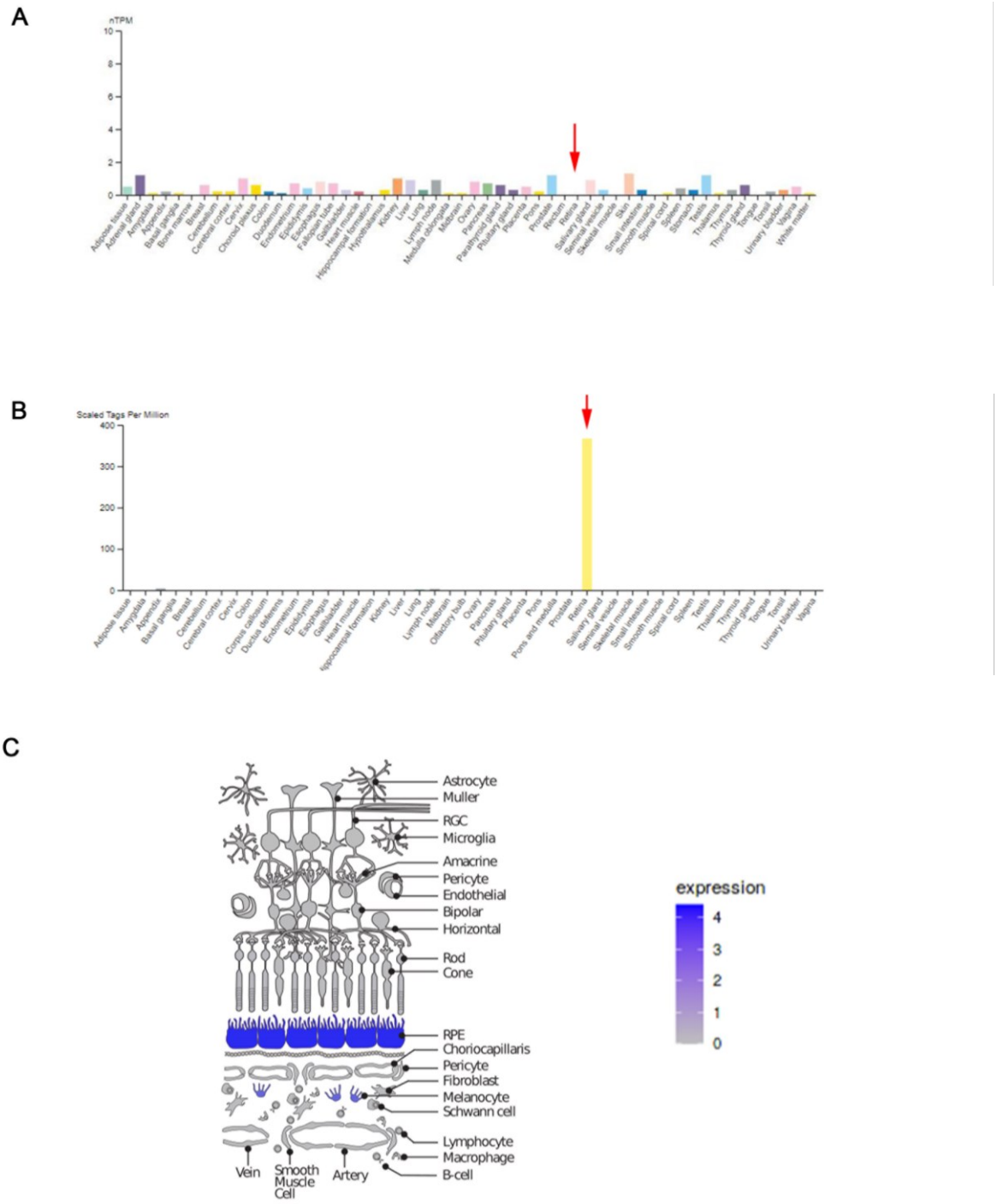

Figure 1-6 Expression of Tetraspanin 10 (TSPAN10)
A: Expression profile of *TSPAN10* using genotype tissue expression (GTeX) [103] and Human protein atlas (HPA) dataset.
Data compiled from single-cell RNA sequencing data from the Human Protein Atlas (www.proteinatlas.org (accessed on 27 June 2022)). Bar chart depicts significant expression of *TSPAN10*. RNA-seq data includes retina only, not RPE. No retinal expression depicted (red arrow). nTPM: normalised protein coding tags per million.
B: Expression profile of *TSPAN10* using Cap Analysis Gene Expression (CAGE) via FANTOM5.
Data compiled from single-cell RNA sequencing data from the Human Protein Atlas (www.proteinatlas.org (accessed on 27 June 2022)). Bar chart depicts significant expression of TSPAN10 in the retina. RNA-seq data includes RPE. High retinal expression seen (red arrow)
C: Heatmap cartoon of *TSPAN10* expression in the retina. Significant expression in the RPE & melanocytes.
Data compiled from single-cell RNA sequencing data from *https://singlecell-eye.com/ [120]*

Within the eye, polymorphisms at *TSPAN10* are associated with myopia [124], astigmatism [124] and strabismus [125]. *TSPAN10* SNPs are also significantly associated with the thickness of retinal layers, with reduced thickness at the foveola and a reduction in the thickness of the retinal nerve fibre layer and ganglion cell layer at the macula reported [126]. Furthermore, some variants at *TSPAN10*, such as rs7503894, have been significantly associated with visual acuity [126], highlighting the importance TSPAN10 may have on the visual pathway. TSPAN10 is thought to play a role in pigmentation, given its association with lighter hair colour [127, 128] and role in eye colour [129, 130]. The possible role such natural variations in pigmentation pathways, such as TSPAN10 may have on retinal development and therefore retinal layer thickness are yet to be elucidated.

The *TSPAN10* SNP associated with an increased risk of AMD is rs6565597, OR 1.13 [71]. This is actually located at the intergenic *NPLOC4-TSPAN10* locus, however, a combination of eQTL and GWAS data suggests the impact of this variant is at *TSPAN10* rather than *NPLOC4* [102]. Furthermore, eQTL data from donor eyes has also identified reduced copy numbers of TSPAN10 in those heterozygous/homozygous for rs6565597 [102]. Recently the rs6565597 variant has again been associated with late AMD, this time in an older age group, specifically those over 90 years, OR 1.46 [131]. This study used the same patient group as the International AMD consortium, however, they were divided by age into four sub-groups, with those over 90 years totalling 969 patients, of which 283 were controls and 686 had late AMD [131].

The function of TSPAN10 in both the eye and specifically the RPE is unknown. We do know that TSPAN10 binds to ADAM10 regulating ADAM10 dependent NOTCH signalling. *In vivo*, ADAM10 regulates NOTCH1 during brain [132], skin [133], intestinal [134], thymocyte [135], and vascular development [136]. The early embryonic lethality of $Adam10^{-/-}$ mice prior to the optic cup formation has precluded any evaluation of the role of ADAM10 in the retina using k.o mice [137]. ADAM10 is indispensable for early retinal development as a key regulator of NOTCH1 signalling. Conversely, mice lacking expression of NOTCH1 and/or NOTCH2 in the RPE do not show significant RPE developmental defects [138] [139]. These mice, however, do show partially penetrant microphthalmia [139], likely due to loss of NOTCH in the ciliary epithelium, resulting in malformation of the ciliary body [140]. Given that mice with reduced NOTCH expression don't show significant RPE developmental defects, it is therefore likely that TSPAN10 k.o embryonic stem cells will develop into RPE. Unfortunately to date a k.o mouse model of TSPAN10 has not been analysed.

TSPAN10 mRNA expression is significantly up regulated in response to Ultraviolet B (UVB) light in fish, suggesting its involvement in the response to UVB [141]. Inhibition of NOTCH2

in the RPE cell line ARPE-19 has been shown to reduce cell apoptosis & reactive oxygen species (ROS) production in response to UVB light versus controls [142], suggesting that NOTCH2 is involved in the UVB light response in RPE cells. Inhibition of NOTCH1 & NOTCH2 has also been shown to reduce RPE cell growth and cell migration [143]. Taken together this could suggest that TSPAN10 influences ADAM10 dependent NOTCH2 signalling in response to UVB light in the RPE.

An extensive literature search for TSPAN10 highlighted a two-fold up-regulation of *TSPAN10* in diabetic mice when compared to controls via next generation RNA-seq transcriptome analysis [144]. Furthermore, fibrovascular retinal membranes from diabetics have been shown to display a 50 - fold reduction in TSPAN10 relative to normal donor retinas [145].

A Search Tool for the Retrieval of Interacting Genes/Proteins (STRING) analysis of TSPAN10 was conducted [146]. STRING uses a curated database of protein interactions such as co-expression and protein homology. STRING extracts protein database associations from Biocarta, BioCyc, GO, KEGG or Reactome. STRING analysis of TSPAN10 confirmed a correlation with ADAM10 and suggested an association with other integrins such as CD9 and CD81, depicted in Figure 1 – 7. STRING analysis also proposed that TSPAN10 has a homology to the mouse protein peripherin-2 (PRPH2). PRPH2 co-immunoprecipitates with the retinal degeneration protein-3 like (RD3L) protein in mice and hence an association with RD3L and TSPAN10 is depicted. RD3L plays a critical role in the regulation of enzymes involved in the nucleotide cycle in photoreceptors [147], and is important for the survival of rods and cones [148]. However, Uniprot analysis [149] of the mouse PRPH2 protein structure in comparison to that of TSPAN10 was conducted and did not reveal even 50% sequence homology. Consequently, the validity of this interaction is questionable.

As evidenced the current literature surrounding TSPAN10 is sparse. Since the completion of the UK Biobank, polymorphisms in TSPAN10 have been implicated in many ocular phenotypes [125, 150, 151]. A greater understanding of TSPAN10 and its interactions may therefore aid several branches of ocular research.

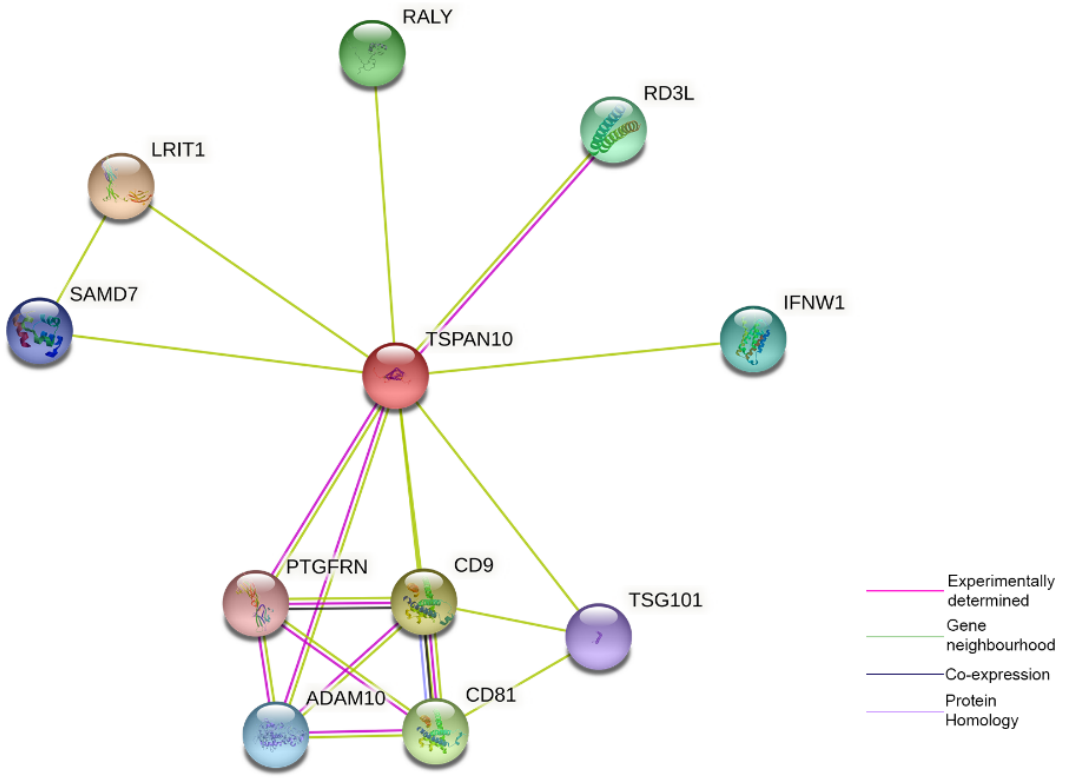

Figure 1-7 Search Tool for the Retrieval of Interacting Genes/Proteins (STRING) analysis of Tetraspanin 10 (TSPAN10)
String analysis of TSPAN10. Coloured lines represent differing methods of validating interactions. All interactions for TSPAN10 are determined from the 'gene neighbourhood' or are experimentally determined.
Data compiled from STRING https://string-db.org/ [146]

1.5 Developing an *in vitro* cellular model

1.5.1 Culturing RPE

A RPE cell culture must be polarized, demonstrating a differentiated and well-demarcated apical-basal phenotype. Furthermore, it should closely approximate RPE gene and protein expression, with the ability to perform RPE specific functions, such as the ingestion and degradation of POS.

To mimic features of BrM, RPE are typically cultured on transwell inserts with differing pore sizes [152, 153] (Figure 1 – 8). This allows the apical expression of Na^+/K^+ ATPase, a key feature of RPE polarity. The presence of a porous underlying substrate helps recapitulate the native RPE environment by allowing the directional secretion of growth factors [154, 155] and extracellular matrix components [156]. Currently, RPE cells are typically cultured on 0.4 µm pore-size inserts as this is felt to produce a phenotype closest to native RPE [157].

Stem-cell derived RPE are also routinely modelled in transwells, with many considering this to be the current gold-standard in RPE modelling.

RPE polarity and differentiation is highly influenced by both plating density and the substrate on which cells are grown. Cells should be organised into an epithelium with cobblestone-like packing, and a barrier function that arises from the precise localisation of junctional complexes at tight junctions.

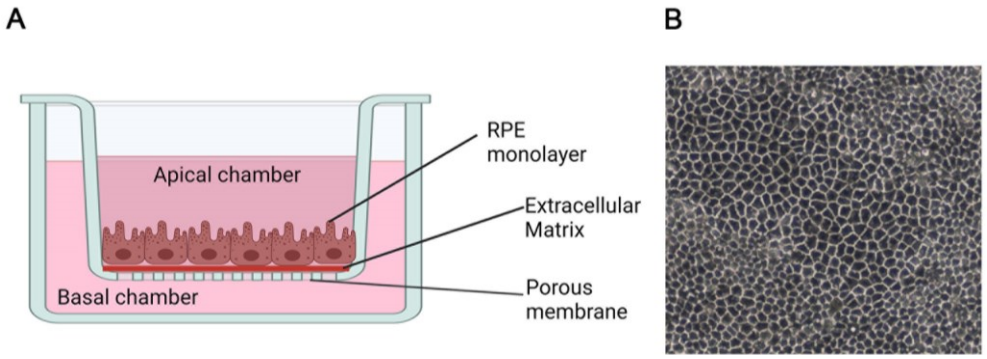

Figure 1-8 Retinal Pigment Epithelial (RPE) cells in culture
A: Schematic of a transwell plate showing RPE cells on a porous membrane within an insert. Image adapted from [158]. Image created using Biorendor.
B: Phase Contrast Image of RPE cells in culture.

1.5.2 RPE Cell lines

There are several RPE cell lines available, including ARPE-19, RPE-J and hTERT RPE-1. Cell lines are incredibly useful since they can proliferate indefinitely and are more robust and easier to work with than primary cells. Unfortunately, given that cell lines are genetically modified, and often extensively passaged, they do have their weaknesses [159], which will be briefly discussed below.

The RPE-J cell line was generated by simian virus 40 (SV40) transformation of primary rat RPE cells [160]. As a result of the SV40 transformation the cells are hypodiploid. Furthermore, they don't express polarity features such as the apical localisation of Na^+/K^+ ATPase [160].

The ARPE-19 cell line was established by selective trypsinisation of primary human RPE derived from the globe of a 19 year old male [152]. In culture ARPE-19 have been demonstrated to have several genetic abnormalities including an unbalanced translocation between chromosome 15q and 19q [161, 162]. Over the years, with numerous passages, the ability of ARPE-19 cells to demonstrate characteristics of differentiated RPE has diminished.

hTERT RPE-1 is a near diploid cell line with an abnormal karyotype [163] that do not develop polarity nor a 'cobblestone' organisation typical of RPE monolayers.

Given the scarce availability of primary RPE and the issues with RPE cell lines, researchers have moved on, with stem-cell derived RPE becoming the new gold standard approach to RPE disease modelling [164, 165].

1.5.3 Differentiation of RPE from human embryonic/pluripotent stem cells

1.5.3.1 Embryonic stem cells (ESC)

Embryonic stem cells (ESC) are found in the inner cell mass of the human blastocyst at an early stage of the developing embryo. In normal embryonic development they disappear after the 7th day post-fertilisation and begin to form the three embryonic tissue layers. ESCs extracted from the inner cell mass during the blastocyst stage can be cultured in the laboratory and under the right conditions will proliferate indefinitely. In 1998, human ESCs were successfully grown in the laboratory for the first time [166]. ESCs grown in this undifferentiated state retain the potential to differentiate into cells of all three embryonic tissue layers. ESC lines have since been established from single cells and have been demonstrated to remain multipotent, whilst maintaining a stable and normal complement of chromosomes [167].

It has been demonstrated that human embryonic stem cell (hESC) derived-RPE cells form highly polarized, hexagonal cells with a cobblestone-like morphology, tight epithelial structure and high pigmentation rate *in vitro*. Such cells have also been shown to recapitulate the RPE phenotype expressing RPE cell markers such as *melanocyte inducing transcription factor* (*MITF)[168], retinal pigment epithelium-specific 65 kDa protein (RPE65) [168], bestrophin – 1 (BEST1) [168], orthodenticle Homeobox 2 (OTX2) [168], premelanosome protein (PMEL) [168], pigment epithelium-derived factor (PEDF) [169],* and *tyrosinase (TYR)* [168] at the gene level, and MITF [169], retinaldehyde-binding protein (CRALBP) [169], RPE65 [169], and zonula occludens-1 (ZO-1) [169] at the protein level. Gene expression in hESC derived RPE has been examined from the start of differentiation to 60 days in culture using single cell RNA sequencing [170]. As expected initially pluripotency genes (*POU5F1, LIN28A, SOX2*) are highly expressed, but are soon downregulated in favour of progenitor genes from days 7-14 (*RAX, PAX6, VSX2*). Eventually at approximately day 30 early RPE maturation genes (*MITF, TYRP1, PMEL, TMEFF2*), intermediate (*TYR, RLBP1*), and finally late (*RPE65, BEST1, RGR*) RPE maturation genes are expressed at approximately day 45 onwards. This expected pattern of gene expression increases our confidence in the use of hESC-derived RPE. Furthermore, the integrity and barrier characteristics of hESC-RPE has been shown to be in keeping with native RPE in

addition to their transport of various drugs and phagocytosis of POS [165, 171-174]. hESC derived RPE show very similar phenotypic and functional properties to native RPE. Such similarities allow hESC-RPE to serve as a relevant *in vitro* model to study the mechanisms of RPE-associated diseases, including retinal degenerations such as AMD.

1.5.3.2 Induced pluripotent stem cells (iPSC)

In 2006, the researchers Takahashi and Yamanaka revolutionised stem cell research. They showed that forced expression of four transcription factors (Oct4, Sox2, Klf4, and c-Myc) was sufficient to convert fibroblasts into ESC-like cells, which they named induced pluripotent stem cells (iPSC) [175]. iPSCs have gained increasing popularity because they can be patient tailored. Within the field of retinal research iPSCs have effectively allowed access to previously unobtainable retinal cells from live patients, enabling *in vitro* modelling.

Several groups have attempted to establish cellular models of AMD using iPSCs from donors with certain AMD risk polymorphisms [176-178]. Common SNPs at chromosomes 1 & 10 (*CFH & ARMS2/HTRA1*) have been modelled, however, the majority of studies have found difficulty proving a significant difference between control and patient-derived cells. Stem cell culture and differentiation is a lengthy and expensive process, therefore small numbers of cell lines are produced meaning statistical differences between cases and controls are difficult to obtain. The following is a brief summary of current stem cell derived RPE models of AMD.

Saini *et al.*, derived hiPSC-RPE from AMD patients who had homozygous/heterozygous genotypes for lead ARMS2/HTRA1 polymorphisms, as well as age-matched unaffected individuals with protective alleles at both loci [176]. No differences in baseline RPE characteristics, such as the expression pattern of RPE signature genes and transepithelial resistance, were found between control and AMD hiPSC-RPE. However, AMD hiPSC-RPE did show elevated expression of complement pathway genes and drusen components, such as *APOE*. This study highlights the most likely heterogeneous nature of AMD as a disease. Minimal differences were seen between control and patient derived RPE. Although long-term culture showed variations in gene expression of drusen components and complement genes, changes in gene expression do not necessarily mean that there are changes in protein expression, therefore further work is needed to understand the implications of ARMS2/HTRA1.

Chang *et al.*, generated hiPSCs from the T cells of patients with intermediate and advanced dry AMD. The hiPSCs were then differentiated into RPE for disease modelling and pharmacological investigations [177]. While both the AMD hiPSC-RPE and control hiPSC-exhibited similar expression of RPE-specific markers such as retinaldehyde binding protein 1

(RLBP1) and RPE65, the AMD hiPSC-RPE displayed higher accumulation of endogenous ROS. The levels of ROS were further heightened in AMD hiPSC-RPE cultures when treated with hydrogen peroxide (H_2O_2). Notably, when several candidate drugs were screened, it was discovered that treatment of both controls and AMD hiPSC-RPE cultures with curcumin significantly reduced ROS levels. This is an important finding given that oxidative stress has been implicated in causing damage to RPE cells in AMD. This study did not select patients and controls based on their genotype/smoking history and other AMD risk factors; therefore, it is difficult to surmise exactly what caused the reduction in ROS.

Hallam *et al.*, conducted a study where they generated hiPSC-RPE from patients with AMD of varying disease severity. All patients included carried the Y402H mutation in the *CFH* gene [178]. Remarkably, in the absence of any external stressors the patient-derived hiPSC-RPE exhibited the presence of drusen-like deposits that contained known drusen proteins, namely APOE and C5b-9, aligning with AMD disease pathology. Additionally, the study revealed increased susceptibly to oxidative stress and impaired autophagy in the AMD hiPSC-RPE cells. The researchers also investigated the potential therapeutic effect of UV light treatment on low and high-risk patient derived hiPSC-RPE. UV light can induce the generation of ROS and subsequent DNA damage. Authors showed that UV light elicited a different response in the low- and high-risk AMD hiPSC-RPE as evaluated by assessing the functional and structural characteristics of the RPE cells after UV treatment.

Yang *et al.*, derived hiPSC-RPE cells from AMD patients and employed Bis-retinoid N-retinyl-N-retinylidene ethanolamine (A2E) and blue light exposure to simulate cellular aging in culture [179]. Interestingly, when compared to control hiPSC-RPE cells derived from individuals with a homozygous protective AMD haplotype at the *CFH* locus, AMD hiPSC-RPE derived from patients with known AMD risk alleles showed impaired SOD2 activity with increased levels of ROS. This finding suggests a potential connection between oxidative stress and the development of AMD in individuals carrying risk alleles at *CFH*.

Golestaneh *et al.*, generated hiPSC-RPE from two AMD patients with abnormal *ARMS2/HTRA1* alleles and one AMD patient with normal *ARMS2/HTRA1* and protective factor B alleles [180]. Consistent with the heightened vulnerability of AMD hiPSC-RPE to oxidative stress [177] Golestaneh *et al.*, reported similar findings of elevated ROS levels and an inability to increase SOD2 expression in response to oxidative stress conditions in AMD hiPSC-RPE. The study also revealed ultrastructural damage and dysfunctional mitochondria in AMD hiPSC-RPE cells.

Sharma et al., recently produced hiPSC-RPE from four patients who were homozygous for the *CFH* rs1061170 SNP, which causes a substitution of tyrosine to histidine, and three

patients who were heterozygous at this locus in comparison to three controls [164]. Increased sub-RPE deposition and RPE atrophy was seen when hiPSC-RPE homozygous for this SNP were treated with complement competent human serum in comparison to hiPSC-RPE with no copies of the targeted SNP.

The problem so far with many hiPSC-derived RPE cellular models of AMD, such as those described above, is their small size and lack of isogenic controls. Furthermore, there is a difference between risk alleles, such as the majority of aforementioned SNPs, and disease-causing mutations. This most likely contributes to the difficulties faced by authors to display significant differences between patients and control derived hiPSCs. In the majority of the aforementioned studies, authors used various drugs or stressors to produce significant differences between AMD and control cell responses. Secondly, genes such as those in the complement & lipoprotein systems, which are often modelled in AMD, mainly have their effects elsewhere in the body. Although, there is evidence of CFH production in the RPE, especially in mice, it has been shown that there is no difference in systemic Factor H levels in AMD patients [181]. Interestingly, recent data demonstrates that Factor H Regulator 4 (FHR-4) is most likely the key molecular player contributing to complement dysregulation in AMD [181]. Systemic FHR-4 levels were found to be increased in AMD, and the strongest AMD-associated CFH locus variant, which is protective for AMD was found to be significantly associated with reduced FHR-4 levels. FHR-4 production is restricted to the liver, with no evidence of expression in the eye therefore, gene-editing of FHR-4 in RPE *in vitro* would be unlikely to yield significant results. Evaluating the effects of risk alleles in a cellular RPE model of AMD may not be appropriate for many variants and in some cases animal models may be more appropriate.

When differentiating RPE from pluripotent stem cells the success of differentiation is often assessed by assaying expression of known cell-type specific genes, either at the mRNA (RT-qPCR) or protein (immunohistochemistry) level. Whilst targeted assays to verify the identity of cells are suitable for protocol development and modelling studies, they don't reveal global gene expression, its similarity or lack thereof to human retinal tissue. There are some studies that have directly investigated global gene expression in an unbiased manner with RNA sequencing [182]. This approach will be recapitulated in this thesis.

1.5.4 Differentiation Method for RPE

There are several differentiation protocols now available to produce RPE in vitro. Originally RPE were generated by simply removing fibroblast growth factor (FGF) from the culture medium [98]. Addition of FGF to retinal cells during the neuroectodermal stage was shown to suppress RPE differentiation but enhance neuroretinal differentiation [183, 184].

Consequently, removal or inhibition of FGF encouraged cells to differentiate down an RPE lineage [185]. During spontaneous differentiation embryoid bodies are formed, which due to their three-dimensional structure induces the formation of three primary germ layers present in the developing embryo. Unfortunately, it has been estimated that using this method only 0.2% of ESCs in an embryoid body will form neural progenitor cells. Consequently, advances in stem cell biology have led to the generation of 'directed differentiation' protocols, where multiple growth factors are added at various time points to encourage cells down an RPE lineage (Figure 1 – 9). Interestingly one group compared direct and spontaneous differentiation methods and found that 5 of 5 hiPSC cultures differentiated to RPE when using the direct method, but only 3 of 5 using the spontaneous method [186]. Subsequently, it seems that directed differentiation is more efficient and was therefore used in this project. The below figure (Figure 1 – 9) outlines various steps in the differentiation of retinal progenitors from pluripotent stem cells. There are several key signalling pathways and transcription factors involved in RPE differentiation. Initially cells are pushed down a neural differentiation pathway to early eye field progenitor cells (EFPC) through the inhibition (**i**) of canonical/β-catenin Wnt signalling, **i** transforming growth factor beta (TGFβ) and **i** bone morphogenic protein (BMP), and activation (**a**) of FGF signalling pathway. **i**BMP is artificially recreated using noggin and is dependent on FGF activity. **i**Wnt occurs through Dickkopf-related protein 1 (DKK-1) and **i**TGFβ with insulin-like growth factor 1 (IGF-1). To differentiate EFPCs to RPE conversely requires **a**canonical/β-catenin Wnt, **a**TGFβ and **i**FGF. Canonical/β-catenin Wnt is manipulated by inhibiting glycogen synthase kinase 3 beta (GSK3β) using a chemical known as CHIR99021. β-catenin is crucial for RPE differentiation as it regulates two key RPE differentiation factors: OTX2 and MITF [187, 188]. **a**TGFβ occurs through the use of Activin A, a member of the TGFβ superfamily. **i**FGF occurs by addition of a chemical inhibitor known as SU5402. The differentiation of RPE from pluripotent stem cells is dependent on the activation and inhibition of multiple signalling pathways at the correct time points with the ultimate aim of recreating embryological development *in vivo*.

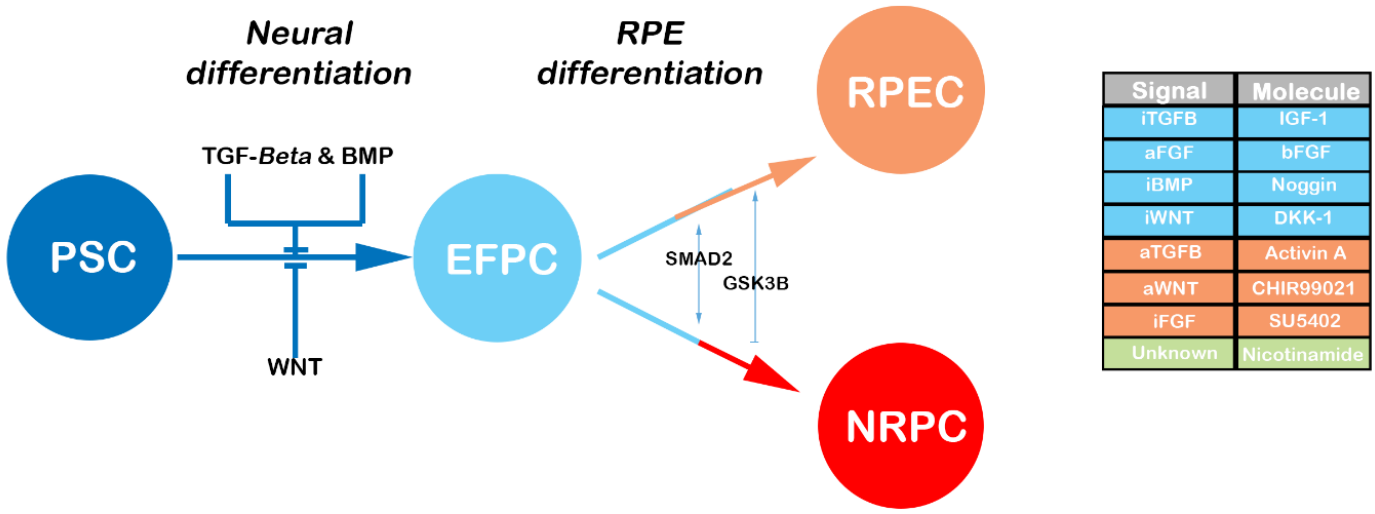

Figure 1-9 Schematic depicting pluripotent stem cell differentiation to retinal progenitor cells
Known signalling pathways and regulators in the differentiation of pluripotent stem cells (PSCs) to RPE cells (RPECs) and neural retinal progenitor cells (NRPCs) via formation of a common eyefield progenitor cell (EFPC). Table depicts small molecules used in the differentiation protocol as substitute endogenous signals and is colour coordinated with the stages of differentiation each molecule is used for. Blunt arrows indicate inhibition.
Differentiation of PSCs to EFPCs is induced by inhibition of TGFβ, BMP and WNT via use of IGF-1, Noggin and DKK-1 respectively; and activation of FGF through addition of FGF. Nicotinamide is also used in the differentiation process, however how it acts is still not fully known.
EFPC to RPE differentiation is induced through inhibition of FGF by adding SU5402 and activation of TGFβ with Activin A and WNT activation with CHIR99021 (an inhibitor of GSK3B).
Abbreviations: i, inhibition; a, activation; TGFβ, transforming growth factor beta; FGF, fibroblast growth factor; BMP, bone morphogenic protein; IGF-1, insulin – like growth factor 1; GSK3β, glycogen synthase kinase 3 beta.
Image adapted from Limnios et *al [97]*.

1.6 CRISPR-Cas-9 Gene Editing

Clustered regularly interspaced short palindromic repeats with Cas9 endonuclease (CRISPR/Cas9) is a ribonucleoprotein complex (RNP) that has revolutionised gene editing. CRISPR/Cas9 is a component of the bacterial immune system that allows bacteria to remember and destroy phages. It consists of a restriction endonuclease complexed with two RNA molecules, crRNA (the customized guide RNA) and tracrRNA (the scaffold RNA). All bacterial crRNAs are complementary to genetic elements of bacteriophages from prior infections. In a re-occurring infection with the same bacteriophage the crRNA guides the RNP complex to complementarily bind and chop the bacteriophage's DNA [189] [190]. The RNA-programable capacity of CRISPR-Cas9 to introduce site specific DNA cuts and its potential for genome editing was established in 2012 [191]. Since then, it has become an extremely useful tool with wide applications in genome engineering in various species and model systems [192].

Since its arrival in the field of gene editing there have been many advances aiding simplicity of CRISPR/Cas9 use. One such example is the linking of two native RNA molecules found in

CRISPR/Cas9 with a synthetic loop to produce a chimera single-guide RNA (sgRNA), instead of using two-part gRNA complexes (consisting of a crRNA and tracrRNA).

The sgRNA has two main features: the RNA scaffold, which forms a secondary structure required for Cas9 binding, and a 20 nucleotide protospacer, complimentary to the target DNA sequence to be edited. Any unique 20 bp region of the genome can be targeted, provided that it is immediately upstream of a protospacer adjacent motif (PAM). For Cas9 originating from S*treptococcus pyogenes,* the PAM sequence is 5`-NGG. The PAM is a limiting factor when selecting sgRNAs since the 20 bp targeting locus must be upstream of 5`-NGG. Once the CRISPR/Cas9 complex is bound to DNA it introduces a double strand DNA (dsDNA) break at 3-4 bp upstream from the 5`-NGG [191, 193, 194]. Cells possess two double strand break repair mechanisms: non-homologous end joining (NHEJ), or homology directed repair (HDR).

In NHEJ non-specific small insertions or deletions (indels) are introduced when re-ligating the two DNA strands. These “indels” could disrupt the open reading frame (ORF) by introducing a premature stop codon and hence k.o a specific gene by targeting its transcripts for nonsense-mediated decay (NMD). If the “indels” introduce extra nucleotides without disrupting the ORF this could lead to faulty protein folding. HDR, on the other hand, occurs during cell division and requires the cells to be in the correct cell cycle phase which makes HDR more infrequent <10% [194, 195]. In the HDR process the double stranded break is repaired via homologous recombination where cells use a donor DNA template homologous to the break point to preserve sequence integrity. Use of a repair template with a specific sequence allows genome editing to be precise. By artificially supplying a donor DNA template an alternative allele could be introduced, for instance, the *CFTR* locus in patient derived intestinal stem cells has been successfully replaced with the correct allele using this technique [196]. Since HDR is less efficient double stranded DNA breaks are mainly repaired via NHEJ. In this case a high number of cell clones must be screened to identify the desired genomic alteration. It is then essential to sequence the targeted locus to validate and quantify the percentage of indels and the number of cell clones carrying indels. These numbers determine the editing efficiency of individual sgRNAs. Figure 1 – 10 displays an overview of the CRISPR/Cas9 gene editing mechanisms.

CRISPR/Cas9 mode of delivery depends on the target organism. A variety of delivery methods exist including *in vitro* transcription, mammalian expression vectors, lentiviral transduction, or delivery of Cas9/sgRNA ribonucleoprotein complexes [197].

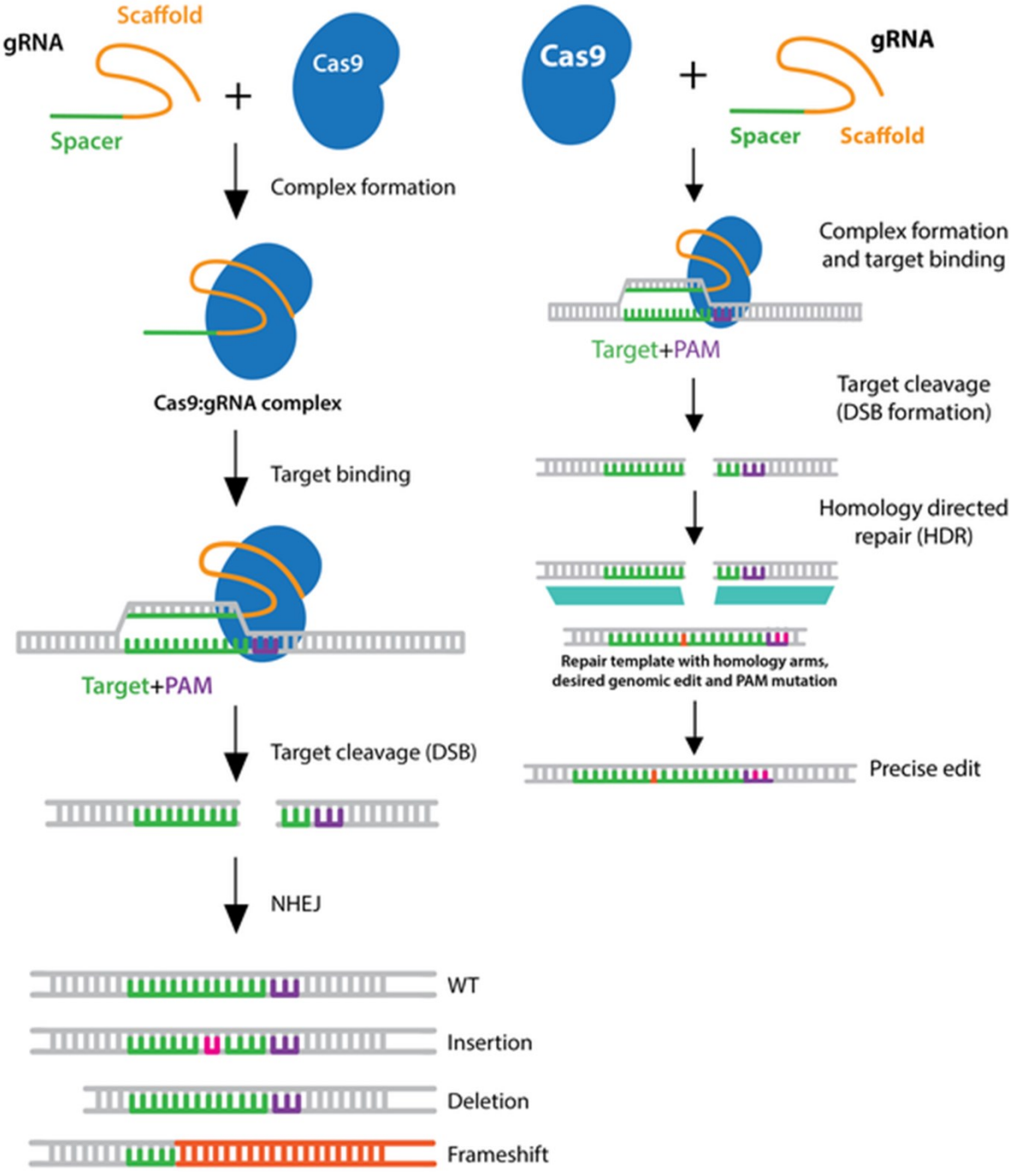

Figure 1-10 An overview of CRISPR/Cas9 gene editing mechanisms
The CRISPR/Cas9 system utilises a single guide RNA (sgRNA) along with the Cas9 endonuclease. The sgRNA comprises a scaffold and a programmable protospacer ("spacer") composed of 20 nucleotides. A protospacer that shares homology with the target genomic DNA locus to be edited is selected. The choice of a suitable sgRNA protospacer is limited by the requirement for it to be immediately upstream of a "protospacer adjacent motif" (PAM). Within the cell, the sgRNA and Cas9 form a complex, that enables the sgRNA to direct the Cas9 towards the desired genomic site. Here, the Cas9 induces a double-strand break (DSB). The cell can repair the DSB through either non-homologous end joining (NHEJ) or homology directed repair (HDR). NHEJ is prone to errors and can lead to random insertions or deletions (indels) at the target site, potentially causing a frameshift resulting in gene knockout. On the other hand, HDR necessitates a repair template with homology to the genomic sequence flanking the DSB. By supplying cells with a repair template containing a specific sequence, such as a point mutation, precise gene editing can be achieved.
Figure from Addgene, copyright 2022.

1.6.1 Comparison to Other Gene Loss-of-Function Tools

To date, there has only been one TSPAN10 loss-of-function cell model, generated using RNA interference (RNAi) in osteoclasts [115]. Gene editing technologies such as CRISPR/Cas9 can generate total gene k.o, providing superiority over the knockdown produced by RNAi.

Earlier genome-engineering technologies, such as zinc finger nucleases (ZFNs) and transcription activator-like effector nucleases (TALENs), share similarities to CRISPR/Cas9 in their ability to generate targeted double-strand breaks to mutate or k.o genes. However, CRISPR/Cas9 has significant advantages over ZFNs and TALENs [198, 199]. It is cheaper, faster and more user-friendly, due to its reliance on RNA/DNA complementarity and the relative ease of reprogramming the sgRNA. In contrast, the process of discovering and creating functional ZFNs or TALENs is time-consuming and often expensive and, once designed for a specific gene, they are not easily adaptable to different targets.

1.6.2 sgRNA Off-target Activity

The CRISPR/Cas9 system is transforming the study and manipulation of the genome. Nevertheless, it is not exempt from limitations. One significant concern has been the off-target activity of CRISPR/Cas9, which occur when the sgRNA binds to locations other than the intended target site [200]. This off-target activity has the potential to introduce unintended mutations, making it a subject of extensive investigation and scrutiny.

1.6.3 Factors influencing sgRNA off-target activity

The probability of sgRNA off-target activity is not thought to occur simply because of excessive sgRNA activity but is felt to be influenced by several factors [200]. Typically, the occurrence of off-target mutagenesis decreases as the number of sgRNA-DNA mismatches increases. Early investigations on sgRNA off-target cleavage in human cell lines indicated that Cas9 cleavage is terminated when four or more mismatches are present [201, 202]. However, in mice and rats, up to eight mismatches have been observed between the sgRNA and an off-target site [200]. The location of mismatches is also important. Those in the PAM-proximal region of the sgRNA are typically not tolerated since this area is crucial for initiating sgRNA-DNA binding. However, mismatches in the PAM-distal portion are more likely to allow Cas9 cleavage. Typically, Cas9 cleavage is hindered by mismatches within the six to fourteen base pairs immediately upstream of a PAM [201, 202], although this varies with both the target gene and cell type. Furthermore, the identity of a mismatch at each position impacts the ability of a sgRNA to induce Cas9 cleavage [203].

Core properties of the sgRNA also affect its function. A GC content between 45 % and 80 % is reported to maximise sgRNA effectiveness [204, 205], whilst self-complementarity between the sgRNA protospacer and scaffold interfere with its function [206].

1.6.4 Predicting sgRNA off-target activity

Given the potential implications of off-target activity, this can be controlled for by precise sgRNA design and the screening of gene edited clones for unintended mutagenesis. As CRISPR/Cas9 gene editing has advanced, so to have the tools to both design sgRNAs and predict off-target activity. Several in silico sgRNA design tools are available for use including Benchling [207], CHOPCHOP [208, 209] and CRISPOR [210]. Such platforms identify sequences adjacent to PAMs as potential sgRNAs and often also provide off-target loci prediction.

Off-target prediction platforms use an alignment algorithm to identify genomic regions of complementarity to the sgRNA and rank them based on the likelihood of cleavage. Potential sgRNAs are given a score based on the likelihood of cleavage, which is derived from several variables such as the number of mismatches, the mismatch identity and position. Such scores aid sgRNA selection with regard to off-target activity.

There are two scoring systems regularly in use, the ‘MIT’ score [201] and the cutting frequency determination (CFD) score [203]. The MIT score outputs an overall specificity score between zero and 100, which is an aggregate of the scores of each off-target for a given sgRNA. A higher score indicates a better outcome, with 100 indicating the absence of predicted off-target activity for the sgRNA. The CFD is calculated for each predicted off-target locus and is the probability (zero to one) that a sgRNA will generate a cut at an off-target site, based on mismatch positions and identities. Furthermore, the CFD also includes single nucleotide DNA or RNA bulges and non-canonical PAMs of the sequence NNG.

Due to variations in the alignment algorithm employed by different tools to identify potential off-target loci, the CFD specificity score can differ among them.

There is also a scoring system to predict sgRNA on-target activity and therefore efficiency at the target site, known as “Rule Set 2” [203]. Consequently, some sgRNA design tools combine multiple scores to help inform choice of sgRNA. For example, Benchling [207] provides a sgRNA “On-Target” efficiency score between zero and 100 in addition to an “Off-Target” score. Benchling considers sgRNAs with an On-Target score greater than 60 to be good guides.

1.6.5 Detection of sgRNA off-target activity

Once the CRISPR/Cas9 system has been used unintended genome editing events can be identified through sequencing. Computationally predicted off-target sites can be inspected for mutagenesis through selective Sanger sequencing.

1.7 Nonsense Mediated Decay (NMD)

Gene expression is dependent on two broad mechanisms, the transcription and then translation of messenger RNA (mRNA). During translation the genetic code in an mRNA transcript is read and used to assemble a chain of amino acids to form a protein. To help eliminate the synthesis of faulty proteins and other incorrectly processed cellular RNAs, cells have evolved surveillance mechanisms to target mRNAs with mutations.

The NMD pathway is one of the most studied RNA surveillance pathways. NMD targets mRNAs with premature termination codons (PTC) for degradation. This ability of the NMD pathway to distinguish normal stop codons from PTCs is crucial for its functionality. In human beings NMD is linked with pre-mRNA splicing; mRNAs with a premature stop codon 50 – 55 nucleotides upstream of the final exon – exon junction are efficiently degraded [211]. This process is signalled by the presence of an exon junction complex (EJC), which is placed 20 – 24 nucleotides upstream of an exon – exon junction during pre-mRNA splicing [212]. EJCs remain associated to the mRNA until they are displaced by the translation machinery. In a faulty transcript, the ribosome encounters a PTC before the final EJC, initiating recruitment of the NMD machinery. The presence of EJCs after the PTC is thought to be the signal recognised by the ribosome to distinguish a PTC from a normal termination codon. It follows that PTCs within 50 to 55 nucleotides of the final exon-exon junction avoid NMD [213].

Interestingly it appears that exon junctional complexes are not equally assembled at all exon – exon junctions, approximately half are present at non-canonical positions [214], the effect of this on the efficiency of NMD is not fully understood. However, ‘faulty’ mRNA transcripts, for example, those with genomic mutations or incorrect RNA processing are efficiently degraded via NMD therefore preventing the production of truncated proteins.

1.8 Project Aims and Hypotheses

Background

Single nucleotide polymorphisms in *TSPAN10* are associated with retinal phenotypes, including AMD. The precise roles of TSPAN10 within the cell remain unclear and must be elucidated to understand if and how it contributes to AMD pathophysiology.

Hypotheses

1. Clinically normal individuals with AMD risk SNPs, including rs6565597 at *NPLOC4/TSPAN10*, have changes in their outer retinal thickness.
2. Expression of TSPAN10 influences known pathogenic mechanisms in AMD

Aims

The project's main aim was to study the cellular roles of TSPAN10 in the RPE with CRISPR/Cas9 gene editing.

Chapter 3: The association between macular thickness and AMD genetic risk variants

Hypothesis

1: Clinically normal individuals with AMD risk SNPs have changes in their outer retinal thickness

Aim

1: To compare the thickness of outer retinal layers in UK Biobank participants with and without AMD risk SNPs in varying combinations.

Chapter 4: Generation of clonal hESC derived RPE using CRISPR/Cas9

Aim

2. To generate biallelic indel mutations in *TSPAN10* resulting in gene k.o and subsequent absence of protein expression in the RPE.

Objectives

2a: To use CRISPR/Cas9 gene editing to generate clonal hESCs with biallelic indel mutations in *TSPAN10*;

2b: To differentiate wild-type and gene-edited hESCs into RPE;

2c: To characterise the effect of biallelic indel mutations on *TSPAN10* transcript expression and TSPAN10 protein levels.

Chapter 5: Phenotypic analysis of TSPAN10 mutant clones

Aim

3: To identify a phenotype associated with k.o of TSPAN10

Objectives

3a: To characterise hESC-RPE for well-known RPE markers;

3b: To assess the ability of hESC-RPE to perform key RPE functions.

Chapter 6: Transcriptomic analysis of TSPAN10 k.o clones

Aim

4. To analyse the transcriptomic profile of TSPAN10 k.o RPE in comparison to WT

Two aims were formed based on the results that are expressed in **Chapters 5 & 6**. Both of which were investigated in **Chapter 7**:

Chapter 7: Investigating the phenotypes identified in TSPAN10 k.o clones in comparison to wild type

Aims

5a: To identify if TSPAN10 k.o RPE are more susceptible to oxidative stress than WT;

5b: To examine differences in melanin synthesis between TSPAN10 k.o and WT cells.

Chapter 8: Further understanding TSPAN10 in the RPE and its interactions

Aims

6a: To examine the effect of TSPAN10 k.o on the matrix metalloprotease ADAM10;

6b: To localise TSPAN10 in the human foetal retina.

2 Materials and Methods

2.1 CRISPR/Cas9 gene editing

2.1.1 Single guide RNA (sgRNA) design

The DNA sequence of the human *TSPAN10* gene was uploaded to the online platform Benchling from Ensembl (ENSG00000182612). Benchling was used with default settings to identify sgRNA sequences for selection within 10 bp of the first ATG start codon in *TSPAN10* Exon 2. The on target and off target scores were calculated using Cas-OFF finder algorithm (http://www.rgenome.net/cas-offinder/) [215]. GC content of sgRNA can affect cleavage efficiency [216, 217], therefore, sgRNAs were designed with a GC content between 40-60%. Two sgRNAs were designed with optimal GC content, a low off target score, and without predicted off-target sites in genes. sgRNA sequences are presented in Table 2-1.

To allow cloning of selected sgRNAs in the expression vector px459-EF1α, BbsI restriction sites were added to the forward and reverse oligonucleotides, ‘CACCG’ to the forward strand and ‘AAAC’ to the reverse (Table 2-1).

Table 2-1 Single guide RNAs (sgRNAs)
Genomic coordinates refer to the human GCh38 genome assembly. Protospacer adjacent motif (PAM) sequences are given in blue, underlined type. The targeted ATG region is highlighted in yellow. BbsI restriction sites are highlighted in green. All sequences are stated in the 5'-3' direction. Benchling [207] On and Off Target scores depicted.

gRNA name	Genomic coordinates of target site (and strand)	gRNA sequence + PAM	Oligonucleotide 1	Oligonucleotide 2	On Target Score	Off Target Score
JL	chr17:81642401-81642423 (+)	CCAGCGTCAAGGATGGAGGAGGG	CACCGCCAGCGTCAAGGATGGAGGA	AAACTCCTCCATCCTTGACGCTGGC	62	34.3
Assembly 2	chr17:81642397-81642419 (+)	TGTTCCAGCGTCAAGGATGGAGG	CACCGTGTTCCAGCGTCAAGGATGG	aaacCCATCCTTGACGCTGGAACAC	63.3	40.2

2.1.2 Cloning of sgRNA in CRISPR vector

Oligonucleotides were ordered from IDT Technologies (see Table 2-1). Each oligonucleotide was diluted in ultra-pure H_2O (ThermoFisher) to a final concentration of 100 µM.

The two guide oligonucleotide strands (forward and reverse) were then annealed and phosphorylated, and the reaction incubated in a thermocycler. Briefly, forward and reverse oligonucleotides were added to ultra-pure H_2O (ThermoFisher) with T4 Ligation buffer (New England Biosciences) and T4 PNK (New England Biosciences). A PCR reaction was then set up at 37°C for 30 minutes, 95°C for 5 minutes, reduced to 25°C by 0.1°C per second and held at 4°C for 30 minutes.

T4 Ligation buffer was used as it contains adenosine triphosphate (ATP) which is used by T4 PNK as a phosphate donor. The recipient cloning plasmid, in this case px459-EF1α, was digested with BbsI restriction enzyme (100ng/µl; Fisher) and ligated as described. 2µl 10x Fast digest (Fisher), 1µl ATP [10mM] (ThermoFisher), 1µl BbsI fast digest (100ng/µl; Fisher), 0.5µl T7 DNA ligase (New England Biolabs), 2µl of phosphorylated and annealed oligonucleotides (1:250 dilution), 0.2µl DTT [100mM] (Promega) and ultra-pure H_2O (ThermoFisher) were added. The reaction was incubated in a thermocycler at 37°C for 5 minutes, 23°C for 5 minutes, cycled 6 times and held at 4°C.

To ensure purity of linear plasmid within the reaction, plasmid safe exonuclease treatment was performed. The ligation reaction was added to 10X Plasmid safe buffer (Cambio), [10mM] ATP (ThermoFisher) and exonuclease (Cambio). The reaction was incubated in a heat block at 37°C for 30 minutes. A map of plasmid px459-EF1α-sgRNA is given in Appendix A, Figure 10 – 1.

2.1.3 Bacterial Transformation

The ligation mix was transformed into chemically competent bacterial cells DH5α (New England Biolabs). Ligation mixture containing plasmid DNA was added to DH5α and placed on ice for 30 mins. Cells were then subjected to a heat shock for 30 seconds at 42°C and placed on ice for 5 minutes. Super Optimal broth with Catabolite repression (SOC) outgrowth media (New England Biolabs) was added to the mixture and placed at 37°C whilst shaking. LB agar plates were made using LB broth agar (Sigma). The reaction was mixed and spread onto an agar plate using a Pasteur pipette (Fisher).

Once successful growth was observed six colonies were selected and further grown in sterile LB broth (Sigma) with ampicillin [1:1000] (Sigma) for 12 hours at 37°C whilst shaking.

2.1.4 Miniprep Purification

Plasmid DNA was extracted using the QIAgen miniprep kit (Qiagen) according to the manufacturer's instructions. The kit contained QIAprep 2.0 spin columns, LyseBlue reagent, RNase A solution, buffers P1, P2, N3, PB and PE. LyseBlue reagent was added to buffer P1 at a ratio of 1:1000. RNase A was added to buffer P1 to a final concentration of 100 µg/ml. A volume of 100 % ethanol (specified on the label of the buffer bottle) was added to buffer PE. All centrifugation steps were carried out at 17,900 g in a table-top microcentrifuge.

5 ml bacterial cultures were pelleted by centrifugation and the supernatant discarded. Pellets were resuspended in 250 µl buffer P1 and transferred to 1.5 ml microcentrifuge tubes. 250 µl buffer P2 was added to lyse cells and mixed thoroughly by inverting the tube multiple times. The reaction turned blue to indicate successful lysis. Care was taken not to allow the lysis reaction to proceed for longer than 5 min. The reaction was neutralised by addition of 350 µl buffer N3. Tubes were inverted several times to facilitate thorough mixing and then centrifuged for 10 min. 800 µl supernatant was applied to QIAprep 2.0 spin columns, centrifuged for 30 seconds and flow-through discarded. Columns were washed with 500 µl buffer PB, spun for 30 seconds and flow-through discarded. Columns were then washed with 750 µl buffer PE, spun for 30 seconds and flow-through discarded. Columns were centrifuged for a further 1 min and then transferred to a clean 1.5 ml microcentrifuge tube. DNA was eluted by incubating the columns with 50 - 100 µl ddH_2O for 1 min at room temperature and then centrifuging for 1 min. A 260/280 ratio of 1.8 and a 260/230 ratio of 2.0-2.2 were accepted as pure for DNA.

2.1.5 Sanger Sequencing

DNA was prepared at a concentration of 100 ng/µl diluted in sterile water. 10 µl per sequencing reaction was supplied to Source BioScience. Any sequencing primers were supplied at a concentration of 3.2 pmol/µl. Primers used for px459-EF1α-sgRNA sequencing depicted in Table 2-2.

Table 2-2 Sequencing Primers for px459-EF1α-sgRNA

Sequencing primer name	Primer sequence (5'-3')
px330_Forward	CATATGCTTACCGTAACTTG
px330_Reverse	AGTTGATAACGGACTAGCCT

2.1.6 Maxiprep Purification

Colonies with the correct recombinant plasmid from the miniprep purification were re-selected and expanded. DNA was extracted using the QIAgen Endofree maxiprep kit

(Qiagen) according to the manufacturer's instructions. The kit contained QIAfilter Cartridges, LyseBlue reagent, RNase A solution, buffers P1, P2, P3, ER, QBT, QC, QN and QBT. LyseBlue reagent was added to buffer P1 at a ratio of 1:1000. RNase A was added to buffer P1 to a final concentration of 100 µg/ml. A volume of 100 % ethanol – specified on the label of the buffer bottle – was added to endotoxin-free water supplied with the kit. All centrifugation steps were carried out at 15,000 x g in a table-top microcentrifuge.

Following transformation, a single bacterial colony with the correct recombinant plasmid was picked and cultured overnight at 37°C in a 15 ml centrifuge tube containing 3 ml of LB broth with ampicillin. 100 µl of the overnight cultured LB broth was used to inoculate 100 ml of LB broth overnight. The 100 ml of LB culture was then divided into two 50 ml centrifuge tubes and the bacteria pelleted by centrifugation at 5,000 g for 15 mins. 45 ml of LB supernatant was removed, the pellets were re-suspended in the remaining 5 ml and added together, re-centrifuged and the supernatant discarded. Pellets were resuspended in 10 ml buffer P1. 10 ml buffer P2 was added to lyse cells and mixed thoroughly by inverting the tube multiple times. The reaction turned blue to indicate successful lysis. Care was taken not to allow the lysis reaction to proceed for longer than 5 min. The reaction was neutralised by addition of 10 ml buffer P3. Tubes were inverted several times to facilitate thorough mixing. The lysate was applied to QIAfilter cartridges and incubated at room temperature for 10 mins. The lysate was filtered through the cartridge into a 50 ml falcon tube. 2.5 ml Buffer ER was added to the filtered lysate, mixed by inverting and incubated on ice for 30 mins. Filtered lysate was added to a QIAGEN-tip and washed twice with Buffer QC. DNA was eluted into a 30 ml endotoxin free tube using 15 ml Buffer QN. DNA was precipitated by adding 10.5 ml isopropanol to eluted DNA, mixed and centrifuged for 30 mins. Supernatant was discarded and the DNA pellet washed with 70 % ethanol and centrifuged for 10 mins. Supernatant was discarded and the pellet left to air dry. DNA was resuspended in Buffer TE. A 260/280 ratio of 1.8 and a 260/230 ratio of 1.8-2.2 were accepted as pure for DNA.

2.2 Electroporation of plasmid gDNA into embryonic stem cells

Electroporation parameters were set on the BTX ECM830 and used as described below (Figure 2 - 1) [218]. For each reaction 1 x 10^6 hESCs in 100 µl of Opti-MEM media (ThermoFisher) were mixed with approximately 10 µg of plasmid DNA (Cas9 plasmid (5 µg). Volumes used differed dependent on DNA concentration. A volume <10 µl was aimed for to improve efficiency. The mixture was added to a 400µL BTX electroporation cuvette with a width of 2 mm (Fisher) and the electroporation reaction set. Following electroporation, the cells were added to a 6 well plate pre-coated with 1 ml of LN521 (Biolamina) per well, and fed with Nutristem hESC XF media + [10µM] Y-27632 (Sigma). Cells were grown for 24 hrs

to allow recovery and time for CRISPR-Cas9 to be translated and re-located back to the nucleus for targeted editing to occur.

Set Parameters											
Poring Pulse						Transfer Pulse					
V	Length (ms)	Interval (ms)	No.	D.rate (%)	Polarity	V	Length (ms)	Interval (ms)	No.	D.rate (%)	Polarity
100	5	50	2	10	+	20	50	50	5	40	+/-

Figure 2-1 Schematic depicting parameters used on BTX ECM830
The poring pulse creates temporary pores in the cell membrane to allow entry of the DNA.
The transfer pulse facilitates the movement of the DNA further into the cell.
Abbreviations: V, Voltage; D rate, death rate.

2.3 Antibiotic clonal selection

After 24 hrs the media was changed on the electroporated cells and replaced with Nutristem hESC XF media + 0.2 µg/ml of puromycin (Fisher). Media was changed daily, and cells photographed to allow monitoring of morphology and death rate. After three days of positive selection with 0.2 µg/ml of puromycin (Fisher) only single cells remained [218], the media was changed without antimicrobials and the cells were allowed to recover and to form colonies.

2.4 Cell expansion

Individual colonies were observed one week post electroporation. 96 well plates were coated with 100 µl of LN521 (Biolamina) per well and incubated at 37 °C for 2 hours, after which it was removed and replaced with Nutristem hESC XF media + [10µM] Y-27632 (Sigma). Colonies were selected using a p200 pipette and transferred in duplicate to a 96 well plate. Duplication of colonies allows for genotyping.

2.5 DNA extraction

Once cells were confluent the media was removed and replaced with 100 µl QuickExtract™ (Lucigen, #QE09050) lysis buffer. Cells were incubated at room temperature for 10 mins and solution transferred to PCR tubes. The mixture was vortexed and incubated in a thermocycler at 65°C for 6 mins, 98°C for 2 mins and held at 10°C. Samples were stored at -20°C.

2.6 Purification of PCR products

PCR products were purified using the ExoSAP-IT Express PCR Product Cleanup kit (Thermofisher) according to the manufacturer's instructions.

2.7 Primer Design

All primers were designed using Primer3 and Benchling software. gDNA and cDNA template sequences from the Homo Sapiens GRCh38 genome assembly were imported into Benchling from the Ensembl genome browser using the 'import DNA sequences' feature. Primers were designed in Benchling using the 'primer wizard' feature, which is powered by Primer3plus [219-221]. Primers were additionally designed in Primer3, the target sequence was copied from Benchling and input into Primer3 online.

All primer sequences in addition to expected product sizes, and annealing temperatures used for each set of primer pairs are detailed in the methods of relevant applications.

2.8 Prediction of knock-out scores

Sanger sequence reads were input into ICE (Synthego) [222] and k.o scores derived. Traces were analysed for homozygosity/heterozygosity and the possibility of mixed populations.

2.9 Off-target mutations

To assess if CRISPR-Cas9 introduced any off-target mutations, nine potential genomic locations predicted with the Cas OFF finder algorithm (http://www.rgenome.net/cas-offinder/) [215] were investigated. These were the top hits with highest likelihood of nonspecific editing with the sgRNA CCAGCGTCAAGGATGGAGGA. A mismatch cut off of 3 was used. A 200-400 bp region spanning the sgRNA binding site was PCR amplified and then sequenced to check for possible indels.

2.10 Karyotyping

2.10.1 Isolation of genomic DNA (gDNA)

The CRISPR-edited hESCs A12 and A2 were cultured until confluence in T25 flasks coated with 5 µg/mL Laminin521 (Biolamina, #LN521) in phosphate-buffered saline (PBS) (+Mg/+Ca^{2+}, PBS Life Technologies, #14190-091). The cells were washed twice with PBS (-Mg/-Ca^{2+}, PBS Life Technologies #14190-094), and detached by incubating with a 0.5 mM solution of EDTA (Life Technologies, #15575-020) in $PBS^{-Mg/-Ca2+}$ for 5 mins at 37°C. After addition of 5 mL Nutristem XF, the cell suspension was centrifuged for 5 mins at 200 x g. gDNA was extracted using the Qiagen QiAamp DNA Micro Kit (Qiagen), using the protocol 'Isolation of Genomic DNA from Tissues', according to the manufacturers' instructions.

2.10.2 Karyotyping

gDNA from hESC clones was shipped to The Wessex Medical Institute where karyotyping was performed. The Wessex Medical Institute reported using the following methods. Array comparative genome hybridization (array-CGH) was performed using Oxford Gene

Technology's (OGT) CytoSure Constitutional v3 60K oligo array, according to the manufacturer's instructions, using Kreatech's pooled control DNA as a reference (Kreatech Diagnostics, Amsterdam, Holland). Slides were scanned using a G2539A Agilent microarray scanner (Agilent Technologies, Wokingham, UK) and analysed using OGT's CytoSure Interpret (v4.9.40) microarray software.

2.11 Tissue Culture

Cell culture work was carried out in a class II biological safety cabinet using aseptic technique in a defined stem cell culture laboratory.

2.11.1 Culture of hESCs

The MasterShef7 human embryonic stem cell line, generated by the Centre for Stem Cell Biology, University of Sheffield, was cultured using standard feeder cell-free conditions, on Laminin-521 (LN521) (Biolamina) coated flasks (maintenance) or 6-well plates (electroporation, differentiation). Flasks were coated with 5 µg/mL Laminin521 (Biolamina, #LN521) in phosphate-buffered saline (PBS) (+Mg/+Ca^{2+}, PBS Life Technologies, #14190-091) either at 37°C, 5% CO_2 for a minimum of 2 hours or at 4°C for minimum of 16 hours with a parafilm sealed lid. Laminin solution was aspirated and the flask covered with the pluripotent stem cell medium NutriStem XF (Biological Industries, #05-100-1A). Cells were seeded at 10,000 cells/cm^2 and left for 48 hours and then fed daily. The cells were passaged every 3 - 4 days at approximately 60 - 90% confluency. When passaged the cells were washed twice with PBS (-Mg/-Ca^{2+}, PBS Life Technologies #14190-094), and detached by incubating with a 0.5 mM solution of EDTA (Life Technologies, #15575-020) in $PBS^{-Mg/-Ca2+}$ for 5 mins at 37°C. After addition of 5 mL Nutristem XF, the cell suspension was centrifuged for 5 minutes at 200 x g and counted before seeding into a fresh flask.

The cells were regularly examined for abnormalities and photographed daily with the EVOS cell imaging system (Thermofisher).

2.11.2 Cell counting

If using trypan blue to mark dead cells, 10 µl cell suspension was mixed with 10 µl trypan blue in a microcentrifuge tube. 10 µl cell suspension (with or without trypan blue) was placed into the well of a haemocytometer. The mean number of cells in the four corner 1 x 1 mm squares was determined. Cell concentration (cells/ml) was calculated as this number multiplies by a dilution factor (if any) multiplied by 10^4, as shown in Equation 2. 1. If trypan blue was used, the dilution factor was 2.

2.11.3 Culture of CRISPR/Cas9 edited hESCs

CRISPR/Cas9 edited clones were selected and continued in culture with daily feeding with Nutristem hESC XF media. Cells were passaged using 0.5mM EDTA (ThermoFisher) approximately every 4 days and closely monitored for signs of differentiation. Cells were expanded up slowly from a LN521 coated 96 well plate (Fisher) to a LN521 coated T25 flask (Fisher) (see section 2.11.1 for details). Prior to cryopreservation cells were re-genotyped to ensure populations were pure and that the expected mutation was still present.

2.11.4 Cryopreservation of hESCs

Cells were washed twice with PBS $^{-Mg-Ca2+}$(ThermoFisher), 0.5mM EDTA added, and cells incubated at 37°C for 5 minutes. Cells were observed under a light microscope (EVOS) at x4 and x 10 magnification to determine detachment. EDTA was diluted with Nutristem hESC XF media and cell elute centrifuged at 200 x g for 5 mins. The supernatant was aspirated, and the cell pellet resuspended in Nutrifreeze media (Biological Industries). Aliquots were placed in cryovials (Corning) and transferred to a MrFrosty freezing container (Sigma), which was placed at -80°C for at least 16 hours prior to placement of cryovials in the liquid nitrogen cryobank.

2.12 Differentiation of hESCs into RPE

A directed differentiation approach was selected [60, 186]. hESCs were grown to 80% confluence. A 12 well plate was coated with hESC qualified Matrigel (Corning) for 1 hr at room temperature. hESCs were passaged as previously described using 0.5 mM EDTA, however, cells were resuspended in retinal differentiation media (RDM). RDM was made using 100 x N2 supplement (ThermoFisher), 50 x B27 supplement (ThermoFisher), 100 x non-essential amino acid (NEAA) (ThermoFisher) and Dulbecco's modified essential medium/nutrient mixture F12 (DMEM/F12) (ThermoFisher).

The following sequence details the timeline and various steps in the directed differentiation protocol:

- Cells were seeded onto Matrigel-coated 12 well plates (Day 0) in RDM and the following growth factors added: 10 mM nicotinamide (Stem Cell Technologies), 50 ng/ml noggin (Peprotech), 10 ng/ml DKK-1 (Peptrotech), and 10 ng/ml IGF-1 (Peprotech).
- The following day (Day 1), media was changed using RDM + the growth factor composition used for Day 0.
- Day 2, media was changed using RDM + 10 mM nicotinamide (Stem Cell Technologies), 5 ng/ml FGF-basic (Peprotech), 10 ng/ml noggin (Peprotech), 10 ng/ml DKK-1 (Peprotech) and 10 ng/ml IGF-1 (Peprotech).

- Day 4, media was changed using RDM + 100 ng/ml activin A (Peprotech), 10 ng/ml DKK-1 (Peprotech) and 10 ng/ml IGF-1 (Peprotech).
- Day 6, media changed using RDM + 100 ng/ml activin A (Peprotech) and 10 μM SU 5402 (Peprotech).
- Days 8,10 and 12: media changed using RDM + 100 ng/ml activin A (Peprotech), 10 μM SU 5402 (Peprotech) and 3 μM CHIR99021 (Peprotech).

At day 15 cells were further passaged (Passage 0). A 6 – well plate was coated with growth-factor reduced (GFR) Matrigel (Corning) for 1 hr at room temperature. GFR Matrigel is a variant of normal Matrigel that has decreased levels of growth factors such as basic FGF, epidermal growth factor, insulin-like growth factor 1, TGFβ, platelet-derived growth factor, and nerve growth factor [223]. Media was aspirated and cells washed twice with DPBS (ThermoFisher). TrypLE Express (ThermoFisher) was added and cells incubated at 37°C for 5 mins. Cells were visualised on an inverted microscope (EVOS XL Core) and once detachment confirmed a cell scraper (Grenier bio-one) was used to gently remove cells. Cells were resuspended in X-VIVO 10 media (Lonza) and centrifuged at 180 x g for 5 mins at room temperature. The cell pellet was resuspended in X-VIVO 10 + 10 μM Y-27632 (Sigma) and cells strained using a nylon mesh cell strainer with 40 μm pores (Fisher). The use of Rock inhibitor (Y-27632) here prevents excessive cell death and allows the cells to maintain stability in a single cell state, whilst they adapt to the new media and extra-cellular matrix. Cells were counted using a haemocytometer and seeded onto GFR Matrigel (Corning) coated plates at 1 x 10^5 cells/cm^2 in X-VIVO 10 (Lonza) +10 μM Y-27632 (Sigma). Media was changed using X-VIVO 10 +10 μM Y-27632 48 hours post-seeding and every 3 days subsequently. After day 7 only X-VIVO 10 was used and media changed every 3 - 4 days. Cells were matured for 28 - 35 days at 37°C, 5% CO_2 with media changes every 3 - 4 days.

Cells were further passaged at day 35 (Passage 1) and day 79 (Passage 2) onto GFR-Matrigel coated T75 flasks (Corning), media changes continued every 3 – 4 days. Cells were passaged as described above, however, Y-27632 was not used. A timeline depicting various passaging steps is shown in Figure 2 – 2. At day 84 cells had reached the end of the differentiation protocol [60] and were therefore considered to be fully differentiated into RPE and ready for cryopreservation and/or use in experiments.

2.12.1 Cryopreservation of hESC-RPE

Day 3 post passage 2, when cells were approximately 84 days old, cells were passaged and resuspended in CryoStor® CS10 (Stem Cell Technologies). 3 x 10^6 cells/ml were placed in cryopreservation vials (Corning) and transferred to a MrFrosty freezing container (Sigma),

which was placed at -80°C for at least 16 hours prior to placement of cryovials in the liquid nitrogen cryobank.

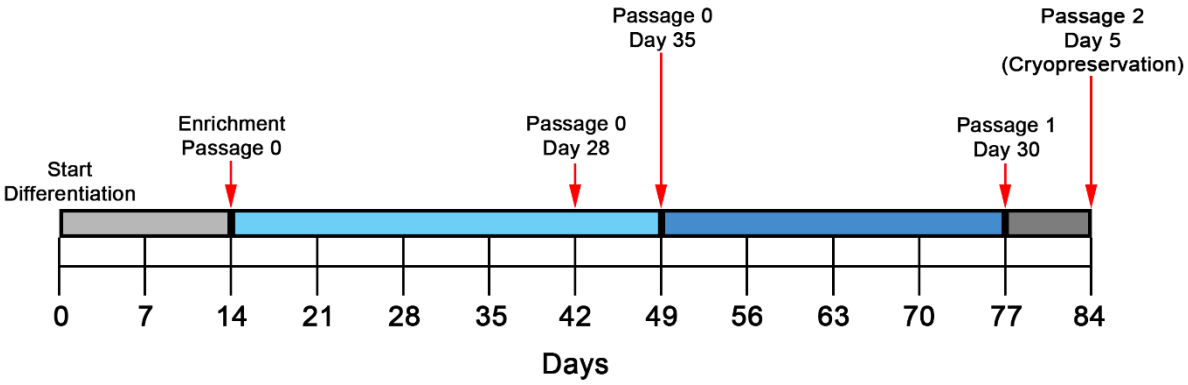

Figure 2-2 Timeline for directed differentiation of human-embryonic stem cells (hESCs) into retinal pigment epithelium (RPE).
Time in days. Various steps in the differentiation protocol highlighted with red arrows.
Schematic adapted from [60]

2.12.2 Culture of hESC-derived RPE on Transwells

Once fully differentiated hESC-RPE were plated onto GFR-matrigel coated 12 mm Transwell Permeable Supports (Corning®). Cells were maintained using X-VIVO 10, with 0.5 ml into the apical compartment and 1.5 ml into the basal. Cells were maintained in culture for at least 35 - 40 days after plating prior to use in experiments. This time point was selected as a minimum given that fully differentiated WT cells displayed good levels of pigmentation by 21 days in culture, and the trans-epithelial electrical resistance (TEER) was >200 Ω/cm^2 from around 35 days. Furthermore, several published reports recommend approximately 6 weeks of culture for stem-cell derived RPE prior to experimental use [164, 176, 224].

2.13 Immunocytochemistry

hESC-derived RPE cells were seeded onto GFR-Matrigel-coated cover slips (Fisher). hESCs were seeded onto laminin-coated cover slips (Fisher). On the day of fixation cells were washed with PBS and fixed in 4% paraformaldehyde (PFA) in PBS (pH 7.4) for 15 mins at room temperature. Cells were washed twice with cold PBS and then blocked with 5% bovine serum albumin (BSA) (Sigma), 1% donkey serum (Sigma) with 0.2% Triton X-100 (Sigma) to permeabilise the cell membrane. After blocking, cells were incubated overnight at 4 °C with primary antibody (Table 2 - 3). Cells were washed three times with cold PBS and incubated with the corresponding secondary antibody (Table 2 - 4) conjugated to AlexaFluor for 1 hr at room temperature. Cells were then incubated with 1 µg/mL of 4',6'-diamino-2-phenylindole (DAPI; Sigma Aldrich, UK) for 5 mins at room temperature (Table 2 – 5), washed three times with PBS, mounted with 80 µL Mowiol 4-88 Mounting Medium and coverslip, and imaged on a Zeiss Axioscope Inverted Compound microscope.

A secondary antibody control was performed for every secondary antibody used in this thesis, where secondary antibody was added alone. Images for controls are presented in Appendix A, Figure 10 – 2.

2.13.1 Immunocytochemistry of Transwells

Transwells were washed, fixed, and blocked as described above (section 2.13). Following which they were removed from their insert using a scalpel and cut into quarters. Each quarter was placed into a 48 well plate using forceps and stained with primary and then secondary antibody as described above. Following DAPI staining transwells were mounted between two coverslips using Mowiol 4-88 Mounting Medium.

2.13.2 Immunocytochemistry of foetal eyes

Human foetal eyes were obtained from the Joint Medical Research Council UK, Wellcome Trust Human Developmental Biology Resource (http://www.hdbr.org/). Human foetal eyes were fixed in 4% PFA in PBS for 30 mins at 4°C. For embedding, samples were washed three times in PBS and equilibrated in 30% sucrose in PBS for cryo-protection at room temperature (RT); once sunk, samples were then orientated and placed into foil moulds containing optimal cutting temperature (OCT) compound, before freezing in methylbutane-dry ice slurry. Tissue sections were cut to 18 µm thickness using a Leica cryostat and collected on SuperfrostTM plus glass slides (VWR). For immunohistochemistry, retinal sections were dried at RT for 15 mins then washed in PBS for 15 mins at 37°C to remove the OCT compound and incubated in blocking buffer (10% foetal bovine serum (FBS) in PBS (Gibco), 1% BSA in PBS) with 0.1% Triton X-100 for 1 hour at RT. Sections were then incubated with primary antibody for 1 hour at RT or overnight at 4°C.

2.13.3 Confocal Microscopy

Confocal image stacks were acquired using a Leica TCS-SP8 laser scanning confocal system attached to a Leica DMi8 automated, inverted microscope frame and using a Leica HC PL Apo 1.3NA x63 glycerol immersion objective under Leica LAS-X software control (Leica microsystems, UK). Images were acquired at 1024 x 1024 pixel count with a scan speed of 600 Hz, 4 line averaging to reduce random electronic noise on the photomultipliers (PMTs), sequential imaging to avoid spectral bleed through between fluorescent channels and system-optimised Z spacing to ensure complete data capture in the Z dimension. For all experiments, samples incubated with secondary antibody only (plus DAPI) were imaged as control samples and used to set the maximum permissible PMT voltage (sensitivity) for each channel whist seeing only trace-level signal. This controlled for both sample autofluorescence and non-specific binding of secondary antibodies. If antibody staining was strong, PMT voltage was decreased, but it was never raised beyond the level set from the control samples.

Table 2-3 Primary antibodies used and their dilutions for immunocytochemistry studies
Details of the primary antibodies used for fluorescence microscopy. Antibodies were diluted in 5% Normal Donkey Serum in 0.1% PBS-Tween 20 (PBST).

Primary Antibodies	Dilution	Catalogue Number	Company
ZO-1 Polyclonal antibody	1:1000	21773-1-AP	Proteintech
OTX2 Polyclonal antibody	1:250	13497-1-AP	Proteintech
TSPAN10 Polyclonal antibody	1:100	14430-1-AP	Proteintech
MITF Monoclonal antibody [D5]	1:250	ab3201	Abcam
Occludin Polyclonal antibody	1:100	71-1500	ThermoFisher
RPE-65 Monoclonal antibody	1:100	ab13826	Abcam
Na^+/K^+ ATPase Monoclonal antibody	1:100	ab7671	Abcam
Best-1 Monoclonal antibody	1:500	ab2182	Abcam
Lamp-1 Polyclonal antibody	1:1000	ab24170	Abcam
Rab-5 Polyclonal antibody	1:200	ab18211	Abcam
Adam10 Monoclonal antibody	1:100	66620-1-Ig	Proteintech
TSPAN10 N-terminal region Monoclonal antibody	1:100	ARP50022_P050	Aviva Systems Biology
SOX2 Polyclonal antibody	1:100	AF2018	Bio-Techne
hNANOG Polyclonal antibody	1:100	AF1997	Bio-Techne
Rhodopsin (RET-P1) Monoclonal antibody	1:1000	MAB5316	Sigma
Rab-7 Monoclonal antibody	1:50	ab50533	Abcam

Table 2-4 Secondary antibodies used and their dilutions for immunocytochemistry
Details of the secondary antibodies used for fluorescence microscopy. Antibodies were diluted in 5% Normal Donkey Serum in 0.1% PBST.

Secondary Antibodies	Dilution	Catalogue Number	Company
Donkey Anti Rabbit IgG Alexa Fluor® 555	1:500	ab150105	Abcam
Donkey Anti-mouse IgG Alexa Fluor® 488	1:500	ab150074	Abcam
Rabbit Anti-goat IgG Alexa Fluor® 488	1:500	A56574	Invitrogen
Goat Anti-mouse IgG Alexa Fluor® 594	1:1000	A-11005	Invitrogen

Table 2-5 Staining reagents used in immunofluorescence studies
Details of the staining reagents used during immunofluorescence experiments. DAPI was reconstituted to 1mg/ml in 1x PBS to form stock solutions. Abbreviations: DAPI: 4', 6'-diamino-2-phenylindole

Product Name	Catalogue Number	Company	Dilution
DAPI	D9542	Sigma Aldrich, UK	1:1500

2.14 RNA extraction

Total RNA was extracted from RPE cells using the RNeasy Micro Kit (Qiagen) with on-column DNase digestion. All cells used were cultured for at least 35 - 40 days prior to RNA extraction. An additional DNAse treatment was performed at the time of extraction using the RNase-Free DNase Set (Qiagen). The concentration of RNA was calibrated using a Nanodrop 1000.

2.15 cDNA synthesis

cDNA was synthesized using the RT-NanoScript2 cDNA Synthesis kit (Primer design) according to the manufacturer's instructions.

2.16 Polymerase Chain Reaction (PCR) & Reverse Transcriptase PCR (RT-PCR)

For each PCR reaction a mastermix was made up using the quantities of reagents defined in Table 2 – 6, including Bioline MyFi Mix (SLS Biosciences), ultra-pure H_2O (ThermoFisher), primer pairs at 10 µM and gDNA or cDNA.

PCR reactions consisted of an initial denaturation step of DNA at 95°C, followed by repeated cycles (35 - 40) consisting of 95°C for 15 seconds for further denaturation, annealing for 15 seconds at a temperature specified for the primer pair in use and extension at 72°C for a duration specified for the primer pair in use. A final elongation for 5 mins at 72°C was used.

A template-free negative control was performed in parallel, which contained 1.0 µl ddH2O instead of cDNA. RT-PCR product sizes were inspected after separation by agarose gel electrophoresis.

Lists of gene targets and primers used in RT-PCR reactions are displayed in Appendix A.

Table 2-6 Quantities of reagents used for PCR and RT-PCR reactions

Reagent	1 X Reaction
Ultra-pure H_2O	11.25 µl
2x MyFi Mix	12.5 µl
Primer Pairs	0.25 µl
cDNA or gDNA	1 µl

2.17 Agarose Gel Electrophoresis

Agarose Gel Electrophoresis was used to separate DNA fragments according to size upon application of an electric field. DNA bands can then be visualised on the agarose gel. The size of the DNA band is determined by comparison with bands of known size created by a 1kb plus DNA ladder (ThermoFisher). A 1 % agarose gel was made by dissolving agarose in 1x tris-acetate-EDTA (TAE) buffer (ThermoFisher) by heating in a microwave. 10 µL 1:20,000 SybrSafe stain (Fisher) was added to visualise the DNA in a later step. The agarose-TAE-SybrSafe solution was poured into a DNA gel mould and left to set with a well comb for 1 hr. The well comb was removed, and the gel tank filled with TAE. 10 µL 1kb plus DNA ladder was loaded onto the gel. 4 µL of DNA loading dye (Qiagen) was added to 25 µL of each sample, and each sample was loaded onto separate wells. Electrophoresis was carried out at 90 V for 40 mins. The gel was imaged using a LiCOR Odyssey (LiCor) as per the manufacturer's instructions.

2.17.1 Gel purification of PCR products

Gel bands were excised on a UV transilluminator and placed in 1.5 ml microcentrifuge tubes. Care was taken to minimise exposure of DNA to UV irradiation. Each gel slice was weighed. DNA was extracted using the Qiagen Gel Extraction kit (Qiagen). The kit contained Buffer QG, Buffer PE, Buffer EB, purification columns and collection tubes. 100 ml of 100 % ethanol was added to the bottle of Buffer PE before use. All centrifugation steps were performed at 13,200 x rpm. 400 µl Buffer QG was added for every 100 mg agarose gel. Gel slices were incubated at 50 °C for 30 min, until the gel was completely dissolved. 3 volumes of Buffer QG to 1 volume of supernatant was added and mixed. Samples were loaded into purification columns attached to collection tubes and spun for 1 min to bind DNA. Flow-through was discarded. Columns were washed by addition of 400 µl Buffer PE and centrifugation for 1 min. Flow-through was discarded. Columns were transferred to clean 1.5 ml microcentrifuge tubes, ensuring the bottoms of columns did not come into contact with flow-through. DNA was eluted by incubating columns with 30 µl Buffer EB for 1 min and then spinning for 1 min. DNA concentration and purity were assayed by NanoDrop 1000 (Thermo Fisher Scientific). A 260/280 ratio of 1.8 and a 260/230 ratio of 1.8-2.2 were accepted as pure for DNA.

2.18 Total RNA sequencing (RNAseq)

2.18.1 RNA extraction for RNAseq

Cells were seeded at $1x10^5$ cells/cm^2 in GFR Matrigel (Fisher) coated T75 flasks (Fisher) and allowed to mature for 40 days. Flasks were washed twice with DPBS. Cells were dissociated with TrypLE Express (ThermoFisher) and placed in an incubator for 5 mins.

Cells were gently dissociated from flasks using a cell scraper (Grenier Bio-one) and added to pre-warmed X-VIVO 10 (Lonza) in a 15 ml falcon tube (Fisher). Cells were pelleted by centrifugation at 180 x g for 5 mins, placed on dry ice and stored at -80°C until RNA isolation.

To isolate RNA the RNeasy Micro Kit (Qiagen) with on-column DNase digestion was used. An additional DNAse treatment was performed at the time of extraction using the RNase-Free DNase Set (Qiagen).

RNA concentration and purity were assayed by NanoDrop 1000 (Thermo Fisher Scientific). A 260/280 ratio of 2.0 and a 260/230 ratio of 1.8-2.2 were accepted as pure for RNA. Concentration and purity of RNA samples used for RNA-seq are provided in Appendix A, Table 10 – 1.

2.18.2 RNA sequencing and alignment

Samples were shipped to Novogene on dry ice. Library preparation and sequencing was performed by Novogene (Novogene (UK) Company Limited). Novogene described its methodologies as follows:

Library preparation: The mRNA present in the total RNA sample is isolated with magnetic beads of oligos d(T)25. This method is known as polyA tailed mRNA enrichment. Subsequently, mRNA is randomly fragmented and cDNA synthesis proceeds through the use of random hexamers and the reverse transcriptase enzyme. Once the synthesis of the first chain is finished, the second chain is synthesised with the addition of an Illumina buffer. With this and together with the presence of dNTPs, RNase H and polymerase I of *Escherichia coli*, the second chain will be obtained by Nick translation. The resulting products go through purification, end-repair, A-tailing and adapter ligation. Fragments of the appropriate size are enriched by PCR, where indexed P5 and P7 primers are introduced, and final products are purified.

The sequencing strategy is Next Generation Sequencing (NGS) based on Illumina's Sequencing Technology by Synthesis (SBS)- detection by fluorescence of the nucleotide added during the synthesis of the complementary chain. The Novaseq6000 sequencing system is used to sequence the libraries. The strategy is paired end 150bp (PE150).

2.18.3 Differential gene expression analysis

Differential gene expression analysis was conducted by NovoGene. Novogene provided the following explanation of their methods:

Differential expression analysis of two conditions/groups (two biological replicates per condition) was performed using the DESeq2R package (1.20.0) [225]. DESeq2 provide

statistical routines for determining differential expression in digital gene expression data using a model based on the negative binomial distribution. The resulting p-values were adjusted using the Benjamini and Hochberg's approach for controlling the false discovery rate. Genes with an adjusted p-value ≤ 0.05 found by DESeq2 were assigned as differentially expressed.

2.18.4 Gene set enrichment analysis (GSEA)

Gene set enrichment analysis (GSEA) was conducted by NovoGene. Novogene provided the following explanation of their methods:

Gene Set Enrichment Analysis (GSEA) is a computational approach to determine if a predefined Gene Set can show a significant consistent difference between two biological states. The genes were ranked according to the degree of differential expression in the two samples, and then the predefined Gene Set were tested to see if they were enriched at the top or bottom of the list. Gene set enrichment analysis can include subtle expression changes. We use the local version of the GSEA analysis tool http://www.broadinstitute.org/gsea/index.jsp, GO, KEGG data set were used for GSEA independently.

2.18.5 GO and KEGG enrichment analysis of differentially expressed genes

GO and KEGG enrichment analysis of differentially expressed genes was performed by Novogene. Novogene provided the following explanation of their methods:

Gene Ontology (GO) enrichment analysis of differentially expressed genes was implemented by the cluster Profiler R package, in which gene length bias was corrected. GO terms with corrected p values less than 0.05 were considered significantly enriched by differential expressed genes. KEGG is a database resource for understanding high-level functions and utilities of the biological system, such as the cell, the organism and the ecosystem, from molecular-level information, especially large-scale molecular datasets generated by genome sequencing and other high-through put experimental technologies (http://www.genome.jp/kegg/). We used clusterProfiler R package to test the statistical enrichment of differential expression genes in KEGG pathways.

2.19 Bulk RNA Sequencing

Bulk RNA sequencing data was downloaded, and abundances of transcripts were quantified using the program Kallisto [226]. Kallisto measurements were imported into the R environment using Tximport package (v1.18.0) [227], where transcript level estimates were sorted by foetal week and the genes *TSPAN10* and *TYR* selected. Transcripts per million were then input into Microsoft excel and analysed using GraphPad Prism.

2.20 Quantitative Real-Time Polymerase Chain Reaction (RT-qPCR)

2.20.1 Primer validation

Primers were validated using WT cDNA. A standard curve was produced for each primer pair, using ten-fold serial dilutions of cDNA template. Standard curves are shown in Appendix A, Figure 10 – 3.

Amplification efficiency (E) was calculated from the slope of each standard curve, using **Equation 2. 2**. Percentage efficiency was calculated using **Equation 2. 3**. The coefficient of determination (R_2) was also calculated for each standard curve using Microsoft Excel (Microsoft Software). These values are given in Appendix A, Table 10 – 2. An efficiency of 90-110 % and R_2<0.980 were deemed acceptable. Melt curves were checked to ensure a single product was generated from each primer pair (indicated by a single melt peak), and to exclude the event of primer-dimers artificially inflating C_q values.

2.20.2 RT-qPCR reactions

Quantitative PCR cDNA samples were diluted to 5 ng/µl with DNAse/RNase free H_2O prior to use. QuantiNova SYBR Green PCR Master Mix (Qiagen) and Quantitect primers (Qiagen) were used.10 µl of MasterMix, 3 µl ddH2O, 2 µl QuantiNova Rox Reference dye, 2 µl primer mix and 3 µl cDNA, were combined in each well of a 96-well plate as per the manufacturer's protocol. Plates used were MicroAmp™ Fast Optical 96-Well Reaction plates (Applied Biosystems™). These were sealed with MicroAmp™ Optical Adhesive Film (Thermofisher). The RT-qPCR was performed using a StepOnePlus™ Real-Time PCR System™ Thermal Cycler running Step One DataAssist™ software (Applied Biosystems™). The following thermocycling program was used: initial denaturation at 95°C for 2 min; 40 cycles of 95°C for 5 sec, 60°C for 10 sec, plate read SYBR fluorophore; melt curve analysis using 95°C for 5 sec, 60°C for 10 sec, increasing to 95°C at +0.1°C/sec, plate read SYBR fluorophore.

Three technical replicates were performed for each sample, and triplicate reactions were performed for each experimental condition. Melt curve analysis was checked to ensure only a single amplicon was amplified. C_q values were exported into Microsoft Excel. The mean C_q of triplicate reactions was calculated and used to determine relative gene expression.

On completion of the reaction all PCR products were resolved on a 1% agarose gel with a 1 kb DNA ladder at 90 V for 1 hr to confirm primer specificity.

Data analysis

The relative expression values for the assayed genes in each sample were calculated using the ΔΔCt method [228], as below. The Applied Biosystems™ software calculated the cycle quantification (C_q) values for each well according to automatic settings. All sample-primer

combinations were plated in triplicate, so that a mean of the three C_q values was taken. The geometric mean of two reference genes (also in triplicate), which were considered stable across treatments was subtracted from the mean sample C_q values. Reference genes were cross-referenced with RNA-seq data to ensure equal expression across cell clones.

$\Delta C_q = C_q$ (target gene) – C_q (reference gene geometric mean)

These values were then subtracted the ΔC_q of a reference sample, in this case the highest ΔC_q value.

$\Delta\Delta C_q = \Delta C_q$ (of each sample) – ΔC_q (reference sample)

This gave a relative expression level for each target gene.

Fold change = $2^{-\Delta\Delta Cq}$

Correlation analysis

A Pearson's correlation analysis was performed for all RT-qPCR reactions with the previously acquired RNAseq data.

2.21 Western Blotting

2.21.1 Total Protein Extraction

Chilled 1X radioimmunoprecipitation assay (RIPA) buffer (Sigma-Aldrich) + 1X cOmplete protease and phosphatase inhibitor cocktail (Roche) was prepared as a lysis buffer. Cells were initially grown in T25 or T75 flasks for 35 - 40 days post passage, and then experiments repeated using cells grown on transwell inserts for 40 days post passage. On ice, cells were washed twice with ice-cold PBS. Cells were incubated with ice-cold lysis buffer for 5 min. Cells were agitated with a cell scraper, homogenised by gentle pipetting and transferred to chilled 1.5 ml microcentrifuge tubes on ice. Samples were incubated on ice for 30 min, during which they were periodically vortexed. Tubes were centrifuged at 14,000 x g at 4 °C for 15 min. Supernatants were transferred to clean 1.5 ml microcentrifuge tubes on ice, taking care not to disturb the DNA pellet. Total protein was quantified by bicinchoninic acid (BCA) protein assay (see below). Samples were diluted in lysis buffer, aliquoted and stored at -80 °C.

2.21.2 BCA Protein Assay

To ensure equal quantities of protein were used in western blotting a BCA protein assay (Pierce, ThermoFisher, UK) was carried out. Standard curves were generated using BSA protein standards at concentrations of 2000µg/ml, 1500µg/ml, 1000µg/ml, 750µg/ml, 500µg/ml, 250µg/ml, 125µg/ml, 25µg/ml, and finally 0µg/ml prepared in RIPA buffer. A 25 µl

volume of known standards and unknown samples were pipetted into allocated wells of a microplate, along with 200 µl of working reagent (50:1 Reagent A: Reagent B). Plates were agitated on an orbital shaker for 30 seconds and were then incubated at 37°C for 30 mins and finally cooled to room temperature. Absorbance was subsequently measured at 562 nm using a microtitre plate reader (SPECTROstar Nano, BMG Labtech, UK). The mean absorbance of replicate wells was calculated. Blank correction was performed by subtraction of the mean blank absorbance from the mean of each standard or unknown. A standard curve was constructed by plotting the blank corrected absorbance of each standard against its known concentration. Concentrations of unknown samples were interpolated from the standard curve.

2.21.3 Western blotting

Total protein was mixed in a 1:1 ratio with 4X Laemmli buffer (LiCor), vortexed, heated at 95 °C for 10 min, spun briefly using a desktop microcentrifuge and vortexed again. 10 - 40 µg/well total protein or 10 µl/well Chameleon® Duo Pre-stained Protein Ladder (LiCor) was loaded into Mini-PROTEAN TGX 10-well 8 - 16 % pre-cast protein gels (Bio-Rad) and resolved at 200 V for 30 – 40 mins in running buffer (Bio-Rad). Protein was transferred to nitrocellulose membranes by dry transfer using a midi trans-blot turbo transfer pack (Bio-Rad). Membranes were dried for 10 mins at 37°C and rehydrated in PBS for 5 mins with gentle shaking. Membranes were rinsed with ddH_2O and incubated with Revert total protein stain 700 (Li-Cor) for 5 mins at room temperature. Total protein stain was removed by incubation for 30 sec with Revert 700 wash solution twice. Membranes were rinsed with ddH_2O and imaged using the 700 infrared channel on the LiCOR Odyssey (LiCor). Membranes were destained by rinsing in ddH_2O and incubated with Revert destaining solution for 5 – 10 min with gentle agitation. Membranes were rinsed with ddH_2O and blocked in Intercept blocking buffer (LiCor) for 1 hr at room temperature with gentle agitation. Membranes were incubated with primary antibodies diluted in blocking buffer for 16 hr at 4 °C. Membranes were washed three times for 5 min in TBS + 0.1 % Tween 20 (TBST), with gentle agitation. Membranes were incubated with secondary antibodies diluted in blocking buffer for 1 hr at room temperature: Goat anti-rabbit IRDye 680RD, 1:5000 (926-68071, Li-COR); Goat anti-mouse IRDye 800RD, 1:5000 (926-32210, Li-COR). Membranes were washed three times for 5 min in TBST, with gentle agitation. Membranes were washed with ddH_2O for 5 min. Membranes were imaged using the 700 and 800 infrared channels on the LiCOR Odyssey (LiCOR).

Table 2 - 7 displays the primary antibodies used in Western blotting experiments.

Table 2-7 Primary antibodies used and their dilutions in Western Blotting experiments

Primary Antibodies	Dilution	Catalogue Number	Company
Adam10 Monoclonal antibody	1:500	ab124695	Abcam
TSPAN10 Polyclonal antibody	1:100	14430-1-AP	Proteintech
Adam10 Monoclonal antibody	1:100	66620-1-Ig	Proteintech
TSPAN10 N-terminal region Monoclonal antibody	1:100	ARP50022_P050	Aviva Systems Biology
Catalase Peroxisome marker	1:1000	ab76024	Abcam
Tyrosinase	1:250	ab738	Abcam

2.22 Transmission Electron Microscopy of hESC-derived RPE

2.22.1 Embedding transwells in resin blocks

hESC-derived RPE cultures were grown on transwells and fixed with primary fixative comprising 3% glutaraldehyde, 4% formaldehyde in 0.1M piperazine-N, N'-bis (PIPES) buffer (pH 7.2) for a minimum of 1 hr. Transwells were then rinsed in 0.1M PIPES buffer and block stained in 2% aqueous uranyl acetate (20 mins). Samples were then dehydrated in an ethanol gradient (30%, 50%, 70%, 95%) for 10 mins each, followed by absolute ethanol twice for 20 mins. A link reagent acetonitrile was then applied for 10 mins, after which samples were incubated overnight in a 1:1 ratio of acetonitrile to Spurr resin (Agar Scientific, Stanstead, UK). The following day samples were submerged in fresh Spurr resin for 6 hrs before embedding and polymerisation in Spurr resin at 60°C for 24 hrs.

2.22.2 Microtomy of transwell resin blocks

Resin blocks were loaded in a Reichert Ultracut E Microtome (Leica Microsystems, UK). A razor blade was initially used to trim the block into a trapezium centred around the sample. The block was then loaded into the cutting arm and a glass knife used to polish the surface before semi-thin sections were taken and stained with toluidine blue. A light microscope was then used to correctly identify sections had been taken in the area of interest. The resin block was re-polished with a glass knife and ultra-thin silver/gold 90nm thick sections cut. Ultra-thin sections were collected on 200 mesh carbon and formvar coated copper/palladium grids, pre-treated with Sodium Hydroxide. Sections were then stained with Reynolds lead

stain. Cross sections of samples were viewed on a Hitachi H7700 (Hitachi High Technology, Japan) Transmission Electron Microscope.

2.23 Trans-Epithelial Electrical Resistance (TEER)

RPE cells were plated on GFR-matrigel coated 12mm Transwell Permeable Supports (Corning®). Resistance readings were measured weekly using the Millicell Electrical Resistance System volt-ohm meter (Millicell ERS-2, Millipore), according to the manufacturer's instructions from 2 to 11 weeks in culture. The electrode was placed in 4 ml 70% ethanol in a 50 ml falcon tube and disinfected for 30 mins at room temperature prior to use. Cultures were removed from the incubator and measurements taken within 2 - 3 mins to ensure temperature stability. The short electrode probe was placed in the apical compartment above the cells, and the longer probe in the basal compartment touching the bottom of the well of the plate. Care was taken to hold the electrode perpendicular to the base of the plate given that variability in the angle of the electrode and depth of immersion can affect resistance measurements. Measurements were performed weekly for all cultures. Measurements were performed in unchanged culture media in triplicate, at three different positions of each well. Averages were used for further analysis. The background resistance was determined from a blank culture insert in the same media coated with the corresponding substrate but without cells and subtracted from the respective experiment condition. Measurements are reported as resistance in ohms multiplied by the area in square centimetres ($\Omega \times cm^2$). Results are presented as mean ± SEM. Statistical hypothesis testing was performed using one-way ANOVA in Prism (GraphPad Software). Post-hoc Dunnett's multiple comparisons tests were then performed between each clone and the WT. Equation 2. 4 displays the method to calculate TEER.

2.24 Enzyme-linked immunosorbent assay (ELISA)

For all ELISAs hESC-RPE cells were cultured on 12mm Transwell Permeable Supports (Corning®) coated with GFR-matrigel. Supernatants from both the apical and basal sides (meaning upper and lower compartments of the Transwell®, respectively) were collected 60 hr after the medium was changed [176]. The optical density readings were measured using a Spectrostar Microplate Reader (SPECTROstar Nano, BMG Labtech, UK).).

2.24.1 Pigment Epithelial Derived Growth Factor ELISA

PEDF secretion levels were measured in duplicate for each differentiation with the commercially available human PEDF ELISA Kit (BioVendor RD191114200R), in accordance with the manufacturer's instructions, after 21 days and 63 days of culture. Conditioned apical and basal media collected from hESC-RPE cultures grown on Transwell® inserts (n=9) was diluted 1:8000 in dilution buffer prior to use in the assay. 100 µl of known PEDF standards,

quality controls, samples and dilution buffer (blank) were applied to allocated wells of a microtitre plate precoated with capture antibody and were incubated for 1 hr on an orbital shaker (ca. 300 rpm). After the incubation period, the wells underwent five consecutive wash cycles using Wash Solution. Subsequently,100 µl of detector antibody was applied to wells and incubated as previously described. Following this, another round of washing was carried out, and 100 µl of the detection enzyme was added to the wells and incubated as previously. Five further washes with Wash Solution were then undertaken. Following this, 100 µl of Substrate Solution was added to each well for 5 mins after which 100 µl of Stop Solution was added.

All incubations were performed at room temperature and two technical replicates were performed for each sample. Optical densities were determined by measuring the absorbance at 450 nm with a microtitre plate reader (SPECTROStar Nano; BMG Labtech, UK), taking into account the 570 nm wavelength correction. Data was analysed in Microsoft Excel and GraphPad Prism.

Details regarding detection components employed can be seen in Table 2 – 8

Table 2-8 Detection components of the BioVendor Human PEDF ELISA
Detection components included within the BioVendor PEDF ELISA used to quantify PEDF levels within conditioned cell culture medium. Abbreviations: PEDF, Pigment Epithelium Derived Factor; HRP, Horseradish Peroxidase.

Detection Component	Details
Capture Antibody	Polyclonal anti-human PEDF
Detector Antibody	Biotinylated polyclonal anti-human PEDF
Detection Enzyme	Streptavidin-HRP
Stabilized Chromagen	Tetramethylbenzidine (TMB)
Substrate Solution	Sulphuric Acid

2.24.2 Human Catalase ELISA

Secreted catalase levels were also measured in duplicates for each differentiation with the commercially available human catalase ELISA Kit (AbCam ab277396) in accordance with the manufacturer's instructions, after 21 days and 63 days of culture. Conditioned media harvested from apical and basal compartments of hESC-RPE cultures (n=9) was diluted 1:25 in the standard diluent buffer prior to use. In brief, 100 µl of known Catalase standards and samples were applied to appropriate wells of a microtitre plate, precoated with capture antibody, and incubated for 2.5 hrs. Plates were subsequently washed four times with 1X Wash Buffer and 100 µl detector antibody was applied to wells for 1 hr, before plates were washed as previously and 100 µl of detection enzyme was added to wells for 45 mins. The final four washes were followed by the addition of 100 µl of Stabilised Chromogen to each

well, and incubation in the dark for 30 mins. Finally, 50 µl of Stop Solution was added to each well. Unless otherwise stated all incubations were performed at room temperature and two technical replicates were performed for each sample. Optical densities were determined by measuring the absorbance at 450 nm with a microtitre plate reader (SPECTROStar Nano; BMG Labtech, UK), taking into account the 570 nm wavelength correction. Data was analysed in Microsoft Excel and GraphPad Prism.

Details regarding detection components employed can be seen in Table 2 – 9

Table 2-9 Detection components of Human Catalase ELISA
Detection components included within the AbCam Catalse ELISA used to quantify Catalase levels within conditioned cell culture medium. Abbreviations: HRP, Horseradish Peroxidase.

Detection Component	Details
Capture Antibody	Polyclonal anti-human Catalase
Detector Antibody	Monoclonal anti-human Catalase Biotin Conjugate
Detection Enzyme	Streptavidin-HRP
Stabilised Chromagen	Tetramethylbenzidine (TMB)
Stop Solution	Sulphuric Acid

2.24.3 Vascular Endothelial Growth Factor ELISA

Secreted levels of human VEGF were quantified using the Novex® human VEGF solid-phase sandwich ELISA (Life technologies, UK) according to the manufacturer's instructions. Conditioned media harvested from apical and basal compartments of hESC-RPE cultures (n=9) was diluted 1:10 in the standard diluent buffer prior to use. It's worth noting that unless specified otherwise, all incubations were conducted at room temperature, and two technical replicates were performed for each sample to ensure the reliability of the results. In brief, the procedure involved the following steps:

- 100 µl of known VEGF standards were administered to the appropriate wells of a microtitre plate. This plate had been pre-coated with a capture antibody and 50 µl of incubation buffer added.
- 50 µl volumes of both samples and control were added to designated wells in duplicate. To these wells, 50 µl of incubation buffer and 50 µl of standard diluent buffer were added. The plates were then incubated for 2 hrs.
- Subsequently, the plates were washed four times with 1X Wash Buffer, and 100 µl of detector antibody was applied to the wells for 1 hr. Following this, the plates were washed again, and 100 µl of detection enzyme was added to the wells for a 30 min incubation.

- After the final four washes, 100 µl of Stabilised Chromogen was added to each well, and the plate was incubated in the dark for 1 hr.
- Finally, 100 µl of Stop Solution was added to each well. In the case of the Chromogen blank, both the detector antibody and detection enzyme were intentionally omitted from the wells.

Optical densities were determined by measuring the absorbance at 450 nm with a microtitre plate reader (SPECTROStar Nano; BMG Labtech, UK), taking into account the 570 nm wavelength correction. Data was analysed in Microsoft Excel and GraphPad Prism.

Details regarding detection components used can be seen in Table 2 – 10.

Table 2-10 Detection components of Novex® Human VEGF ELISA
Details of detection components included in the Novex® Human VEGF ELISA used to quantify VEGF levels within conditioned cell culture medium. Abbreviations: VEGF, Vascular Endothelial Growth Factor; HRP, Horseradish Peroxidase.

Detection Component	Details
Capture Antibody	Polyclonal anti-human VEGF 165
Detector Antibody	Monoclonal anti-human VEGF Biotin Conjugate
Detection Enzyme	Streptavidin-HRP
Stabilised Chromagen	Tetramethylbenzidine (TMB)
Stop Solution	Sulphuric Acid

2.25 Assessment of melanin synthesis and melanogenesis

2.25.1 DOPA-Oxidase Activity Assay

DOPA-oxidase activity was assessed in all differentiations of all cell clones. Briefly cells cultured for 40-45 days in T75 flasks were lysed using 1X radioimmunoprecipitation assay (RIPA) buffer (Sigma-Aldrich) + 1X cOmplete protease and phosphatase inhibitor cocktail (Roche), and the protein concentration was measured by BCA assay (Thermo Scientific™ Pierce™ BCA Protein Assay Kit). Samples were then diluted to 4 µg/µl and 30 µl used for DOPA-oxidase assays. Samples were added to a 96 well plate in duplicate and 150 µl of a phosphate buffer (Sigma) with l-3,4-dihydroxyphenylalanine L-DOPA 1 mM (Sigma) and 3-methyl- 2-benzothiazolinonehydrazone hydrochloride 6 mM (MBTH) (Sigma) added. DOPA-oxidase activity was then measured as the accumulation of the downstream product, dopachrome. The enzymatic activity was recorded by measuring the absorbance of dopachrome at 492 nm using a plate reader (SPECTROStar Nano; BMG Labtech, UK). This was performed at regular intervals at 37°C from the start of the L-DOPA treatment at 0 min for 30 min intervals until 180 min.

2.25.2 Slide Scanner Microscopy

The Olympus BX51 microscope with robotic slide loader was used to capture brightfield images of slides. Initially an overview scan was taken. Five 1 x 1 mm squares were then selected for imaging transwell sections in detail. Three of the 1 x 1 mm squares were selected for each slide for analysis, any section with image distortion or blurring was not included. Three slides were imaged for each cell population.

2.25.3 Pigmentation Image Analysis

Brightfield images were anonymised and analysed in Fiji (ImageJ). Initially to measure the level of pigmentation the background pixel values were set to 0 and black. Images were then duplicated, and the colour channels split, with the red channel selected. The black dots, representing transwell pores were thresholded, with maximum threshold based on the least pigmented image and set to 90. The thresholded selections were then transferred to the original image. The original image was then converted to an 8-bit grey image to allow thresholding and calculation of the mean grey value, representative of pigment. A threshold of 0 – 205 was selected based on the least pigmented image. The threshold was then applied to create a binary image.

This process was repeated for each image and the mean grey values calculated ± standard deviation.

2.25.4 Addition of L-Dopa to hESC-RPE

Fully differentiated hESC-RPE were grown on GFR-matrigel coated 12mm Transwell Permeable Supports (Corning®) for at least 40 days. L-DOPA (Enzo Life Sciences) was added to the apical transwell compartment at two concentrations, 1 μM and 2 μM, diluted in X-VIVO 10, in triplicate with every media change for 28 days. This was performed for all differentiations of all cell lines. At day 28 transwells were washed x 3 in DPBS (Fisher) and fixed with 4% PFA. Transwell membranes were then cut from inserts and fixed between two coverslips using Mowiol 4-88 Mounting Medium. Slides were imaged using an Olympus VS110 scanner.

2.26 Determination of antioxidant enzyme activity and oxidative stress

2.26.1 Catalase Assay

Catalase (CAT) activity was measured in cell lysates from all differentiations of all cell clones using a kit from Cayman Chemical Company (Ann Arbor, Michigan, USA). The CAT assay kit is based on the reaction of methanol with the CAT enzyme in the presence of H_2O_2 to form formaldehyde. Formaldehyde reacts with Purpald (4-amino-3-hydrazino- 5-mercapto-1,2,4-triazole), leading to the production of a purple colour with absorbance at 540 nm. The

absorbance is positively correlated with the activity of the CAT enzyme. CAT activity was expressed as nmol/min/mg protein after normalisation to the total protein amount, which was measured using the BCA Protein Assay (section 2.20.2).

2.26.2 Measurement of intracellular reactive oxygen species (ROS)

The generation of intracellular ROS was determined using the 2'-7'dichlorofluorescein diacetate (DCFH-DA) assay (Abcam). Cells were plated in Nunc 96 well black optical – bottom plates (ThermoFisher) for 6 weeks. 24 hrs prior to the assay cells were treated with varying concentrations of H_2O_2. The DCFH-DA assay was performed as per the manufacturers' instructions. Briefly, 10 µm DCFH-DA was added to wells for 40 mins at 37°C. Cells were then washed twice with PBS. 96 well plates were immediately measured at the fifth minute and then at 30-minute intervals up to 180 minutes in a fluorescent microplate reader at excitation 495 nm and emission 530 nm. Results were expressed as mean fluorescence intensity (MFI) corresponding to relative reactive oxygen species (ROS) production.

2.27 Phagocytosis assay

A pulse-chase feeding assay was selected and the method from Ratnayaka et al followed [229].

2.27.1 Photoreceptor Outer Segment (POS) Isolation

Fresh whole porcine eyes were obtained from Upton's of Basset butchers (Southampton, UK). Eyes were dissected the same day and the retinas isolated using a sterile scalpel and dissecting microscope. An incision was made at the ora serata following which the anterior segment and lens were removed. The retina was then extracted and added to KCl buffer (0.3M KCl, 10mM HEPES, 0.5mM $CaCl_2$, 1mM $MgCl_2$; pH 7.0) with 48% (w/v) sucrose solutions and ciprofloxacin 10µg/ml. Porcine retinas were then homogenised by gentle shaking for 2 mins. The solution was then centrifuged at 5000 x g for 5 mins and the resulting supernatant passed through a sterile gauze into new Eppendorf tubes and diluted 1:1 in KCl buffer devoid of sucrose. The resulting solution was subsequently centrifuged at 4000 x g for 7 mins. Following this the pellet of POS was washed 3 times in PBS by centrifugation at 4000 x g for 7 mins. POS pellets were then resuspended in X-VIVO 10 with 2.5% sucrose (w/v), Aliquots were stored at -80^{o}C prior to use.

2.27.2 POS Tagging with FITC

The isolated POS were covalently labelled with the fluorescent dye Fluorescein Isothiocyanate (FITC) to facilitate their visualisation in ensuing experiments. The POS were suspended in a 1.5 ml FITC stock solution (2 mg/ml FITC isomer 1; ThermoFisher, UK, prepared in 0.1 M

Na_2CO_3 buffer at pH 9.5). This mixture was placed on a rotating plate (Stuart STR9 Rocking Platform; Camlab Ltd, UK) in the dark for 1 hour to allow for the covalent attachment of the FITC conjugate. Afterward, the POS-FITC solution underwent centrifugation at 3000 x g for 4 mins at 20°C. The solution containing unbound FITC was removed, and the FITC-labelled POS pellets were resuspended in X-VIVO 10 with 2.5% sucrose, divided into aliquots, and stored at -80°C.

2.27.3 BCA protein assay

To determine the concentration of FITC-POS prepared in section 2.29.2, a BCA protein assay (Pierce, ThermoFisher, UK) was conducted as per the manufacturer's instructions (see section 2.21.2 for more details regarding the method). All standards were prepared in X-VIVO 10 with 2.5% sucrose.

2.27.4 Pulse-chase POS feeding

Mature hESC-RPE monolayers from both WT and TSPAN10 k.o cells were fed POS using a pulse-chase method [229, 230]. WT cells were either treated with 100 µM hydrogen peroxide (H_2O_2; Sigma Aldrich, UK) for 24 hours [231], or left untreated as a control. Initially cells were chilled to 17^{o}C for 30 mins (Enviro-Genie, Fisher Scientific, UK), after which they were fed POS-FITC at 4 µg/cm^2 [232] and kept at 17^{o}C for an additional 30 mins to facilitate maximal binding but minimise internalisation. Subsequently, the medium was removed to eliminate any unbound POS, and fresh pre-warmed media added. RPE monolayers were then returned to a humidified incubator at 37^{o}C with 5% CO_2 for 4, 6, 12 or 24 hrs prior to fixation.

2.27.5 Data acquisition

Cells were stained for endosomal and lysosomal markers, and/or for the tight junction marker occludin as described in sections 2.13 and 2.13.1. All antibodies used and their concentrations are reported in Tables 2 - 3 and 2 - 4. All images were acquired using a Leica SP8 (Leica Microsystems, UK) confocal laser scanning microscope. Z-stacks were taken for each field of view using sequential scanning and system optimised settings. For quantification of attached (total) and internalised POS, z-stacks for each hESC-RPE line were taken at 63× magnification and 0.33 µm interval. The numbers of POS were quantified using ImageJ Image Processing and Analysis software (ImageJ, https://imagej.nih.gov/ij/). Quantification of POS-FITC co-localisation with endocytic and lysosomal compartments was performed using a method by Ratnayaka et al [229], which utilises the software Volocity (Perkin Elmer, UK). Initially image z-stacks were opened in FIJI (ImageJ) and channels split into the colours red, green and blue. To remove the incidence of false co-localisation the average background pixel intensities were measured for both red and green channels, which was then subtracted from the whole image. Red and green channels were then merged and

saved as a composite image which was opened in Volocity. The aim was to analyse co-localisation of red and green. Volocity uses the Costes et al automated statistical algorithm to analyse co-localisation between the red and green channels [233]. A region of interest was drawn around a POS which was identified as being internalised by review of the Z-stack images. For each time point/condition 30 cells were analysed for all differentiations of all cell clones (n=9). Co-localisation values were then averaged for each cell clone and plotted as a function of time in GraphPad Prism. A two-way ANOVA was used to compare the extent of colocalization at varying time points to WT untreated cells.

2.27.6 Costes et al method of colocalization quantification

Various techniques have been developed to quantify colocalization, where specific coefficients are used to measure the extent of colocalization. Currently, the most widely accepted method is the one described by Costes et al. [258]. In this study, colocalization quantification was performed using this method, which is integrated into the Volocity software package (PerkinElmer, UK).

The Costes et al. method employs a threshold-based automatic algorithm, eliminating the need for user-defined thresholds. This approach reduces subjectivity and enhances the reliability of the results. The algorithm operates as follows: it calculates a linear least square fit line for the pixel intensity scatterplot, where the x and y axes represent the intensities of the two fluorochromes. A threshold is set for one axis, and its intersection with the least square fit line determines the corresponding threshold for the other axis. The Pearson correlation coefficient (r) is then computed for the data below these thresholds. Iteratively, the thresholds are adjusted until the correlation coefficient approaches zero. Subsequently, data points where both fluorochrome intensities exceed the Costes thresholds are plotted on 2D scatterplots for each analysed image. These Costes thresholds are indicated by black regions along the axes, providing a qualitative measure of colocalization [258]. The Pearson correlation coefficient and Manders split coefficients yield quantitative results, defining the extent of association and co-occurrence between the two fluorochromes [258][259]. These calculations are based solely on the intensities above the Costes thresholds.

In this study, the Manders coefficients were utilized to quantify colocalization between the fluorochromes. The presented coefficient values indicate the fraction of red coinciding with green and vice versa. The Manders colocalization metrics were chosen over the Pearson correlation coefficient. This decision was based on the fact that Manders metrics offer independence from signal proportionality, and they provide results that are intuitively easier to interpret [259]

2.28 Flow Cytometry

To allow cell sorting by flow cytometry hESC-RPE cultured for 40 days were dissociated into single cells using a papain dissociation system (Lorne laboratories). Briefly cells were incubated with papain for 30 mins to allow dissociation, following which a 1:10 OVO solution was added for 5 mins. Dissociated cells were spun over a 100% OVO suspension at 200 x g for 5 mins, resuspended in 1% BSA solution (Sigma) and counted using a haemocytometer.

Cells were blocked on ice for 30 mins after which they were stained for PE Mouse Anti-Human CD140b (BD Biosciences 558821, clone [28D4], 20μg/mL) and FVD eFluor® 506 (Invitrogen, 65-0866, 0.5μL/sample) conjugated antibodies, diluted in 1% BSA (Sigma). Cells were incubated with the conjugated antibodies at 4°C for 30 mins. Cells were then washed twice and resuspended in 1% BSA. Compensation beads (BD Biosciences) were used to control for spectral overlap between different fluorochromes. Stained cells were sorted for CD140b using a BD FACS Aria Fusion Cell Sorter (BD Biosciences) using the BD FACSDiva software (BD Biosciences).

2.29 Assessment of outer retinal layer thickness

2.29.1 Study cohort selection and data acquisition, UK Biobank

The UK Biobank constitutes a large-scale, multi-site cohort study encompassing 502,682 individuals, all of whom are residents of the United Kingdom and were enrolled through the National Health Service. The primary objective of the UK Biobank data resource is to facilitate in-depth exploration of the genetic and environmental factors that influence major diseases in later stages of life [313]. A comprehensive overview of the study's methodology has been previously published [312]. Between 2006 and 2010, participants underwent thorough assessments at 22 examination centres, which encompassed extensive baseline questionnaires, physical measurements, and the collection of biological samples. As part of these assessments, participants completed a touchscreen self-administered questionnaire that inquired about their lifestyle and environmental exposures, with a particular focus on tobacco smoking habits, including both current and past smoking status (UK Biobank Data Field number: 20116).

Additionally, after the initial baseline evaluations, 23% of UK Biobank members, equivalent to N=117,279 individuals, also took part in an ophthalmic examination, which is detailed more comprehensively in Chan et al and Cumberland et al [314, 315].

For most participants, genotyping data was available, and the processes related to their acquisition, imputation, and quality control are described in Bycroft et al [234].

2.29.2 Inclusion & exclusion criteria

The data set used was the same as described in Chua et al*.,* [235], therefore our exclusion criteria were equivalent. Briefly, the initial analysis included participants of European ancestry who underwent SD-OCT as part of the UK Biobank data collection. To minimize potential influences from population genetic structure, the study sample was restricted to unrelated individuals of European descent. European ancestry was verified using genetic data from study participants. Exclusion criteria included participants who withdrew their consent, had poor SD-OCT signal strength, missing thickness values from any Early Treatment Diabetic Retinopathy Study (ETDRS) subfield, image quality score <45, poor centration certainty, or poor segmentation certainty using Topcon Advanced Boundary Segmentation (TABS^{TM}) software [236]. SD-OCT measurements falling outside a range of 3 standard deviations were also removed. Additionally, participants with the following characteristics were also excluded from the study: refractive error $\pm$ 6 dioptres (D); visual acuity worse than 0.1 logMAR; IOPcc of <6 mmHg or >21 mmHg; self-reported AMD or a recorded AMD diagnosis (ICD10 code), self-reported glaucoma or ocular disorders. Patients with diabetes, neurodegenerative diseases, or diabetic neuropathy were likewise not included. Figure 2 – 3 shows how many individuals were included after application of the exclusion criteria.

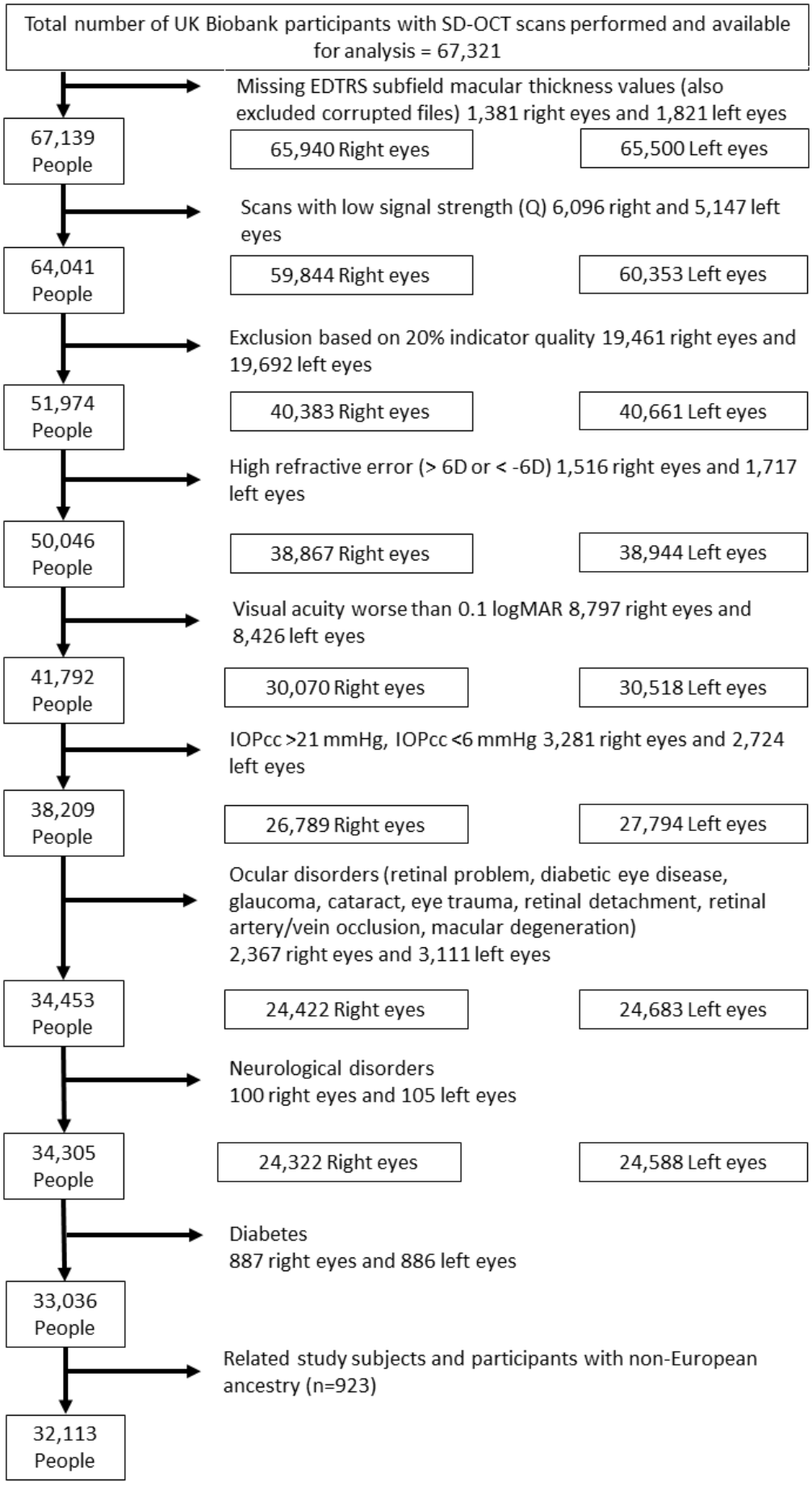
Total number of UK Biobank participants with SD-OCT scans performed and available for analysis = 67,321
Missing EDTRS subfield macular thickness values (also excluded corrupted files) 1,381 right eyes and 1,821 left eyes
67,139 People
65,940 Right eyes
65,500 Left eyes
Scans with low signal strength (Q) 6,096 right and 5,147 left eyes
64,041 People
59,844 Right eyes
60,353 Left eyes
Exclusion based on 20% indicator quality 19,461 right eyes and 19,692 left eyes
51,974 People
40,383 Right eyes
40,661 Left eyes
High refractive error (> 6D or < -6D) 1,516 right eyes and 1,717 left eyes
50,046 People
38,867 Right eyes
38,944 Left eyes
Visual acuity worse than 0.1 logMAR 8,797 right eyes and 8,426 left eyes
41,792 People
30,070 Right eyes
30,518 Left eyes
IOPcc >21 mmHg, IOPcc <6 mmHg 3,281 right eyes and 2,724 left eyes
38,209 People
26,789 Right eyes
27,794 Left eyes
Ocular disorders (retinal problem, diabetic eye disease, glaucoma, cataract, eye trauma, retinal detachment, retinal artery/vein occlusion, macular degeneration)
2,367 right eyes and 3,111 left eyes
34,453 People
24,422 Right eyes
24,683 Left eyes
Neurological disorders
100 right eyes and 105 left eyes
34,305 People
24,322 Right eyes
24,588 Left eyes
Diabetes
887 right eyes and 886 left eyes
33,036 People
Related study subjects and participants with non-European ancestry (n=923)
32,113 People

Figure 2-3 Flowchart depicting SD-OCT inclusion and exclusion criteria
Abbreviations: D = dioptre; EDTRS = Early Treatment Diabetic Retinopathy Study; IOP = intraocular pressure; logMAR = logarithm of the minimum angle of resolution; OCT = optical coherence tomography; SD = spectral domain.
Reproduced from Kaye et al (2021) [150] under the terms of the Creative Commons Licence.

2.29.3 Ethical considerations

The UK Biobank study obtained ethical approval from the North West Research Ethics Committee (06/ MRE08/65) and secured informed written consent from its participants, adhering to the principles outlined in the Declaration of Helsinki. No further ethical approval was needed here to utilise the previously acquired UK Biobank data.

2.29.4 Genotyping for AMD risk polymorphisms

For most UK Biobank participants, genotyping data was available. The processes related to their acquisition, imputation, and quality control are described in Bycroft et al [234].

For the purposes of our analyses we extracted the genotypic information for all loci associated with AMD described elsewhere [71]; high quality information was obtained for 33/34 such SNPs, because no high quality genotypes were available in the UK Biobank for the rarer rs142450006 SNP

2.29.5 Optical Coherence Tomography (OCT)

SD-OCT imaging was performed using the Topcon 3D OCT 1000 Mk2 (Topcon Corp., Tokyo, Japan) after visual acuity, autorefraction and IOP measurements were collected. OCT images were obtained under mesopic conditions, without pupillary dilation, using the 3D macular volume scan (512 A-scans per B-scan; 128 horizontal B-scans in a 6 × 6-mm raster pattern) [237, 238].

2.30 List of equations

All equations used in this thesis can be found in Appendix B.

2.31 Overview of experimental design

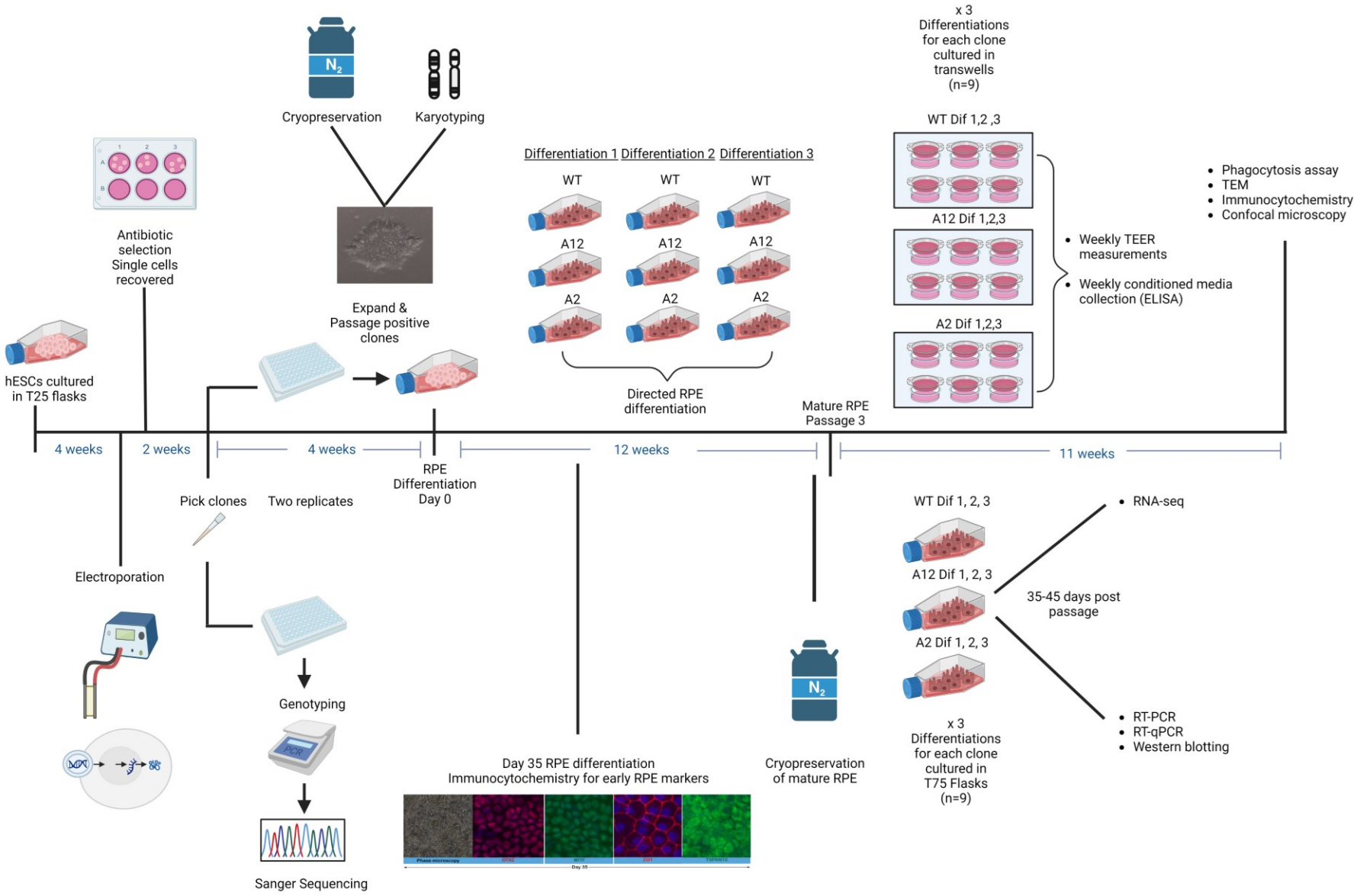
Cryopreservation
Karyotyping
Antibiotic selection Single cells recovered
Expand & Passage positive clones
hESCs cultured in T25 flasks
Differentiation 1 Differentiation 2 Differentiation 3
WT
A12
A2
Directed RPE differentiation
x 3 Differentiations for each clone cultured in transwells (n=9)
WT Dif 1,2 ,3
A12 Dif 1,2,3
A2 Dif 1,2,3
Weekly TEER measurements
Weekly conditioned media collection (ELISA)
Phagocytosis assay
TEM
Immunocytochemistry
Confocal microscopy
Mature RPE Passage 3
4 weeks
2 weeks
4 weeks
12 weeks
11 weeks
Pick clones
Two replicates
RPE Differentiation Day 0
Electroporation
Genotyping
PCR
Sanger Sequencing
Day 35 RPE differentiation Immunocytochemistry for early RPE markers
Cryopreservation of mature RPE
WT Dif 1, 2, 3
A12 Dif 1, 2, 3
A2 Dif 1, 2, 3
35-45 days post passage
RNA-seq
RT-PCR
RT-qPCR
Western blotting
x 3 Differentiations for each clone cultured in T75 Flasks (n=9)

Figure 2-4 Overview of Experimental Design
Schematic depicting experimental design from hESCs to CRISPR/Cas-9 edited hESC derived RPE. Time points of cells at which each experimental procedure was performed are highlighted, including various vessels in which cells were grown. Of note, further detail for RPE directed differentiation highlighted elsewhere.
Image produced using BioRender.

3 The Association between macular thickness and AMD genetic risk variants

Genetic investigations have proven instrumental in unveiling the underlying mechanisms of AMD. Remarkable progress has been made through GWAS, leading to the identification of SNPs within genes that increase the risk of disease [71, 239]. Notably, SNPs in genes located on chromosome 1 in the CFH-CFHR1-5 cluster and near the ARMS2 and HTRA1 genes on chromosome 10 contribute to nearly 80% of AMD's genetic risk [71, 83, 85]. Possessing at least one CFH risk allele alone is linked to a population attributable risk fraction for early and late AMD of 10% and 53%, respectively [82].

Despite our growing knowledge of genetic loci associated with AMD risk, the precise molecular processes behind these interactions remain incompletely understood. Furthermore, it remains uncertain whether individuals carrying common risk polymorphisms exhibit retinal abnormalities before the clinical onset of AMD. A recent study examined the correlation between AMD susceptibility-altering variants within CFH-CFHR5 and ARMS2/HTRA1 and macular retinal thickness in both healthy individuals and those with AMD [240]. The findings indicated thicker retinas in the perifoveal region among healthy individuals with a protective CFHR1/3 deletion, while individuals with early or intermediate AMD and ARMS2/HTRA1 risk alleles displayed thinner retinas compared to those with CFH-CFHR5 risk alleles. Despite substantial research on the effects of polymorphisms on chromosomes 1 and 10, including their impact on retinal thickness [240, 241], little attention has been given to the additional genetic loci, such as rs6565597 at *NPLOC4 -TSPAN10,* uncovered in the Fritsche et al GWAS, particularly in individuals without AMD [71].

Optical coherence tomography (OCT) imaging has transformed our comprehension of retinal disorders, including AMD. Spectral-domain OCT (SD-OCT) imaging produces cross-sectional images of retinal layers by utilizing differences in optical reflectivity among different layers of retinal cells, extending from the retinal nerve fibre layer to the RPE. Advanced segmentation algorithms enable the measurement of retinal layer thickness based on variations in optical reflectivity, making it possible to identify boundaries between retinal layers *in vivo* [242]. The UK Biobank, one of the world's largest prospective cohorts, offers a wealth of medical, lifestyle, and extensive genetic sequencing data, including comprehensive information on ophthalmic conditions [243, 244]. This extensive dataset presents an opportunity to investigate how high-risk AMD genetic loci affect changes in the thickness of the outer retinal layers in clinically healthy participants from the UK Biobank population. This research has the potential to shed light on the mechanisms through which these genetic loci contribute to AMD development and uncover novel biomarkers for clinical application.

Hypothesis: Individuals with AMD risk SNPs but without AMD show changes to their outer retinal thickness.

The aim of this chapter was to analyse the association of outer retinal thickness measurements with the presence of AMD risk SNPs in healthy individuals.

3.1 Methods

This section describes chapter specific methodological analysis for Chapter 3. For in depth technical protocols please refer to Chapter 2, section 2.29.

3.1.1 Segmentation and analysis of outer retinal layers

We selected four SD-OCT measurements of outer retinal layer thickness to analyse the outer-retinal layer related boundaries as represented in Figure 3 – 1: inner nuclear layer - retinal pigment epithelium (INL-RPE), retinal pigment epithelium-Bruch's membrane (RPE-BM), and the specific sublayers of the photoreceptor: inner nuclear layer-external limiting membrane (INL-ELM); external limiting membrane-inner segment outer segment (ELM-ISOS); and inner segment outer segment-retinal pigment epithelium (ISOS-RPE) [236, 245]. The accuracy of the segmentation is described by Yang et al [246]. Additional details on how we used the algorithm to segment UKBB images are described by Keane et al and Patel et al [238, 245]. Briefly, the segmentation approach incorporates an automated evaluation of signal strength, image alignment, and identification of segmentation errors. In line with previous work we classified subpar images, as those with a signal strength <45, as assessed using the TABS algorithm. All segmentation measurements were calculated up to, but not including the boundary layer. The TABS segmentation algorithm was employed to delineate the outer retinal layers [238]. The INL-ELM is a proxy measure of the synaptic terminal of the photoreceptor. The ELM-ISOS is representative of the photoreceptor inner segment. The ISOS-RPE measurement is representative of the photoreceptor outer segment. The RPE-BM measurement represents the RPE and BM complex. The anatomy of the outer retinal layers corresponds with the OCT boundaries observed in the retina (Figure 3 – 1), hence the layers have been defined using the above specific definitions.

Two measurements were collated for each outer retinal layer, average and central thickness. Central thickness measurements represent the central 1 mm subfield area of the SD-OCT scan, corresponding to the fovea. Average measurements represent the mean thickness of outer retinal layers in the macula.

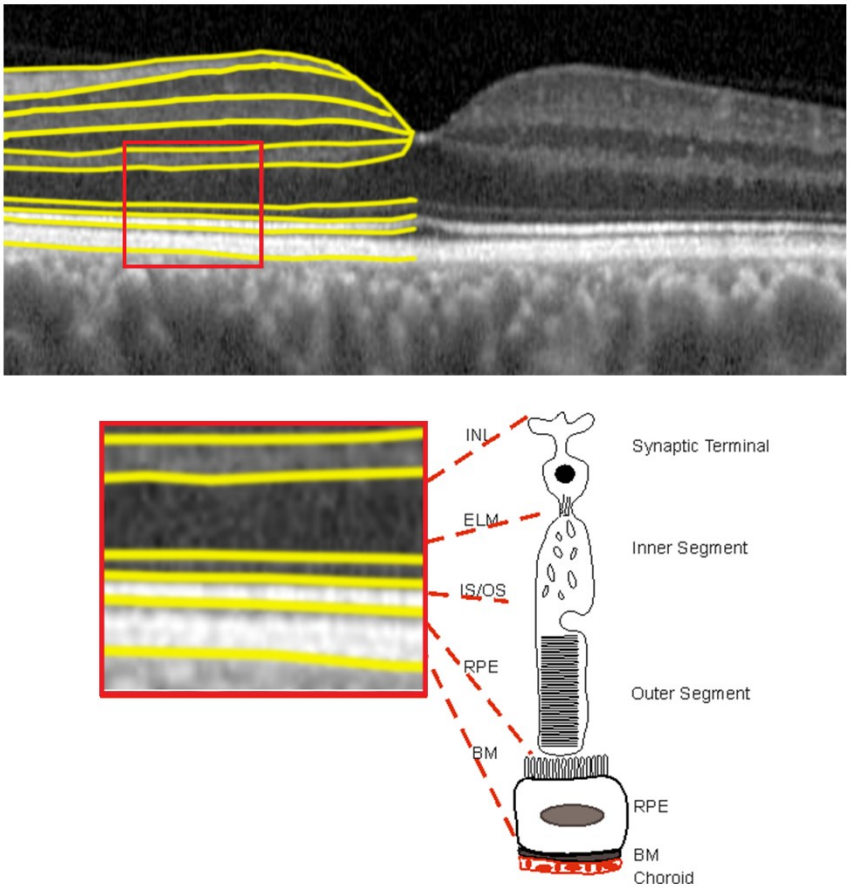

Figure 3-1 Optical coherence tomography with segmentation in half the image and a schematic demonstrating corresponding outer retinal layers in relation to photoreceptor segments and retinal pigment epithelium.
Inner nuclear layer- External limiting membrane (INL-ELM) representative of the synaptic terminal. External limiting membrane—Inner and outer segments (ELM-ISOS) representative of the photoreceptor inner segment. Inner and outer segments—Retinal pigment epithelial thickness (ISOS-RPE), representative of the photoreceptor outer segment. Retinal pigment epithelium—Bruch's membrane (RPE-BM) representative of the RPE and BM complex.
Reproduced from Kaye et al., (2021) [150] under the terms of the Creative Commons Licence.

For the purposes of our analyses we extracted the genotypic information for all loci associated with AMD described elsewhere [71]; high quality information was obtained for 33/34 such SNPs, because no high quality genotypes were available in the UK Biobank for the rarer rs142450006 SNP.

3.1.2 Statistical analyses

The following section was reproduced from Kaye et al [150].

'Descriptive analyses were conducted using *epiDisplay* package in R (https://www.r-project.org/). Means and standard errors were calculated for normally distributed continuous variables. Categorical variables were characterized by computing frequencies and percentages.

To test the associations between selected AMD markers and outer retinal layer thickness measurements, we built linear models adjusted for age, sex, refraction and smoking habits of the study participants. In addition, we also computed polygenic risk scores (PRS) of AMD using alleles and effect and built linear models to assess PRS association with measurement of outer retinal layer thickness.

To further explore the possibility of an interaction between AMD risk-altering genotypes and their potential to non-linearly influence outer retinal layer thickness, we built linear regression models that, in addition to the above parameters, also included a genetic interaction (GI) term and individual AMD variants as independent predictors and each of the four SD-OCT measurements (ELM-ISOS, ISOS-RPE, INL-ELM and RPE-BM), as outcomes. Each of the average and central SD-OCT measurements was respectively tested for the unique pairwise combinations of SNPs that were previously found in association with any of the SD-OCT parameters beyond Bonferroni multiple testing correction. The latter was conservatively defined on the basis of 33 SNPs and 15 unique pairs of SNPs assessed in the GI analyses, multiplied by the number of SD-OCT measurements. We did not consider central and average measurements to be independent.

To further explore the relationship between AMD and outer retinal layer thickness measurements, we built Mendelian Randomization models (MR), testing potential causal associations between AMD and four different measurements of outer retinal layer thickness.

Regression tests, although generally robust statistical tools for identifying associations between two variables, do not provide insights into the nature of that relationship. Such an association can result from a causal influence of either variable on the other, or both variables may be influenced by other known or unknown factors, often not incorporated into the model. Mendelian randomization is a relatively new group of cross-sectional causal inference statistical methods [247, 248] designed to specifically investigate the direction of causation in the relationship between two correlated variables. Mendelian randomization examines the hypothesis that a specific trait, referred to as an "exposure" in this context, whose variability is at least partially explained by the impact of established genetic loci (referred to as "instruments"), causally affects certain phenotypic expressions of another trait

or disease, termed the "outcome." These methods emulate randomized trials by effectively comparing individuals who are randomly assigned based on their possession of a high or low load of alleles predisposing to the exposure. This assignment adheres to Mendel's law of segregation and is not influenced by the presence of the outcome phenotype.

In this study, we chose as instrumental variables genetic markers that independently (r^2<0.1) located in each genomic region associated with AMD. These instrumental variables were selected from previously published AMD GWAS [71]. The effect of these genes is a good approximation of the subsequent likelihood of AMD in individuals who currently present no objective signs of the disease. To minimize bias, we removed variants that showed substantial associations with SD-OCT parameters. To establish causality, we performed two types of experiments: first, where AMD-associated variants were used as the exposure variable, and SD-OCT measurements were the outcome, and then the inverse experiment where variants associated with outer retinal layer thickness served as an exposure variable and AMD was the outcome. The two-sample analyses were conducted using *MendelianRandomization* package in R. Several MR tests, including "simple median", "inverse-variance weighted", and "MR-Egger", were applied to assess causality. These tests are mutually complementary, and their results are usually interpreted together [249].'

3.1.2.1 Mendelian Randomization

Mendelian randomization (MR) is used to investigate causal relationships between risk factors and outcomes using observational data. In MR modelling there is an assumption that genetic variants, in this case AMD risk polymorphisms, are valid instrumental variables. For this to hold true a genetic variant used in MR must be A) associated with the risk factor; B) not associated with any confounder of the risk factor–outcome association; and C) not associated with the outcome conditional on the risk factor and confounders [250]. MR-Egger is a statistical technique utilized in situations where the instrumental variable assumptions are not met, yet a less stringent assumption is fulfilled [251]. MR-Egger is commonly used for summarised genetic data and was therefore selected for use in our analysis. MR-Egger comprises three components: (1) an evaluation for directional pleiotropy, (2) an assessment for causal impact, and (3) an estimation of the causal effect. The MR-Egger method can assess whether genetic variants have pleiotropic effects on the outcome that differ on average from zero (directional pleiotropy), as well as to provide a consistent estimate of the causal effect. MR-Egger is performed by modifying weighted linear regression. Instead of setting the intercept term to zero, it is instead estimated as part of the analysis [251].

Directional pleiotropy refers to a situation in genetic studies where a single genetic variant affects multiple traits or outcomes, but the effects of that variant on different traits have

consistent directions, either positive or negative. In other words, if a genetic variant is associated with an increased risk of one trait or outcome, it tends to also be associated with an increased risk (or decreased risk) of other traits or outcomes. This is in contrast to non-directional pleiotropy, where the effects of a genetic variant on different traits may vary in direction. Assessing directional pleiotropy is important in MR to ensure that the genetic variant used as an instrument for a particular exposure is not influencing the outcome through pathways other than the exposure of interest.

Another analysis tool used in our MR was Inverse variance weighted (IVW). This is a statistical method used to estimate the causal effect of an exposure on an outcome. In IVW, each genetic variant's causal estimate is weighted by the inverse of its variance, which reflects the precision of its effect estimate. Essentially, variants with more precise effect estimates are given greater weight in the analysis.

The IVW method assumes that all genetic variants used are valid instruments for the exposure and satisfy certain assumptions, such as the absence of horizontal pleiotropy (i.e., the genetic variants only affect the outcome through the exposure of interest). By combining the causal estimates from multiple genetic variants using IVW, the aim is to obtain a more precise and unbiased estimate of the causal effect of the exposure on the outcome.

Simple median analysis was also employed in our MR. This is conducted by taking the causal estimate for each genetic variant (the effect size of the variant on the outcome, in this case AMD genetic risk on outer retinal layer thickness) and using the median of these causal estimates across all variants. The median estimate is then considered as the overall causal effect estimate of the exposure on the outcome.

3.2 Results

3.2.1 Study population demographics

The final study cohort consisted of 32,132 participants from the UK Biobank, all of European ancestry. Among them, 48% were male, and the mean age was 57 years (± 8). A total of 54% of the participants self-reported as 'never smoked.' Additional detailed demographic information about the study subjects can be seen in Table 3 – 1. The distribution of outer retinal thickness measurements for INL-ELM, ELM-ISOS, and ISOS-RPE closely resembled a normal distribution (Appendix C, Figure 12 – 1).

Table 3-1 Characteristics of the study participants (N=32,113).
The fields "(%, N)" and (mean (SD)) denote percentage, number of study participants, means and standard deviations respectively. SE, standard error.

Characteristics	Statistics
Demographic characteristics	
Sex (%, N)	
Women	51.97 % (16,688)
Men	48.03 % (15,425)
Age (mean (SD))	56.6 (8)
SE	0.02 (1.95)
Smoking status (%, N)	
Never-smokers	54.12 % (17,378)
Ever-smokers	45.88 % (14,735)
SD-OCT measurements (µm)	
INL-ELM (center)	108.9 (9.4)
INL-ELM (average)	80.9 (6.1)
ELM-ISOS (center)	28.4 (1.8)
ELM-ISOS (average)	23.6 (1.4)
ISOS-RPE (center)	42.9 (5.4)
ISOS-RPE (average)	38.2 (3.5)
RPE_BM (center)	26.1 (4.3)
RPE_BM (average)	25.3 (2.8)

3.2.2 Average Outer Retinal Layer Thickness and AMD Risk SNPs

Initially we tested the association between AMD susceptibility-increasing alleles and outer-retinal layer thickness measurements. We identified several nominally significant associations with average SD-OCT measurements (Table 3 – 2, Appendix C Table 12 – 1), of which 10 remained significant after multiple testing corrections ($p < 0.0004$ (0.05/(4 × 33)). The strongest association ($p = 3.34 \times 10^{-54}$) was observed between rs3138141, a variant located near the boundary between an intron and the third exon of the retinol dehydrogenase 5 (*RDH5*) gene and the average INL-ELM layer thickness (Table 3 – 2).

Very significant associations were also found between rs10922109 within the *CFH* gene ($p = 1.47 \times 10^{-49}$) and rs6565597 within the *NPLOC4-TSPAN10* gene ($p = 1.00 \times 10^{-38}$) and RPE-BM average layer thickness.

3.2.3 Central Outer Retinal Layer Thickness and AMD Risk SNPs

Associations with central SD-OCT measurements, approximated to represent the fovea were also discovered (Table 3 – 3, Appendix C Table 12 – 2). The statistically strongest association was found between ISOS-RPE layer thickness and the *RDH5* variant rs3138141 $p = 7.21 \times 10^{-46}$). Additionally, we also observed a strong association between the same marker (rs3138141; $p = 1.22 \times 10^{-44}$) and INL-ELM layer thickness. There was a significant association between RPE-BM layer thickness and the variant rs6565597 ($p = 5.12 \times 10^{-45}$) located in the intergenic region between the *NPLOC4* and *TSPAN10* genes.

3.2.4 Polygenic Risk Score (PRS)

Genes linked to AMD risk were strongly correlated with various measures of outer-retinal layer thickness. Notably, the central thickness of ISOS-RPE showed the most significant correlation with a cumulative PRS derived from AMD-associated variants, resulting in decreased thickness (beta = -0.52, $p = 1.37 \times 10^{-67}$). The incorporation of age, sex, and smoking status yielded only marginal enhancements to the predictive capacity of the model. However, AMD-related genes appeared to exert minimal influence on the variability of SD-OCT measurements, particularly when compared to factors such as smoking and age (Appendix C, Table 12 – 3). The AMD PRS accounted for only 0.2–6% of the variability in SD-OCT measurements. Generally, an elevated AMD-risk PRS was strongly linked to decreased thickness in layers containing the RPE (ISOS-RPE and RPE-BM, both centrally and on average), and to a lesser extent, with thickening in layers encompassing the external limiting membrane (INL-ELM and ELM-ISOS, both centrally and on average), albeit with less statistical significance.

3.2.5 Gene-Gene Interactions

We took the SNPs that were previously associated with any parameter of average and central outer-retinal layer thickness measurements, and specifically looked for non-linear gene by gene interactions of pairs of SNPs. Table 3 – 4 displays the results for all gene–gene interactions affecting outer retinal layer thickness. Interactions involving the *NPLOC4-TSPAN10* SNP rs6565597 appeared to correlate with notable changes in outer retinal layer thickness. Specifically, the interaction between the AMD-predisposing alleles *NPLOC4-TSPAN10* (rs6565597.T) and *CFH* (rs10922109.C) significantly increased the average thickness of the INL-ELM (Fig. 8–3) (beta = 0.25; p = 0.0004). However, this association did not maintain significance after correcting for multiple testing (p = 0.08).

Conversely, we observed that the interaction between the AMD-predisposing rs6565597 T allele (*NPLOC4-TSPAN10*) and the rs61985136 T allele (*RAD51B*) was nominally linked to a decreased central thickness of the ISOS-RPE layer. Nevertheless, this association did not remain significant after Bonferroni correction (beta = -0.23, p = 0.0009, Bonferroni-adjusted p = 0.15).

3.2.6 Mendelian Randomization

Mendelian randomization (MR) analyses were used to explore the causality of the observed associations between outer retinal thickness and AMD risk polymorphisms. Directional pleiotropic relationships were uncovered between AMD risk and various measurements of outer retinal layer thickness. As shown in Table 3 – 5 the results revealed a predisposition to AMD caused a significant decrease in the thickness of the central area of the ISOS-RPE layer (MR-Egger p = 0.04) with no evidence of pleiotropy (MR-Egger intercept p = 0.36). While there was some evidence linking AMD risk with measurements of other outer retinal layers in our dataset, these associations were not significant across all MR tests.

Table 3-2 Significant associations between average SD-OCT measurements and AMD variants

Chr	Variant	Gene	EA	NEA	*ELM-ISOS*			*INL-ELM*			*ISOS-RPE*			*RPE-BM*		
					Beta	SE	p-value	Beta	SE	p-value	Beta	SE	p-value	Beta	SE	p-value
1	rs10922109	CFH	C	A	0.018	0.011	0.1	−0.036	0.048	0.5	−0.26	0.03	6.63×10^{-20}	−0.322	0.022	1.47×10^{-49}
6	rs429608	PBX2	G	A	0.022	0.015	0.1	0.017	0.065	0.8	−0.19	0.04	6.08×10^{-07}	−0.08	0.03	0.01
6	rs943080	VEGFA	T	C	−0.003	0.011	0.8	−0.048	0.047	0.3	0.005	0.03	0.9	−0.084	0.021	8.83×10^{-05}
7	rs7803454	PILRA	T	C	0.029	0.014	0	0.199	0.059	0.0008	0.245	0.04	5.15×10^{-12}	−0.107	0.027	7.67×10^{-05}
9	rs10781182	RORB	T	G	0.001	0.012	1	0.215	0.051	2.11×10^{-05}	−0.05	0.03	0.1	0.024	0.023	0.3
10	rs3750846	ARMS2	C	T	0.014	0.013	0.3	0.074	0.057	0.2	−0.26	0.03	5.32×10^{-14}	−0.068	0.026	0.01
12	rs3138141	BLOC1S1 - RDH5	A	C	0.049	0.012	0.0001	0.824	0.053	3.34×10^{-54}	0.389	0.03	2.44×10^{-34}	0.091	0.024	0.0002
14	rs61985136	RAD51B	T	C	0.027	0.011	0.02	0.223	0.049	5.35×10^{-06}	0.038	0.03	0.2	−0.052	0.022	0.02
17	rs6565597	NPLOC4-TSPAN10	T	C	−0.039	0.015	0.0008	−0.374	0.05	8.76×10^{-14}	0.377	0.03	4.25×10^{-36}	−0.3	0.023	1.00×10^{-38}
19	rs2230199	C3	G	C	−0.019	0.014	0.2	−0.061	0.058	0.3	0.16	0.04	5.04×10^{-06}	0.042	0.027	0.1

Table 3-3 Significant associations between central SD-OCT measurements and AMD variants

Ch	Variant	Gene	EA	NEA	*ELM-ISOS*			*INL-ELM*			*ISOS-RPE*			*RPE-BM*		
					Beta	SE	p	Beta	SE	p	Beta	SE	P	Beta	SE	p
1	rs10922109	CFH	C	A	0.061	0.015	2.94×10^{-05}	0.016	0.075	0.8	−0.601	0.043	3.45×10^{-44}	−0.330	0.034	5.02×10^{-22}
4	rs10033900	CFI	T	C	0.025	0.014	0.08	0.023	0.074	0.8	−0.168	0.042	7.50×10^{-05}	0.032	0.034	0.3
6	rs429608	PBX2	G	A	0.012	0.020	0.6	−0.101	0.102	0.3	−0.450	0.059	1.92×10^{-14}	−0.030	0.047	0.5
7	rs7803454	PILRA	T	C	−0.017	0.018	0.4	0.187	0.094	0.05	0.127	0.054	0.02	−0.190	0.043	8.38×10^{-06}
10	rs3750846	ARMS2	C	T	0.047	0.018	0.01	0.102	0.090	0.3	−0.682	0.052	2.36×10^{-39}	0.011	0.041	0.8
12	rs3138141	BLOC1S1-RDH5	A	C	−0.032	0.016	0.05	1.178	0.084	1.22×10^{-44}	0.686	0.048	7.21×10^{-46}	0.129	0.038	0.001
14	rs61985136	RAD51B	T	C	0.048	0.015	0.001	0.324	0.077	2.93×10^{-05}	0.023	0.045	0.6	−0.027	0.035	0.4
17	rs6565597	NPLOC4-TSPAN10	T	C	−0.061	0.015	8.08×10^{-05}	−0.388	0.079	9.67×10^{-07}	0.407	0.046	4.20×10^{-19}	−0.509	0.036	5.12×10^{-45}
19	rs2230199	C3	G	C	−0.029	0.018	0.1	−0.068	0.092	0.5	0.275	0.053	2.15×10^{-07}	0.003	0.042	0.9

Columns “Variant”, “EA” and “NEA” list variants that were included in the model, and their risk alleles (EA, effect alleles for which the effect sizes are reported and NEA, non-effect alleles). Fields “Beta”, “SE” and “P” denote the change in SD-OCT measurements, standard errors and p-values of observed associations. The tables include significant linear regression results for 32,113 unrelated participants from UK Biobank participants. Models were adjusted for sex, age, spherical equivalent, smoking status.

Table 3-4 SD-OCT variance predicted by a model adjusted by for sex, age, spherical equivalent, smoking status and Polygenic Risk Score (PRS).
The model included SD-OCT measurements as dependent variables and PRS as an independent predictor. PRS was calculated using 33 AMD-associated variants. Columns "Beta", "SE" and "p-value" show the changes in the measurements per standard deviation in PRS dosage increase, and standard errors and p-values of the associations. Fields "R^2 (Null model)" and "R^2 (Model adjusted for PRS)" include R^2 of the null model, adjusted for sex, age, spherical equivalent and smoking status, and the model additionally adjusted for PRS.

Measurement	Beta	SE	p-value	PRS model R^2	Null model R^2
ELM-ISOS (average)	0.02	0.01	0.01	0.0668	0.0666
ELM-ISOS (center)	0.05	0.01	$2.39x10^{-06}$	0.0189	0.0183
INL-ELM (average)	0.10	0.03	0.004	0.0559	0.0556
INL-ELM (center)	0.14	0.05	0.006	0.0163	0.0160
ISOS-RPE (average)	-0.18	0.02	$3.46x10^{-20}$	0.0038	0.0012
ISOS-RPE (center)	-0.52	0.03	$1.37x10^{-67}$	0.0191	0.0098
RPE-BM (average)	-0.18	0.02	$7.21x10^{-34}$	0.0420	0.0376
RPE-BM (center)	-0.15	0.02	$9.58x10^{-11}$	0.0390	0.0378

Table 3-5 Results of linear models testing the effects of 10 most significant AMD SNP interactions on SD-OCT measurements.
Models were adjusted for sex, age, spherical equivalent, smoking status. Field "Variants" displays rs ID numbers and the risk alleles of the variants included in the interactions, that were nominally associated with outer-retinal layers. The column “Measurement” lists SD-OCT measurements that were tested. The columns "Beta","SE","p-value" and “Adjusted p-value” denote the change of SD-OCT measurements (in μm), standard errors, 95% confidence intervals, p-values and Bonferroni-corrected p-values for each tested interaction. The table includes results for 32,132 participants from UK Biobank participants.

Variants	Genes	Beta	SE	p-value	Measurement	Adjusted p-value
rs10922109_C * rs6565597_T	CFH NPLOC4-TSPAN10	0.25	0.072	0.0004	INL-ELM (average)	0.08
rs6565597_T * rs61985136_T	NPLOC4-TSPAN10 RAD51B	-0.23	0.068	0.0009	ISOS-RPE (center)	0.16
rs429608_G * rs61985136_T	PBX2 RAD51B	-0.15	0.058	0.008	ISOS-RPE (average)	1
rs3750846_C * rs429608_G	ARMS2 PBX2	0.29	0.113	0.01	INL-ELM (average)	1
rs6565597_T * rs61985136_T	NPLOC4-TSPAN10 RAD51B	-0.11	0.045	0.01	ISOS-RPE (average)	1
rs10922109_C * rs6565597_T	CFH NPLOC4-TSPAN10	0.28	0.114	0.01	INL-ELM (center)	1
rs61985136_T * rs429608_G	RAD51B PBX2	-0.21	0.087	0.02	ISOS-RPE (center)	1
rs6565597_T * rs10033900_T	NPLOC4-TSPAN10 CFI	-0.12	0.051	0.02	RPE-BM (center)	1
rs3750846_C * rs943080_T	ARMS2 VEGFA	-0.05	0.019	0.01	ELM-ISOS (average)	1
rs429608_G * rs943080_T	PBX2 VEGFA	0.22	0.092	0.01	INL-ELM (average)	1

Table 3-6 Results of Mendelian randomisation analyses testing the causal association between AMD and four different SD-OCT measurements.
Columns "Exposure" and "Outcome" include the names of the tested traits. Field "Method" lists the names of the tests that were used to assess causality. The columns "Estimate", "SE", "95% CI" and "p-value" denote respectively the MR models coefficients, standard errors and 95% confidence intervals computed by each method. The coefficient units denote the difference in SD-OCT measurements between AMD cases and controls. Statistically significant tests are shown in **bold** ($p \leq 0.05$). For an exposure to be associated with an outcome all MR tests need to be significant. Here this only applies to central ISOS-RPE thickness.

Exposure	Outcome	Method	Estimate	SE	95% CI		p-value
AMD	ISOS-RPE (center)	Simple median	-0.38	0.14	-0.65	-0.12	**0.005**
		Weighted median	-0.58	0.12	-0.82	-0.34	**1.61×10^{-06}**
		IVW	-0.34	0.13	-0.60	-0.09	**0.008**
		MR-Egger	-0.60	0.30	-1.18	-0.01	**0.04**
		(intercept)	0.04	0.04	-0.05	0.13	0.35
AMD	ELM-ISOS (center)	Simple median	0.04	0.03	-0.01	0.09	0.09
		Weighted median	0.05	0.01	0.02	0.08	**0.0003**
		IVW	0.05	0.01	0.02	0.07	**0.0003**
		MR-Egger	0.05	0.02	0.02	0.08	**0.003**
		(intercept)	0.00	0.01	-0.01	0.01	0.64
AMD	INL-ELM (center)	Simple median	0.24	0.14	-0.03	0.52	0.08
		Weighted median	0.08	0.07	-0.05	0.21	0.22
		IVW	0.08	0.06	-0.04	0.19	0.19
		MR-Egger	0.03	0.08	-0.13	0.18	0.75
		(intercept)	0.03	0.03	-0.03	0.08	0.33
AMD	RPE-BM (center)	Simple median	0.12	0.07	-0.01	0.25	0.08
		Weighted median	0.01	0.04	-0.06	0.08	0.77
		IVW	0.03	0.04	-0.04	0.10	0.40
		MR-Egger	-0.01	0.05	-0.10	0.09	0.91
		(intercept)	0.01	0.01	-0.01	0.04	0.31
AMD	ISOS-RPE (average)	Simple median	-0.15	0.07	-0.29	-0.02	**0.03**
		Weighted median	-0.14	0.07	-0.28	0.00	**0.05**
		IVW	-0.14	0.06	-0.26	-0.01	**0.03**
		MR-Egger	-0.21	0.14	-0.49	0.07	0.14
		(intercept)	0.01	0.02	-0.03	0.06	0.57
AMD	ELM-ISOS (average)	Simple median	0.03	0.02	-0.01	0.07	0.15
		Weighted median	0.02	0.01	0.00	0.05	**0.04**
		IVW	0.03	0.01	0.01	0.04	**0.01**
		MR-Egger	0.02	0.01	0.00	0.05	0.06
		(intercept)	0.00	0.00	-0.01	0.01	0.92
AMD	INL-ELM (average)	Simple median	0.23	0.09	0.05	0.41	**0.01**
		Weighted median	0.05	0.05	-0.04	0.15	0.29
		IVW	0.07	0.04	-0.02	0.15	0.12
		MR-Egger	0.02	0.06	-0.09	0.13	0.73
		(intercept)	0.02	0.02	-0.01	0.06	0.22
AMD	RPE-BM (average)	Simple median	0.07	0.05	-0.02	0.17	0.13
		Weighted median	-0.06	0.02	-0.11	-0.01	**0.02**

		IVW	-0.04	0.03	-0.11	0.02	0.16
		MR-Egger	-0.06	0.05	-0.15	0.03	0.20
		(intercept)	0.01	0.01	-0.02	0.03	0.65

3.3 Interpretation and Interim Discussion

This Chapter attempts to examine the correlation between AMD genetic variants and changes in outer retinal layer thickness within a large normal population. Our focus on the outer retina stemmed from the hypothesis that AMD-associated genes might impact the thickness of photoreceptor and RPE layers. Our findings unveil a discernible yet intricate relationship between outer retinal thickness and the presence of AMD risk SNPs. By scrutinizing changes in individual retinal layers instead of overall retinal thickness, we gain deeper insights into potential structural alterations.

Crucially, by studying individuals without AMD, rather than those already diagnosed, we can pinpoint structural changes that may precede the onset of the disease. By using Mendelian randomization modelling with AMD risk polymorphisms, we identified a statistically significant decrease in ISOS-RPE thickness. This consistent pattern persisted when retinal thickness was modelled using cumulative AMD risk in the form of a PRS. Notably, these findings held true even after adjusting for factors like age, sex, spherical equivalent, and smoking status, all known to influence retinal thickness [235, 252]. Thus, it can be inferred that AMD risk is causatively linked to thinner ISOS-RPE measurements in the general population in those without an AMD diagnosis. One plausible explanation for this is that AMD-related pathological processes may commence much earlier in life, with ISOS-RPE thinning serving as an early indicator of disease onset. The ISOS-RPE measurement serves as a surrogate for the POS. While there remains some debate regarding the anatomical correlates of the hyperreflective bands observed on OCT imaging [253], we observed significant thinning of this measurement, particularly centrally, in the presence of AMD risk SNPs. The POS comprises numerous infolded plasma membrane discs housing visual pigments. Inflammation and oxidative stress lead to a reduction in POS length [254], rendering it a marker of photoreceptor health. ISOS-RPE thinning emerged as the most profoundly significant change in our PRS analysis involving the presence of AMD risk SNPs. Notably, POS shortening has been documented in the normal fellow eyes of late AMD patients [255], and OCT scans in AMD patients show a reduction in photoreceptor layer thickness over time [256], further underscoring its relevance in understanding AMD progression. In the healthy retina, photoreceptors maintain a relatively stable length by continuously regenerating new outer segments from their base while simultaneously shedding mature outer segments, which are then engulfed by the RPE through phagocytosis. Alterations in the length of POS could stem from degeneration of photoreceptors preceding their death or changes in RPE phagocytosis efficiency. In AMD, rod photoreceptors degenerate before cones, particularly in the perifoveal region. Additionally, early in the disease process, before identifiable AMD fundus features emerge, there is evidence of delayed rod-mediated dark adaptation [257].

Such a shortening of POS may disrupt the retinoid cycle, leading to delayed rod-mediated dark adaptation. This delay could induce previously undetectable changes in the fundus of otherwise healthy individuals. POS shortening thus emerges as a potential biomarker for pre-disease AMD.

The PRS analysis also unveiled an association between a notable decrease in RPE-BM thickness associated with the presence of AMD risk SNPs. This finding holds particular significance in the context of AMD, as most clinical and histological manifestations initially manifest in the RPE and BrM. BrM is compromised in nAMD, and the accumulation of drusenoid deposits between the RPE and BrM represents one of the earliest signs of AMD. Additionally, BrM plays a vital role in maintaining photoreceptor health. Interestingly, aging has been linked to an increase in BrM thickness [258]. Prior studies have indicated that RPE-BM thickness decreases with age [236], suggesting that if BrM thickens, the RPE must undergo significant thinning as individuals age. The results presented here cannot definitively determine whether individuals with normal ocular health but possessing AMD risk polymorphisms exhibit prematurely thin RPE layers or thinner BrM. However, our analysis has intriguingly revealed that in the presence of a high genetic risk for AMD, there is a significant reduction in the thickness of both the ISOS-RPE and the RPE-BM. This observation suggests that premature thinning of the RPE may be a key contributing factor in the development of AMD.

We detected evidence supporting both additive and non-additive effects of several established AMD genetic loci on outer retinal thickness. Interestingly, we did not find any interactive or individual effects for the widely studied AMD risk SNPs rs1061170 (Y402H) in *CFH* or rs10490924 (A69S) in *ARMS2* on retinal layer thickness. However, we identified several gene–gene interactions, all involving the *NPLOC4-TSPAN10* SNP rs6565597. Specifically, we observed a statistically significant increase in the average thickness of the INL-ELM in the presence of AMD-predisposing alleles at the *CFH* (rs10922109) and *NPLOC4-TSPAN10* (rs6565597) loci. In this additive model, homozygosity for the *CFH* protective allele (AA) combined with the *NPLOC4-TSPAN10* risk allele (TT) resulted in a significant thinning of the INL-ELM (Figure 3 – 2). This finding suggests a notable influence of the *CFH* protective allele on INL-ELM thickness. The INL-ELM serves as a proxy measure encompassing synaptic terminals, axons, and the nucleus of photoreceptors, including the outer plexiform and outer nuclear layers. Interestingly, in this case, interactions involving AMD-predisposing alleles unexpectedly led to a thicker measurement, contradicting the overall trend towards thinning observed in most of our results.

Presence of the AMD risk-associated allele, rs6565597, appeared to generally cause a significant thinning of outer retinal layers in normal individuals in this study. Whether these changes to outer retinal thickness put individuals at an increased risk of AMD is currently not known. Interestingly, thinning of the RPE-BM layer correlates with the TEM data shown in Chapter 6, section 6.2.2 where TSPAN10 k.o hESC-RPE were significantly shorter than WT cells. We know that individuals with rs6565597 have reduced copy numbers of *TSPAN10*, if this translates into reduced levels of TSPAN10 protein this could help explain the result. Participants in this study were all of European ancestry, confirmed by their genetic data (see Chapter 2 section 2.28.2 for inclusion & exclusion criteria). Interestingly others have shown that black or mixed-race participants have a significantly thicker RPE-BM in comparison to white individuals regardless of age [236]. We know from our phenotypic data that TSPAN10 likely influences RPE pigmentation. Taken together this could help to explain our results. One interesting possibility would be to look at the RPE-BM thickness of individuals with albinism to understand if they have RPE-BM thinning.

Our analysis also revealed a thinning of both the layer representing the POS and that representing the RPE in the presence of AMD risk SNPs. Consequently, it is highly plausible that individuals with ostensibly normal ocular examinations, yet carrying AMD risk alleles, may harbour previously undetected changes to these layers prior to the onset of symptoms.

One limitation of this work is the potential misclassification of AMD status. The average age of the Biobank cohort is 56.58 ± 7.98 years; hence, there could be individuals with early fundal signs of AMD who were unaware of their condition at the time of recruitment. Additionally, it would have been insightful to ascertain if any of the participants had a family history of AMD, but unfortunately, this information was not available in the UK Biobank dataset. Therefore, we regard the studied population as "normal" in the population-based context, where AMD or other retinopathies are anticipated to be exceedingly rare and unlikely to significantly alter the properties of the population distribution, which constituted the primary focus of this work.

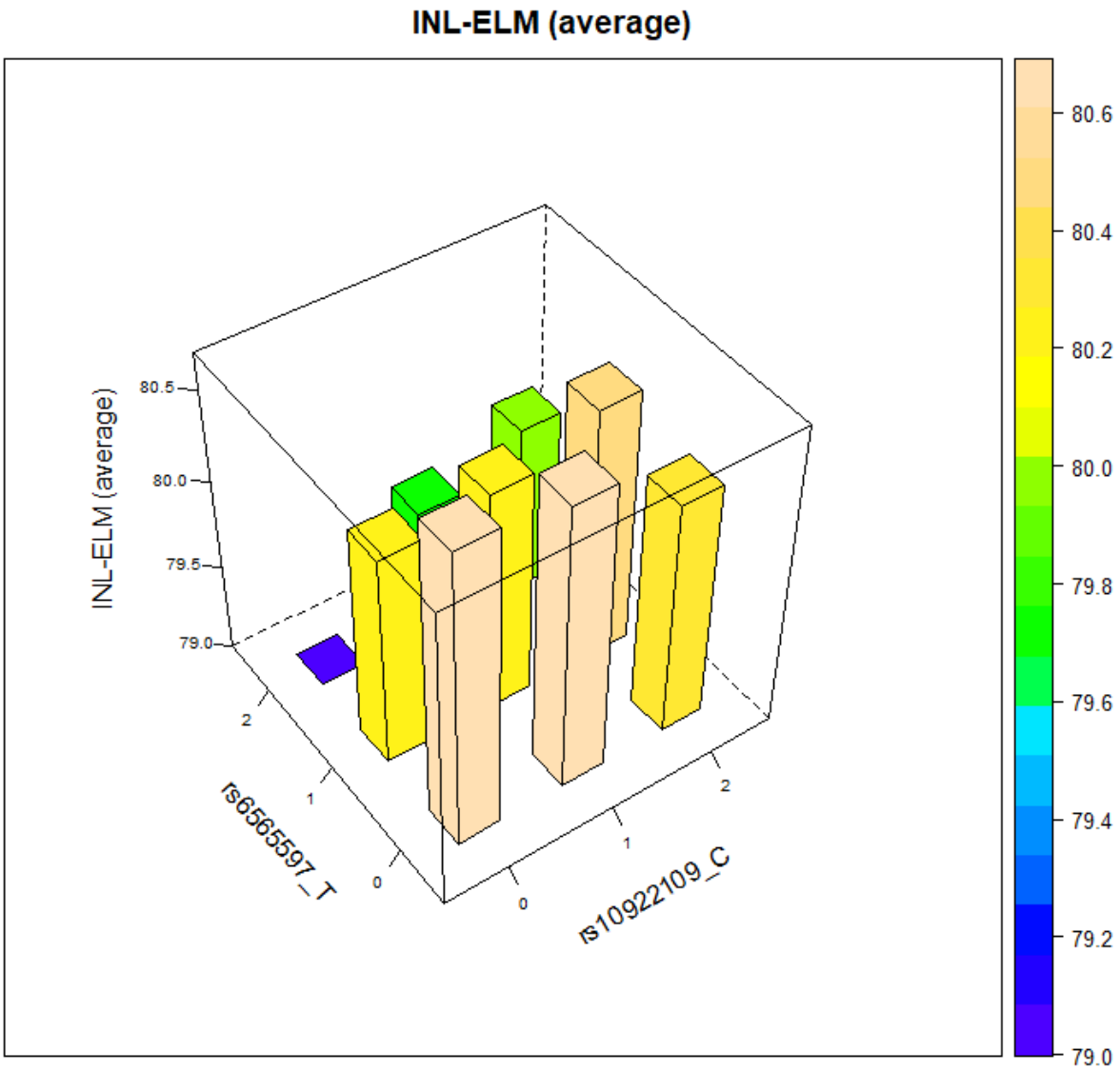

rs6565597_T (NPLOC4-TSPAN10); rs10922109 (CFH);

p=0.0004; Adjusted p-value=0.08

Figure 3-2 Association of the INL-ELM thickness with two common AMD-associated genetic polymorphisms (rs10922109 and rs6565597)
The dosage of the AMD-predisposing alleles at these SNP loci (C and T respectively) is shown in the x- and y-axes. Values of 0, 1 and 2 denote number of the AMD risk alleles present in individual genotypes (i.e. risk allele is not present, heterozygous or homozygous genotypes for that allele respectively). The average INL-ELM thickness for each combination of these genotypes is given in the z-axis (for the sake of clarity the minimum was set to 79.0 μm).
Reproduced from Kaye et al (2021) [150] under the terms of the Creative Commons Licence.

4 Generation of Clonal hESC derived RPE using Crispr/Cas9

4.1 Generation of a TSPAN10 knock out human embryonic stem cell (hESC) clone (Objective 1a)

The CRISPR/Cas9 plasmid px459-EF1α (V2.0 Addgene, # 62988) encodes two expression cassettes: the unaltered Cas9 endonuclease from S. pyogenes (SpCas9) and a single guide RNA (sgRNA) (see Appendix A Figure 10 - 1). The architecture of pX459 is such that a pair of annealed oligonucleotides, complementary to the 20-nucleotide target site and its 3' PAM, can be seamlessly cloned in to create a complete CRISPR expression vector containing the sgRNA of choice ("pX459-gRNA"; see Figure 4 – 1). An individual CRISPR expression vector can be created for each sgRNA, as required.

The px459 vector used was previously adapted by the Zeng laboratory to encode a wild type Cas9 enzyme fused with two nuclear localisation signals (NLS) to increase the efficiency of Cas9 import into the nucleus, as depicted in Figure 4 – 1 [194]. px459 also includes a puromycin resistance cassette to allow antibiotic selection. Furthermore, the usual chicken β-actin promoter in px459 was adapted, the promoter used in this study was EF1α [218] to enhance expression in hESCs (px459-EF1α). The px459 encodes a U6-sgRNA cassette with a BbsI site for cloning our target specific sgRNA to then obtain a final plasmid. The sgRNA is cloned at the BbsI restriction site upstream and adjacent to the sgRNA scaffold. U6 is the RNA polymerase III promoter driving the expression of small hairpin RNAs in this case the Cas9 sgRNA expression.

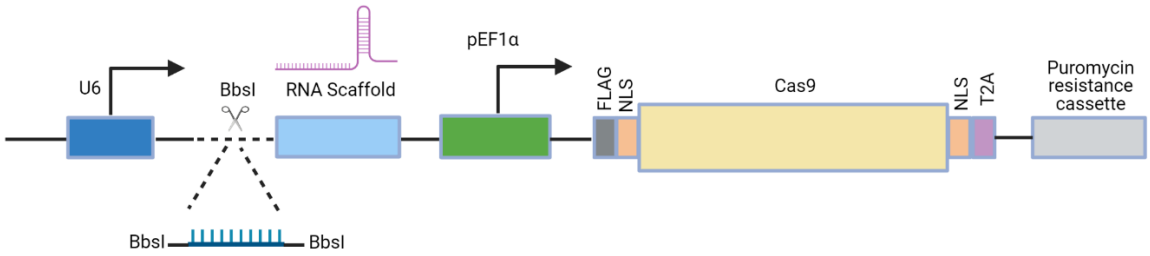

Figure 4-1 Schematic depicting edited px459 plasmid to include the EF1α promoter
Image created using Biorender.

To generate biallelic indel mutations in *TSPAN10* a CRISPR strategy which utilised the NHEJ pathway (see Figure 1 – 10 in Chapter 1) was sufficient. This pathway can introduce random indels into the target gene and requires only SpCas9 and the sgRNA. Two sgRNAs were used independently to generate TSPAN10 k.o clones, to control for both Cas9 failure and off-target mutagenesis. The Benchling CRISPR design tool was used to design sgRNAs. Within the constraint of being adjacent to an "NGG" PAM site, the sgRNAs were selected on the basis of having a high MIT and CFD specificity score (as close to 100 as

possible; see description in section 1.6 of Chapter 1), thereby indicating high on- and low off – target activity, see section 2.1.1, Table 2 – 1 for relevant scores.

TPSAN10 is encoded by a relatively short DNA sequence and contains only four exons. Six transcripts are encoded, of which five are produced and three are protein coding (Table 4 – 1). All generated and protein coding transcripts contain exon 2, therefore this region was selected as a target site. There is one methionine present in exon 2 at 81,637,486bp. Upstream of this start codon was targeted by sgRNAs to target the open reading frame and allow generation of a frameshift mutation and subsequently, k.o or scramble the protein.

Table 4-1 TSPAN10 Transcripts
All transcripts encoded by TSPAN10, taken from ENSEMBL. Six transcripts are encoded, of which four are protein coding, all of which contain the targeted ATG at exon 2.

Name	BP	Protein	Biotype	Contains Exon 2 ATG
TSPAN10-203	1840	355aa	Protein Coding	Yes
TSPAN10-205	2330	235aa	Protein Coding	Yes
TSPAN10-206	1856	355aa	Protein Coding	Yes
TSPAN10-204	1868	235aa	Nonsense mediated decay	Yes
TSPAN10-202	1896	No protein	Processed transcript	No
TSPAN10-201	1716	No protein	Retained intron	Yes

The *TSPAN10* sequence was also examined for alternative AUG codons, as leaky translation initiation from up- [259, 260] or down-stream [261, 262] start codons has been documented for other genes. Table 4 – 2 lists the locations of all AUG codons within or just upstream of the*TSPAN10* coding sequence and the lengths and molecular weights of proteins that could arise if they were to initiate translation, although there is currently no evidence of translation initiation from an alternative AUG in *TSPAN10*.

Table 4-2 AUG Translation Initiation Codons within the human TSPAN10 transcript
The canonical start codon is shaded green; positions are with respect to the A of the AUG codon within the full-length 1182 bp coding sequence and 393 amino acid protein. Non-AUG start codons can initiate translation, but these can take different forms and so could not be identified [263].

Exon	Position in protein	Resulting protein length (aa)	Predicted protein MW (kDa)
1	1	393	40.82
2	39	354	36.65
3	159	234	24.3

The two sgRNAs designed are displayed in Table 4 – 3 alongside their MIT specificity, CFD specificity and Rule Set 2 on-target efficiency scores (descriptions of which are given in section 1.6 of Chapter 1). Figure 4 – 2 depicts the alignment of the two sgRNAs with the target region.

Table 4-3 gRNAs used for CRISPR/Cas9 Gene Editing
PAM is underlined; MIT and CFD specificity scores are calculated by different methods to predict likelihood of Cas9 cleavage at off-target loci; Rule Set 2 on-target specificity score indicates likelihood of Cas9 cleavage at the target locus.

sgRNA	Target exon	gRNA sequence + PAM	MIT specificity score	CFD specificity score	Rule Set 2 on-target efficiency score
JL	2	CCAGCGTCAAGGATGGAGGAGGG	54	73	62
Assembly 2	2	TGTTCCAGCGTCAAGGATGGAGG	74	88	63

Following introduction of sgRNAs into the plasmid px459, mini-prep to extract DNA and Sanger sequencing was performed to select plasmids containing the correct sequence. Two were selected for maxi-prep, JL-6 and Assembly 2,2. Both JL-6 and Assembly 2,2 contained the forward and reverse sequences for their respective sgRNAs as depicted in Figures 4 – 3 and 4 – 4.

Primers were designed using Benchling for genotyping of exon 2 in TSPAN10 and PCR conditions optimised. Combinations of primer pairs were tested at varying annealing temperatures (see Appendix D, Table 13 – 1, Figure 13 – 1). Primer pair TSPAN10 Genotyping Forward 1 + TSPAN10 Genotyping Reverse 3 at 62°C annealing was selected.

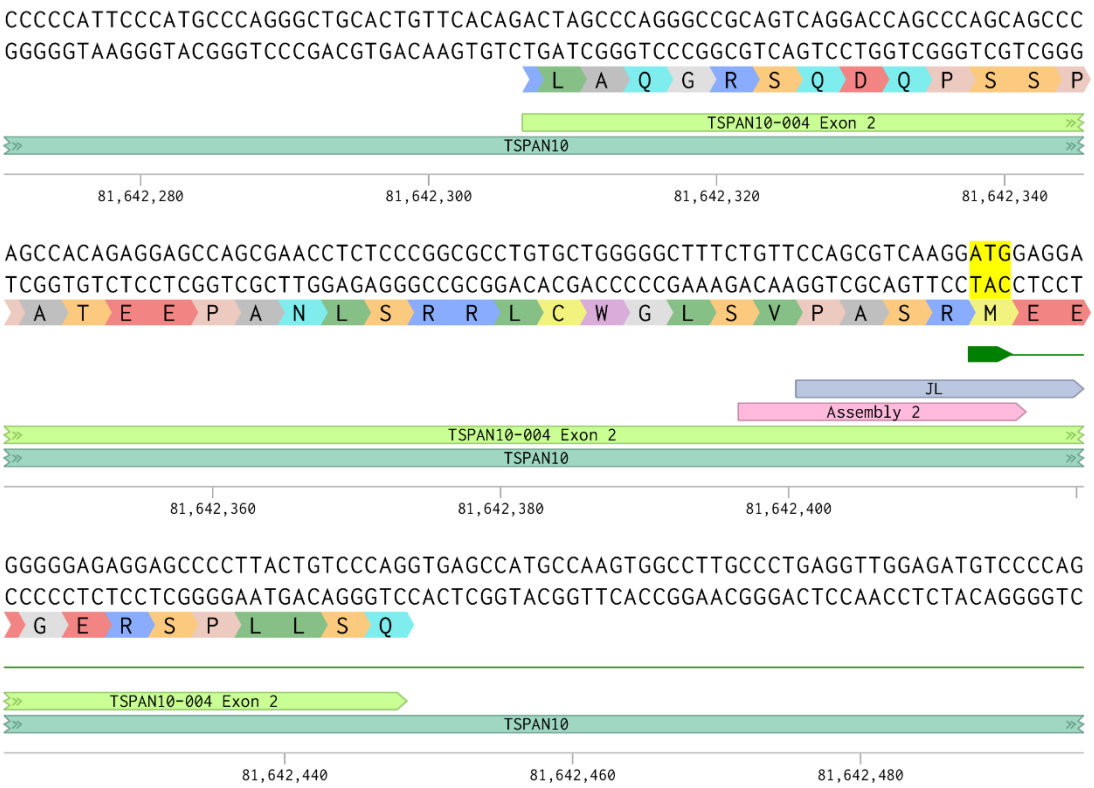

Figure 4-2 Snapshot of annotated genomic DNA for TSPAN10 Exon 2
The ATG Methionine (M) is highlighted in yellow. The two guides JL and Assembly 2 are depicted in lilac and pink respectively, showing their alignment with the target region.
Image generated in Benchling

hESCs were cultured as described in Chapter 2 and plasmid DNA JL-6 and Assembly 2,2 introduced into cells via electroporation. Cell colonies were selected using puromycin selection and surviving single cells expanded. Genomic DNA (gDNA) was extracted from cell clones that survived puromycin selection and therefore presumed to contain plasmid DNA.

PCR for TSPAN10 gDNA was performed and the PCR product from those samples with bands sent for Sanger sequencing (Figure 4 – 5). Two cell clones, A2 and A12 were found to contain indels in the target region. Both clones were homozygous for indels, with A2 containing a 7 bp deletion and A12 a 1 bp insertion (Figure 4 – 5). Predicted k.o scores were calculated for both clones and found to be 100% and 99%, respectively (Table 4 - 4) [222]. Knock-outs were predicted to occur through NMD due to a PTC more than 50 to 55 nucleotides upstream of the final exon-exon junction (Figure 4 – 6) [213]. These two clones were taken forward to the next stage for differentiation into RPE.

Cell clone name	KO-Score (%)	KI-Score	R^2	Guide Sequences
A11 JL6	22	None	0.97	CCAGCGTCAAGGATGGAGGA
A9 JL6	0	None	1	CCAGCGTCAAGGATGGAGGA
A12 JL6	99	None	0.99	CCAGCGTCAAGGATGGAGGA
A2 JL6	100	None	1	CCAGCGTCAAGGATGGAGGA
A1 jl6	34	None	0.95	CCAGCGTCAAGGATGGAGGA
A8 JL6	42	None	0.97	CCAGCGTCAAGGATGGAGGA
B2 Assembly 2	0	None	1	TGTTCCAGCGTCAAGGATGG
B5 Assembly 2	0	None	1	TGTTCCAGCGTCAAGGATGG
B3 Assembly 2	0	None	1	TGTTCCAGCGTCAAGGATGG
B8 Assembly 2	0	None	1	TGTTCCAGCGTCAAGGATGG
B10 Assembly 2	0	None	1	TGTTCCAGCGTCAAGGATGG
B6 Assembly 2	0	None	1	TGTTCCAGCGTCAAGGATGG
B9 Assembly 2	0	None	1	TGTTCCAGCGTCAAGGATGG

Table 4-4 Knock out scores for human embryonic stem cell (hESC) clones
Sanger sequencing reads were input into Synthego [222] and knock-out scores calculated. (A) clones contain the sgRNA JL-6 and (B) clones the sgRNA Assembly 2. No B-clones were successful. Two A clones, A12 and A2 (highlighted in green) produced high knock-out scores.

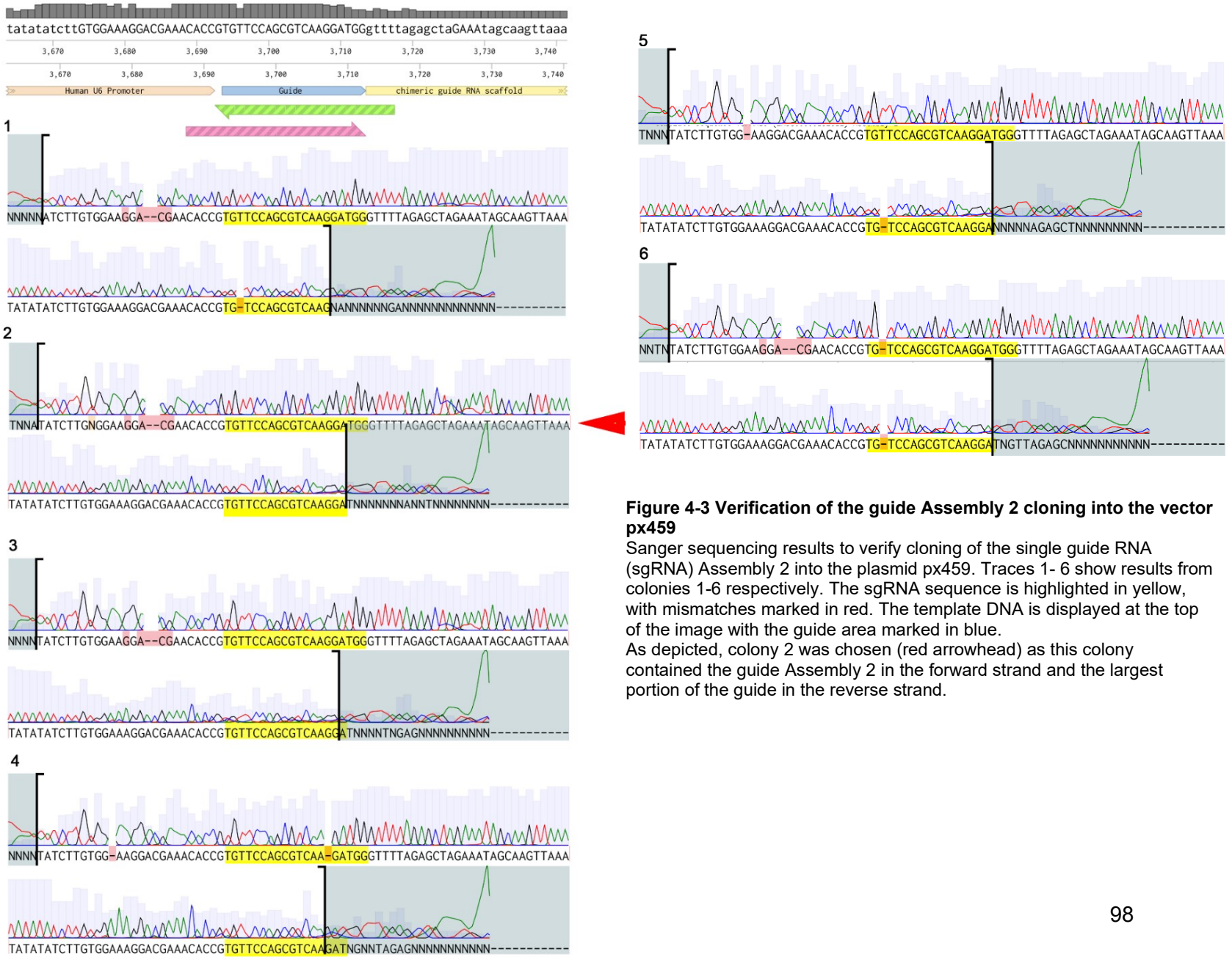

Figure 4-3 Verification of the guide Assembly 2 cloning into the vector px459
Sanger sequencing results to verify cloning of the single guide RNA (sgRNA) Assembly 2 into the plasmid px459. Traces 1- 6 show results from colonies 1-6 respectively. The sgRNA sequence is highlighted in yellow, with mismatches marked in red. The template DNA is displayed at the top of the image with the guide area marked in blue.
As depicted, colony 2 was chosen (red arrowhead) as this colony contained the guide Assembly 2 in the forward strand and the largest portion of the guide in the reverse strand.

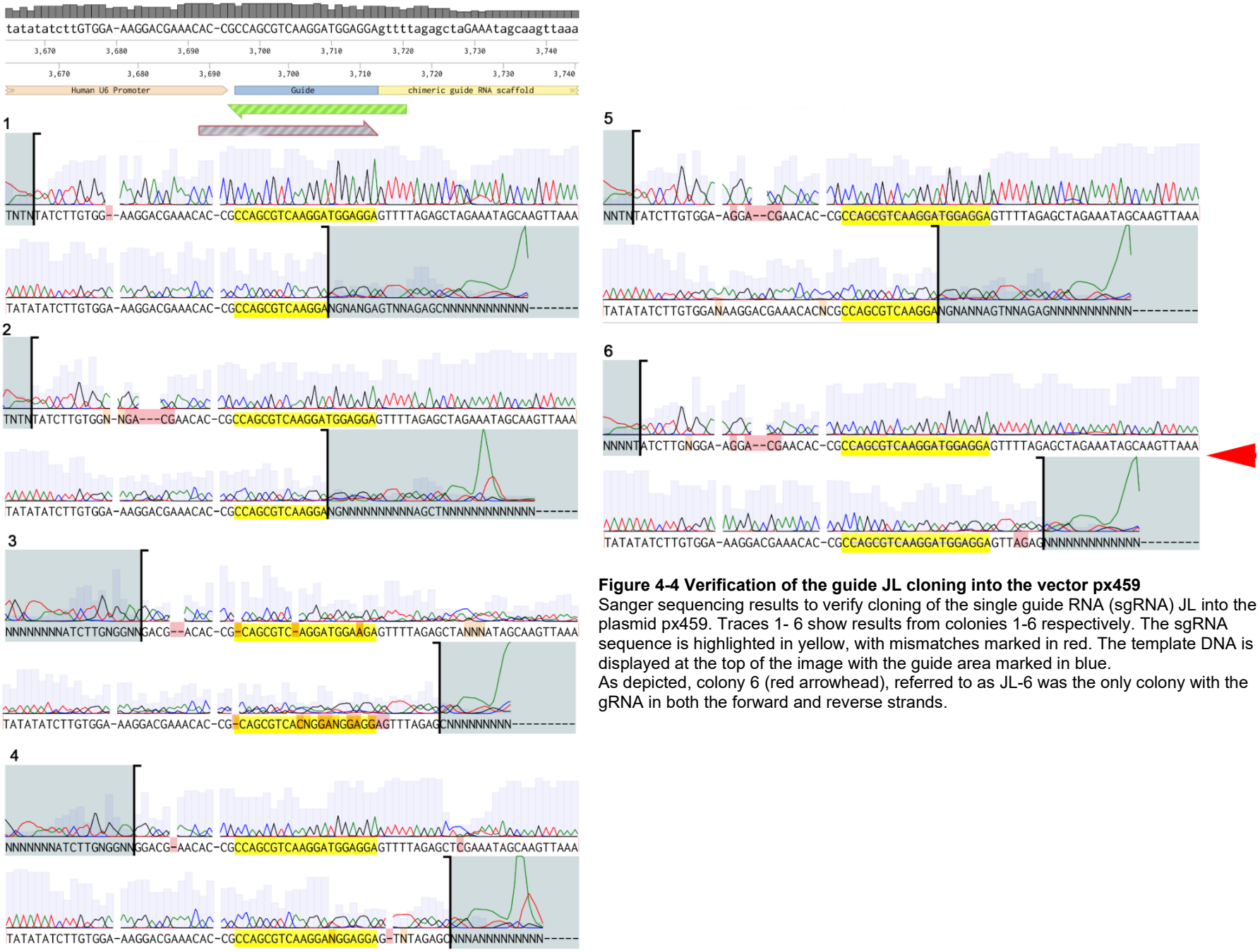

Figure 4-4 Verification of the guide JL cloning into the vector px459
Sanger sequencing results to verify cloning of the single guide RNA (sgRNA) JL into the plasmid px459. Traces 1- 6 show results from colonies 1-6 respectively. The sgRNA sequence is highlighted in yellow, with mismatches marked in red. The template DNA is displayed at the top of the image with the guide area marked in blue.
As depicted, colony 6 (red arrowhead), referred to as JL-6 was the only colony with the gRNA in both the forward and reverse strands.

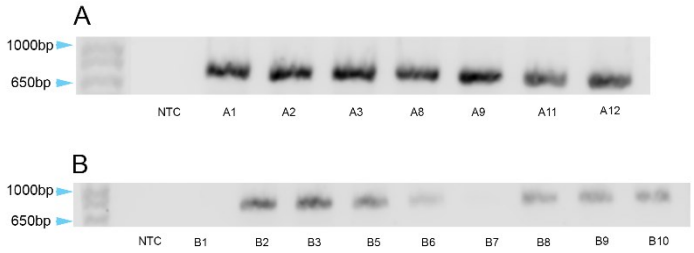

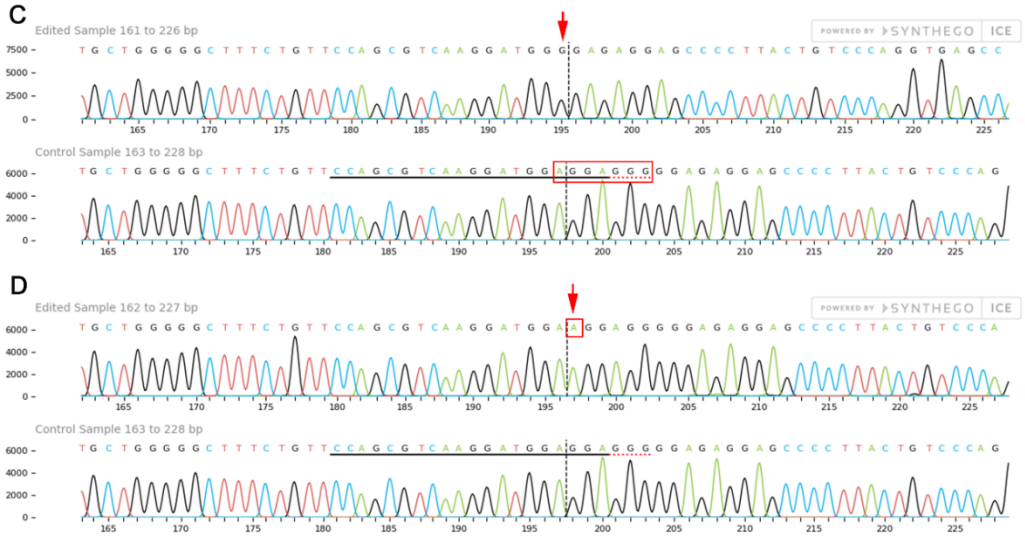

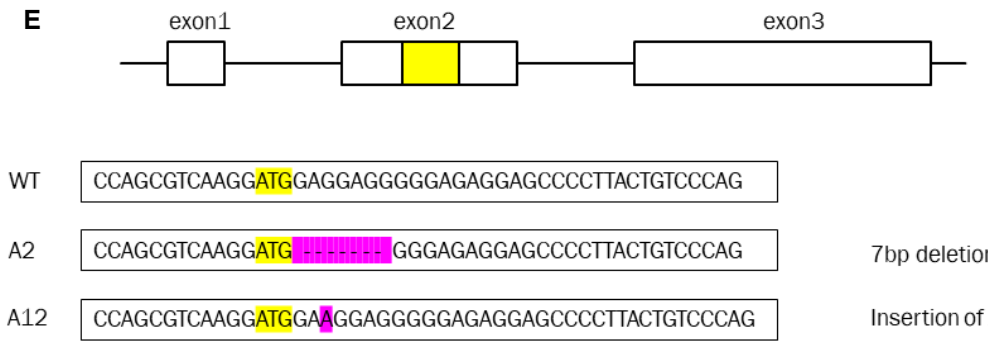

Figure 4-5 Selecting embryonic stem cell (hESC) clones with TSPAN10 insertions and/or deletions (indels)

A&B Polymerase Chain Reaction (PCR) using TSPAN10 primers to genotype hESC clones electroporated with plasmid px459 containing sgRNA.

- **(A)** Clones A1-A12 were generated using CRISPR plasmid px459 containing the single guideRNA (sgRNA) JL-6.
- **(B)** Clones B1-B10 were generated using CRISPR plasmid px459 containing the sgRNA Assembly 2,2.
- **(C)** **Sanger sequence traces for hESC clone A2** (top sequence) vs WT (bottom sequence). 7 bp deletion from 194 bp in clone A2 outlined in red.
- **(D)** **Sanger sequence traces for hESC clone A12** (top sequence) vs WT (bottom sequence). 1 bp insertion of A at 197 bp in clone A12 outlined in red.
- **(E)** **Schematic demonstrating genomic DNA insertions/deletions present in hESC clones.** WT sequence with ATG region highlighted. A2 clone sequence with 7 bp deletion emphasised in purple. A12 clone sequence with insertion of A highlighted in purple.

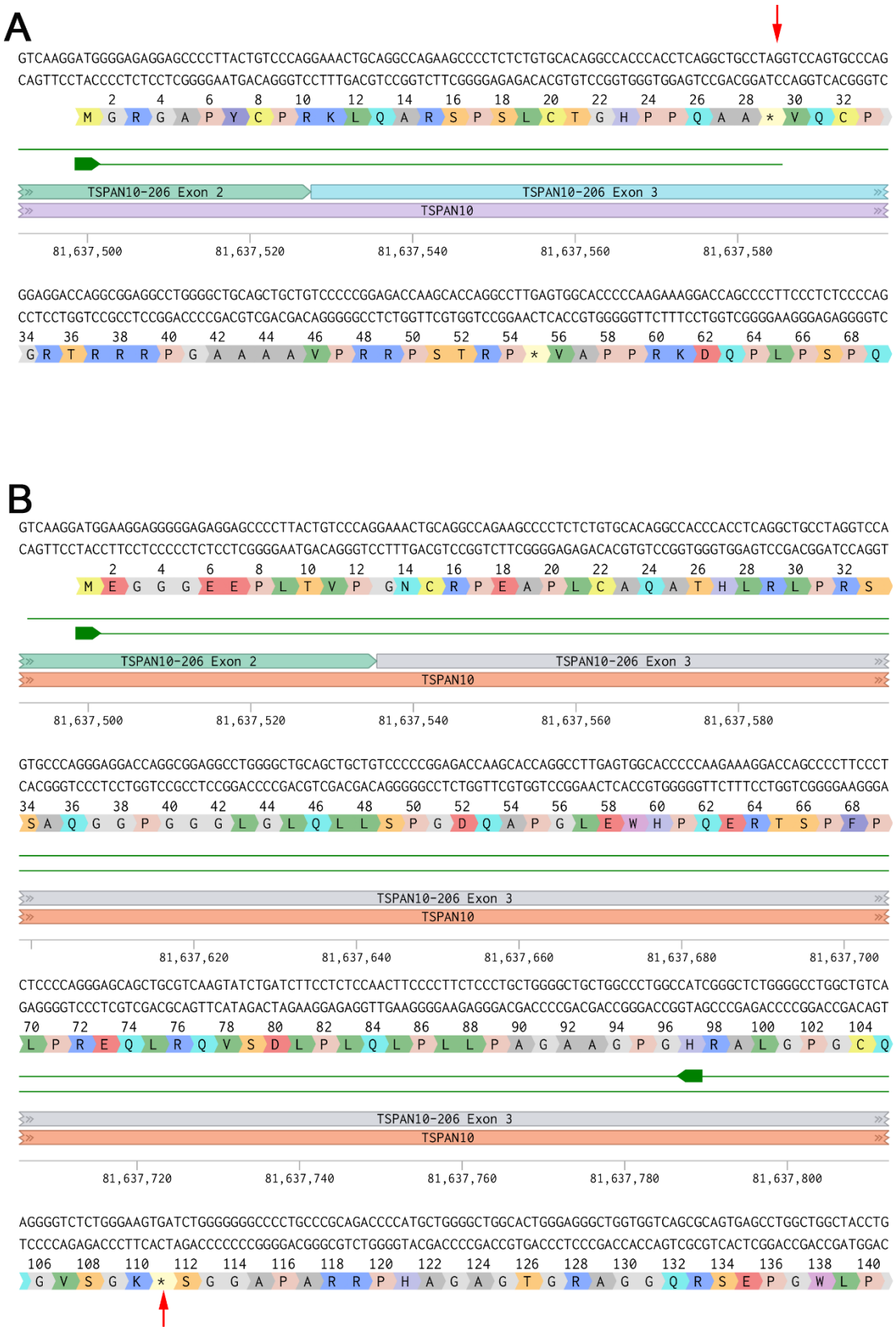

Figure 4-6 Schematics demonstrating the result of indels on the coding sequence in TSPAN10 k.o cells
Snapshots of TSPAN10 coding sequence post CRISPR/Cas9 modification for clones A2 and A12.
Red arrows highlight the first PTC for each clone.
A: Proposed resultant transcript for A2
B: Proposed resultant transcript for A12

4.1.1 Confirmation of hESC pluripotency

Following the production of the hESC CRISPR Cas9 mediated cell clones A2 and A12 immunofluorescence microscopy was performed to confirm markers of pluripotency. Cells were grown on laminin coated coverslips for 2 - 3 days, fixed with 4% PFA and stained for the pluripotency markers SOX2 and NANOG (Chapter 2, Table 2 – 3). Both clones showed expression of SOX2 and NANOG in addition to displaying typical embryonic stem cell morphology (Figure 4 – 7). Subsequently, both cell clones were taken forward for differentiation to RPE.

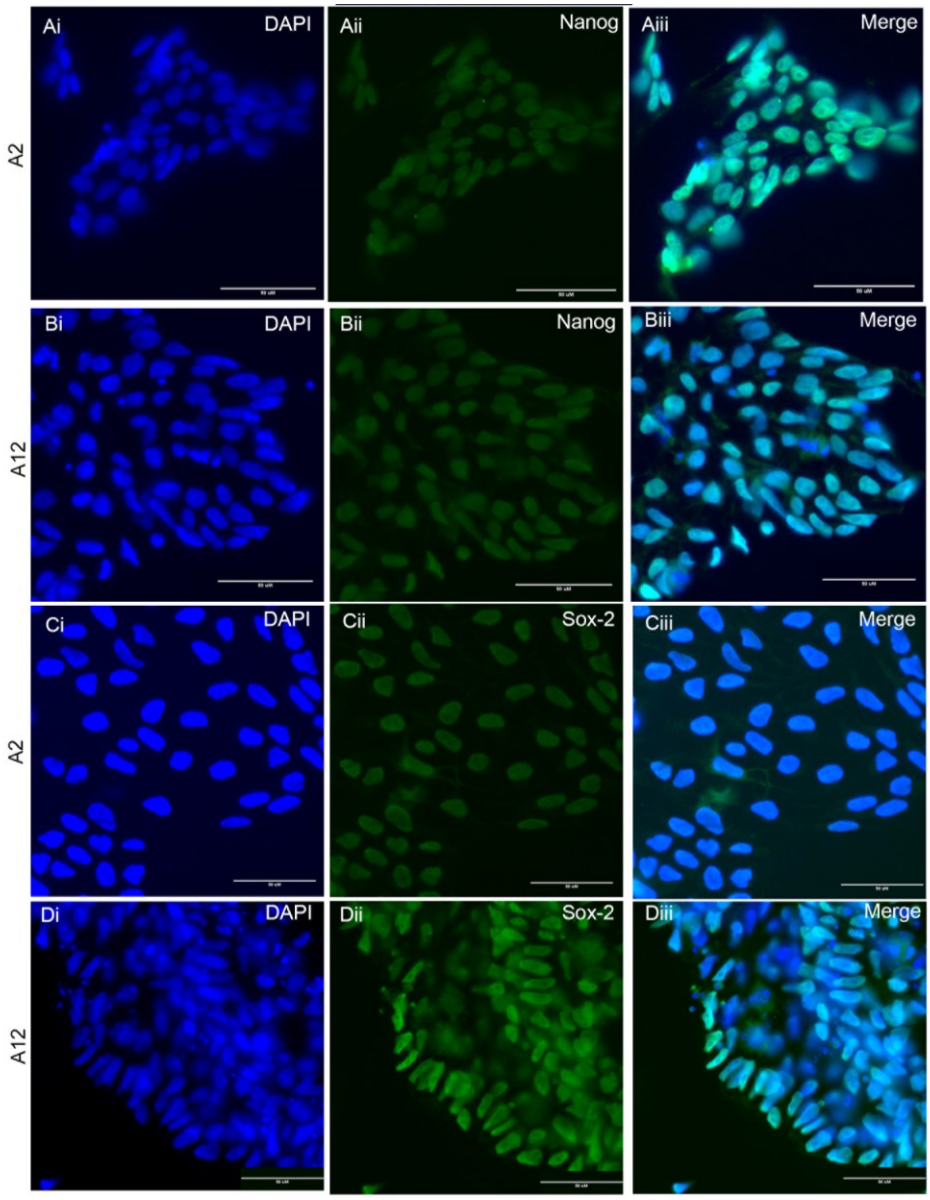

Figure 4-7 Immunocytochemistry of human embryonic stem cells (hESCs) for pluripotency markers
Immunofluorescence images illustrating the expression of pluripotency markers in hESCs. Nuclei are counterstained with DAPI (blue).
Ai-Aii. A2 express the pluripotency marker NANOG
Bi-Bii. A12 express the pluripotency marker NANOG
Ci-Cii. A2 express the pluripotency marker SOX-2
Di-Dii. A12 express the pluripotency marker SOX-2
Abbreviations: DAPI; 4',6-diamidino-2-phenylindole. Scale bars represent 50μm.

4.2 Generation of hESC-derived RPE (Objective 1b)

To differentiate hESCs into RPE a directed differentiation method was selected (see Chapter 1 section 1.5.4 and Chapter 2, section 2.12 for detail). The directed differentiation method was amended to remove use of antimicrobial agents. Antimicrobials have been shown to reduce both the growth rate and differentiation of hESCs [264]. Furthermore, the effects of antimicrobials on differentiations would be a variable unaccounted for in transcriptomic and further analysis, given that antimicrobials are known to alter gene expression and regulation [265].

Three separate differentiations were generated for each of WT, A2 (100% KO) and A12 (99% KO) to allow for robust comparison. Differentiation is a lengthy process with multiple steps over a period of 84 days. A detailed report of the steps involved is reported in section 2.12. Figures 4 – 8 & 4 – 9 highlight various stages in the initial differentiation process including identification of unwanted cell types, such as neural patches that were manually removed. Cells were initially stained for PAX6 an early eye field marker (data not shown) however, this did not distinguish between neural retina progenitor cells, the main contaminators. A key transcription factor in RPE differentiation is MITF [266], consequently, cells were stained with MITF to distinguish phenotypic features of those inducted into an RPE fate. In addition to neural patches identified at day 19, cells grouped into rosette structures did not stain for MITF (Figure 4 – 9) and were consequently removed from cultures using a P200 pipette.

Stem cell derived RPE initially resemble foetal RPE in culture (Figure 4 – 10). At this early stage (day 31 of the directed differentiation protocol) cells appear disordered and are significantly less pigmented (Figure 4 – 10). At day 31 cells do not have the classical hexagonal RPE shape, although immunocytochemistry for tight junction markers such as zonula occludens-1 (ZO-1) shows some semblance of a hexagonal shape (Figure 4 – 11). Furthermore, at this early stage they express key RPE transcription factors, such as Orthodenticle Homeobox 2 (OTX2) and MITF (Figures 4 – 12 & 4 – 13). RPE were cultured for a minimum of 35 – 40 days post completion of the directed differentiation protocol [60] to obtain a mature phenotype (Figure 4 – 14).

Figure 4 – 15 portrays an overview of the steps involved in directed differentiation and the time points at which certain RPE markers are seen.

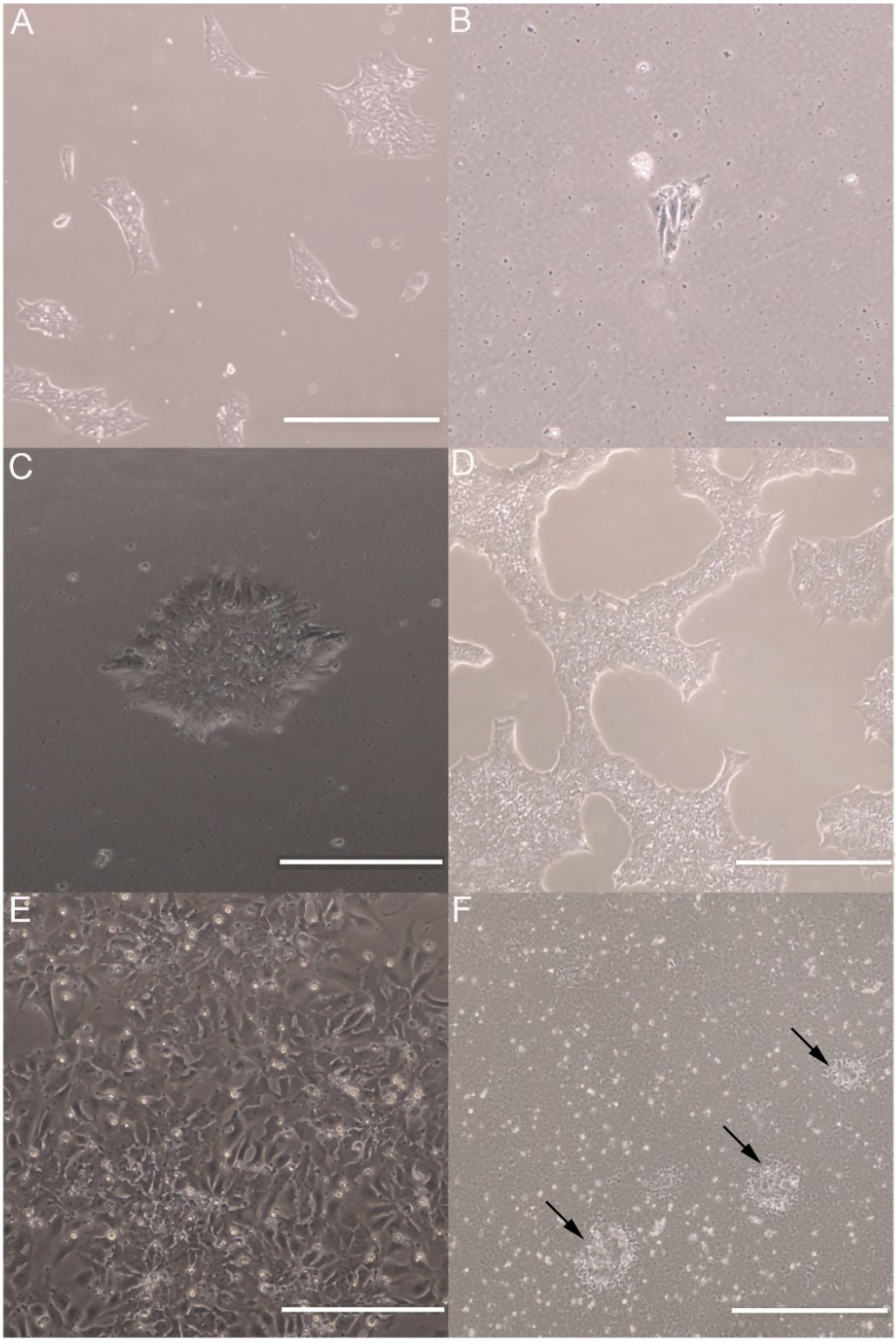

Figure 4-8 Phase contrast imaging of human embryonic stem cells (hESCs) and directed differentiation to retinal pigment epithelium (RPE)
A: WT hESCs day 2 post passage (4x)
B: Single cells day 2 post puromycin treatment (10x)
C: Single cell colonies day 5 post puromycin treatment. (10x)
D: CRISPR/Cas-9 edited cell clone A2 hESCs prior to directed differentiation (4x), day 4 post passage
E: Day 1 directed differentiation. (20x)
F: Day 19 directed differentiation, black arrows show large clumps which most likely correspond with neural rosettes. (4x)
Scale bars in A,D,F represent 600µm. Scale bars in B-C 250µm. Scale bar in E 125µm

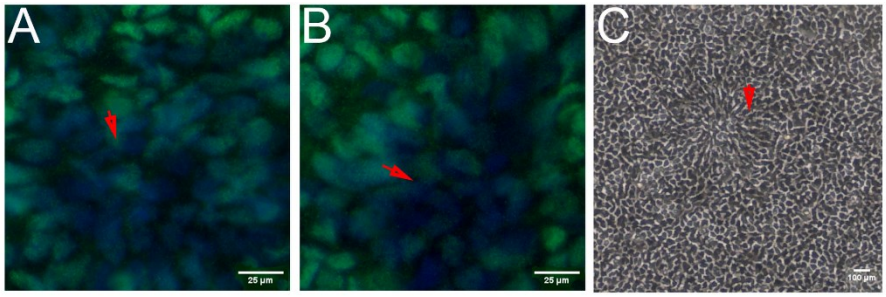

Figure 4-9 Identification and removal of non-RPE cell types
A & B. Representative staining of MITF (green) and DAPI (blue) in nuclei. Red arrows identify absence of MITF staining in rosette shaped structures at Day 25 differentiation. Scale bars represent 25µm.
C Phase contrast image of differentiating hESC-RPE in culture at Day 25 directed differentiation. Red arrow highlights rosette arrangement of cells corresponding with images A & B. Scale bar represents 250µm.

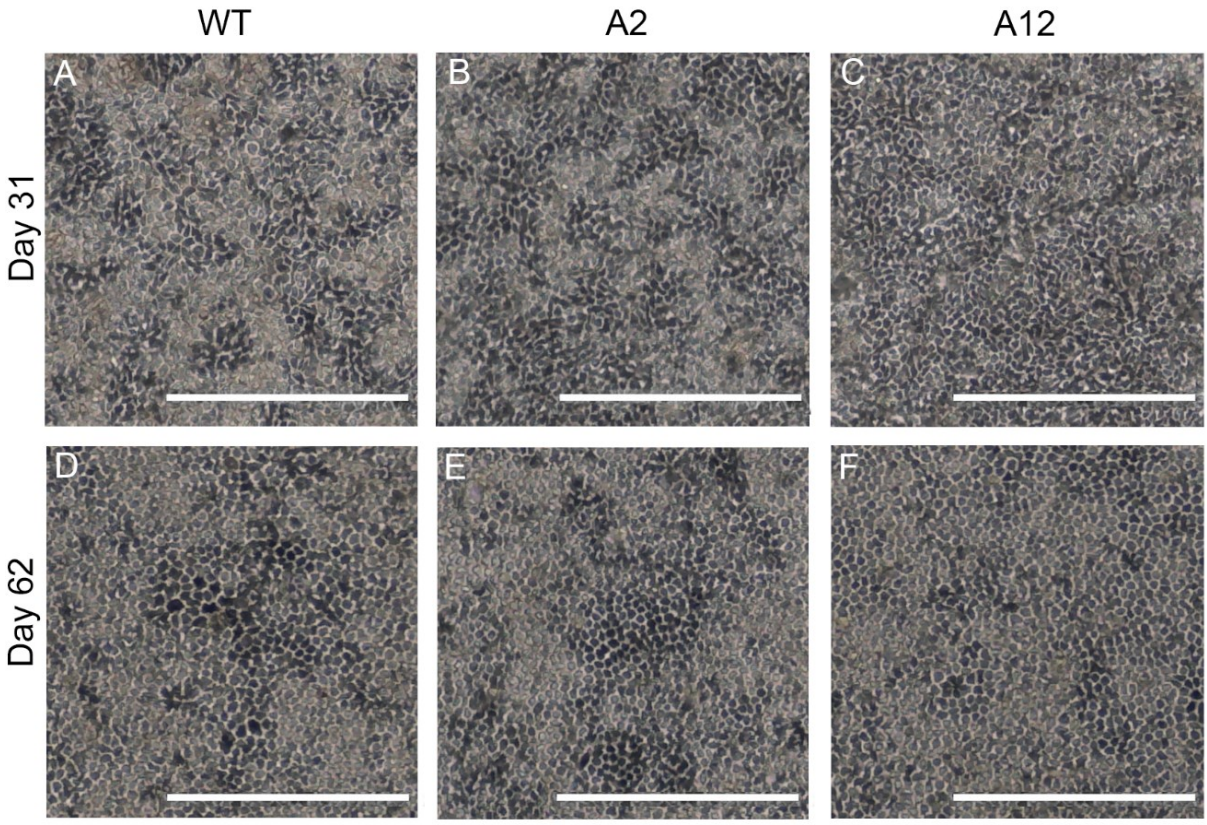

Figure 4-10 Phase contrast imaging of human embryonic stem cells (hESCs) during directed differentiation to retinal pigment epithelium (RPE) days 31-62
Images **A-C** show clumping of cells with layering. Areas of possible pigmentation evident. Cells are developing a more hexagonal shape. Cells appear disordered.
Images **D-F** show increased hexagonal appearance of cells with areas of darker pigmentation.
Scale bars represent 250 µm

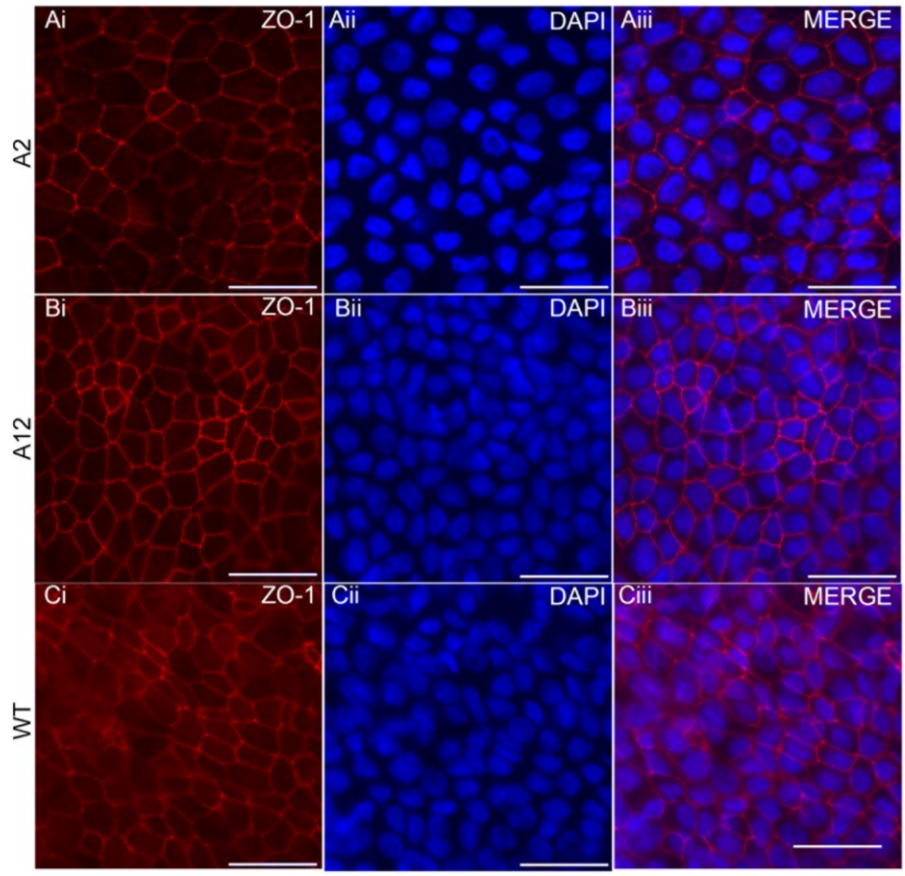

Figure 4-11 Immunocytochemistry of human embryonic stem cell (hESC) derived retinal pigment epithelium (RPE) at day 35 differentiation for ZO-1.
Ai, Bi, Ci Staining of tight junctions with ZO-1 (red). ZO-1 localised to cell-cell junctions in both WT and TSPAN10 k.o cells. Some cells display hexagonal morphology. No difference is evident between WT and TSPAN10 k.o cells.
Aii, Bii, Cii Nuclear DAPI stain (blue)
Aiii, Biii, Ciii. Merged images of ZO-1 and DAPI stains.
Abbreviations: DAPI; 4',6-diamidino-2-phenylindole. Scale bars represent 25μm
Immunocytochemistry performed for three differentiations from all three clones (n=9).

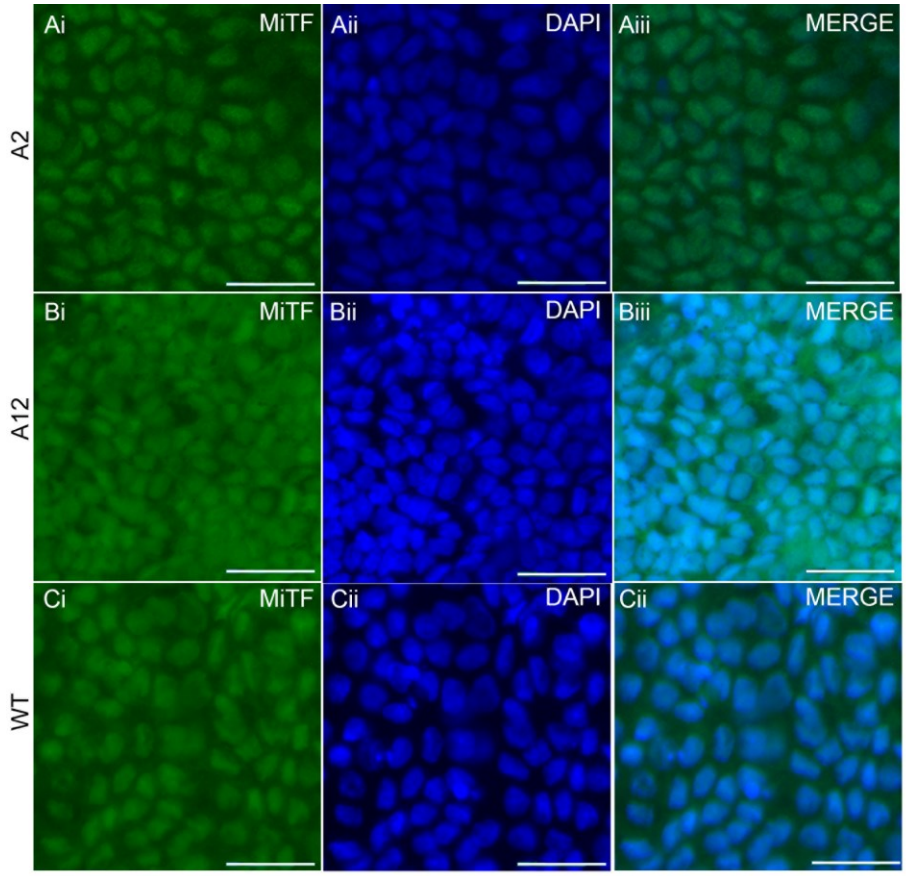

Figure 4-12 Immunocytochemistry of human embryonic stem cell (hESC) derived retinal pigment epithelium (RPE) at day 35 differentiation for MITF.
Ai, Bi, Ci Staining for MITF a key regulator of RPE differentiation, localised to the nucleus (green). No difference is evident between WT and TSPAN10 k.o cells.
Aii, Bii, Cii Nuclear DAPI stain (blue)
Aiii, Biii, Ciii. Merged images of MITF and DAPI stains.
Abbreviations: DAPI; 4',6-diamidino-2-phenylindole. Scale bars represent 25μm
Immunocytochemistry performed for three differentiations from all three clones (n=9).

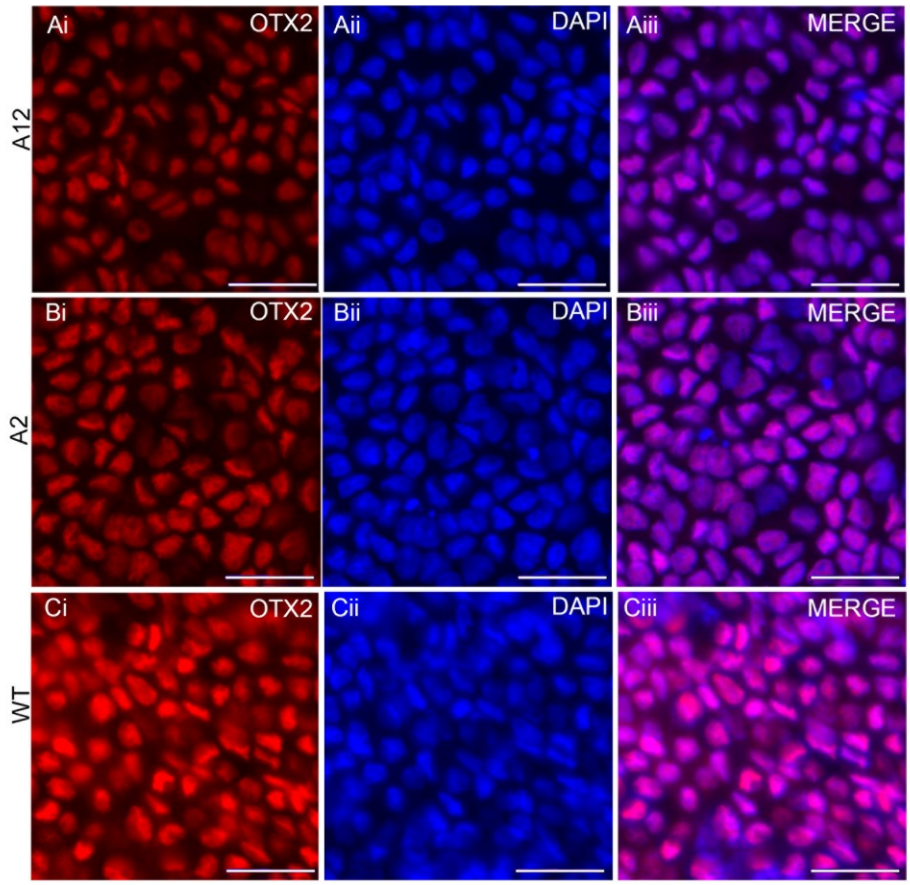

Figure 4-13 Immunocytochemistry of human embryonic stem cell (hESC) derived retinal pigment epithelium (RPE) at day 35 differentiation for OTX2.
Ai, Bi, Ci Staining for OTX2 a key regulator of RPE differentiation, localised to the nucleus (red). No difference is evident between WT and TSPAN10 k.o cells.
Aii, Bii, Cii Nuclear DAPI stain (blue)
Aiii, Biii, Ciii. Merged images of MITF and DAPI stains.
Abbreviations: DAPI; 4',6-diamidino-2-phenylindole. Scale bars represent 25µm
Immunocytochemistry performed for three differentiations from all three clones (n=9).

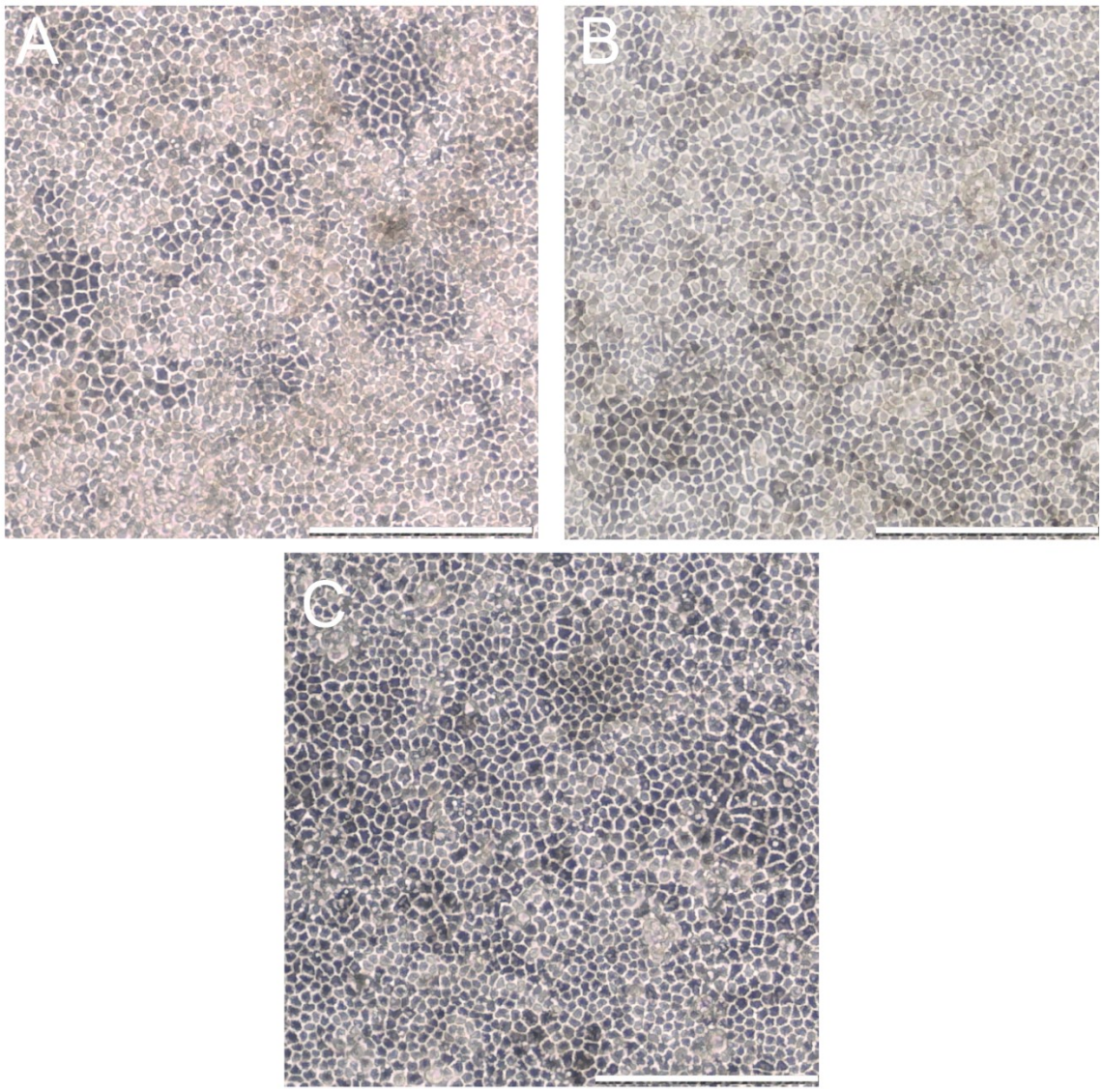

Figure 4-14 Phase contrast imaging of human embryonic stem cell derived retinal pigment epithelium (hESC-RPE) day 110 directed differentiation.
A: Clone A2 day 110.
B: Clone A12 day 110.
C: Wild type (WT) cells day 110.
All images show hexagonal shaped cells with a cobblestone morphology and varying degrees of pigmentation. WT cells (**C**) appear more pigmented than A2 (**A**) & A12 (**B**).
Scale bars represent 250 μm

Figure 4-15 Stages in directed differentiation of retinal pigment epithelium (RPE) cells from human embryonic stem cells (hESCs)
Timeline demonstrating various characteristics of hESC-RPE during directed differentiation. At Day 1 characteristic hESC are seen. Day 7-10 shows disorganised immature cells. By day 19 cells have started to resemble immature RPE. At day 35 cells resemble RPE and immunocytochemistry staining for RPE markers confirms this. Abbreviations: OTX2, Orthodenticle Homeobox 2; MITF, Melanocyte inducing transcription factor; ZO-1, Zonula occludens – 1; TSPAN10, Tetraspanin 10.

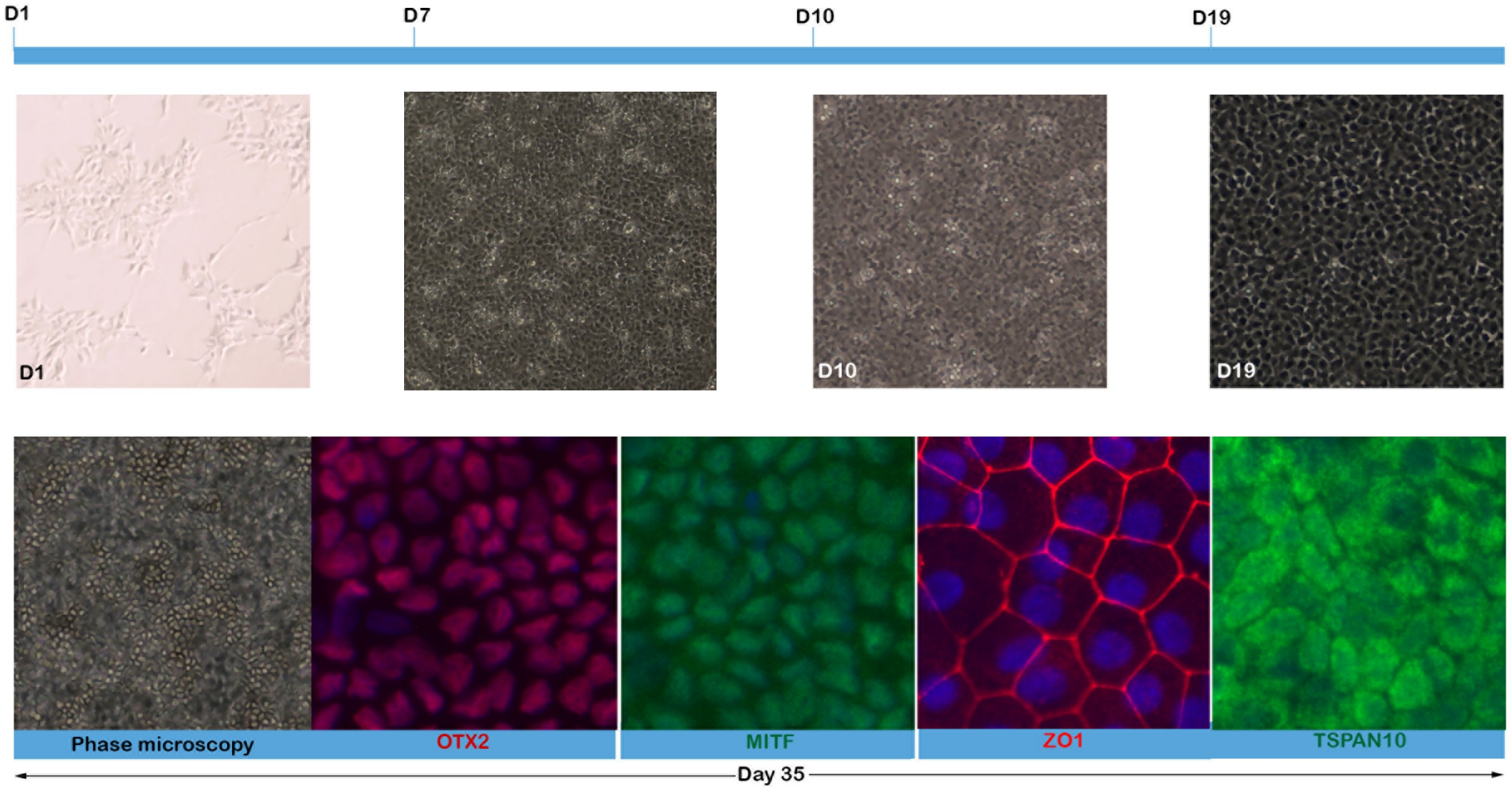

4.2.1 Karyotyping of CRISPR/Cas9 edited cell clones

ESCs in long term culture can develop and accumulate recurrent genomic abnormalities and copy number variations that can be detrimental to basic research. Some copy number variations can lead to selective advantages and reduce differentiation capacities, subsequently it is important to monitor and verify the genomic integrity of hESC cultures as a key measure of quality control. Furthermore, CRISPR/Cas9 gene editing can introduce unwanted genomic abnormalities.

CRISPR/Cas9 edited hESCs were therefore karyotyped. Karyotyping was performed by the Wessex Medical Institute therefore no credit can be taken for this work. Array comparative genome hybridization showed no new pathogenic mutations in either A2 or A12. A deletion in chromosome 7 in the *DFNA5* gene, classified as a variant of uncertain significance, was identified in both TSPAN10 mutants and WT and is therefore unlikely to have been introduced by long-term passage or gene editing (see Appendix D, Figures 13 – 2 & 13 – 3 for karyotyping results). This change in the *DFNA5* gene is most likely a genetic trait of the blastocyst from which the mastershef7 hESC line is derived.

4.2.2 Screening of predicted gRNA off-target loci for mutagenesis

For each gRNA designed, potential off-target loci were predicted using the Cas OFF finder algorithm (http://www.rgenome.net/cas-offinder/) and a mismatch cut-off of three employed. The generated lists of off targets that were output by Cas OFF finder were ranked by number of mismatches. Table 4 – 5 lists the top nine predicted off - target loci. Primers were designed to sequence the top nine predicted off - target loci and PCR performed (see Appendix D, Figure 13 – 4) [218]. PCR reactions with amplicons of the expected product size were examined by Sanger sequencing (Figure 4 – 16). A 7 bp deletion was seen at off target site 4 in the TSPAN10 k.o A2. This was input into the genome browser Ensembl and the sequence ‘BLASTed’ [267]. The 7 bp deletion is at an intergenic location, with no known regulatory variants or SNPs at the site, it was therefore concluded to be non – pathogenic. A substitution of C->G was also seen at off target site 3 in both TSPAN10 mutants and WT cells. Again, this was in an intergenic region and given its presence in WT cells was deemed to be a normal variant, although no SNPs have been reported at this location. Examination in the UCSC genome browser [268] revealed a G at this position is also seen in the Rhesus monkey, Elephant and Dog, meaning it’s not highly conserved and therefore unlikely to be a regulatory sequence.

Table 4-5 Top nine predicted off target loci
PAM is underlined; mismatches between the sgRNA on-target and off-target sequences are shown in red; the chromosome and position at which the off-target site is found are reported in addition to the strand. The column off target refers to the name given to each specific locus for the purpose of this thesis.

Off-target DNA sequence + PAM	Chromosome	Position	Direction	Mismatches	Off Target
CCAGCACCAAGGAGGGAGGAAGG	chr8	1914086	+	3	5
TCAGCGTCAAGGATGAAGGATGG	chr5	142223136	-	2	4
CCAGCTTTGAGGATGGAGGAAGG	chr20	59505209	-	3	9
CCAGTGTCAAGGCTTGAGGATGG	chr2	148592319	+	3	2
CCAGAGTAAAGGATGGAGGAAGG	chr2	168339209	+	2	1
CCAGGGTCAGGGGTGG	chr12	89392162	+	3	7
CCAGCAGCAAGGATGGTGGAGGG	chr4	189658739	-	3	3
CCAGCGGGAAGGATGCAGGAAGG	chr17	14974956	-	3	8
CCAGCTTCAAAGATGGAGGGAGG	chr10	3180569	-	3	6

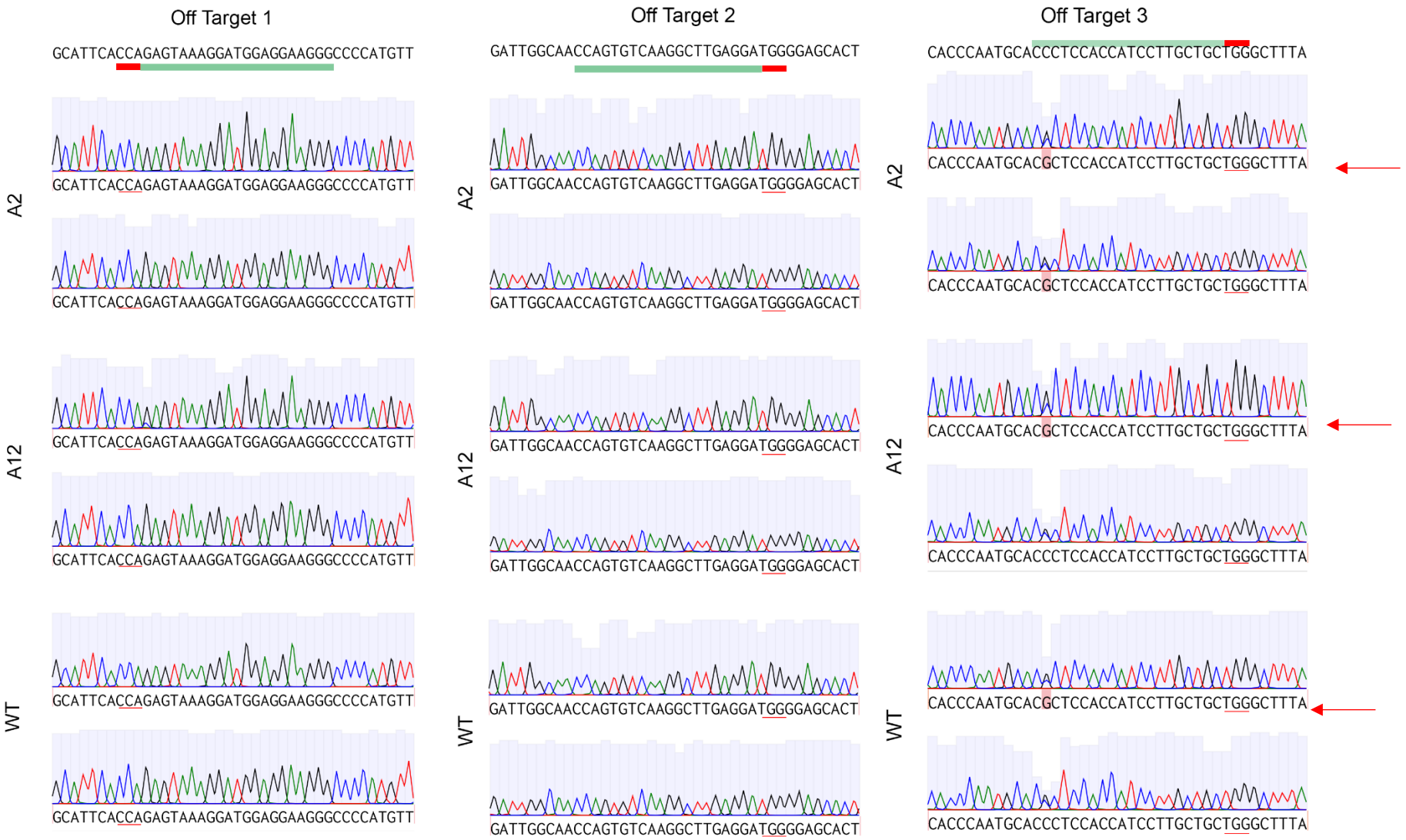
Off Target 1
GCATTCACCAGAGTAAAGGATGGAGGAAGGGCCCCATGTT
A2
GCATTCACCAGAGTAAAGGATGGAGGAAGGGCCCCATGTT
GCATTCACCAGAGTAAAGGATGGAGGAAGGGCCCCATGTT
A12
GCATTCACCAGAGTAAAGGATGGAGGAAGGGCCCCATGTT
GCATTCACCAGAGTAAAGGATGGAGGAAGGGCCCCATGTT
WT
GCATTCACCAGAGTAAAGGATGGAGGAAGGGCCCCATGTT
GCATTCACCAGAGTAAAGGATGGAGGAAGGGCCCCATGTT
Off Target 2
GATTGGCAACCAGTGTCAAGGCTTGAGGATGGGGAGCACT
A2
GATTGGCAACCAGTGTCAAGGCTTGAGGATGGGGAGCACT
GATTGGCAACCAGTGTCAAGGCTTGAGGATGGGGAGCACT
A12
GATTGGCAACCAGTGTCAAGGCTTGAGGATGGGGAGCACT
GATTGGCAACCAGTGTCAAGGCTTGAGGATGGGGAGCACT
WT
GATTGGCAACCAGTGTCAAGGCTTGAGGATGGGGAGCACT
GATTGGCAACCAGTGTCAAGGCTTGAGGATGGGGAGCACT
Off Target 3
CACCCAATGCACCCTCCACCATCCTTGCTGCTGGGCTTTA
A2
CACCCAATGCACGCTCCACCATCCTTGCTGCTGGGCTTTA
CACCCAATGCACGCTCCACCATCCTTGCTGCTGGGCTTTA
A12
CACCCAATGCACGCTCCACCATCCTTGCTGCTGGGCTTTA
CACCCAATGCACCCTCCACCATCCTTGCTGCTGGGCTTTA
WT
CACCCAATGCACGCTCCACCATCCTTGCTGCTGGGCTTTA
CACCCAATGCACCCTCCACCATCCTTGCTGCTGGGCTTTA

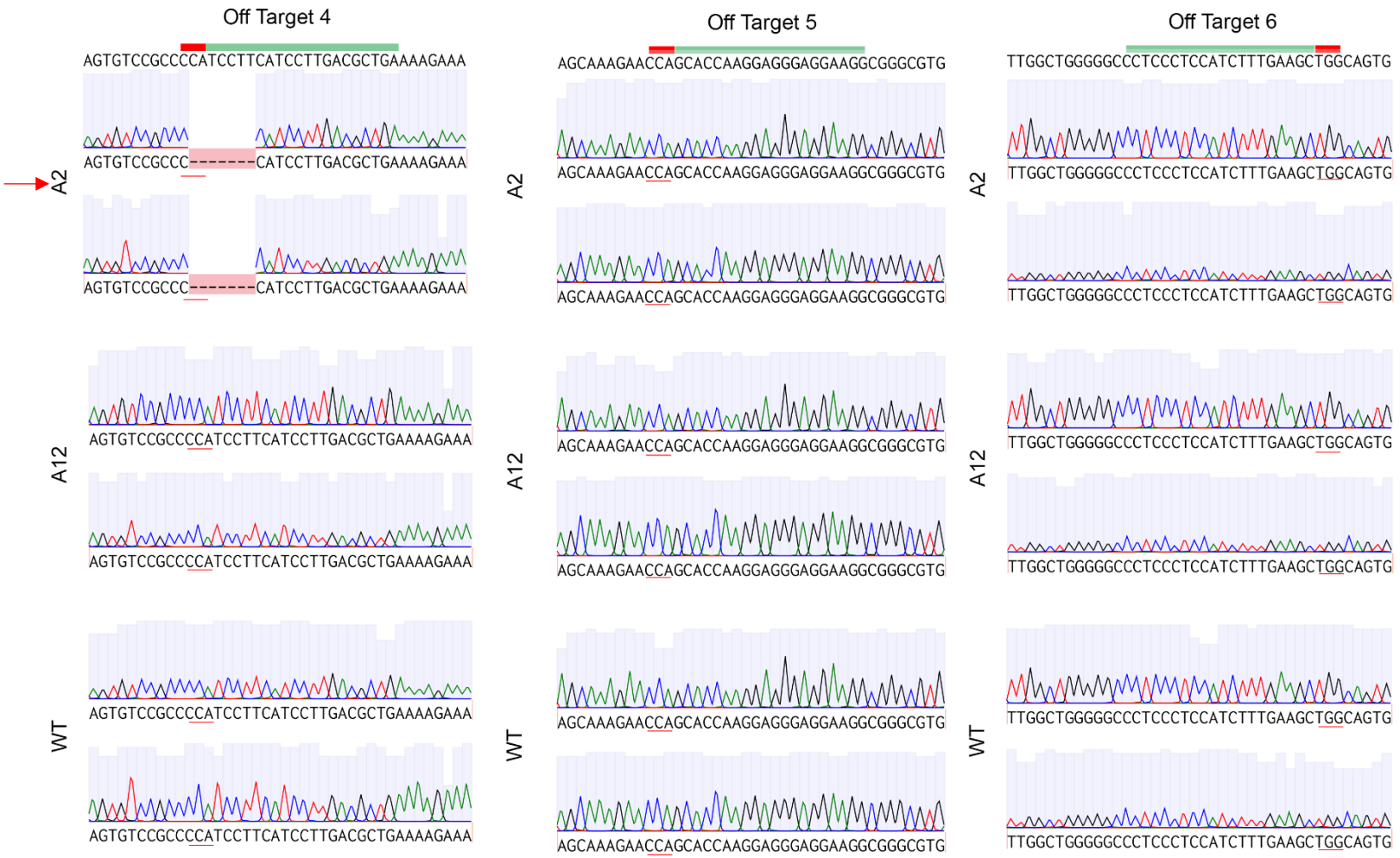
Off Target 4
Off Target 5
Off Target 6
A2
A12
WT
AGTGTCCGCCCCATCCTTCATCCTTGACGCTGAAAAGAAA
AGTGTCCGCCC-------CATCCTTGACGCTGAAAAGAAA
AGCAAAGAACCAGCACCAAGGAGGGAGGAAGGCGGGCGTG
TTGGCTGGGGGCCCTCCCTCCATCTTTGAAGCTGGCAGTG

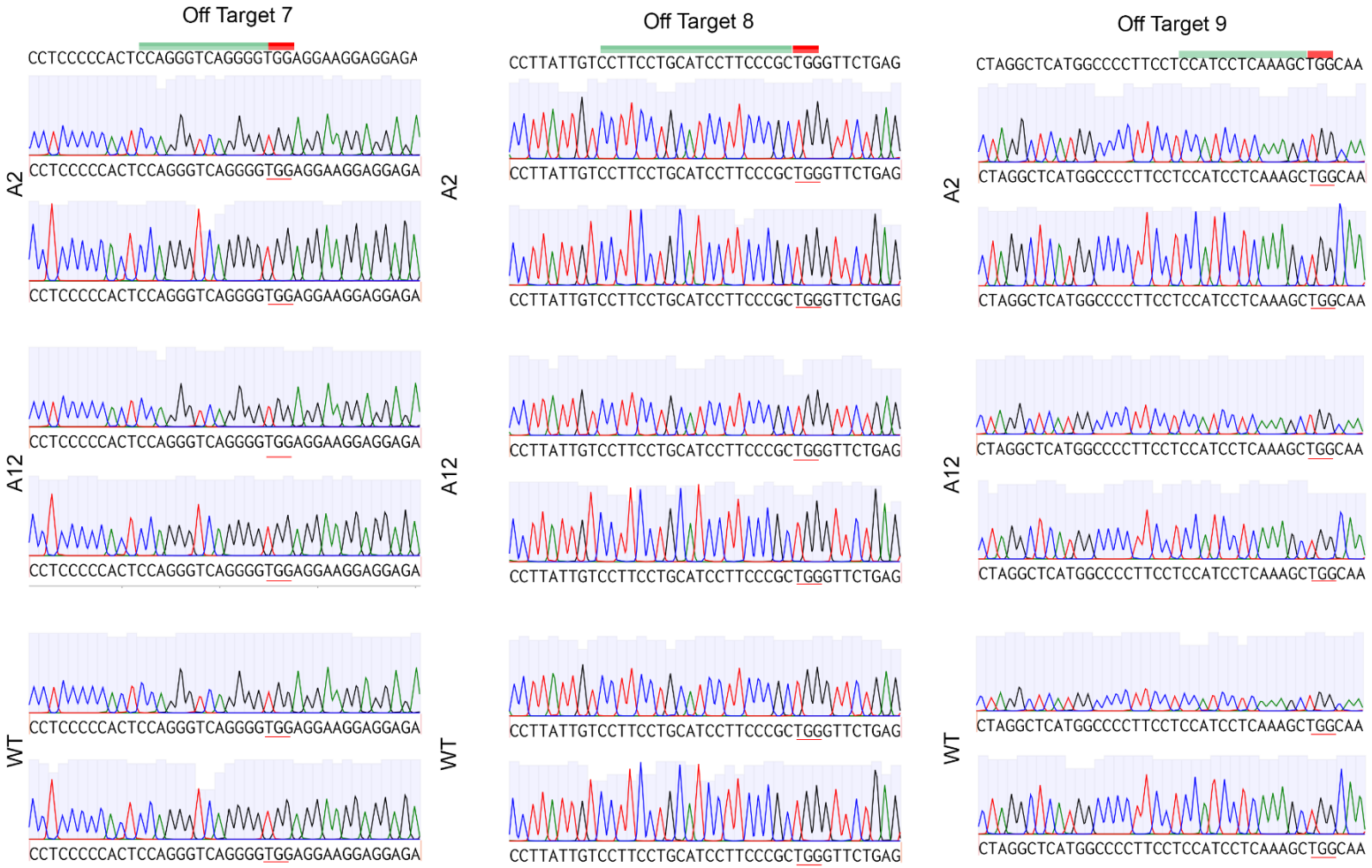

Figure 4-16 Chromatograms of off - target loci sequencing for TSPAN10 mutants and WT cells
Sequences are of the predicted sgRNA off-target locus + PAM site. The PAM is underlined in red.
Off target 4 in TSPAN10 k.o A2 shows a 7bp deletion.
A substitution of C->G is seen at Off Target 3 in both TSPAN10 mutants and WT cells.

4.3 Characterisation of the effect of biallelic indel mutations on *TSPAN10* transcript expression and TSPAN10 protein levels (Objective 1c)

To confirm k.o of TSPAN10 at both the mRNA and protein level a variety of techniques were employed including immunocytochemistry, RT-PCR, qRT-PCR and western blotting.

4.3.1 Immunocytochemistry

Cells were stained for TSPAN10 early in the differentiation process to confirm absence of TSPAN10 in knock-out cell clones A2 and A12. At day 35 differentiation WT cells (differentiations 1, 2 & 3) stained strongly for TSPAN10 using a polyclonal antibody (Proteintech) (Figure 4 – 17). As expected, both predicted k.o cell clones showed only background staining for TSPAN10 (differentiations 1, 2 & 3), suggesting that they do not contain the TSPAN10 protein (Figure 4 – 17). These early results suggested the full TSPAN10 protein was not produced in the presumed TSPAN10 k.o cell clones.

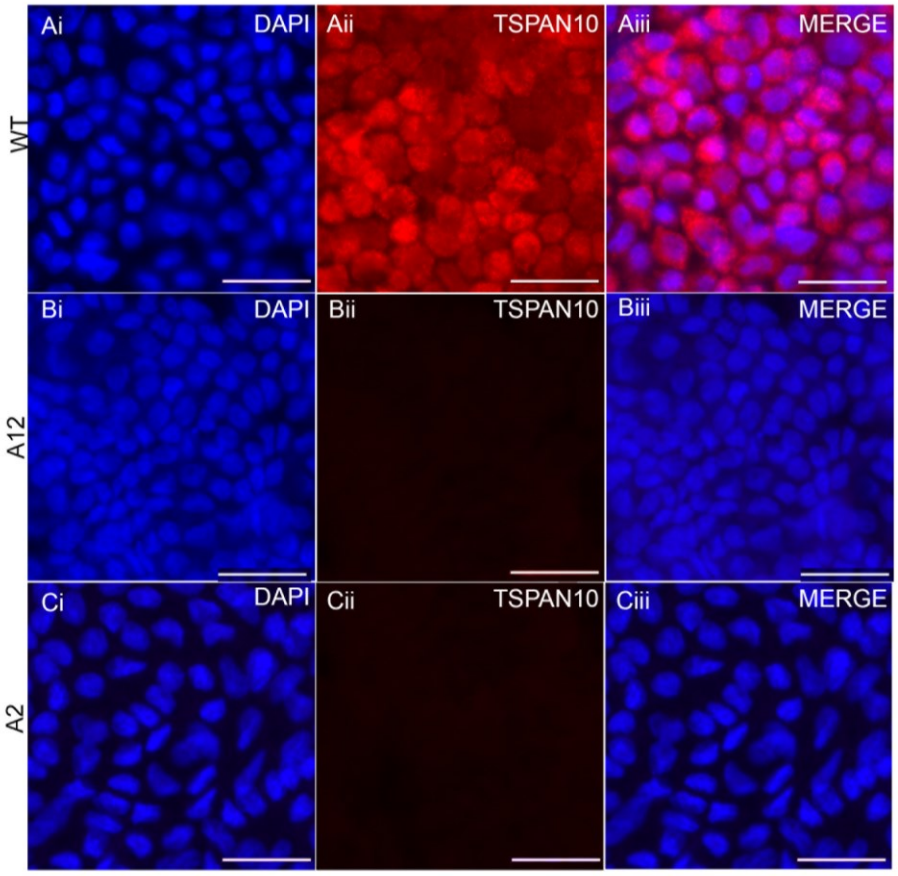

Figure 4-17 Immunocytochemistry of Day 35 hESC-RPE for TSPAN10
Ai, Bi. Ci Nuclei stained with DAPI (blue)
Aii, Bii, Cii Representative staining of TSPAN10 (red). WT cells display strong expression of TSPAN10.
Aiii, Biii, Ciii Merged images showing dual DAPI and TSPAN10 staining. TSPAN10 k.o cell clones A2 & A12 show only DAPI staining with no expression of TSPAN10.
Scale bars represent 25µm
Immunocytochemistry performed for three differentiations from all three clones (n=9).

4.3.2 Western Blotting

Traditional western blotting of cell lysates grown on transwells from day 40 post differentiation hESC-RPE was used to confirm absence of TSPAN10 protein in cell clones A2 and A12. Complete absence of product is seen in all differentiations of A2 (n=3) and A12 (n=3), where-as WT differentiations (1, 2 & 3) produce a product of the expected size at 38 kDa (Figure 4 – 18). A comparison to total protein stain confirms presence of protein in all cell clones and differentiations and acts as a loading control. Three differentiations were used for each clone and three technical repeats performed. These results confirm absence of TSPAN10 protein in day 40 mature RPE cells. The corresponding BCA assay can be found in Appendix A, Figure 10 – 8.

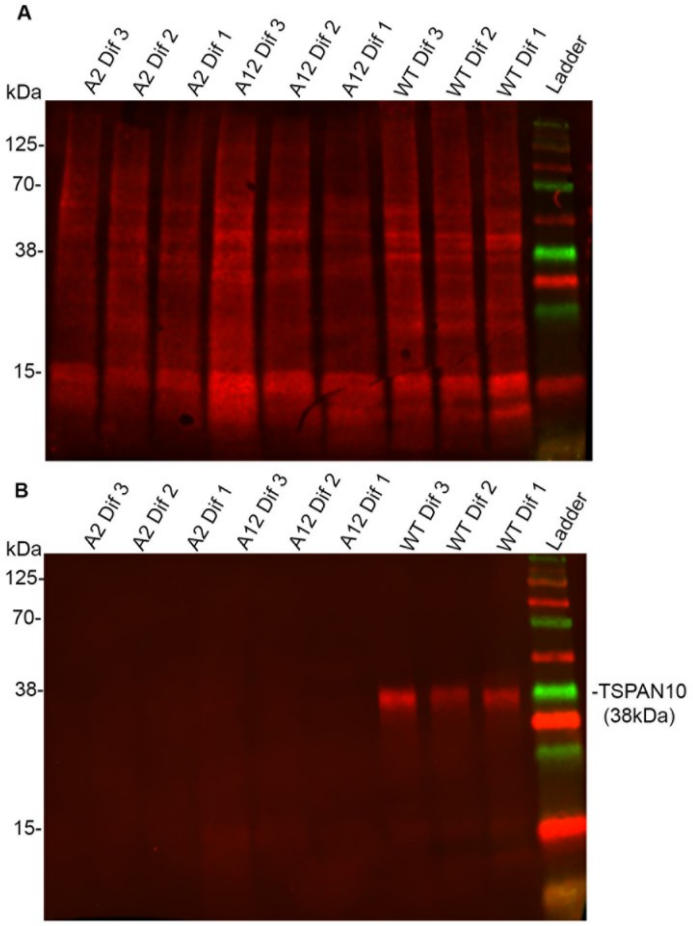

Figure 4-18 Western Blot for TSPAN10 protein in *TSPAN10* mutant and WT hESC-RPE cells
A: A total protein stain (Revert 700) was performed as a control to ensure equal loading of lysates.
B: A TSPAN10 protein blot using the Proteintech polyclonal Ab indicates that both clones and all differentiations are true knockouts.
N=3 technical repeats performed.

4.3.3 RT-PCR for *TSPAN10* in hESC-RPE

To confirm absence of the TSPAN10 mRNA transcript RT-PCR was performed. A significant number of primers spanning exon-exon boundaries were designed and tested (Appendix D

Table 13 – 2, Figure 13 – 6). TSPAN10 is GC rich (69% GC content), consequently primer design is more complex.

Primers were designed to produce a large product to encompass as much of TSPAN10's transcript as possible, the forward primer selected was in exon 2 and the reverse primer in exon 4 (Figure 4 – 19). This RT-PCR showed a product of the expected size (826bp) in WT hESC-RPE day 40 post-differentiation (n=3), but no product in day 40 post-differentiation TSPAN10 k.o cells for all differentiations (A2=3, A12=3). In fact, two amplicons were seen in the WT cells, one at 826bp and the other at approximately 188bp, corresponding with the possibility of alternative splicing at exon 3. Exon 3 is 638bp and the expected product was 826bp, therefore a product of 188bp would not contain exon 3. To confirm if this additional product is seen in other cell types this RT-PCR was repeated using retinal organoid cDNA. As depicted in Figure 4 – 19C, only the day 40 WT hESC-RPE produced two products, the second smaller product was not seen in the retinal organoid control, suggesting the possibility of alternative splicing occurring at TSPAN10 in mature RPE, possibly of exon 3 (638bp).

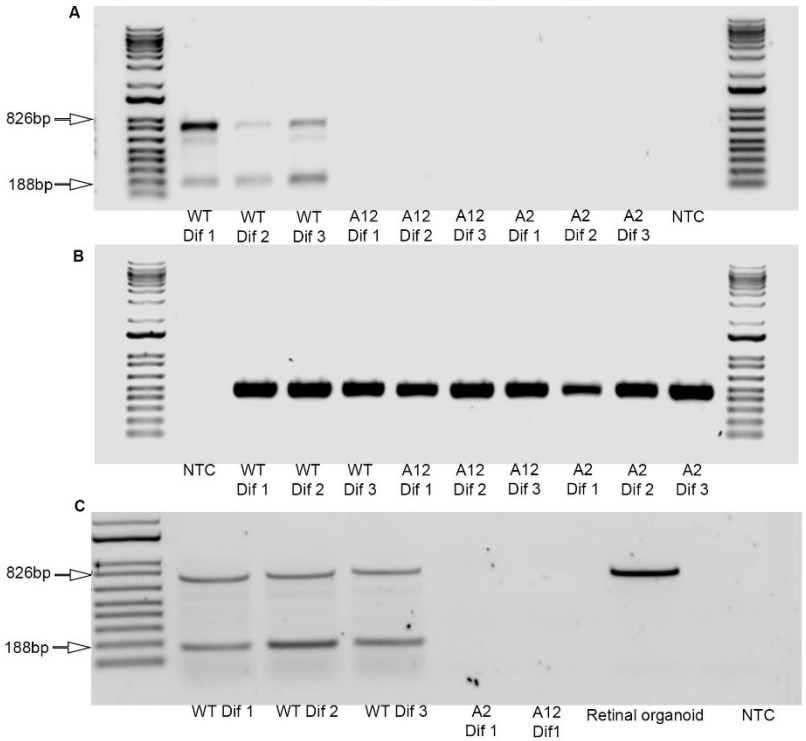

Figure 4-19 RT-PCR for TSPAN10 & GAPDH day 40 hESC-RPE
A: RT-PCR for TSPAN10 in day 40 hESC-RPE. Expected product size 826 bp. Two amplicons visible for all WT cells, no product seen for *TPSAN10* mutants.
B: Control RT-PCR for GAPDH in day 40 hESC-RPE. Expected product size 450 bp. Acts as loading control and confirms good quality cDNA.
C: Repeat RT-PCR TSPAN10 using day 40 hESC-RPE and retinal organoid control. WT hESC-RPE produced two products, the expected product at 826bp and a second product at approximately 188bp. Retinal organoid control only produced one product and TSPAN10 k.o cells did not produce any amplicons.

4.3.4 RT-qPCR for *TSPAN10* in hESC-RPE

RT-qPCR was used to assess TSPAN10 transcript stability and production in day 40 post differentiation hESC-RPE from each differentiation of each clone (n=9) (see Figure 4 – 20). Samples were run in triplicate. All samples were run on an agarose gel post RT-qPCR for robustness (see Appendix D Figures 13 – 7 to 13 – 13). A reduction in TSPAN10 transcript levels was observed to varying degrees in both mutant clones. Interestingly both A2 and A12 did show some production of TSPAN10 mRNA, although markedly reduced in comparison to WT at day 40 (Figure 4 – 20). In fact, the mean ΔΔCq values for each clone were significantly different, as assessed with the One-way ANOVA, (**WT** 19.15 ± 2.35, **A12** 4.08 ± 1.85, **A2** 1.35 ± 0.64) p = 0.02 (WT vs A12), p = 0.002 (WT vs A2). These RT-qPCR results were compared to the RNA-seq data (see Chapter 5), and the mean fold change was comparable (**WT** 4.73, **A12** 2.00, **A2** 1). A Pearson correlation analysis was performed to compare the RNA-seq data with the RT-qPCR, which further confirmed their similarity (R^2 =0.78, *p*=0.004) (see Appendix D, Figure 13 – 14). The primers used in this RT-qPCR were QuantiTect primers (Qiagen), who report the amplicon produced is 176 bp spanning exons 2 and 3. A map of the primer locations is detailed in Figure 4 – 20. The combination of these results confirmed that a small amount of *TSPAN10* transcript is produced in the *TSPAN10* mutant clones A2 and A12, the relevance of this will be discussed in section 3.4. Both TSPAN10 k.o clones should produce transcripts that are degraded by NMD given the frameshift mutations and PTCs. Furthermore, given that RT-PCR of WT hESC-RPE produces two amplicons the possibility of alternative splicing was investigated (see section

3.4).

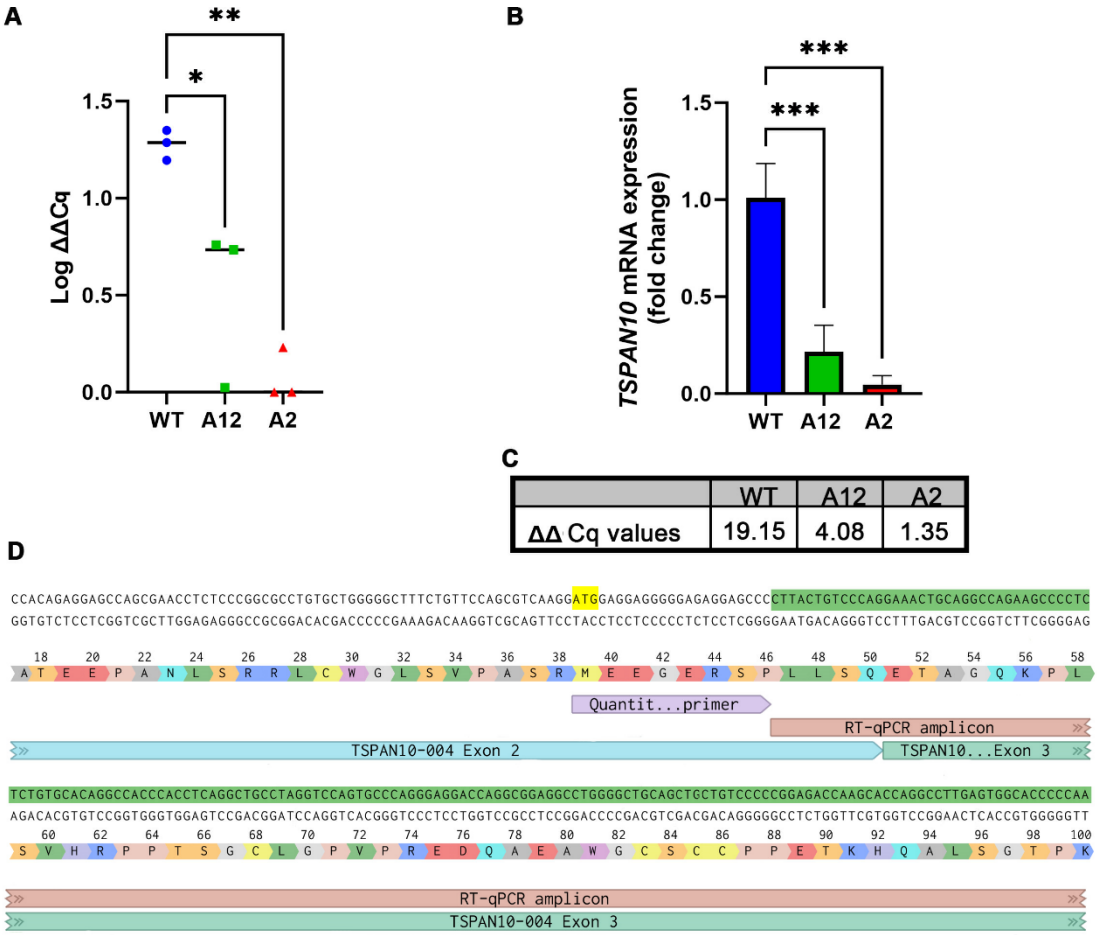

Figure 4-20 RT-qPCR quantification of *TSPAN10* mRNA expression in day 40 hESC-RPE TSPAN10 mutant cells
A: Log ΔΔCq, normalised *TSPAN10* mRNA expression relative to highest ΔCq value where each point is an independent experiment, N=3. WT vs A12 p = 0.0183, WT vs A2 p = 0.0022.
B: Normalised mRNA expression relative to mean wild type ΔCq value. Bars depict mean fold-change and error bars show SEM of three independent experiments. WT vs A12 p = 0.0006, WT vs A2 p = 0.0002.
C: Table depicting mean ΔΔCq values for all cell clones.
D: Representation of amplified sequence. Highlighted in yellow is the target ATG in exon 2 and highlighted in green is the amplicon spanning exons 2 and 3.
Statistical analysis One-way ANOVA with Dunnett's correction

4.4 Alternative splicing at TSPAN10 in the RPE

It was expected that the TSPAN10 k.o mutants would produce short mRNA transcripts that would undergo NMD due to the introduction of frameshift mutations and a PTC, and therefore would be undetectable through RT-qPCR and RNA-seq. Figure 4 – 20 in section 4.3 clearly demonstrates the presence of TSPAN10 transcript in both A12 and A2, detected through RT-qPCR, although at a significantly reduced amount. Furthermore, the amplified transcript in RT-qPCR was reported by Qiagen, who supplied the primers, to contain the exon 2 – 3 boundary and then a portion of the beginning of exon 3. Our targeted ATG was in exon 2, with both A12 and A2 then producing a PTC in exon 3 (see section 4.1, figure 4 – 6). Consequently, it was concluded that both A12 and A2 were producing some TSPAN10 transcript. When RNA is extracted from cell lysates this portrays a snapshot of the cell cycle. We don't know at what point faulty transcripts undergo NMD, therefore it is true that some transcript will be available for amplification in RT-qPCR. Given that no protein is produced (Figures 4 – 17 & 4 – 18), we assume that transcripts are degraded, however an alternative theory is that we are just unable to detect the small, truncated proteins translated from these faulty transcripts due to the limited TSPAN10 antibodies available. Because some transcript was detected, we decided to amplify and sequence it, to help understand what exactly was being produced.

To investigate this further, primers were designed to try and amplify the transcripts via RT-PCR. A significant number of primers were designed spanning exons 1 – 3, as shown in Table 4 – 6. Exon 4 was not included in the design as previously when the transcript aimed to amplify the whole region including exon 4 (Figure 4 – 19) no product was seen for A12 nor A2.

Table 4-6 Primers used for TSPAN10 RT-PCR

Primer name	Primer sequence (5'-3')	Amplicon size (bp)	RT-PCR Figure
E2 forward	ACAGAGGAGCCAGCGAAC	826	3 – 21 A
Reverse 5	TGACAGAGGCTCCATCTTCG		
E1 forward 3	GCAAAGACGAGCATCCGAAG	548	3 – 21 B
Reverse RK 3	CCCCAGATCACTTCCCAGAG		
E1 forward 3	GCAAAGACGAGCATCCGAAG	674	3 – 21 C
Reverse 2	CCCAGAGAAGCCACGTAACA		

Figure 4 – 21 displays a schematic of the amplified exons and all successful RT-PCR reactions for TSPAN10. Primers that successfully amplified a product for A12 gave no band for A2 (Figure 4 – 21 C), therefore a smaller region was targeted (Figure 4 – 21 B), suggesting that the A2 transcript is smaller than that for A12. As was the case for all previous RT-PCRs for TSPAN10, WT hESC-RPE produced two products. Bands from RT-PCRs (Figure 4 – 21 B & C) were excised, purified and sent for Sanger sequencing. Both

A12 and A2 produced transcripts that contained a truncated version of WT exon 3, but not exon 2 (Figure 4 – 22). This suggested that exon 2, which is 142 bp, was alternatively spliced, producing a product containing exon 1 and some of exon 3. This is exemplified in the forward strand of A2 (Figure 4 – 22), which shows, what looks to be nonsense code, but is in fact the end portion of exon 1.

Further answers were sought to understand what happens in the WT cells. Figures 4 – 21 B & C show the production of two amplicons roughly 150 bp apart for all WT cells, exon 2 is 142 bp long, therefore alternative splicing at exon 2 could explain these double bands. Figure 4 – 21 A also shows two products for WT cells, however, the first amplicon is at the expected size and the second amplicon approximately 200 bp. If exon 3 was alternatively spliced, this would give a product for this reaction of 188 bp. This smaller product was not seen in TSPAN10 k.o mutants, reconfirming the hypothesis that the clones A12 and A2 produce transcript containing exon 1 and a portion of WT exon 3. Consequently, it was surmised that both exons 2 and 3 of TSPAN10 can be alternatively spliced in RPE cells.

To further understand this splicing pattern RNA sequencing results (discussed in Chapter 6) were examined in detail at the TSPAN10 region to look for alternative splicing. Sashimi plots were created using the Integrative Genomics Viewer (IGV) software [269, 270]. Sashimi plots visualise splice junctions from aligned RNA seq data and an inbuilt gene annotation track, in this instance the reference genome. Sashimi plots were developed for TSPAN10 specifically focussing on exons 2 and 3 (Figure 4 – 23). As depicted in the figure the coverage for each alignment is plotted as a bar graph, and arcs representing splice junctions connect exons with the number of reads split across the junction displayed numerically (junction depth). A minimum depth of 50 was selected in this instance. Figure 4 – 23 shows alternative splicing of exon 2 in many of the differentiations. This is especially depicted in the WT clone, where all differentiations show alternative splicing of exon 2. However, this is only seen in A2 differentiation 2 and A12 differentiations 1 and 2, this discrepancy is most likely due to copy numbers as there is significantly reduced transcript seen in the k.o clones in comparison to WT. This data confirms that exon 2 of TSPAN10 can be alternatively spliced in RPE cells. This is not reported on the UCSC genome browser or other genomic databases. Consequently, if exon 2 is alternatively spliced out in a small number of transcripts then the CRISPR/Cas9 induced indels will not be translated leading to the possibility of a truncated protein.

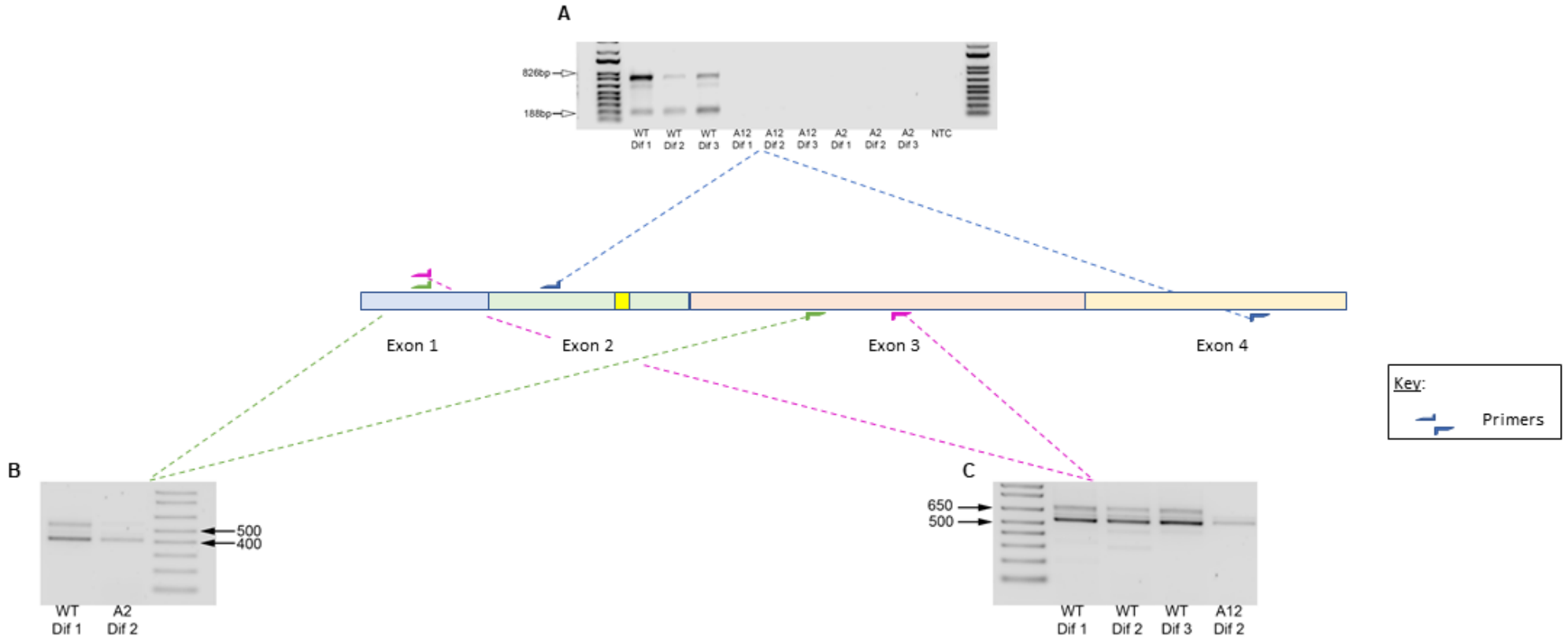

Figure 4-21 Map of TSPAN10 exons and RT-PCR experiments performed
The four exons of *TSPAN10* are shown with the target ATG location approximated in exon 2 with a yellow square.
Locations of primers used for each RT-PCR are shown along with the corresponding gel.
A: Amplicons seen in WT differentiations only. (Expected size 826 bp). Second product seen at 188 bp.
B: Two amplicons seen in WT dif 1, the fainter larger product being the expected size. One amplicon seen in A2 dif 2, smaller than expected size. (Expected size 548 bp)
C: Two amplicons seen in WT differentiations, the fainter larger product being the expected size. One amplicon in A12 dif 2, smaller than expected size. (Expected size 674 bp).

Figure 4-22 Chromatograms sequencing the exon 2 - exon 3 junction in *TSPAN10*
Chromatograms developed using Benchling display Sanger sequencing results from RT-PCR of TSPAN10. Yellow highlighted areas demonstrate location of the gRNA. The template at the top of the image shows exon 2 in turquoise and exon 3 in green.
WT hESC-RPE display expected sequencing results for exon 2. Both TSPAN10 k.o mutants A2 and A12 transcripts do not contain exon 2.
The sequence of the forward strand of A2 matched to exon 2 is actually the sequence of the end of exon 1. Both A2 and A12 display the correct sequence for the start of exon 3.

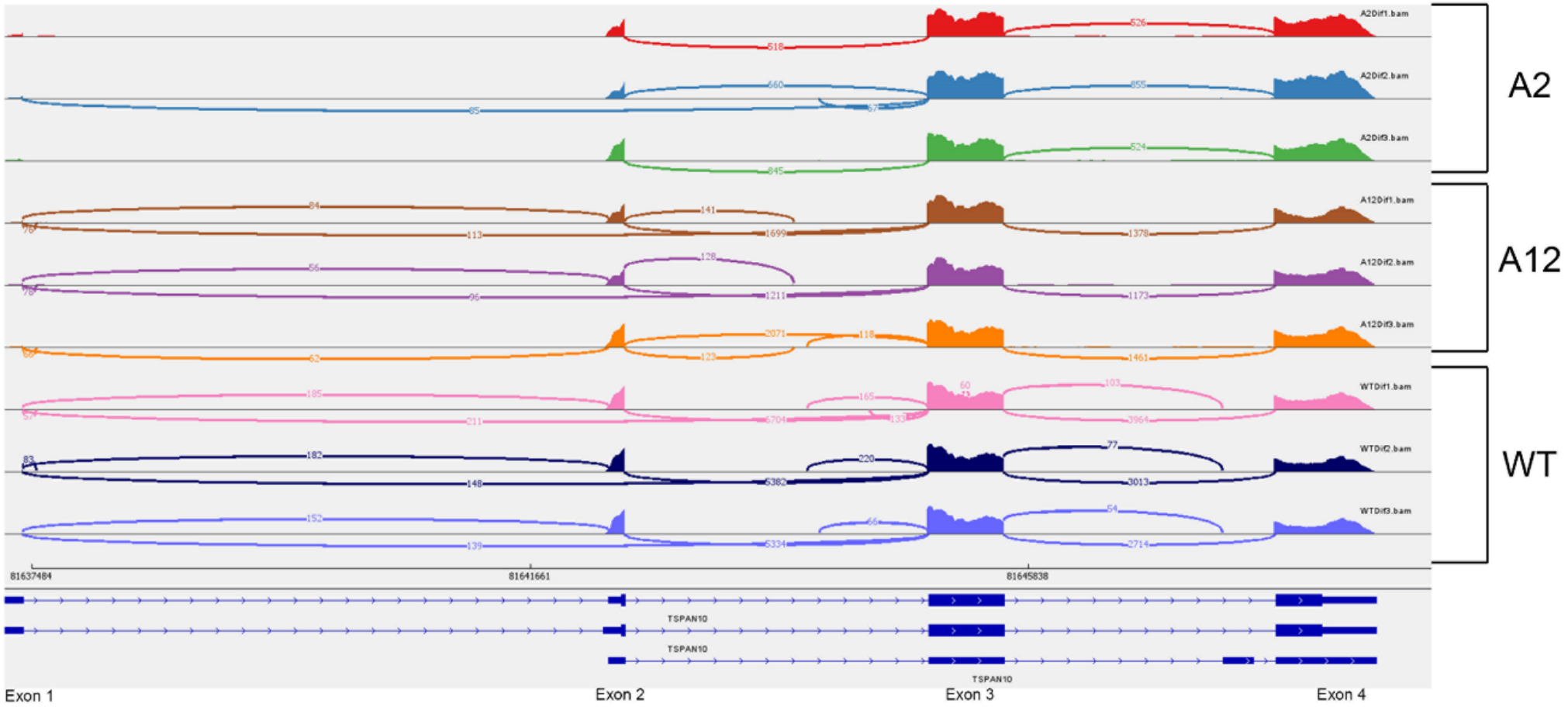

Figure 4-23 Sashimi plot visualising TSPAN10 splice junctions
Sashimi plot created using Integrative Genomics Viewer (IGV) depicting splicing patterns at TSPAN10 in the RNA seq data (Chapter 5).
Alternative splicing of exon 2 is depicted in all WT differentiations and in some knockout differentiations including A2 2, A12 1 and A12 2. However, the copy numbers are significantly reduced in knockout clones in comparison to WT, and furthermore, the majority of transcript appears to include exon 2, demonstrated by the high copy numbers between exons 2 and 3.

4.4.1 Predicting protein structures of alternative transcripts

Section 4.3, Figures 4 – 17 & 4 – 18, clearly demonstrate that no WT TSPAN10 protein was detected in TSPAN10 k.o - mutants. The antibody used was polyclonal, unfortunately we do not know the precise location of the epitopes targeted. We cannot rule out the possibility that a short, truncated protein is produced from A12 and A2 that does not contain any of the epitopes recognised by our polyclonal antibody. Consequently, the sequences for both transcripts were input into Consurf [271-273] and Alphafold [274], along with WT, and predicted protein structures discerned (Figures 4 – 24 & 4 – 25). As evidenced if either transcript produced a protein it would be a truncated version of the WT, with significantly reduced helices, but containing the N-terminal region of the protein. The only way to truly understand if and what proteins are being produced would be mass spectrometry of products, however that is out of the scope of this thesis.

4.4.2 Probing for truncated TSPAN10 proteins

All TSPAN10 k.o transcripts were predicted to contain all or part of the N-terminal region of the protein. Fortunately, a monoclonal antibody targeting the N-terminal portion of the TSPAN10 protein was located and purchased to probe for truncated proteins.

4.4.2.1 Immunocytochemistry

Mature hESC-RPE were stained for TSPAN10 to confirm absence of TSPAN10 in k.o cell clones A2 and A12. Fully mature WT cells (differentiations 1, 2 & 3) stained strongly for TSPAN10 using the monoclonal antibody targeting the N-terminal region (Aviva Systems Biology) (Figure 4 – 26). The staining pattern was again punctate cytoplasmic. Interestingly both predicted k.o cell clones showed only background staining for TSPAN10 (differentiations 1, 2 & 3), suggesting that they do not contain a truncated TSPAN10 protein (Figure 4 – 26). These results suggest that a truncated TSPAN10 protein is not produced in the presumed TSPAN10 k.o cell clones, and therefore that any transcript produced is degraded.

4.4.2.2 Western Blotting

Traditional western blotting of cell lysates grown on transwells from day 40 post differentiation hESC-RPE were used to confirm absence of truncated TSPAN10 protein in cell clones A2 and A12. Complete absence of product is seen in all differentiations of A2 (n=3) and A12 (n=3), where-as WT differentiations (1, 2 & 3) produce a product of the expected size at 37kDa (Figure 4 – 27). A comparison to total protein stain confirms presence of protein in all cell clones and differentiations and acts as a loading control. Three differentiations were used for each clone and three technical repeats performed. These

results confirm absence of TSPAN10 protein in day 40 mature RPE cells. The corresponding BCA assay can be found in Appendix D, Figure 13 – 5

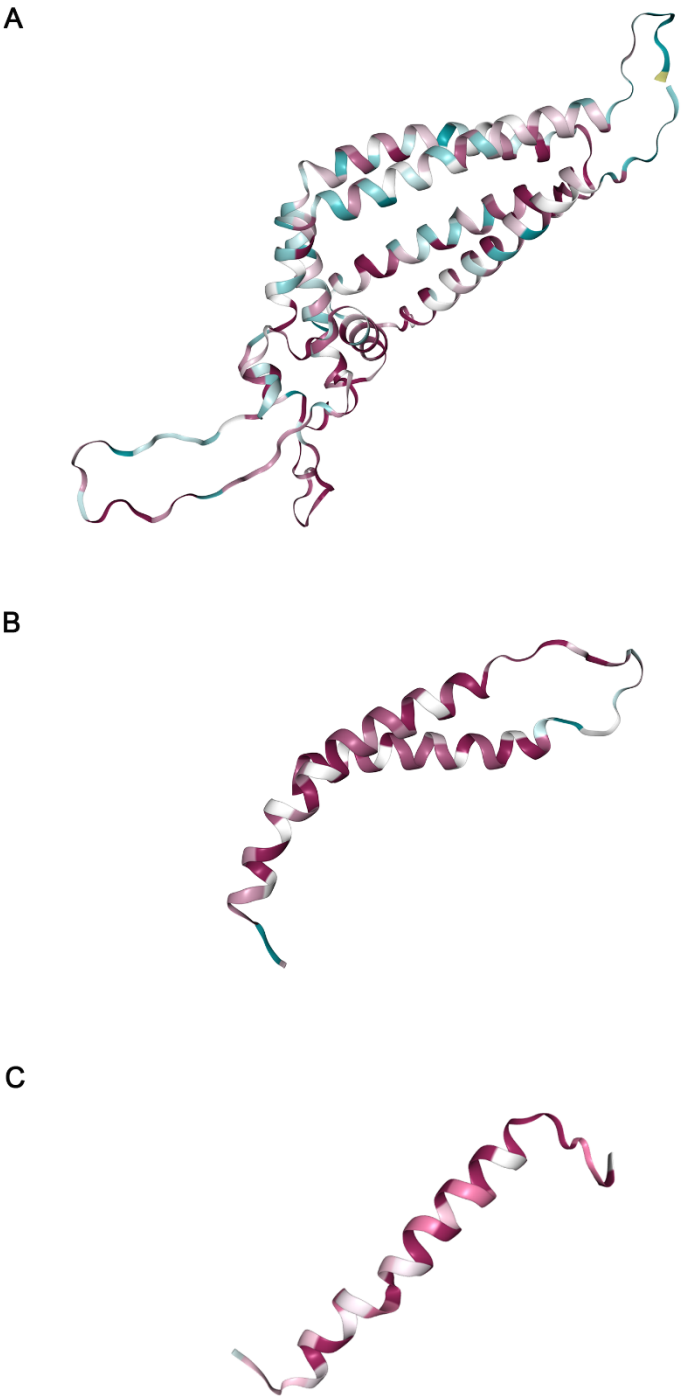

Figure 4-24 Predicted protein structures of WT TSPAN10 and mutant TSPAN10
Predicted protein structures generated using Consurf [271-273] for **A**: WT TSPAN10; **B**: A12 and **C**: A2. WT sequence downloaded from ENSEMBL. **B** & **C** Structures derived from A12 and A2 sequencing results, representing shortened versions of exon 3 TSPAN10.

Colour scheme represents evolutionary conservation of protein structure, where pink is highly conserved and blue least conserved. The helical structures appear to be highly evolutionary conserved.

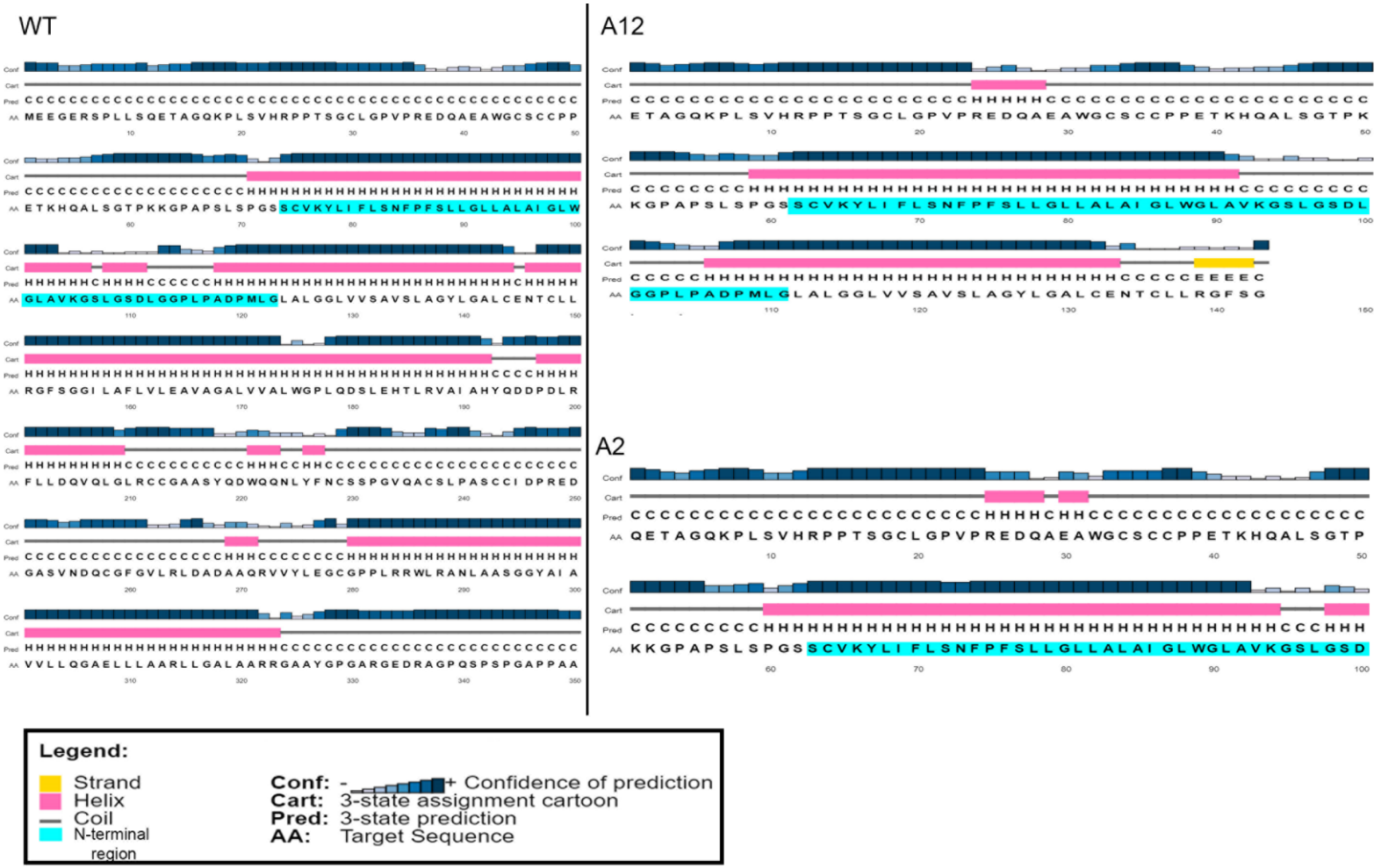

Figure 4-25 TSPAN10 protein secondary fold prediction
Predictions produced with Consurf [271-273] Blue bars above indicate the confidence of the prediction; alpha helices are represented by pink rectangles; beta strands are shown by yellow rectangles; coiled domains are represented by a black line; amino acid (AA) sequence is shown below; a one letter symbol indicates the secondary structure in which each residue is predicted to reside (H, alpha helix; E, beta strand; C, coil). Turquoise highlights represent N-terminal sequence present in each clone. WT & A12 contain the full N-terminal sequence, shortened version in A2.
WT protein is predicted to contain nine helices, whereas A12 to contain three and A2 four.

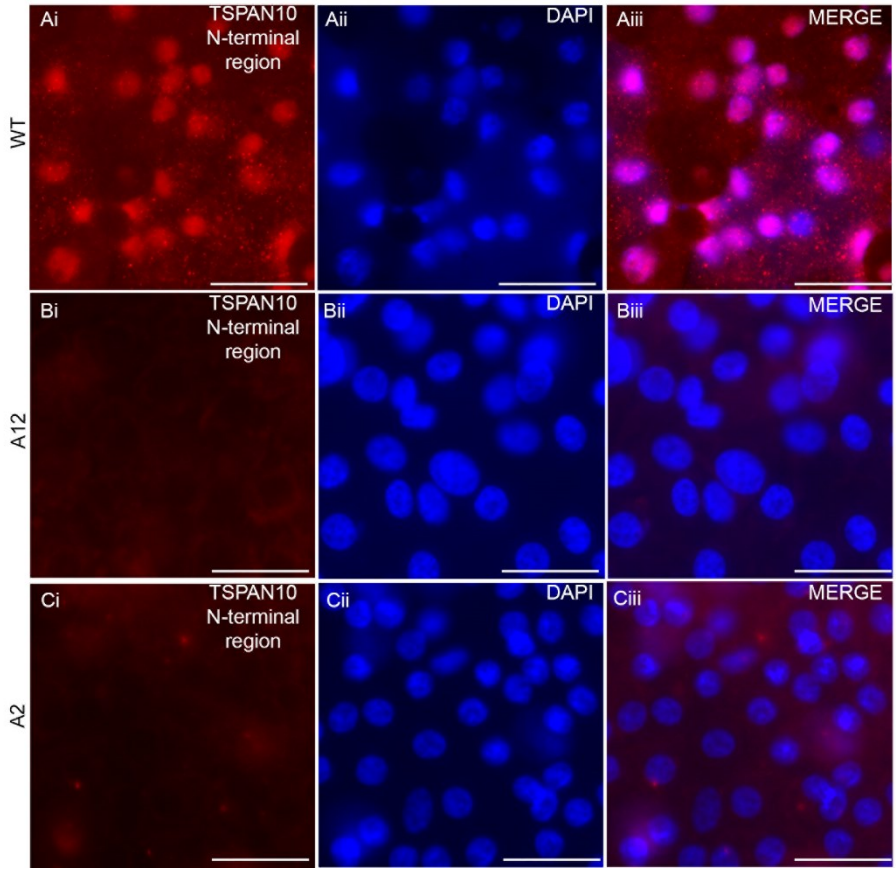

Figure 4-26 Immunocytochemistry staining for TSPAN10 N-Terminal Region in WT and TSPAN10 mutant hESC-RPE

Ai, Bi. Ci Representative staining of TSPAN10 N-Terminal region with Proteintech monoclonal Ab (red). WT cells display strong expression of TSPAN10, punctate cytoplasmic and nuclear staining.
Aii, Bii, Cii Nuclei stained with DAPI (blue)
Aiii, Biii, Ciii Merged images showing dual DAPI and TSPAN10 staining. TSPAN10 k.o cell clones A2 & A12 show only DAPI staining with some background red staining.
Scale bars represent 25µm
Immunocytochemistry performed for three differentiations from all three clones (n=9).

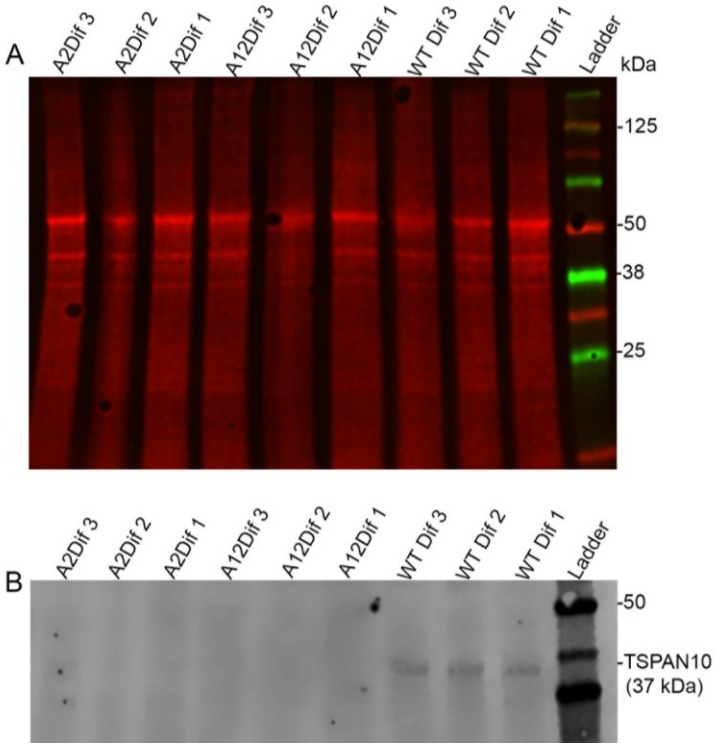

Figure 4-27 Western blot for TSPAN10 N-terminal Region in hESC-RPE
A: Revert 700 Total protein stain was performed as a control to ensure equal loading of lysates.
B: TSPAN10 protein blot using a monoclonal Ab targeting the N-terminal region demonstrates a band in WT cells only (37kDa)-. Demonstrating that both clones, A12 and A2 and all differentiations of these clones are true knockouts.
N=3 technical repeats performed

4.5 Interpretation and Interim Discussion

The CRISPR/Cas9 system was used to perform gene editing, guided by in silico sgRNA design. The use of CRISPR in hESCs allows a pure clonal population to be produced, given that clones were derived from single cells. Consequently, Sanger Sequencing confirmed biallelic indel mutations in both selected clones, with predicted k.o scores of 99% (A12) and 100% (A2), Table 4 – 4.

A general point regarding the CRISPR/Cas9 system was the efficiency and success of the two sgRNAs designed, JL and Assembly 2. Assembly 2 had a higher MIT specificity score (74) and Rule Set 2 on target score (63) than JL (54 and 62, respectively), however only clones produced using the JL guide were successful at introducing indels. The reasons for the failure of the gRNA Assembly 2 are likely related to the concentration of the DNA introduced to the cells. Following maxi-prep JL-6 was at a much higher concentration than Assembly 2, therefore a small volume could easily be introduced to the hESCs to give a total concentration of 10 µg. However, for Assembly 2 a larger volume of plasmid DNA was delivered to give a similar concentration of DNA. Given that two indels were produced by JL-6 there was no need to repeat the maxi-prep and electroporation with the Assembly-2 guide.

Interestingly the indels produced by the JL guide were an insertion (A12) and a deletion (A2) (see Figure 3 – 5). According to the literature deletions are more common than insertions [275]. As chromosomal rearrangements can arise from gene editing [276, 277], karyotyping was performed for both clones (A2 & A12), see Appendix D, Figures 13 – 2 & 13 – 3. No variants of significance were identified for either clone in comparison to WT. Interestingly a deletion in the *DFNA5* gene was seen in both WT and TSPAN10 k.o cells, which was identified as a variant of unknown significance. Given that the deletion was also present in WT cells this indicates several options for its occurrence. Firstly, that the mutation was present in the blastocyst from which the hESCs were derived, or secondly that the ESCs acquired this deletion during early passaging. Non-syndromic hearing impairment is associated with mutations in *DFNA5* [278], however the variant seen in our hESCs has not been associated with any clinical phenotypes to date. Consequently, this variant is unlikely to affect the results presented in this thesis.

CRISPR/Cas9 edited cells must always be screened for off-target loci. The number of off-targets screened varies in the literature with some groups performing whole genome sequencing [279]. Typically, authors tend to screen the top 10 off-target hits, initially focussing on those that are within exons [218]. Here we screened the top 9 off-target hits, given that this encompassed all targets with up to 3 mismatches for the guide JL. Screening the top 10 would include targets with 4 mismatches, of which there were a large number. We saw no changes in exons nor promoter regions, however the clone A2 did produce a homozygous 7 bp deletion at off-target 4 within an intron as evidenced in Figure 4 – 16. This change was in chromosome 5 and found to be intronic, therefore it was assumed that it would not impact the validity of the A2 clone, given that this change is unlikely to impact the role of TSPAN10.

Electroporation was used to insert the correct plasmid DNA into the hESCs. Electroporation was selected over other methods such as lentiviral transduction given that hESCs have been shown to respond to and recover well from electroporation [280]. Furthermore, this reduces the risk of unknown effects to the cells that a lentiviral vector could cause.

hESCs were differentiated into RPE using a previously published and verified method [60]. A directed differentiation method was chosen, given that this produces RPE cells faster and at higher purity [186]. The alternative method, spontaneous differentiation [98], involves removal of FGF from cell culture media and then the eventual selection of pigmented clones. The spontaneous method is useful for RPE production for *in vivo* transplantation [281], given the reduction in growth factors and other xeno-additives, a concern that was not relevant to this project. Furthermore, given the associations TSPAN10 has with pigmentation [127, 129],

or to be more specific, the lack of, selecting cells based on pigmentation was felt not to be appropriate for this project, especially with regard to the TSPAN10 k.o clones. With any differentiation protocol, there will undoubtedly be production of unwanted cell types. The main contaminant in the described differentiations appeared to be neural retinal cells. This cell type was initially seen at approximately day 10 (Figure 4 – 8 F). Removal of cells with a non-RPE phenotype is included in several RPE differentiation protocols at an early stage [60] [61]. This was undertaken using a P200 pipette tip, however discerning early RPE from early neural retina or fibroblasts was challenging, especially given the low numbers of neural retina present in cultures. A subset of cells were then fixed and stained for the early RPE cell marker MITF (Figure 4 – 9), to allow identification of morphologically distinct areas with negative staining that could be used to identify non-RPE progenitors. These were identified as rosette structures and removed using a P200 pipette tip in all differentiations.

Carriers of the rs6565597 SNP at *NPLOC4/TSPAN10*, which is associated with AMD [71], have reduced copy numbers of *TSPAN10* mRNA [102], with those homozygous for the risk allele expressing the lowest transcript numbers. This was ascertained by genotyping and performing RNA sequencing of donor eyes from both normal individuals and those with AMD [102], indicating that presence of rs6565597 leads to reduced *TSPAN10* mRNA levels, which could lead to reduced TSPAN10 protein, suggesting that reduced levels of TSPAN10 is a risk factor for AMD. By knocking-out the *TSPAN10* gene we aimed to produce a more extreme phenotype in culture, with the ultimate aim of understanding how changes in TSPAN10 expression might impact AMD. Initially to confirm k.o of TSPAN10 immunocytochemistry of differentiating hESCs (day 35 of directed differentiation) was performed for all differentiations from all clones (n=9), Figure 4 – 17. A2 & A12 showed only DAPI staining, with no evidence of TSPAN10 expression. The antibody used was a polyclonal antibody, therefore it has multiple epitopes and should capture any TSPAN10 protein produced. These results suggest that the TSPAN10 protein is produced during the differentiation process of hESCs to RPE in WT cells at day 35, but not in the TSPAN10 k.o clones. Immunocytochemistry staining for TSPAN10 was not performed earlier than day 35, therefore we cannot currently say at what point in the differentiation of RPE that TSPAN10 is first produced. TSPAN10 appears to be localised mainly to the RPE in the adult retina [102], however immunocytochemical staining for TSPAN10 in the foetal retina will also be performed (Chapter 8) to understand if this expression pattern remains the same, or if TSPAN10 is also expressed in other retinal cell types at an earlier stage. Given that this immunocytochemistry experiment was not performed on fully-differentiated hESC derived RPE we repeated it using day 40 post differentiation cells grown on transwells and the same result was seen with A2 and A12 showing only DAPI staining (data not shown).

Western blotting enabled re-validation of TSPAN10 k.o. This was performed on fully-differentiated hESC-RPE (day 35 - 40 post differentiation). Bands at the expected size (38kDa) were seen for all three WT differentiations, but not in the TSPAN10 k.o clones (Figure 4 – 18). The antibody used was the same as that in the immunocytochemistry experiment and is polyclonal. There is currently a paucity of antibodies commercially available against TSPAN10. Consequently, we cannot confirm the specific epitopes targeted in this experiment. Ideally this experiment would be repeated using several monoclonal TSPAN10 antibodies with different epitopes at known locations, to ensure a truncated protein is not produced. However, we can assume that the absence of a product in the TSPAN10 k.o clones and presence of a product in the WT indicates that a TSPAN10 protein is not being produced in A2 and A12. Furthermore, this helps to confirm the validity of the antibody.

TSPAN10 produces six transcripts, of which four are protein coding, see Table 4 – 1. RT-PCR and RT-qPCR were used to understand if any transcript remained in the TSPAN10 k.o clones A2 and A12. RT-PCR using a forward primer in exon 2 and reverse primer in exon 4 showed a band at the expected size in all differentiations of the WT, however no bands were seen for each of the three differentiations of A2 nor A12. In fact, two bands were seen in the WT clones (Figure 4 – 19), of which the second unexpected product appeared to be approximately 200 bp, however this was not evident in non-RPE (Figure 4 – 19). This experiment was repeated more than three times and using different cDNA, however the same result occurred. Consequently, it was surmised that TSPAN10 must be alternatively spliced in RPE. As previously discussed, there is a paucity of literature investigating TSPAN10. There is no mention of alternative splicing in the available databases, such as The UCSC Genome Browser [268]. If TSPAN10 is alternatively spliced, this raised the possibility that a transcript could be produced in our k.o clones. RT-qPCR showed the production of some transcript for both A2 and A12, albeit at a significantly reduced amount to WT, Figure 4 – 20. The forward primer used in this reaction spanned the exon 2/3 junction, and the reverse primer was in exon 3, according to Qiagen (Figure 4 – 20). This result was surprising given that the ATG targeted by our CRISPR/Cas9 sgRNA was in exon 2, therefore we did not expect our TSPAN10 k.o clones to produce a product as all transcripts should undergo NMD. However, the RNA used in this RT-qPCR experiment only shows a snapshot of the cells' life cycle, therefore it is possible that any transcript identified had not yet been targeted to NMD. A further possibility is that if there is alternate splicing of TSPAN10, then an alternate ATG could be used, thereby avoiding the indels we introduced in exon 2. To further understand if a smaller transcript is produced in the k.o clones several primers were designed to amplify varying lengths of cDNA (Figure 4 – 21). It appeared that A2 did still

produce some transcript, albeit a shorter product (approximately 400 bp) and A12 also produced a transcript (approximately 500 bp). Interestingly, k.o cells only showed one product for RT-PCR reactions, whereas WT cells continually showed two. This implied that exon 2, which is targeted in our k.o populations could be alternatively spliced. We aimed to confirm this through sequencing, Figure 4 – 22. The transcripts sequenced from A2 and A12 did not contain exon 2 (Figure 4 – 22), however the larger product produced from WT cells did. To understand fully the splicing pattern for TSPAN10 in the RPE we used the data produced from our RNA sequencing experiments (Chapter 6). Figure 4 – 23 shows a Sashimi Plot produced for all differentiations of all cell clones focussed in on exons 2 and 3 for TSPAN10. This demonstrates alternate splicing of exon 2, especially evident in the WT clones, due to reduced copy numbers in TSPAN10 k.o cells. The alternate splicing of exon 2 explains the shortened transcript production in our k.o cells.

We then aimed to model potential protein products that could be produced from a shortened TSPAN10 transcript. As mentioned, our TSPAN10 polyclonal antibody did not show a product in A2 nor A12, however we do not know where the epitopes for this antibody are. Subsequently, we used both Consurf and AlphaFold to model possible protein structures produced by A2 & A12 and compared them to WT protein, see Figures 4 – 24 & 4 – 25. Interestingly, both the A2 and A12 predicted protein structures contain some or all of the TSPAN10 N-terminal region (Figure 4 – 25). Fortunately, we were able to identify another TSPAN10 antibody (Aviva Systems Biology) that targets the TSPAN10 N-terminal region and is monoclonal. The protein structures predicted for A12 & A2 both contain some or all of the N-terminal region, as shown in Figure 4 – 25. Consequently, western blotting and immunocytochemistry experiments were performed using this new N-terminal antibody. As displayed in Figure 4 – 27, no bands were seen on western blotting in any of the differentiations of A12 nor A2. A faint band was seen in all differentiations of WT cells at the expected molecular weight. This was further confirmed in immunocytochemistry experiments (Figure 4 – 26), which demonstrate fluorescence in WT cells, but only background signal in A2 nor A12. However, this antibody was very difficult to work with and did not produce results that were as clean as those seen in Section 4.3.1 and 4.3.2, with the WT showing very faint bands on western blot. Despite this, the absence of a product in A12 and A2 reassures us that these shortened transcripts do not produce a protein product in our k.o cells. There is no current literature available on the stability, half-life nor further information on the structure of TSPAN10. Other C8 tetraspanins have been more thoroughly investigated, including TSPAN15, whose crystal structure was recently determined revealing a conserved ADAM10 binding site [282]. The interaction of TSPAN10 in RPE cells with experimentally predicted protein partners such as ADAM10 will be investigated in Chapter 7.

One unexpected benefit of some transcript production in A2 and A12 is the closer semblance of our cells to the picture seen in those with the AMD risk SNP rs6565597, where *TSPAN10* copy numbers are reduced [102]. However, the cells are still a far more extreme phenotype, especially given the apparent lack of protein production.

In conclusion, this chapter demonstrates the successful use of CRISPR/Cas9 to reduce *TSPAN10* transcript and k.o TSPAN10 protein production in hESCs. Furthermore, the successful differentiation of hESCs to RPE is shown, however this will be discussed further in the following chapter.

5 Identification of a phenotype associated with knockout of TSPAN10

To identify a phenotype caused by TSPAN10 k.o in RPE cells validation was first sought to confirm that hESCs were correctly differentiated to healthy RPE. All cells were therefore characterised for the presence of vital RPE morphological and functional features *in vitro*.

5.1 Expression of RPE markers

5.1.1 Immunocytochemistry

The expression of RPE specific markers was examined through immunofluorescence to verify structural adaptation and maturation of RPE monolayers. hESC-RPE were grown on transwell inserts as this is felt to recapitulate the native BRB (see Chapter 1, Section 1.5). Cells were probed for the mid-late tight junction protein occludin at day 60 post differentiation to assess the formation of BRB complexes (Figure 5 – 1). During the differentiation process at day 35 cells grown on cover slips were probed for the early tight-junction protein ZO-1 (Chapter 4, Section 4.2, Figure 4 – 11). WT cells and both TSPAN10 k.o mutant clones showed bright staining for both early and mid-late tight-junction markers. Both ZO-1 and occludin staining was continuous along intercellular junctions, indicating high expression of junctional complexes. A hexagonal cobblestone morphology was evident in WT cells and largely present in TSPAN10 mutants, although less pronounced.

Day 60 post differentiation cells grown on transwells were then stained for the RPE specific marker retinoid isomerohydrolase, RPE-specific 65 KDa protein (RPE-65) (Figure 5 – 2). RPE-65 is crucial for visual function, as it converts all-*trans* to 11-*cis*-retinoids [283]. RPE-65 staining showed punctate expression within the cytoplasm of all cells, confirming presence of a key RPE marker.

RPE polarisation is vital for many functions including the directional secretion of proteins, the absorption of stray light and phagocytosis of shed POS (see section 1.2 in Chapter 1). The specialisation of apical and basal membrane proteins is crucial for polarisation, and therefore day 60 post differentiation cells grown on transwells were examined for the apically expressed protein Na^+/K^+ ATPase. Apical expression of Na^+/K^+ ATPase was confirmed in all cell clones and differentiations (n=9) (Figure 5 – 3), however in the TSPAN10 mutants expression appeared predominantly apicolateral, with some evidence of lateral expression in the WT but significantly less.

Finally, cells were also stained for the RPE marker Bestrophin (Best-1), which is localised basolaterally and within the eye exclusively found in the RPE (Figure 5 – 4). Cells were also co-stained for the tight-junction marker ZO-1 (Figure 5 – 4). Best-1 is believed to act as a

channel protein, controlling the flow of chloride ions through the basolateral membrane of the RPE cell. Cells showed continuous Best-1 staining, however this was much weaker comparatively to their ZO-1 staining. These images were taken using a standard fluorescence microscope, not using the confocal microscope, consequently we are unable to confirm the basolateral location of this marker.

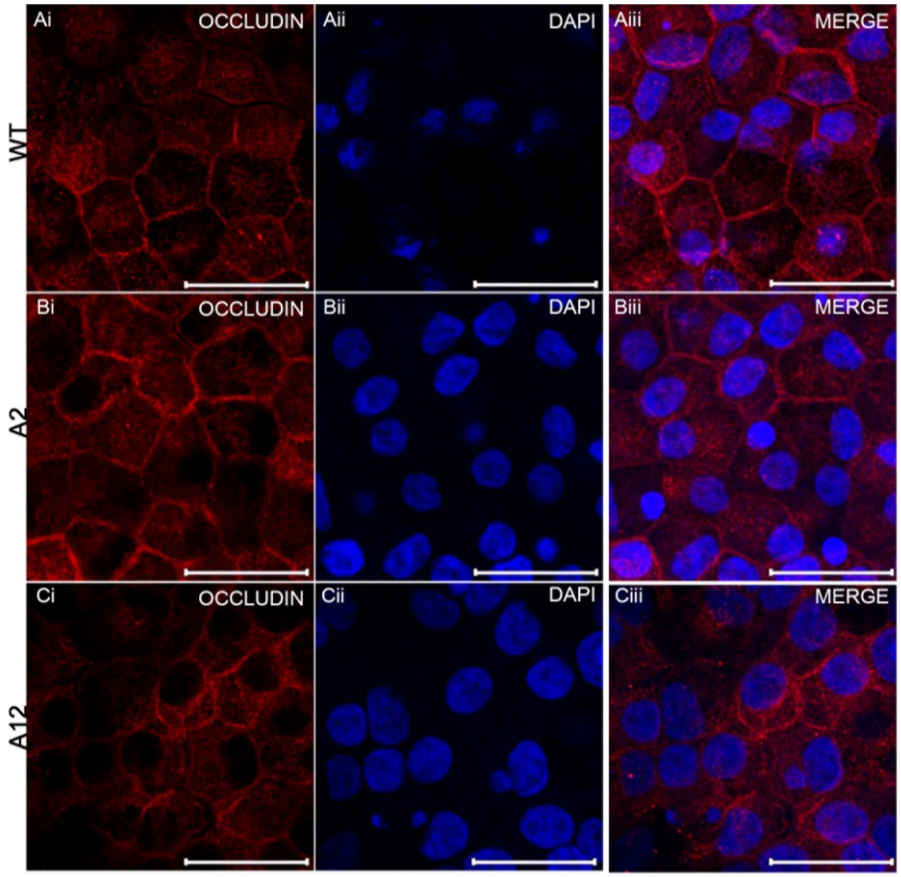

Figure 5-1 Immunocytochemistry for Occludin in day 60 hESC-RPE
Ai, Bi. Ci Representative staining of Occludin (red).
Aii, Bii, Cii Nuclei stained with DAPI (blue)
Aiii, Biii, Ciii Merged images showing dual DAPI and Occludin staining.
Scale bars represent 25μm
Immunocytochemistry performed for three differentiations from all three clones (n=9). hESC-RPE cultured on transwells for 60 days.

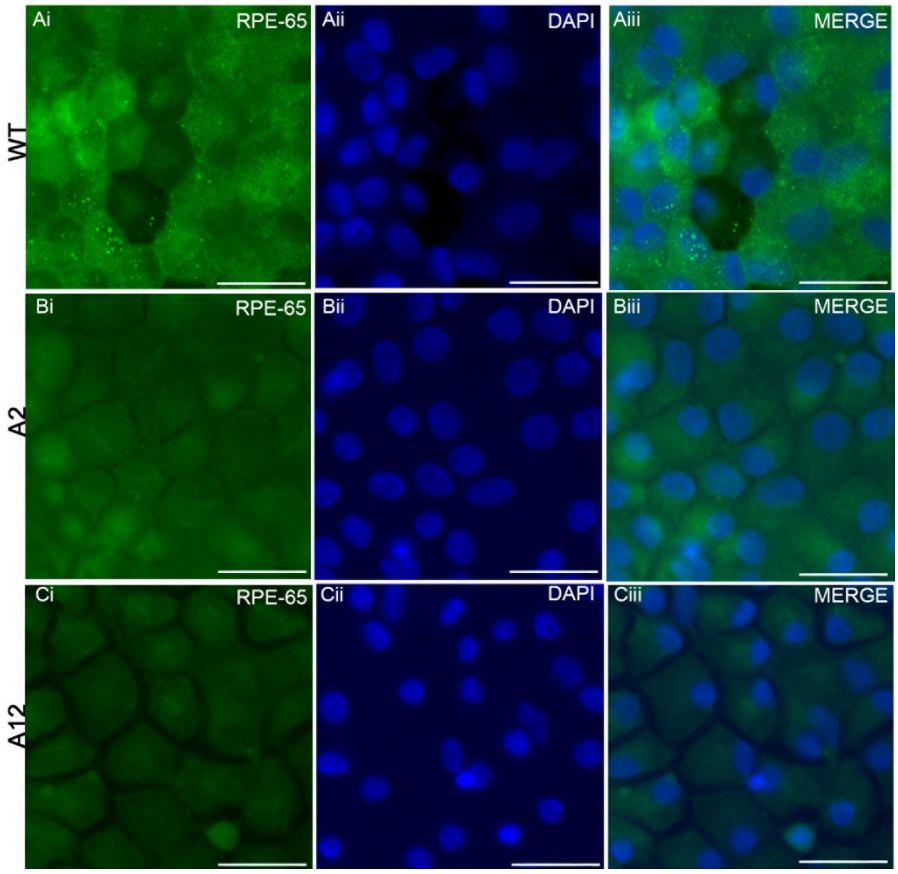

Figure 5-2 Immunocytochemistry for RPE-65 in day 60 hESC-RPE
Ai, Bi. Ci Representative staining of RPE-65 (green).
Aii, Bii, Cii Nuclei stained with DAPI (blue)
Aiii, Biii, Ciii Merged images showing dual DAPI and RPE-65 staining.
Scale bars represent 25μm
Immunocytochemistry performed for three differentiations from all three clones (n=9). hESC-RPE cultured on transwells for 60 days.

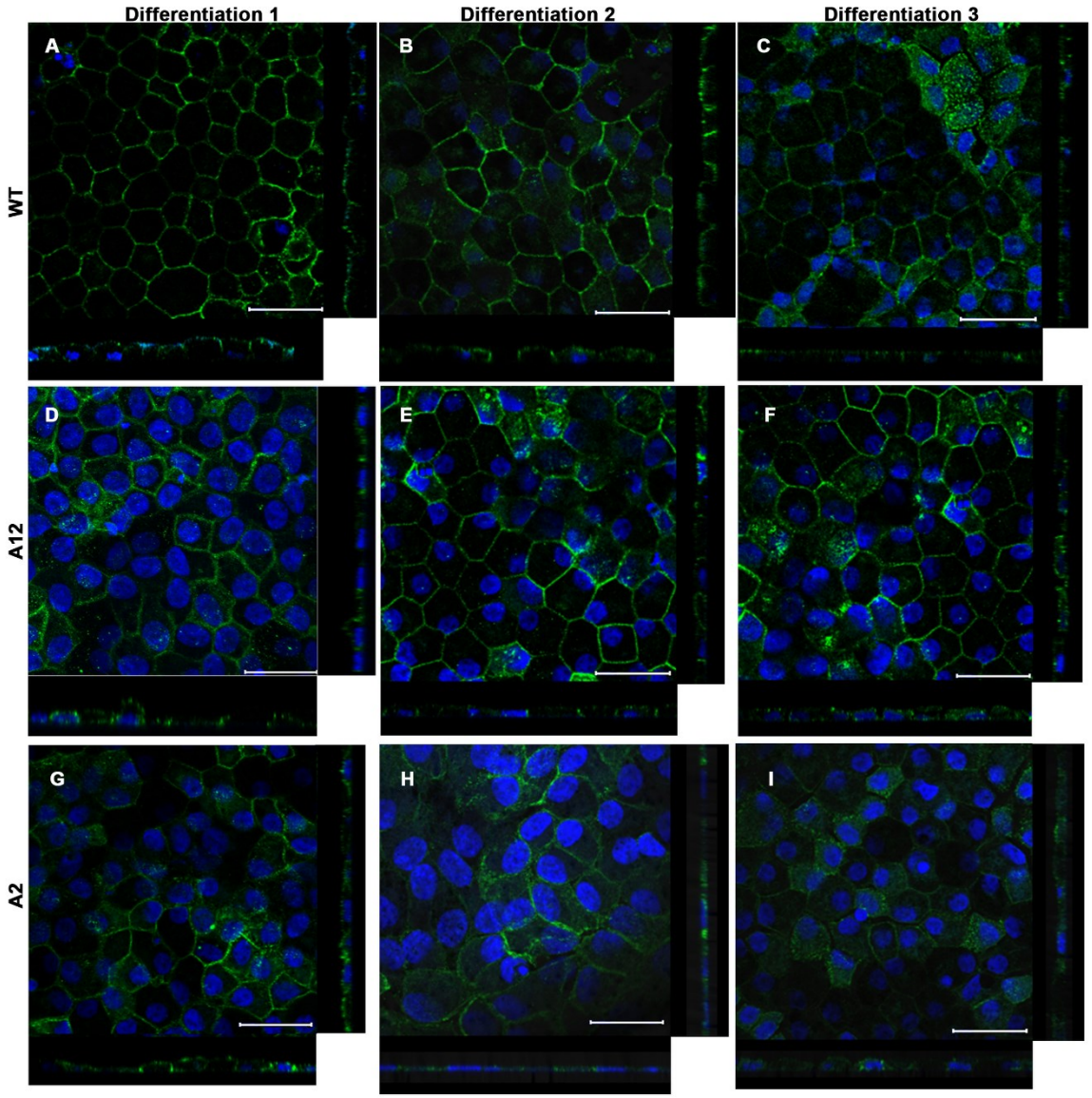

Figure 5-3 Immunocytochemistry for Na+/K+ ATPase in day 60 hESC-RPE
Confocal z-stack images of immunofluorescent labelling for the RPE marker Na^+/K^+-ATPase (green) and nuclear stain DAPI (blue) of hESC-RPE cultured on transwells for 60 days (n=3 for each clone).
A: WT 1, B: WT 2, C: WT 3, D: A12 1, E: A12 2, F: A12 3, G: A2 1, H: A2 2, I: A2 3.
Predominantly apical localisation of Na^+/K^+-ATPase pump in WT cells.
Apical localisation still present in A2 and A12, however less well demarcated, appears more apico-lateral.
Scale bars represent 25μm.

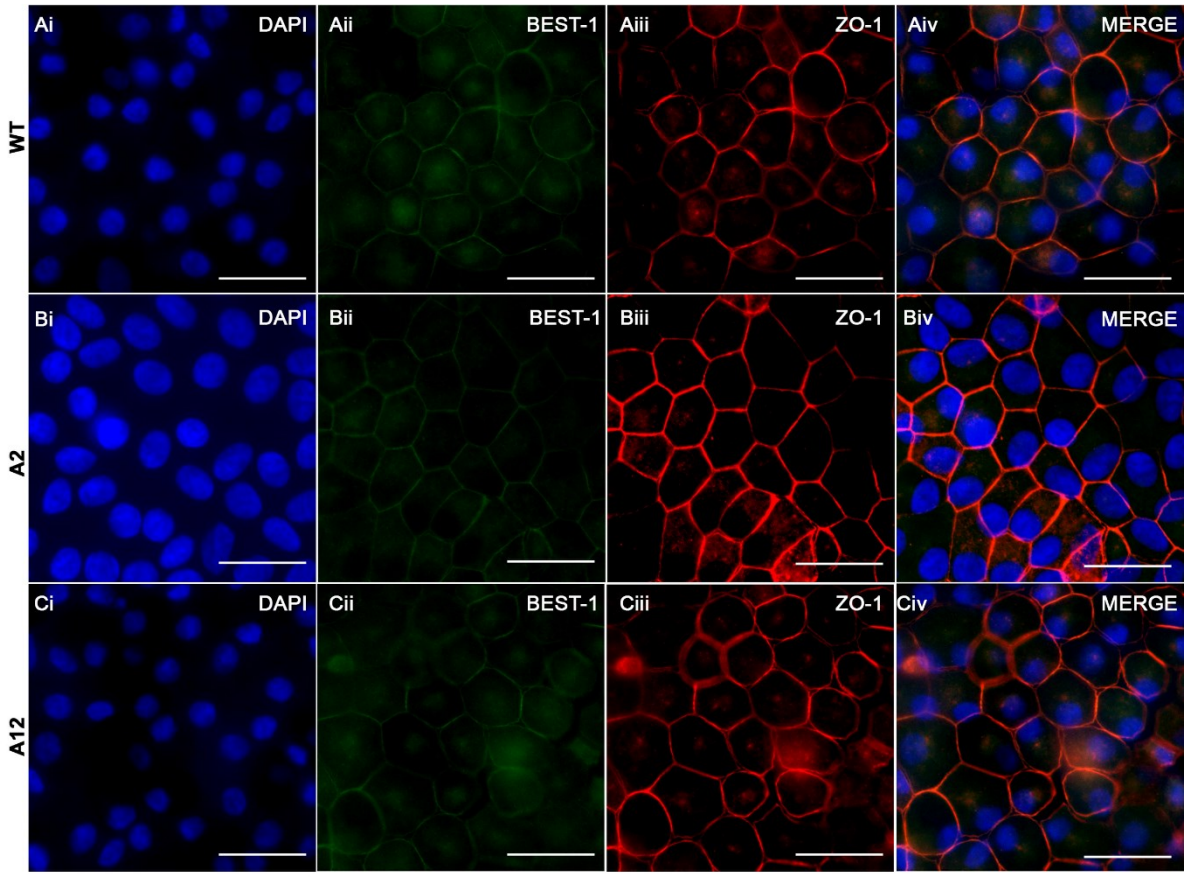

Figure 5-4 Immunocytochemistry for Best-1 and ZO-1 in day 60 hESC-RPE
Ai, Bi. Ci Nuclei stained with DAPI (blue)
Aii, Bii, Cii Representative staining of Best-1 (green). Best-1 staining weak for WT and TSPAN10 mutants.
Aiii, Biii, Ciii Representative staining of ZO-1 (red).
Aiv, Biv. Civ Merged images showing DAPI, Best-1 and ZO-1 staining.
Scale bars represent 25μm
Immunocytochemistry performed for three differentiations from all three clones (n=9). hESC-RPE cultured on transwells for 60 days

5.1.2 RT-PCR

cDNA was made from hESC-RPE at day 40 post differentiation cultured on transwells and RT-PCR performed for expression profiling of RPE specific markers including Best-1, an integral membrane protein localised to the basolateral plasma membrane. All differentiations for all cell clones including WT and TSPAN10 k.o mutants produced amplicons of the expected size, confirming expression of Best-1 (Figure 5 – 5). RT-PCR for the RPE specific marker RPE-65 showed expression of an amplicon of the expected size in all differentiations for all cell clones (Figure 5 – 5).

Tyrosine Kinase c-mer (MerTK) is a tyrosine kinase expressed at the apical surface of the RPE. It is a key regulator of the recognition and internalisation of POS during phagocytosis. RT-PCR for MerTK showed production of an amplicon of the expected size for all differentiations for all cell clones including WT and TSPAN10 k.o mutants, confirming expression of MerTK in hESC-RPE (Figure 5 – 5). The housekeeping gene *GAPDH* was used as a control in these experiments to control for RNA integrity (Figure 5 – 5). Primer sequences are displayed in Appendix D, Table 13 – 5.

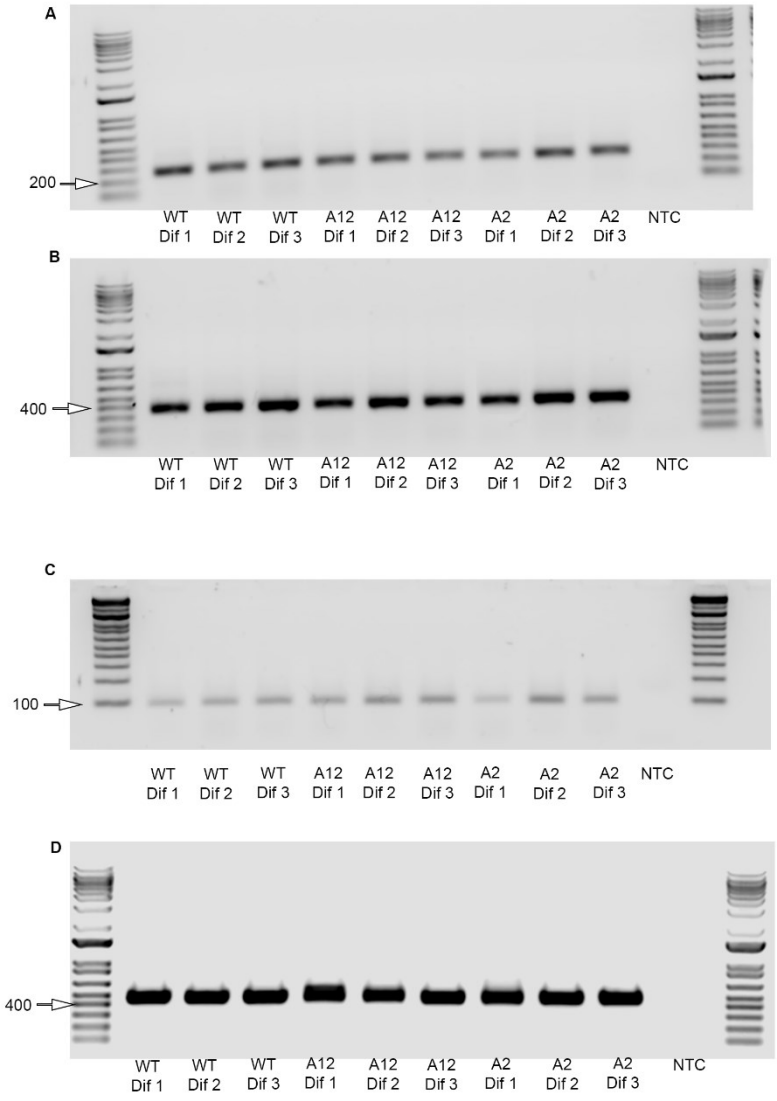

Figure 5-5 RT-PCR of cell clones A2, A12 and WT cDNA for retinal pigment epithelium (RPE) markers
A: RT-PCR for RPE-65 for all clones and differentiations (279bp).
B: RT-PCR for Bestrophin-1 (Best-1) for all clones and differentiations (359bp).
C: RT-PCR for MerTk for all clones and differentiations (95bp).
D: RT-PCR for GAPDH for all clones and differentiations (450bp).

5.1.3 RT-qPCR

To confirm equal expression of RPE markers between WT and TSPAN10 k.o mutants RT-qPCR was performed for RPE-65, Best-1, Tyrosinase and MerTK (Figure 5 – 6). cDNA was produced from hESC-RPE cultures at day 40 post differentiation for all differentiations of all cell clones (n = 9). Samples were run in triplicate. No significant differences were seen between WT cells and clones A2 or A12. This confirmed all cell clones including TSPAN10 k.o mutants displayed equal expression of RPE markers. To further validate these results a Pearson correlation analysis was performed to compare the RNA-seq data (Chapter 6) with the RT-qPCR results for RPE markers (Appendix D, Figures 13 – 15 & 13 – 16). Figure 13 – 15 shows the correlation for RPE-65 (R^2 =0.60, p=0.02) and Figure 13 – 16 the correlation for Best-1 (R^2 =0.67, p=0.01). There was no correlation seen for Tyrosinase nor MerTK.

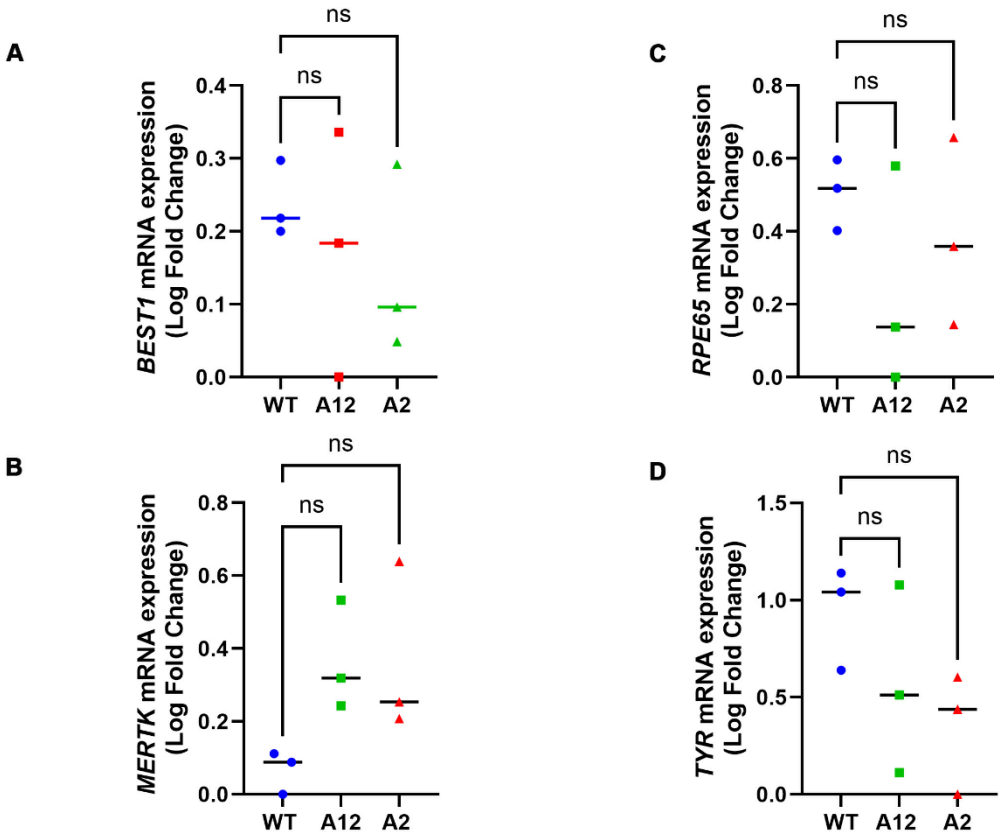

Figure 5-6 RT-qPCR validation of expression of RPE markers in hESC-RPE day 40 in culture post differentiation
Normalised mRNA expression relative to mean wild type ΔCq value. Bars depict mean fold-change and error bars show SEM of three independent experiments. Statistical analysis One-way ANOVA with Dunnett's correction.

A: BEST1. No significant differences seen between WT and TSPAN10 k.o cells.
B: MertK. No significant differences seen between WT and TSPAN10 k.o cells.
C: RPE-65. No significant differences seen between WT and TSPAN10 k.o cells
D: Tyrosinase. No significant differences seen between WT and TSPAN10 k.o cells

5.2 Directional secretion of growth factors

The artificial BRB created by the porous membrane of the transwell insert in combination with hESC-RPE cells produces an *in vitro* system in which inter-compartmental communication must occur via the hESC-RPE monolayer. Polarised secretion of pigment epithelium-derived factor (PEDF) and vascular-endothelial growth factor (VEGF) in RPE monolayers can be used as a benchmark of RPE monolayer health and function [284]. Evidence of hESC-RPE cell polarisation was observed via the apical localisation of Na^+/K^+ATPase using confocal microscopy in Section 5.1.1. Subsequently, the secretion profile of hESC-RPE was examined.

ELISA quantification was performed on conditioned apical and basal media harvested from 63-day old hESC-RPE cultures to determine the level and directional secretion of growth factors from the RPE (Figure 5 – 7). Samples were run in duplicate for each differentiation of each cell clone. Student's unpaired two-tailed t-test was used to analyse differences between apical and basal concentrations for each differentiation of each clone (Data not shown). Mean VEGF differences between apical and basal secretion for each cell clone were assessed using a one-way ANOVA with Tukey's correction (Figure 5 – 7). At 63 days WT basal secretion (2.49 ± 0.67 ng/ml) was significantly greater than apical secretion (0.58 ± 0.15 ng/ml), ($p<0.05$). In the TSPAN10 k.o clones, both A12 and A2 showed increased basal over apical secretion, especially A12, however this was not statistically significant (Figure 5 – 7a). In fact, A2 showed near equal apical and basal VEGF secretion, with a statistically significant increase in apical VEGF secretion when compared to WT apical VEGF (Student's two-tailed t-test, $p<0.05$).

PEDF secretion was also assessed using ELISA quantification of conditioned apical and basal media harvested from 63-day old hESC-RPE cultures (Figure 5 – 7b). After 63 days in culture PEDF was preferentially secreted to the apical compartment in WT (7.50 ± 2.55 µg/ml), A12 (9.48 ± 0.75 µg/ml) and A2 (7.19 ± 2.23 µg/ml) compared to basolateral secretion of WT (2.62 ± 1.39 µg/ml), A12 (2.46 ± 0.89 µg/ml) and A2 (2.02 ± 0.43 µg/ml) ($p < 0.05$).

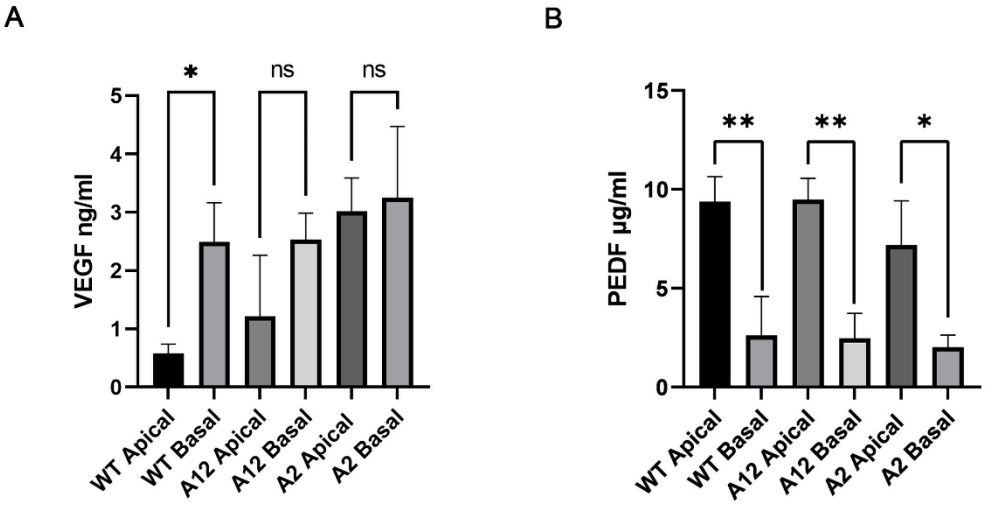

Figure 5-7 Secretion of growth factors from hESC-RPE
A: Secretion of vascular endothelial growth factor (VEGF) from hESC-RPE
ELISA quantification of VEGF was performed on conditioned media harvested from the apical and basal compartments of hESC-RPE after 63-days in culture on transwell inserts.
There was a statistically significant increase in basal vs apical conditioned media VEGF at 63 days for WT cells. There was no statistically significant differences in basal vs apical conditioned media VEGF for the TSPAN10 k.o clones A12 and A2.
Results are expressed as mean + SD for three separate differentiations for each cell clone. Statistical analysis performed using one way ANOVA with Tukey's correction for multiple comparisons. *p<0.05
B: Secretion of pigment derived epithelial growth factor (PEDF) from hESC-RPE
ELISA quantification of PEDF was performed on conditioned media harvested from the apical and basal compartments of hESC-RPE after 63-days in culture on transwell inserts. Results are mean + SD for three separate differentiations for each cell clone. Each sample was run in duplicate.
PEDF was significantly higher in apical compared to basal conditioned media at 63-days for WT p=0.007; A12 p=0.0018; A2 p=0.018
Statistical analysis performed using One-way ANOVA with Tukey's correction for multiple comparisons.
**p<0.01, *p<0.05

5.3 Blood-retinal barrier formation

To evaluate the functional ability of tight-junction complexes observed in section 4.1.1 TEER measurements were performed over an 11-week period. High TEER indicates integrity of an epithelial monolayer, in which cell-cell junctions, especially tight junctions, provide a barrier function to prevent paracellular permeability. Conversely, loss of epithelial barrier integrity, indicated by low TEER, reflects increased epithelium permeability which may indicate cell-cell junction disruption.

TEER readings were performed weekly over an 11-week period, there was a steady increase in TEER values for all differentiations of both WT and TSPAN10 k.o mutants over time, peaking at approximately 63 days (Figure 5 - 8). Interestingly TSPAN10 k.o mutants appeared to have a higher TEER than WT hESC-RPE at most time points. This was tested using one-way ANOVAs with Dunnett's post-hoc correction at all time points and a statistically significant difference seen between WT and TSPAN10 k.o mutants for all differentiations ($p<0.0001$) up to 56 days (data not shown). At 63 days the majority of cells reached peak resistance values, there was still a highly significant difference between the majority of TSPAN10 k.o mutant differentiations and WT ($p<0.0001$), except for WT differentiation 1 & A12 differentiation 2, and WT differentiation 2 & A12 differentiation 2.

Mean TEER values for WT, A12 and A2 clones at 63 days are displayed in Figure 5 – 9A. There was a significant difference between WT and A12 ($p=0.01$), and WT and A2 ($p<0.01$) clones (one way ANOVA with post-hoc Dunnett's correction). Figure 5 – 9B reports the individual TEER values of differentiations at this time point. Taken together these results suggest that all hESC-derived RPE have good epithelial barrier integrity with a TEER around 200 $\Omega.cm^2$, in line with previous reports [285].

However, the differences between TSPAN10 k.o and WT cells suggest that a phenotype of TSPAN10 k.o could be an increased TEER, and therefore increased barrier function and reduced paracellular permeability.

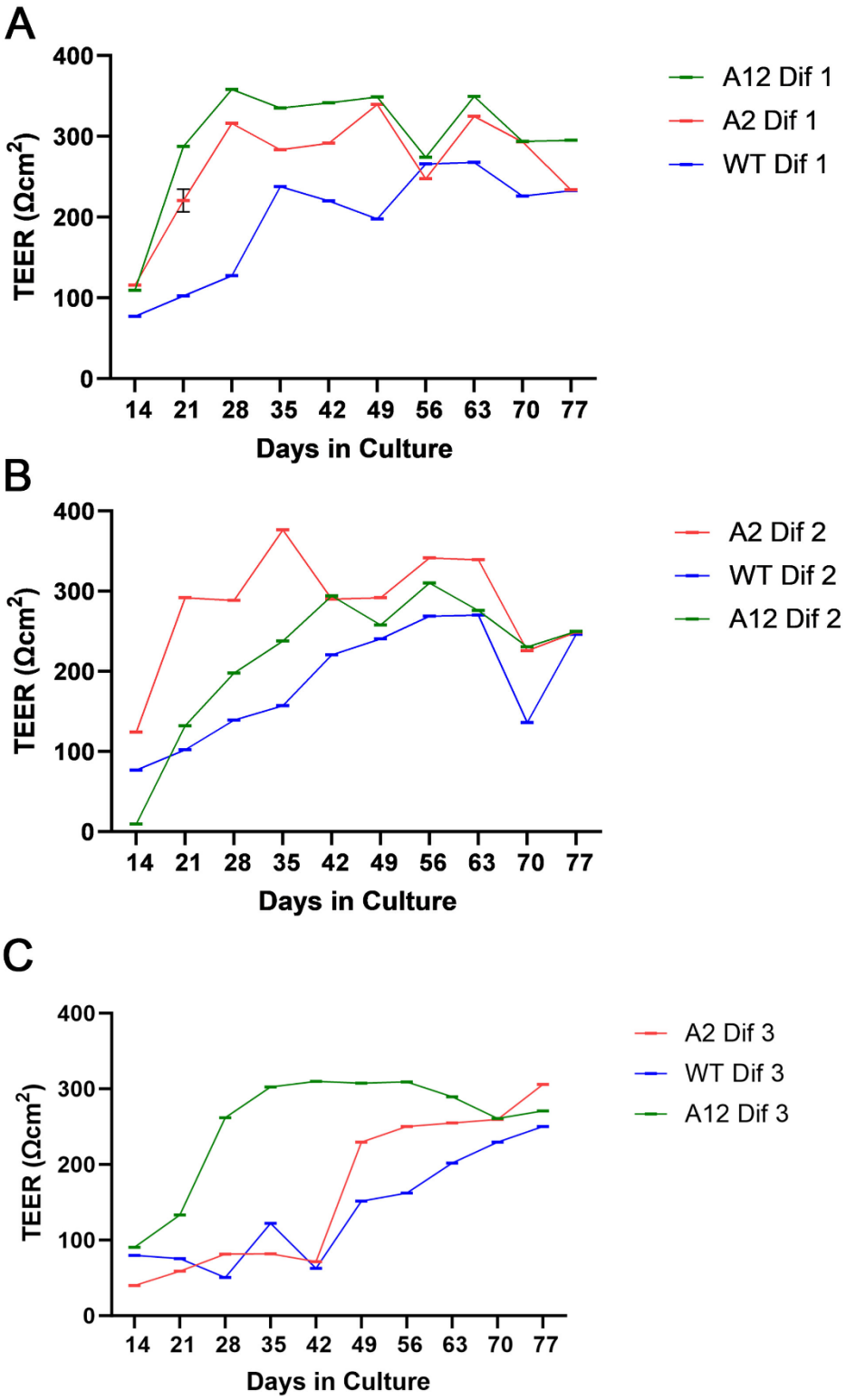

Figure 5-8 Transepithelial electrical resistance (TEER) in TSPAN10 mutant and WT clones.
High TEER indicates epithelial barrier integrity and is influenced by tight junctions.
TEER plotted over time in days as mean ± SD. An increase in TEER is seen in all differentiations and clones over time.

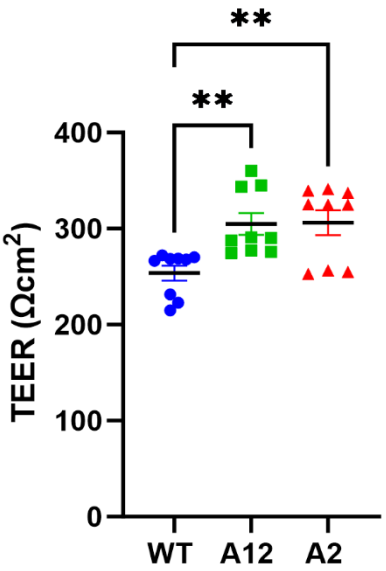

Cell clone & differentiation	TEER (Ωcm^2) at 63 days
WT Dif 1	267.68 ± 0.91
WT Dif 2	270.29 ± 1.54
WT Dif 3	223.19 ± 1.44
A12 Dif 1	349.44 ± 1.07
A12 Dif 2	275.76 ± 1.07
A12 Dif 3	289.46 ± 1.44
A2 Dif 1	324.8 ± 0.18
A2 Dif 2	339.24 ± 1.68
A2 Dif 3	254.74 ± 1.53

Figure 5-9 Mean Transepithelial electrical resistance (TEER) in TSPAN10 mutant and WT clones at day 63
Scatter dot plots for TEER values measured from separate inserts for each cell line, mean value shown by black line, and error bars show SEM of three differentiations Three separate differentiation experiments displayed for each cell line. One-way ANOVA with Dunnett's multiple comparison post-hoc test used for statistical analysis. **p<0.01
Significantly increased TEER in TSPAN10 mutants versus WT.
Table displays individual TEER values (mean, n=3) for each differentiation. All differentiations have a TEER > 200Ωcm^2.

5.4 Phagocytic ability

Phagocytosis is a key function of the RPE. The phagocytic function of our RPE monolayers was analysed by feeding fluorescently-labelled POS to WT and TSPAN10 k.o cultures. hESC-RPE were grown on transwells for at least 40 days, 4 hrs following a POS load cells were fixed and stained for RPE markers to discern individual cells. Three images were taken for each differentiation of each cell line. The number of attached and internalised POS were counted per frame using Fiji (Image J). No differences between the number of attached (p=0.9474) and internalised (p=0.9939) POS between TSPAN10 k.o and WT cells were seen, statistical analysis with one way ANOVA (Figure 5 – 10). This confirms that our cell cultures can effectively phagocytose POS despite TSPAN10 k.o.

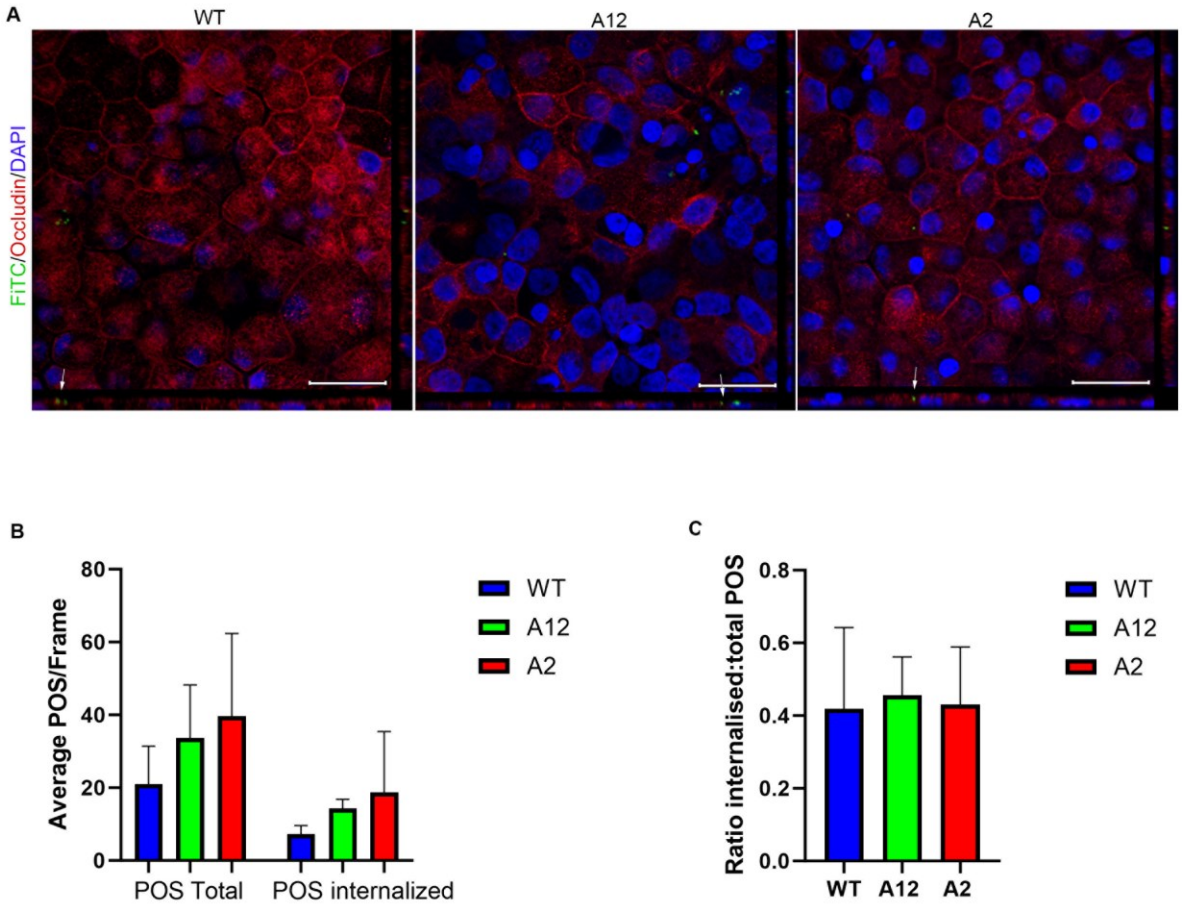

Figure 5-10 Phagocytic ability of hESC-RPE
A: Confocal z-stack images 4 hrs after feeding porcine POS labelled with FiTC. White arrows indicate internalised POS (green). Occludin (red) and DAPI (blue) detected to visualise cells. Scale bar 25 µm
B: Bar chart showing quantification of average number of POS/frame, n = 3 cell lines with three replicate confocal frames (63× magnification) each. Error bars indicate SD.
C: Bar chart showing ratio of internalised to total POS. n = 3 cell lines with three replicate confocal frames (63× magnification) each. Error bars indicate SD.

5.5 Interpretation and Interim Discussion

This chapter explores the differentiation of hESCs into healthy RPE through validation of a healthy RPE phenotype. Stem cell derived RPE are the current gold standard for *in vitro* RPE modelling studies [164, 165], however confirmation of successful differentiation must first be determined before cells can be used for downstream applications. We used a combination of techniques to confirm expression of RPE specific markers, initially immunocytochemistry was performed (Figures 5 – 1 & 5 – 2) demonstrating expression of the mid-late tight junction marker occludin, and the RPE marker RPE65. Such markers are typically expressed by stem-cell derived RPE by differentiation day 60 [170]. We saw expression in all differentiations for all clones. In WT & k.o cells ZO-1 staining is continuous along intercellular junctions, indicating high expression of junctional complexes. Staining for tight-junction markers highlights the typical RPE cobblestone morphology, which is clearly seen in WT cells but is not as uniform in the k.o clones. One thought for this appearance is that the TSPAN10 k.o cells are less mature than their WT counterparts, given that less mature hESC-RPE typically have a more disorganised appearance [286]. Stem cell derived RPE developed for transplantation purposes are typically assessed by their degree of cobble stoning and pigmentation [285], with those that are more pigmented and with the most uniform appearance felt to be superior. Both such features can be assessed by eye allowing the cell sample to maintain viability, something which is not feasible when assessing a cells' protein and or gene expression. Consequently, one could surmise that the TSPAN10 k.o clones are inferior RPE differentiations in comparison to WT and/or that they are less mature. Given that this same pattern of reduced cobble stoning and pigmentation (discussed further in Chapter 7) is seen in all differentiations for both clones (n = 6) in comparison to WT (n = 3). It may suggest that TSPAN10 is involved in RPE differentiation and/or RPE maturation. Another explanation could relate to a direct effect of TSPAN10 on cell morphology. TSPAN10 belongs to the tetraspanin family, which are all membrane spanning proteins. Members of the tetraspanin family such as CD151 have been shown to regulate cell morphology [287]; given this familial classification TSPAN10 k.o could impact the cell membrane and therefore affect cell morphology, which could also explain the less uniform cobblestone appearance identified. Assessment of cobblestone morphology can be measured through an automated process [288], removing any risk of bias through self-assessment and allowing a more robust numerical comparison of clones. However, a numerical representation of cobblestone morphology is not standardly performed for most stem-cell derived RPE studies [165, 289].

RT-PCR and RT-qPCR were used to confirm the expression of relevant RPE markers (Figures 5 – 5 & 5 – 6). All differentiations for all clones expressed *RPE-65*, *Best1* and

MerTk, with no significant differences seen in expression levels between TSPAN10 k.o cells and WT. These results reconfirm an RPE phenotype in our stem cell derived RPE, and further help to validate the RPE differentiation protocol used [60]. Expression of the above selected genes are commonly used in the literature to confirm correct differentiation of stem cells into RPE [170, 176]. Further clarification of correct RPE signature gene expression will be sought from the RNAseq data in Chapter 6.

Pearson correlation analyses were performed to compare the RT-qPCR results to the RNAseq data (Chapter 6). The Pearson correlation coefficient (R^2) is the most common way of measuring a linear correlation. It is a number between –1 and 1 that measures the strength and direction of the relationship between two variables, in this case the RT-qPCR and RNAseq data. As a rule of thumb, an R^2 value greater than 0.5 shows a strong correlation between two variables. The R^2 values for RPE-65 and Best-1 were both >0.5, and both p-values were <0.05, inferring that the correlation coefficient is statistically significant. This was not true for the other RPE markers MerTK and Tyrosinase. While both RNAseq and RT-qPCR approaches estimate expression by quantifying the abundance of transcripts, the methods involve different experimental and bioinformatic processing procedures, which can influence correlation. Furthermore, the normalisation method used to obtain final expression estimates from the raw RT-qPCR data can be a source of differences between RT-qPCR and RNAseq estimates.

Stem-cell derived RPE are typically grown on transwells to allow RPE maturation. The transwell membrane supports the growth of epithelial cells in a uniform monolayer, promoting the formation of tight junctions as well as the acquisition of polarity, which is critical to RPE cell function. Furthermore, culture on the transwell membranes enables functional testing of TEER and polarised secretion of molecules to verify the quality of the RPE monolayer.

Initially to determine the presence of functional plasma membrane polarity within cultures Na^+/K^+ ATPase expression was assessed using immunocytochemistry. RPE polarity is required for its anti-photoxidative, vectoral transport, directional protein secretion and phagocytic functions [20]. In contrast to epithelia from both the kidney and gall bladder, Na^+/K^+ ATPase is mainly expressed on the RPE apical surface where it is thought to facilitate the process of phototransduction and has been implicated in the regulation of a well-differentiated, polarised epithelial phenotype [20]. This has led to its frequent use in the characterisation of RPE from a variety of sources including cell lines, primary RPE and stem cell derived RPE. Here, immunocytochemistry for Na^+/K^+ ATPase confirmed apical expression and hence RPE polarity (Figure 5 – 3) for all differentiations of all clones. The z

axis snapshots did however reveal apicolateral staining for the k.o cells, whereas WT cells appeared taller with more apical than apicolateral staining. It may be that the TSPAN10 k.o cells have reduced polarity in comparison to WT. As previously discussed, tetraspanins are membrane proteins, Na^+/K^+ ATPase is also situated in the outer plasma membrane of cells [290]. Consequently, if TSPAN10 k.o alters the plasma membrane then this could affect other membrane proteins such as Na^+/K^+ ATPase.

Tight junctions are apical intracellular junctions which not only control paracellular permeability across the epithelium, but also act as a physical barrier to maintain distinct apical and basolateral membrane compositions [23]. The functional integrity of these tight-junction complexes was examined in section 5.3 through TEER, which is a measure of paracellular ion movement. TEER is largely influenced by tight junctions, but also by other cell-cell and cell-substrate interactions [291-293]. By approximately day 40 (week 6) all cell clones and differentiations, had reached a TEER of at least 200 Ωcm^2 .This is in keeping with the literature, with hESC derived RPE typically reaching a TEER of between 150-200 Ωcm^2 by day 40 in culture [285]. In fact, a study by Michelet *et al*, reported 'pure' RPE populations to have a maximum TEER of 158 Ωcm^2 with the TEER increasing with the degree of pigmentation. We saw the opposite, WT cells were more pigmented than TSPAN10 k.o clones, however the TSPAN10 k.o cells had a significantly increased TEER. The TEER figures we saw are also similar to those reported for adult human RPE (178 Ωcm^2) [294]. Interestingly all differentiations of both TSPAN10 k.o mutants showed an increased TEER relative to WT. This was analysed at weekly timepoints over 11 weeks, and there was a statistically significant increase in the TEER of TSPAN10 k.o mutants versus WT seen at all timepoints. This suggests that TSPAN10 k.o is possibly increasing the integrity of tight junctions in hESC-RPE. Currently the reasons for this are unknown, one possibility is that k.o of TSPAN10 causes an upregulation of another member of the tetraspanin family, which consequently increases the integrity of tight junctions and therefore the TEER. We have examined tight junctions in our hESC-RPE using immunofluorescence staining with antibodies against ZO-1 and occludin (Figures 5 – 1 & 5 – 4), however we have not examined aherens junctions. It is difficult to accurately quantify expression using immunofluorescence, with qualitative assessments typically used [295], therefore changes in gene expression in TSPAN10 k.o cells versus WT will be thoroughly examined using the RNA-seq dataset (Chapter 6) to further understand this TEER phenotype, including the expression of RPE tight junction genes such as occludin, ZO-1, the Claudin family [26] and adherens junction genes.

We also explored the directional secretion capability of RPE monolayers. This characteristic is highly desirable in *in vitro* cultures as growth factors are selectively secreted either from

the RPE's basal or apical membrane to serve distinct and directional functions. The compartmentalised nature of the transwell system makes it conducive for examining and preserving this directional secretion, allowing the measurement of protein concentrations in both the apical and basal compartments. Given their well-established native secretion patterns, PEDF and VEGF concentrations in the media are frequently used as functional indicators of polarity. Here we utilized this to validate our hESC-derived RPE cultures.

PEDF secretion was analogous to native RPE, favouring directional secretion from the apical surface. PEDF concentrations were comparable to that reported in stem cell derived RPE cultures [170]. This was seen at both 21 days and 63 days, with no difference between the two time points. Da Cruz and colleagues report that PEDF secretion increases as RPE matures and then declines after ~80 days in culture [296]. This was not true for our cultures. Furthermore, there was no difference evident between PEDF secretion in TSPAN10 k.o versus WT cultures. This is corroborated by the RNAseq data, where PEDF was not called as a differentially expressed gene (Chapter 6).

VEGF is typically secreted in a polarised manner from the basal aspect of RPE cells [297, 298]. Here, WT cells showed a preference for basal VEGF secretion, which was comparable to that reported in stem cell derived RPE cultures [299]. Conversely, there was no statistically significant difference in basal vs apical VEGF secretion for both TSPAN10 k.o clones, although the A12 clone did show a preference for basal VEGF secretion. (Figure 5 – 7A).

VEGF and PEDF exert a certain yin/yang effect, with PEDF antagonising VEGF signalling [300-302]. PEDF is an anti-angiogenic and anti-apoptotic photoreceptor trophic factor with a potent neurotrophic effect [303]. Whereas VEGF is an angiogenic factor secreted by the RPE to maintain the choriocapillaris [303]. Our TSPAN10 k.o cells did not show the expected polarised basal secretion of VEGF. When *VEGFA* gene expression was analysed in our RNAseq data set (Chapter 6) there was no evidence of increased expression in WT nor either of the TSPAN10 k.o clones. It appears that VEGF in our TSPAN10 mutant hESC-derived RPE is not secreted in a polarised manner, especially for the A2 clone. Whether this is a drawback of our cultured cells or related to the TSPAN10 k.o given the differences between WT and A2 is not known. Interestingly, others have shown that treatment of stem-cell derived RPE with H_2O_2 to mimic oxidative stress causes a significant increase in the secretion of VEGF [299]. If the TSPAN10 k.o clones are intuitively more stressed than their WT counterparts this could explain the VEGF ELISA result, although one would expect an equal increase in VEGF basal secretion in comparison to WT, not just apical as seen here.

Finally, we examined the phagocytic ability of our RPE cultures. The RPE possesses a high phagocytic capacity to accommodate the constant proteolytic burden of POS renewal. In fact, each cell is responsible for the diurnal removal of up to 30-50 POS tips daily [35, 304]. All differentiations of all cell clones were able to internalise POS after a POS challenge, with no differences evident between WT and TSPAN10 k.o cells.

In summary, Chapter 5 validates the identity of the hESC-RPE within this culture system, supporting their use in downstream experiments.

6 Transcriptomic analysis of TSPAN10 k.o clones

RNA-seq was used to investigate gene expression in the TSPAN10 mutants A12 and A2 in comparison to WT hESC-RPE. The aim was to identify transcriptional changes common to A12 and A2 that occurred as a result of TSPAN10 k.o.

In RNA-seq, gene expression level is estimated by the abundance of transcripts that map to the genome. Read counts are proportional to gene expression level, gene length and sequencing depth.

Cells were cultured in T75 flasks for 40 days post differentiation. RNA samples from each differentiation for each clone were isolated and sent to NovoGene Europe for sequencing (WT n=3, A12 n=3, A2 n=3). NovoGene also performed the initial gene expression analysis, therefore no credit can be taken for this work. Log2 fold-change of gene-coding RNA expression and associated adjusted p-values (p_{adj}) were calculated by comparison of gene hit counts between cell lines. Two comparisons were made. A2 and A12 differentiations were each compared to WT differentiations. For analysis of RNA-seq data, the following assumption was made:

Assumption: Transcription changes common to A2 and A12 (compared to WT) were caused by the loss of *TSPAN10*.

Initially validity of data was checked by confirming the number of mapped reads per sample. The number and percentage of reads aligned to the human genome (GRCh38) ratio should be higher than 70%. This was performed by NovoGene Europe and results presented in Table 6 – 1. All samples had mapped reads >90%.

Log2 fold-change data were subjected to two analysis pipelines: (i) gene set enrichment analysis (GSEA), to identify over-represented sets of genes, such as those involved in a particular signalling pathway; and (ii) differential gene expression analysis, to investigate individual genes of interest.

Genes with an absolute log2 fold-change >1.00 and a p_{adj} <0.05 were called as differentially expressed genes (DEGs), as per NovoGene Europe, both are commonly used empirical values in RNAseq projects. A12 had 489 DEGs in comparison to WT, were as A2 had 152. Augmented differential gene expression was not surprising in both A12 and A2 given the previously described phenotypes. Compared to WT, A12 and A2 shared 49 upregulated and 64 downregulated DEGs, representing changes assumed to be caused by the loss of *TSPAN10.*

Table 6-1 Number of mapped reads per sample
Number and percentage of reads aligned to the genome; the ratio should be higher than 70%.

Sample Name	Mapped reads (number) (% of total reads)
WTDif1	43592768 (91.95%)
WTDif2	48268788 (91.26%)
WTDif3	40080474 (92.78%)
A12Dif1	36138158 (92.94%)
A12Dif2	44500778 (92.75%)
A12Dif3	44215714 (93.18%)
A2Dif1	43793588 (92.83%)
A2Dif2	44137342 (93.19%)
A2Dif3	36556120 (93.5%)

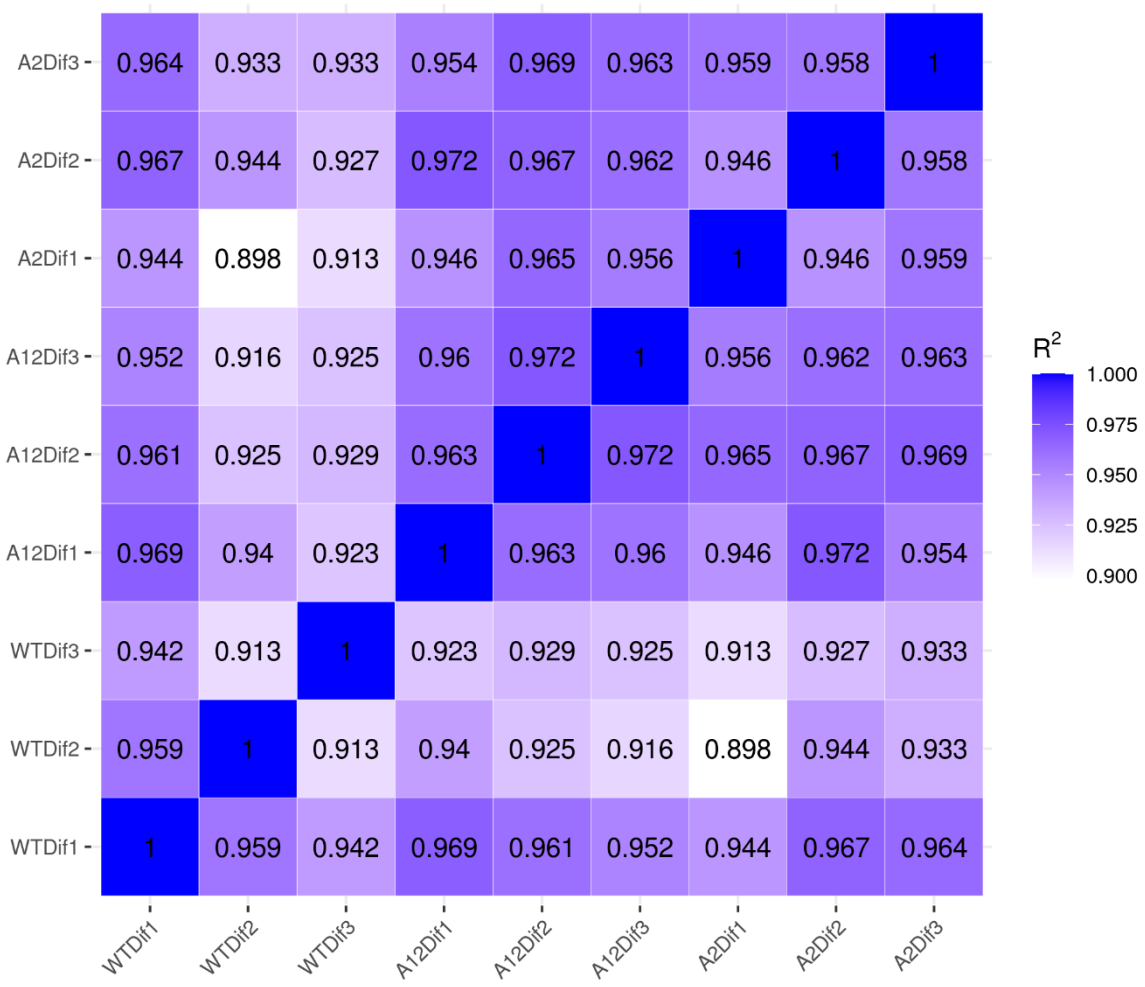

Figure 6-1 Pearson correlation analysis between samples
R^2: Square of Pearson correlation coefficient (r)
The closer the correlation coefficient is to 1, the higher similarity the samples have. The square of the Pearson correlation coefficient should be greater than 0.92 (under ideal experiment conditions) but ideally R^2 should be greater than 0.8.
Figure produced by NovoGene Europe.

The correlation of the gene expression levels between samples plays an important role in verifying reliability and sample selection. This both demonstrates the repeatability of the RNA-seq experiment and estimates the differential gene expression analysis. According to all gene expression levels of each sample, the correlation coefficient of samples between groups was calculated and drawn as heat maps, performed by NovoGene Europe. The higher the correlation coefficient of the sample, the closer the expression pattern. The correlation coefficient matrix is shown in Figure 6 – 1. Under ideal conditions the R^2 should be >0.92 for highly correlated samples, however values greater than 0.8 are acceptable. These results demonstrate almost all differentiations for all cell clones had an R^2 >0.92, therefore, all cell clones were similar despite TSPAN10 k.o. Samples with an R^2 < 0.92 included A2 dif 1 vs WT dif 2 (0.898); A2 dif 1 vs WT dif 3 (0.913); A12 dif 1 vs WT dif 2 (0.916), and WT dif 3 vs WT dif 2 (0.913). This correlation analysis estimates that TSPAN10 k.o does not cause hESC-RPE to be greatly different to their WT counterparts in terms of the transcriptome.

A principal component analysis (PCA) was also undertaken to evaluate intergroup differences and intragroup sample duplication. PCA analysis on the gene expression value, Fragments Per Kilobase of transcript sequence per Millions base pairs sequenced (FPKM) of all samples was performed by NovoGene Europe (Figure 6 – 2). Under ideal conditions, the samples between groups should be dispersed and the samples within groups should be gathered together. PCA is a multivariate dimensionality reduction analysis method. A dataset is a group of points in a multidimensional space and the PCA method moves all data points to a new coordinate system without changing their relative spatial position, making their projections have the largest variances in the new coordinate [305]. In this new coordinate system, the axis with the largest variance of projection is PC1 and the second largest one is PC2. The key of PCA is to reduce the dimension of the data under the premise of keeping the data as much as possible. This method ignores the less relevant variables to describe the relations between different samples. In the PCA analysis for all differentiations of hESC-RPE the TSPAN10 k.o mutants appeared to localise together for all differentiations (A2 and A12). However, the WT differentiations appear to be relatively dispersed relative to PC2 (Figure 6 – 2).

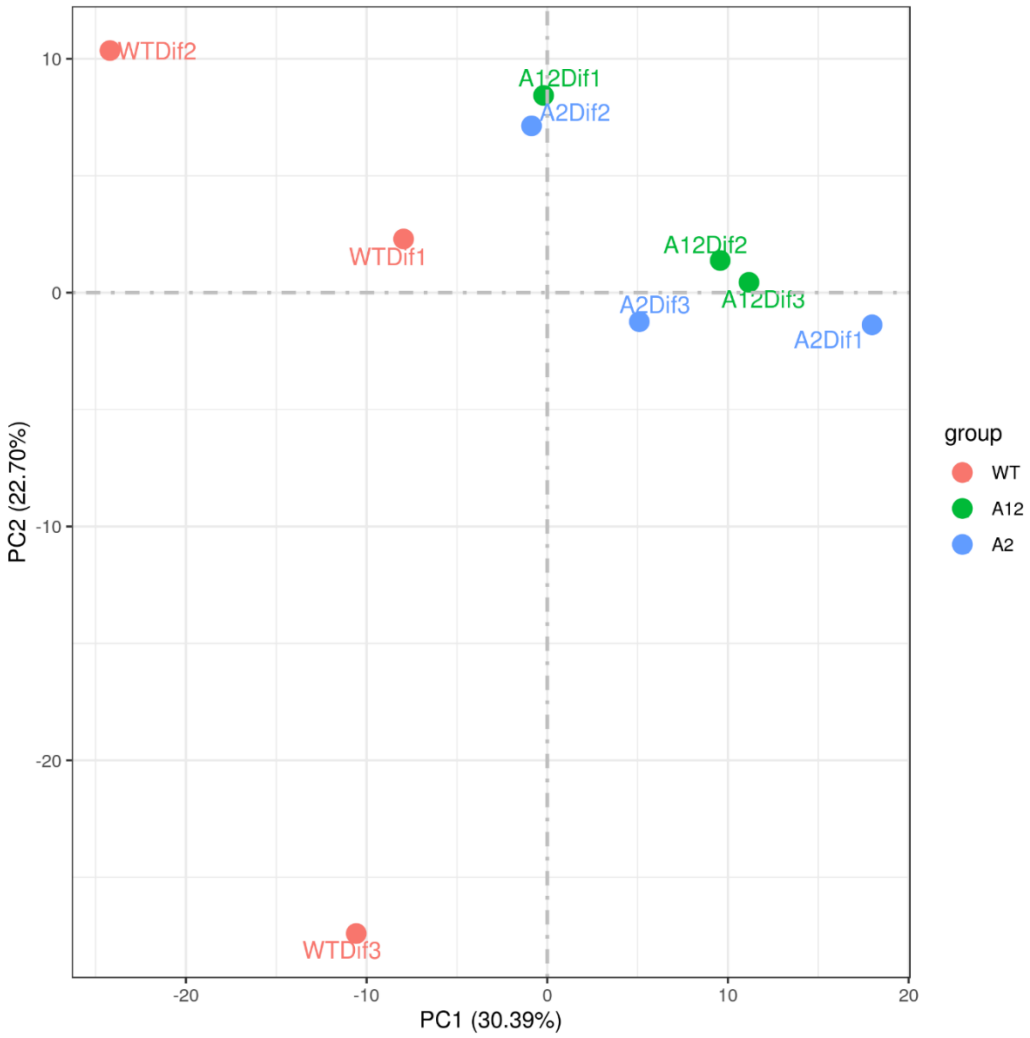

Figure 6-2 2D Principal component analysis (PCA) of hESC-RPE
Two-dimensional map displaying PCA of hESC-RPE. PCA should differ between groups, and samples within groups should localise together. The TSPAN10 k.o mutants appear to localise together for all differentiations (A2 and A12). However, the WT differentiations appear to be slightly dispersed relative to principal component 2. Figure produced by NovoGene Europe.

6.1 Differential Gene Expression Analysis

As a first avenue of investigation, *TSPAN10* expression was investigated in A12 and A2 compared to WT. *TSPAN10* mRNA levels derived from RNA-seq followed the same trend as those determined by RT-qPCR (see Chapter 4, Figure 4 – 20). A2 showed a significant log2 fold-change of -2.24 in *TSPAN10* (p_{adj}= 3.20 x 10^{-20}), whereas that in A12 was still significant, but less so, at -1.25 (p_{adj}= 5.63 x 10^{-8}). *TSPAN10* was therefore a differentially expressed gene in both A2 and A12.

TSPAN10 is a member of the tetraspanin family, therefore it is possible that down-regulation of *TSPAN10* could be compensated by up-regulation of another member of the tetraspanin family. Up-regulated DEGs for both A2 and A12 vs WT were compared. A12 showed

significant up-regulation of the tetraspanin TSPAN18 (p_{adj}= 6.74 x 10^{-6}, log2 fold change = 2.78). This was not, however, replicated in A2, where TSPAN18 was again up regulated (log2 fold change = 1.69), but this was not significant after correction for multiple testing (padj = 0.07) (Figure 6 – 3).

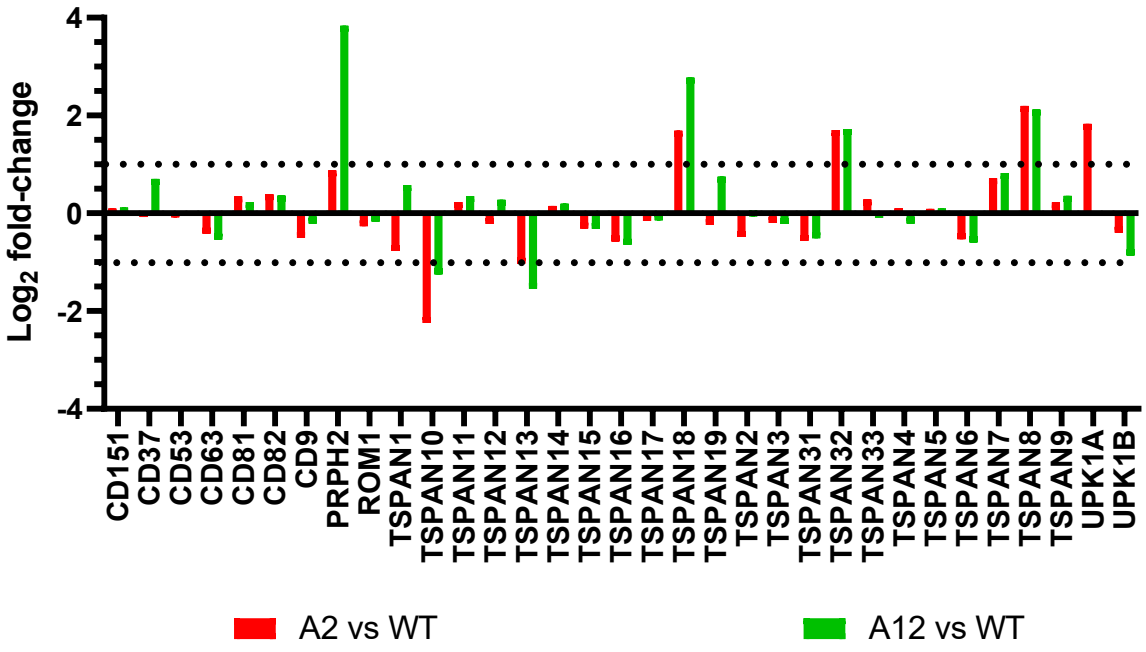

Figure 6-3 Expression of the tetraspanin genes
Coloured bars show the log2 fold-change of gene expression in the comparisons A2 and A12 to WT. Horizontal dashed lines indicate the minimum and maximum log2 fold-change thresholds required for a gene to be considered differentially expressed.

Those genes with the greatest fold change for both A12 and A2 versus WT were examined. 114 DEGs were identified, including 49 upregulated and 64 downregulated DEGs. Of those down-regulated 24 DEGs showed complete absence of transcript in one or both TSPAN10 mutants (summarised in Table 6 - 2). The majority of genes with complete absence of transcript in TSPAN10 mutants are involved in the nuclear factor kappa B (NF-kB) pathway e.g. *NLRP2* and *IRAK4*, or are zinc-fingers, which have a diverse number of roles in the cell including protein folding, lipid binding and regulation of apoptosis.

Table 6-2 Differentially expressed genes (DEGs) with no expression in either TSPAN10 k.o mutant
Genes significantly down-regulated in A12 and A2 vs WT where transcript levels are zero for a TSPAN10 k.o mutant.
Numbers represent Fragments per kilo base of transcript per million mapped fragments (FPKM) corrected to 2 decimal places.
Genes highlighted in pale green are zinc fingers. Genes highlighted in pink belong to the NF-kB pathway. Genes grouped via function.

WTDif1	WTDif2	WTDif3	A12Dif1	A12Dif2	A12Dif3	A2Dif1	A2Dif2	A2Dif3	Gene	Function
2.7	2.28	1.85	0	0	0	0	0	0	NLRP2	NF-kB
1.95	2.39	2.03	0	0	0	0	0	0	IRAK4	NF-kB
1.48	1.71	2.19	0	0	0	0.49	0.46	0.22	ZNF558	Zinc finger
0.82	0.75	0.7	0	0	0	0	0	0	ZNF736	Zinc finger
0.73	0.92	0.48	0	0.02	0	0	0	0	ZNF572	Zinc finger
0.15	0.33	0.13	0	0	0	0	0	0	ZNF208	Zinc finger
0.27	0.54	0.33	0	0	0	0	0	0	ZNF676	Zinc finger
0.4	0.3	0.49	0	0.01	0	0	0	0	ZXDA	Zinc finger
0.1	0.15	0.1	0	0	0	0	0	0	ZNF726	Zinc finger
0.26	0.26	0.15	0	0	0	0	0	0	ZNF728	Zinc finger
0.32	0.31	0.4	0.02	0	0	0	0	0	ZBED6CL	Zinc finger
3.41	6.62	2.4	0	0	0	1.2	1.92	1.61	FPGT	GDP-L-fucose synthesis
0.59	0.83	0.45	0	0	0	0	0	0	PUS7L	Pseudouridine synthesis
0.14	0.09	0.19	0	0	0	0	0	0	TSPYL5	Cell growth
0.8	0.52	0.29	0	0	0	0	0	0	TCEAL5	Transcriptional regulation
0.43	0.28	0.12	0	0.02	0	0.06	0	0.01	PCDHGA3	Calcium ion binding
4.03	4	3.99	0	0	0	0	0	0	TRIM4	Unknown
10.87	12.17	9.05	0	0	0	0	0	0	AL592183.1	Unknown
0.26	0.18	0.22	0	0	0	0	0	0	AC003973.3	Unknown
3.18	4.57	2.14	0	0	0	0	0	0	LINC02506	Non-coding RNA
0.44	0.62	0.35	0	0	0	0	0	0	MIR4458HG	Non-coding RNA
0.57	0.84	0.53	0	0	0	0.05	0.08	0.09	FNBP1P1	Pseudogene
0.06	0.08	0.08	0	0	0	0	0	0	TPTEP1	Pseudogene
0.27	0.48	0.02	0	0	0	0	0	0	C9orf64	Pseudogene

Secondly, those genes with the most significant p_{adj} for both A2 and A12 versus WT were analysed. The catalase gene (*CAT*) was significantly down-regulated in both A2 (log2 fold-change -2.33, $p_{adj} = 1.39 \times 10^{-20}$) and A12 (log2 fold-change -1.52, $p_{adj} = 1.05 \times 10^{-7}$) compared to WT. Catalase is a key enzyme in the cell which catalyses the decomposition of hydrogen peroxide, a reactive oxygen species [306]. Catalase activity has been previously reported to be associated with AMD [306]. This will be examined further in Chapter 6.

DEGs specifically related to the eye included *RAX* (Retina And Anterior Neural Fold Homeobox) which contributes to retinal development and was significantly up-regulated in both A2 (log2 fold-change 1.83, $p_{adj} = 0.014$) and A12 (log2 fold-change 2.31, $p_{adj} = 5.63 \times 10^{-8}$) compared to WT. RAX is essential for the proliferation of retinal progenitor cells and their subsequent differentiation into various retinal cell types including those that constitute the RPE. RAX helps maintain the identity of retinal cells, and in the RPE it functions as an RPE-specific gene promoter seen in RPE progenitor cells. Consequently, the increased levels of expression in TSPAN10 k.o clones hint at possibly a more immature phenotype or likeness to RPE progenitor cells. However, to counter this theory, a study by Lidgerwood et al analysing RPE transcriptomic and proteomic signatures in hESC-RPE at varying ages in culture reported no changes in RAX expression regardless of age [307]. RAX is key in the maintenance of retinal identity by regulating the expression of genes specific to retinal development and function. This ensures that RPE cells develop correctly and acquire their specialized functions, such as pigment production and light absorption. RAX has several other key functions in the eye and is pivotal in eye development, subsequently it is difficult to hypothesise exactly why there is upregulation of *RAX* in TSPAN10 k.o cells, however it most likely suggests that TSPAN10 may influence RPE development.

Interphotoreceptor matrix proteoglycan 2 (*IMPG2*) was also significantly up-regulated in both A2 (log2 fold-change 2.52, $p_{adj} = 0.03$) and A12 (log2 fold-change 3.13, $p_{adj} = 5.39 \times 10^{-6}$) compared to WT. Mutations in *IMPG2* are known to cause retinitis pigmentosa. IMPG2 is unique to the inter-photoreceptor matrix, mice k.o for IMPG2 show abnormal accumulation of its sister proteoglycan, IMPG1, at the boundary between the outer segment (OS) and RPE [308]. This in turn affects the interaction between RPE microvilli and the POS. There were however no significant differences in IMPG1 expression between WT and TSPAN10 k.o cells.

By producing two different clones (A2 and A12) with TSPAN10 k.o, the two transcriptomic data sets can be combined to assess the effects of TSPAN10 k.o. This was performed by designing an analysis pipeline in Kallisto [226] using the Bam files generated by Novo Gene

Europe. Combining the datasets reduced the number of hits, with only 17 genes called as DEGs, Table 6 – 3. A similar pattern was seen to the analysis of the individual clones, with *TSPAN10, CAT*, zinc-finger genes, heat shock proteins genes and those involved in the NF-KB pathway called as DEGs.

DEGs of interest are marked on the volcano plots shown in Figure 6 – 4, which displays the significant up and down regulated genes for both A12 and A2. Of note the scale bars differ between graphs A and B, this is a reflection of the larger spread of fold change and significance seen in the A12 clone. Furthermore, as previously mentioned there were many more DEGs that reached significance in the A12 mutant in comparison to the A2 mutant.

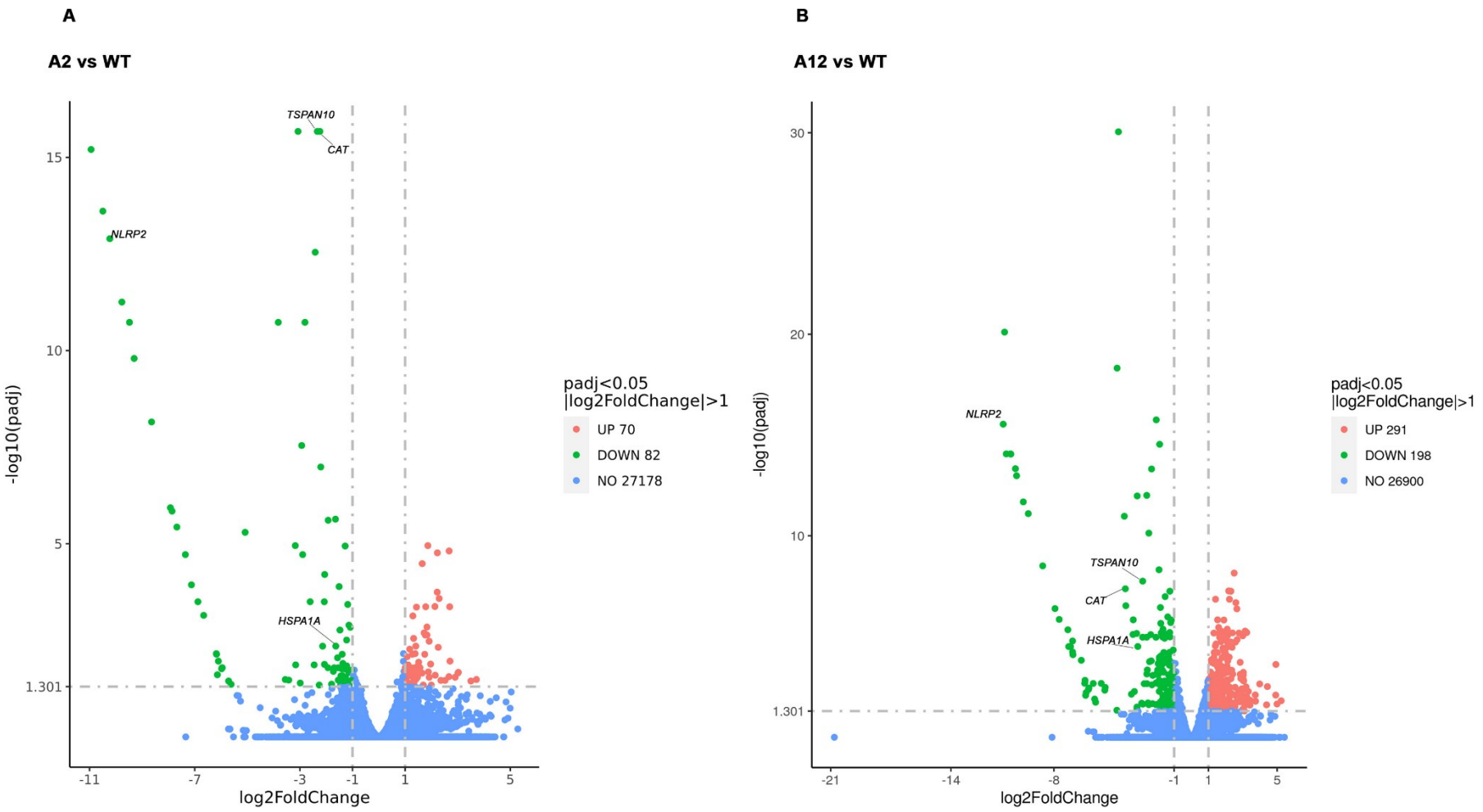

Figure 6-4 Volcano plots displaying significantly differentially expressed genes (DEG) for TSPAN10 mutants vs WT
A: A2 vs WT, B A12 vs WT.
padj<0.05, log2FoldChange>1
DEGs highlighted include *TSPAN10, CAT, NLRP2 & HSPA1A*
Many more DEGs for A12 vs WT than A2. Note the different scales in A & B, representing differences in both the significance and fold change.

Table 6-3 Differentially expressed genes in A2 & A12 combined versus WT
Differentially expressed genes in A12 and A2 vs WT.
Numbers represent Fragments per kilo base of transcript per million mapped fragments (FPKM) corrected to 2 decimal places. Genes grouped via function.
Abbreviations: The B-statistic (B) is the log-odds that that gene is differentially expressed; The moderated t-statistic (t) is the ratio of the M-value to its standard error, where the M-value is the log2-fold change (logFC).
Genes highlighted in pale green are zinc fingers. Genes highlighted in pink belong to the NF-kB pathway. Genes highlighted in blue are involved in the oxidative stress response. Genes highlighted in orange are related to the extracellular matrix.
A positive log-odds (B) means a gene is more likely to be differentially expressed.

Gene	Function	logFC	Mean Expression	t	p.val	p.adj	B
TSPAN10	?	-1.55	5.28	-6.91	1.67E^{-05}	0.03	3.36
CAT	Antioxidant	-1.84	6.34	-6.9	1.69E^{-05}	0.03	3.35
HSPA1A	Heat shock protein	-1.52	5.48	-5.96	6.72E^{-05}	0.05	2.01
MAP10	Cytoskeleton organisation	-2.38	0.56	-6.55	2.79E^{-05}	0.04	2.1
CDH19	Cadherin	-1.7	4.32	-6.32	3.91E^{-05}	0.04	2.55
IAH1	Lipase	-4.57	1.62	-7.9	4.40E^{-06}	0.01	3.89
RARRES2	Adipokine	-1.69	5.07	-6.47	3.13E^{-05}	0.04	2.76
ZNF736	Zinc finger	-3.61	0.67	-7.88	4.56E^{-06}	0.01	3.43
ZNF229	Zinc finger	-3.6	1.54	-8.82	1.42E^{-06}	0.01	4.7
H1F0	Histone	-2.34	1.56	-8.53	2.02E^{-06}	0.01	4.44
H2AFJ	Histone	-2.02	4.21	-7.94	4.18E^{-06}	0.01	4.63
IRAK4	NF-kB	-1.7	3.77	-6.85	1.82E^{-05}	0.03	3.24
AKAP5	Calmodulin binding Associated with RP	-1.3	5.32	-6.97	1.55E^{-05}	0.03	3.44
TAS1R3	Taste	1.52	2.49	6.14	5.11E^{-05}	0.05	1.95
PTPRB	Phosphatase activity	-1.4	3.19	-6.06	5.77E^{-05}	0.05	2.15
ATP2B4	Calcium homeostasis	0.96	5.77	6	6.34E^{-05}	0.05	2.08
FCHO1	Endocytosis	2.2	1.6	5.99	6.46E-05	0.05	1.34

Finally, genes commonly expressed by mature RPE were compared in TSPAN10 k.o cells versus WT to confirm purity of the RPE populations. Genes were selected based on those frequently associated with mature RPE in the literature [170, 307], Figure 6 – 5. No differentially expressed RPE genes were identified for either clone. Re-iterating both that the

cells were efficiently differentiated to RPE and that there is no significant difference in purity between clones.

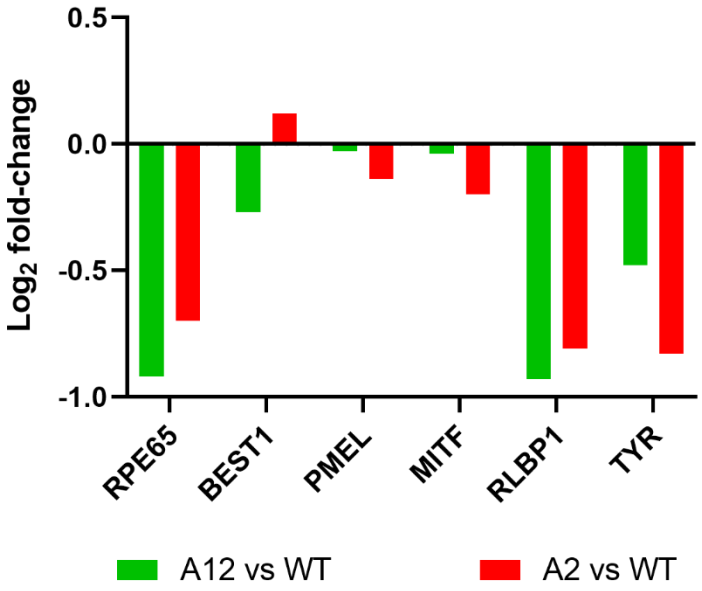

Figure 6-5 Expression of RPE signature genes
Coloured bars show the log2 fold-change of gene expression in the comparisons of A2 and A12 to WT. No genes were differentially expressed. There was reduced expression of RPE-65, RLBP1 and TYR in both k.o clones, however this did not reach significance.

To gain a broader picture of DEGs gene set enrichment analysis (GSEA) was requested and the analysis performed by NovoGene Europe. GSEA employs ranked gene lists to compute an enrichment score (ES) for gene sets, assessing the degree of over-representation of genes within these sets at the extremes of the ranked list [309]. Subsequently, it evaluates the significance of the enrichment score for each specific gene set, yielding a nominal p-value, and mitigates the impact of multiple hypothesis testing by computing normalized enrichment scores (NES) and the false discovery rate (FDR) for each. GSEA condenses extensive and intricate omics datasets into a more manageable structure, aiding in data interpretation. Moreover, it can uncover pathway effects that might go unnoticed in single-gene analysis. A key advantage of GSEA is its reliance on the complete transcriptomics dataset, eliminating the need for a p-value cutoff, which can restrict the discovery of biologically meaningful results. An FDR threshold of <0.25 was used to control for false positive results [309], this was calculated using the Benjamini and Hochberg's approach for controlling the FDR [310].

6.1.1 Hallmark Gene Set Enrichment

The enrichment of a range of well-defined biological processes was explored using the Molecular Signature Database (MSigDB) of 50 "Hallmark" gene sets [311]. The Hallmark

gene sets were defined to reduce noise and redundancy across gene sets, to provide robust enrichment analysis results. They therefore served as a solid foundation for GSEA in this study.

With an FDR<0.25 only one gene set was significantly positively enriched in the Hallmark Gene set enrichment analysis for A12 in comparison to WT, 'positive regulation of dendrite extension', no gene sets were negatively enriched. Additionally using the same criteria only one gene set was significant for A2 vs WT, with negative enrichment of the gene set 'Serine phosphorylation of STAT protein', no gene sets were positively enriched.

Dendrites are processes of neuronal cells, within the retina there are three types of neuronal cells photoreceptors, bipolar cells and ganglion cells. The RPE interacts with photoreceptors constantly *in vivo*, through the recycling of POS and transport of ions, water and vitamin A, subsequently the enrichment of the gene set 'positive regulation of dendrite extension' in A12 in comparison to WT could refer to this interaction. The individual genes involved in this gene set were further examined to identify those driving this enrichment and possible associations to RPE function (Table 6 – 4). Only one gene, *WNT5A* was significant after correction for multiple testing. *WNT5A* encodes a member of the WNT family that signals through both the canonical and non-canonical WNT pathways and is reported to play an essential role in regulating developmental pathways during embryogenesis. As previously discussed, to differentiate hESC to RPE requires activation of the canonical WNT pathway (Chapter 1, section 1.5). Interestingly a group of synaptotagmins are included in this gene set, namely SYT1, SYT4 and SYT17. Synaptotagmins are synaptic vesicle-specific integral membrane proteins. In the retina SYT17 is mainly localised to the RPE [312], and as shown in Table 6 – 4 there was high expression of SYT17 in both A12 and WT cells, with increased expression in A12. SYT17 is reported to play multiple roles in intracellular membrane trafficking. In neurons SYT17 is localised to the Golgi where it controls import of cargo from the ER, and the early endosome, with loss of SYT17 disrupting endocytic trafficking [313]. *SYT17* was not called as a DEG in the A2 dataset, however *WNT5A* was, although this was not significant after correction for multiple testing.

Table 6-4 Further examination of gene set 'positive regulation of dendrite extension'
Numbers in A12 and WT columns represent Fragments per kilo base of transcript per million mapped fragments (FPKM) corrected to 2 decimal places.
Only one gene was significant after correction for multiple testing- **bold.**

A12	WT	log2FoldChange	pvalue	padj	gene_name
260.83	167.03	0.64	0.011	0.16	CPNE5
881.69	674.21	0.38	0.056	0.35	SYT17
161.80	75.19	1.10	0.0025	0.06	SYT1
37.55	7.61	2.29	0.004	0.09	SYT4
392.00	196.65	0.994	0.0007	**0.02**	WNT5A
17.61	4.99	1.81	0.012	0.16	UNC13A

STAT proteins are latent cytoplasmic transcription factors activated by various extracellular signalling proteins. Upon activation, through serine phosphorylation STAT proteins can up-regulate the transcription of various target genes. Given this large and non-specific role of STAT proteins, no association can be made in relation to the A2 phenotype vs WT.

There were several interesting positive and negatively correlated gene sets based on the TSPAN10 k.o mutant phenotype which did not meet the FDR<0.25 criteria but had moderate nominal enrichment scores and highly significant nominal *p*-values. This included ‘polarised epithelial cell differentiation’, which was positively enriched in A12 (NES 1.41) and ‘establishment of apical-basal cell polarity (NES 1.43). ‘Collagen trimer’, was positively enriched in both A12 (NES 1.43) and A2 (NES 1.39). Positive regulation of oxidative stress induced cell death was positively enriched in A12 vs WT (NES 1.41)

An interesting negatively correlated gene set included ‘pigment granule organisation’, which was negatively enriched in A12 vs WT (NES -1.37).

Epithelial cells are typified by apical-basal polarity. Tight junctions are apical intracellular junctions which not only control paracellular permeability across the epithelium, but also act as a physical barrier to maintain distinct apical and basolateral membrane compositions [23]. Given the increase in TEER seen in TSPAN10 mutants in comparison to WT cells the positive enrichment of gene sets ‘polarised epithelial cell differentiation’ and ‘establishment of apical-basal cell polarity’ is interesting. However, these gene sets only had high nominal enrichment scores in the A12 clone, not in the A2 clone therefore they cannot account for phenotypes common to both cell populations.

The negative enrichment of the gene set ‘pigment granule organisation’ in A12 vs WT cells aligns with the phenotype seen in TSPAN10 k.o hESC-RPE. This will be discussed further in Chapter 7.

Overall given the limited number of DEGs called there were very few Hallmark gene sets enriched in our TSPAN10 k.o cells in comparison to WT.

6.1.2 GO enrichment

The second gene sets employed were the GO gene sets [314, 315], which is a major bioinformatics classification system to unify the presentation of gene properties across all species. These 580 gene sets describe subcellular locations of gene product activity. It includes three main branches: cellular component (CC), molecular function (MF) and biological process (BP). Expression of genes localised to specific cellular component(s) may therefore be feasibly altered by loss of *TSPAN10.* The GO gene sets were used to identify cellular locations, biological processes and molecular functions of positively- or negatively enriched gene product activity. GO pathway enrichment was performed for both A2 and A12 vs WT by NovoGene Europe. GO terms with $p_{adj} < 0.05$ are significant enrichment. Figures 6 – 6 and 6 – 7 depict GO enrichment for A12 and A2. 31 GO terms were significantly enriched with a nominal p-value of <0.05 and an FDR of <0.25 in at least one comparison. GO terms are hierarchical and there is overlap between parent terms, enriched GO gene sets were displayed on a bar chart (Figures 6 – 6 & 6 – 7). Terms related to misfolded protein binding were negatively enriched in both k.o clones (Figure 6 – 6). This may indicate a molecular function affected by k.o of *TSPAN10*.

DEGs within the gene set 'misfolded protein binding' were examined, given that this is the only enrichment set common to both k.o clones (Figure 6 – 8). Those genes which reached the log2fold change threshold included several heat shock proteins, namely *HSPA2 (*A2 log2fold= -3.55*, padj=0.03,* A12 log2fold= -2.89*, padj=0.02), HSPA1A (*A2 log2fold= -1.03*, padj=0.01,* A12 log2fold= -1.55*, padj=1.22 x* 10^{-5}*), HSPA13 (*A2 log2fold = -1.39, *padj*=0.007*,* A12 log2fold = -1.12 *padj=0.006) and HSPA9 (*A2 log2fold= -1.18, *padj=0.56,* A12 log2fold= *-1.22, padj =0.44)*.

There were 10 GO CC terms significantly positively enriched in A12 in comparison to WT, terms included extracellular matrix, basement membrane and contractile fibre, indicating possible subcellular locations affected by k.o of *TSPAN10.* No GO terms were positively enriched for the clone A2 after correction for multiple testing, therefore only results for A12 are displayed in Figure 6 – 7. The enrichment of basement membrane and extracellular matrix terms coincides with the results seen for TSPAN10 mutant TEER displayed in Chapter 5. However, as previously stated, these terms were specific only to A12, not to A2 and therefore such changes cannot be specifically aligned to TSPAN10 k.o.

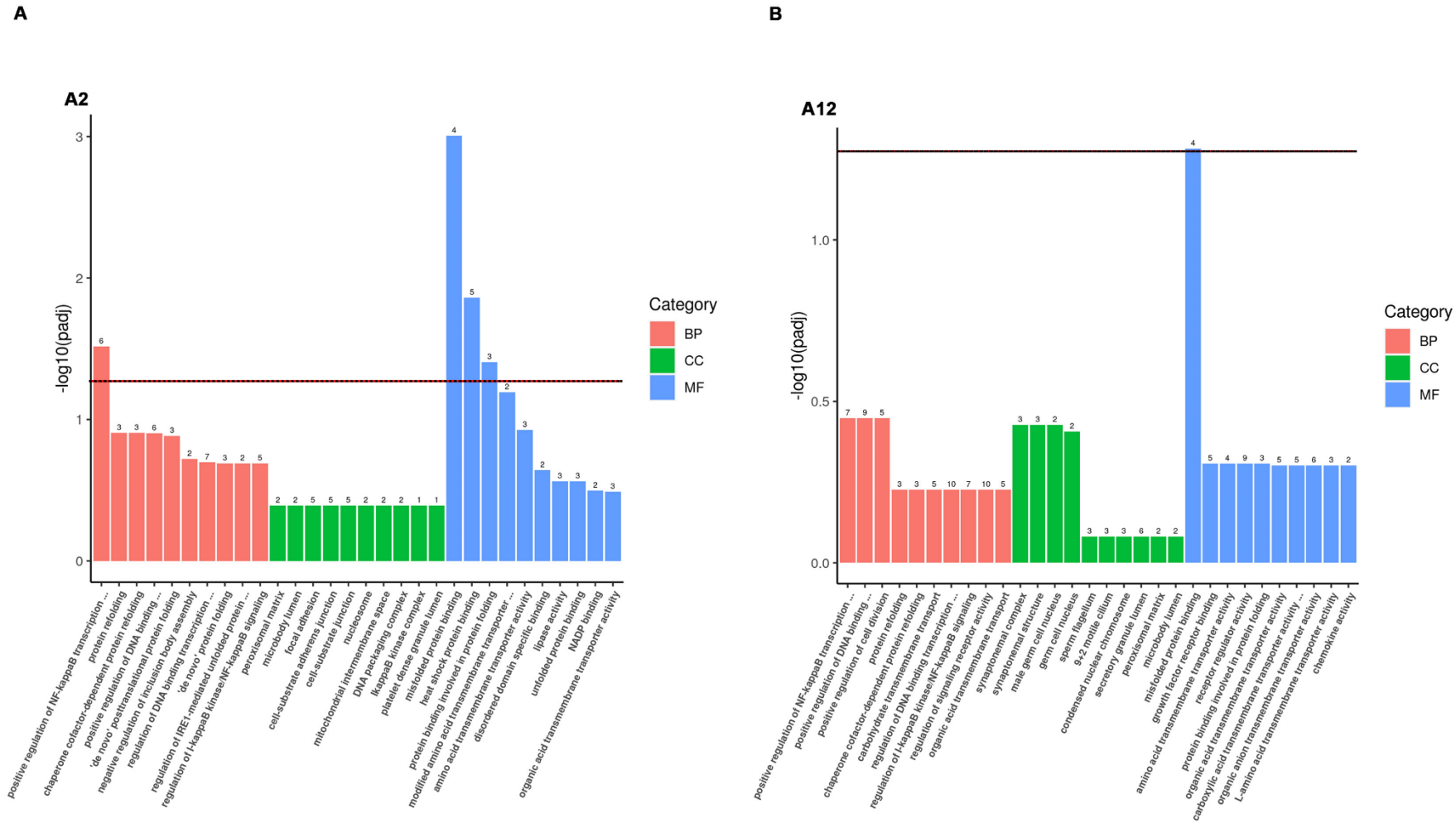

Figure 6-6 Negatively enriched GO terms for A2 vs WT and A12 vs WT
Histograms represent GO enriched terms for TSPAN10 k.o mutant A2 in comparison to WT (**A**) or A12 in comparison to WT (**B**). Red bars indicate GO terms that are biological processes (BP), green bars cell components (CC) and blue bars molecular functions (MF).
Red and black dashed line shows significance level of padj =0.05, where > -log10(0.05) is significant.
For A2 four terms reached the significance threshold, three molecular function terms: misfolded protein binding, heat shock protein binding, and protein binding involved in protein folding. One biological process term reached the significance threshold, positive regulation of NF-kappa B transcription factor activity.
For A12 only one term reached the significance threshold, the molecular function term, misfolded protein binding.

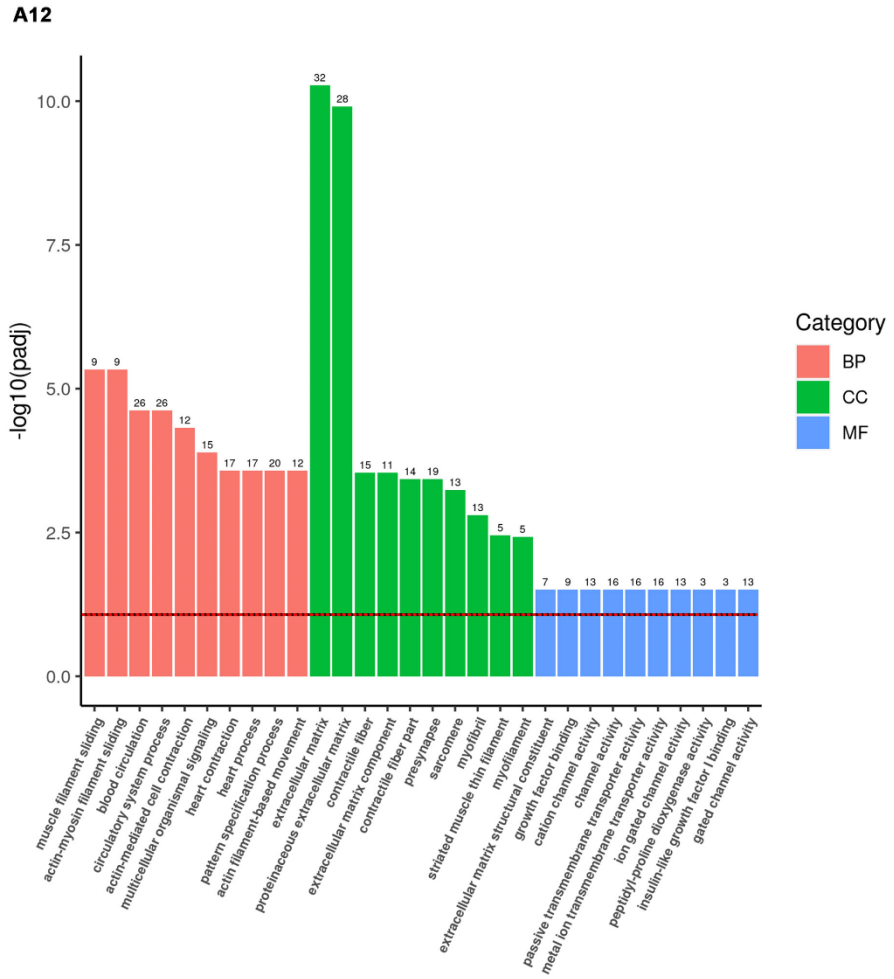

Figure 6-7 Significant positively enriched GO terms for A12 vs WT
Bar chart represents positively enriched GO terms for TSPAN10 k.o mutant A12 in comparison to WT. Red bars indicate GO terms that are biological processes (BP), green bars cell components (CC) and blue bars molecular functions (MF).
Red line shows significance level of padj =0.05, where > -log10(0.05) is significant.
Multiple significantly enriched GO terms for A12 vs WT. The most significant being the biological process term, extracellular matrix.

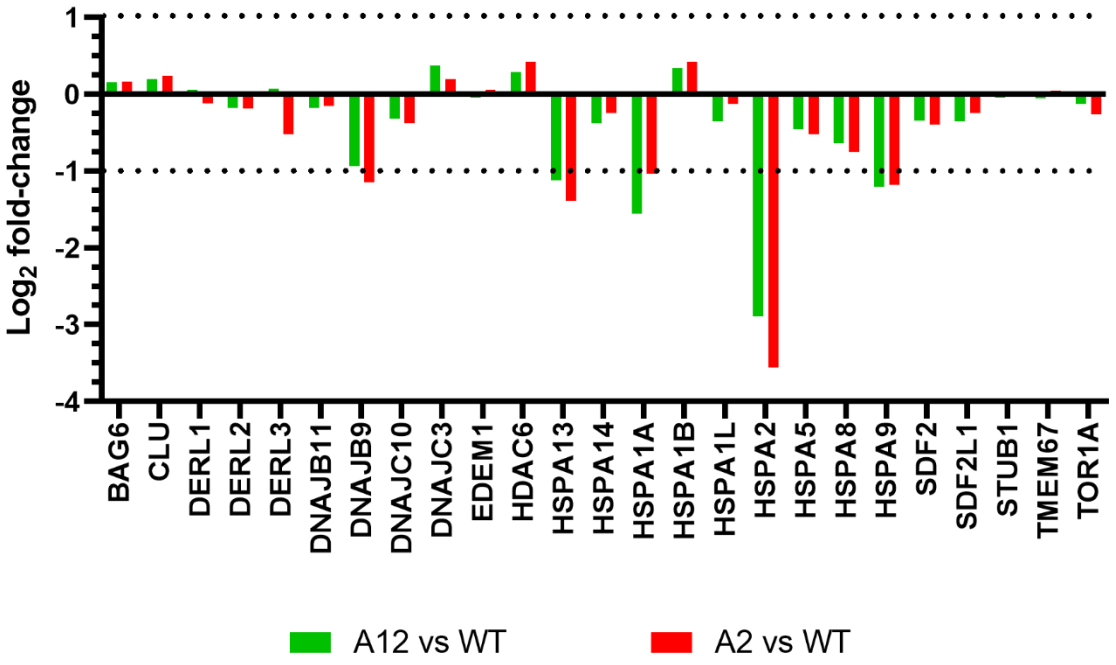

Figure 6-8 Expression of genes in the GO term 'misfolded protein binding' gene set
Coloured bars show the log2 fold-change of gene expression in the comparisons of A2 and A12 to WT. Horizontal dashed lines indicate the minimum and maximum log2 fold-change thresholds required for a gene to be considered differentially expressed.
Several heat shock proteins are differentially expressed in both A2 and A12, including HSPA2, HSPA1A, HSPA13 and HSPA9.

6.1.3 Reactome enrichment

Reactome enrichment analysis was used to identify pathways that are significantly enriched in TSPAN10 k.o versus WT RPE. Reactome is a curated database of biological pathways in humans, encompassing a wide range of cellular processes and functions [316]. Reactome pathway enrichment was performed for both A2 and A12 vs WT by NovoGene Europe. Reactome terms with $p_{adj} < 0.05$ are significant enrichment. Analysis of differentially expressed signalling pathways (Figure 6 – 9) shows that pathways involved in collagen degradation and formation, extracellular matrix degradation and organisation, and muscle contraction are very significantly enriched in both A12 and A2 vs WT. These linked terms are highlighted in Figure 6 – 9 with purple arrows for those involving collagen, green arrows for pathways involving the extracellular matrix and pink arrows for muscle contraction. The top 20 positive most significantly enriched pathways are shown in Figure 6 – 9, ranked by significance. There were many more genes involved in the enriched pathways for A12 than A2, denoted by the large difference in count sizes between the graphs 6 – 9A and 6 – 9B. For example, the pathway ‘Degradation of the extracellular matrix’ has a count of 4 for A2 but 13 for A12.

Interestingly the GO terms extracellular matrix and proteinaceous extracellular matrix were very significantly positively enriched for A12, aligning with the Reactome pathway analysis. When the Reactome gene sets for extracellular matrix degradation and organisation and collagen degradation and formation were analysed for the A2 clone the same DEGs recurred, namely *COL1A2, COL7A1* and *COL16A1*. For the A12 clone in the same gene sets, the aforementioned collagen genes were differentially expressed in addition to several others. *COL1A2* encodes the α-2 chain of type I collagen, which is a major component of the extracellular matrix. Within the RPE type I collagen provides structural support, aids with barrier function and helps with cell adhesion and matrix organisation. *COL7A1* encodes type VII collagen, which is also a key component of the extracellular matrix. While direct associations between *COL7A1* mutations and specific retinal diseases may not be well-established, disruptions in type VII collagen can theoretically affect the RPE's adhesion to BrM and its overall function. This could contribute to retinal conditions where the integrity of the RPE and its barrier function are compromised, such as AMD. *COL16A1* encodes type XVI collagen, which is not a major structural component like type I collagen, but it is involved in the organization and stabilization of the extracellular matrix.

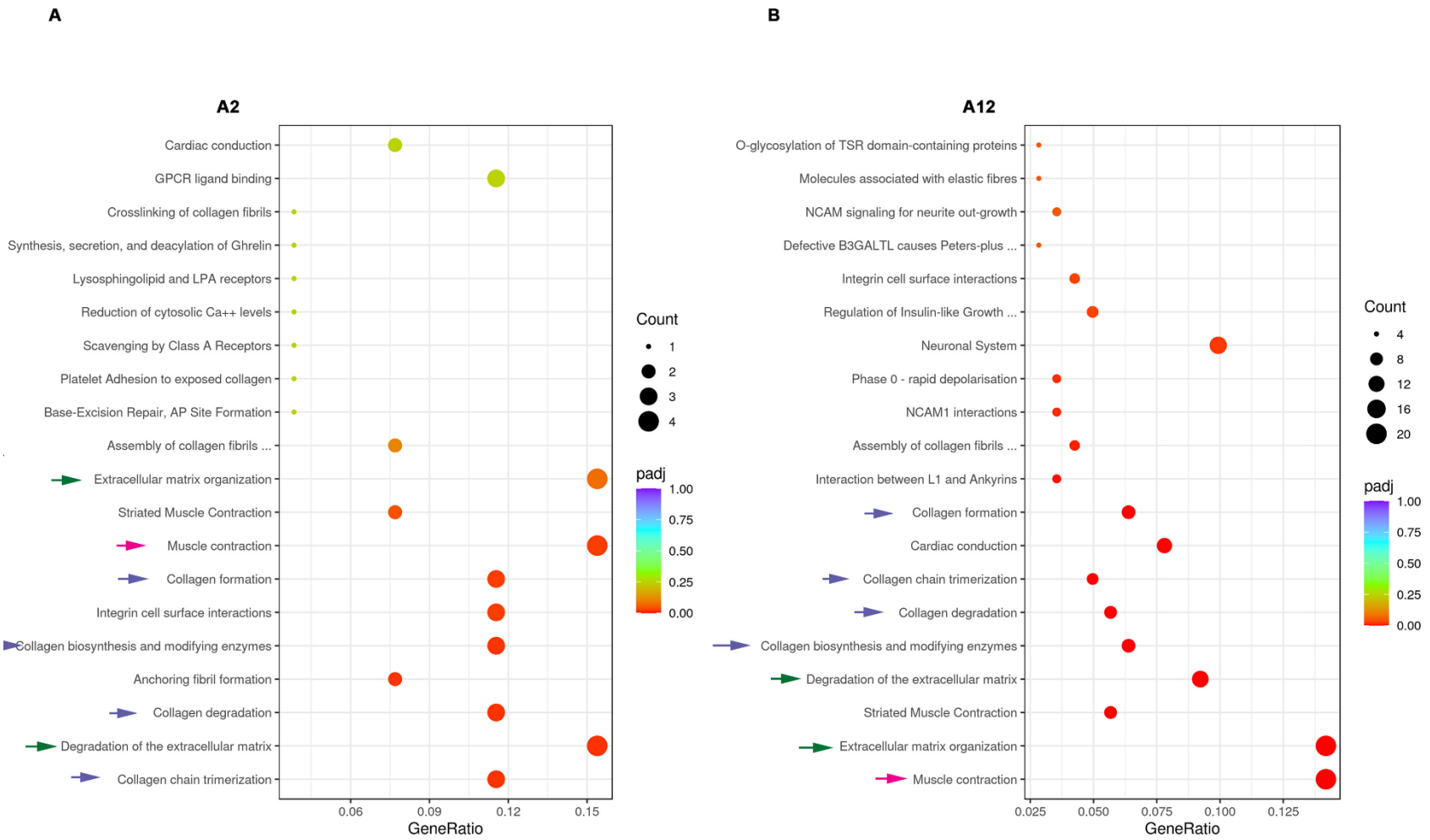

Figure 6-9 Dot-plots representing the significance of the top 20 positively enriched pathways ranked by significance (Reactome PA).
Genes are clustered into pathway terms based on membership of Reactome pathways. Count is the number of genes involved in the pathway. Gene Ratio is the ratio of the genes involved in the pathway to the total number of genes analysed. P adjust is the adjusted p-value. Note the different Count sizes between A2 and A12.
A: Dot plot represents A2 vs WT, **B**: dot plot represents A12 vs WT.
Purple arrows highlight pathways involved in collagen synthesis/degradation. Green arrows highlight pathways involved in extracellular matrix organisation/degradation. Pink arrows highlight pathways involved in muscle contraction.

6.2 Interpretation and Interim Discussion

RNAseq was used to probe transcriptional changes in A12 and A2 compared to WT in hESC-RPE. GSEA was used to identify Hallmark gene sets, GO gene sets and Reactome pathways that were significantly negatively or positively enriched in each k.o relative to WT cells. Individual DEGs were also scrutinized. It was assumed that transcriptional changes common to A12 and A2 were caused by the loss of TSPAN10.

Current analysis of transcriptomic data confirms significant reduction of *TSPAN10* transcript in both mutants A12 and A2 in comparison to WT cells, adding to the results presented in Chapter 4. When both TSPAN10 k.o clones were analysed together a small number of DEGs were identified in comparison to WT (Table 6 – 3). Those identified were also seen as DEGs when A2 and A12 were analysed individually. Such genes included those related to oxidative stress, such as catalase (*CAT*) and a heat shock protein (*HSPA1A*), zinc fingers (*ZNF736* & *ZNF229*), a cadherin (*CDH19*) and the NFκB pathway (*IRAK4*). DEGs with no coverage in one of the two TSPAN10 k.o, but expression in WT were also examined (Table 6 – 2). Again, those identified mainly represent genes involved in the NFκB pathway and zinc fingers. However, the majority of zinc finger genes actually have low expression in the WT, suggesting their involvement in the RPE may be limited, therefore making them less interesting targets. DEGs identified belonging to the NFκB pathway when A2 and A12 were analysed independently include *NLRP2*, *IRAK4*, and *IRAK1*. All were differentially expressed in A12 and A2 with good coverage in the WT. Interestingly ‘regulation of NF-kB signalling’ was negatively enriched in both A12 and A2 versus WT in the GO gene enrichment sets, although this was not statistically significant. ‘Positive regulation of NF-kB signalling’ was also negatively enriched and statistically significant for the A2 clone (Figure 6 – 6). The NFκB family of transcription factors play a pivotal role in regulating the inflammatory response, immune function, and malignant transformation [317]. Canonical NFκB activation from an inflammatory stimulus leads to the inhibition of autophagy [318], resulting in the accumulation of misfolded proteins, a potential source of sub-RPE drusen deposits [319] linking this diverse pathway to AMD. iPSC-RPE derived from a patient with a truncating mutation in the NEMO gene (a negative regulator of NF-κB signalling) produce sub-RPE APOE-positive deposits when treated with complement incompetent human serum [164]. Furthermore, NF-kB polymorphisms have been associated with AMD in a high-altitude population [320]. In our transcriptomic data NF-kB signalling was negatively enriched, suggesting reduced NFκB activation. The NF-kB family is a diverse system with multiple targets and effectors. It appears to have a role in AMD pathophysiology, however here only a small number of DEGs related to this large pathway were identified, and no gene sets related to NF-κB signalling were significantly enriched. The genes identified are connected to

the NF-κB pathway, however, they have varying roles. *IRAK1* is partially responsible for interleukin-1 (IL-1) induced upregulation of NF-κB [321, 322]. *IRAK4* encodes a kinase that activates NF-κB in both the Toll-like receptor and T-cell receptor signalling pathways [321, 322]. NLRP2 appears to be involved with the inflammasome as it can regulate both caspase-1 and NF-kB [321, 322]. Consequently, no firm conclusions can be drawn on the current data with regard to TSPAN10's interaction with the NF-κB family. Given that *IRAK1* was differentially expressed when both A2 and A12 were combined one avenue of investigation could be an ELISA for IL-1.

Two genes directly related to the oxidative stress response were identified as DEGs, *CAT* and *HSPA1A*. Catalase is an antioxidant enzyme which catalyses the conversion of the reactive oxygen species (ROS) H_2O_2 to H_2O and O_2. Catalase was identified as an interesting target and will be discussed further in Chapter 7, section 7.1. *HSPA1A* codes for a heat shock protein, HSP70-1, which is stress inducible. Gene set enrichment analysis highlighted misfolded protein binding to be negatively enriched in both k.o clones in comparison to WT (Figure 6 – 8). When this gene set was analysed the main genes that were significantly down-regulated were all members of the heat shock protein 70 family, including *HSPA1A*. Correct protein folding is an essential cellular function controlled by heat shock proteins. Aberrant protein folding underlies many age-related degenerative processes and is thought to be associated with AMD. Cells typically increase the expression of heat shock proteins in order to normalise their growth conditions in response to various environmental stress factors such as oxidative stress. The heat shock proteins function as molecular chaperones by preventing the accumulation of cellular cytotoxic protein aggregates and assisting in correct folding of both nascent and misfolded proteins.

We saw significantly reduced levels of gene expression for four members of the heat shock protein 70 family in comparison to WT (Figure 6 – 8). If reduced TSPAN10 expression is associated with reduced heat shock protein expression, then this could indicate a mechanism via which TSPAN10 is implicated in AMD, given that patients with the TSPAN10 AMD risk SNP have reduced copy numbers of TSPAN10. Further work to explore the relationship of TSPAN10 with oxidative stress in the RPE can be found in Chapter 7.

Reactome pathways were also examined for TSPAN10 mutant clones in comparison to WT. With several "up" pathways reaching significance, specifically those related to the extracellular matrix. Interestingly more pathways showed significance when only the "up" category was analysed rather than "all". This most likely indicates that the pathways associated with upregulated genes are more strongly represented in the Reactome database compared to the complete set of genes (which includes both upregulated and downregulated

genes). Several reasons for this include differential gene expression, where downregulated genes may not cluster into specific pathways as strongly as upregulated genes, diluting the overall significance when all genes are considered. Furthermore, upregulated genes might be involved in highly specific and well-defined pathways relevant to the condition being studied, (in this case AMD) whereas the overall gene set might include genes with diverse functions that do not collectively point to a specific pathway.

Initially when the gene sets from each clone were first examined a Pearson correlation analysis was conducted (Figure 6 – 1). This demonstrated minimal differences between differentiations for each cell clone and furthermore, limited differences between each clone, i.e. WT versus TSPAN10 k.o (Figure 6 – 1). This therefore suggests that TSPAN10 k.o causes only small differences in the transcriptome of hESC-RPE. This is further reinforced by the relatively small number of hits reported in this chapter, namely 114 DEGs. Cells in culture typically do not reflect those *in vivo*, given that they are not privy to the same stressors. We aimed to k.o TSPAN10 to create an exaggerated model in the hope that our cells would develop an obvious phenotype, including differences in transcript expression in comparison to WT. Cells in culture have an ample supply of nutrients and minimal exposure to light damage and other external stressors. Consequently, despite TSPAN10 k.o, the transcriptome profiles of our k.o cells did not differ significantly to their WT counterparts. This is also reflected by the relatively low number of DEGs seen when both the A2 and A12 clones are combined in comparison to WT (Table 6 – 3), and the limited gene sets that were enriched.

Certain differences between the cells may only be obvious following a stress event. Ageing is associated with vision decline and delayed dark adaptation, both of which are direct consequences of tissue stress and retinal damage [323]. The introduction of a variety of stressors that a normal individual will typically experience including exposure to natural light, free radicals and ROS into the RPE culture model may more accurately recapitulate the ageing state [324]. Furthermore, on a day-to-day basis RPE cells typically phagocytose POS. This phagocytic activity may be accompanied by a respiratory burst, a rapid eruption of ROS [59], which stresses the cells. The cells used to acquire this RNA-seq data were not privy to any of the aforementioned stressors, which may be masking potential TSPAN10 targets. Typically, RPE derived from iPSCs are subjected to stress events prior to RNA-seq analysis, such as the use of complement competent human serum [164] or H_2O_2 [177] (see section 1.5.3.2). We assumed that using a k.o model would alleviate this requirement and produce more hits than we acquired. However, using an external stressor in this instance would muddy the waters as it would be difficult to know which effect was due to TSPAN10 k.o and which from the stress event.

Transcriptomic analysis produces a very large volume of data that can be examined in many ways and related to cellular phenotypes. This transcriptomic evaluation provides a basis to help highlight the role of TSPAN10 in the RPE. A summary of key transcriptional changes in the TSPAN10 k.o lines A12 and A2 is depicted in Figure 6 – 10.

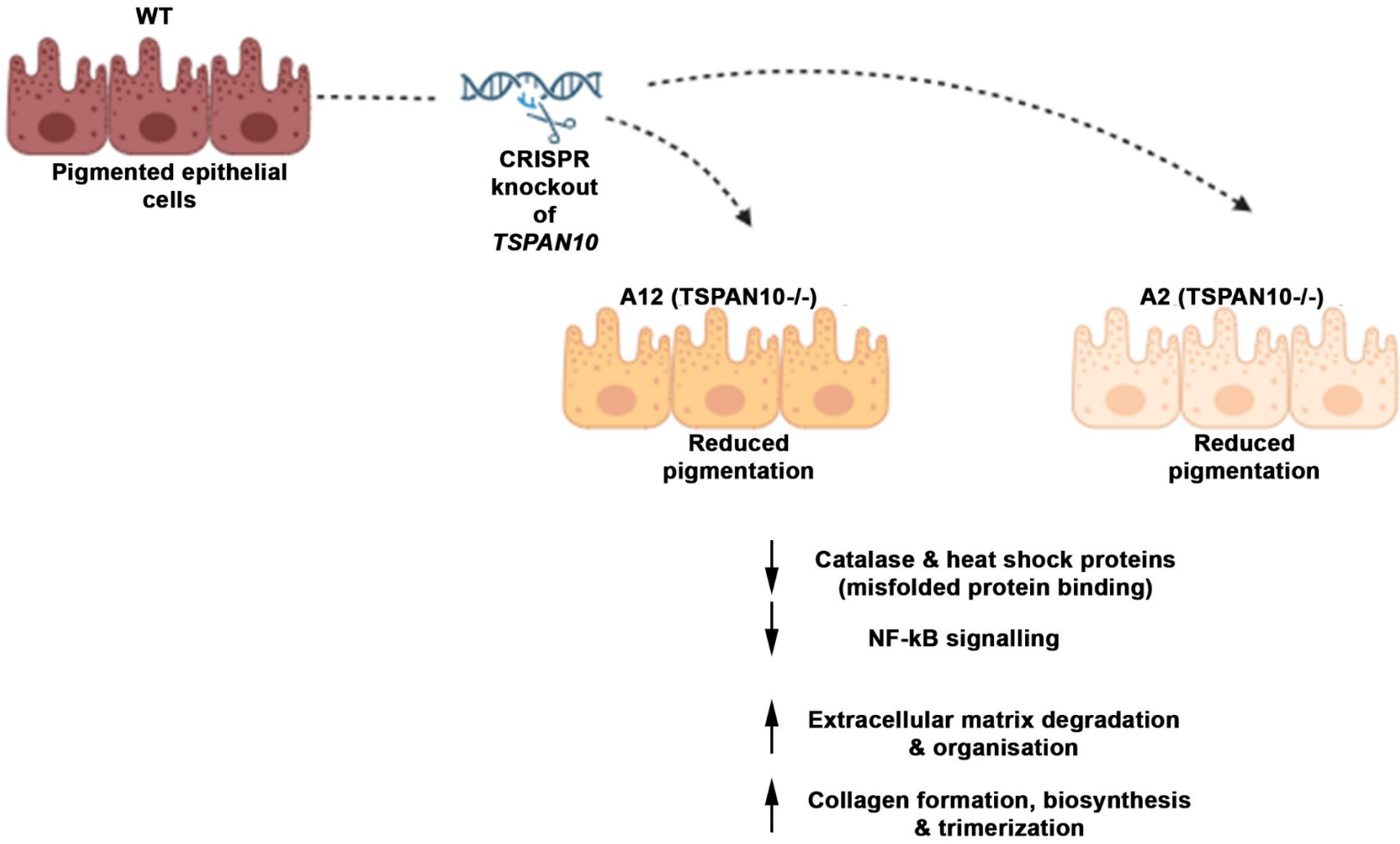

Figure 6-10 Summary of key transcriptional changes in TSPAN10 k.o cells
TSPAN10 k.o RPE show reduced expression of antioxidant enzymes and heat shock proteins, signifying its involvement in oxidative stress. In comparison to WT, TSPAN10 k.o cells show transcriptional changes in genes related to the extracellular matrix and collagen formation. Image created using Biorender.com

7 Investigating the phenotypes identified in TSPAN10 k.o clones in comparison to wild type

7.1 TSPAN10 has a role in oxidative stress in the RPE

Oxidative stress has been implicated in the pathogenesis of AMD for many years. Reactive oxygen species (ROS) generation has long been considered to have harmful consequences for the RPE. One of the DEGs in the RNA-seq data with the highest fold change for both TSPAN10 k.o mutants was catalase (*CAT*). *CAT* was significantly reduced in both A12 and A2 in comparison to WT. Catalase is fundamental to the cell, catalysing the conversion of hydrogen peroxide (H_2O_2) to H_2O and O_2 [323]. Given the changes in *CAT* expression in TSPAN10 k.o mutants identified through RNA-seq, we aimed to understand if this pattern was seen for the catalase enzyme and furthermore to establish if k.o of TSPAN10 results in increased oxidative stress in the RPE.

7.1.1 Investigating catalase enzymatic activity in the RPE

Initially western blotting was performed for catalase using day 40-45 post-differentiation hESC-RPE. Total protein staining showed equal loading of lysates, however staining for catalase revealed a reduction in all differentiations of A12 (n=3) and A2 (n=3) in comparison to WT (n=3) (Figure 7 – 1 A & B). Three biological replicates and three technical repeats were performed and gave very similar results. Consequently, it was surmised that TSPAN10 k.o RPE produce a reduced amount of the catalase antioxidant enzyme in comparison to WT.

We then aimed to establish whether there is a reduction in catalase enzymatic activity between WT and TSPAN10 k.o whole cell lysates. This was achieved through a catalase activity assay (Cayman chemical). There was a statistically significant reduction in catalase activity in TSPAN10 k.o cells A12 ($p=0.0137$) and A2 ($p=0.0082$) in comparison to WT at baseline in hESC-RPE cultured for 40 days post differentiation (Figure 7 – 1 C). The results of this assay suggest that catalase is less active in TSPAN10 k.o cells therefore less H_2O_2 is converted to H_2O and O_2 in comparison to WT, culminating in increased oxidative stress.

Finally, an ELISA for catalase of conditioned apical media from WT and TSPAN10 k.o mutants grown on transwell inserts revealed a similar pattern. At 21 days in culture a significant reduction in catalase was seen in both A12 ($p=0.04$) and A2, ($p=0.01$) in comparison to WT (data not shown), and this was even more significant at 63 days A12 ($p=0.0002$) and A2, ($p<0.0001$) (Figure 7 – 1 D).

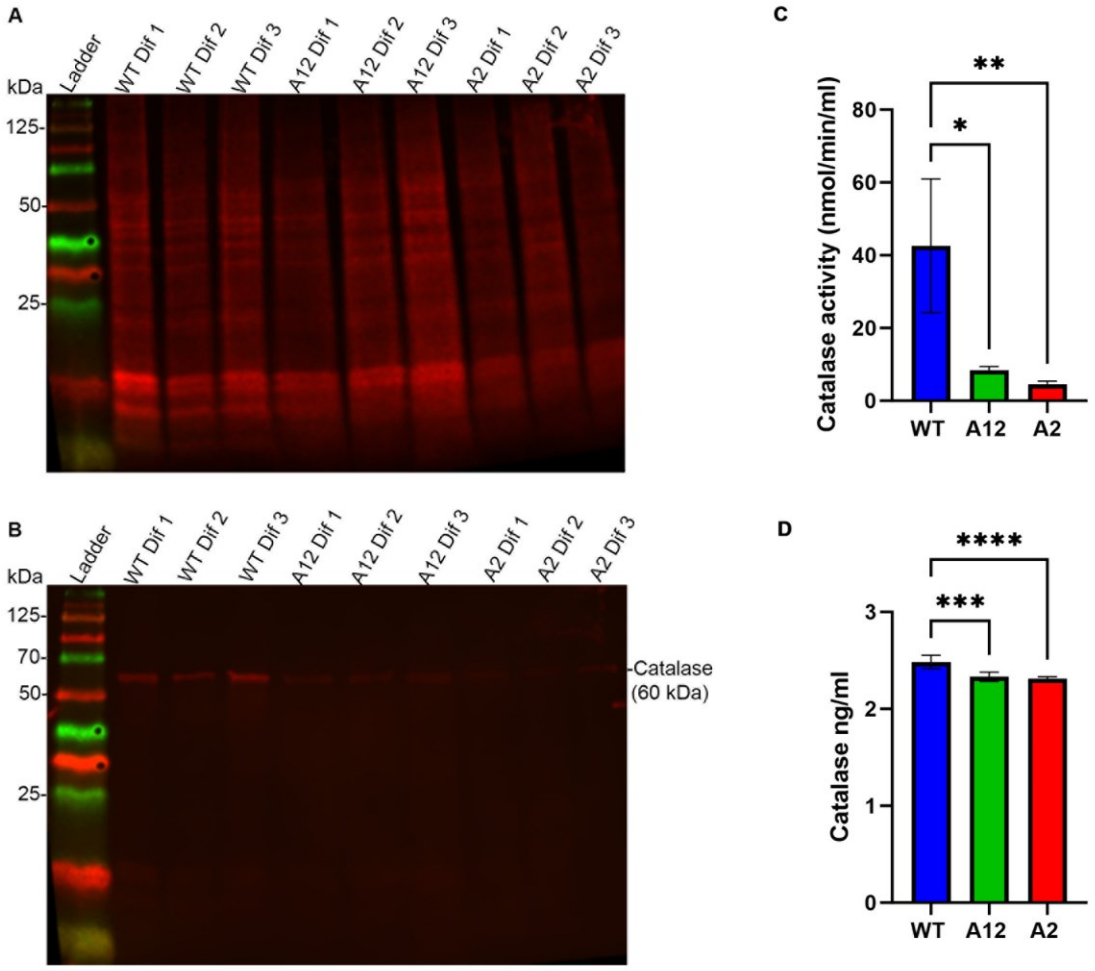

Figure 7-1 Study of catalase in hESC-RPE
Western Blot for Catalase the peroxisome marker in TPSAN10 mutant and WT hESC-RPE cells
A: A total protein stain (Revert 700) was performed as a control to ensure equal loading of lysates.
B: A Catalase protein blot using the Abcam monoclonal Ab indicates that catalase protein expression is reduced in all differentiations of A12 and A2 in comparison to WT.
N=3 technical repeats performed.
C: Determination of the antioxidant enzyme catalase activity in hESC-RPE
Catalase activity during basal conditions determined for wild-type and the TSPAN10 knockout cell lines A12 and A2. Enzyme activity expressed as means ± SD of three differentiations for each cell line, where each differentiation was repeated in triplicate. Statistical significance with respect to WT cells using One-way ANOVA with Dunnett's multiple comparison post-hoc test. $p \leq 0.05$ (*), $p \leq 0.01$ (**)
D: ELISA quantification of catalase was performed on conditioned media harvested from the apical compartments of hESC-RPE after 63 days in culture on transwell inserts. Bars show mean of three differentiations for each cell clone. Error bars show SD of three differentiations. One-way ANOVA with Dunnett's multiple comparison post-hoc test used for statistical analysis. ****p<0.0001, ***p=0.0002, *p<0.05

7.1.2 Quantification of ROS production in the RPE

Having established that TSPAN10 k.o cells show reduced catalase enzyme production and activity in comparison to WT we then sought to understand if this reduced antioxidant activity translated into increased ROS. hESC-RPE were either treated with H_2O_2 at 100 µM or 200 µM or X-VIVO 10 media for 24 hrs and ROS production quantified from 0 – 180 mins at 30 min intervals using a DCFDA assay (Abcam) (Figure 7 – 2). 100 µM of H_2O_2 was chosen because it is a similar concentration to that seen in the human vitreous [325].

At baseline there was a statistically significant increase in ROS production in TSPAN10 k.o cells in comparison to WT from 90 mins onwards. This difference steadily increased and was maximal at 180 mins A12 ($p = 0.02$) A2 ($p = 0.001$). There were no differences observed between TSPAN10 k.o and WT cell ROS production in the presence of 100 or 200 µM of H_2O_2. All three cell lines showed similarly increasing ROS production over time in the presence of H_2O_2. Interestingly the level of ROS production in TSPAN10 k.o cells under basal conditions was very similar to that seen in H_2O_2 treated WT cells. These results further suggest that TSPAN10 has a role in oxidative stress in the RPE.

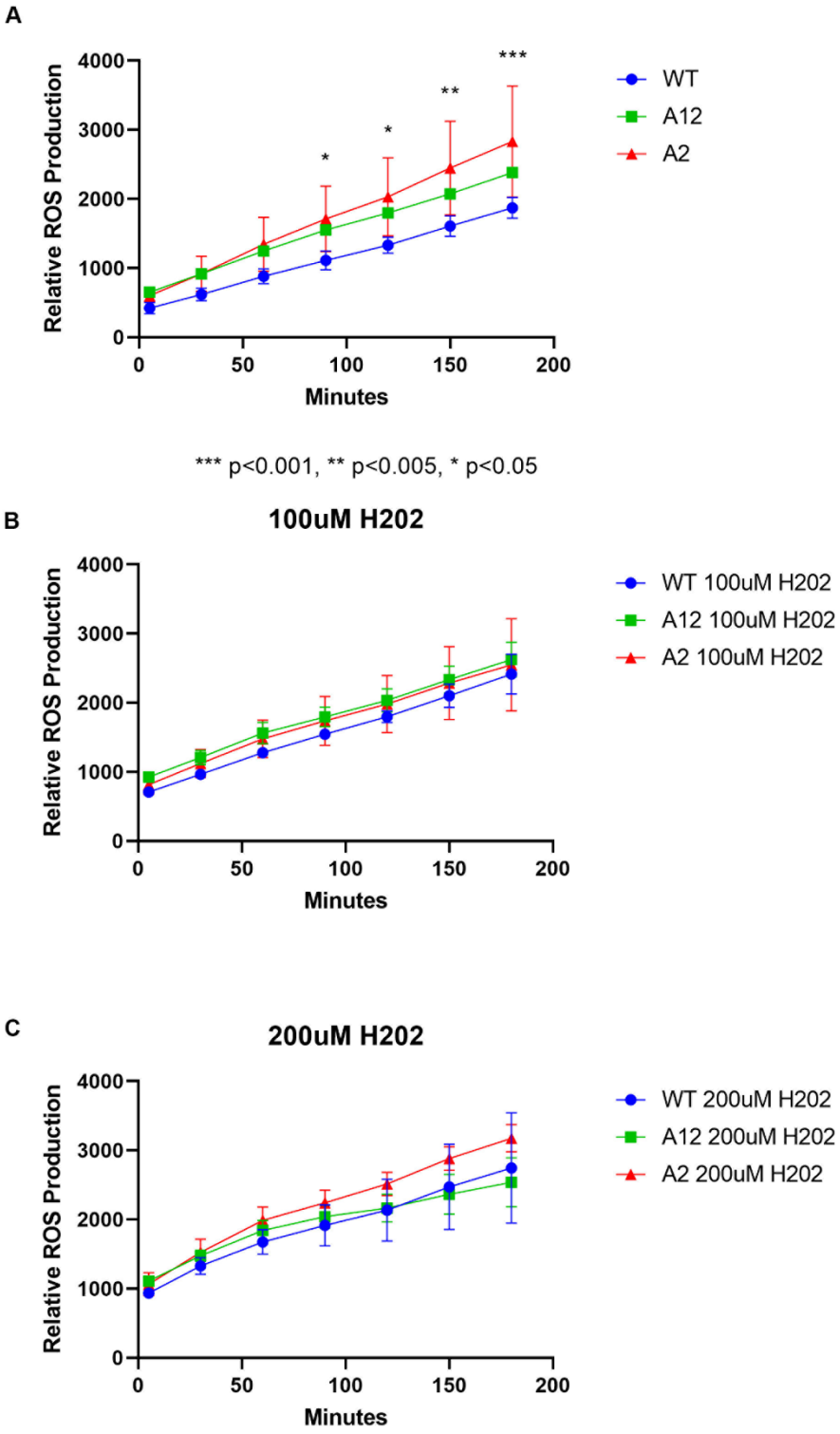

Figure 7-2 TSPAN10 knockout hESC-RPE produce increased reactive oxygen species (ROS)
Reactive oxygen species (ROS) production is significantly higher in TSPAN10 knockout hESC-RPE under basal conditions in comparison to WT (**A**). (**B** & **C**) Both WT and TSPAN10 knockout cells are equally susceptible to H_2O_2 and show no difference in ROS production under stress conditions.
Statistical comparison conducted using a two-way ANOVA with Dunnett's multiple comparison test. Significant differences are indicated as $p \leq 0.05$ (*), $p \leq 0.005$ (**) and $p \leq 0.001$ (***).

7.1.3 Functional implications of increased oxidative stress

Changes in the balance of ROS and antioxidant enzymes can have significant functional consequences, which in turn effect cellular phenotype. Phagocytosis of POS is a key function of the RPE and trafficking of POS through the endosomal and lysosomal systems is known to be modulated by changes in oxidative stress [231]. Interestingly TSPAN10 has been reported to localise ADAM10 to late endosomes in HeLa cells, and other C8 tetraspanins are known to localise ADAM10 to both endosomes and lysosomes [113]. Consequently, we conducted a functional experiment to assess whether the k.o of TSPAN10 translated to an impairment of POS trafficking, specifically through the endosomal and lysosomal pathways. To ensure that POS were correctly tagged with FiTC WT cells were fed POS and after 4 hrs fixed and stained with anti-rhodopsin antibody, which is a marker of photoreceptors. Co-localisation of rhodopsin with FiTC confirmed that porcine POS had been correctly extracted and tagged with FiTC (Figure 7 – 4 B). Co-localisation was quantified using an automated quantification method described by Costes et al [233], which allows for an unbiased assessment of the number of POS molecules co-localising with another marker, such as rhodopsin, where 1.0 represents 100% co-localisation (see chapter 2 section 2.29 for a more detailed method). Fluorescently-labelled POS were then fed to WT and TSPAN10 k.o cultures, and the effect of TSPAN10 k.o was evaluated across the duration of the experiment by quantifying FITC-POS co-localisation with the early endosomal marker Rab5 [326] and the lysosomal membrane-associated protein (LAMP-1) used as a marker of lysosomes [327]. Furthermore, to mimic oxidative stress conditions a subset of WT cells were treated with 100 μM H_2O_2 for 24 hrs prior to POS feeding. This concentration of H_2O_2 was chosen given that it has previously been used in equivalent studies [328, 329] and is similar to that seen in the human vitreous [325].

To quantify the extent of Rab5 or LAMP1 co-localisation with FiTC-tagged POS scatterplots for red vs. green channel intensities were generated for 10 cells from each image, with three images taken from each differentiation for each cell clone and were subject to the Costes et al. statistical algorithm to determine maximum threshold intensities and quantify the extent of fluorophore overlap.

Initially co-localisation of FITC-POS with Rab5 or LAMP1 were assessed only in differentiation 3 of WT, A12 and A2 to assess for changes common to both k.o cell types inferring that differences were a result of TSPAN10 k.o. Trafficking of cargos through the early endosome was not affected by TSPAN10 k.o (Figure 7 – 3). Although co-localisation of Rab5 with FITC-POS in A2 was significantly reduced in comparison to WT at 12 ($p < 0.0001$) and 24 hrs ($p < 0.0001$), this was not seen in the A12 clone, which mimicked WT cells. Consequently, given the time and expense involved in this assay it was not repeated in the

biological replicates, differentiations 1 and 2. Conversely, there were changes seen in the co-localisation of FITC-POS and LAMP1 common to both A12 and A2 in comparison to WT. Subsequently, POS trafficking to the lysosome was assessed in all three differentiations for WT and both TSPAN10 k.o cell lines (A2 and A12).

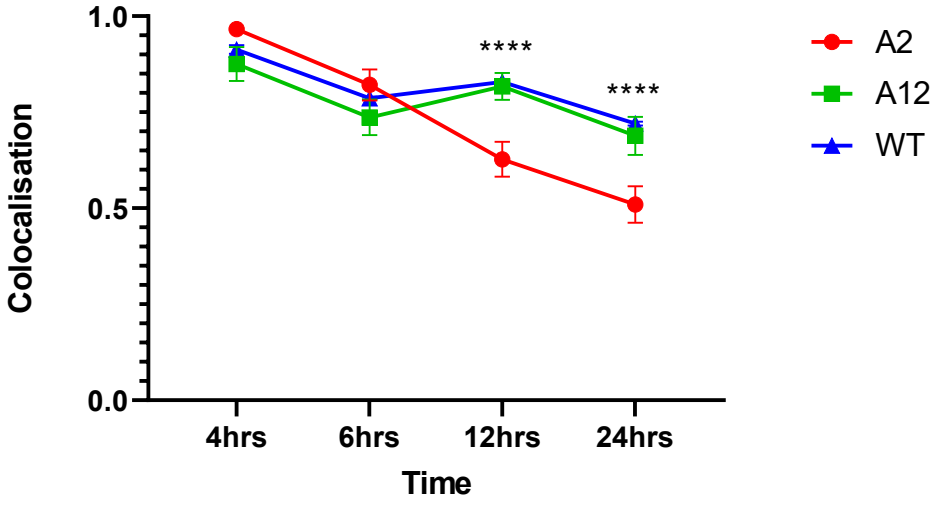

Figure 7-3 Evaluation of cargo trafficking to early endosomes over 24hrs
hESC-RPE cells fed fluorescently labelled photoreceptor outer segments (POS) were observed to be trafficked to early endosomes within the first 4 hrs following a POS dose. The extent of colocalization of POS (green) with early endosomes, labelled with anti-Rab-5 (red) was determined using an unbiased automated algorithm described by Costes et al. Data are shown for WT and the two TSPAN10 knockout clones A12 and A2. Only differentiation three was examined. No differences were observed between WT and TSPAN10 knock-out cells, implying that TSPAN10 knock-out does not affect trafficking of cargos to early endosomes. The y-axis shows the extent of colocalization, where 1.0 = 100% colocalization. Data from a minimum of 3 images per time-point per cell line and at least n= 10 cells/image. Statistical comparison conducted using a two-way ANOVA with Sidak's multiple comparison test. Significant differences are indicated as $p \leq 0.0001$ (****).

In WT hESC-RPE POS co-localisation with LAMP1 increased over time, peaking at 12 hrs post POS feed, and then slowly reducing at 24 hrs (Figures 7 – 4 & 7 – 5). Comparatively TSPAN10 k.o hESC-RPE showed significantly increased co-localisation of POS and LAMP1 in comparison to WT at 4 hrs (A2 $p<0.0001$) (A12 $p<0.0001$), 6 hrs (A2 $p<0.0001$) (A12 $p<0.0001$), 12 hrs for A2 ($p<0.0001$) and 24 hrs (A2 $p<0.0001$) (A12 $p<0.0001$). POS appeared to be prematurely trafficked to lysosomes in TSPAN10 k.o cells. This pattern resembled that seen by others when RPE are treated with H_2O_2 to mimic oxidative stress [231]. Consequently, WT hESC-RPE were treated with 100 μM H_2O_2. POS trafficking in TSPAN10 k.o cells (Figure 7 – 5 A & B) mimicked that seen when WT cells were treated with H_2O_2 (Figure 7 – 5 C). Importantly there was no difference in the expression of LAMP1 between our WT and TSPAN10 k.o cells according to our RNAseq data (Chapter 6)

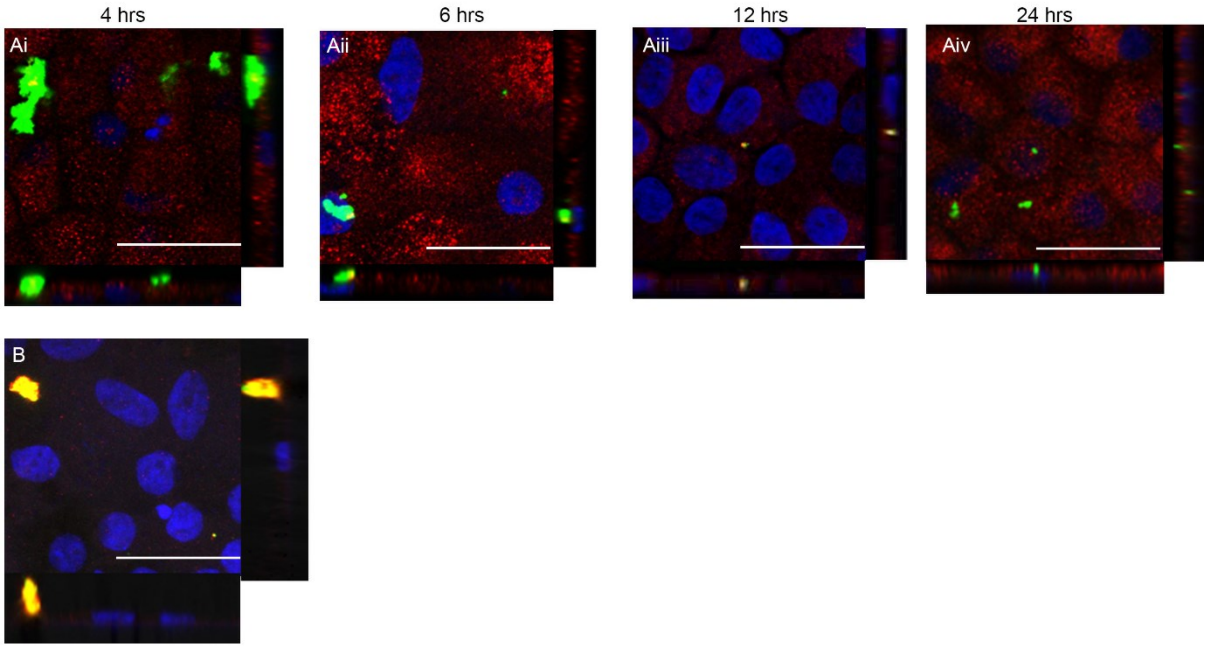

Figure 7-4 POS trafficking in the RPE to lysosomes
A: Representative confocal images taken after a POS feeding assay showing trafficking of POS (green) in lysosomal compartments (stained with Lamp1 red). Nuclei stained with DAPI (blue)
Ai: 4 hrs after commencement of feeding assay. Colocalised vesicles appear yellow. Small area of colocalization visible
Aii: 6 hrs after commencement of feeding assay. Colocalised vesicles appear yellow. Small area of colocalization visible
Aiii: 12 hrs after commencement of feeding assay. Colocalised vesicles appear yellow.
Aiv: 24 hrs after commencement of feeding assay. Colocalised vesicles appear yellow.
B: Representative confocal image taken 4 hrs after a POS feed showing sustained conjugation of FiTC (green) to POS (stained with rhodopsin red).

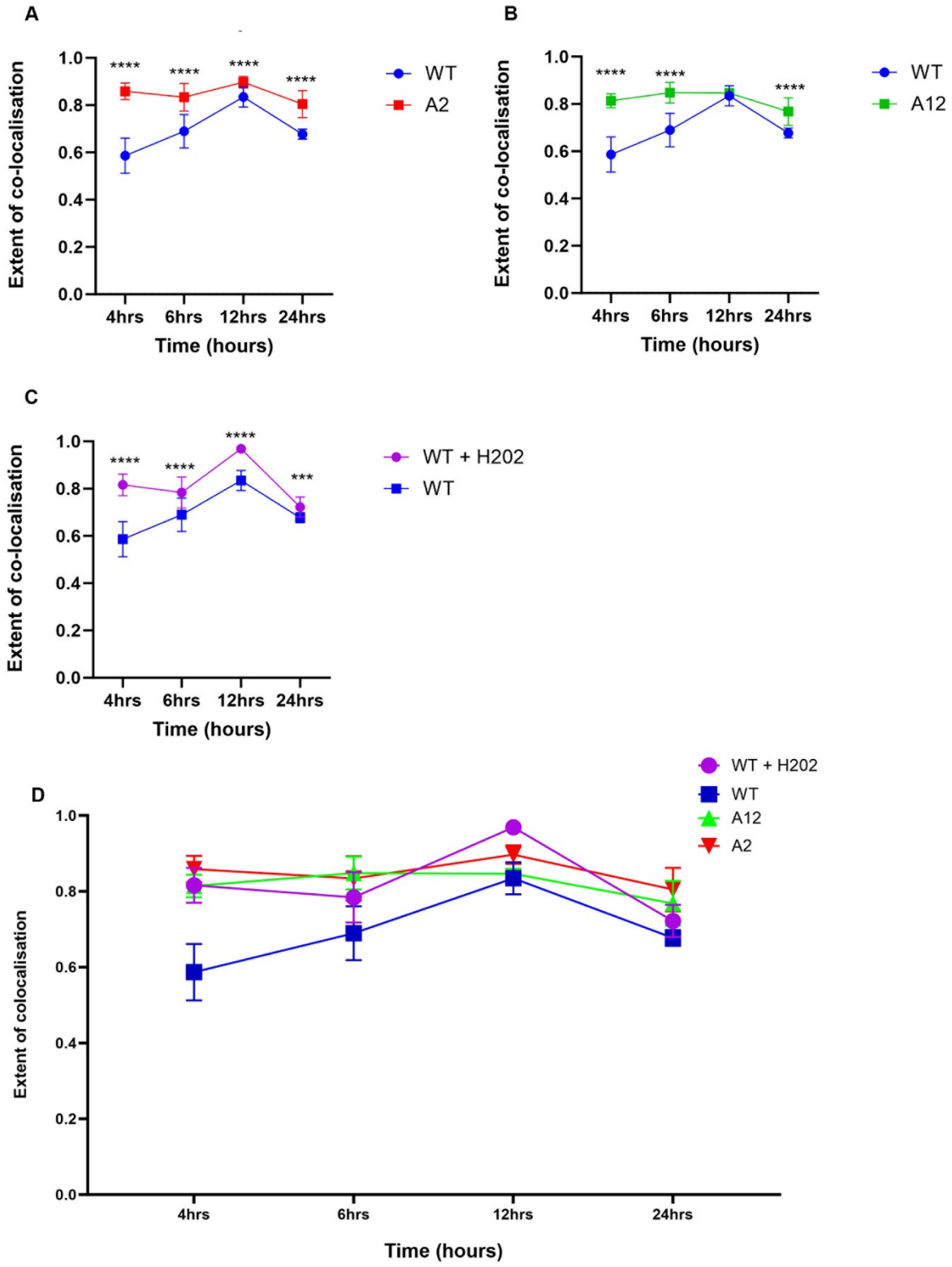

Figure 7-5 Evaluation of POS cargo trafficking to lysosomes over 24hrs
hESC-RPE cells fed fluorescently labelled photoreceptor outer segments (POS) were observed to be trafficked to lysosomes within the first 24 hrs following a POS dose. The extent of colocalization of POS (green) with lysosomes, labelled with anti-Lamp1 (red) was determined using an unbiased automated algorithm described by Costes et al. Data are shown for WT, the two TSPAN10 knockout clones A2 (A) and A12 (B) and WT cells treated with hydrogen peroxide for 24hrs to mimic oxidative stress (C).
(D) The mean of all cell lines and conditions shown together emphasising how the TSPAN10 knock out cell lines mimic oxidatively stressed RPE for the first two time points (4hrs and 6hrs). Emphasising how cargos are prematurely trafficked to lysosomes in TSPAN10 knock out and oxidatively stressed WT cells.

The y-axis shows the extent of colocalization, where 1.0 = 100% colocalization. Data from a minimum of 9 images per time-point per cell line (3 from each differentiation) and at least n= 10 cells/image. Statistical comparison conducted using a two-way ANOVA with Sidak's multiple comparison test. Significant differences are indicated as $p \leq 0.001$ (***). $p \leq 0.0001$ (****).

7.1.4 TSPAN10 is localised to the late endosome

Given that TSPAN10 appears to have an impact on POS trafficking to the lysosome, we questioned how this mechanism may occur. There are reports that TSPAN10 localises ADAM10 to the late endosome [113] (which is further explored in Chapter 8). Consequently, we aimed to understand if TSPAN10 itself is localised to late endosomes in the RPE. To achieve this, we conducted an immunocytochemistry experiment staining for both the late endosome marker Rab7 [326, 330] and TSPAN10 in WT hESC-RPE grown on transwells for at least 40 days post differentiation, imaged using confocal microscopy. Rab7 (green) showed significant co-localisation with TSPAN10 (red), demonstrated by the yellow areas seen in Figure 7 – 6 Aiv.

Scatterplots for red vs. green channel intensities were generated for three images from three WT differentiations and were subject to the Costes et al. statistical algorithm to determine maximum threshold intensities and quantify the extent of fluorophore overlap between Rab7 and TSPAN10. For the images displayed in Figure 7 – 6 panel A 95.5% of red and 88.0% of green were calculated as colocalised with green (Rab7) and red (TSPAN10) respectively. Costes overlap coefficients, M1 and M2, for the images analysed are shown in the table in Figure 7 – 6 C. On average, 89.0 ± 2.0% of Rab7 was reported to colocalise with TSPAN10, supporting the presence of TSPAN10 within RPE late endosomes. Standard deviation of statistical data indicated a small degree of spread within overlap coefficients, demonstrating variation in the amount of Rab7/TSPAN10 co-localisation between differentiations. However, all data points, except M1 from WT Dif 3, fell within one standard deviation of the mean. This, in addition to the calculated SEM for both M1 and M2 coefficients, which is close to 0, validates a sample cohort representative of the late endosome population.

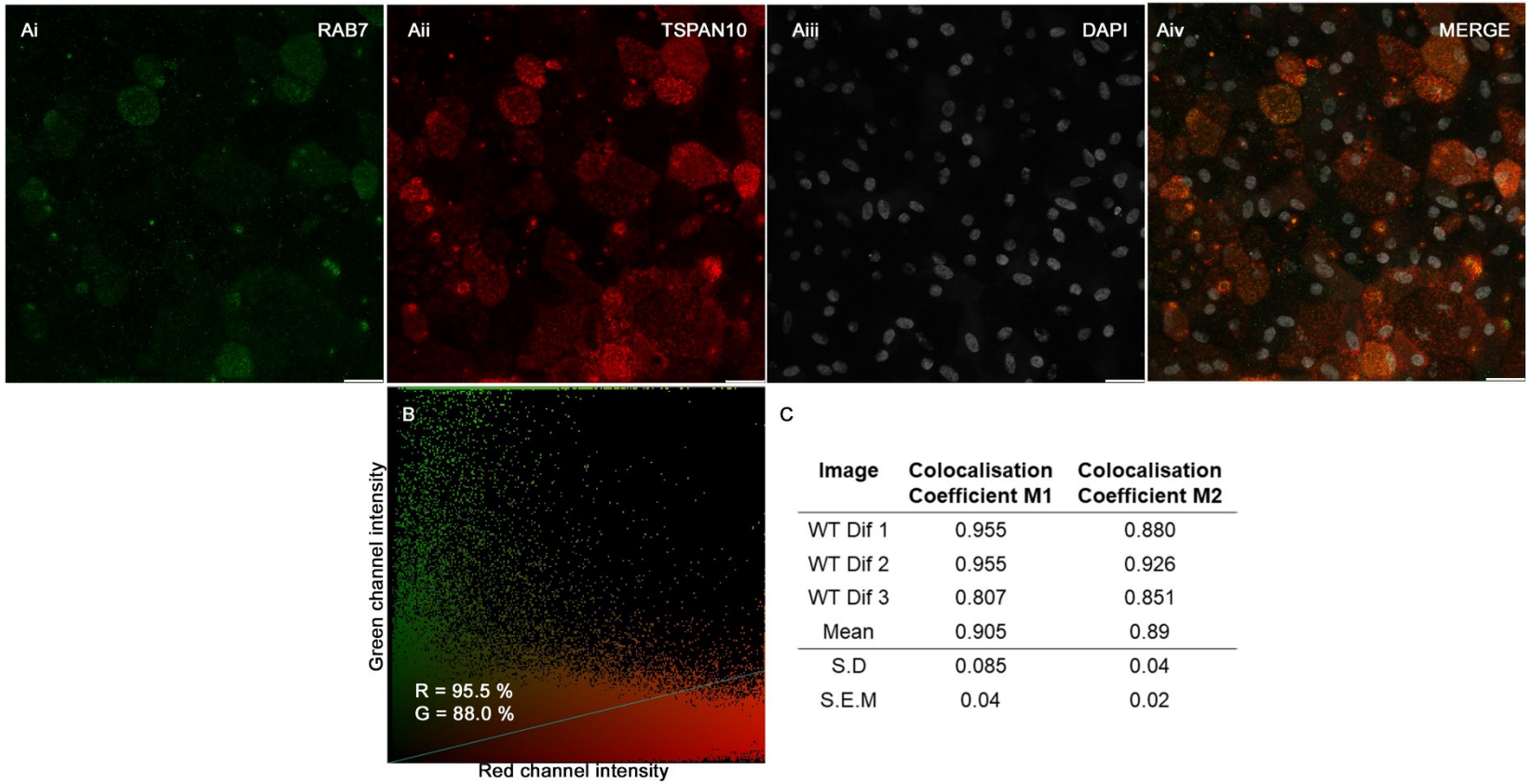

C

Image	Colocalisation Coefficient M1	Colocalisation Coefficient M2
WT Dif 1	0.955	0.880
WT Dif 2	0.955	0.926
WT Dif 3	0.807	0.851
Mean	0.905	0.89
S.D	0.085	0.04
S.E.M	0.04	0.02

Figure 7-6 Assessment of TSPAN10 and Rab7 co-localisation in wild-type hESC-RPE
Ai-Aiv: Confocal micrographs to assess co-localisation of Rab7 (green) with TSPAN10 (red) in WT hESC-RPE.DAPI nuclear stain shown in grey.
B Scatterplot of green (Rab7) and red (TSPAN10) pixel intensities for panel A. The results indicate 95.5% of red (TSPAN10) is colocalised with green (Rab7) and 88.0% of green (Rab7) is colocalised with red (TSPAN10). Intensities below the threshold determined by the Costes et al. algorithm for the x and y axis are not shown (black).
C: Quantification of Rab7 and TSPAN10 co-localisation in WT hESC-RPE. Costes overlap coefficients M1 and M2 indicate the percentage of red (TSPAN10) colocalised with green (Rab7) and green colocalised with red respectively. The results show 89.0 ± 2.0% of Rab7 is colocalised with TSPASN10. Measurements are presented for 3 differentiations. Quantification was performed in the Volocity software suite (PerkinElmer, UK).
Scale bars 25 µm

7.2 TSPAN10 has a role in pigmentation of the RPE

The RPE is formed of a single layer of polygonal cells, which are pigmented. This pigmented characteristic is a key defining feature of RPE, allowing the cell type to be easily distinguished. The RPE appears dark brown due to its melanin content, which helps reduce damage to the retina from UV light *in vivo*. Melanin loss and photobleaching has been shown to occur as the RPE ages, with a 2.5- fold decrease in melanin content by the age of 90 [244]. This loss of melanin is associated with decreased antioxidant activity of the RPE [244]. In fact, the melanin content of the eye is reported to be inversely proportional to the incidence of AMD [245] and significantly less macular pigments are observed in AMD patients compared to healthy individuals [246]. However, the potential role of melanosomal pigments in the RPE in AMD is relatively understudied. The presence of pigment is a key phenotype of the RPE and was therefore examined in hESC-RPE.

During the differentiation process, WT cultures showed evidence of pigmentation at approximately differentiation day 30 macroscopically. When examined under the microscope, there were scattered areas of cells with dark pigmentation evident (Figure 7 – 7A). TSPAN10 k.o mutants did not appear pigmented at this same time point to the eye, however examination of the A12 clone under the microscope showed a few small areas with pigmented cells (Figure 7 – 7A iii). A2 did not show any pigmentation at day 30 differentiation.

TSPAN10 k.o mutants continued to show significantly less pigmentation, despite the length of time in culture. Figure 7 - 7 B is a photograph of hESC-RPE cultured for 9 weeks on transwell inserts post differentiation, a stark difference in the amount of pigmentation between WT and TSPAN10 k.o mutants is evident. WT cells are a characteristic brown colour with mottled darker areas of pigment visible. Both A2 and A12 are a yellow/cream colour. WT cells remained pigmented throughout most of the differentiation process and regained pigment within 2 weeks after passaging post-differentiation. This was not true for either TSPAN10 k.o, only a small amount of pigmentation was evident in differentiated cells from the A2 and A12 clones.

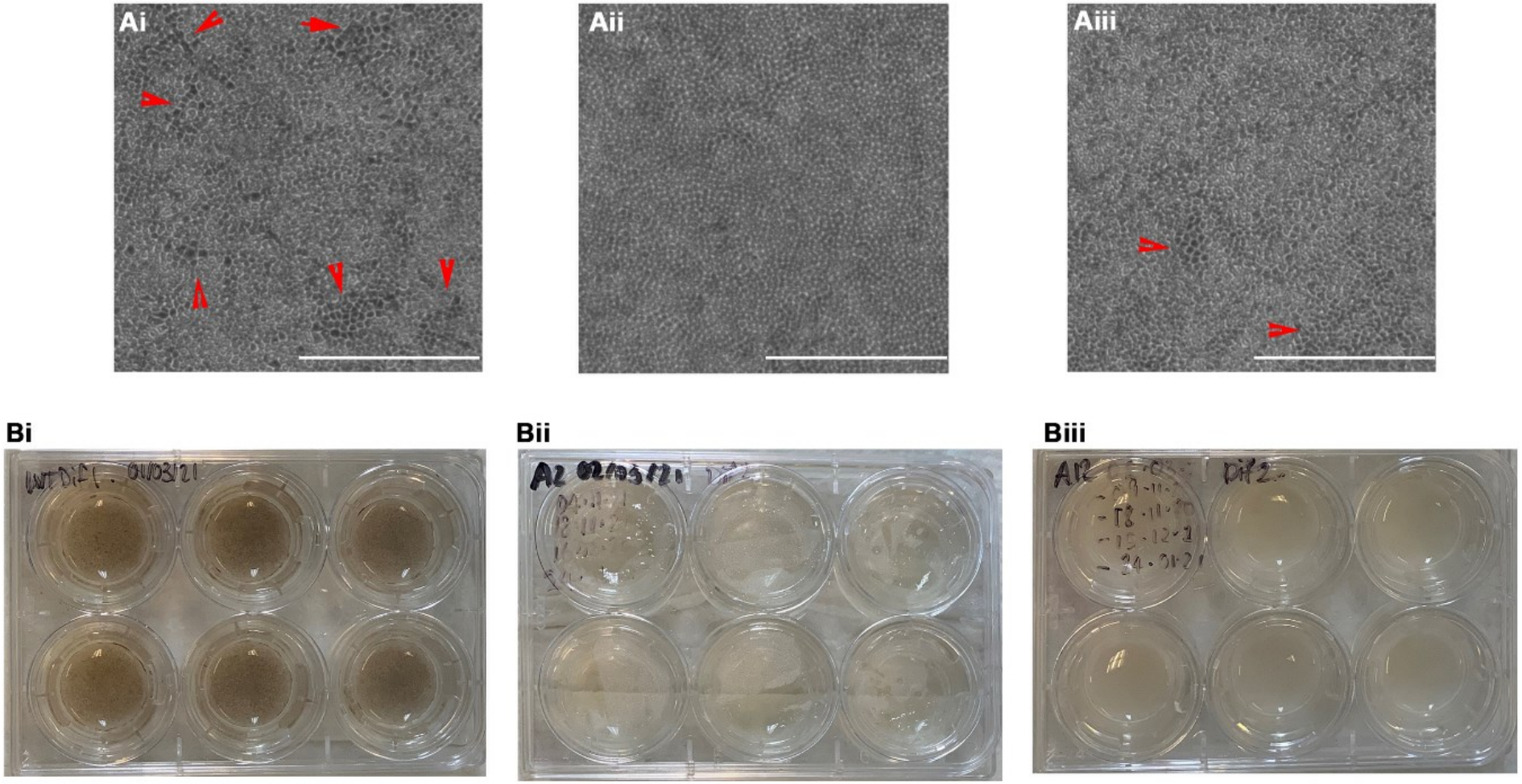

Figure 7-7 Phase contrast imaging of hESC-RPE displaying pigmentation at day 30 directed differentiation and pigmentation differences at day 60.
At differentiation day 30 cells start to show evidence of pigmentation. Scale bars represent 375µm
Red arrows highlight pigmented areas of cells. WT shows significantly more pigmentation than TSPAN10 k.o mutants.
Ai: WT **Aii**: A2 **Aiii**: A12
B: Photographs of hESC-RPE in culture on 6-well transwell inserts, differing amounts of pigmentation evident
Bi: WT**. Bii**: A2**. Biii**: A12. WT cells show classic brown mottled pigmentation macroscopically. Both TSPAN10 k.o mutants are a pale yellow/cream.

7.2.1 Tyrosinase function

Tyrosinase is a key enzyme of melanogenesis, without tyrosinase the formation of melanin is not possible [247]. Tyrosinase catalyses three reactions in melanin synthesis: the hydroxylation of L-tyrosine to 3,4-dihydroxyphenyl-L-alanine (L-DOPA), the oxidation of L-DOPA to dopaquinone and the oxidation of 5,6-dihydroxyindole to 5,6-dihydroxyquinone. Given the key role of tyrosinase in pigmentation, its expression was compared in WT and TSPAN10 k.o hESC-RPE 40 days post differentiation using RT-qPCR (Chapter 5, Figure 5 – 6D). Interestingly no differences in tyrosinase expression were seen between WT cells and the TSPAN10 k.o mutants A2 nor A12. This result is confirmed in our RNAseq data, where tyrosinase was not called as a DEG (A2 vs WT padj = 0.16; A12 vs WT padj = 0.38).

Despite the minimal differences in tyrosinase mRNA expression, due to the reduction of pigmentation seen in our k.o cultures we investigated tyrosinase protein production through western blotting. Western blotting of day 40 post differentiation hESC-RPE cell lysates showed a significant reduction in tyrosinase expression in TSPAN10 k.o cells in comparison to WT where two products were seen at 50kDa and 70kDa (Figure 7 – 8). This suggests that despite similar mRNA production TSPAN10 k.o leads to reduced tyrosinase protein expression. Given that tyrosinase is crucial for the formation of melanin this result helps to explain why TSPAN10 mutant cells are significantly less pigmented than their WT counterparts. There was however some tyrosinase protein production in TSPAN10 mutant cells, therefore a DOPA-oxidase assay was undertaken to assess the ability of the tyrosinase present to catalyse the oxidation of L-DOPA to dopaquinone.

One of the most widely used *in vitro* assays to measure the dopa oxidase activity of tyrosinase is the dopachrome method [265]. The formation of dopachrome from L-dopa is measured spectrophotometrically. None of the intermediates between L-dopa and dopachrome show absorbance in the visible spectrum, and the autoxidation of dopaquinone is very rapid, therefore none of these intermediate products interfere with the reaction. The MBTH assay is a revised version of the dopachrome assay. Besthorn's hydrazone (3-methyl- 2-benzothiazolinonehydrazone hydrochloride), or MBTH is used to trap dopaquinone formed from the oxidation of L-DOPA as a stable compound. MBTH reacts with dopaquinone by a Michael addition reaction forming a dark pink product, the levels of which can be monitored continuously using a spectrophotometer. It is assumed that the reaction of MBTH with dopaquinone is very rapid relative to the enzyme catalysed oxidation of L-DOPA. Thus, the rate of production of the pink pigment can be used as a quantitative measure of enzyme activity. The MBTH assay of dopa oxidase activity is thought to be theoretically sounder than the traditional dopachrome assay [264]. Furthermore, the MBTH assay is reported to be approximately seven times more sensitive than the dopachrome assay in terms of rate of

absorbance increase [264]. Consequently, the MBTH assay was chosen as a measure of tyrosinase activity. There was a significant reduction in tyrosinase activity in TSPAN10 k.o cells in comparison to WT throughout the assay, (Figure 7 – 9 A). By 180 minutes all WT differentiations had reached the maximum threshold at 490 nm absorbance, however both TSPAN10 mutants, A12 and A2 showed only approximately 50% of this activity at 180 minutes, Figure 7 – 9 B. Consequently, we can infer that TSPAN10 k.o cells have reduced tyrosinase activity. Given that this was common to both clones A12 and A2 and all differentiations it is likely that reduced tyrosinase activity is a phenotype related to TSPAN10 k.o.

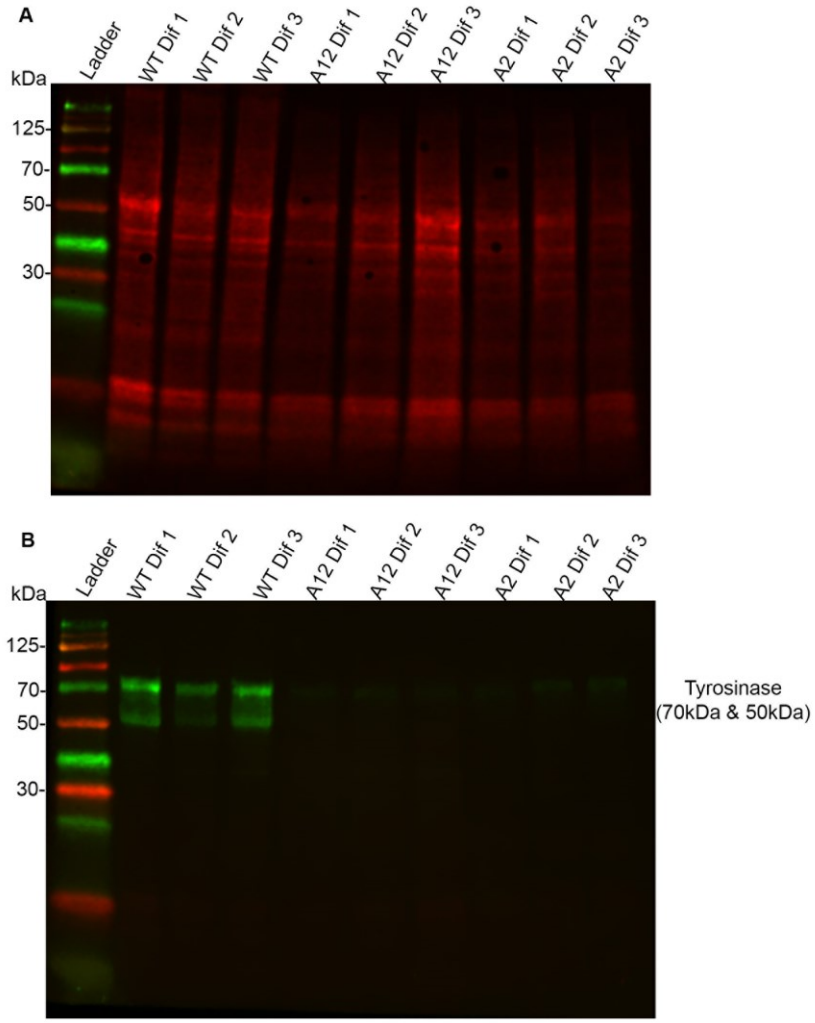

Figure 7-8 Western Blot for Tyrosinase in TPSAN10 mutant and WT hESC-RPE cells
A: A total protein stain (Revert 700) was performed as a control to ensure equal loading of lysates.
B: A Tyrosinase protein blot using the Abcam monoclonal Ab (60kDa) indicates that tyrosinase protein expression is reduced in all differentiations of A12 and A2 in comparison to WT.
N=3 technical repeats performed

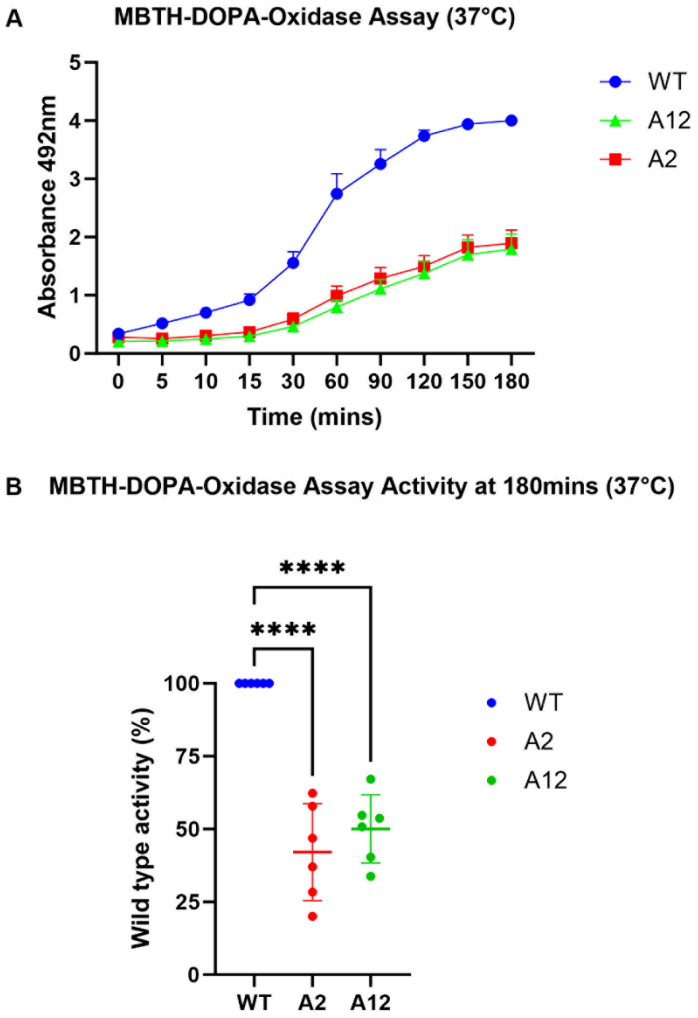

Figure 7-9 Tyrosinase activity in wild-type and TSPAN10 mutant hESC-RPE
The absorbance of dopaquinone, a product synthesised by the transformation of L-DOPA by tyrosinase was quantified as a measure of tyrosinase activity in wild-type and TSPAN10-mutant cell lines (A2 and A12). Cumulative production of dopaquinone (**A**) was quantified from the start of L-DOPA treatment (0 min) to 180 min. Statistical differences between cell lines were analysed at 180 min (**B**). Data are shown as mean ± SD and statistically significant differences between groups are indicated by asterisks (****p < 0.0001).

7.2.2 Transmission electron microscopy of hESC-RPE

RPE cells appear pigmented due to the presence of melanin granules. To further investigate the morphology, apicobasolateral specialisation and melanosome content of hESC-RPE ultrastructural adaptions of cells grown on Transwell® inserts were analysed by transmission electron microscopy (TEM) (Figures 7 – 10, 7 – 11 & 7 – 12). hESC-RPE displayed polarised membrane domains, with well-defined apical microvilli (Figures 7 – 10 & 7 – 11, Ai-Aiii) and basal infolds (Figure 7 – 11, Ci-Ciii). Apically localised melanosomes/pigment granules (Figures 7 – 10 & 7 – 11, Bi-Biii) were also evident, however there was a significant reduction in melanosomes evident in TSPAN10 k.o cells in comparison to WT (Figure 7 – 12). Cellular junctions including tight junctions and adherens junctions were also seen in micrographs, typically found co-distributed along adjacent cell membranes. Tight junctions were localised to the apical axis of the RPE at the point of cell-to-cell contact and were visualised as darker points of contact between cells in TEM sections (Figure 7 – 10 C). Four ultrastructural characteristics were chosen for comparison between WT and TSPAN10 k.o RPE, namely mean cell height, number of stage III and IV melanosomes per cell, number of sub-RPE fibrous long-spaced (FLS) collagen deposits per cell and average length of apical microvilli per cell. All comparator images were used at the same magnification. For cell height and apical microvilli measurements three readings were taken per cell perpendicular to the transwell membrane on which the cell was attached. Cells not attached to the transwell membrane were not included. Three cells were analysed per differentiation and three differentiations per cell line (n=9). Cell height measurements for WT hESC-RPE were in keeping with those previously reported [331, 332], however there was a statistically significant reduction in the height of both A12 and A2 cells in comparison to WT (Figure 7 – 12 A). No differences in apical microvilli height, nor numbers of sub-RPE FLS collagen were seen between WT and TSPAN10 k.o cells (Figure 7 – 12 C & D). There was however a significant reduction in the number of mature stage III and IV melanosomes seen between WT and TSPAN10 k.o cells (Figure 7 – 12 B). Numbers of mature melanosomes were identified using previously published criteria [333, 334], namely the presence of melanin granules marked a melanosome as mature (Figure 7 – 12 E). The number of mature melanosomes seen in WT cells was comparable to those previously reported [334], however for TSPAN10 k.o cells there was approximately a 4-fold reduction seen (A2 vs WT $p=0.0002$, A12 vs WT $p=0.0004$).

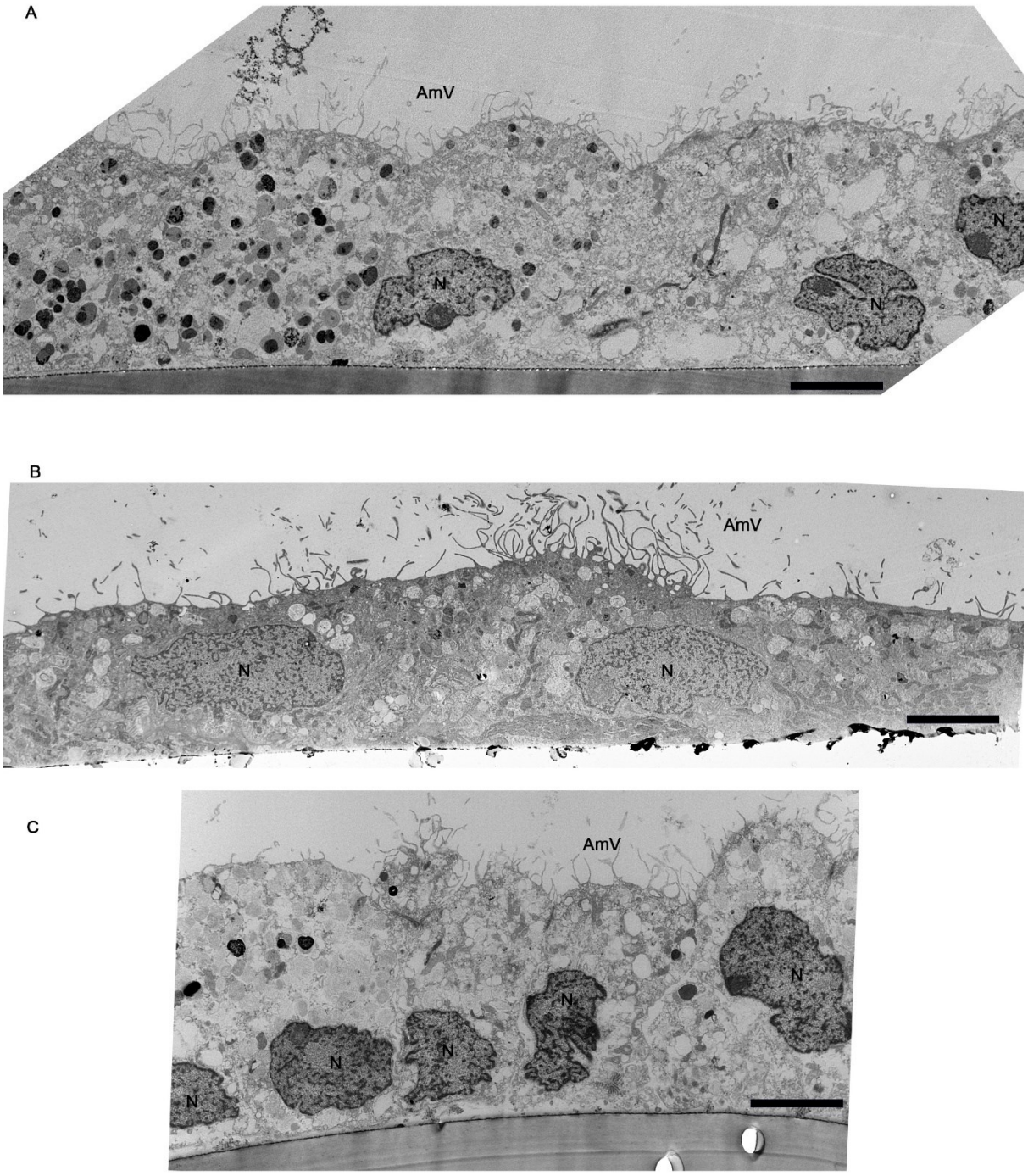

Figure 7-10 Transmission Electron Microscopy (TEM) of hESC-RPE
Examination of RPE ultrastructure using TEM.
A: WT; **B**: A2; **C**: A12
RPE cells from both TSPAN10 k.o mutants and WT cells display apical microvilli. WT cells clearly show a significantly increased number of melanin granules in comparison to TSPAN10 k.o mutants. Sub-RPE FLS collagen is seen in both WT cells and TSPAN10 k.o mutants. Furthermore, all cells contain vacuoles.
Abbreviations: AmV apical microvilli, N nucleus

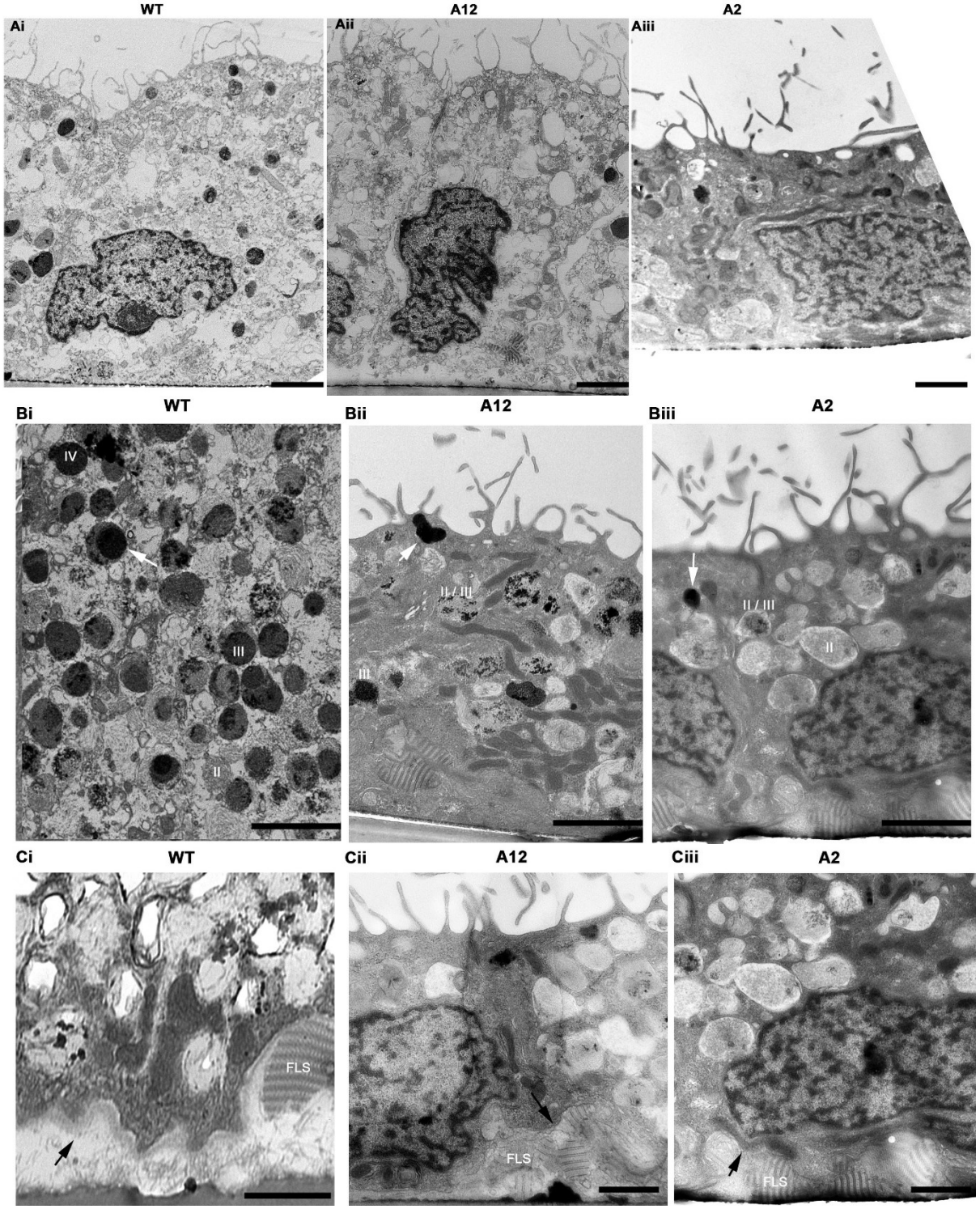

Figure 7-11 RPE ultrastructure analyses by TEM
A significant difference was observed in cell height between WT and TSPAN10 mutants (**Ai-Aiii**). WT cells displayed significantly increased numbers of stage III and IV melanosomes in comparison to TSPAN10 k.o cells (**Bi-Biii**).
There was no difference in the amount of sub-RPE fibrous-long spaced collagen (FLS) deposits between WT and TSPAN10 k.o cells, nor differences in basal laminar area (**Ci-Ciii**). Black arrows depict basal infolds.
Vacuoles were evident in both WT and TSPAN10 k.o cells.
Black arrows depict basal infolds, white arrows depict stage 4 melanosomes.
Abbreviations: FLS: Fibrous-long spaced collagen, II: Stage 2 melanosomes, III: Stage 3 melanosomes
Scale bars in A represent 2 μm, B = 1μm and C = 1μm.

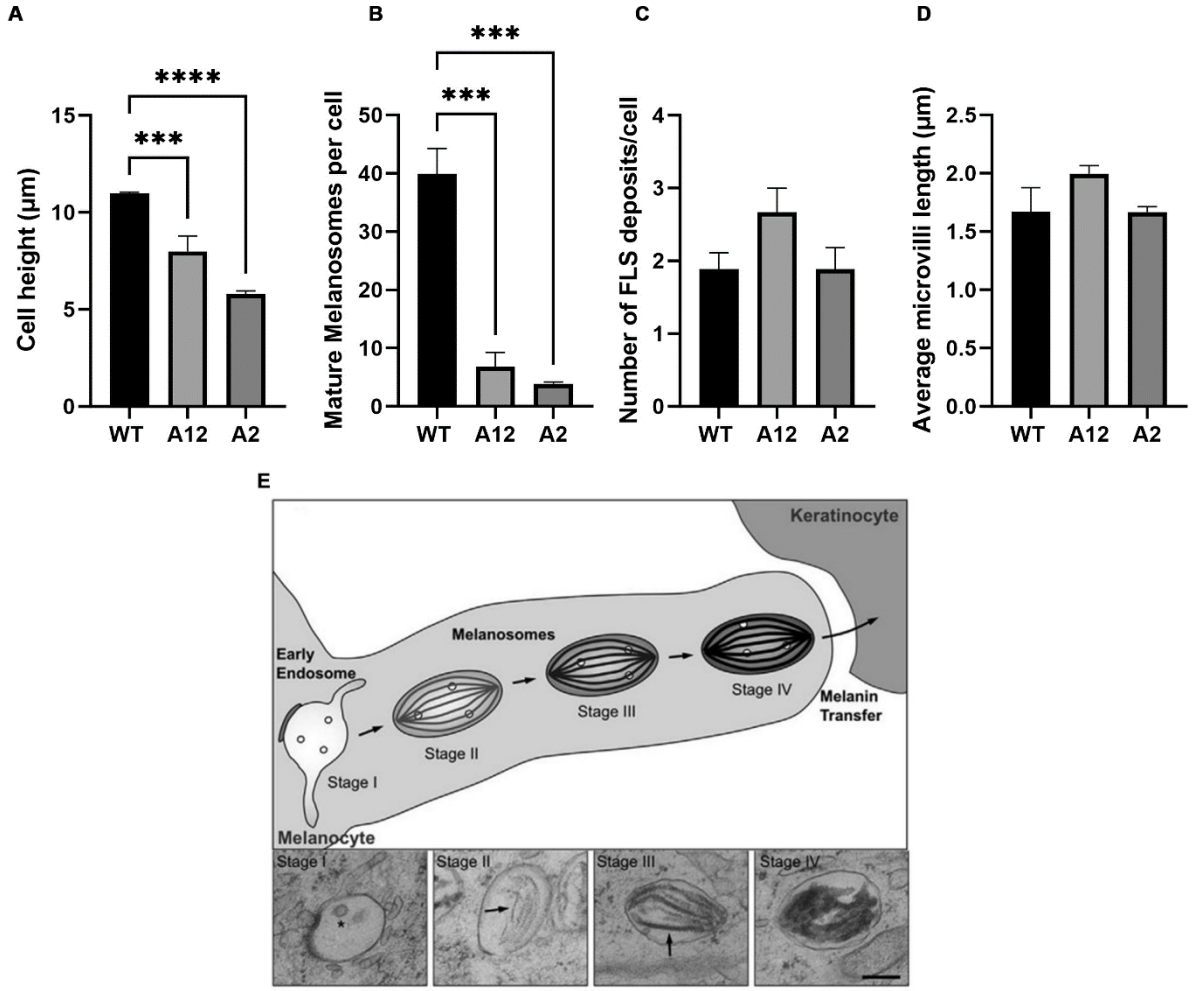

Figure 7-12 Graphical representation of RPE ultrastructure analysis using TEM in hESC-RPE
Bar charts demonstrate average RPE characteristics identified using transmission electron microscopy (TEM).
A: Significant reduction in RPE average cell height in TSPAN10 k.o mutant clones in comparison to WT.
B: Significant increase in the number of Stage III and IV (mature) melanosomes per cell for WT cells in comparison to TSPAN10 k.o mutants.
C: No differences seen in the number of sub-RPE FLS collagen per cell
D: No differences seen in the average apical microvilli length
Three cells examined per image at x 4200 magnification. Three differentiations per cell clone (N=9). For cell height measurements three readings taken per cell and averaged. For apical microvilli measurements three microvilli measurements were taken per cell and averaged.
Error bars represent SEM. Statistical analysis with One-way ANOVA
**** $p<0.001$ ***$p<0.005$
E: Schematic and images taken from [333]. Upper image demonstrating melanosome biogenesis in skin melanocytes. Pre-melanosomes defined as Stage I and Stage II melanosomes with no melanin deposition. Stage III and IV mature melanosomes with melanin evident. Ultrastructure of melanosome stages from TEM shown in below images. Stage I (pre) melanosome with intraluminal vesicles (*). Stage II (pre) melanosome characterised by intraluminal amyloid sheets (arrow), upon which electron dense melanin deposits in Stage III (mature) melanosomes, denoted with black arrow. Stage IV melanosomes show filling of the lumen with melanin. Scale bar represents 200nm.

7.2.3 Fluorescence Activated Cell Sorting

One possible criticism of this work is if RPE cultures are not pigmented then should they be included? Typically, when RPE are differentiated from stem cells they are selected based on their pigmentation. I did not perform this step in the differentiation process as it was hypothesized that TSPAN10 could affect RPE pigmentation. Recently a newly discovered RPE marker CD140b [248] has been reported to allow selective sorting of RPE cells, producing a population that are increasingly pigmented. Consequently, we aimed to sort hESC-RPE from both WT and TSPAN10 mutant cells based on CD140b and to then compare pigmentation levels. It was hypothesized that if k.o sorted cells became equally pigmented to WT, then this would suggest that previously noted changes in pigment are unrelated to TSPAN10. However, if positively selected TSPAN10 k.o RPE cells remained less pigmented than their WT counterparts, this would help to confirm that TPSAN10 k.o is driving such changes.

Flow cytometry allows for the examination of individual cellular attributes as they traverse a light beam, assessing parameters such as cell dimensions, granularity, and fluorescence intensity following treatment with fluorochrome-conjugated antibodies. These measurements are attained by examining how cells scatter laser light or emit fluorescent signals. Forward scattering of light by a cell provides information about its size in relation to other cells, whereas side scattering of light indicates the internal intricacy or granularity within the cell.

Fluorochromes linked to either the primary antibody or to a secondary antibody that binds to the primary antibody can be used to quantify the relative fluorescence intensity of each cell. This provides a direct assessment of the number of antigens present on or within a specific cell. In this work directly conjugated antibodies were used. Compensation beads stained with fluorochrome-conjugated antibodies of interest were used to provide distinct positive and negative stained populations.

Fluorescence-activated cell sorting (FACS) can be used to purify specific cell populations based on the phenotypes detected by flow cytometry. Cell types typically express a unique combination of antigens on the plasma membrane that can distinguish one cell population from another. The phenotype of a cell is determined by the presence or absence of a light signal, indicating positive or negative expression of a specific surface molecule. Following detection, cells exhibiting the same phenotype are directed to a specific collection tube according to their electrical charge.

Aside from FACS, there are alternative methods like magnetic-activated cell sorting (MACS) that rely on cell surface markers to isolate specific cell populations. MACS uses magnetic beads conjugated with antibodies to target particular cell surface molecules. When the

antibodies interact with their antigens, the magnetic beads-coated cells can be separated from those without coatings as they pass through a magnetic field. However, MACS has a limitation compared to FACS because it can target only a limited number of molecules. Unfortunately, there are not currently MACS beads targeting CD140b, therefore FACS was chosen.

Initially the CD140b antibody was titrated to ensure optimal staining, reduce background fluorescence and the risk of false negatives. The RPE cell line ARPE19 cultured for 3 months (gifted by Dr J.Dewing) was used as a positive control to preserve hESC-RPE samples. A serial dilution of the manufacturer's recommended concentration was tested, and the staining index calculated, displayed in Appendix D Figure (13 – 17). A concentration of 20 µl per test was selected.

hESC-RPE cultured for at least 40 days were dissociated and sorted for CD140b using FACS. Three separate experiments were conducted with sorting of differentiations 1, 2 and 3 for each cell line occurring one week apart. Figure 7 – 13A shows the gating strategy used and Figure 7 – 13B the distribution of CD140b positive cells for each cell type and differentiation. Interestingly there were more TSPAN10 k.o than WT CD140b positive cells. The mean % of WT CD140b positive cells across the three differentiations was 45.0%, however this was 65.9% for A12 and 60.2% for A2. A One-way ANOVA did not show statistical significance for these differences.

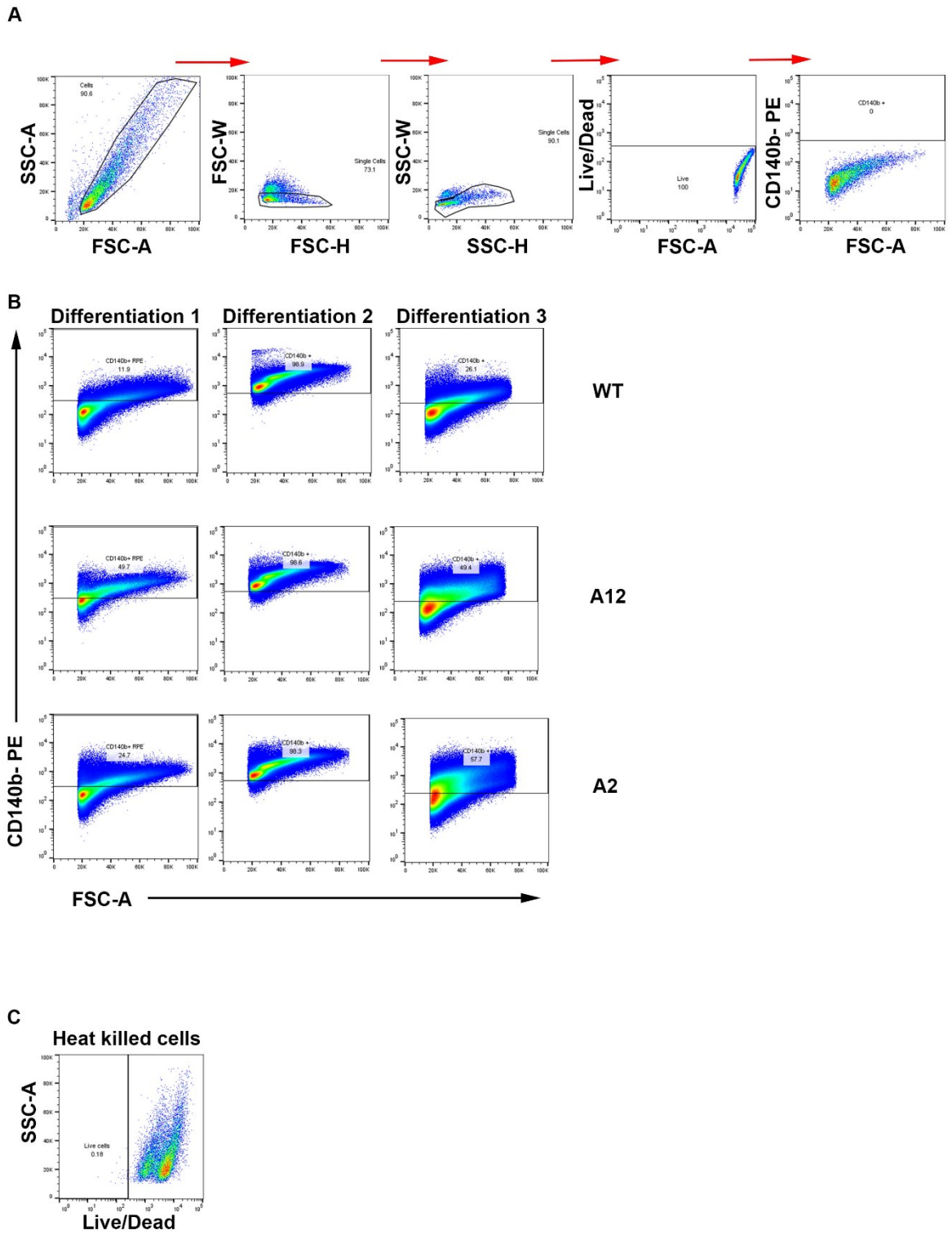

Figure 7-13 Fluoresence Activated Cell Sorting of hESC-RPE cells

(A) hESC-RPEs gated through the FSC-A vs SSC-A plot were further interrogated by the ratios of height to width in forward scatter and side scatter, in addition to their ability to uptake the live/dead cell marker eFluor 506. Live CD140b$^+$ hESC-RPE cells were then selected for cell sorting as shown in B.

(B) Comparison of CD140b$^+$ cells between WT and TSPAN10 k.o cells shows an increase in CD140b$^+$ cells in TSPAN10 k.o cell lines in comparison to WT.

(C) Heat killed cell control. All cells are gated as positive for the live/dead marker.

7.2.4 CD140b sorted hESC-RPE pigmentation differences.

To understand if CD140b sorted cells become more pigmented despite TSPAN10 k.o sorted cells were re-plated into positive and negative populations and cultured on transwell inserts for 45 days. Differences in pigmentation were observed throughout culture in the WT populations, however no obvious differences were seen in CD140b positive and negative TSPAN10 k.o cell lines. To quantify differences in pigmentation, cells were fixed, and bright-field images taken. Five 1 x 1 mm fields of view for each cell line and differentiation were captured, and the best three images selected based on image quality. All images were imported into Fiji (Image J), thresholded, converted to a binary image and the mean grey value calculated (method depicted in Figure 7 – 14). There was a significant difference seen between CD140b positive and negative cells in all differentiations of WT hESC-RPE (Figure 7 – 15 Aiii, Di), with a mean % area pigmented for CD140b positive cells of 56.5% and CD140b negative cells of 28.4%, $p<0.0001$. However, this was not seen in the A12 and A2 TSPAN10 k.o clones (Figure 7 – 15 Biii & Ciii). Interestingly there was an anomaly seen in A2 differentiation 2 (Figure 7 – 15 Ciii), where there was a statistically significant difference in pigmentation between CD140b positive and negative cells ($p<0.0001$, analysed with Two-way ANOVA), however this was not seen for the other two differentiations of A2. Although when the results of the three differentiations were combined this result did skew the mean, so that a difference of 2.17 % pigmentation in CD140b positive cells versus 1.16% in CD140b negative cells was significantly different ($p=0.038$, analysed using student's two-tailed t-test). Given that these changes in pigmentation were not common to all differentiations of all k.o clones and the small differences in pigmentation reported for A2 differentiation 2 it was concluded that sorting of TSPAN10 k.o cells for CD140b would not allow TSPAN10 k.o cells to become pigmented to a similar level as WT cells. Overall, these results suggest that sorting of RPE for CD140b does increase the pigmentation of the population. Given that this was not true for TSPAN10 k.o cells it adds to the evidence that TSPAN10 is involved in RPE pigmentation.

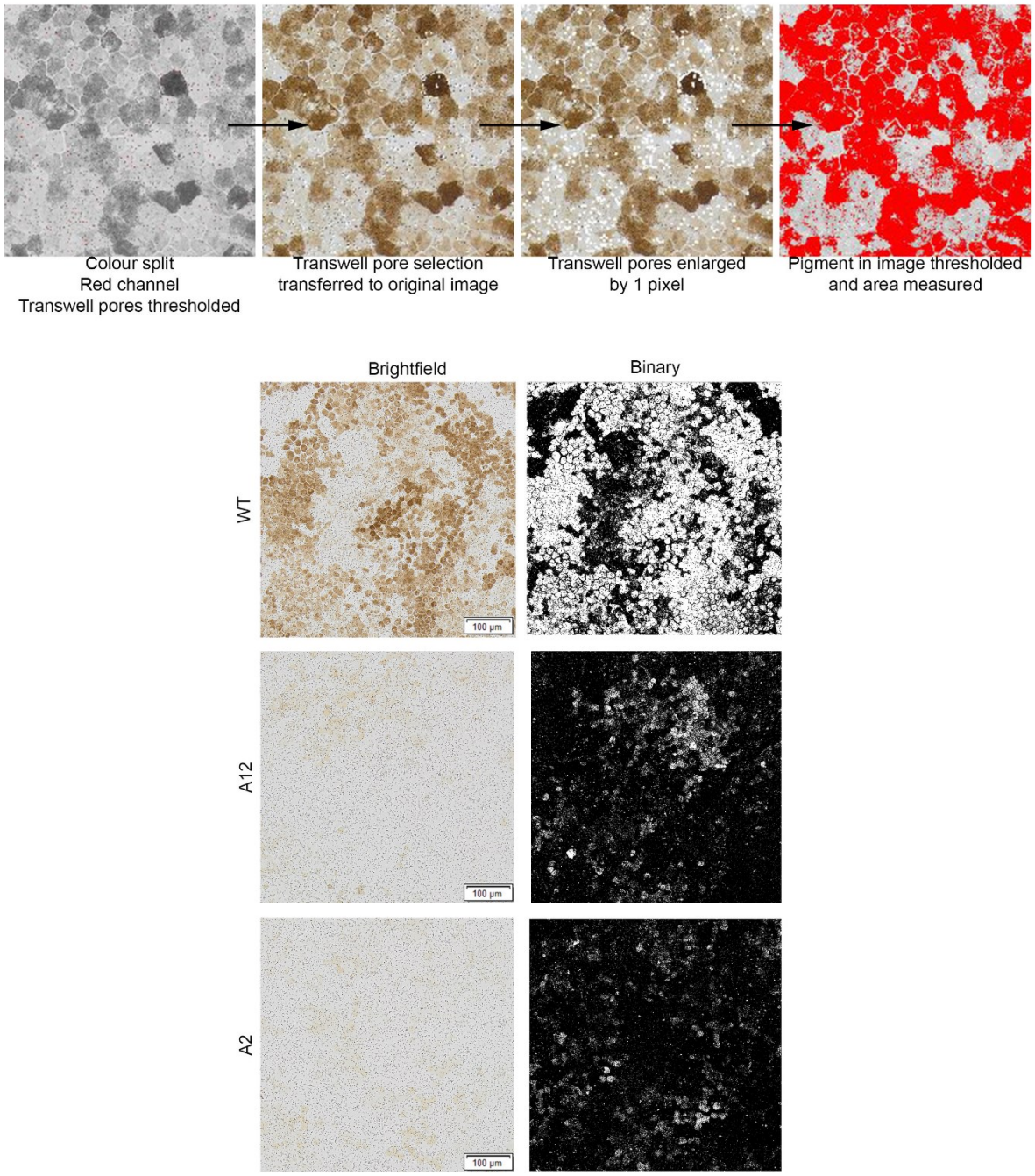

Figure 7-14 Thresholding of brown pigment in brightfield images of hESC-RPE
Depiction of the steps taken to quantify the level of pigmentation in hESC-RPE cultures.
Initial images show the splitting of channels into red, blue and green and thresholding of the red channel to remove transwell pores to prevent false positives. Subsequent images show the conversion of WT, A12 and A2 brightfield images into binary images where brown pigment has been thresholded (pigment depicted as white, no pigment depicted as black).
Scale bars represent 100 µm.

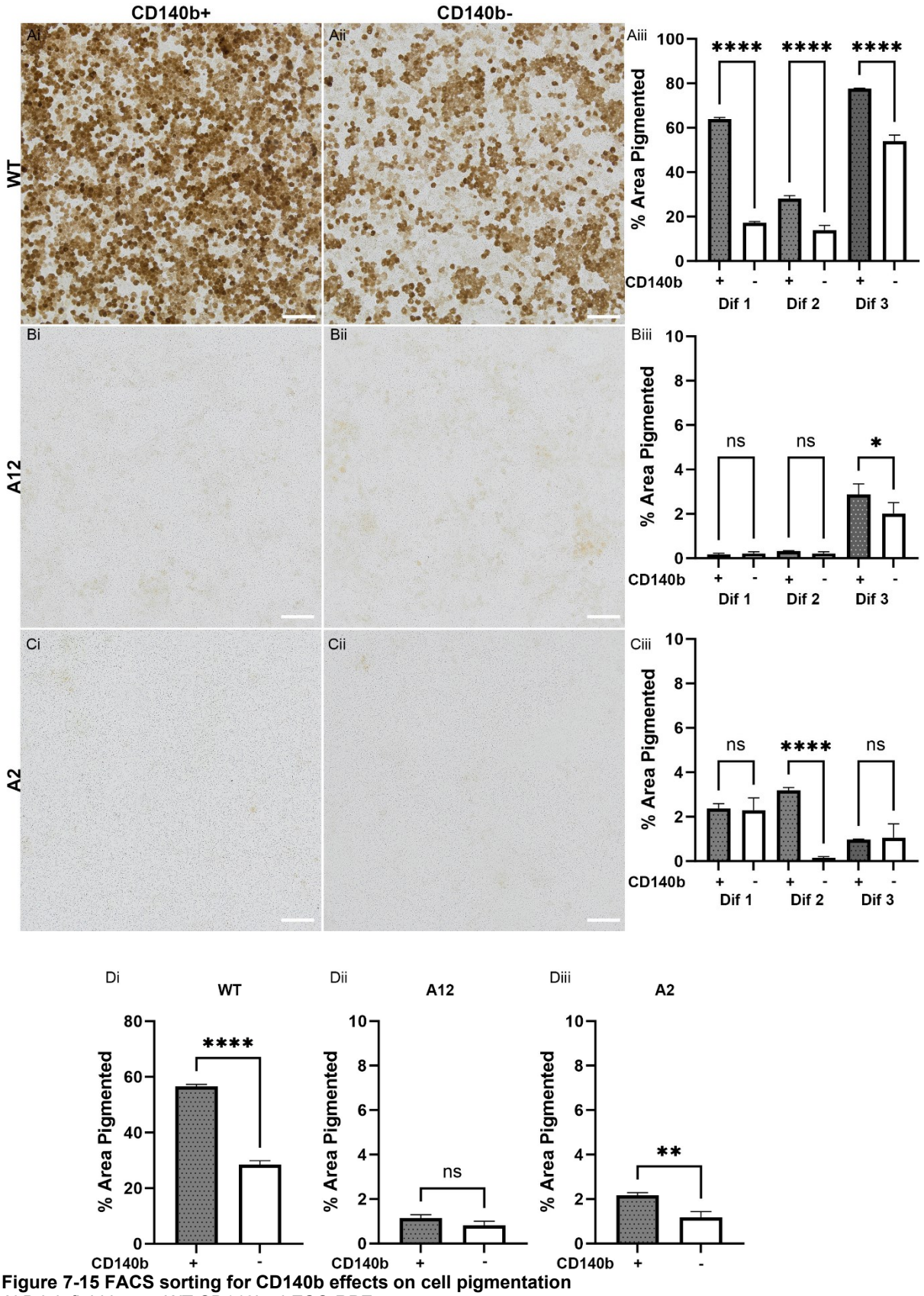

Figure 7-15 FACS sorting for CD140b effects on cell pigmentation
Ai Brightfield image WT CD140b+ hESC-RPE
Aii Brightfield image WT CD140b- hESC-RPE
Aiii Bar chart displaying the % area of pigmented WT cells. Significant differences seen between CD140b+ and CD140b- cells.
Bi Brightfield image A12 CD140b+ hESC-RPE
Bii Brightfield image A12 CD140b- hESC-RPE

Biiii Bar chart displaying the % area of pigmented A12 cells. Significant difference seen between CD140b+ and CD140b- cells for differentiation 3. No significant differences seen for other differentiations.
Ci Brightfield image A2 CD140b+ hESC-RPE
Cii Brightfield image A2 CD140b- hESC-RPE
Ciii Bar chart displaying the % area of pigmented A2 cells. Significant difference seen between CD140b+ and CD140b- cells for differentiation 2. No significant differences seen for other differentiations.
Di Bar chart depicts mean % area pigmented for WT CD140b + and – FACS sorted cells. Significant difference evident.
Dii Bar chart depicts mean % area pigmented for A12 CD140b + and – FACS sorted cells. No significant difference seen, cells have very little pigmentation.
Diii Bar chart depicts mean % area pigmented for A2 CD140b + and – FACS sorted cells. Significant difference seen although cells still have very little pigmentation,
Scale bars represent 100μm
Statistical analysis in A-C with Two-way ANOVA where each positive and negative population in each differentiation of each clone were compared.
Statistical analysis in D with Student's two-tailed t-test ****p<0.0001, *** p<0.001, **p<0.005, *p<0.05

7.2.5 L-Dopa and hESC-RPE pigmentation

Melanin synthesis is a complex biological process that occurs within melanosomes, small subcellular lysosome-like organelles [335]. The rate limiting step in melanin synthesis is the hydroxylation of L-tyrosine to L-DOPA which is catalysed by tyrosinase. We saw a significant reduction in tyrosinase production and function in our TSPAN10 k.o hESC-RPE (section 6.2.1). Consequently, we aimed to understand if the lack of pigmentation in these cells could be rescued by the addition of exogenous L-DOPA.

hESC-RPE were cultured on transwells for 40 days post differentiation and then treated with L-DOPA at two concentrations, 1 μM and 2 μM by adding the drug apically to transwells during media changes for 28 days. Apical addition was felt to be sufficient given that L-Dopa is released into the subretinal space apical to the RPE when melanin synthesis occurs [336]. A starting concentration of L-Dopa at 1 μM was chosen because it has been shown that addition of 1 μM L-Dopa to RPE cells causes an influx in intracellular Ca^{2+} [336]. Melanosomes are known to store Ca^{2+}, and reductions in melanosomal Ca^{2+} are correlated with reduced pigmentation [337]. After 28 days of treatment cells were fixed and brightfield images taken of five 1 x 1 mm sections for each condition. The three best images were then selected, thresholded and mean grey values calculated, see Chapter 2 section 2.26 and Figure 7 – 14 for further details of the method.

We saw no change in pigmentation in WT or TSPAN10 k.o cells with the addition of L-Dopa at either 1 or 2 μM. As depicted in Figure 7 – 16 TSPAN10 k.o cells A12 and A2 remained unpigmented despite treatment with L-Dopa, and there were no changes in the amount of pigment present in WT cells.

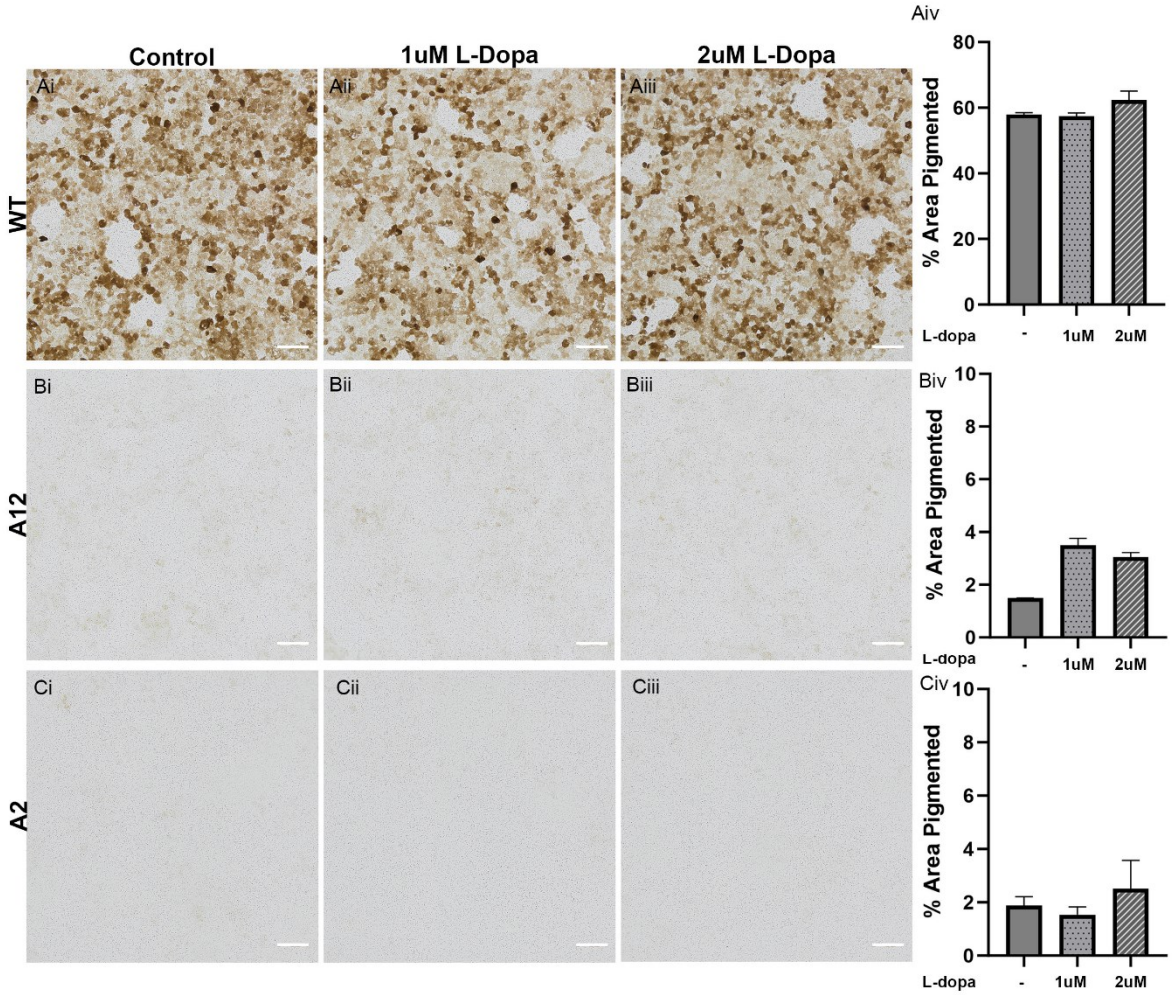

Figure 7-16 L-Dopa treatment of hESC-RPE
Day 40 hESC-RPE were treated with L-Dopa at varying concentrations for 28 days after which pigmentation levels were assessed using ImageJ.
Ai: Brightfield image of control WT hESC-RPE
Aii: Brightfield image of WT hESC-RPE treated with 1μM L-Dopa
Aiii: Brightfield image of WT hESC-RPE treated with 2μM L-Dopa
Aiv: Bar chart depicting % area of pigmentation for WT. No significant differences seen between treatment groups.
Bi: Brightfield image of control A12 hESC-RPE
Bii: Brightfield image of A12 hESC-RPE treated with 1μM L-Dopa
Biii: Brightfield image of A12 hESC-RPE treated with 2μM L-Dopa
Biv: Bar chart depicting % area of pigmentation. No significant differences seen between treatment groups.
Ci: Brightfield image of control A2 hESC-RPE
Cii: Brightfield image of A2 hESC-RPE treated with 1μM L-Dopa
Ciii: Brightfield image of A2 hESC-RPE treated with 2μM L-Dopa
Civ: Bar chart depicting % area of pigmentation. No significant differences seen between treatment groups.
Three 1 x 1 mm images analysed for each condition and differentiation, three differentiations per cell clone (n=9).
Statistical analysis Two-way ANOVA with Dunnett's correction.
Scale bar represents 100 μm.

7.3 Interpretation and Interim Discussion

Experiments in this chapter aimed to identify and further examine a phenotype associated with the k.o of TSPAN10, to test the hypothesis that k.o cell lines will exhibit consistent and specific phenotypes that may underlie the risk of AMD in TSPAN10. Two specific phenotypes of TSPAN10 k.o RPE were studied, increased oxidative stress and a reduction in pigmentation.

7.3.1 Oxidative Stress

ROS is a broad term that encompasses oxygen free radicals, which have unpaired electrons, such as superoxide (O2−•), as well as oxidising agents that are not free radicals such as hydrogen peroxide (H_2O_2) [244]. ROS can be both endogenous and exogenous. The main endogenous source of ROS is the mitochondrial electron transport chain, however there are several other sources including peroxisomes and the endoplasmic reticulum, where oxygen consumption is high [245]. There are many exogenous ROS sources including tobacco smoke and fatty acids in foods [245], both of which are associated with AMD [246, 247]. Consequently, oxidative stress has long been investigated in relation to AMD [241]. Catalase is a key antioxidant enzyme, catalysing the conversion of the ROS H_2O_2 to H_2O and O_2.[241] The activity of catalase is closely linked to the mechanisms of ROS degradation. Catalase is localised within the peroxisomes of the RPE [248, 249]. Interestingly, almost all patients with a peroxisomal disorder, regardless of the mutation present with a form of retinopathy [338, 339].

One of the DEGs in our RNA-seq data with the highest fold change for both TSPAN10 k.o mutants was catalase (*CAT*) (Chapter 5). Consequently, we first aimed to understand if this reduced mRNA expression translated into reduced protein production. Western blotting for catalase showed a significant reduction in expression in TSPAN10 mutant cells from all differentiations in comparison to WT (Figure 7 - 1 A & B). Three technical repeats of this experiment were performed for robustness. This result reinforced our RNA-seq data, suggesting that TSPAN10 k.o cells produce less of the antioxidant enzyme catalase.

As previously mentioned, catalase is an enzyme, therefore we next sought to measure catalase function in our hESC-RPE. Typically, catalase activity is measured using calorimetric assays analysing the breakdown of H_2O_2 [252]. We chose an assay designed by Cayman Chemical which exploits the peroxidatic function of catalase based on the reaction of catalase with methanol in the presence of H_2O_2. Catalase activity was significantly reduced in both TSPAN10 mutants in comparison to WT (Figure 7 – 1 C). Given that TSPAN10 k.o cells produce less catalase it is difficult to state whether this reduced activity is

directly because of reduced production or if the catalase that is produced has reduced enzymatic activity or a combination of the two.

Finally, we aimed to understand how much catalase was present in our cultures without undergoing cell lysis. We used apical and basal conditioned media collected from our hESC-RPE cultures to perform a sandwich ELISA (Figure 7 – 1 D). Despite being statistically significant we only saw a small fold change in catalase secretion in our TSPAN10 k.o cells versus WT (Figure 7 – 1D). This may be related to the limited amount of stress these cells are under in culture given their constant supply of nutrients. Furthermore, given that catalase is mainly localised to the peroxisome or the secondary lysosome differences in catalase in the conditioned cell media are likely to be limited.

Catalase activity in the RPE has been previously studied and found to be approximately 6-fold higher than in other ocular tissues [306]. Interestingly, given its antioxidant effects catalase activity decreases in the RPE with both age and macular degeneration [306]. Furthermore, the immunoreactivity of catalase in the cytoplasm and lysosomes of macular RPE cells from eyes with and without AMD show an age-dependent reduction [340]. Our results show that TSPAN10 k.o hESC-RPE produce less catalase and have reduced catalase activity. Therefore, we can cautiously conclude that TSPAN10 affects catalase expression in human RPE, hinting at a possible mechanism for its role in AMD risk. As discussed, catalase is an antioxidant enzyme, therefore one can assume that reductions in catalase activity would result in increased oxidative stress. To ensure that this was true in our cultures we conducted a DCFDA assay to measure oxidative stress under both basal conditions and those of increased stress using H_2O_2. DCFDA is a fluorogenic dye that measures hydroxyl, peroxyl and other ROS activity within the cell. TSPAN10 k.o cells produced increased ROS levels in comparison to WT cells under basal conditions (Figure 7 – 2 A). Interestingly, when treated with 100μM and 200μM concentrations of H_2O_2 TSPAN10 mutants did not show an increased susceptibility to oxidative stress in comparison to WT (Figures 7 – 2 B & C). These results collaborate our RNAseq data (Chapter 6), which showed a significant difference in heat-shock protein (HSP) expression in TSPAN10 mutant cells in comparison to WT. The production of HSP is a universal nonspecific response of a cell to any form of stress and is one of the most ancient methods of cell protection. The most commonly produced HSP is HSP70, made up of 11 genes in humans, the HSP70 protein is created in response to stress, but also under basal conditions [341]. A deficiency or excess of antioxidants modulates the activation of heat-shock factor and subsequent HSP70 synthesis [342]. At baseline our TSPAN10 k.o cells show increased production of ROS, this could be related to the reduced production of the antioxidant enzyme catalase and the reduced expression of HSPs such as HSP70 (as discussed in Chapter 6).

An imbalance between ROS and antioxidant production can have significant consequences for the cell. RPE cells are the most actively phagocytic cells in the human body, internalising and processing POS from overlying photoreceptors as part of the visual cycle. Phagocytosis is a key role of the RPE that is reduced by increased oxidative stress [343]. The accumulation of partially degraded POS as lipofuscin and its photo-oxidative derivatives in the ageing RPE is a key feature of diseases such as AMD [344]. Such derivatives of POS can accumulate within the lysosome especially under conditions associated with oxidative stress [19, 345]. The lysosome is integral to the RPE's phagocytic capacity and is essential for retinal proteostasis. This is of particular importance to POS phagocytosis, which is reliant on an operational endo-lysosomal system to accommodate the high proteolytic burden exerted on the RPE. We then aimed to understand the impact of TSPAN10 k.o on RPE phagocytosis and the trafficking of POS through the endosomal and lysosomal pathways. It has previously been shown that increased oxidative stress in RPE cells, induced through addition of H_2O_2 leads to the premature trafficking of POS to lysosomes [231]. This was shown using an RPE cell line ARPE19, in which peak trafficking of POS to lysosomes occurred at 24 hrs post POS feed. Interestingly in our hESC-RPE WT cells we saw peak trafficking to lysosomes occurring around 12 hrs, with a reduction in co-localisation at 24 hrs indicating reduced trafficking to the lysosome at this point (Figure 7 – 5). These differences between ARPE19 cells and our hESC-RPE might be explained by the closer semblance of hESC-RPE to native RPE, favouring more efficient phagocytosis as cultures mature [346]. Our results showed premature trafficking of POS to the lysosome in both TSPAN10 k.o clones at 4 and 6 hrs in comparison to WT (Figure 7 – 5). These results were very similar to the response of WT cells treated with H_2O_2, which showed increased trafficking of POS to the lysosome at all time points over 24 hrs in comparison to WT (Figure 7 – 5). POS cargos have been shown to bind to the RPE within approximately 1 - 2 hrs of exposure, they are then engulfed between 4 - 6 hrs and digested within 16 – 20 hrs [347, 348]. During this time course POS cargos are shuttled from early endosomes to late endosomes, lysosomes, and finally autophagosomes, with some degree of flexibility. POS cargos could bypass early and intermediate compartments under conditions of oxidative stress to prematurely co-localise with lysosomes, which could explain the results described here. Rapid trafficking of POS that has bypassed upstream processing events might increase the chances of proteolytically indigestible material accumulating within RPE lysosomes. This process may serve as a potential mechanism for lipofuscin biogenesis, as lipofuscin, once formed, is known to resist degradation and cannot be transported out of the cell through exocytosis [349]. Lipofuscin is known to prevent cellular renewal and promote the misfolding of intracellular proteins by increasing the sensitivity of RPE cells to oxidative stress [350, 351] Notably, the build-up of high molecular weight aggregates within lysosomes and related organelles is a prominent

feature in degenerative conditions such as AMD.[352-354]. Subsequently, we can deduce that k.o of TSPAN10 leads to increased oxidative stress in the RPE and premature trafficking of POS to the lysosome, which may serve as a mechanism for lipofuscin formation and hence increase the likelihood of AMD.

We do not currently understand how TSPAN10 may be influencing the described changes in oxidative stress within the RPE. There are reports of TSPAN10 influencing the trafficking of ADAM10 to the late endosome [113]. Therefore, we hypothesised that if TSPAN10 is also localised to the late endosome it could help to explain the reported results. We saw very high levels of co-localisation of the late endosome marker Rab7 [326] with TSPAN10 in all differentiations of WT hESC-RPE using immunocytochemistry (Figure 7 – 6). The staining pattern of both Rab7 and TSPAN10 was nearly identical. This was not performed for the cell lines A12 and A2 given their lack of TSPAN10 protein. Rab7 is commonly used as a late endosome/phagosome marker and can help to distinguish between intracellular vesicles such as late phagosomes/endosomes vs lysosomes. However, there is evidence to suggest that some lysosomes are also positive for Rab7 [231, 355]. With Rab7 appearing critical for the maintenance of a functional lysosome compartment and the aggregation and fusion of late endocytic structures/lysosomes [355]. Overall, the significant colocalisation of TSPAN10 with Rab7 (89%) suggests that TSPAN10 is localised to the late endosome in RPE cells, where it is therefore able to exert its effects on trafficking of POS cargos and influence the response of the cell to oxidative stress.

7.3.2 Pigmentation

The second phenotype of our hESC-RPE further examined was their pigmentation. The RPE contains three main types of pigment granules: melanin, lipofuscin and melanolipofuscin [50, 356]. Each of the three pigment granules develop at differing time points in human RPE. Lipofuscin, which is significantly associated with diseases such as AMD accumulates with increasing age and melanolipofuscin is seen predominantly in aged RPE [357]. Within this chapter we specifically focused on melanin and melanosomes, the organelle in which melanin is synthesised.

Melanosomes form during a brief period of embryogenesis, by the 14th week of foetal development melanosomes of all maturation stages are seen and melanosome synthesis typically concludes a few weeks later [50, 52]. Melanogenesis in the RPE is comprised of four morphologically distinct melanosomal stages I to IV [358]. Stage I melanosomes, also known as premelanosomes, lack pigment and exhibit characteristic intraluminal striations. During stage II tyrosinase-filled vesicles originating from the Golgi apparatus enter the premelanosome. Stage III is marked by the integration of tyrosinase and other melanogenic

proteins into the melanosomal membrane, which facilitates melanin synthesis. Once the organelle is filled with melanin, it is characterised as a mature stage IV melanosome [359], see Chapter 1, Figure 1 – 4. Following this period of melanogenesis new melanin is formed at a very low level, if at all [360]. Melanosome formation seen during embryogenesis can be replicated in stem-cell derived RPE [50, 361].

Key prerequisites for melanogenesis include the presence of premelanosomes and the synthesis of tyrosinase and other melanogenic proteins. Melanin formation is not possible without tyrosinase [55] a rate limiting enzyme that is only synthesized in postnatal RPE, and not in the adult RPE [52, 335, 360]. In the absence of tyrosinase activity no melanin is formed [52, 360]. Because of the oxidative capabilities of tyrosinase and melanin precursors, along with their tendency to generate radicals and cause oxidative stress, it's essential for them to be isolated within the premelanosome. Interestingly we saw no changes in tyrosinase expression between TSPAN10 k.o and WT hESC-RPE when analysed by both RNAseq and RT-qPCR (Chapter 5, Figure 5 – 6D). However macroscopically it was evident that all k.o cultures were significantly less pigmented than their WT counterparts both during and post-differentiation (Figure 7 – 7). Subsequently, western blotting for tyrosinase was performed to understand if k.o cultures produce similar amounts of tyrosinase protein to WT, despite the equivalent PCR results. Figure 7 – 8 shows an example of a western blot, with a significant reduction in tyrosinase seen in all differentiations of all TSPAN10 k.o cells. Furthermore, when tyrosinase function was examined, we saw a significant reduction in TSPAN10 k.o cells versus WT (Figure 7 – 9). These results could suggest that TSPAN10 interacts with tyrosinase or is crucial for tyrosinase production and/or function. Melanosomes from fair-skinned individuals are known to have low tyrosinase activity due to a more acidic pH, whilst melanosomes from dark- skinned individuals have a more neutral pH and higher tyrosinase activity [362, 363]. Unfortunately, we did not measure the pH of our RPE, but we do know that TSPAN10 k.o cells have significantly reduced tyrosinase activity compared to WT, in addition to being less pigmented. It would be interesting to understand if TSPAN10 k.o affects the pH of RPE at baseline, as this could indicate both an idea of its function and help to explain its influence on pigmentation.

Melanosomes can produce two types of melanin, eumelanin which is photoprotective and pheomelanin which is phototoxic. The synthesis of both types of melanin generates ROS. RPE cells mainly contain the darker pigment eumelanin [364, 365]. Interestingly, regional differences in pigmentation occur within the eye, with darker pigmentation seen at the macula [366]. Melanin synthesis is influenced by ROS which can be generated or derived from multiple intracellular compartments. In the cytoplasm, low levels of H_2O_2 have been shown to regulate the cAMP signalling cascade that activates the transcription of

melanogenic enzymes [367], in addition to increasing the activity of tyrosinase [368]. During the initial steps of melanin synthesis where tyrosinase oxidizes both L-tyrosine to L-DOPA and L-DOPA to L-DOPAquinone, superoxides are generated [369]. Despite this generation of ROS, multiple studies have demonstrated that eumelanin also has ROS-buffering capacity, through scavenging OH^-[370], singlet oxygen [371] and superoxide anions [372]. This coincides with the data depicted in Figure 6 – 2A showing that WT cells, which are more pigmented, have reduced ROS at baseline. Interestingly pigmentation is reported to correlate directly with the activity of catalase in human melanocytes *in vitro* [373]. This aligns with the work discussed in this chapter showing reduced catalase activity in less pigmented k.o cells (Figure 7 – 1).

As previously mentioned, the ageing RPE is severely burdened by oxidative stress and the subsequent production of free radicals [243, 261]. Melanin pigmentation in the RPE plays a direct role in shielding the macula from oxidative harm [374, 375]. Moreover, epidemiological data suggests that individuals with lower levels of pigmentation may be at a heightened risk for diseases related to oxidative stress. For instance, in a prospective cohort study encompassing a diverse range of ethnicities in the United States, Caucasian participants were found to have a fivefold higher likelihood of developing AMD than participants of African descent [376, 377]. Hispanic and Asian participants demonstrated intermediate risk levels. Even after adjusting for established risk factors such as body mass index, hypertension, diabetes, smoking, and alcohol consumption, the observed disparities persisted [376, 377]. Albinism as a risk factor for developing AMD would support this hypothesis, but whether individuals with albinism indeed face a slightly elevated risk remains uncertain. The possible late-onset clinical diagnosis of AMD in albinism patients may go unnoticed since these patients are rare and have a low VA already early in life. If TSPAN10 is involved in the melanin synthesis pathway within the RPE as suggested by our results, this could indicate its involvement in AMD risk.

There is some thought within the academic community that L-DOPA supplementation could alter AMD risk. Oral L-DOPA treatment in Parkinson patients has been shown to reduce the risk of AMD, or delay disease onset [378]. Additionally in a small pilot study, treatment naïve patients with wet AMD were given oral L-DOPA which increased VA and delayed the onset of anti-VEGF injections [379]. It is thought that decreased pigmentation in the RPE may lead to less L-DOPA, and subsequently increased VEGF secretion [380]. Given the proposed role exogenous L-DOPA may have we attempted to rescue the reduced pigmentation in our k.o hESC-RPE through apical addition of L-DOPA (Figure 7 – 16). No changes in pigmentation were seen for WT nor k.o cells over a 28-day period. It could be that the concentrations of L-DOPA selected were too weak to cause an effect, or that the drug was not administered for

a long enough time, or at the wrong time point. Given the effect TSPAN10 k.o has on tyrosinase activity, with respect to the reduced oxidation of L-DOPA to L-DOPAquinone (Figure 7 – 9) it was unlikely for exogenous addition of L-DOPA to have any effect.

A defining feature of the RPE is their pigmentation. Typically, during RPE differentiation cells are selected based on this and further cultured. We did not perform this step as evidence from other studies suggested TSPAN10 may be involved in pigmentation [127-130]. Instead RPE were sorted using FACS for a novel RPE cell surface marker (CD140b) [361] and their pigmentation compared between CD140b positive and negative populations. A significant difference was evident between WT cells, with no difference between FACS sorted cells for A12 and A2, despite a large number of cells expressing CD140b (Figure 7 – 13). This result in addition to the molecular work described in previous chapters detailing expression of RPE markers allows us to rule out the possibility that our cells are less pigmented due to failed differentiations. Ideally this sorting would have occurred as part of the differentiation process, however a sterile FACS machine was only installed on site after a large proportion of this work had been conducted.

But does the amount of pigmentation matter? Many human stem cell-derived cultures are challenged by high amounts of variation, furthermore, hESC-RPE cultures do not always mature with the same speed. Consequently, virtually all RPE differentiation studies use pigmentation as a maturation marker instead of time. This appears to be a reliable benchmark and is easy to use because it is clearly visible. However, even though pigmentation seems to be a good biomarker for RPE development, the level of pigmentation does not reflect the maturation state of hESC-RPE. With regard to their gene expression profile and functional annotation, cells appear to be at a similar developmental stage at both early and late pigmentation stages [381]. Importantly both early and late pigment cells show the expression of well-known RPE markers [381].

To add to the evidence that TSPAN10 is involved in RPE pigmentation ultrastructural analysis of cells was conducted using TEM. Melanosomes in various stages were identified and counted, with a significant difference in the numbers of stage III/IV melanosomes (where melanin synthesis occurs) seen in k.o cells. During Stage III of melanogenesis, the melanogenic enzymes tyrosinase, TYRP1 (tyrosinase-related protein 1) and TYRP2 (tyrosinase-related protein 2), along with ion transport proteins ATP7A (copper-transporting ATPase 1), OCA2 (oculocutaneous albinism II), and SLC45A2 are translocated from the trans-Golgi network to the melanosome membrane. We saw a reduction in tyrosinase protein production in our k.o cells, which could help explain the reduction in stage III and IV melanosomes. Although we did not examine protein production of the other aforementioned

melanogenic enzymes and proteins, our RNAseq data (Chapter 6) demonstrates that they were not called as DEGs. Consequently, we can conclude that the decrease in tyrosinase seen because of TSPAN10 k.o likely leads to a reduction in the maturation of melanosomes and production of melanin. Defects in melanosome biogenesis are associated with retinal disease, and a deficit of melanin pigment in the RPE is associated with aging and AMD. The data displayed corroborate these findings and demonstrate disrupted melanogenesis in TSPAN10 k.o RPE cells.

We also used our TEM data to examine other characteristics of our hESC-RPE. The number of sub-RPE FLS collagen per cell was compared in WT and TSPAN10 k.o mutants. No significant differences were seen. FLS collagen is thought to be a combination of collagen and proteoglycans, formed by depolymerisation of native collagen fibrils [360]. The presence of sub-RPE FLS is generally associated with pathological changes in the extracellular matrix, especially in diseases like AMD, and indicates abnormal remodelling of BrM. In vivo, clumps of FLS collagen are found primarily in the outer collagenous layer or embedded in the basement membrane of the choriocapillaris [382] [383]. FLS collagen is often seen in stem cell derived RPE cells in culture [331]. The presence of FLS collagen can reflect the activity of extracellular matrix production by RPE cells, a feature of differentiated and functional RPE. As RPE cells mature, they often start producing components of the extracellular matrix, including collagen. The presence of FLS collagen in RPE cells in culture may suggest that they are becoming more specialised and taking on some of their normal in vivo functions, such as contributing to the structural integrity of BrM.

We also used our TEM data to examine the height of our hESC-RPE. We saw a significant reduction in the height of our k.o cells in comparison to WT, with WT cells falling within the normal range [332] (10-14μm). Given that both A12 and A2 were shorter than their WT counterparts we can infer that this may be a result of TSPAN10 k.o. Several reasons are hypothesised for this. Firstly, this could be related to the development of the k.o cells, if TSPAN10 interferes with the differentiation process, producing a truncated, immature RPE cell. The maturation of the RPE begins with activation of the tyrosinase promoter, which marks the onset of melanogenesis [384]. Consequently, if the cells are shorter because they are more immature secondary to TSPAN10 k.o this phenotype could relate to their lack of tyrosinase and subsequently melanin.

The height differences reported could also relate to the RPE not typically being a homogenous population. Several groups have described their heterogeneity both *in vivo* and in culture [385-387]. We attempted to control for these differences by using three separate RPE differentiations and analysing 3 cells per population (n=9). Another explanation for this

height difference could be a less dense cell population, allowing cells to spread out, increasing their surface area and subsequently reducing their height. We aimed to prevent this by plating the same number of cells in each condition and ensured that all cultures were treated the same.

There is variability between RPE at the macula and cells in the periphery. Those at the macula have a smaller diameter, a typical height of 12μm and a higher melanin content [388], however cells in the periphery are much bigger with diameters of up to 60μm and varying heights [17]. It could be that TSPAN10 k.o cells have a phenotype more in keeping with peripheral RPE cells. This would also align with the reduced melanin content described.

Finally, this shortened RPE does have some alignment with clinical findings. Chapter 8 describes a clinical study undertaken examining the thickness of the outer retinal layers in healthy adults with AMD risk SNPs, including the risk SNP at *NPLOC4/TSPAN10* rs6565597 [150]. One finding, which was discussed in more detail in Chapter 3 is the thinning of the RPE-BM layer in those individuals carrying rs6565597. This clinical result corroborates the data reported here that TSPAN10 k.o RPE are shorter than their WT counterparts. We know that as the RPE ages the cells at the macula become less dense and less hexagonal, with increased diameters and eccentricity [19, 386]. This likely relates to cell loss, with the remaining cells spreading out to fill the gaps. If TSPAN10 k.o affects RPE morphology and carriers of the SNP rs6565597 have less copies of TSPAN10, then one could infer that this may be a role of this understudied gene and help to explain its part in AMD risk.

8 Further understanding TSPAN10 in the RPE and its interactions

8.1 TSPAN10 and ADAM10

As previously discussed, (Chapter 1, section 1.4) there is a paucity of literature surrounding TSPAN10 and its role in the RPE. TSPAN10 belongs to the C8 tetraspanins all of which are reported to interact with and regulate the function of the transmembrane protease ADAM10. When processed into its mature active form ADAM10 cleaves the extracellular domains of membrane-anchored proteins, processing a number of substrates involved in diverse biological processes. String analysis of TSPAN10 (Chapter 1, Figure 1 – 7) reveals an experimentally confirmed interaction with ADAM10, however on further examination of this work it appears that of all the C8 tetraspanins, the interplay between TSPAN10 and ADAM10 is relatively poor. Recently the crystal structure of the C8 tetraspanin TSPAN15 has been resolved, a supposedly close relative of TSPAN10 [282]. TSPAN15 is known to form a complex with ADAM10 that is active as a protease in the plasma membrane [389] and selectively promotes N-cadherin shedding by ADAM10 [390]. Consequently, we aimed to understand if TSPAN10 k.o affects ADAM10 expression or maturation. Initially the protein structure of TSPAN10 was mapped using AlphaFold2 [391] and the extracellular domain examined for a conserved ADAM10 binding site similar to that seen in TSPAN15 [282]. As shown in Figure 8 – 1, the extracellular domain of TSPAN10 contains two of the conserved amino acids seen in the hypervariable region of the TSPAN15 ectodomain that correspond to the ADAM10 binding site (N166, Y168, H169). N166 is seen at N224 and Y168 at Y226, however H169 is replaced with an F (Phenylalanine) in all other C8 tetraspanins including TSPAN10 (Figure 8 – 1) [392]. Importantly the predicted structures for our TSPAN10 mutants, A12 and A2 do not contain this extracellular domain and therefore do not contain the conserved ADAM10 binding site (Figures 8 – 1 & 8 – 2). Consequently, we aimed to examine the effect this would have on ADAM10 expression.

Initially RT-qPCR was performed for ADAM10 and there were no significant differences in mRNA expression between TSPAN10 k.o cells and WT (Figure 8 – 3). This result was comparable to our RNA seq data (Chapter 6), where ADAM10 was not called as a DEG as there were no differences in ADAM10 mRNA expression between TSPAN10 mutants and WT hESC-RPE. To understand the implications TSPAN10 k.o might have on ADAM10 protein expression western blotting was performed using two different ADAM10 monoclonal antibodies. As shown in Figures 8 – 4 and 8 – 5, there were no obvious differences in ADAM10 protein expression between WT and TSPAN10 mutant hESC-RPE. These lack of differences in ADAM10 expression both at the transcript and protein level were surprising. Subsequently, immunocytochemistry was performed for both ADAM10 and TSPAN10 to look

for co-localisation within the cell (Figure 8 – 6). As shown, ADAM10 appears to mainly localise apically in the RPE, whereas TSPAN10 seems to be cytoplasmic, with no evidence of co-localisation between the two. Interestingly not all cells showed ADAM10 staining. In the WT cultures, the majority of cells had some form of apical staining with a few exceptions, however in the TSPAN10 k.o cells many showed weak staining for ADAM10. The staining pattern also differed between k.o and WT cells. In the k.o lines ADAM10 staining appeared to cover almost the entire apical surface of the cell, whereas in the WT staining was typically seen at the cell borders.

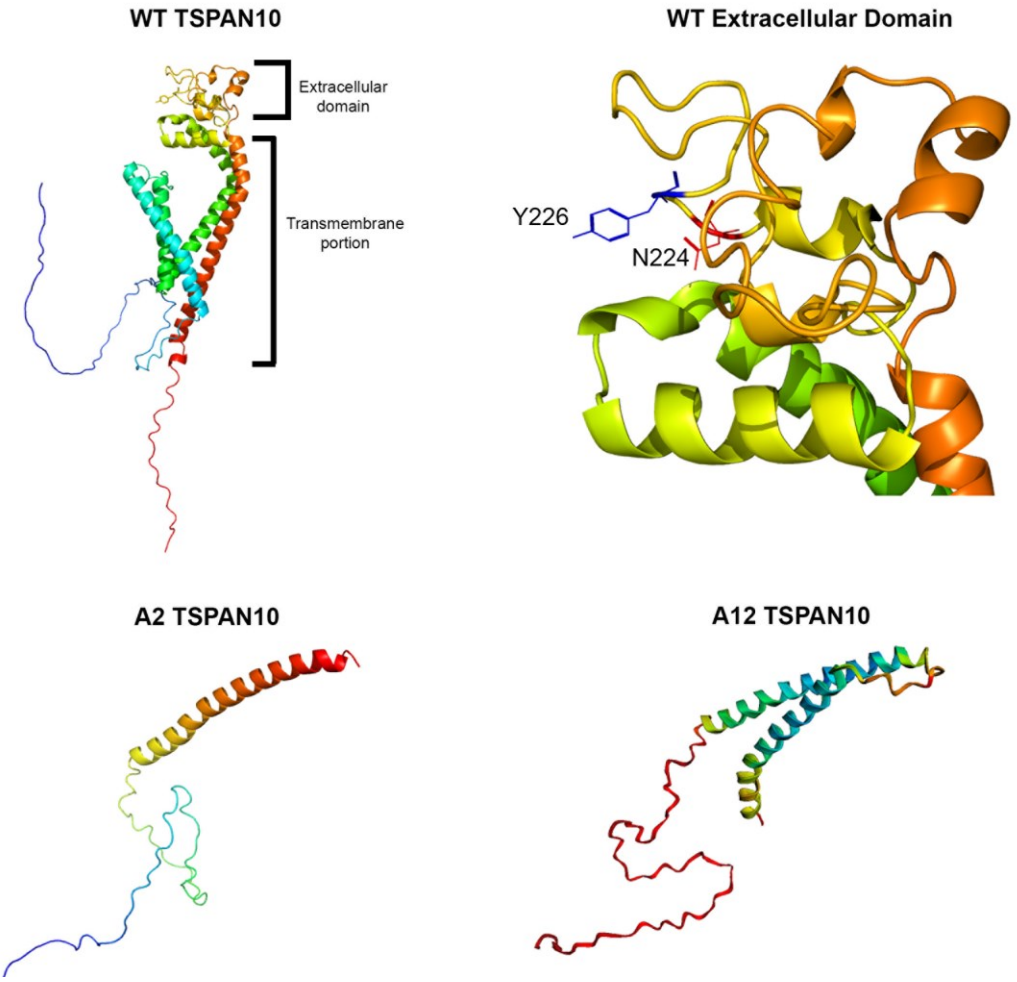

Figure 8-1 Alphaprot generated protein structures of WT TSPAN10 and knockout predicted structures
The crystal structure of WT TSPAN10 is predicted including the extracellular domain where ADAM10 is thought to bind, and the transmembrane portion of WT TSPAN10.
The predicted crystal structures of both A2 and A12 are also shown, neither contain the conserved ADAM10 extracellular binding site.

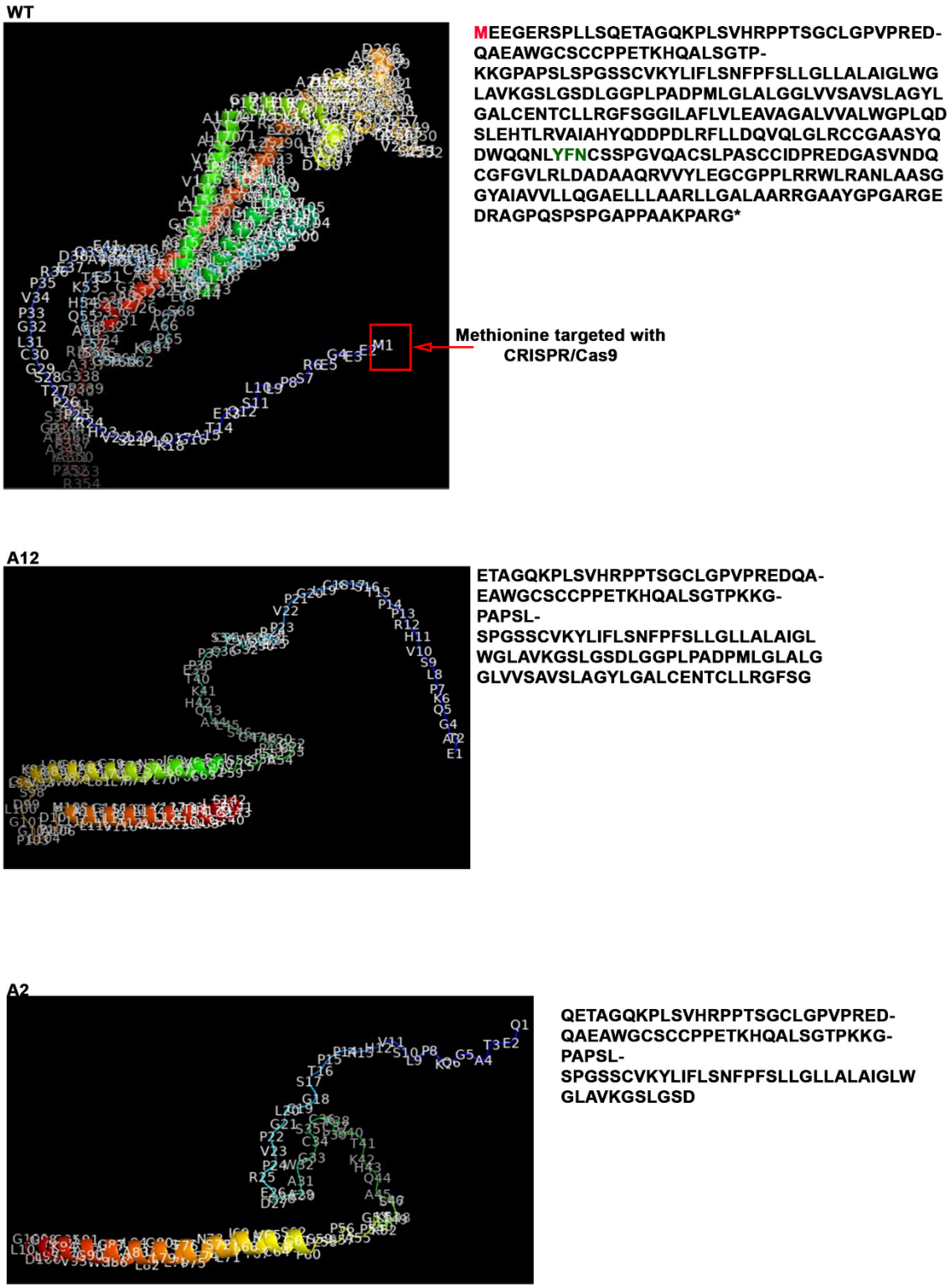

Figure 8-2 Amino acid labelled Alphaprot generated protein structures of WT TSPAN10 and TSPAN10 knockout predicted structures

The crystal structure of WT TSPAN10 is displayed with all amino acid residues labelled, including the start codon methionine (M1) which is labelled in red and the ADAM10 binding domain in green. Predicted protein structures of the TSPAN10 mutant clones A12 and A2 depicted from mRNA sequencing data. All amino acid residues are labelled using standard convention, where the number depicts the order of the sequence and the letter the amino acid. Amino acid sequences are shown in text adjacent to each crystal structure.

As shown, neither A12 nor A2 predicted structures contain the amino acid sequence coded for in TSPAN10 exon 2, including the start codon methionine (M1). Instead A12 starts with E (glutamic acid) and A2 Q (glutamine). Furthermore, neither A12 nor A2 contain the ADAM10 binding domain.

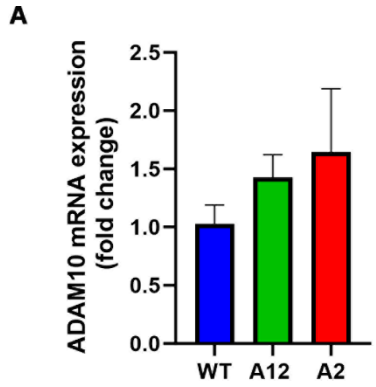

Figure 8-3 RT-qPCR quantification of ADAM10 mRNA expression in WT and TSPAN10 mutant cell lines
A: Normalised ADAM10 mRNA expression relative to mean WT cells. Bars show mean fold-change and error bars depict SEM of three independent experiments and three biological replicates. Statistical analysis One-way ANOVA with Dunnett's correction.

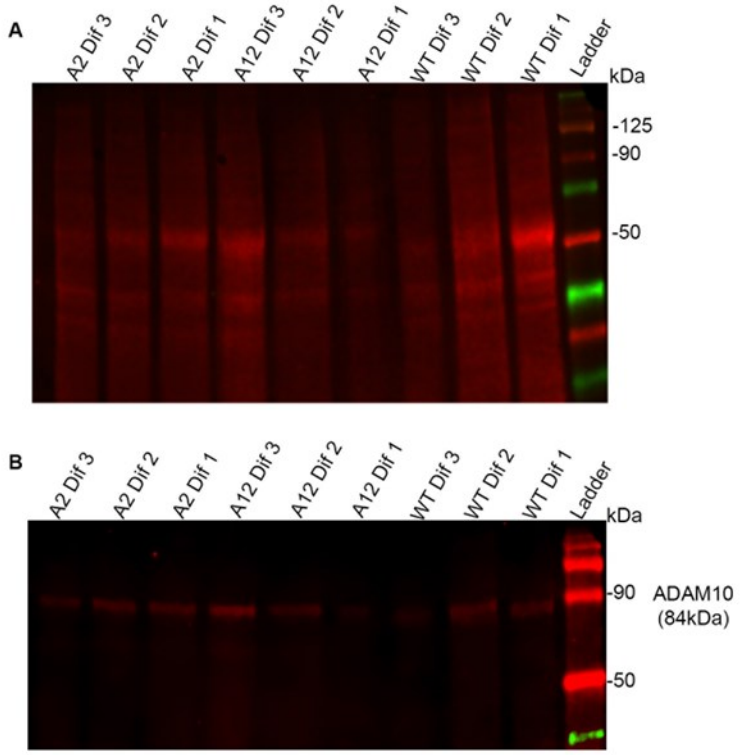

Figure 8-4 Western blot for ADAM10 in WT and TSPAN10 mutant hESC-RPE
A: A total protein stain (Revert 700) was performed as a control to ensure equal loading of lysates.
B: An ADAM10 protein blot using the Abcam monoclonal Ab (84kDa) indicates that ADAM10 protein expression is similar in TSPAN10 k.o cells A12 and A2 in comparison to WT.
N=3 technical repeats performed

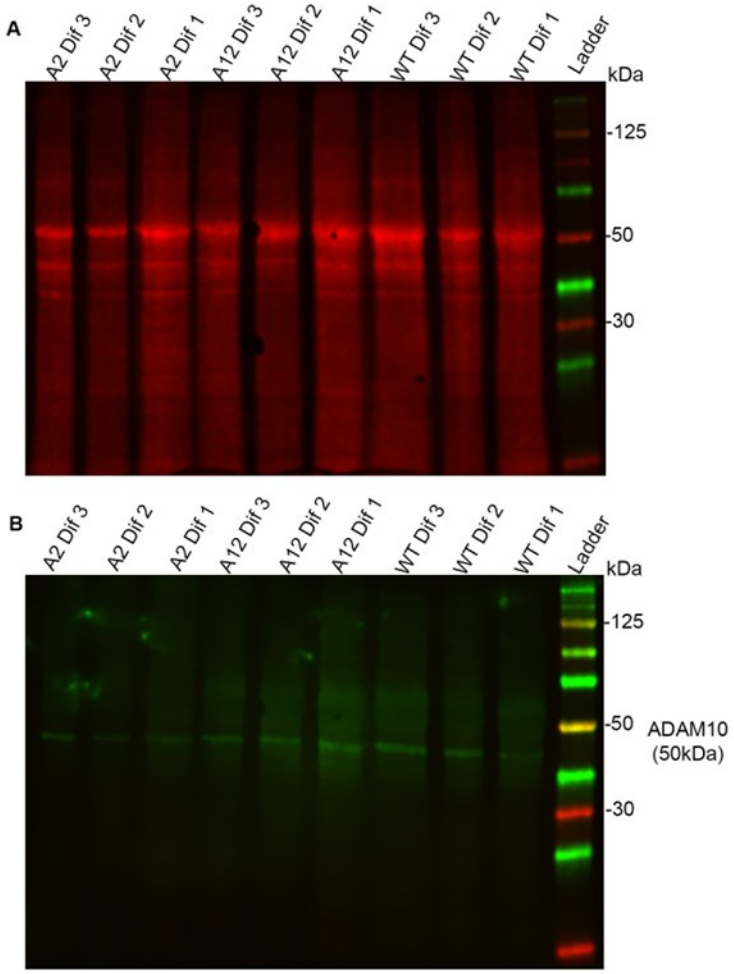

Figure 8-5 Western blot for ADAM10 in WT and TSPAN10 mutant hESC-RPE
A: A total protein stain (Revert 700) was performed as a control to ensure equal loading of lysates.
B: An ADAM10 protein blot using the Proteintech monoclonal Ab (84kDa) indicates that ADAM10 protein expression is similar in TSPAN10 k.o cells A12 and A2 in comparison to WT.
N=3 technical repeats performed

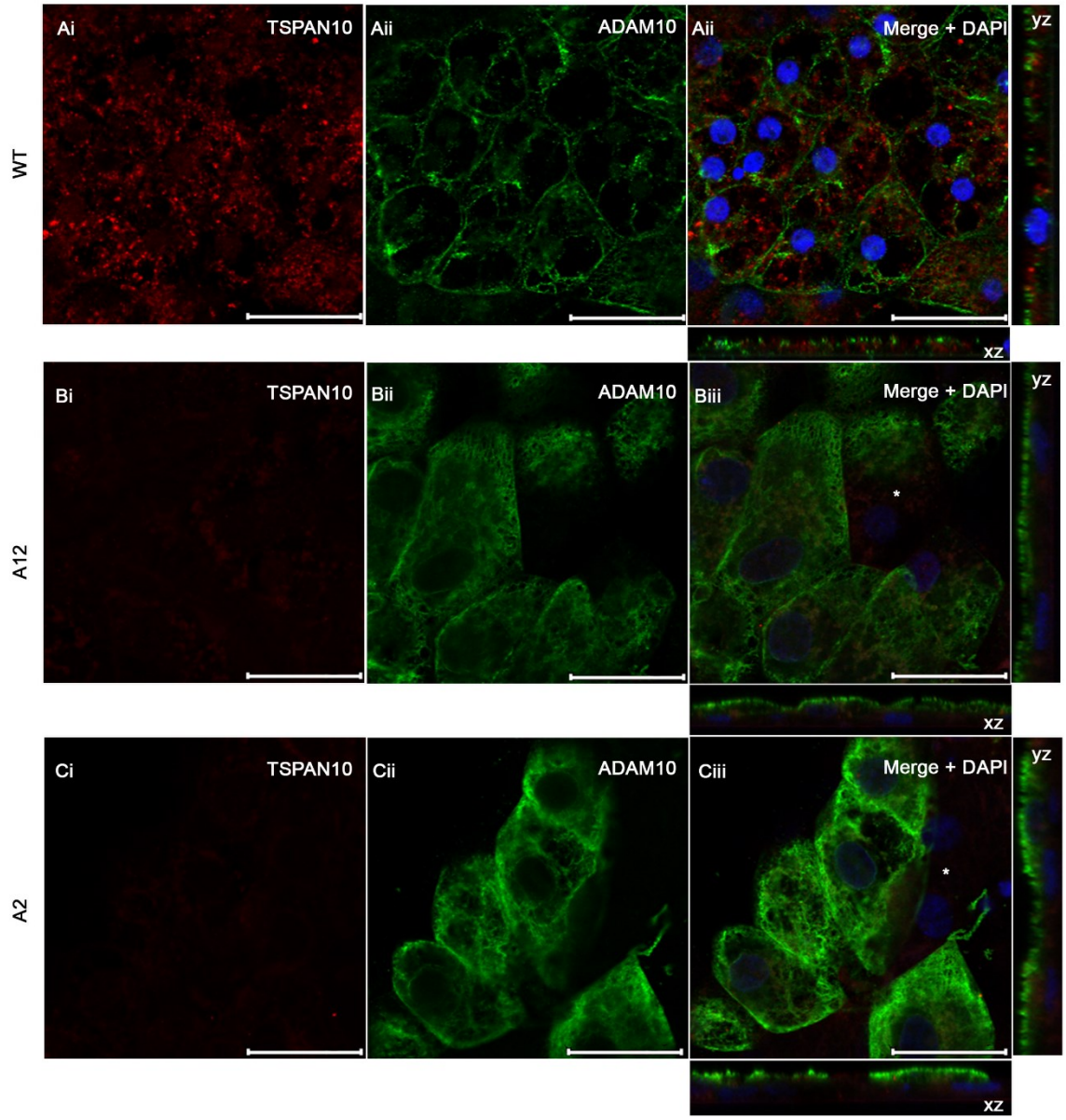

Figure 8-6 Immunocytochemistry for ADAM10 and TSPAN10 co-localisation in hESC-RPE
Confocal z-stack images of WT and TSPAN10 mutant hESC-RPE. ADAM10 (green), TSPAN10 (red) and DAPI (blue)
Ai-Aiii: WT cells express TSPAN10 with a typical punctate staining pattern and cytoplasmic location. ADAM10 staining in a fibrinous, lattice type pattern. It appears to mainly follow cell borders. There is no evidence of colocalization between TSPAN10 & ADAM10. ADAM10 staining appears to be apicolateral in z-section views.
Bi-Biii: A12, ADAM10 staining seen apically in a fibrinous lattice type pattern. Only background staining for TSPAN10 seen. * depicts A12 cells within the same culture with no ADAM10 expression.
Ci-Ciii: A2, ADAM10 staining seen apically in a fibrinous lattice type pattern. Only background staining for TSPAN10 seen. * depicts A2 cells within the same culture with no ADAM10 expression.
Scale bar 25 µm

8.2 TSPAN10 in the developing retina

RNAseq data tells us that *TSPAN10* is expressed in the RPE and melanocytes within the adult eye [120]. Stem cell derived RPE are often described to more closely resemble the foetal RPE rather than the adult. Given that little is known about TSPAN10 especially in the developing retina I aimed to understand where TSPAN10 is expressed in the human foetal retina through immunocytochemistry. 16 weeks foetal eyes were sectioned and stained for the RPE marker BEST-1, the photoreceptor marker rhodopsin and TSPAN10. There was no co-expression of TSPAN10 with rhodopsin, suggesting that at this early stage TSPAN10 is not localised to primitive photoreceptors (Figure 8 – 7). Best-1 staining allowed identification of the foetal RPE, however TSPAN10 staining was very weak (Figure 8 – 8). Disparate weak TSPAN10 staining was seen in the primitive choroid (Figure 8 – 8). Choroidal staining of TSPAN10 could represent melanocytes within the primitive choroid.

To gain a better picture of *TSPAN10* expression during foetal development RNA seq data was used from the openly available data set from the Tang group [393]. Data was available from foetal week 5 – 6, up to week 24 for the RPE and neural retina. Figure 8 – 9 depicts *TSPAN10* expression in both the RPE (pink) and neural retina (green). Each data point represents the average expression levels from at least two embryos. As shown in Figure 8 – 9 *TSPAN10* expression is greater in the RPE than the neural retina. Furthermore, *TSPAN10* expression reduces at 17 weeks, which may explain the immunocytochemistry results in figures 8 – 7, & 8 – 8, where little to no TSPAN10 was seen in the 16-week foetal eye.

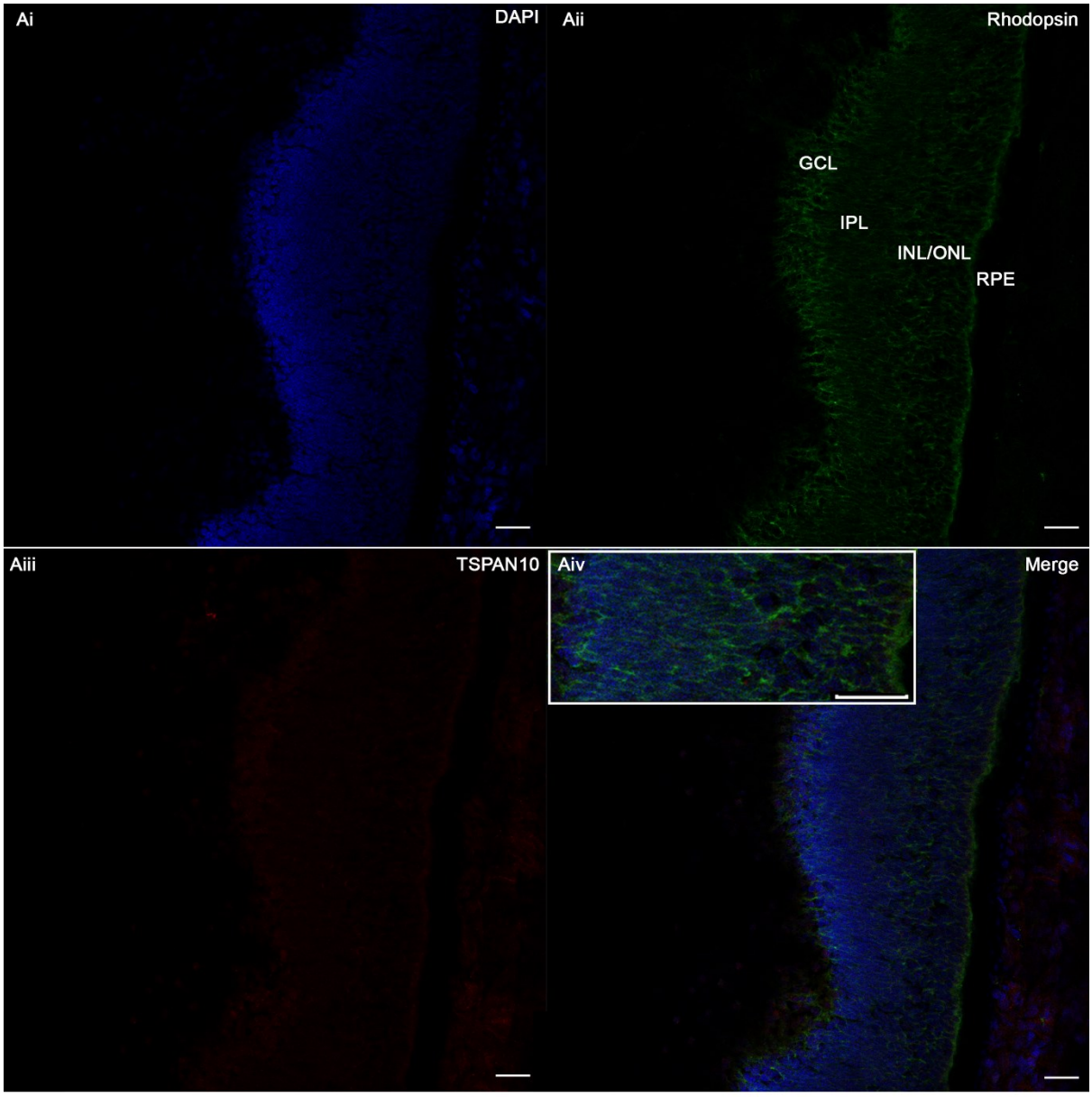

Figure 8-7 Immunocytochemistry for Rhodopsin and TSPAN10 of human foetal retina at 16 weeks gestation.
Human foetal retina at 16 weeks gestation was sectioned and stained for the photoreceptor marker rhodopsin and TSPAN10 to understand the distribution of TSPAN10 during retinal development.
Ai: DAPI nuclear stain (blue)
Aii: Rhodopsin stain (green). Staining of the primitive photoreceptor layer evident. Some staining to the INL/ONL, IPL and GCL.
Aiii: TSPAN10 stain (red). Non-specific weak staining within the primitive choroid, no obvious co-staining of photoreceptors with rhodopsin.
Aiv: Merged image. With magnified section shown.
Scale bar 25μm. Abbreviations: DAPI; 4',6-diamidino-2-phenylindole. RPE, Retinal pigment epithelium. CH, Choroid. GCL, ganglion cell layer. IPL, inner plexiform layer. INL, inner nuclear layer. ONL, outer nuclear layer.

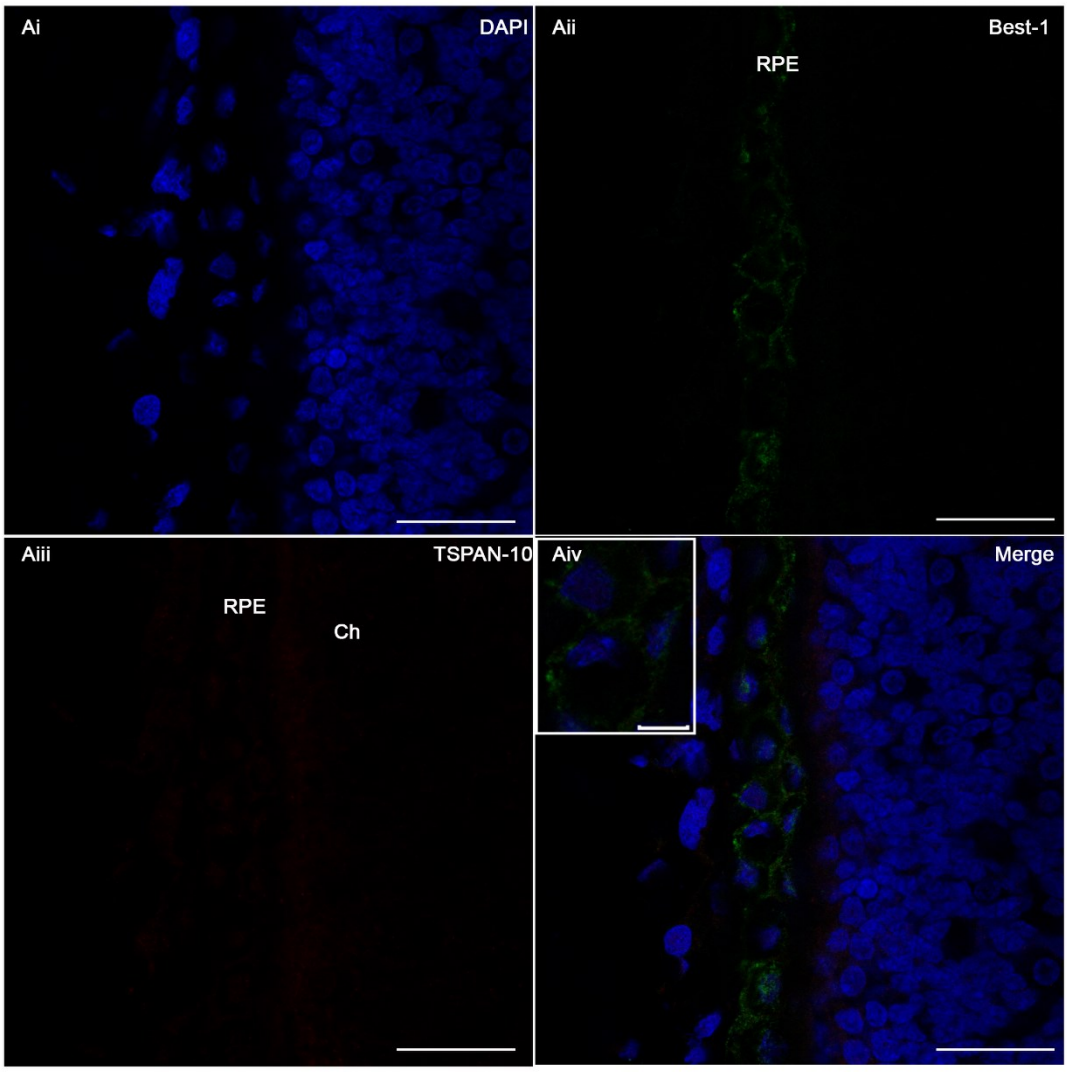

Figure 8-8 Immunocytochemistry for BEST1 and TSPAN10 in human foetal retina at 16 weeks gestation. Human foetal retina at 16 weeks gestation was sectioned and stained for the RPE marker bestrophin (Best-1) and TSPAN10 to understand the distribution of TSPAN10 during retinal development.
Ai: DAPI nuclear stain (blue)
Aii: Best-1 stain (green). Staining of the RPE layer evident.
Aiii: TSPAN10 stain (red). Non-specific weak staining of the primitive choroid, suggestion of some weak staining at the RPE.
Aiv: Merged image. With magnified section showing BEST1 staining pattern. Scale bar in magnified section 5μm Scale bar 25μm. Abbreviations: DAPI; 4',6-diamidino-2-phenylindole. RPE, Retinal pigment epithelium. Ch, Choroid.

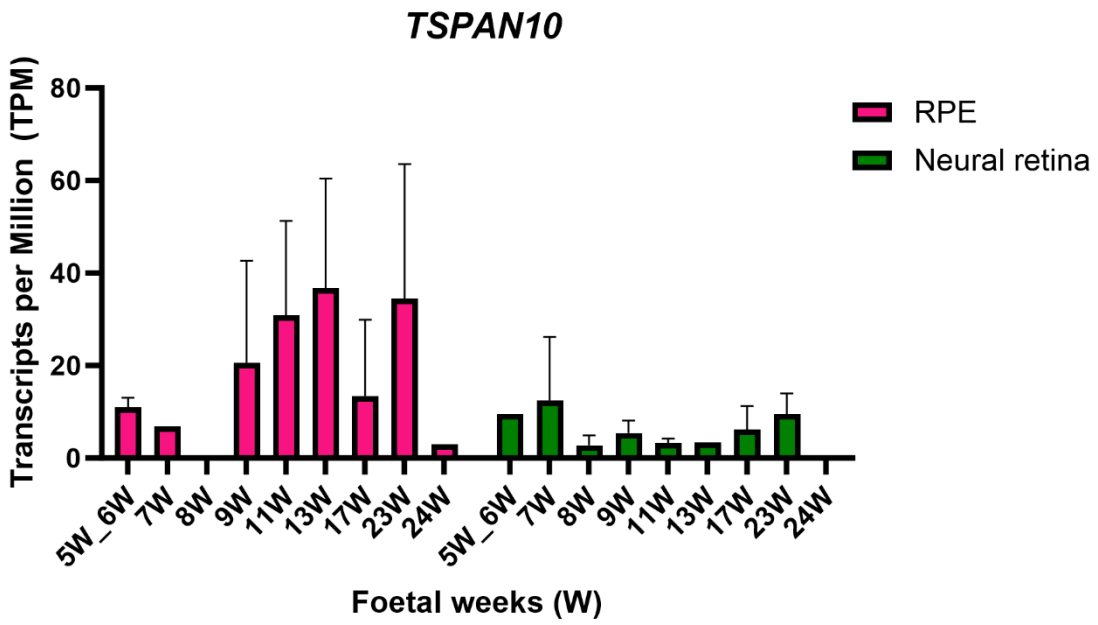

Figure 8-9 TSPAN10 expression in the human foetal eye during development
Bar chart depicts *TSPAN10* mRNA expression in the RPE and neural retina from weeks 5/6 to week 24 of foetal development. The RPE is shown in pink and neural retina in green.
Bars depict mean expression and error bars show SD of at least two embryos.
TSPAN10 expression is greater in the RPE than the neural retina throughout this period of foetal development, peaking at 13 weeks before reducing and then increasing at 23 weeks.
Data from the openly available data set from the Tang group [393]

8.3 Interpretation and Interim Discussion

The work presented in this chapter aims to further probe the pre-existing knowledge of TSPAN10's molecular interactions and its expression in the developing retina.

8.3.1 ADAM10

Despite prior reports of TSPAN10 interacting with ADAM10 we found little evidence for such an interaction. In fact, despite loss of the extracellular domain containing the ADAM10 binding site in our TSPAN10 mutants, there were no differences in ADAM10 mRNA nor protein expression. There were, however, some differences seen with regard to ADAM10 staining. WT cells showed a fibrinous lace like pattern which followed cellular borders in an apical distribution. Both A12 and A2 also showed only apical staining, however this appeared to almost coat the surface of the cell and was continuous. Interestingly some cells showed only weak ADAM10 staining in both the WT and TSPAN10 mutant populations, this may be related to the heterogeneity in cultures, or possibility differences in cell maturity given that ADAM10 expression differs dependent on developmental stage [302]. ADAM10 is one of the principal proteases involved in the activation of the TNF-α and EGF receptor pathways by shedding of the membrane bound proteins pro-TNF-α and EGF receptor ligands [303, 304]. The distribution of ADAM10 in the developing eye has been studied in the chicken where ADAM10 mRNA is expressed in the RPE between embryonic day 5 and 7, however the large amount of dark pigmentation in the RPE makes the expression difficult to visualise at later developmental stages [302]. There is evidence to suggest that a close family member of ADAM10, ADAM9, is involved in the development of the RPE. Loss of ADAM9 function results in disorganisation of RPE cells [394], which in turn interrupts photoreceptor cell functions, leading to speculation that the ADAMs may remodel the extracellular matrix between the RPE and photoreceptor outer segments. If true, this could help to explain the apical distribution of ADAM10 we saw in our RPE. Data from single-cell RNA sequencing reports ADAM10 expression to be distributed throughout the retina [312]. Interestingly a study investigating transcriptomic and proteomic signatures of the RPE in AMD reported increased ADAM10 expression in iPSC-RPE derived from GA donors in comparison to controls [395]. Furthermore, as seen here ADAM10 expression was not apparent in all iPSC-RPE cells [395]. ADAM10 expression has also been shown to increase in older post-mortem eyes, localising mainly in the RPE and drusenoid deposits [396]. ADAM10 has been shown to be basolaterally sorted in polarised Madin-Darby canine kidney epithelial cells [307]. There are no definitive reports of its localisation in the RPE. However as discussed this is likely dependent on its conformation, given that ADAM10 can interact with many partner proteins [306].

Given the multiple roles of ADAM10 it is difficult to hypothesise why we saw subtle differences in the staining pattern. One explanation could be competition with other C8 tetraspanins. TspanC8 tetraspanins have a different impact on the cleavage of various ADAM10 substrates [397]. Removing TSPAN10 from the competition in our k.o cultures could allow other tetraspanins to regulate ADAM10's substrate selectivity. Interestingly, by using ADAM10 deletion mutants and ADAM10 chimeras with ADAM17, the most closely related ADAM to ADAM10, Noy et al have shown that TspanC8 engage ADAM10 in subtly different ways, leading the authors to suggest that they might direct substrate specificity by constraining ADAM10 into defined conformations [398].

Further evidence for this tetraspanin compensation comes from Drosophila where depletion of one or two of the Drosophila TspanC8 produced only mild defects, however depletion of all three significantly impacted Notch regulated developmental processes [113]. In relation to ADAM10 this has been shown in prostate epithelial cells, where ablation of Tspan15 leads to increased expression of Tspan5, and subsequently promotion of its association with ADAM10 and its exit from the ER [397]. Whereas over expression of Tspan15 strongly diminishes the association of Tspan5 with ADAM10 [397]. The simplest explanation for these results is that the competition between these tetraspanins for the association with ADAM10 may yield a pool of free tetraspanins which is retained in the ER in the case of Tspan5 or is quickly endocytosed and eliminated in the case of Tspan15. Our RNAseq data (Chapter 6) did not find a significant change in any of the other TspanC8 after Bonferroni correction in our k.o lines, however there were three tetraspanins (TSPAN18, TSPAN8 and TSPAN32) with increased expression that reached the minimum Log2fold change threshold to be considered as differentially expressed (Figure 6 – 3).

Overall, our experiments did not find convincing evidence for TSPAN10 interacting with ADAM10, however any such interaction could be highly transient, or occur at a specific time point which we have not captured.

8.3.2 TSPAN10 in the developing retina

TSPAN10 staining in the developing retina was not convincing at 16 weeks gestation. Previously published works have shown TSPAN10 staining in the adult retina only [102]. However, we did see good expression of both the RPE marker Best-1 and the photoreceptor marker Rhodopsin. Our results therefore suggest that the TSPAN10 protein is not expressed at this developmental stage.

To help understand TSPAN10 expression throughout foetal development I used freely available RNA seq data from foetal eyes at varying stages of gestation (week 5/6 to week 24) [393]. The data used was bulk RNA sequencing data from RPE and neural retina cells.

As depicted in Figure 8 – 9 *TSPAN10* expression is greater in the RPE than the neural retina throughout development. Expression appears to gradually increase up to 13 weeks in the RPE before reducing and then increasing again at 23 weeks. Unfortunately, we do not have data between 13 and 17 weeks, nor 17 and 23 weeks. The reduction in expression at 17 weeks aligns with the immunocytochemistry data where TSPAN10 expression was very weak, almost undetectable in 16-week foetal eyes. The foetal expression data helps to confirm that TSPAN10 is largely expressed in the RPE. In the human foetal eye the RPE layer begins to differentiate around embryonic day 30, with pigment particles found in RPE cells at embryonic day 35 [50]. The generation of new melanosomes in the human RPE is thought to be complete by around week 14 [399], with a mixture of all four stages of melanosomes seen by weeks 8 – 14 [400]. Around 27 weeks gestation all melanosomes are melanized and matured to stage IV [400]. We saw peak TSPAN10 expression at week 13, this aligns with the generation of new melanosomes in the RPE, which is reported to stop at approximately week 14. However, when compared to the expression pattern of tyrosinase (Appendix D, Figure 13 – 18) there are no obvious similarities, furthermore, TYR expression is nearly 5-fold greater than TSPAN10 in the developing RPE at the stages examined. Given the reduced pigmentation seen in the TSPAN10 mutants in this thesis, this RNA expression pattern adds to the idea that TSPAN10 is involved in pigmentation and more specifically melanosome formation.

9 Discussion

9.1 Overview of key results

This projects main aim was to probe the role of TSPAN10 in the cell, and in particular the RPE to help gain some insight into the possible role TSPAN10 may play in AMD.

AMD is a debilitating, blinding disease affecting a large proportion of adults in the western world. Although a complex disease with multiple risk factors, genetics are thought to play a large contributary role in disease susceptibility. Many genetic loci have been determined to be associated with AMD, however a large proportion are either not expressed in the RPE or have their main effects elsewhere in the body. TSPAN10 was selected in this study as a target, given that it is mainly localised to the RPE and therefore *in vitro* RPE cell models will give us some understanding of the role TSPAN10 has in the retina.

The project was subdivided into several aims, with 5a and 5b emerging after an initial body of work had been undertaken. They were as follows:

1: To compare the thickness of outer retinal layers in UK Biobank participants with and without AMD risk SNPs in varying combinations

2: To generate biallelic indel mutations in *TSPAN10* resulting in gene k.o and subsequent absence of protein expression in the RPE.

3: To identify a phenotype associated with k.o of *TSPAN10*.

4: To analyse the transcriptomic profile of TSPAN10 k.o RPE in comparison to WT.

5a: To identify if TSPAN10 k.o RPE are more susceptible to oxidative stress than WT.

5b: To examine differences in melanin synthesis between TSPAN10 k.o and WT cells.

6a: To examine the effect of TSPAN10 k.o on the matrix metalloprotease ADAM10.

6b: To localise TSPAN10 in the human foetal retina.

The aforementioned aims were explored in Chapters 3 – 8. Discussions will not be repeated, but the content and main conclusions of these chapters will be summarised with regards to their respective aims.

The major focus of Chapter 3 was to align AMD risk SNPs with changes in outer retinal layer thickness *in vivo*. We saw significant thinning of the photoreceptor layer and RPE-BM with the presence of AMD risk SNPs. Interestingly the rs6565597 SNP at *NPLOC4/TSPAN10*

was very significantly associated with RPE-BM thinning, helping to emphasise the role TSPAN10 has in the RPE and align with the TEM data presented in Chapter 7. rs6565597

My first objective was to k.o the functional TSPAN10 protein, presented in Chapter 4. An extensive literature search suggests that this has not been achieved before and there are currently no published works investigating the molecular role of TSPAN10 in the RPE. Knocking-out the functional protein and assessing the cellular phenotype highlights if TSPAN10 is crucial to basic RPE functions. Furthermore, by differentiating hESCs to RPE the role TSPAN10 has in RPE development, may become evident. There were several options to k.o the TSPAN10 protein, one of which was introducing a faulty gene into a cell line, such as ARPE-19 or primary RPE through a vector such as with lentiviral transfection. This approach was not chosen given that ARPE-19 do not fully demonstrate a normal RPE phenotype, and primary RPE are both difficult to acquire and only survive in culture for a limited number of passages (see Chapter 1, section 1.5.2). Furthermore, use of a cell line does not ensure a clonal population where all cells contain the select genetic mutant. CRISPR/Cas9 gene editing was chosen and employed to ablate TSPAN10 gene function in hESCs that were then differentiated into RPE cells, more details regarding CRISPR/Cas9 can be found in Chapter 1, section 1.6. hESCs were used as they provide a uniform genetic background, which is not possible with patient samples and hiPSCs. Furthermore, they have a high proliferation rate allowing colonies to readily form from single cells, thereby ensuring clonal populations. We chose to use a robust embryonic stem cell line and differentiate these cells into RPE, increasing the likelihood that the hESC-RPE cells would have both a normal karyotype and be stable in culture.

The first key contribution of this project was a set of clonal TSPAN10$^{-/-}$ hESCs for the study of TSPAN10 function. Biallelic indel mutations in TSPAN10 always resulted in k.o at the protein level, due to absence of TSPAN10 protein, but did not result in transcript instability. Given that the indels in each clone are different, the subsequent short transcripts produced also differed between clones. Selected clones were karyotyped as CRISPR can induce detrimental chromosomal rearrangements [276]. Diploid cell lines which did not express TSPAN10 protein were chosen for phenotypic studies.

A further output from this project was the discovery that TSPAN10 is alternatively spliced in the RPE (Chapter 4, section 4.4). Our data suggests that TSPAN10 is alternatively spliced at exon 3 where there is an alternative ATG, producing a short transcript. This transcript is not reported on Ensembl or any other genome browser website. If there is alternative splicing in TSPAN10, then there is the possibility that a transcript will be produced in the TSPAN10 k.o mutants, that does not undergo NMD. We believe this is the most likely explanation for our

results in Chapter 4. Despite this alternate splicing we did not detect any TSPAN10 protein in our samples (Chapter 4, sections 4.3.2 & 4.4).

In this project hESC-RPE have been successfully produced via directed differentiation and TSPAN10 k.o cell clones produced. hESC-derived RPE have been produced by many groups over the last decade and there are now several working protocols to differentiate cells [7] [8]. Directed differentiation was chosen as this is reported to be both highly efficient and produces a relatively pure population of RPE. Three differentiations for A2, A12 and WT were generated approximately one week apart to allow both a robust statistical analysis and for potential differentiation failure. Differentiations can fail for many reasons including cell plating density, passage number of initial stem cell populations, purity of stem cell populations, the quality of reagents used and the handling of cells. The successful differentiation of hESC to RPE as confirmed in Chapter 5 can be seen as another outcome of this thesis.

To ensure purity of RPE cell sorting was considered during the differentiation process. As discussed in Chapter 7 there are two main methods of cell sorting, magnetic cell separation beads (MACS) and fluorescence activated cell sorting (FACS). CD140b is reported to be a selective cell surface marker for RPE [361], however there are currently no magnetic beads available for this marker, therefore this approach was not taken. FACS was also considered, unfortunately at the time cells were differentiated there was not a sterile FACS machine available for use in our facility. Cells were cultured without antimicrobials therefore the risk of contamination was too high, especially given the time and expenditure involved in producing the hESC-RPE. Of note, cell sorting is not routinely performed in many published stem-cell derived RPE studies.

Chapter 5 examined the phenotype of TSPAN10 mutant and WT hESC-RPE. Like all epithelial cells, RPE are typified by apical-basal polarity. Tight junction proteins play an important role in the establishment and maintenance of this polarity [23], controlling paracellular permeability across the epithelium, and acting as a physical barrier to maintain distinct apical and basolateral membrane compositions [23]. The functional integrity of these tight-junction complexes was examined in Chapter 5, section 5.3 through TEER, which is a measure of paracellular ion movement. Interestingly all differentiations of both TSPAN10 k.o mutants showed an increased TEER relative to WT. This suggests that TSPAN10 k.o is somehow increasing the integrity of tight junctions in hESC-RPE. There are several reasons this could be happening, the first being production of a truncated TSPAN10 protein, which is transported to the cellular tight junctions or cell membrane reducing paracellular permeability. However, Chapter 4, section 4.4.2 discredits this possibility. The second is that

TSPAN10 k.o causes up-regulation of another gene involved in tight junction formation or maintenance to compensate for the loss of TSPAN10. Interestingly *claudin-19* was up-regulated in A12 in comparison to WT (log2 fold change 0.86, p_{adj} =0.03), however this fold change did not meet the threshold for *claudin-19* to be called as a DEG. Furthermore, this was not seen in the A2 mutant and therefore is unlikely to explain the increased TEER seen. Other genes involved in tight junction formation and or maintenance were examined, however no significant changes were seen common to both TSPAN10 mutants. The transcriptomic analysis discussed in Chapter 6 did however show enrichment of extracellular matrix and collagen pathways for both A12 and A2. Collagen is an essential component of the RPE's extracellular matrix and basement membrane, particularly in BrM, which is largely composed of Type IV collagen. It provides structural support, influences cell behaviour, and plays a critical role in maintaining the health and function of the RPE. Changes in collagen composition and structure can impact RPE function and are implicated in age-related retinal diseases, such as AMD. In the context of TEER positive enrichment of collagen pathways, including collagen synthesis and formation in the TSPAN10 mutants could help to explain the described TEER differences. This may be through tight junction formation and stability as a result of a collagen rich extracellular matrix, interaction of collagen with integrins to promote tight junction formation, and influences on cell adhesion [401]. A further consideration when using TEER is that measurements often underestimate the resistance due to tight junctions. TEER is used to estimate the resistance of the pore pathway, for solutes to cross the strands of tight junctions, however, it is actually an amalgamation of the paracellular resistance and the plasma membrane resistances [14]. Consequently, only when the plasma membrane resistance is much higher than the resistance of the tight junctions is the pore pathway actually measured. A further reason for TEER underestimation is that the unit of $\Omega \times cm^2$, is based on the area of the plasma membrane, but the area used is actually that of the transwell filter. RPE cells typically have varying plasma membranes with some cultures showing few microvilli and basal infoldings, whilst other cultures have extensive elaborations of the plasma membrane. The data in Chapter 7, section 7.2.2 shows the TEM evaluation of the RPE cultures presented in this thesis, with WT cells being significantly taller than TSPAN10 mutants, which could result in an increased plasma membrane area. Such an underestimation of plasma membrane area in the WT may account for the differences in TEER seen.

Chapter 6 of this thesis outlines the results of transcriptomic analysis of WT hESC-RPE in comparison to the TSPAN10 k.o mutant clones A12 and A2. There were many DEGs common to both A12 and A2, and therefore inferred to be caused by TSPAN10 k.o. The examination of gene sets showed enrichment of the GO molecular function gene set

'misfolded protein binding' in both A12 and A2 in comparison to WT. Chronic light exposure and oxidative stress within the RPE is known to induce protein misfolding. Healthy RPE comprise intracellular protein quality control mechanisms to repair and or remove misfolded proteins from the cytoplasm. Several retinal diseases, including AMD, show a reduction in the RPE's ability to effectively clear intracellular proteins. For example, lipofuscin induced oxidative stress in the RPE has been associated with an increase in the number of intracellular misfolded proteins [402]. This results in the accumulation of waste material both inside and adjacent to the RPE monolayer. We saw changes in the processing of POS to the lysosome in our TSPAN10 mutants (Chapter 7, section 7.1.3), in line with those changes seen under oxidative stress (Chapter 7, section 7.1.3). When the GO term misfolded protein binding was examined, the main genes driving this change were heat shock proteins (HSPs). The HSP70 (Heat Shock Protein 70) family is a group of four highly conserved proteins that play crucial roles in protein folding, protection against stress, and protein homeostasis. The HSP70 proteins are encoded by the closely linked, stress-inducible and intronless genes, *HSPA1A* and *HSPA1B* [403]. *HSPA1A* was called as a DEG when both the A12 and A2 datasets were combined (Chapter 6, Table 6 – 3), with reduced expression seen in the TSPAN10 k.o clones in comparison to WT. HSPs form an essential partnership with proteasomes and lysosomes in the chaperone mediated autophagy process [404]. The HSP70 family is present in lysosomal fractions of RPE cells [329] and may affect the permeabilization of lysosomes [405]. In Chapter 7 we saw altered processing of POS through the lysosome in TSPAN10 k.o cells. Currently we are not able to determine exactly how/if TSPAN10 interacts with heat shock proteins, nor how it alters POS processing through the lysosome. However, these results hint at a theoretical mechanism for TSPAN10 in AMD risk linking together 1) increased oxidative stress in the cell leading to 2) the build-up of misfolded and damaged proteins in the cytoplasm, which in turn 3) results in cell damage.

Chapter 7 explores the two phenotypes identified as a consequence of TSPAN10 k.o; increased oxidative stress, and reduced pigmentation. We saw significantly reduced catalase production and activity in TSPAN10 mutant RPE, translating into increased ROS production at baseline and localization of POS to the lysosome equivalent to cells treated with hydrogen peroxide. Interestingly, this examination of POS trafficking helped localize TSPAN10 to the late endosome in the cell. Both TSPAN10 mutants were significantly less pigmented than WT cells, with reduced expression and activity of tyrosinase. Cell sorting of cultures for the RPE specific cell marker CD140b did not increase pigmentation of TSPAN10 mutants, however it did for WT cells. This result helped to solidify that it was likely the loss of TSPAN10 causing changes in pigmentation. TEM analysis of cells showed reductions in melanosome numbers in TSPAN10 mutants, in addition to shortened cells in comparison to

WT. Previous studies have shown TSPAN10 to be highly correlated with genes involved in ion transport and vesicle trafficking through co-expression analyses in RNA-seq data [102]. Interestingly vesicle trafficking is key for melanin synthesis, suggesting a potential role for TSPAN10 in the cell and possibly explaining its role in AMD susceptibility. Understanding where in the pigmentation pathway TSPAN10 has an effect is a key next step.

Chapter 8 suggests that TSPAN10 does not interact with ADAM10 in the RPE, contrary to the small body of literature available on TSPAN10's partner proteins. A preliminary study also examined TSPAN10 during RPE and neural retina development with TSPAN10 expression gradually increasing and peaking at 13 weeks in the RPE, aligning with melanin synthesis and melanosome generation [50].

A number of phenotypes relating to the characteristics of cells appeared to vary in a manner reciprocal to the level of *TSPAN10* transcript expressed by the cell line. Varying features between the two k.o clones are displayed in Table 9 – 1. The A12 clone was seen to express more *TSPAN10* transcript than A2 (Figure 4 – 21). For example, A12 secretion of VEGF was relatively similar to that seen by WT cells, whereas for A2 there was no apical/basal polarity for VEGF secretion (Figure 5 – 7). The A12 clone macroscopically and microscopically (as seen on TEM) were more pigmented than A2 (Figures 7 – 10, 7 – 11, 7 – 12). Furthermore, the A12 clone had increased tyrosinase activity in comparison to A2 (Figure 7 – 9). A12 RPE cells were taller than A2 cells (Figure 7 – 12). A12 cells had more *CAT* enzyme than A2 (Figure 7 – 1) and consequently A2 cells produced more ROS at baseline than A12 (Figure 7 – 2). When all the results are re-examined it is clear that A2 appears to be a more severe phenotype than A12, as outlined in Table 9-1. This pattern is evocative of that underlying a proposed mechanism of genetic compensation that has been documented in zebrafish and cell lines, which ameliorates phenotypic severity in k.o (but not knockdown) models by upregulation of compensating genes [406-408]. Compensating genes described thus far have been paralogues or have otherwise shared sequence homology with the faulty gene. According to one suggested mechanism, the response is elicited by the remnants of mRNAs that have undergone NMD, which are proposed to bind to homologous genes and instigate their upregulation [407]. This notion of phenotype severity is interesting when we align it with the human data showing individuals with the rs6565597 SNP for AMD risk have reduced copy numbers of *TSPAN10* [102].

Table 9-1 Contrasting features of TSPAN10 knock out clones A12 and A2

Feature	A12	A2
TSPAN10 transcript expression (RT-qPCR)	Mean ΔΔCq 4.08 ± 1.85	Mean ΔΔCq 1.35 ± 0.64
TSPAN10 transcript size (RT-PCR)	500bp product	400bp product
TSPAN10 transcript expression vs WT (RNAseq)	Log2 fold-change -1.25 (p_{adj}= 5.63 x 10^{-8})	Log2 fold-change -2.24 (p_{adj}= 3.20 x 10^{-20}),
VEGF secretion apical:basal	1.21:2.53 ng/ml	3.10:3.24 ng/ml
PEDF secretion apical:basal	9.49:2.46 µg/ml	7.19:2.02 µg/ml
TEER (Ωcm^2)	304.88 Ωcm^2	306.26 Ωcm^2
NaK+ATPase expression	Apico-lateral	Apico-lateral
CD140b expression (% of total)	65.9%	60.2%
Mature melanosome numbers per cell	5.78	3.88
Cell height (µm)	7.99	5.80
Dopa-oxidase assay absorbance at 180mins as a % of WT activity	47.1%	41.6%
Number of differentially expressed genes	489	152
Gene set enrichment	30 positively enriched GO terms. 1 negatively enriched GO term	4 negatively enriched GO terms.
ROS production at baseline at 180 mins (relative ROS production)	2382	2830
Catalase activity (nmol/ml/min)	8.44 nmol/ml/min	4.47 nmol/ml/min
Phagocytic ability, ratio internal:total POS	0.46	0.43
Processing of POS Cargos vs WT (Lamp1 co-localisation)	Significantly different at 4, 6 and 24 hrs. No difference at 12 hrs	Significantly different at all time points (4,6,12 & 24 hrs)

The rs6565597 SNP at *NPLOC4-TSPAN10* is an intergenic SNP, predicted to cause a missense mutation with a substitution of C to T. It was originally reported to have an Odds Ratio of 1.13 [71] for advanced AMD, which has since been shown to increase to 1.46 in those aged 90 years and older [131]. eQTL data revealed rs6565597 to be associated with expression of *TSPAN10*, with presence of hetero or homozygosity for the SNP reducing expression of *TSPAN10* [102]. eQTL contribute to understanding causality by identifying genetic variants associated with gene expression levels. If the eQTL variant influences the phenotype only through gene expression, this supports a causal role of gene expression. Colocalization tests evaluate whether the same genetic variant is associated with both gene expression (eQTL) and a trait or disease in the same region, in this case AMD. If there is a high probability that the same variant affects both expression and the trait, this supports a causal relationship. Colocalization strengthens the case that the genetic effect on disease may act through modulation of gene expression, rather than through a different mechanism. For rs6565597 at *TSPAN10* colocolization of eQTL data and the AMD GWAS data [71] suggest that genetic variation driving decreased expression of TSPAN10 is causal for an increased risk of AMD (colocalization probability 0.96) [102]. This causal association with gene expression influenced our decision to knock-out *TSPAN10*.

Aside from its association with AMD little else is known about this SNP. We have shown a significant association of hetero or homozygosity for rs6565597 with outer retinal thickness, specifically a reduction in ISOS-RPE and RPE-BM thickness (Chapter 3). The results throughout this thesis are in agreement with the idea that reduced expression of *TSPAN10* is causal for increased AMD risk. Initially we saw reduced cell polarity (VEGF secretion and NaK^{+}ATPase expression) and reduced cell height with TSPAN10 k.o. With reduced pigmentation and mature melanosomes and increased oxidative stress associated with TSPAN10 k.o. This is all in keeping with TSPAN10 expression being causally linked with AMD risk, as we know in AMD cells become depigmented [409], show increased levels of oxidative stress [58] and in end stage disease there is epithelial to mesenchymal transition which is associated with decreased polarisation and reduced cell height [410].

9.2 Interplay between pigmentation and oxidative stress

In humans there is an inverse relationship between RPE lipofuscin concentration and RPE melanin concentration [153]. Lipofuscin is a pigment that accumulates in RPE cells as a by-product of the phagocytosis of POS. Lipofuscin accumulation is both a marker and a consequence of oxidative stress. Excess accumulation of lipofuscin leads to cellular dysfunction, especially in post-mitotic cells such as the RPE. This known interplay between oxidative stress, melanin and lipofuscin helps us speculate the role of TSPAN10 in the RPE

and the phenotypes seen here. TSPAN10 appears to be localised to the late endosome, shown through its colocalization with Rab7 (Chapter 7, Figure 7 – 6). Interestingly Rab7 also associates with early and intermediate stage melanosomes [411], regulating the transport of immature melanosomes in melanocytes, and more specifically the transport of both tyrosinase and tyrosinase-related protein 1 from the late-endosome to the melanosome [412, 413]. TSPAN10 k.o results in reduced tyrosinase protein production and activity (Chapter 7, Figures 7 – 8 & 7 – 9), however there is no obvious correlation between *TSPAN10* and *TYR* mRNA expression in the foetal retina (Chapter 8), and TSPAN10 k.o does not affect *TYR* mRNA expression (Chapter 7). If TSPAN10 interacts with the tyrosinase protein or perhaps Rab7 in the late endosome acting as some sort of molecular switch this could influence the transport of tyrosinase from the late endosome to the melanosome. One of the most well-studied tetraspanins in the context of pigmentation is CD63. It is involved in the formation and maturation of melanosomes. CD63 is also a marker of late endosomes and lysosomes and helps in the proper sorting and functioning of enzymes such as tyrosinase, which is critical for melanin production. These functions of CD63 in the context of pigmentation help to propose potential ways in which TSPAN10 is involved. However, although CD63 belongs to the broader tetraspanin family, it is not specifically a C8 tetraspanin like TSPAN10.

Melanogenic enzymes, including tyrosinase, are generally thought to be transported to melanosomes via endosomes, and several gene products responsible for genetic pigmentation disorders, e.g., BLOC complexes and certain Rabs, are actually involved in endosomal transport [57, 414-416]. However, the precise roles of these gene products in each of the tyrosinase transport events (e.g., ER-to-Golgi transport, transport from the Golgi, and endosomal transport) are not fully understood, and somewhat conflicting results have been reported. Given the endosomal location of TSPAN10, the reduced tyrosinase production in TSPAN10 k.o cells and the significant reduction/absence of mature melanosomes in TSPAN10 k.o cells this may suggest TSPAN10 is involved in the transport of tyrosinase, specifically the endosomal transport, however this is highly speculative and needs experimental verification.

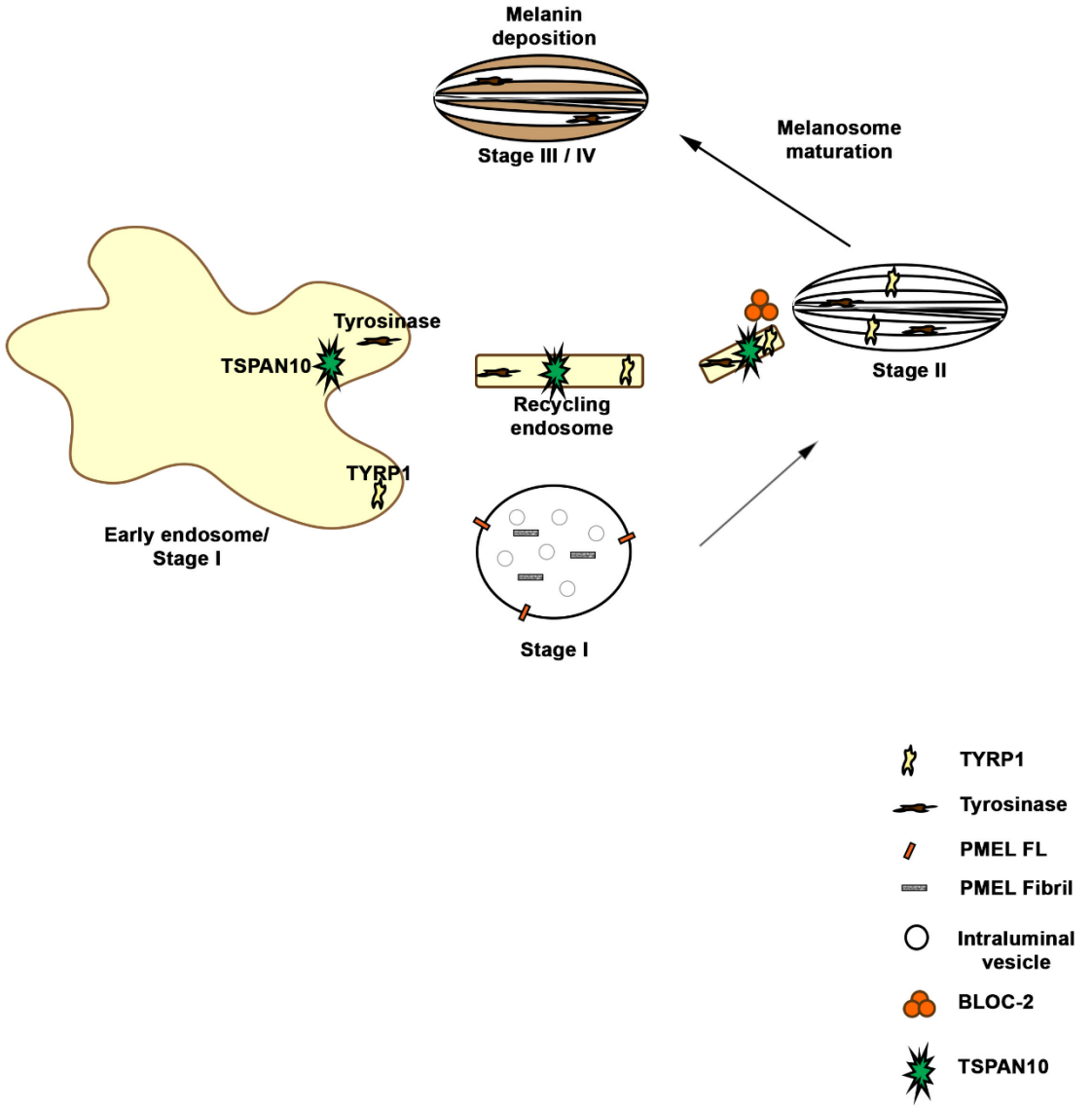

Figure 9-1 Proposed role for TSPAN10 in the melanosomal pathway
Schematic depicting endosomal and melanosomal transport systems and the proposed role of TPSAN10. PMEL fibrils emanate from intraluminal vesicles in the vacuolar portion of early endosomes

Melanin protects the RPE cells from oxidative damage as it is able to scavenge reactive free radicals [417], quench electronically excited states [56] and sequester redox-active metal ions [418]. With age, not only is there a loss of melanin granules but the remaining granules undergo an age-related change. The granules become increasingly complex, due to the fusion of melanin with lipofuscin, therefore, reducing its photoprotective role [56]. The reduction in melanin content with age is reported to result from its oxidative degradation by ROS generated by lipofuscin, as part of melanolipofuscin granules [419]. This close relationship of melanin and oxidative stress creates a certain chicken and egg scenario when examining the function of TSPAN10. Are the TSPAN10 mutant cells more stressed because they have less pigment? Or does increased ROS in the TSPAN10 mutant RPE lead to reduced pigmentation? Furthermore, do TSPAN10 mutant cells have less catalase and

HSPs because they are less pigmented, rather than this being a direct consequence of TSPAN10 k.o? Catalase activity influences the rate of melanin synthesis [420]. High levels of catalase activity within melanosomes can accelerate the breakdown of H_2O_2, which in turn may regulate the activity of tyrosinase. High levels of H_2O_2 can inhibit tyrosinase activity by various mechanisms, including the oxidation of critical cysteine residues in the enzyme's active site. Catalase activity within melanosomes may also influence the quality of melanin pigment produced. Therefore, if TSPAN10 is upstream of catalase, is it this interaction, reducing catalase production that results in the reduced tyrosinase activity and pigmentation seen? Clearly, there is a strong correlation between pigmentation and oxidative stress, and given the phenotypes seen in this thesis there must be some interplay with TSPAN10. Future work could involve analysing other elements of the pigmentation pathway in TSPAN10 k.o cells. Furthermore, it would be interesting to understand if those with the AMD risk SNP at *TSPAN10* also have fair hair and skin.

9.3 Implications for AMD research, treatments and pathology

Despite the large number of genetic loci associated with AMD, only a small number have been thoroughly examined [89]. Several novel targets, such as the polymorphism at *NPLOC4/TSPAN10* have not been investigated. AMD is thought to be a complex disease, consequently, future treatments may need to be tailored to the recipient.

TSPAN10 appears to act upstream of the antioxidant enzyme catalase, influencing its production. Oxidative stress is critical in AMD, with the macula positioned in a high oxidative stress environment. If TSPAN10 k.o reduces catalase production in the RPE, then attempting to increase TSPAN10 production or function could produce the alternate result. TSPAN10 is a good target given its predominant location in the RPE in the retina, consequently, specific targeting would hopefully produce less unwanted effects in other tissues of the eye. If we understood how TSPAN10 affects catalase expression, this would help to identify further targets to bolster catalase production and subsequently increase antioxidant function.

We know from our human study (Chapter 3) that the AMD risk SNP at *NPLOC4/TSPAN10* is associated with reduced thickness of both the RPE-BM and POS [150]. Furthermore, we saw a reduction in the height of our TSPAN10 k.o RPE (Chapter 7), which adds to the notion that *TSPAN10* expression may be associated with thickness of the RPE. Thinning of the RPE [421] and photoreceptor layer [226, 422] are both seen in AMD. There is debate as to which occurs first, if photoreceptor thinning is a result of RPE dysfunction (as their supportive cells) [423], or if it is the primary insult [424]. From the data presented within this thesis it is not possible to deduce how TSPAN10 may influence both RPE and photoreceptor

thickness, or to conclude if a thinning in one layer causes reciprocal thinning in the other. This association of TSPAN10 expression with RPE thickness, does however, add to the body of evidence for TSPAN10's role in AMD. Future work could involve analysing outer retinal layer thickness in a TSPAN10 k.o mouse model, to see if it correlates with the results presented here.

9.4 Limitations

WT cells used in this project did not undergo the CRISPR procedure, therefore any stresses this may have placed on the cell was not comparable between WT and mutants. One possibility to circumvent this is to use WT clones, which have been exposed to a sgRNA, but upon sequencing, no change in the target region produced. Another method might use WT cells that have been transfected with the pX459 plasmid that does not contain a sgRNA protospacer sequence. Thus, phenotypic changes caused by plasmid overexpression and/or the CRISPR procedure (i.e. electroporation and clonal isolation) might be captured. Of course, there is a limit to the number of clones that can feasibly be maintained and experimented on in parallel. This is a drawback of using clones.

Ideally a rescue experiment would be performed to 'knock-in' the TSPAN10 gene in our mutant cells. Our original method employed in the hESCs (CRISPR/Cas9 with puromycin selection) allowed us to isolate single cells ensuring clonal lines were created. This is not feasible in fully differentiated RPE therefore selecting cells with the 'knock-in' would require screening a significant number of cells and extensive selection criteria. Unfortunately, with limited time and resources this would be difficult to achieve.

The transcriptomic data in this thesis (Chapter 6) utilised cells grown on T75 GFR-matrigel coated flasks, whereas all other data is from RPE cells grown on GFR-matrigel coated transwell membranes. At the time of data collection there was concern over the quality of mRNA that could be achieved from the smaller number of cells grown on transwells versus flasks, to ensure high read depth and quality control. Cells grown in flasks still displayed the significant differences in pigmentation reported throughout this thesis for WT versus TSPAN10 k.o cells and showed expression of key RPE markers. All RT-PCR, RT-qPCR and western blotting data was originally undertaken on hESC-RPE grown in flasks; however this was repeated using cells cultured for a similar period of time on transwells and equivalent results seen. RPE cells grown on transwells are reported to display features of highly differentiated RPE, with transwell membranes allowing a monolayer of cells to form. This difference in culture conditions for the transcriptomic data could explain the lower than expected number of differentially expressed genes for the two TSPAN10 k.o clones versus WT (Chapter 6). Importantly all RNA seq data that was used for further investigation into

TSPAN10 function was verified using RT-qPCR from RPE cells grown on transwell membranes in addition to other molecular techniques. Stem-cell derived RPE cells grown on transwells represent the gold standard for RPE and in hindsight RNA sequencing data should have used cells grown in these culture conditions.

9.5 Future directions

We have uncovered several phenotypes associated with TSPAN10 k.o in this thesis, however, cannot fully conclude how TSPAN10 has such effects. With insights from the literature the following suggestions are proposed as avenues for future investigation.

9.5.1 Understanding how TSPAN10 affects melanin synthesis

We saw a reduction in tyrosinase production and activity in TSPAN10 k.o RPE. Tyrosinase is synthesised in the endoplasmic reticulum (ER) where it is glycosylated, folded and then transported to the Golgi [425]. It is then folded and packaged into vesicles and finally sorted to melanosomes. If tyrosinase is not adequately glycosylated in the ER the incompletely modified protein is held there [426]. To understand if TSPAN10 k.o leads to incomplete glycosylation of tyrosinase an Endoglycosidase H Assay could be conducted [426]. By analyzing the glycosylation pattern of tyrosinase using the Endoglycosidase H assay, one can infer the maturation status of the enzyme and its potential functionality in the melanin synthesis pathway. This would increase our understanding of how TSPAN10 effects pigmentation.

We examined hESC-RPE morphology using TEM, including an assessment of melanosome number and maturation status. For melanosomes to correctly form and mature their pH must be tightly controlled [427]. Stage I and II melanosomes are acidic organelles, however tyrosinase is only weakly active above pH 6, therefore melanosomes must neutralize as they mature to promote tyrosinase function [427]. To understand if TSPAN10 affects the pH of maturing melanosomes, therefore inhibiting tyrosinase function we could initially measure the pH of our hESC-RPE using a fluorescent pH sensitive dye such as Lyosensor or Seminaphtharhodafluor-1 (SNARF-1) [428] and quantifying the fluorescence intensity. This would give an indication as to whether TSPAN10 k.o alters the pH and may signpost how it influences pigmentation.

We used confocal microscopy to look for colocalization of TSPAN10 with the late endosome marker Rab7. However, we do not know if TSPAN10 also localizes to melanosomes. Immunogold labelling electron microscopy is a powerful technique for studying the detailed cellular and subcellular localisation of proteins and other molecules, providing valuable insights into their functions and interactions within the cell [429]. This would enable us to

determine the precise subcellular localisation of TSPAN10 within the RPE, a crucial step to understand its full function.

9.5.2 Assessing phenotypes associated with the AMD risk SNP rs6565597

Initially the aim was to design a sgRNA to recapitulate the AMD risk SNP rs6565597 in hESC-RPE, through CRISPR/Cas9 HDR. HDR is notoriously difficult in comparison to NHEJ, the technique employed to obtain the TSPAN10 k.o mutants discussed here. The success rate is much smaller and given the constraints of targeting a single base pair the sgRNA design is also more difficult. Additionally, the differentiation process to RPE takes considerable time, and often non-coding SNPs can have subtle effects. Gaining a further understanding of the role TSPAN10 has in the RPE has helped signpost how the rs6565597 SNP is a risk factor for AMD. However, the next step would be to insert rs6565597 into RPE and look for changes in pigmentation and oxidative stress in the cells.

10 Appendix A

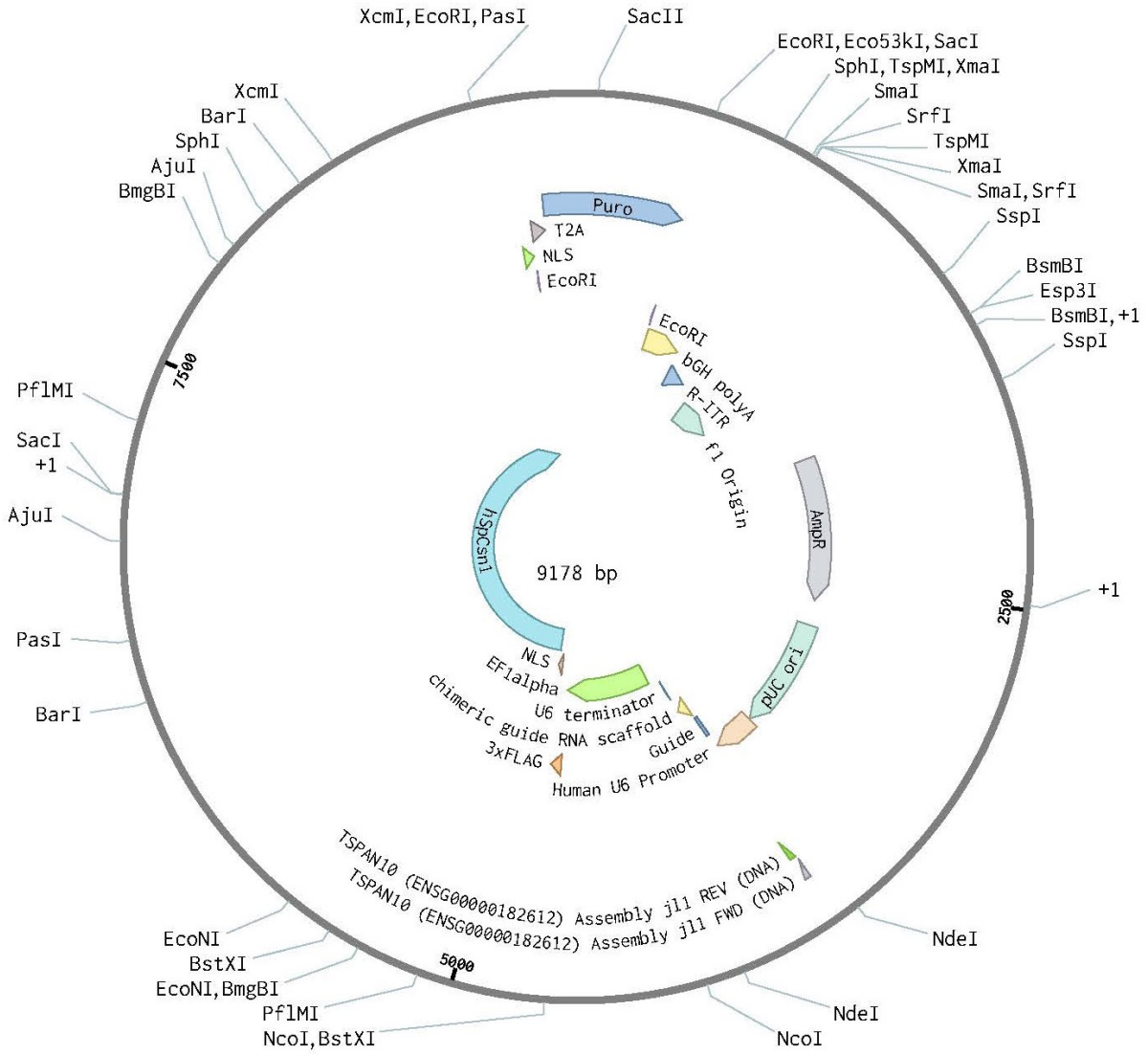

Figure 10-1 Plasmid map px459-EF1α-sgRNA
Adaptation of pX459-U6-Chimeric_BB-CBh-hSpCas9 (“pX459; Addgene)
Figure generated with Benchling

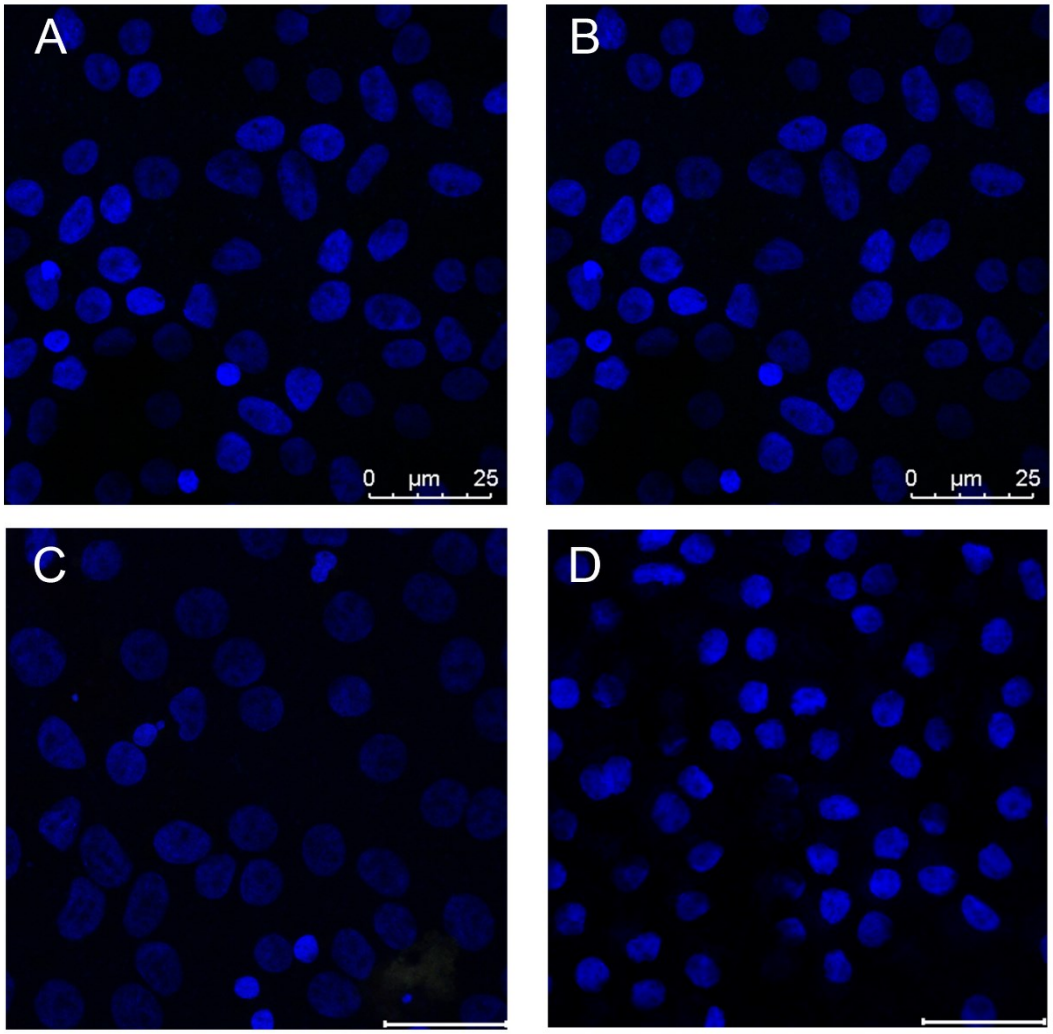

Figure 10-2 Secondary antibody controls employed in determining the expression of RPE specific markers within hESC-RPE
In hESC-RPE cells incubated in blocking buffer alone no staining was observed when probed with **A** Donkey Anti-mouse IgG Alexa Fluor® 488 (Abcam) (green), **B** Donkey Anti-rabbit IgG Alexa Fluor® 555 (Abcam) (red), **C** Rabbit Anti-goat IgG Alexa Fluor® 488 (Invitrogen) (green) or **D** Goat Anti-mouse IgG Fluor® 594 (red). Nuclei are counterstained with DAPI (blue). Abbreviations: DAPI, 4',6-diamidino-2-phenylindole. Scale bars representative of 25 µm.

Table 10-1 RNA concentration and purity for RNA sequencing
Concentration and purity were assayed by NanoDrop 1000 (Thermo Fisher Scientific).

Sample	Concentration (ng/µl)	260/280 ratio	260/230 ratio
WT Dif 1	291.5	2.06	2.00
WT Dif 2	183.9	2.03	1.80
WT Dif 3	212.5	2.06	1.81
A12 Dif 1	260.8	2.05	1.87
A12 Dif 2	283.6	2.05	1.86
A12 Dif 3	263.9	2.06	1.80
A2 Dif 1	678.9	2.03	1.86
A2 Dif 2	354.6	2.07	1.85
A2 Dif 3	341.8	2.03	1.82

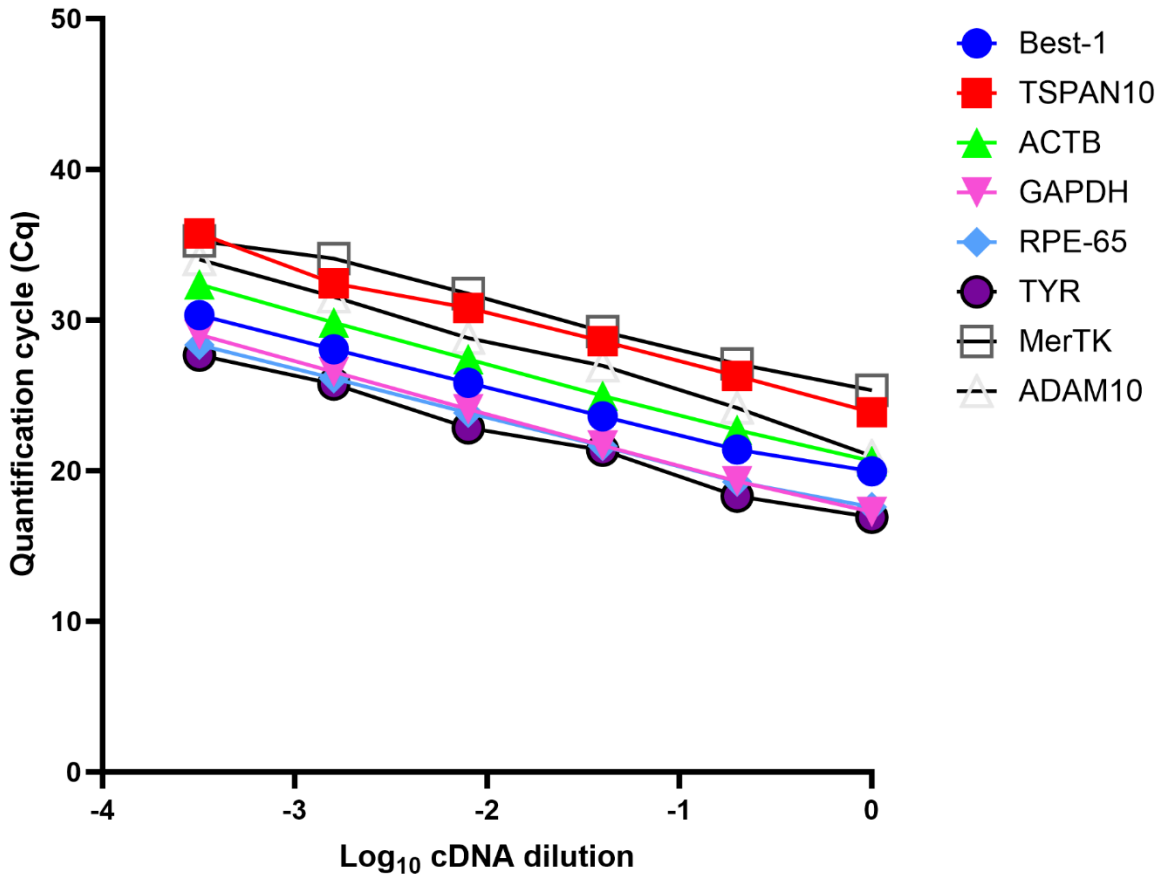

Figure 10-3 Standard curves of RT-qPCR primers generated with ten-fold serial dilutions of cDNA template.

Table 10-2 Summary of RT-qPCR primer validation

Primer Pair	Ta (°C)	Efficiency, E	Efficiency (%)	R^2
Best-1	60	2.04	104.17	0.99
TSPAN10	60	2.02	102.13	0.99
ACTB	62	1.98	97.95	0.99
GAPDH	62	1.97	97.16	0.99
RPE-65	60	2.08	108.76	0.99
TYR	60	2.06	106.66	0.99
ADAM10	60	1.95	95.11	0.99
MERTK	60	2.10	110.03	0.99

11 Appendix B

List of Equations

Equation 2. 1: To calculate cell concentration

Cell concentration (cells/ml) = mean no. cells in corner squares x dilution factor x 10^4

Equation 2. 2: To calculate primer amplification efficiency from standard curves made with ten-fold dilutions of template

E= $10^{-1/slope}$

Equation 2.3 To calculate percentage primer amplification efficiency

% Efficiency = (E-1) x 100

Equation 2.4 To calculate transepithelial electrical resistance (TEER)

TEER (Ωcm^2) = R_{tissue} (Ω) x surface area (cm^2)

12 Appendix C

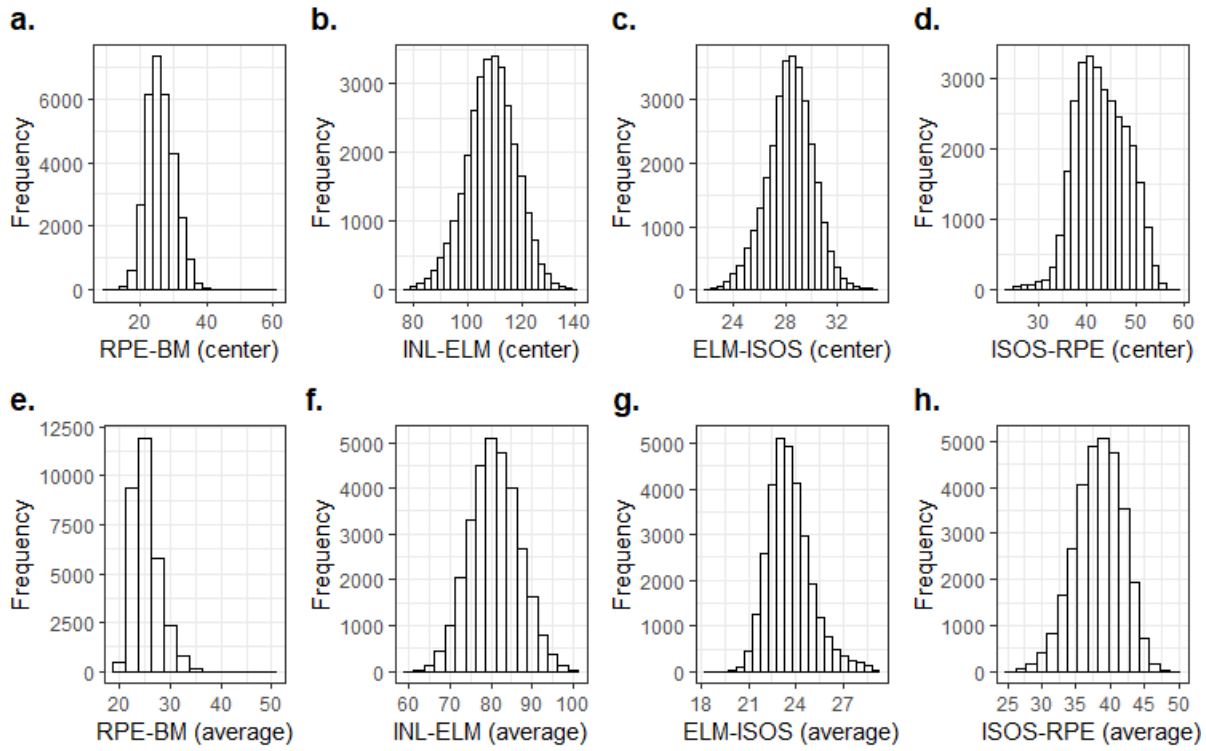

Figure 12-1 Distributions of SD-OCT measurements in the UK Biobank cohort.
A-H Depict bar charts showing the distribution of outer retinal thickness measurements in the UK Biobank cohort. The distribution of outer retinal thickness measurements for INL-ELM, ELM-ISOS and ISOS-RPE, resembled a normal distribution; however, RPE-BM thickness (A & E) followed a leptokurtic distribution.
Reproduced from Kaye et al (2021) [150] under the terms of the Creative Commons Licence.

Table 12-1 Associations between average spectral-domain optical coherence tomography (SD-OCT) measurements and risk AMD variants.
Columns “Variant”, “EA” and “NEA” list variants that were included in the model, and their risk alleles (EA, effect alleles for which the effect sizes are reported and NEA, non-effect alleles). Fields “Beta”, “SE” and “P” denote the change in SD-OCT measurements, standard errors and p-values of observed associations. The table includes significant linear regression results for 32,113 unrelated participants from UK Biobank participants. Models were adjusted for sex, age, spherical equivalent, smoking status.

						ELM-ISOS			*INL-ELM*			*ISOS-RPE*			*RPE-BM*		
Chr	**BP**	**Variant**	**Gene**	**EA**	**NEA**	**Beta**	**SE**	**p-value**	**Beta**	**SE**	**p-value**	**Beta**	**SE**	**p-value**	**Beta**	**SE**	**p-value**
1	196704632	rs10922109	CFH	C	A	0.02	0.01	0.1	-0.036	0.048	0.5	**-0.26**	**0.03**	**$6.63x10^{-20}$**	**-0.322**	**0.022**	**$1.47x10^{-49}$**
2	228086920	rs11884770	COL4A3	C	T	-0.01	0.01	0.3	0.065	0.053	0.2	-0.01	0.03	0.7	0.028	0.024	0.2
3	99180668	rs140647181	COL8A1	C	T	-0.02	0.04	0.7	0.458	0.193	0.02	-0.27	0.12	0.02	0.094	0.088	0.3
3	64715155	rs62247658	ADAMTS9	C	T	0.01	0.01	0.3	0.034	0.048	0.5	0.009	0.03	0.8	-0.046	0.022	0.03
4	110659067	rs10033900	CFI	T	C	0.001	0.01	0.9	-0.002	0.047	1	-0.08	0.03	0.003	-0.012	0.021	0.6
5	35494448	rs114092250	SPEF2	G	A	0.01	0.03	0.7	0.135	0.146	0.4	-0.09	0.09	0.3	0.021	0.067	0.8
5	39327888	rs62358361	C9	T	G	0.1	0.05	0.1	0.3	0.227	0.2	-0.1	0.14	0.5	-0.101	0.104	0.3
6	31930462	rs429608	PBX2	G	A	0.02	0.01	0.1	0.017	0.065	0.8	**-0.19**	**0.04**	**$6.08x10^{-07}$**	-0.08	0.03	0.01
6	43826627	rs943080	VEGFA	T	C	-0.00	0.01	0.8	-0.048	0.047	0.3	0.005	0.03	0.9	**-0.084**	**0.021**	**$8.83x10^{-05}$**
7	104756326	rs1142	KMT2E	T	C	-0.00	0.01	0.8	-0.026	0.049	0.6	-0.03	0.03	0.3	-0.024	0.022	0.3
7	99991548	rs7803454	PILRA	T	C	0.03	0.01	0	0.199	0.059	0.0008	**0.245**	**0.04**	**$5.15x10^{-12}$**	**-0.107**	**0.027**	**$7.67x10^{-05}$**
8	23082971	rs13278062	TNFRSF10A	T	G	-0.01	0.01	0.4	0.023	0.047	0.62	0.005	0.03	0.8	0.006	0.022	0.8
9	76617720	rs10781182	RORB	T	G	0.00	0.01	1	**0.215**	**0.051**	**$2.11x10^{-05}$**	-0.05	0.03	0.1	0.024	0.023	0.3
9	101923372	rs1626340	TGFBR1	G	A	0.02	0.01	0.2	0.055	0.057	0.3	0.065	0.03	0.06	0.001	0.026	1
9	107661742	rs2740488	ABCA1	A	C	-0.01	0.01	0.7	-0.059	0.053	0.3	-0.04	0.03	0.2	0.014	0.024	0.6
9	73438605	rs71507014	TRPM3	G	GC	0.01	0.01	0.2	0.121	0.048	0.01	0.035	0.03	0.23	0.027	0.022	0.2
10	24999593	rs12357257	ARHGAP21	A	G	0.01	0.01	0.6	0.045	0.057	0.4	-0.04	0.03	0.21	0.012	0.026	0.6
10	124215565	rs3750846	ARMS2	C	T	0.01	0.01	0.3	0.074	0.057	0.2	**-0.26**	**0.03**	**$5.32x10^{-14}$**	-0.068	0.026	0.01
12	56115778	rs3138141	BLOC1S1-RDH5	A	C	**0.05**	**0.01**	**0.0001**	**0.824**	**0.053**	**$3.34x10^{-54}$**	**0.389**	**0.03**	**$2.44x10^{-34}$**	**0.091**	**0.024**	**0.0002**
12	112132610	rs61941274	ACAD10	A	G	-0.07	0.03	0.03	0.222	0.15	0.1	0.289	0.09	1.27E-03	-0.169	0.069	0.01
13	31821240	rs9564692	B3GALTL	C	T	-0.01	0.01	0.5	0.055	0.052	0.3	0.005	0.03	0.9	0.014	0.024	0.6
14	68769199	rs61985136	RAD51B	T	C	0.03	0.01	0.02	**0.223**	**0.049**	**$5.35x10^{-06}$**	0.038	0.03	0.2	-0.052	0.022	0.02
15	58680954	rs2043085	LIPC	C	T	-0	0.01	0.8241	-0.061	0.048	0.2	0.014	0.03	0.6	-0.069	0.022	0.002
16	56997349	rs5817082	CETP	C	CA	0.02	0.01	0.2	-0.048	0.053	0.4	-0.08	0.03	1.09E-02	0.017	0.024	0.5
16	75234872	rs72802342	CTRB2	C	A	-0.01	0.02	0.6	-0.141	0.09	0.1	-0.08	0.05	0.13	0.021	0.041	0.6
17	26649724	rs11080055	TMEM97	C	A	-0	0.01	0.9	0.025	0.047	0.6	0.01	0.03	0.73	0.01	0.021	0.7

17	79526821	rs6565597	NPLOC4-TSPAN10	T	C	-0.04	0.01	0.0008	**-0.374**	**0.05**	**8.76×10^{-14}**	**0.377**	**0.03**	**4.25×10^{-36}**	**-0.3**	**0.023**	**1.00×10^{-38}**
19	6718387	rs2230199	C3	G	C	-0.02	0.01	0.2	-0.061	0.058	0.3	**0.16**	**0.04**	**5.04×10^{-06}**	0.042	0.027	0.1
19	45411941	rs429358	APOE	T	C	-0.02	0.01	0.3	0.104	0.065	0.1	-0.05	0.04	0.2	0.022	0.03	0.5
19	1031438	rs67538026	CNN2	C	T	0	0.01	0.8	0.032	0.049	0.5	-0.05	0.03	0.1	0.015	0.022	0.5
20	56653724	rs201459901	C20orf85	T	TA	0	0.02	0.9	0.26	0.102	0.01	-0.08	0.06	0.2	0.075	0.047	0.1
22	33105817	rs5754227	SYN3	T	C	0.03	0.02	0.1	-0.012	0.07	0.9	-0.09	0.04	0.04	0.084	0.032	0.01
22	38476276	rs8135665	SLC16A8	T	C	0.01	0.01	0.3	0.084	0.059	0.2	-0	0.04	0.94	-0.057	0.027	0.04

Table 12-2 Associations between central spectral-domain optical coherence tomography (SD-OCT) measurements and risk AMD variants
Columns “Variant”, “EA” and “NEA” list variants that were included in the model, and their risk alleles (EA, effect alleles for which the effect sizes are reported and NEA, non-effect alleles). Fields “Beta”, “SE” and “P” denote the change in SD-OCT measurements, standard errors and p-values of observed associations. The table includes significant linear regression results for 32,113 unrelated participants from UK Biobank participants. Models were adjusted for sex, age, spherical equivalent, smoking status.

						ELM-ISOS			*INL-ELM*			*ISOS-RPE*			*RPE-BM*		
Chr	**BP**	**Variant**	**Gene**	**EA**	**NEA**	**Beta**	**SE**	**P**	**Beta**	**SE**	**P**	**Beta**	**SE**	**P**	**Beta**	**SE**	**P**
1	196704632	rs10922109	CFH	C	A	**0.061**	**0.015**	**$2.94x10^{-05}$**	0.016	0.075	0.8	**-0.601**	**0.043**	**$3.45x10^{-44}$**	**-0.330**	**0.034**	**$5.02x10^{-22}$**
2	228086920	rs11884770	COL4A3	C	T	-0.013	0.016	0.4	0.089	0.084	0.3	-0.018	0.048	0.7	0.043	0.038	0.3
3	99180668	rs140647181	COL8A1	C	T	0.052	0.059	0.4	0.497	0.305	0.1	-0.474	0.175	0.01	0.186	0.139	0.2
3	64715155	rs62247658	ADAMTS9	C	T	0.016	0.015	0.3	-0.022	0.075	0.8	0.073	0.043	0.09	-0.048	0.034	0.2
4	110659067	rs10033900	CFI	T	C	0.025	0.014	0.08	0.023	0.074	0.8	**-0.168**	**0.042**	**$7.50x10^{-05}$**	0.032	0.034	0.3
5	35494448	rs114092250	SPEF2	G	A	-0.026	0.045	0.6	0.239	0.231	0.3	-0.332	0.133	0.01	0.207	0.105	0.05
5	39327888	rs62358361	C9	T	G	0.108	0.070	0.1	0.168	0.358	0.6	-0.297	0.206	0.1	0.085	0.163	0.6
6	31930462	rs429608	PBX2	G	A	0.012	0.020	0.6	-0.101	0.102	0.3	**-0.450**	**0.059**	**$1.92x10^{-14}$**	-0.030	0.047	0.5
6	43826627	rs943080	VEGFA	T	C	0.027	0.014	0.06	0.028	0.074	0.7	-0.102	0.042	0.02	0.047	0.034	0.2
7	99991548	rs7803454	PILRA	T	C	-0.017	0.018	0.4	0.187	0.094	0.05	0.127	0.054	0.02	**-0.190**	**0.043**	**$8.38x10^{-06}$**
7	104756326	rs1142	KMT2E	T	C	-0.014	0.015	0.4	-0.087	0.077	0.3	-0.156	0.044	0.0004	0.010	0.035	0.8
8	23082971	rs13278062	TNFRSF10A	T	G	0.019	0.014	0.2	0.072	0.074	0.3	-0.012	0.043	0.8	0.019	0.034	0.6
9	73438605	rs71507014	TRPM3	G	GC	-0.016	0.015	0.3	0.027	0.076	0.7	0.054	0.044	0.2	0.052	0.035	0.1
9	76617720	rs10781182	RORB	T	G	0.012	0.016	0.4	0.107	0.080	0.2	-0.100	0.046	0.03	0.046	0.036	0.2
9	101923372	rs1626340	TGFBR1	G	A	-0.016	0.018	0.4	0.020	0.090	0.8	0.114	0.052	0.03	0.002	0.041	1.0
9	107661742	rs2740488	ABCA1	A	C	0.015	0.016	0.4	0.053	0.084	0.5	-0.054	0.048	0.3	0.043	0.038	0.3
10	24999593	rs12357257	ARHGAP21	A	G	0.015	0.017	0.4	0.028	0.090	0.8	-0.118	0.051	0.02	0.039	0.041	0.3
10	124215565	rs3750846	ARMS2	C	T	0.047	0.018	0.01	0.102	0.090	0.3	**-0.682**	**0.052**	**$2.36x10^{-39}$**	0.011	0.041	0.8
12	56115778	rs3138141	BLOC1S1-RDH5	A	C	-0.032	0.016	0.05	**1.178**	**0.084**	**$1.22x10^{-44}$**	**0.686**	**0.048**	**$7.21x10^{-46}$**	0.129	0.038	0.001
12	112132610	rs61941274	ACAD10	A	G	-0.018	0.046	0.7	0.630	0.237	0.01	0.402	0.136	0.003	-0.078	0.108	0.5
13	31821240	rs9564692	B3GALTL	C		0.004	0.016	0.8	0.031	0.082	0.7	-0.036	0.047	0.4	0.033	0.037	0.4
14	68769199	rs61985136	RAD51B	T	C	0.048	0.015	0.001	**0.324**	**0.077**	**$2.93x10^{-05}$**	0.023	0.045	0.6	-0.027	0.035	0.4
15	58680954	rs2043085	LIPC	C	T	0.006	0.015	0.7	-0.127	0.076	0.09	-0.001	0.044	1.0	-0.031	0.035	0.4
16	56997349	rs5817082	CETP	C	CA	0.019	0.016	0.2	-0.006	0.084	0.9	-0.140	0.048	0.004	-0.007	0.038	0.9
16	75234872	rs72802342	CTRB2	C	A	-0.005	0.028	0.9	-0.117	0.142	0.4	-0.173	0.082	0.03	0.009	0.065	0.9
17	26649724	rs11080055	TMEM97	C	A	0.014	0.014	0.3	-0.121	0.074	0.1	0.003	0.042	0.9	-0.048	0.034	0.2

17	79526821	rs6565597	NPLOC4-TSPAN10	T	C	**-0.061**	**0.015**	**8.08×10^{-05}**	**-0.388**	**0.079**	**9.67×10^{-07}**	**0.407**	**0.046**	**4.20×10^{-19}**	**-0.509**	**0.036**	**5.12×10^{-45}**
19	6718387	rs2230199	C3	G	C	-0.029	0.018	0.1	-0.068	0.092	0.5	**0.275**	**0.053**	**2.15×10^{-07}**	0.003	0.042	0.9
19	45411941	rs429358	APOE	T	C	-0.010	0.020	0.6	0.035	0.102	0.7	-0.206	0.059	0.0004	-0.025	0.047	0.6
19	1031438	rs67538026	CNN2	C	T	0.000	0.015	1.0	0.155	0.077	0.05	-0.073	0.044	0.1	0.006	0.035	0.9
20	56653724	rs201459901	C20orf85	T	TA	0.062	0.031	0.05	0.326	0.161	0.04	-0.025	0.092	0.8	0.094	0.073	0.2
22	33105817	rs5754227	SYN3	T	C	0.016	0.021	0.5	0.065	0.110	0.6	-0.101	0.063	0.1	0.054	0.050	0.3
22	38476276	rs8135665	SLC16A8	T	C	0.021	0.018	0.2	0.175	0.093	0.06	0.005	0.053	0.9	-0.118	0.042	0.01

Table 12-3 Association between SD-OCT measurements and age
Fields “Beta”, “SE” and “P” denote the change in SD-OCT measurements (µm change per year), standard errors and p-values of observed associations.

	Beta	**SE**	**p-value**
INL-ELM (average)	0.05006	0.006589	3.13×10^{-14}
INL-ELM (center)	0.003	0.0042	0.42
ELM-ISOS (center)	-0.021	0.0013	1.45×10^{-61}
ELM-ISOS (average)	-0.036	0.000972	4.49×10^{-288}
ISOS-RPE (center)	-0.062	0.004	1.98×10^{-61}
ISOS-RPE (average)	-0.002	0.002	0.34
RPE-BM (center)	-0.081	0.003	8.8×10^{-161}
RPE-BM (average)	-0.043	0.002	8.94×10^{-112}

13 Appendix D

Table 13-1 Primers tested for TSPAN10 genotyping

Primer name	Primer sequence (5'-3')
TSPAN10 Genotyping Forward 1	AAGCAGAGGCCTCCTTAAGCTC
TSPAN10 Genotyping Reverse 1	CCCCTCAACCCAATCTCAGCAT
TSPAN10 Genotyping Reverse 2	CCTGCACCCTGAGCCAAAGATT
TSPAN10 Genotyping Forward 3	CTGACCCTGCAGAGCTGAAGTC
TSPAN10 Genotyping Reverse 3	CTCACGCAATCTTCCCTCCTCA

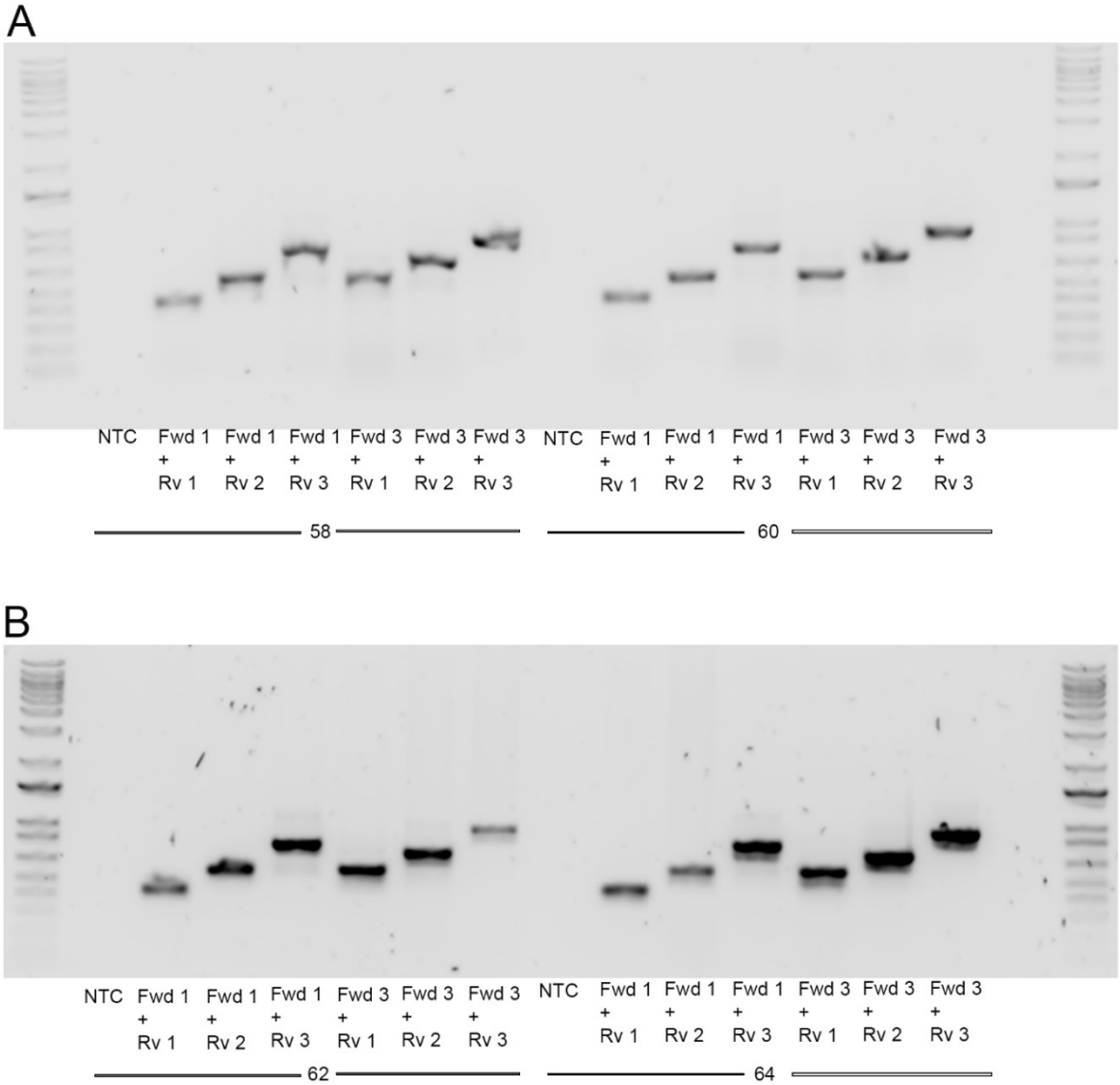

Figure 13-1 A&B Polymerase Chain Reaction (PCR) using TSPAN10 primer pairs.
PCR of TSPAN10 primer pairs using genomic DNA (gDNA) from retinal organoids at varying temperatures and in varying combinations to assess the most robust primer pair.

(A) Temperatures 58°C and 60°C.

(B) Temperatures 62°C and 64°C. Primer pair Forward 1 + Reverse 3 at 62°C selected.

Figure 13-2 Karyotyping report for A2
Report and data generated by Wessex Medical Institute therefore no credit can be taken for this work. Array comparative genome hybridization showed no new pathogenic mutations

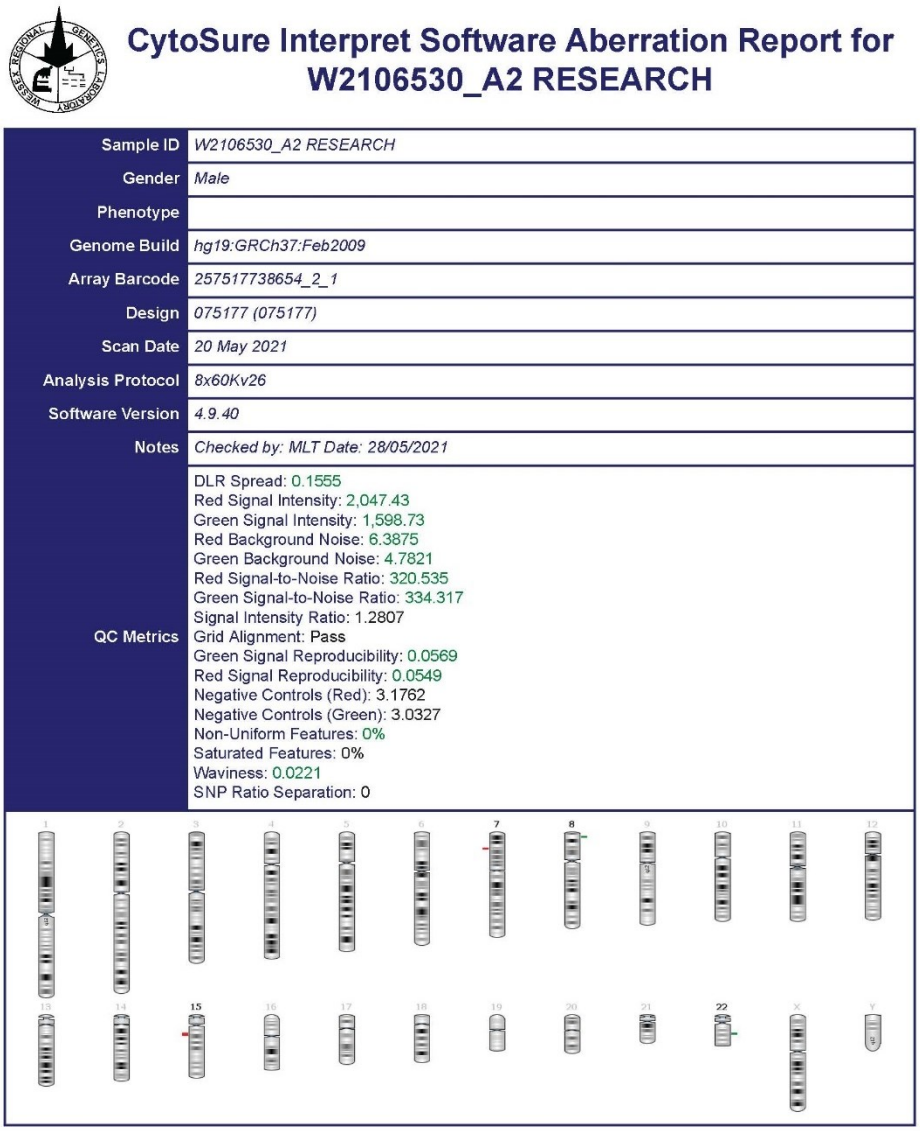

CytoSure Interpret Software Aberration Report for W2106530_A2 RESEARCH

Sample ID	*W2106530_A2 RESEARCH*
Gender	*Male*
Phenotype	
Genome Build	*hg19:GRCh37:Feb2009*
Array Barcode	*257517738654_2_1*
Design	*075177 (075177)*
Scan Date	*20 May 2021*
Analysis Protocol	*8x60Kv26*
Software Version	*4.9.40*
Notes	*Checked by: MLT Date: 28/05/2021*
QC Metrics	DLR Spread: 0.1555 Red Signal Intensity: 2,047.43 Green Signal Intensity: 1,598.73 Red Background Noise: 6.3875 Green Background Noise: 4.7821 Red Signal-to-Noise Ratio: 320.535 Green Signal-to-Noise Ratio: 334.317 Signal Intensity Ratio: 1.2807 Grid Alignment: Pass Green Signal Reproducibility: 0.0569 Red Signal Reproducibility: 0.0549 Negative Controls (Red): 3.1762 Negative Controls (Green): 3.0327 Non-Uniform Features: 0% Saturated Features: 0% Waviness: 0.0221 SNP Ratio Separation: 0

W2106530_A2 RESEARCH

	Chromosome	Cytogenetic Location	Start	Stop	Size	Gain/ Loss	ISCN Notation	Classification (Initial)	Mean Log Ratio
1	7	p15.3	24736891	24782638	45.75Kb	Loss	arr[hg19] 7p15.3(24,736,891-24,782,638)x1	VOUS: deletion	-0.8095
2	8	p23.1	7113656	7881316	767.66Kb	Gain	arr[hg19] 8p23.1(7,113,656-7,881,316)x3	Benign: W track	0.6425
3	15	q13.2	30491415	30653918	162.5Kb	Loss	arr[hg19] 15q13.2(30,491,415-30,653,918)x1	Likely Benign: 2 or more studies on DGV	-0.8909
4	15	q13.3	32445861	32465711	19.85Kb	Loss	arr[hg19] 15q13.3(32,445,861-32,465,711)x1	Likely Benign: 2 or more studies on DGV	-0.814
5	22	q12.2	30053587	30054342	755b	Gain	arr[hg19] 22q12.2(30,053,587-30,054,342)x3	BS-Batch specific	0.4507

W2106530_A2 RESEARCH

Aberration 1

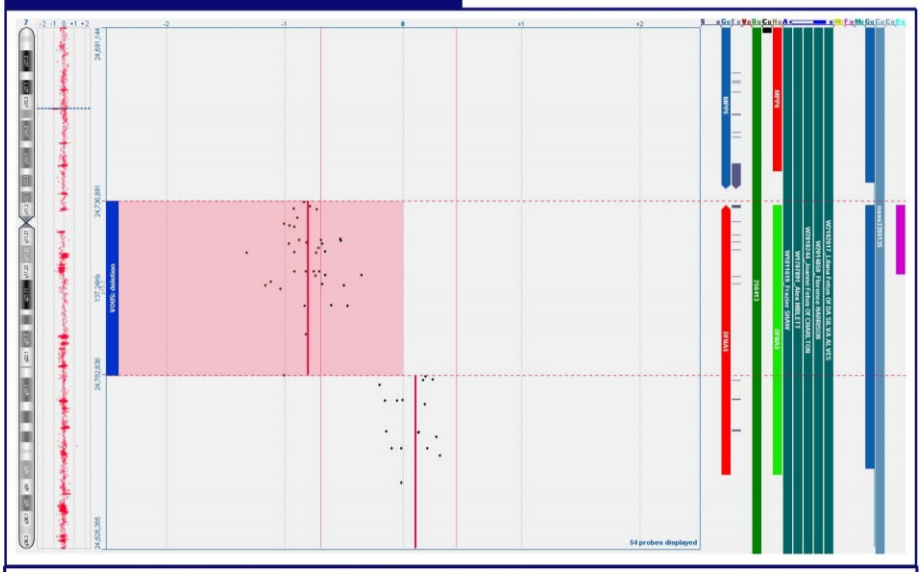

ISCN Notation :	*arr[hg19] 7p15.3(24,736,891-24,782,638)x1*	**Gain/Loss :**	*Loss*
Mean Log Ratio :	*-0.8095*	**Size :**	*45.75Kb*
Classification (Initial) :	*VOUS: deletion*	**Chromosome :**	*7*
Start :	*24736891*	**Stop :**	*24782638*
Cytogenetic Location :	*p15.3*	**Size (Max) :**	*92.77Kb*
Start (Max) :	*24690218*	**Stop (Max) :**	*24782985*
Detection Method :	*CBS*		
Comments :	*?*		
Genes :	*DFNA5;*		
Syndromes :			
DECIPHER Patients :	*252a2a282c24; 252b2a252528; 252c262b2b27; 25282b28; 25282c292c2b; 252823232426; 2529252b2c2c; 2528292b2c25; 25282b242c25; 262327252b26; 252829272426;*		
OMIM Genes :	*DFNA5;*		
# OMIM Genes :	*1*		

Figure 13-3 Karyotyping report for A12
Report and data generated by Wessex Medical Institute therefore no credit can be taken for this work. Array comparative genome hybridization showed no new pathogenic mutations

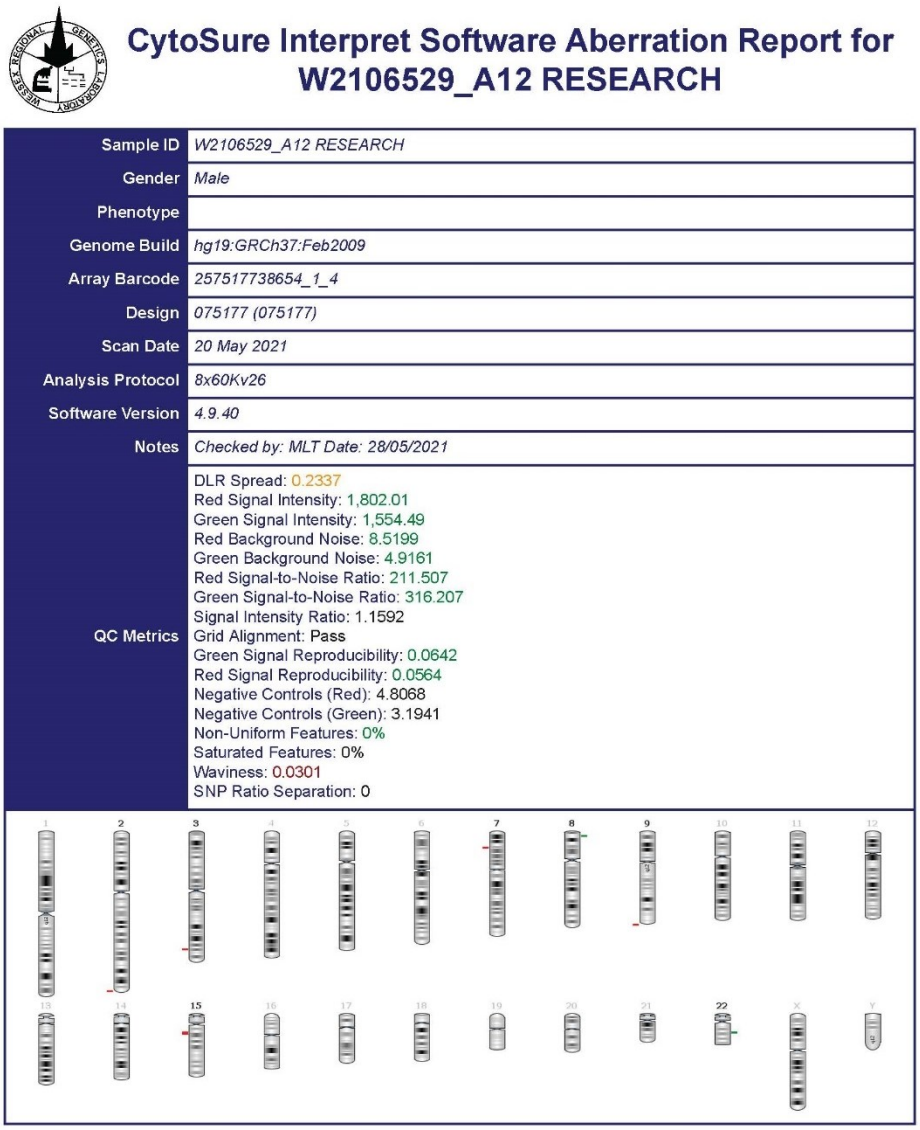

CytoSure Interpret Software Aberration Report for W2106529_A12 RESEARCH

Sample ID	*W2106529_A12 RESEARCH*
Gender	*Male*
Phenotype	
Genome Build	*hg19:GRCh37:Feb2009*
Array Barcode	*257517738654_1_4*
Design	*075177 (075177)*
Scan Date	*20 May 2021*
Analysis Protocol	*8x60Kv26*
Software Version	*4.9.40*
Notes	*Checked by: MLT Date: 28/05/2021*
QC Metrics	DLR Spread: 0.2337 Red Signal Intensity: 1,802.01 Green Signal Intensity: 1,554.49 Red Background Noise: 8.5199 Green Background Noise: 4.9161 Red Signal-to-Noise Ratio: 211.507 Green Signal-to-Noise Ratio: 316.207 Signal Intensity Ratio: 1.1592 Grid Alignment: Pass Green Signal Reproducibility: 0.0642 Red Signal Reproducibility: 0.0564 Negative Controls (Red): 4.8068 Negative Controls (Green): 3.1941 Non-Uniform Features: 0% Saturated Features: 0% Waviness: 0.0301 SNP Ratio Separation: 0

Page **1** of **3**

W2106529_A12 RESEARCH

	Chromosome	Cytogenetic Location	Start	Stop	Size	Gain/ Loss	ISCN Notation	Classification (Initial)	Mean Log Ratio
1	2	q37.3	240321947	240322855	908b	Loss	arr[hg19] 2q37.3(240,321,947-240,322,855)x1	BS-Batch specific	-0.7628
2	3	q26.32	176914910	176916228	1.32Kb	Loss	arr[hg19] 3q26.32(176,914,910-176,916,228)x1	BS-Batch specific	-0.8524
3	7	p15.3	24736891	24782638	45.75Kb	Loss	arr[hg19] 7p15.3(24,736,891-24,782,638)x1	VOUS: deletion	-0.7915
4	8	p23.1	7113656	7881316	767.66Kb	Gain	arr[hg19] 8p23.1(7,113,656-7,881,316)x3	Benign: W track	0.6966
5	9	q34.3	140513155	140513578	423b	Loss	arr[hg19] 9q34.3(140,513,155-140,513,578)x1	BS-Batch specific	-0.8366
6	15	q13.2	30491415	30653918	162.5Kb	Loss	arr[hg19] 15q13.2(30,491,415-30,653,918)x1	Likely Benign: 2 or more studies on DGV	-0.8924
7	15	q13.3	32445861	32465711	19.85Kb	Loss	arr[hg19] 15q13.3(32,445,861-32,465,711)x1	Likely Benign: 2 or more studies on DGV	-0.9172
8	22	q12.2	30053587	30054342	755b	Gain	arr[hg19] 22q12.2(30,053,587-30,054,342)x3	BS-Batch specific	0.5567

W2106529_A12 RESEARCH

Aberration 3

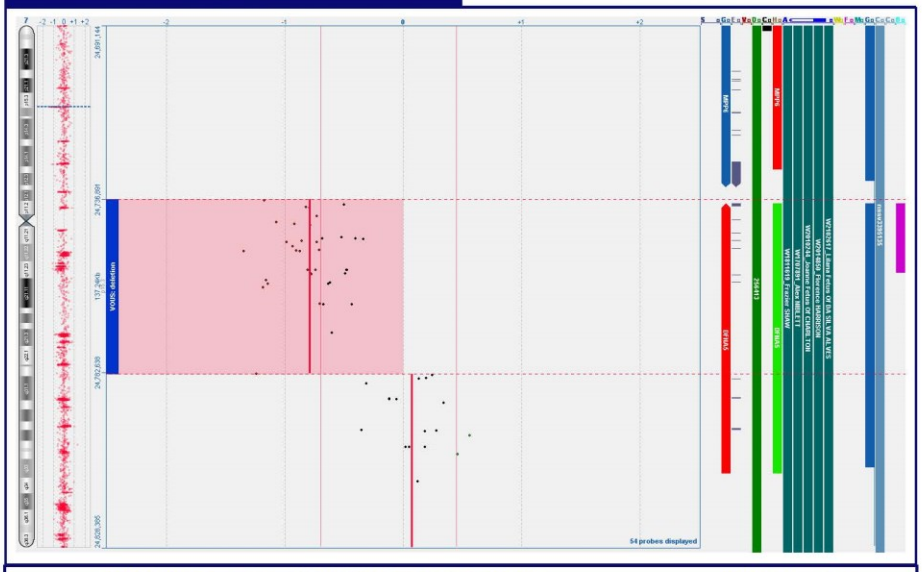

ISCN Notation :	*arr[hg19] 7p15.3(24,736,891-24,782,638)x1*	**Gain/Loss :**	*Loss*
Mean Log Ratio :	*-0.7915*	**Size :**	*45.75Kb*
Classification (Initial) :	*VOUS: deletion*	**Chromosome :**	*7*
Start :	*24736891*	**Stop :**	*24782638*
Cytogenetic Location :	*p15.3*	**Size (Max) :**	*92.77Kb*
Start (Max) :	*24690218*	**Stop (Max) :**	*24782985*
Detection Method :	*CBS*		
Comments :	*?*		
Genes :	*DFNA5;*		
Syndromes :			
DECIPHER Patients :	*252a2a282c24; 252b2a252528; 252c262b2b27; 25282b28; 25282c292c2b; 252823232426; 2529252b2c2c; 2528292b2c25; 25282b242c25; 262327252b26; 252829272426;*		
OMIM Genes :	*DFNA5;*		
# OMIM Genes :	*1*		

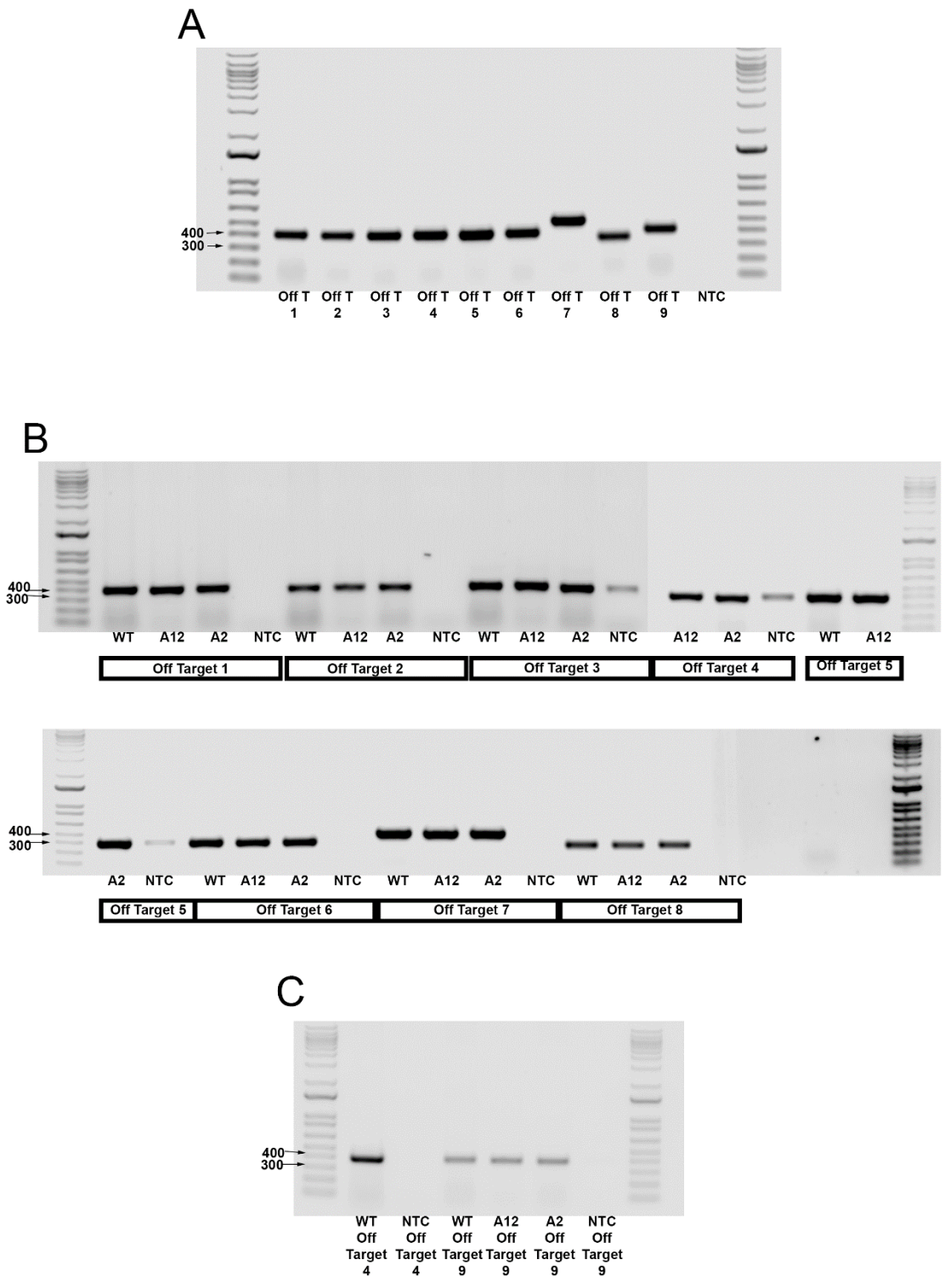

Figure 13-4 PCR for off-target primer selection and PCR for off-target hits in hESC-RPE gDNA
A: PCR of primers designed and tested for off-target hits
B: PCR of hESC-RPE gDNA for off target hits using primers tested in A
C: PCR of hESC-RPE gDNA for off target hits using primers tested in A
All sequencing reactions from **B** & **C** were then sent for Sanger sequencing.

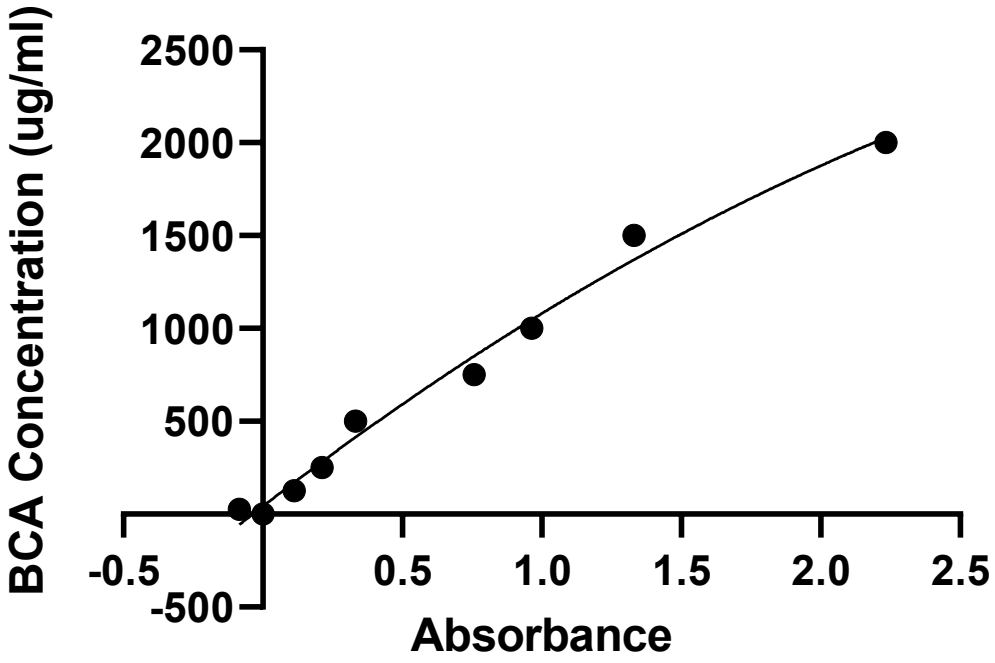

Figure 13-5 BCA Protein Assay standard curve
Standard curve created using Microsoft excel and GraphPad Prism

Table 13-2 Primers tested for TSPAN10 RT-PCR

TSPAN10 Primer Name	Sequence
Forward 1	atgcacaGACTAGCCCAGG
Forward 2	tctccatgcacaGACTAGCC
Forward 5	CTTCCTCCTCGACCAAGTCC
Reverse 1	GTCCTGGTAGTGGGCGATG
Reverse 2	GGGGAGCTGCAGTTAAAGTAC
Reverse 4	TTCTGGCCTGCAGTTTCCT
Reverse 5	TGACAGAGGCTCCATCTTCG

Table depicts various primers tested; selected primers highlighted in green

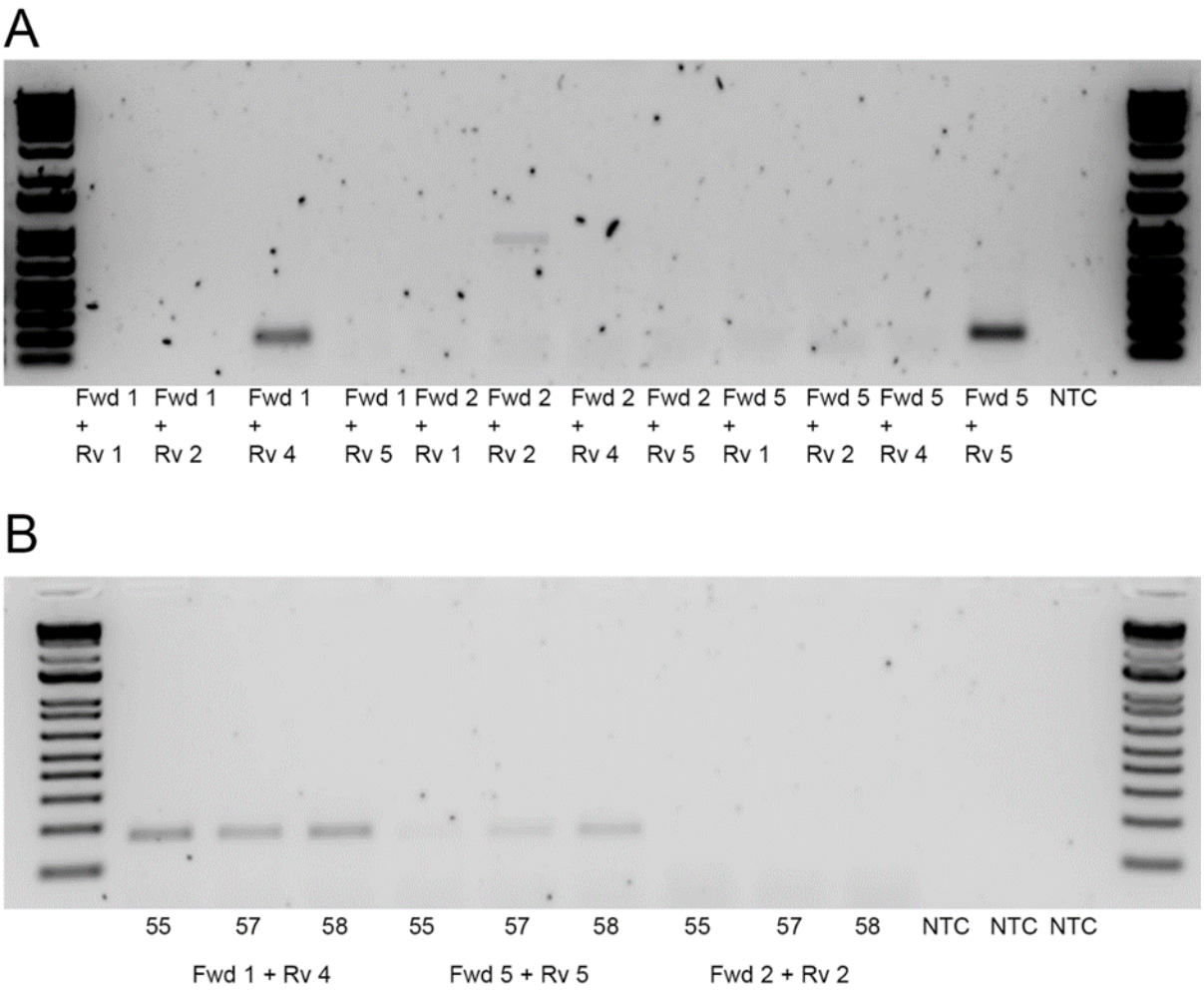

Figure 13-6 Primers designed for RT-PCR of cDNA from human embryonic stem cell (hESC) derived retinal pigment epithelium (RPE) for TSPAN10

(A) RT-PCR results for TSPAN10 primer combinations as shown in Table 13 – 2

(B) Primer combinations successful in (**A**) selected. PCR results for selected primer combinations at varying temperatures

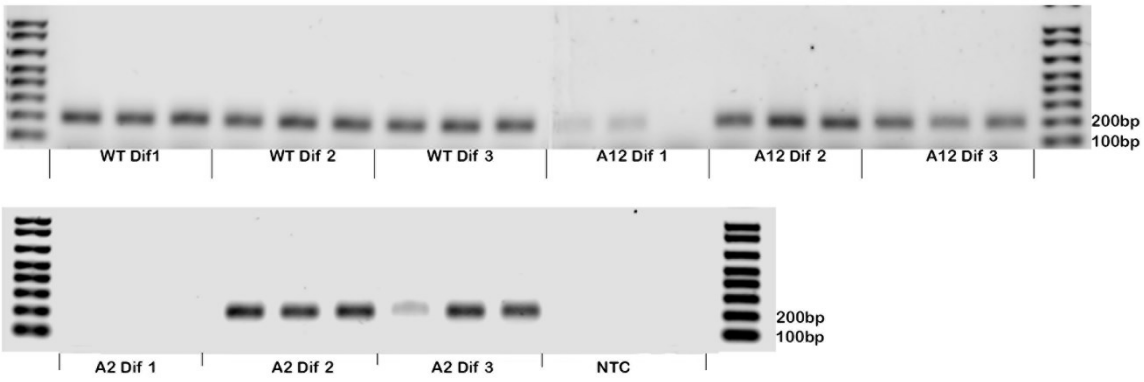

Figure 13-7 Gel electrophoresis of RT-qPCR products for TSPAN10

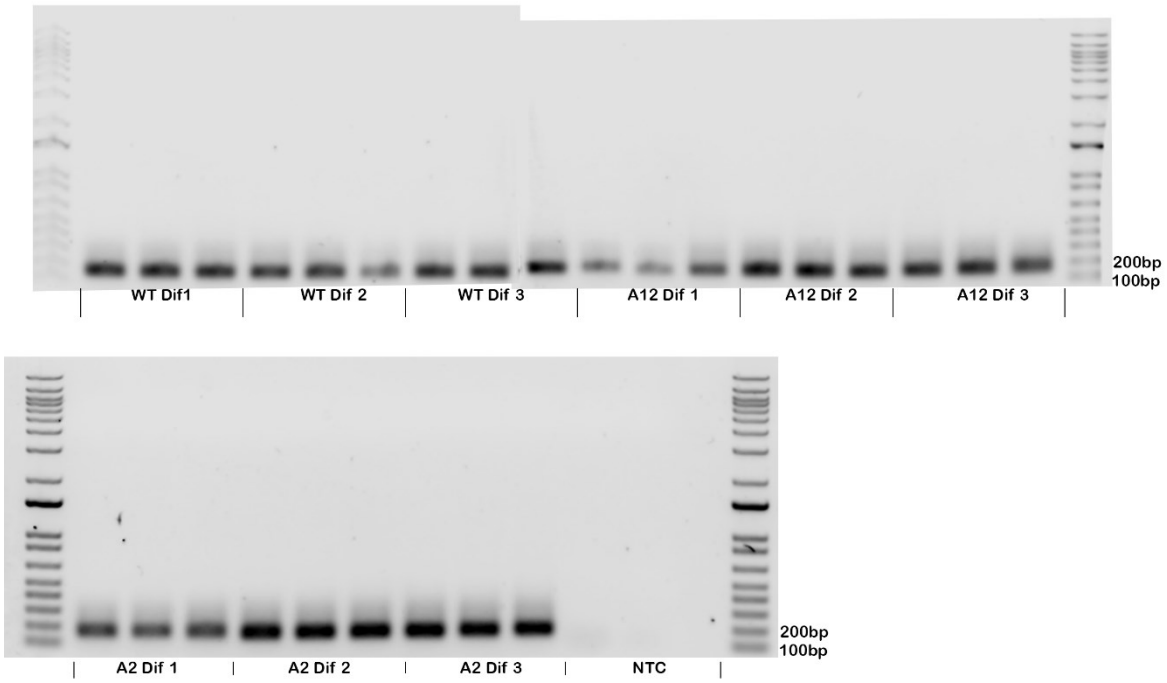

Figure 13-8 Gel electrophoresis of RT-qPCR products for Beta Actin

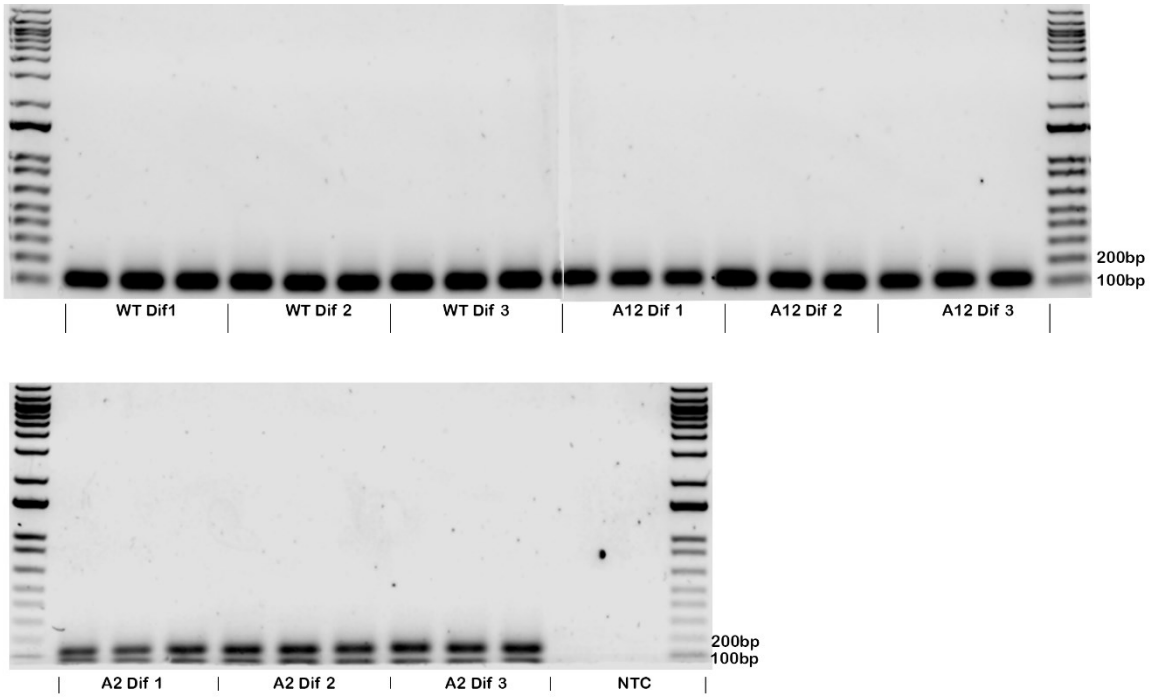

Figure 13-9 Gel electrophoresis of RT-qPCR products for GAPDH

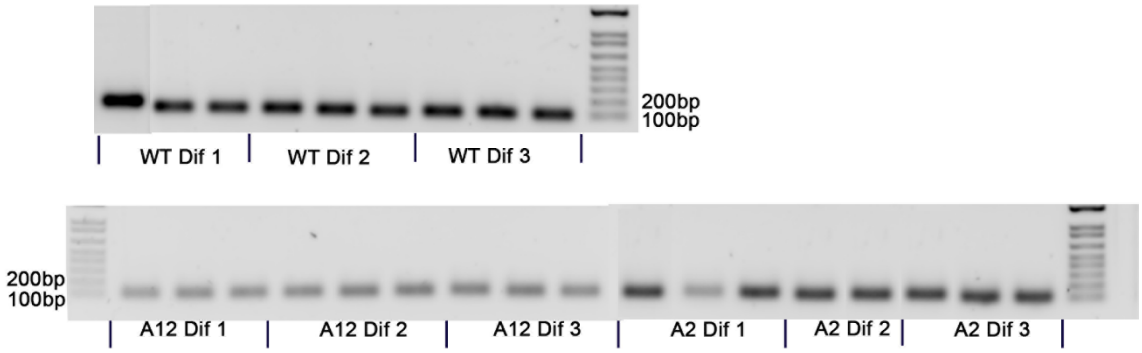

Figure 13-10 Gel electrophoresis of RT-qPCR products for ADAM10

Figure 13-11 Gel electrophoresis of RT-qPCR products for RPE65

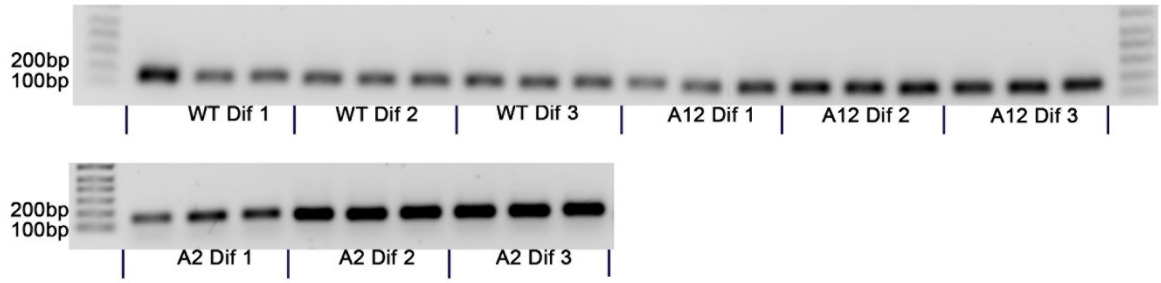

Figure 13-12 Gel electrophoresis of RT-qPCR products for Tyrosinase

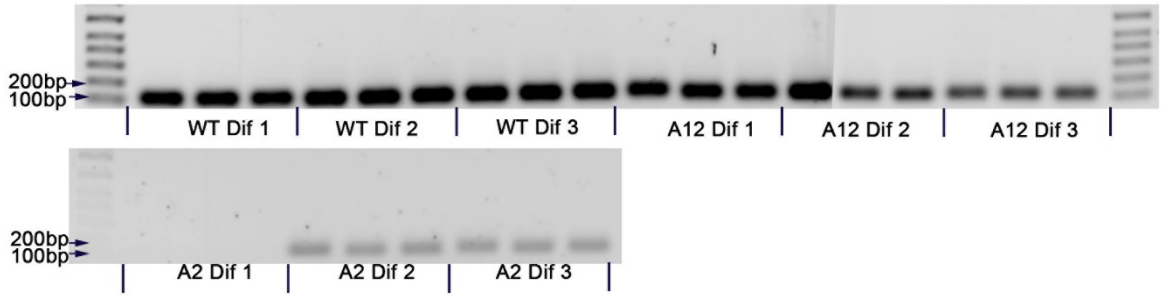

Figure 13-13 Gel electrophoresis of RT-qPCR products for MERTK

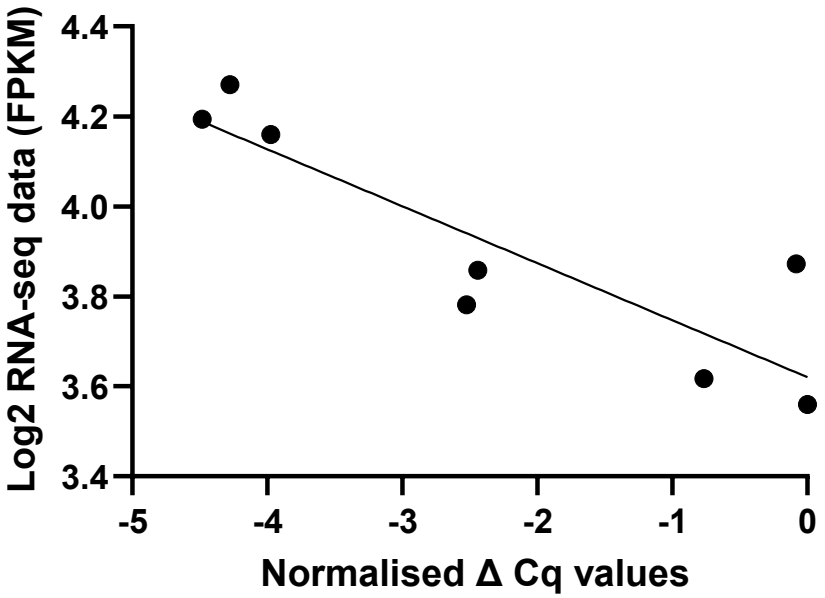

Figure 13-14 Pearson Correlation Analysis of RNA-seq data and RT-qPCR data for TSPAN10
Confirmation of similarity between RT-qPCR data and RNA-seq data for TSPAN10.
R^2 =0.78, *p*= 0.004

Table 13-3 Primer sequences used for RT-PCR of RPE markers.

Primer Name	Sequence (5'-3')
RPE-65 Fwd	GCC CTC CTG CAC AAG TTT GAC TTT
RPE-65 Rv	AGT TGG TCT CTG TGC AAG CGT AGT
Best 1 Fwd	ATT TAT AGG CTG GCC CTC ACG GAA
Best 1 Rv	TGT TCT GCC GGA GTC ATA AAG CCT
MerTK Fwd	GTGAGGCAGCGTGCATGAAAG
MerTK Rv	GGGCTTTGGGATGCCTTGAG

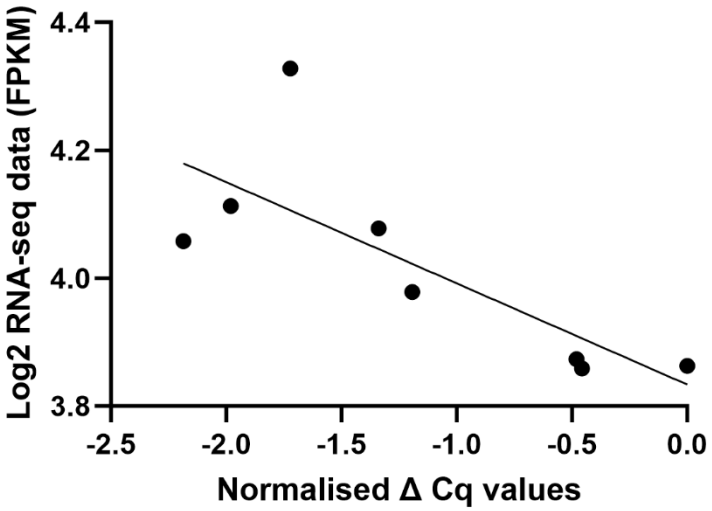

Figure 13-15 Pearson Correlation Analysis of RNA-seq data and RT-qPCR data for RPE65
Confirmation of similarity between RT-qPCR data and RNA-seq data for RPE65.
R^2 =0.60, *p*= 0.02

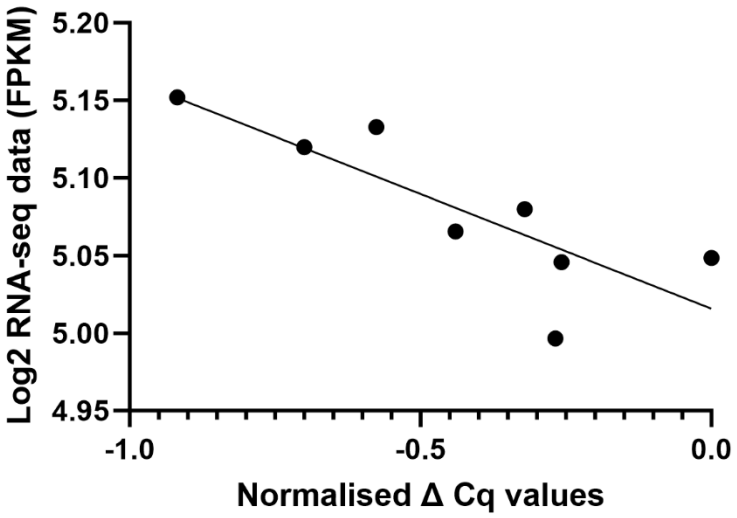

Figure 13-16 Pearson Correlation Analysis of RNA-seq data and RT-qPCR data for BEST1

Confirmation of similarity between RT-qPCR data and RNA-seq data for RPE65.
R^2 =0.67, *p*= 0.01

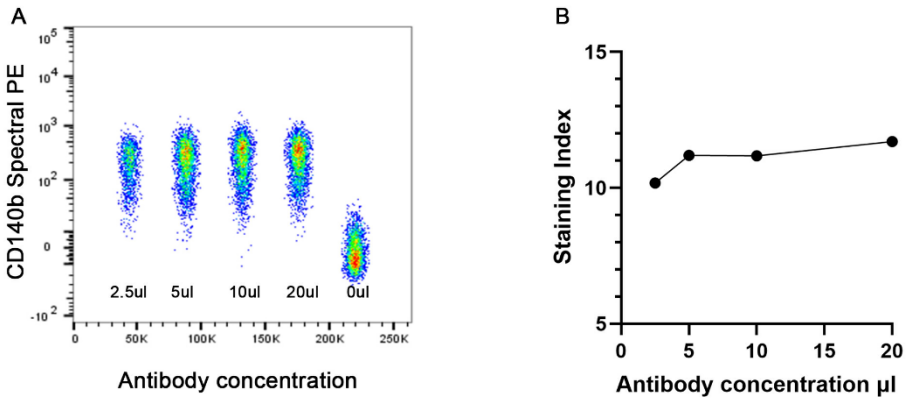

Figure 13-17 Titration and calculation of staining index for CD140b antibody
A: CD140b staining of ARPE19 cells grown in culture for 3 months. Varying antibody concentrations displayed.
B: Staining index calculated for the CD140b-PE antibody. 20 µl of antibody per test produced the highest staining index and was therefore selected.

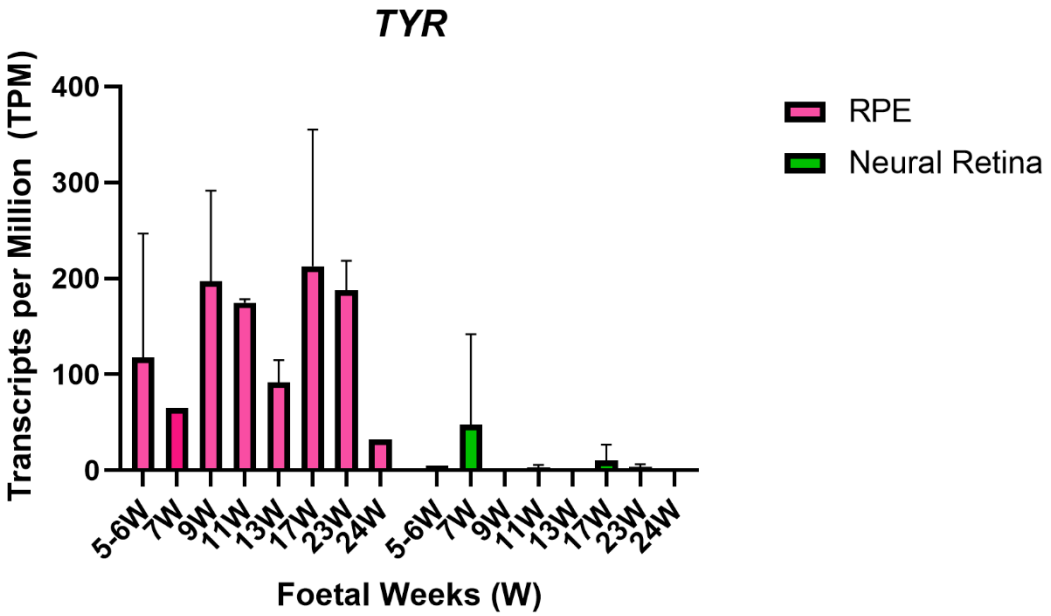

Figure 13-18 Tyrosinase expression in the developing foetal eye
Bar chart depicts *TYR* (tyrosinase) mRNA expression in the RPE and neural retina from weeks 5/6 to week 24 of foetal development. The RPE is shown in pink and neural retina in green.
Bars depict mean expression and error bars show SD of at least two embryos.
TYR expression is greater in the RPE than the neural retina throughout this period of foetal development, there is no specific pattern to tyrosinase expression.
Data from the openly available data set from the Tang group [393]

References

1. Blindness, G.B.D., C. Vision Impairment, and S. Vision Loss Expert Group of the Global Burden of Disease, *Causes of blindness and vision impairment in 2020 and trends over 30 years, and prevalence of avoidable blindness in relation to VISION 2020: the Right to Sight: an analysis for the Global Burden of Disease Study.* Lancet Glob Health, 2021. **9**(2): p. e144-e160.

2. Freud, S., J. Riviere, and Sigmund Freud Collection (Library of Congress), *Civilization and its discontents*. 1930, New York,: J. Cape & H. Smith. 144 p.

3. Scott, A.W., et al., *Public Attitudes About Eye and Vision Health.* Jama Ophthalmology, 2016. **134**(10): p. 1111-1118.

4. Fritsche, L.G., et al., *Age-related macular degeneration: genetics and biology coming together.* Annu Rev Genomics Hum Genet, 2014. **15**: p. 151-71.

5. John V. Forrester, A.D.D., Paul G. McMenamin, Fiona Roberts, Eric Pearlman,, *The Eye (Fourth Edition)*. Chapter 2 - Embryology and early development of the eye and adnexa. 2016. 103-129.

6. Young, R.W., *The renewal of rod and cone outer segments in the rhesus monkey.* J Cell Biol, 1971. **49**(2): p. 303-18.

7. Keeling, E., et al., *3D-Reconstructed Retinal Pigment Epithelial Cells Provide Insights into the Anatomy of the Outer Retina.* Int J Mol Sci, 2020. **21**(21).

8. Volland, S., et al., *A comparison of some organizational characteristics of the mouse central retina and the human macula.* PLoS One, 2015. **10**(4): p. e0125631.

9. Ts'o, M.O. and E. Friedman, *The retinal pigment epithelium. 3. Growth and development.* Arch Ophthalmol, 1968. **80**(2): p. 214-6.

10. Booij, J.C., et al., *The dynamic nature of Bruch's membrane.* Prog Retin Eye Res, 2010. **29**(1): p. 1-18.

11. Hogan, M.J. and J. Alvarado, *Studies on the human macula. IV. Aging changes in Bruch's membrane.* Arch Ophthalmol, 1967. **77**(3): p. 410-20.

12. Triviño, A.d.H., R.; Rojas, B.; Gallego, B.I.; Ramírez, A.I.; Salazar, J.J.; Ramírez, J.M. , *Effects ofHypercholesterolaemia in the Retina.* Ocular Diseases, 2012.

13. Campbell, M. and P. Humphries, *The blood-retina barrier: tight junctions and barrier modulation.* Adv Exp Med Biol, 2012. **763**: p. 70-84.

14. Rizzolo, L.J., et al., *Integration of tight junctions and claudins with the barrier functions of the retinal pigment epithelium.* Prog Retin Eye Res, 2011. **30**(5): p. 296-323.

15. Klaassen, I., C.J. Van Noorden, and R.O. Schlingemann, *Molecular basis of the inner blood-retinal barrier and its breakdown in diabetic macular edema and other pathological conditions.* Prog Retin Eye Res, 2013. **34**: p. 19-48.

16. Sparrow, J.R., D. Hicks, and C.P. Hamel, *The retinal pigment epithelium in health and disease.* Curr Mol Med, 2010. **10**(9): p. 802-23.

17. Strauss, O., *The retinal pigment epithelium in visual function.* Physiol Rev, 2005. **85**(3): p. 845-81.

18. Rozanowski, B., et al., *Human RPE melanosomes protect from photosensitized and iron-mediated oxidation but become pro-oxidant in the presence of iron upon photodegradation.* Invest Ophthalmol Vis Sci, 2008. **49**(7): p. 2838-47.

19. Feeney-Burns, L., E.S. Hilderbrand, and S. Eldridge, *Aging human RPE: morphometric analysis of macular, equatorial, and peripheral cells.* Invest Ophthalmol Vis Sci, 1984. **25**(2): p. 195-200.

20. Lehmann, G.L., et al., *Plasma membrane protein polarity and trafficking in RPE cells: past, present and future.* Exp Eye Res, 2014. **126**: p. 5-15.

21. Wimmers, S., M.O. Karl, and O. Strauss, *Ion channels in the RPE.* Prog Retin Eye Res, 2007. **26**(3): p. 263-301.

22. Boulton, M. and P. Dayhaw-Barker, *The role of the retinal pigment epithelium: topographical variation and ageing changes.* Eye (Lond), 2001. **15**(Pt 3): p. 384-9.

23. Shin, K., V.C. Fogg, and B. Margolis, *Tight junctions and cell polarity.* Annu Rev Cell Dev Biol, 2006. **22**: p. 207-35.

24. Rizzolo, L.J., *Barrier properties of cultured retinal pigment epithelium.* Exp Eye Res, 2014. **126**: p. 16-26.

25. Van Itallie, C.M. and J.M. Anderson, *Claudins and epithelial paracellular transport.* Annu Rev Physiol, 2006. **68**: p. 403-29.

26. Colegio, O.R., et al., *Claudins create charge-selective channels in the paracellular pathway between epithelial cells.* Am J Physiol Cell Physiol, 2002. **283**(1): p. C142-7.

27. Peng, S., et al., *Claudin-19 and the barrier properties of the human retinal pigment epithelium.* Invest Ophthalmol Vis Sci, 2011. **52**(3): p. 1392-403.

28. McCarthy, K.M., et al., *Occludin is a functional component of the tight junction.* J Cell Sci, 1996. **109 (Pt 9)**: p. 2287-98.

29. Chiba, H., et al., *Transmembrane proteins of tight junctions.* Biochim Biophys Acta, 2008. **1778**(3): p. 588-600.

30. Stevenson, B.R., et al., *Identification of ZO-1: a high molecular weight polypeptide associated with the tight junction (zonula occludens) in a variety of epithelia.* J Cell Biol, 1986. **103**(3): p. 755-66.

31. Bazzoni, G., et al., *Interaction of junctional adhesion molecule with the tight junction components ZO-1, cingulin, and occludin.* J Biol Chem, 2000. **275**(27): p. 20520-6.

32. Fanning, A.S., et al., *The tight junction protein ZO-1 establishes a link between the transmembrane protein occludin and the actin cytoskeleton.* J Biol Chem, 1998. **273**(45): p. 29745-53.

33. Furuse, M., et al., *Direct association of occludin with ZO-1 and its possible involvement in the localization of occludin at tight junctions.* J Cell Biol, 1994. **127**(6 Pt 1): p. 1617-26.

34. Itoh, M., et al., *The 220-kD protein colocalizing with cadherins in non-epithelial cells is identical to ZO-1, a tight junction-associated protein in epithelial cells: cDNA cloning and immunoelectron microscopy.* J Cell Biol, 1993. **121**(3): p. 491-502.

35. Kevany, B.M. and K. Palczewski, *Phagocytosis of retinal rod and cone photoreceptors.* Physiology (Bethesda), 2010. **25**(1): p. 8-15.

36. Mazzoni, F., H. Safa, and S.C. Finnemann, *Understanding photoreceptor outer segment phagocytosis: use and utility of RPE cells in culture.* Exp Eye Res, 2014. **126**: p. 51-60.

37. Feng, W., et al., *Mertk triggers uptake of photoreceptor outer segments during phagocytosis by cultured retinal pigment epithelial cells.* J Biol Chem, 2002. **277**(19): p. 17016-22.

38. Finnemann, S.C. and R.L. Silverstein, *Differential roles of CD36 and alphavbeta5 integrin in photoreceptor phagocytosis by the retinal pigment epithelium.* J Exp Med, 2001. **194**(9): p. 1289-98.

39. Finnemann, S.C., et al., *Phagocytosis of rod outer segments by retinal pigment epithelial cells requires alpha(v)beta5 integrin for binding but not for internalization.* Proc Natl Acad Sci U S A, 1997. **94**(24): p. 12932-7.

40. Bobu, C. and D. Hicks, *Regulation of retinal photoreceptor phagocytosis in a diurnal mammal by circadian clocks and ambient lighting.* Invest Ophthalmol Vis Sci, 2009. **50**(7): p. 3495-502.

41. Kinnunen, K., et al., *Molecular mechanisms of retinal pigment epithelium damage and development of age-related macular degeneration.* Acta Ophthalmol, 2012. **90**(4): p. 299-309.

42. Ji, C.H. and Y.T. Kwon, *Crosstalk and Interplay between the Ubiquitin-Proteasome System and Autophagy.* Mol Cells, 2017. **40**(7): p. 441-449.

43. Dawson, D.W., et al., *Pigment epithelium-derived factor: a potent inhibitor of angiogenesis.* Science, 1999. **285**(5425): p. 245-8.

44. King, G.L. and K. Suzuma, *Pigment-epithelium-derived factor--a key coordinator of retinal neuronal and vascular functions.* N Engl J Med, 2000. **342**(5): p. 349-51.

45. Steele, F.R., et al., *Pigment epithelium-derived factor: neurotrophic activity and identification as a member of the serine protease inhibitor gene family.* Proc Natl Acad Sci U S A, 1993. **90**(4): p. 1526-30.

46. Burns, M.S. and M.J. Hartz, *The retinal pigment epithelium induces fenestration of endothelial cells in vivo.* Curr Eye Res, 1992. **11**(9): p. 863-73.

47. Campochiaro, P.A., *Retinal and choroidal neovascularization.* J Cell Physiol, 2000. **184**(3): p. 301-10.

48. Schiaffino, M.V., *Signaling pathways in melanosome biogenesis and pathology.* Int J Biochem Cell Biol, 2010. **42**(7): p. 1094-104.

49. Summers, C.G., *Vision in albinism.* Trans Am Ophthalmol Soc, 1996. **94**: p. 1095-155.

50. Boulton, M.E., *Studying melanin and lipofuscin in RPE cell culture models.* Exp Eye Res, 2014. **126**: p. 61-7.

51. Kinnear, P.E., B. Jay, and C.J. Witkop, Jr., *Albinism.* Surv Ophthalmol, 1985. **30**(2): p. 75-101.

52. Rozanowska, M., *Properties and Functions of Ocular Melanins and Melanosomes.* Melanins and Melanosomes: Biosynthesis, Biogenesis, Physiological, and Pathological Functions, 2011: p. 187-224.

53. Riley, P.A., *Melanins and melanogenesis.* Pathobiol Annu, 1980. **10**: p. 223-51.

54. Mason, H.S., *The chemistry of melanin; mechanism of the oxidation of dihydroxyphenylalanine by tyrosinase.* J Biol Chem, 1948. **172**(1): p. 83-99.

55. Oetting, W.S. and R.A. King, *Molecular basis of albinism: mutations and polymorphisms of pigmentation genes associated with albinism.* Hum Mutat, 1999. **13**(2): p. 99-115.

56. Sarna, T., et al., *Loss of melanin from human RPE with aging: possible role of melanin photooxidation.* Exp Eye Res, 2003. **76**(1): p. 89-98.

57. Raposo, G. and M.S. Marks, *The dark side of lysosome-related organelles: specialization of the endocytic pathway for melanosome biogenesis.* Traffic, 2002. **3**(4): p. 237-48.

58. Beatty, S., et al., *The role of oxidative stress in the pathogenesis of age-related macular degeneration.* Surv Ophthalmol, 2000. **45**(2): p. 115-34.

59. Miceli, M.V., M.R. Liles, and D.A. Newsome, *Evaluation of oxidative processes in human pigment epithelial cells associated with retinal outer segment phagocytosis.* Exp Cell Res, 1994. **214**(1): p. 242-9.

60. Foltz, L.P. and D.O. Clegg, *Rapid, Directed Differentiation of Retinal Pigment Epithelial Cells from Human Embryonic or Induced Pluripotent Stem Cells.* J Vis Exp, 2017(128).

61. Choudhary, P., et al., *Directing Differentiation of Pluripotent Stem Cells Toward Retinal Pigment Epithelium Lineage.* Stem Cells Transl Med, 2017. **6**(2): p. 490-501.

62. Wong, W.L., et al., *Global prevalence of age-related macular degeneration and disease burden projection for 2020 and 2040: a systematic review and meta-analysis.* Lancet Glob Health, 2014. **2**(2): p. e106-16.

63. Jonas, J.B., C.M.G. Cheung, and S. Panda-Jonas, *Updates on the Epidemiology of Age-Related Macular Degeneration.* Asia Pac J Ophthalmol (Phila), 2017. **6**(6): p. 493-497.

64. Gehrs, K.M., et al., *Age-related macular degeneration--emerging pathogenetic and therapeutic concepts.* Ann Med, 2006. **38**(7): p. 450-71.

65. Tolentino, M.J., et al., *Angiography of fluoresceinated anti-vascular endothelial growth factor antibody and dextrans in experimental choroidal neovascularization.* Arch Ophthalmol, 2000. **118**(1): p. 78-84.

66. Moshfeghi, A.A., et al., *Systemic bevacizumab (Avastin) therapy for neovascular age-related macular degeneration: twenty-four-week results of an uncontrolled open-label clinical study.* Ophthalmology, 2006. **113**(11): p. 2002 e1-12.

67. Heier, J.S., et al., *Pegcetacoplan for the treatment of geographic atrophy secondary to age-related macular degeneration (OAKS and DERBY): two multicentre, randomised, double-masked, sham-controlled, phase 3 trials.* Lancet, 2023. **402**(10411): p. 1434-1448.

68. Khanani, A.M., et al., *Efficacy and safety of avacincaptad pegol in patients with geographic atrophy (GATHER2): 12-month results from a randomised, double-masked, phase 3 trial.* Lancet, 2023. **402**(10411): p. 1449-1458.

69. Age-Related Eye Disease Study 2 Research, G., *Lutein + zeaxanthin and omega-3 fatty acids for age-related macular degeneration: the Age-Related Eye Disease Study 2 (AREDS2) randomized clinical trial.* JAMA, 2013. **309**(19): p. 2005-15.

70. Seddon, J.M., et al., *Rare variants in CFI, C3 and C9 are associated with high risk of advanced age-related macular degeneration.* Nat Genet, 2013. **45**(11): p. 1366-70.

71. Fritsche, L.G., et al., *A large genome-wide association study of age-related macular degeneration highlights contributions of rare and common variants.* Nat Genet, 2016. **48**(2): p. 134-43.

72. Vingerling, J.R., et al., *Age-related macular degeneration and smoking. The Rotterdam Study.* Arch Ophthalmol, 1996. **114**(10): p. 1193-6.

73. Smith, W., et al., *Risk factors for age-related macular degeneration: Pooled findings from three continents.* Ophthalmology, 2001. **108**(4): p. 697-704.

74. Mitchell, P., et al., *Smoking and the 5-year incidence of age-related maculopathy: the Blue Mountains Eye Study.* Arch Ophthalmol, 2002. **120**(10): p. 1357-63.

75. Green, W.R., *Histopathology of age-related macular degeneration.* Mol Vis, 1999. **5**: p. 27.

76. Li, C.M., et al., *Distribution and composition of esterified and unesterified cholesterol in extra-macular drusen.* Exp Eye Res, 2007. **85**(2): p. 192-201.

77. Rudolf, M., et al., *Prevalence and morphology of druse types in the macula and periphery of eyes with age-related maculopathy.* Invest Ophthalmol Vis Sci, 2008. **49**(3): p. 1200-9.

78. Curcio, C.A., et al., *Aging, age-related macular degeneration, and the response-to-retention of apolipoprotein B-containing lipoproteins.* Prog Retin Eye Res, 2009. **28**(6): p. 393-422.

79. McLeod, D.S., et al., *Relationship between RPE and choriocapillaris in age-related macular degeneration.* Invest Ophthalmol Vis Sci, 2009. **50**(10): p. 4982-91.

80. Sohn, E.H., et al., *Choriocapillaris Degeneration in Geographic Atrophy.* Am J Pathol, 2019. **189**(7): p. 1473-1480.

81. Wang, D.G., et al., *Large-scale identification, mapping, and genotyping of single-nucleotide polymorphisms in the human genome.* Science, 1998. **280**(5366): p. 1077-82.

82. Klein, R., et al., *Risk alleles in CFH and ARMS2 and the long-term natural history of age-related macular degeneration: the Beaver Dam Eye Study.* JAMA Ophthalmol, 2013. **131**(3): p. 383-92.

83. Fritsche, L.G., et al., *Age-related macular degeneration is associated with an unstable ARMS2 (LOC387715) mRNA.* Nat Genet, 2008. **40**(7): p. 892-6.

84. Ryoo, N.K., et al., *Thickness of retina and choroid in the elderly population and its association with Complement Factor H polymorphism: KLoSHA Eye study.* PLoS One, 2018. **13**(12): p. e0209276.

85. Rivera, A., et al., *Hypothetical LOC387715 is a second major susceptibility gene for age-related macular degeneration, contributing independently of complement factor H to disease risk.* Hum Mol Genet, 2005. **14**(21): p. 3227-36.

86. Strunz, T., et al., *A transcriptome-wide association study based on 27 tissues identifies 106 genes potentially relevant for disease pathology in age-related macular degeneration.* Sci Rep, 2020. **10**(1): p. 1584.

87. Lauwen, S., et al., *Increased pro-MMP9 plasma levels are associated with neovascular age-related macular degeneration and with the risk allele of rs142450006 near MMP9.* Mol Vis, 2021. **27**: p. 142-150.

88. Peters, F., et al., *Regulation of ABCA1 by AMD-Associated Genetic Variants and Hypoxia in iPSC-RPE.* Int J Mol Sci, 2022. **23**(6).

89. Strunz, T., et al., *Learning from Fifteen Years of Genome-Wide Association Studies in Age-Related Macular Degeneration.* Cells, 2020. **9**(10).

90. Tucker, B.A., et al., *Exome sequencing and analysis of induced pluripotent stem cells identify the cilia-related gene male germ cell-associated kinase (MAK) as a cause of retinitis pigmentosa.* Proc Natl Acad Sci U S A, 2011. **108**(34): p. E569-76.

91. Gallagher, M.D. and A.S. Chen-Plotkin, *The Post-GWAS Era: From Association to Function.* Am J Hum Genet, 2018. **102**(5): p. 717-730.

92. Gusev, A., et al., *Partitioning heritability of regulatory and cell-type-specific variants across 11 common diseases.* Am J Hum Genet, 2014. **95**(5): p. 535-52.

93. Maurano, M.T., et al., *Systematic localization of common disease-associated variation in regulatory DNA.* Science, 2012. **337**(6099): p. 1190-5.

94. Visscher, P.M., et al., *10 Years of GWAS Discovery: Biology, Function, and Translation.* Am J Hum Genet, 2017. **101**(1): p. 5-22.

95. Strohmeyer, T., et al., *Correlation between retinoblastoma gene expression and differentiation in human testicular tumors.* Proc Natl Acad Sci U S A, 1991. **88**(15): p. 6662-6.

96. Hu, J. and D. Bok, *A cell culture medium that supports the differentiation of human retinal pigment epithelium into functionally polarized monolayers.* Mol Vis, 2001. **7**: p. 14-9.

97. Limnios, I.J., et al., *Efficient differentiation of human embryonic stem cells to retinal pigment epithelium under defined conditions.* Stem Cell Res Ther, 2021. **12**(1): p. 248.

98. Buchholz, D.E., et al., *Derivation of functional retinal pigmented epithelium from induced pluripotent stem cells.* Stem Cells, 2009. **27**(10): p. 2427-34.

99. Kim, S., et al., *Generation, transcriptome profiling, and functional validation of cone-rich human retinal organoids.* Proc Natl Acad Sci U S A, 2019. **116**(22): p. 10824-10833.

100. Westra, H.J. and L. Franke, *From genome to function by studying eQTLs.* Biochim Biophys Acta, 2014. **1842**(10): p. 1896-1902.

101. Gusev, A., et al., *Integrative approaches for large-scale transcriptome-wide association studies.* Nat Genet, 2016. **48**(3): p. 245-52.

102. Orozco, L.D., et al., *Integration of eQTL and a Single-Cell Atlas in the Human Eye Identifies Causal Genes for Age-Related Macular Degeneration.* Cell Rep, 2020. **30**(4): p. 1246-1259 e6.

103. Ratnapriya, R., et al., *Retinal transcriptome and eQTL analyses identify genes associated with age-related macular degeneration.* Nat Genet, 2019. **51**(4): p. 606-610.

104. Hogan, M.J., *Macular Diseases: Pathogenesis. Electron Microscopy of Bruch's Membrane.* Trans Am Acad Ophthalmol Otolaryngol, 1965. **69**: p. 683-90.

105. Hogan, M.J., *Role of the retinal pigment epithelium in macular disease.* Trans Am Acad Ophthalmol Otolaryngol, 1972. **76**(1): p. 64-80.

106. Sarks, S.H., *Ageing and degeneration in the macular region: a clinico-pathological study.* Br J Ophthalmol, 1976. **60**(5): p. 324-41.

107. Sarks, J.P., S.H. Sarks, and M.C. Killingsworth, *Evolution of geographic atrophy of the retinal pigment epithelium.* Eye (Lond), 1988. **2 (Pt 5)**: p. 552-77.

108. Cha, J. and I. Lee, *Single-cell network biology for resolving cellular heterogeneity in human diseases.* Exp Mol Med, 2020. **52**(11): p. 1798-1808.

109. Reppert, N. and T. Lang, *A conserved sequence in the small intracellular loop of tetraspanins forms an M-shaped inter-helix turn.* Scientific Reports, 2022. **12**(1): p. 4494.

110. Felbor, U., H. Schilling, and B.H. Weber, *Adult vitelliform macular dystrophy is frequently associated with mutations in the peripherin/RDS gene.* Hum Mutat, 1997. **10**(4): p. 301-9.

111. Dryja, T.P., et al., *Dominant and digenic mutations in the peripherin/RDS and ROM1 genes in retinitis pigmentosa.* Invest Ophthalmol Vis Sci, 1997. **38**(10): p. 1972-82.

112. Haining, E.J., et al., *The TspanC8 subgroup of tetraspanins interacts with A disintegrin and metalloprotease 10 (ADAM10) and regulates its maturation and cell surface expression.* J Biol Chem, 2012. **287**(47): p. 39753-65.

113. Dornier, E., et al., *TspanC8 tetraspanins regulate ADAM10/Kuzbanian trafficking and promote Notch activation in flies and mammals.* J Cell Biol, 2012. **199**(3): p. 481-96.

114. Prox, J., et al., *Tetraspanin15 regulates cellular trafficking and activity of the ectodomain sheddase ADAM10.* Cell Mol Life Sci, 2012. **69**(17): p. 2919-32.

115. Zhou, J., et al., *Downregulation of Notch modulators, tetraspanin 5 and 10, inhibits osteoclastogenesis in vitro.* Calcif Tissue Int, 2014. **95**(3): p. 209-217.

116. Atlas, H.P.; Available from: proteinatlas.org.

117. Uhlen, M., et al., *Towards a knowledge-based Human Protein Atlas.* Nat Biotechnol, 2010. **28**(12): p. 1248-50.

118. Takahashi, H., et al., *5' end-centered expression profiling using cap-analysis gene expression and next-generation sequencing.* Nat Protoc, 2012. **7**(3): p. 542-61.

119. Wistow, G., et al., *Expressed sequence tag analysis of human RPE/choroid for the NEIBank Project: over 6000 non-redundant transcripts, novel genes and splice variants.* Mol Vis, 2002. **8**: p. 205-20.

120. Mullins, J.J., *https://singlecell-eye.com/.* 2020.

121. Seong, I., et al., *Sox10 controls migration of B16F10 melanoma cells through multiple regulatory target genes.* PLoS One, 2012. **7**(2): p. e31477.

122. Gao, X., et al., *Screening of tumor grade-related mRNAs and lncRNAs for Esophagus Squamous Cell Carcinoma.* J Clin Lab Anal, 2021. **35**(6): p. e23797.

123. Saint-Pol, J., et al., *Regulation of the trafficking and the function of the metalloprotease ADAM10 by tetraspanins.* Biochem Soc Trans, 2017. **45**(4): p. 937-44.

124. Shah, R.L., et al., *Genome-wide association studies for corneal and refractive astigmatism in UK Biobank demonstrate a shared role for myopia susceptibility loci.* Hum Genet, 2018. **137**(11-12): p. 881-896.

125. Plotnikov, D., et al., *A commonly occurring genetic variant within the NPLOC4-TSPAN10-PDE6G gene cluster is associated with the risk of strabismus.* Hum Genet, 2019. **138**(7): p. 723-737.

126. Currant, H., et al., *Genetic variation affects morphological retinal phenotypes extracted from UK Biobank optical coherence tomography images.* PLoS Genet, 2021. **17**(5): p. e1009497.

127. Morgan, M.D., et al., *Genome-wide study of hair colour in UK Biobank explains most of the SNP heritability.* Nat Commun, 2018. **9**(1): p. 5271.

128. Hysi, P.G., et al., *Genome-wide association meta-analysis of individuals of European ancestry identifies new loci explaining a substantial fraction of hair color variation and heritability.* Nat Genet, 2018. **50**(5): p. 652-656.

129. Liu, F., et al., *Digital quantification of human eye color highlights genetic association of three new loci.* PLoS Genet, 2010. **6**(5): p. e1000934.

130. Simcoe, M., et al., *Genome-wide association study in almost 195,000 individuals identifies 50 previously unidentified genetic loci for eye color.* Sci Adv, 2021. **7**(11).

131. Schick, T., et al., *The Effect of Genetic Variants Associated With Age-Related Macular Degeneration Varies With Age.* Invest Ophthalmol Vis Sci, 2020. **61**(14): p. 17.

132. Jorissen, E., et al., *The disintegrin/metalloproteinase ADAM10 is essential for the establishment of the brain cortex.* J Neurosci, 2010. **30**(14): p. 4833-44.

133. Weber, S., et al., *The disintegrin/metalloproteinase Adam10 is essential for epidermal integrity and Notch-mediated signaling.* Development, 2011. **138**(3): p. 495-505.

134. Tsai, Y.H., et al., *ADAM10 regulates Notch function in intestinal stem cells of mice.* Gastroenterology, 2014. **147**(4): p. 822-834 e13.

135. Tian, L., et al., *ADAM10 is essential for proteolytic activation of Notch during thymocyte development.* Int Immunol, 2008. **20**(9): p. 1181-7.

136. Glomski, K., et al., *Deletion of Adam10 in endothelial cells leads to defects in organ-specific vascular structures.* Blood, 2011. **118**(4): p. 1163-74.

137. Hartmann, D., et al., *The disintegrin/metalloprotease ADAM 10 is essential for Notch signalling but not for alpha-secretase activity in fibroblasts.* Hum Mol Genet, 2002. **11**(21): p. 2615-24.

138. Schouwey, K., et al., *RBP-Jkappa-dependent Notch signaling enhances retinal pigment epithelial cell proliferation in transgenic mice.* Oncogene, 2011. **30**(3): p. 313-22.

139. Ha, T., et al., *The Retinal Pigment Epithelium Is a Notch Signaling Niche in the Mouse Retina.* Cell Rep, 2017. **19**(2): p. 351-363.

140. Zhou, Y., et al., *Notch2 regulates BMP signaling and epithelial morphogenesis in the ciliary body of the mouse eye.* Proc Natl Acad Sci U S A, 2013. **110**(22): p. 8966-71.

141. Lu, Y., et al., *Molecular genetic response of Xiphophorus maculatus-X. couchianus interspecies hybrid skin to UVB exposure.* Comp Biochem Physiol C Toxicol Pharmacol, 2015. **178**: p. 86-92.

142. Liu, L., et al., *The inhibition of NOTCH2 reduces UVB-induced damage in retinal pigment epithelium cells.* Mol Med Rep, 2017. **16**(1): p. 730-736.

143. Liu, W., et al., *Blockage of Notch signaling inhibits the migration and proliferation of retinal pigment epithelial cells.* ScientificWorldJournal, 2013. **2013**: p. 178708.

144. Kandpal, R.P., et al., *Transcriptome analysis using next generation sequencing reveals molecular signatures of diabetic retinopathy and efficacy of candidate drugs.* Mol Vis, 2012. **18**: p. 1123-46.

145. Ishikawa, K., et al., *Microarray analysis of gene expression in fibrovascular membranes excised from patients with proliferative diabetic retinopathy.* Invest Ophthalmol Vis Sci, 2015. **56**(2): p. 932-46.

146. Szklarczyk, D., et al., *The STRING database in 2021: customizable protein-protein networks, and functional characterization of user-uploaded gene/measurement sets (vol 49, pg D605, 2021).* Nucleic Acids Research, 2021. **49**(18): p. 10800-10800.

147. Azadi, S., L.L. Molday, and R.S. Molday, *RD3, the protein associated with Leber congenital amaurosis type 12, is required for guanylate cyclase trafficking in photoreceptor cells.* Proc Natl Acad Sci U S A, 2010. **107**(49): p. 21158-63.

148. Chang, B., et al., *New mouse primary retinal degeneration (rd-3).* Genomics, 1993. **16**(1): p. 45-9.

149. UniProt, C., *UniProt: the universal protein knowledgebase in 2021.* Nucleic Acids Res, 2021. **49**(D1): p. D480-D489.

150. Kaye, R.A., et al., *Macular thickness varies with age-related macular degeneration genetic risk variants in the UK Biobank cohort.* Sci Rep, 2021. **11**(1): p. 23255.

151. Hannah Currant, P.H., Tomas W Fitzgerald...Anthony P Khawaja et al, *Genetic variation affects morphological retinal phenotypes extracted from UK Biobank Optical Coherence Tomography images*, in *medRxiv*. 2020.

152. Dunn, K.C., et al., *ARPE-19, a human retinal pigment epithelial cell line with differentiated properties.* Exp Eye Res, 1996. **62**(2): p. 155-69.

153. Bhutto, I. and G. Lutty, *Understanding age-related macular degeneration (AMD): relationships between the photoreceptor/retinal pigment epithelium/Bruch's membrane/choriocapillaris complex.* Mol Aspects Med, 2012. **33**(4): p. 295-317.

154. Kay, P., Y.C. Yang, and L. Paraoan, *Directional protein secretion by the retinal pigment epithelium: roles in retinal health and the development of age-related macular degeneration.* J Cell Mol Med, 2013. **17**(7): p. 833-43.

155. Paraoan, L., et al., *Secretory proteostasis of the retinal pigmented epithelium: Impairment links to age-related macular degeneration.* Prog Retin Eye Res, 2020. **79**: p. 100859.

156. Benedicto, I., et al., *Concerted regulation of retinal pigment epithelium basement membrane and barrier function by angiocrine factors.* Nat Commun, 2017. **8**: p. 15374.

157. Klingeborn, M., et al., *Directional Exosome Proteomes Reflect Polarity-Specific Functions in Retinal Pigmented Epithelium Monolayers.* Sci Rep, 2017. **7**(1): p. 4901.

158. Lynn, S.A., et al., *Ex-vivo models of the Retinal Pigment Epithelium (RPE) in long-term culture faithfully recapitulate key structural and physiological features of native RPE.* Tissue Cell, 2017. **49**(4): p. 447-460.

159. Beebe, D.C., *The use of cell lines to "model" ocular tissues: cautionary tales.* Invest Ophthalmol Vis Sci, 2013. **54**(8).

160. Nabi, I.R., et al., *Immortalization of polarized rat retinal pigment epithelium.* J Cell Sci, 1993. **104 (Pt 1)**: p. 37-49.

161. Fasler-Kan, E., et al., *The Retinal Pigment Epithelial Cell Line (ARPE-19) Displays Mosaic Structural Chromosomal Aberrations.* Methods Mol Biol, 2018. **1745**: p. 305-314.

162. Hazim, R.A., et al., *Rapid differentiation of the human RPE cell line, ARPE-19, induced by nicotinamide.* Exp Eye Res, 2019. **179**: p. 18-24.

163. Kuznetsova, A.V., A.M. Kurinov, and M.A. Aleksandrova, *Cell models to study regulation of cell transformation in pathologies of retinal pigment epithelium.* J Ophthalmol, 2014. **2014**: p. 801787.

164. Sharma, R., et al., *Epithelial phenotype restoring drugs suppress macular degeneration phenotypes in an iPSC model.* Nat Commun, 2021. **12**(1): p. 7293.

165. Carr, A.J., et al., *Molecular characterization and functional analysis of phagocytosis by human embryonic stem cell-derived RPE cells using a novel human retinal assay.* Mol Vis, 2009. **15**: p. 283-95.

166. Thomson, J.A., et al., *Embryonic stem cell lines derived from human blastocysts.* Science, 1998. **282**(5391): p. 1145-7.

167. Amit, M., et al., *Clonally derived human embryonic stem cell lines maintain pluripotency and proliferative potential for prolonged periods of culture.* Dev Biol, 2000. **227**(2): p. 271-8.

168. Peng, S., et al., *Engineering a blood-retinal barrier with human embryonic stem cell-derived retinal pigment epithelium: transcriptome and functional analysis.* Stem Cells Transl Med, 2013. **2**(7): p. 534-44.

169. Hongisto, H., et al., *Comparative proteomic analysis of human embryonic stem cell-derived and primary human retinal pigment epithelium.* Sci Rep, 2017. **7**(1): p. 6016.

170. Petrus-Reurer, S., et al., *Molecular profiling of stem cell-derived retinal pigment epithelial cell differentiation established for clinical translation.* Stem Cell Reports, 2022. **17**(6): p. 1458-1475.

171. Vaajasaari, H., et al., *Toward the defined and xeno-free differentiation of functional human pluripotent stem cell-derived retinal pigment epithelial cells.* Mol Vis, 2011. **17**: p. 558-75.

172. Onnela, N., et al., *Electric impedance of human embryonic stem cell-derived retinal pigment epithelium.* Med Biol Eng Comput, 2012. **50**(2): p. 107-16.

173. Juuti-Uusitalo, K., et al., *Efflux protein expression in human stem cell-derived retinal pigment epithelial cells.* PLoS One, 2012. **7**(1): p. e30089.

174. Savolainen, V., et al., *Impedance spectroscopy in monitoring the maturation of stem cell-derived retinal pigment epithelium.* Ann Biomed Eng, 2011. **39**(12): p. 3055-69.

175. Takahashi, K. and S. Yamanaka, *Induction of pluripotent stem cells from mouse embryonic and adult fibroblast cultures by defined factors.* Cell, 2006. **126**(4): p. 663-76.

176. Saini, J.S., et al., *Nicotinamide Ameliorates Disease Phenotypes in a Human iPSC Model of Age-Related Macular Degeneration.* Cell Stem Cell, 2017. **20**(5): p. 635-647 e7.

177. Chang, Y.C., et al., *The generation of induced pluripotent stem cells for macular degeneration as a drug screening platform: identification of curcumin as a protective agent for retinal pigment epithelial cells against oxidative stress.* Front Aging Neurosci, 2014. **6**: p. 191.

178. Hallam, D., et al., *An Induced Pluripotent Stem Cell Patient Specific Model of Complement Factor H (Y402H) Polymorphism Displays Characteristic Features of Age-Related Macular Degeneration and Indicates a Beneficial Role for UV Light Exposure.* Stem Cells, 2017. **35**(11): p. 2305-2320.

179. Yang, J., et al., *Validation of genome-wide association study (GWAS)-identified disease risk alleles with patient-specific stem cell lines.* Hum Mol Genet, 2014. **23**(13): p. 3445-55.

180. Golestaneh, N., et al., *Repressed SIRT1/PGC-1alpha pathway and mitochondrial disintegration in iPSC-derived RPE disease model of age-related macular degeneration.* J Transl Med, 2016. **14**(1): p. 344.

181. Cipriani, V., et al., *Increased circulating levels of Factor H-Related Protein 4 are strongly associated with age-related macular degeneration.* Nat Commun, 2020. **11**(1): p. 778.

182. Barabino, A., et al., *Deregulation of Neuro-Developmental Genes and Primary Cilium Cytoskeleton Anomalies in iPSC Retinal Sheets from Human Syndromic Ciliopathies.* Stem Cell Reports, 2020. **14**(3): p. 357-373.

183. Lamba, D.A., et al., *Efficient generation of retinal progenitor cells from human embryonic stem cells.* Proc Natl Acad Sci U S A, 2006. **103**(34): p. 12769-74.

184. Guillemot, F. and C.L. Cepko, *Retinal fate and ganglion cell differentiation are potentiated by acidic FGF in an in vitro assay of early retinal development.* Development, 1992. **114**(3): p. 743-54.

185. Kuwahara, A., et al., *Generation of a ciliary margin-like stem cell niche from self-organizing human retinal tissue.* Nat Commun, 2015. **6**: p. 6286.

186. Leach, L.L., et al., *Induced Pluripotent Stem Cell-Derived Retinal Pigmented Epithelium: A Comparative Study Between Cell Lines and Differentiation Methods.* J Ocul Pharmacol Ther, 2016. **32**(5): p. 317-30.

187. Fujimura, N., et al., *Spatial and temporal regulation of Wnt/beta-catenin signaling is essential for development of the retinal pigment epithelium.* Dev Biol, 2009. **334**(1): p. 31-45.

188. Westenskow, P., S. Piccolo, and S. Fuhrmann, *Beta-catenin controls differentiation of the retinal pigment epithelium in the mouse optic cup by regulating Mitf and Otx2 expression.* Development, 2009. **136**(15): p. 2505-10.

189. Barrangou, R., et al., *CRISPR provides acquired resistance against viruses in prokaryotes.* Science, 2007. **315**(5819): p. 1709-12.

190. Wiedenheft, B., S.H. Sternberg, and J.A. Doudna, *RNA-guided genetic silencing systems in bacteria and archaea.* Nature, 2012. **482**(7385): p. 331-8.

191. Jinek, M., et al., *A programmable dual-RNA-guided DNA endonuclease in adaptive bacterial immunity.* Science, 2012. **337**(6096): p. 816-21.

192. Doudna, J.A. and E. Charpentier, *Genome editing. The new frontier of genome engineering with CRISPR-Cas9.* Science, 2014. **346**(6213): p. 1258096.

193. Liu, Y., et al., *In Vitro CRISPR/Cas9 System for Efficient Targeted DNA Editing.* mBio, 2015. **6**(6): p. e01714-15.

194. Ran, F.A., et al., *Double nicking by RNA-guided CRISPR Cas9 for enhanced genome editing specificity.* Cell, 2013. **154**(6): p. 1380-9.

195. Miyaoka, Y., et al., *Systematic quantification of HDR and NHEJ reveals effects of locus, nuclease, and cell type on genome-editing.* Sci Rep, 2016. **6**: p. 23549.

196. Schwank, G., et al., *Functional repair of CFTR by CRISPR/Cas9 in intestinal stem cell organoids of cystic fibrosis patients.* Cell Stem Cell, 2013. **13**(6): p. 653-8.

197. Sander, J.D. and J.K. Joung, *CRISPR-Cas systems for editing, regulating and targeting genomes.* Nat Biotechnol, 2014. **32**(4): p. 347-55.

198. Gaj, T., C.A. Gersbach, and C.F. Barbas, 3rd, *ZFN, TALEN, and CRISPR/Cas-based methods for genome engineering.* Trends Biotechnol, 2013. **31**(7): p. 397-405.

199. Gupta, R.M. and K. Musunuru, *Expanding the genetic editing tool kit: ZFNs, TALENs, and CRISPR-Cas9.* J Clin Invest, 2014. **124**(10): p. 4154-61.

200. Anderson, K.R., et al., *CRISPR off-target analysis in genetically engineered rats and mice.* Nat Methods, 2018. **15**(7): p. 512-514.

201. Hsu, P.D., et al., *DNA targeting specificity of RNA-guided Cas9 nucleases.* Nat Biotechnol, 2013. **31**(9): p. 827-32.

202. Cho, S.W., et al., *Analysis of off-target effects of CRISPR/Cas-derived RNA-guided endonucleases and nickases.* Genome Res, 2014. **24**(1): p. 132-41.

203. Doench, J.G., et al., *Optimized sgRNA design to maximize activity and minimize off-target effects of CRISPR-Cas9.* Nat Biotechnol, 2016. **34**(2): p. 184-191.

204. Montague, T.G., et al., *CHOPCHOP: a CRISPR/Cas9 and TALEN web tool for genome editing.* Nucleic Acids Res, 2014. **42**(Web Server issue): p. W401-7.

205. Wang, T., et al., *Genetic screens in human cells using the CRISPR-Cas9 system.* Science, 2014. **343**(6166): p. 80-4.

206. Thyme, S.B., et al., *Internal guide RNA interactions interfere with Cas9-mediated cleavage.* Nat Commun, 2016. **7**: p. 11750.

207. Benchling, [Biology Software], 2020.

208. Labun, K., et al., *CHOPCHOP v3: expanding the CRISPR web toolbox beyond genome editing.* Nucleic Acids Res, 2019. **47**(W1): p. W171-W174.

209. Labun, K., et al., *CRISPR Genome Editing Made Easy Through the CHOPCHOP Website.* Curr Protoc, 2021. **1**(4): p. e46.

210. Concordet, J.P. and M. Haeussler, *CRISPOR: intuitive guide selection for CRISPR/Cas9 genome editing experiments and screens.* Nucleic Acids Res, 2018. **46**(W1): p. W242-W245.

211. Thermann, R., et al., *Binary specification of nonsense codons by splicing and cytoplasmic translation.* EMBO J, 1998. **17**(12): p. 3484-94.

212. Le Hir, H., et al., *The exon-exon junction complex provides a binding platform for factors involved in mRNA export and nonsense-mediated mRNA decay.* EMBO J, 2001. **20**(17): p. 4987-97.

213. Nagy, E. and L.E. Maquat, *A rule for termination-codon position within intron-containing genes: when nonsense affects RNA abundance.* Trends Biochem Sci, 1998. **23**(6): p. 198-9.

214. Le Hir, H., J. Sauliere, and Z. Wang, *The exon junction complex as a node of post-transcriptional networks.* Nat Rev Mol Cell Biol, 2016. **17**(1): p. 41-54.

215. Bae, S., J. Park, and J.S. Kim, *Cas-OFFinder: a fast and versatile algorithm that searches for potential off-target sites of Cas9 RNA-guided endonucleases.* Bioinformatics, 2014. **30**(10): p. 1473-5.

216. Liu, X., et al., *Sequence features associated with the cleavage efficiency of CRISPR/Cas9 system.* Sci Rep, 2016. **6**: p. 19675.

217. Doench, J.G., et al., *Rational design of highly active sgRNAs for CRISPR-Cas9-mediated gene inactivation.* Nat Biotechnol, 2014. **32**(12): p. 1262-7.

218. Nazlamova, L., et al., *Generation of a Cone Photoreceptor-specific GNGT2 Reporter Line in Human Pluripotent Stem Cells.* Stem Cells, 2022. **40**(2): p. 190-203.

219. Untergasser, A., et al., *Primer3--new capabilities and interfaces.* Nucleic Acids Res, 2012. **40**(15): p. e115.

220. Koressaar, T. and M. Remm, *Enhancements and modifications of primer design program Primer3.* Bioinformatics, 2007. **23**(10): p. 1289-91.

221. Koressaar, T., et al., *Primer3_masker: integrating masking of template sequence with primer design software.* Bioinformatics, 2018. **34**(11): p. 1937-1938.

222. Synthego, I.A., *https://ice.synthego.com/#/.*

223. Vukicevic, S., et al., *Identification of multiple active growth factors in basement membrane Matrigel suggests caution in interpretation of cellular activity related to extracellular matrix components.* Exp Cell Res, 1992. **202**(1): p. 1-8.

224. Sharma, R., et al., *Triphasic developmentally guided protocol to generate retinal pigment epithelium from induced pluripotent stem cells.* STAR Protoc, 2022. **3**(3): p. 101582.

225. Love, M.I., W. Huber, and S. Anders, *Moderated estimation of fold change and dispersion for RNA-seq data with DESeq2.* Genome Biol, 2014. **15**(12): p. 550.

226. Bray, N.L., et al., *Near-optimal probabilistic RNA-seq quantification.* Nat Biotechnol, 2016. **34**(5): p. 525-7.

227. Soneson, C., M.I. Love, and M.D. Robinson, *Differential analyses for RNA-seq: transcript-level estimates improve gene-level inferences.* F1000Res, 2015. **4**: p. 1521.

228. Livak, K.J. and T.D. Schmittgen, *Analysis of relative gene expression data using real-time quantitative PCR and the 2(-Delta Delta C(T)) Method.* Methods, 2001. **25**(4): p. 402-8.

229. Ratnayaka, J.A., E. Keeling, and D.S. Chatelet, *Study of Intracellular Cargo Trafficking and Co-localization in the Phagosome and Autophagy-Lysosomal Pathways of Retinal Pigment Epithelium (RPE) Cells.* Methods Mol Biol, 2020. **2150**: p. 167-182.

230. Hall, M.A., Toshka, *Kinetic Studies of Rod Outer Segment Binding and Ingestion by Cultured Rat RPE Cells.* Experimental Eye Research, 1987. **45**: p. 907-922.

231. Keeling, E., et al., *Oxidative Stress and Dysfunctional Intracellular Traffic Linked to an Unhealthy Diet Results in Impaired Cargo Transport in the Retinal Pigment Epithelium (RPE).* Mol Nutr Food Res, 2019. **63**(15): p. e1800951.

232. Krohne, T.U., et al., *Effects of lipid peroxidation products on lipofuscinogenesis and autophagy in human retinal pigment epithelial cells.* Experimental Eye Research, 2010. **90**(3): p. 465-471.

233. Costes, S.V., et al., *Automatic and quantitative measurement of protein-protein colocalization in live cells.* Biophys J, 2004. **86**(6): p. 3993-4003.

234. Bycroft, C., et al., *The UK Biobank resource with deep phenotyping and genomic data.* Nature, 2018. **562**(7726): p. 203-209.

235. Chua, S.Y.L., et al., *Associations with photoreceptor thickness measures in the UK Biobank.* Sci Rep, 2019. **9**(1): p. 19440.

236. Ko, F., et al., *Associations with Retinal Pigment Epithelium Thickness Measures in a Large Cohort: Results from the UK Biobank.* Ophthalmology, 2017. **124**(1): p. 105-117.

237. Chua, S.Y.L., et al., *Cohort profile: design and methods in the eye and vision consortium of UK Biobank.* BMJ Open, 2019. **9**(2): p. e025077.

238. Keane, P.A., et al., *Optical Coherence Tomography in the UK Biobank Study - Rapid Automated Analysis of Retinal Thickness for Large Population-Based Studies.* PLoS One, 2016. **11**(10): p. e0164095.

239. Fritsche, L.G., et al., *Seven new loci associated with age-related macular degeneration.* Nat Genet, 2013. **45**(4): p. 433-9, 439e1-2.

240. Zouache, M.A., et al., *Macular retinal thickness differs markedly in age-related macular degeneration driven by risk polymorphisms on chromosomes 1 and 10.* Sci Rep, 2020. **10**(1): p. 21093.

241. Oeverhaus, M., et al., *Genetic Polymorphisms and the Phenotypic Characterization of Individuals with Early Age-Related Macular Degeneration.* Ophthalmologica, 2017. **238**(1-2): p. 6-16.

242. Yang, Q., et al., *Automated segmentation of outer retinal layers in macular OCT images of patients with retinitis pigmentosa.* Biomed Opt Express, 2011. **2**(9): p. 2493-503.

243. Sudlow, C., et al., *UK Biobank: An Open Access Resource for Identifying the Causes of a Wide Range of Complex Diseases of Middle and Old Age.* Plos Medicine, 2015. **12**(3).

244. Allen, N., et al., *UK Biobank: Current status and what it means for epidemiology.* Health Policy and Technology, 2012. **1**(3): p. 123-126.

245. Patel, P.J., et al., *Spectral-Domain Optical Coherence Tomography Imaging in 67 321 Adults: Associations with Macular Thickness in the UK Biobank Study.* Ophthalmology, 2016. **123**(4): p. 829-40.

246. Yang, Q., et al., *Automated layer segmentation of macular OCT images using dual-scale gradient information.* Opt Express, 2010. **18**(20): p. 21293-307.

247. Lawlor, D.A., et al., *Mendelian randomization: using genes as instruments for making causal inferences in epidemiology.* Stat Med, 2008. **27**(8): p. 1133-63.

248. Burgess, S., D.S. Small, and S.G. Thompson, *A review of instrumental variable estimators for Mendelian randomization.* Stat Methods Med Res, 2017. **26**(5): p. 2333-2355.

249. Zheng, J., et al., *Recent Developments in Mendelian Randomization Studies.* Curr Epidemiol Rep, 2017. **4**(4): p. 330-345.

250. Didelez, V. and N. Sheehan, *Mendelian randomization as an instrumental variable approach to causal inference.* Stat Methods Med Res, 2007. **16**(4): p. 309-30.

251. Bowden, J., G. Davey Smith, and S. Burgess, *Mendelian randomization with invalid instruments: effect estimation and bias detection through Egger regression.* Int J Epidemiol, 2015. **44**(2): p. 512-25.

252. Ooto, S., et al., *Effects of age, sex, and axial length on the three-dimensional profile of normal macular layer structures.* Invest Ophthalmol Vis Sci, 2011. **52**(12): p. 8769-79.

253. Tao, L.W., et al., *Ellipsoid zone on optical coherence tomography: a review.* Clin Exp Ophthalmol, 2016. **44**(5): p. 422-30.

254. Kamoshita, M., et al., *AMPK-NF-kappaB axis in the photoreceptor disorder during retinal inflammation.* PLoS One, 2014. **9**(7): p. e103013.

255. Nagai, N., et al., *Macular Pigment Optical Density and Photoreceptor Outer Segment Length as Predisease Biomarkers for Age-Related Macular Degeneration.* J Clin Med, 2020. **9**(5).

256. Lamin, A., et al., *Changes in volume of various retinal layers over time in early and intermediate age-related macular degeneration.* Eye (Lond), 2019. **33**(3): p. 428-434.

257. Mullins, R.F., et al., *The ARMS2 A69S Polymorphism Is Associated with Delayed Rod-Mediated Dark Adaptation in Eyes at Risk for Incident Age-Related Macular Degeneration.* Ophthalmology, 2019. **126**(4): p. 591-600.

258. Ramrattan, R.S., et al., *Morphometric analysis of Bruch's membrane, the choriocapillaris, and the choroid in aging.* Invest Ophthalmol Vis Sci, 1994. **35**(6): p. 2857-64.

259. Wang, X.Q. and J.A. Rothnagel, *5'-untranslated regions with multiple upstream AUG codons can support low-level translation via leaky scanning and reinitiation.* Nucleic Acids Res, 2004. **32**(4): p. 1382-91.

260. Girard, G., A.P. Gultyaev, and R.C. Olsthoorn, *Upstream start codon in segment 4 of North American H2 avian influenza A viruses.* Infect Genet Evol, 2011. **11**(2): p. 489-95.

261. Liu, J., et al., *Initiation of translation from a downstream in-frame AUG codon on BRCA1 can generate the novel isoform protein DeltaBRCA1(17aa).* Oncogene, 2000. **19**(23): p. 2767-73.

262. Kochetov, A.V., et al., *The role of alternative translation start sites in the generation of human protein diversity.* Mol Genet Genomics, 2005. **273**(6): p. 491-6.

263. Kearse, M.G. and J.E. Wilusz, *Non-AUG translation: a new start for protein synthesis in eukaryotes.* Genes Dev, 2017. **31**(17): p. 1717-1731.

264. Cohen, S., et al., *Antibiotics reduce the growth rate and differentiation of embryonic stem cell cultures.* Tissue Eng, 2006. **12**(7): p. 2025-30.

265. Ryu, A.H., et al., *Use antibiotics in cell culture with caution: genome-wide identification of antibiotic-induced changes in gene expression and regulation.* Sci Rep, 2017. **7**(1): p. 7533.

266. Adijanto, J., et al., *Microphthalmia-associated transcription factor (MITF) promotes differentiation of human retinal pigment epithelium (RPE) by regulating microRNAs-204/211 expression.* J Biol Chem, 2012. **287**(24): p. 20491-503.

267. Harrison, P.W., et al., *Ensembl 2024.* Nucleic Acids Res, 2024. **52**(D1): p. D891-D899.

268. Kent, W.J., et al., *The human genome browser at UCSC.* Genome Research, 2002. **12**(6): p. 996-1006.

269. Thorvaldsdottir, H., J.T. Robinson, and J.P. Mesirov, *Integrative Genomics Viewer (IGV): high-performance genomics data visualization and exploration.* Brief Bioinform, 2013. **14**(2): p. 178-92.

270. Robinson, J.T., et al., *Integrative genomics viewer.* Nat Biotechnol, 2011. **29**(1): p. 24-6.

271. Ashkenazy, H., et al., *ConSurf 2016: an improved methodology to estimate and visualize evolutionary conservation in macromolecules.* Nucleic Acids Res, 2016. **44**(W1): p. W344-50.

272. Ashkenazy, H., et al., *ConSurf 2010: calculating evolutionary conservation in sequence and structure of proteins and nucleic acids.* Nucleic Acids Res, 2010. **38**(Web Server issue): p. W529-33.

273. Celniker, G., et al., *ConSurf: Using Evolutionary Data to Raise Testable Hypotheses about Protein Function.* Israel Journal of Chemistry, 2013. **53**(3-4): p. 199-206.

274. Jumper, J., et al., *Highly accurate protein structure prediction with AlphaFold.* Nature, 2021. **596**(7873): p. 583-589.

275. Shin, H.Y., et al., *CRISPR/Cas9 targeting events cause complex deletions and insertions at 17 sites in the mouse genome.* Nat Commun, 2017. **8**: p. 15464.

276. Kosicki, M., K. Tomberg, and A. Bradley, *Repair of double-strand breaks induced by CRISPR-Cas9 leads to large deletions and complex rearrangements.* Nat Biotechnol, 2018. **36**(8): p. 765-771.

277. Cullot, G., et al., *CRISPR-Cas9 genome editing induces megabase-scale chromosomal truncations.* Nat Commun, 2019. **10**(1): p. 1136.

278. Yu, C., et al., *A 3-nucleotide deletion in the polypyrimidine tract of intron 7 of the DFNA5 gene causes nonsyndromic hearing impairment in a Chinese family.* Genomics, 2003. **82**(5): p. 575-9.

279. Tsai, S.Q., et al., *GUIDE-seq enables genome-wide profiling of off-target cleavage by CRISPR-Cas nucleases.* Nat Biotechnol, 2015. **33**(2): p. 187-197.

280. Ruby, K.M. and B. Zheng, *Gene targeting in a HUES line of human embryonic stem cells via electroporation.* Stem Cells, 2009. **27**(7): p. 1496-506.

281. Nommiste, B., et al., *Stem cell-derived retinal pigment epithelium transplantation for treatment of retinal disease.* Prog Brain Res, 2017. **231**: p. 225-244.

282. Lipper, C.H., et al., *Crystal structure of the Tspan15 LEL domain reveals a conserved ADAM10 binding site.* Structure, 2022. **30**(2): p. 206-214 e4.

283. Moiseyev, G., et al., *RPE65 is the isomerohydrolase in the retinoid visual cycle.* Proceedings of the National Academy of Sciences of the United States of America, 2005. **102**(35): p. 12413-12418.

284. Kamao, H., et al., *Characterization of human induced pluripotent stem cell-derived retinal pigment epithelium cell sheets aiming for clinical application.* Stem Cell Reports, 2014. **2**(2): p. 205-18.

285. Michelet, F., et al., *Rapid generation of purified human RPE from pluripotent stem cells using 2D cultures and lipoprotein uptake-based sorting.* Stem Cell Research & Therapy, 2020. **11**(1).

286. Al-Ani, A., et al., *In Vitro Maturation of Retinal Pigment Epithelium Is Essential for Maintaining High Expression of Key Functional Genes.* Int J Mol Sci, 2020. **21**(17).

287. Yamada, M., et al., *The tetraspanin CD151 regulates cell morphology and intracellular signaling on laminin-511.* FEBS J, 2008. **275**(13): p. 3335-51.

288. Joshi, R., et al., *Automated Measurement of Cobblestone Morphology for Characterizing Stem Cell Derived Retinal Pigment Epithelial Cell Cultures.* J Ocul Pharmacol Ther, 2016. **32**(5): p. 331-9.

289. Vugler, A., et al., *Elucidating the phenomenon of HESC-derived RPE: anatomy of cell genesis, expansion and retinal transplantation.* Exp Neurol, 2008. **214**(2): p. 347-61.

290. Galva, C., P. Artigas, and C. Gatto, *Nuclear Na+/K+-ATPase plays an active role in nucleoplasmic Ca2+ homeostasis.* J Cell Sci, 2012. **125**(Pt 24): p. 6137-47.

291. Chen, S., R. Einspanier, and J. Schoen, *Transepithelial electrical resistance (TEER): a functional parameter to monitor the quality of oviduct epithelial cells cultured on filter supports.* Histochem Cell Biol, 2015. **144**(5): p. 509-15.

292. Lo, C.M., C.R. Keese, and I. Giaever, *Cell-substrate contact: another factor may influence transepithelial electrical resistance of cell layers cultured on permeable filters.* Exp Cell Res, 1999. **250**(2): p. 576-80.

293. Srinivasan, B., et al., *TEER measurement techniques for in vitro barrier model systems.* J Lab Autom, 2015. **20**(2): p. 107-26.

294. Blenkinsop, T.A., et al., *Human Adult Retinal Pigment Epithelial Stem Cell-Derived RPE Monolayers Exhibit Key Physiological Characteristics of Native Tissue.* Invest Ophthalmol Vis Sci, 2015. **56**(12): p. 7085-99.

295. Terryn, C., et al., *Rapid method of quantification of tight-junction organization using image analysis.* Cytometry A, 2013. **83**(2): p. 235-41.

296. da Cruz, L., et al., *Phase 1 clinical study of an embryonic stem cell-derived retinal pigment epithelium patch in age-related macular degeneration.* Nat Biotechnol, 2018. **36**(4): p. 328-337.

297. Blaauwgeers, H.G., et al., *Polarized vascular endothelial growth factor secretion by human retinal pigment epithelium and localization of vascular endothelial growth factor receptors on the inner choriocapillaris. Evidence for a trophic paracrine relation.* Am J Pathol, 1999. **155**(2): p. 421-8.

298. Kokkinaki, M., N. Sahibzada, and N. Golestaneh, *Human induced pluripotent stem-derived retinal pigment epithelium (RPE) cells exhibit ion transport, membrane potential, polarized vascular endothelial growth factor secretion, and gene expression pattern similar to native RPE.* Stem Cells, 2011. **29**(5): p. 825-35.

299. Chen, L., et al., *Oxidative stress differentially impacts apical and basolateral secretion of angiogenic factors from human iPSC-derived retinal pigment epithelium cells.* Sci Rep, 2022. **12**(1): p. 12694.

300. Ohno-Matsui, K., et al., *Novel mechanism for age-related macular degeneration: an equilibrium shift between the angiogenesis factors VEGF and PEDF.* J Cell Physiol, 2001. **189**(3): p. 323-33.

301. Bhutto, I.A., et al., *Pigment epithelium-derived factor (PEDF) and vascular endothelial growth factor (VEGF) in aged human choroid and eyes with age-related macular degeneration.* Exp Eye Res, 2006. **82**(1): p. 99-110.

302. Haurigot, V., et al., *Long-term retinal PEDF overexpression prevents neovascularization in a murine adult model of retinopathy.* PLoS One, 2012. **7**(7): p. e41511.

303. Falk, T., R.T. Gonzalez, and S.J. Sherman, *The yin and yang of VEGF and PEDF: multifaceted neurotrophic factors and their potential in the treatment of Parkinson's Disease.* Int J Mol Sci, 2010. **11**(8): p. 2875-900.

304. Bonilha, V.L., *Age and disease-related structural changes in the retinal pigment epithelium.* Clin Ophthalmol, 2008. **2**(2): p. 413-24.

305. Koch, C.M., et al., *A Beginner's Guide to Analysis of RNA Sequencing Data.* Am J Respir Cell Mol Biol, 2018. **59**(2): p. 145-157.

306. Liles, M.R., D.A. Newsome, and P.D. Oliver, *Antioxidant enzymes in the aging human retinal pigment epithelium.* Arch Ophthalmol, 1991. **109**(9): p. 1285-8.

307. Lidgerwood, G.E., et al., *Transcriptomic Profiling of Human Pluripotent Stem Cell-derived Retinal Pigment Epithelium over Time.* Genomics Proteomics Bioinformatics, 2021. **19**(2): p. 223-242.

308. Salido, E.M. and V. Ramamurthy, *Proteoglycan IMPG2 Shapes the Interphotoreceptor Matrix and Modulates Vision.* J Neurosci, 2020. **40**(20): p. 4059-4072.

309. Subramanian, A., et al., *Gene set enrichment analysis: a knowledge-based approach for interpreting genome-wide expression profiles.* Proc Natl Acad Sci U S A, 2005. **102**(43): p. 15545-50.

310. Benjamini, Y. and Y. Hochberg, *Controlling the False Discovery Rate - a Practical and Powerful Approach to Multiple Testing.* Journal of the Royal Statistical Society Series B-Statistical Methodology, 1995. **57**(1): p. 289-300.

311. Liberzon, A., et al., *The Molecular Signatures Database (MSigDB) hallmark gene set collection.* Cell Syst, 2015. **1**(6): p. 417-425.

312. Voigt, A.P., et al., *Spectacle: An interactive resource for ocular single-cell RNA sequencing data analysis.* Exp Eye Res, 2020. **200**: p. 108204.

313. Ruhl, D.A., et al., *Synaptotagmin 17 controls neurite outgrowth and synaptic physiology via distinct cellular pathways.* Nat Commun, 2019. **10**(1): p. 3532.

314. Ashburner, M., et al., *Gene ontology: tool for the unification of biology. The Gene Ontology Consortium.* Nat Genet, 2000. **25**(1): p. 25-9.

315. The Gene Ontology, C., *The Gene Ontology Resource: 20 years and still GOing strong.* Nucleic Acids Res, 2019. **47**(D1): p. D330-D338.

316. Milacic, M., et al., *The Reactome Pathway Knowledgebase 2024.* Nucleic Acids Res, 2024. **52**(D1): p. D672-D678.

317. Cancer Genome Atlas Research, N., *Comprehensive genomic characterization defines human glioblastoma genes and core pathways.* Nature, 2008. **455**(7216): p. 1061-8.

318. Trocoli, A. and M. Djavaheri-Mergny, *The complex interplay between autophagy and NF-kappaB signaling pathways in cancer cells.* Am J Cancer Res, 2011. **1**(5): p. 629-49.

319. Golestaneh, N., et al., *Dysfunctional autophagy in RPE, a contributing factor in age-related macular degeneration.* Cell Death Dis, 2017. **8**(1): p. e2537.

320. Xin, Y., et al., *Association between NF-kB polymorphism and age-related macular degeneration in a high-altitude population.* PLoS One, 2021. **16**(6): p. e0251931.

321. Stelzer, G., et al., *The GeneCards Suite: From Gene Data Mining to Disease Genome Sequence Analyses.* Curr Protoc Bioinformatics, 2016. **54**: p. 1 30 1-1 30 33.

322. Safran, M., et al., *GeneCards Version 3: the human gene integrator.* Database (Oxford), 2010. **2010**: p. baq020.

323. Tokarz, P., K. Kaarniranta, and J. Blasiak, *Role of antioxidant enzymes and small molecular weight antioxidants in the pathogenesis of age-related macular degeneration (AMD).* Biogerontology, 2013. **14**(5): p. 461-82.

324. Leong, Y.C., et al., *Molecular pathology of Usher 1B patient-derived retinal organoids at single cell resolution.* Stem Cell Reports, 2022. **17**(11): p. 2421-2437.

325. Halliwell, B., M.V. Clement, and L.H. Long, *Hydrogen peroxide in the human body.* FEBS Lett, 2000. **486**(1): p. 10-3.

326. Chavrier, P., et al., *Localization of low molecular weight GTP binding proteins to exocytic and endocytic compartments.* Cell, 1990. **62**(2): p. 317-29.

327. Saftig, P. and J. Klumperman, *Lysosome biogenesis and lysosomal membrane proteins: trafficking meets function.* Nat Rev Mol Cell Biol, 2009. **10**(9): p. 623-35.

328. Mitter, S.K., et al., *Dysregulated autophagy in the RPE is associated with increased susceptibility to oxidative stress and AMD.* Autophagy, 2014. **10**(11): p. 1989-2005.

329. Ryhanen, T., et al., *Crosstalk between Hsp70 molecular chaperone, lysosomes and proteasomes in autophagy-mediated proteolysis in human retinal pigment epithelial cells.* J Cell Mol Med, 2009. **13**(9B): p. 3616-31.

330. Guerra, F. and C. Bucci, *Multiple Roles of the Small GTPase Rab7.* Cells, 2016. **5**(3).

331. Hongisto, H., et al., *In vitro stem cell modelling demonstrates a proof-of-concept for excess functional mutant TIMP3 as the cause of Sorsby fundus dystrophy.* J Pathol, 2020. **252**(2): p. 138-150.

332. Forrester, J.V., et al., *The eye : basic sciences in practice*. 2016, Elsevier: Edinburgh.

333. Benito-Martinez, S., et al., *Research Techniques Made Simple: Cell Biology Methods for the Analysis of Pigmentation.* J Invest Dermatol, 2020. **140**(2): p. 257-268 e8.

334. George, A., et al., *In vitro disease modeling of oculocutaneous albinism type 1 and 2 using human induced pluripotent stem cell-derived retinal pigment epithelium.* Stem Cell Reports, 2022. **17**(1): p. 173-186.

335. Marks, M.S. and M.C. Seabra, *The melanosome: membrane dynamics in black and white.* Nat Rev Mol Cell Biol, 2001. **2**(10): p. 738-48.

336. Lopez, V.M., et al., *L-DOPA is an endogenous ligand for OA1.* PLoS Biol, 2008. **6**(9): p. e236.

337. Zhang, Z., et al., *Mitochondrial NCKX5 regulates melanosomal biogenesis and pigment production.* J Cell Sci, 2019. **132**(14).

338. Kumar, R., et al., *The peroxisome: an update on mysteries 3.0.* Histochem Cell Biol, 2024. **161**(2): p. 99-132.

339. Das, Y., D. Swinkels, and M. Baes, *Peroxisomal Disorders and Their Mouse Models Point to Essential Roles of Peroxisomes for Retinal Integrity.* Int J Mol Sci, 2021. **22**(8).

340. Frank, R.N., R.H. Amin, and J.E. Puklin, *Antioxidant enzymes in the macular retinal pigment epithelium of eyes with neovascular age-related macular degeneration.* Am J Ophthalmol, 1999. **127**(6): p. 694-709.

341. Pastukhov Iu, F., et al., *[Protein 70 kDa in control of sleep and thermoregulation].* Zh Evol Biokhim Fiziol, 2008. **44**(1): p. 65-71.

342. Bianchi, A., et al., *Oxidative stress-induced expression of HSP70 contributes to the inhibitory effect of 15d-PGJ2 on inducible prostaglandin pathway in chondrocytes.* Free Radic Biol Med, 2014. **76**: p. 114-26.

343. Qin, S. and G.W. De Vries, *alpha2 But not alpha1 AMP-activated protein kinase mediates oxidative stress-induced inhibition of retinal pigment epithelium cell phagocytosis of photoreceptor outer segments.* J Biol Chem, 2008. **283**(11): p. 6744-51.

344. Wang, A.L., et al., *Autophagy and exosomes in the aged retinal pigment epithelium: possible relevance to drusen formation and age-related macular degeneration.* PLoS One, 2009. **4**(1): p. e4160.

345. Datta, S., et al., *The impact of oxidative stress and inflammation on RPE degeneration in non-neovascular AMD.* Prog Retin Eye Res, 2017. **60**: p. 201-218.

346. Westenskow, P.D., et al., *Using flow cytometry to compare the dynamics of photoreceptor outer segment phagocytosis in iPS-derived RPE cells.* Invest Ophthalmol Vis Sci, 2012. **53**(10): p. 6282-90.

347. Lakkaraju, A., S.C. Finnemann, and E. Rodriguez-Boulan, *The lipofuscin fluorophore A2E perturbs cholesterol metabolism in retinal pigment epithelial cells.* Proc Natl Acad Sci U S A, 2007. **104**(26): p. 11026-31.

348. Finnemann, S.C., L.W. Leung, and E. Rodriguez-Boulan, *The lipofuscin component A2E selectively inhibits phagolysosomal degradation of photoreceptor phospholipid by the retinal pigment epithelium.* Proc Natl Acad Sci U S A, 2002. **99**(6): p. 3842-7.

349. Jung, T., N. Bader, and T. Grune, *Lipofuscin: formation, distribution, and metabolic consequences.* Ann N Y Acad Sci, 2007. **1119**: p. 97-111.

350. Kaemmerer, E., et al., *Effects of lipid peroxidation-related protein modifications on RPE lysosomal functions and POS phagocytosis.* Invest Ophthalmol Vis Sci, 2007. **48**(3): p. 1342-7.

351. Terman, A. and U.T. Brunk, *Lipofuscin.* Int J Biochem Cell Biol, 2004. **36**(8): p. 1400-4.

352. Ferrington, D.A., D. Sinha, and K. Kaarniranta, *Defects in retinal pigment epithelial cell proteolysis and the pathology associated with age-related macular degeneration.* Prog Retin Eye Res, 2016. **51**: p. 69-89.

353. Hyttinen, J.M., et al., *Clearance of misfolded and aggregated proteins by aggrephagy and implications for aggregation diseases.* Ageing Res Rev, 2014. **18**: p. 16-28.

354. Kaarniranta, K., et al., *Mechanisms of protein aggregation in the retinal pigment epithelial cells.* Front Biosci (Elite Ed), 2010. **2**(4): p. 1374-84.

355. Bucci, C., et al., *Rab7: a key to lysosome biogenesis.* Mol Biol Cell, 2000. **11**(2): p. 467-80.

356. Mason, H.S., *A classification of melanins.* Ann N Y Acad Sci, 1948. **4**: p. 399-404.

357. Feeney, L., *Lipofuscin and melanin of human retinal pigment epithelium. Fluorescence, enzyme cytochemical, and ultrastructural studies.* Invest Ophthalmol Vis Sci, 1978. **17**(7): p. 583-600.

358. Lopes, V.S., et al., *Melanosome maturation defect in Rab38-deficient retinal pigment epithelium results in instability of immature melanosomes during transient melanogenesis.* Mol Biol Cell, 2007. **18**(10): p. 3914-27.

359. Seiji, M., et al., *Subcellular localization of melanin biosynthesis.* Ann N Y Acad Sci, 1963. **100**: p. 497-533.

360. Sarna, T., *Properties and Function of the Ocular Melanin - a Photobiophysical View.* Journal of Photochemistry and Photobiology B-Biology, 1992. **12**(3): p. 215-258.

361. Plaza Reyes, A., et al., *Identification of cell surface markers and establishment of monolayer differentiation to retinal pigment epithelial cells.* Nat Commun, 2020. **11**(1): p. 1609.

362. Chen, Q., et al., *Measurement of Melanin Metabolism in Live Cells by [U-(13)C]-L-Tyrosine Fate Tracing Using Liquid Chromatography-Mass Spectrometry.* J Invest Dermatol, 2021. **141**(7): p. 1810-1818 e6.

363. Fuller, B.B., D.T. Spaulding, and D.R. Smith, *Regulation of the catalytic activity of preexisting tyrosinase in black and Caucasian human melanocyte cell cultures.* Exp Cell Res, 2001. **262**(2): p. 197-208.

364. Hu, D.N., J.D. Simon, and T. Sarna, *Role of ocular melanin in ophthalmic physiology and pathology.* Photochem Photobiol, 2008. **84**(3): p. 639-44.

365. Sanyal, S. and G.H. Zeilmaker, *Retinal damage by constant light in chimaeric mice: implications for the protective role of melanin.* Exp Eye Res, 1988. **46**(5): p. 731-43.

366. Boulton, M., et al., *Age-related changes in the morphology, absorption and fluorescence of melanosomes and lipofuscin granules of the retinal pigment epithelium.* Vision Res, 1990. **30**(9): p. 1291-303.

367. Kim, H.E. and S.G. Lee, *Induction of ATP synthase beta by H2O2 induces melanogenesis by activating PAH and cAMP/CREB/MITF signaling in melanoma cells.* Int J Biochem Cell Biol, 2013. **45**(7): p. 1217-22.

368. Karg, E., et al., *Hydrogen peroxide as an inducer of elevated tyrosinase level in melanoma cells.* J Invest Dermatol, 1993. **100**(2 Suppl): p. 209S-213S.

369. Koga, S., M. Nakano, and S. Tero-Kubota, *Generation of superoxide during the enzymatic action of tyrosinase.* Arch Biochem Biophys, 1992. **292**(2): p. 570-5.

370. Korytowski, W. and T. Sarna, *Bleaching of melanin pigments. Role of copper ions and hydrogen peroxide in autooxidation and photooxidation of synthetic dopa-melanin.* J Biol Chem, 1990. **265**(21): p. 12410-6.

371. Sarna, T., I.A. Menon, and R.C. Sealy, *Photosensitization of melanins: a comparative study.* Photochem Photobiol, 1985. **42**(5): p. 529-32.

372. Bustamante, J., et al., *Role of melanin as a scavenger of active oxygen species.* Pigment Cell Res, 1993. **6**(5): p. 348-53.

373. Maresca, V., et al., *Correlation between melanogenic and catalase activity in in vitro human melanocytes: a synergic strategy against oxidative stress.* Pigment Cell Melanoma Res, 2008. **21**(2): p. 200-5.

374. Bergen, A.A., et al., *On the origin of proteins in human drusen: The meet, greet and stick hypothesis.* Prog Retin Eye Res, 2019. **70**: p. 55-84.

375. de Jong, S., et al., *Implications of genetic variation in the complement system in age-related macular degeneration.* Prog Retin Eye Res, 2021. **84**: p. 100952.

376. Klein, R., et al., *Prevalence of age-related macular degeneration in the US population.* Arch Ophthalmol, 2011. **129**(1): p. 75-80.

377. Klein, R., et al., *Associations of candidate genes to age-related macular degeneration among racial/ethnic groups in the multi-ethnic study of atherosclerosis.* Am J Ophthalmol, 2013. **156**(5): p. 1010-1020 e1.

378. Brilliant, M.H., et al., *Mining Retrospective Data for Virtual Prospective Drug Repurposing: L-DOPA and Age-related Macular Degeneration.* Am J Med, 2016. **129**(3): p. 292-8.

379. Figueroa, A.G., et al., *Levodopa Positively Affects Neovascular Age-Related Macular Degeneration.* Am J Med, 2021. **134**(1): p. 122-128 e3.

380. Bakker, R., et al., *The retinal pigmentation pathway in human albinism: Not so black and white.* Prog Retin Eye Res, 2022. **91**: p. 101091.

381. Bennis, A., et al., *Stem Cell Derived Retinal Pigment Epithelium: The Role of Pigmentation as Maturation Marker and Gene Expression Profile Comparison with Human Endogenous Retinal Pigment Epithelium.* Stem Cell Rev Rep, 2017. **13**(5): p. 659-669.

382. Holz, F.G., et al., *Ultrastructural findings in autosomal dominant drusen.* Arch Ophthalmol, 1997. **115**(6): p. 788-92.

383. van der Schaft, T.L., et al., *Is basal laminar deposit unique for age-related macular degeneration?* Arch Ophthalmol, 1991. **109**(3): p. 420-5.

384. Jeffery, G., *The retinal pigment epithelium as a developmental regulator of the neural retina.* Eye (Lond), 1998. **12 (Pt 3b)**: p. 499-503.

385. Starnes, A.C., et al., *Multi-nucleate retinal pigment epithelium cells of the human macula exhibit a characteristic and highly specific distribution.* Vis Neurosci, 2016. **33**: p. e001.

386. Bhatia, S.K., et al., *Analysis of RPE morphometry in human eyes.* Mol Vis, 2016. **22**: p. 898-916.

387. Farjood, F., et al., *Identifying biomarkers of heterogeneity and transplantation efficacy in retinal pigment epithelial cells.* J Exp Med, 2023. **220**(12).

388. Weiter, J.J., et al., *Retinal pigment epithelial lipofuscin and melanin and choroidal melanin in human eyes.* Invest Ophthalmol Vis Sci, 1986. **27**(2): p. 145-52.

389. Koo, C.Z., et al., *The tetraspanin Tspan15 is an essential subunit of an ADAM10 scissor complex.* J Biol Chem, 2020. **295**(36): p. 12822-12839.

390. Seipold, L., et al., *In vivo regulation of the A disintegrin and metalloproteinase 10 (ADAM10) by the tetraspanin 15.* Cell Mol Life Sci, 2018. **75**(17): p. 3251-3267.

391. Mirdita, M., et al., *ColabFold: making protein folding accessible to all.* Nat Methods, 2022. **19**(6): p. 679-682.

392. Binger, K.J. and M.D. Wright, *Seeing your partner: Structural elucidation of the first C8 tetraspanin protein.* Structure, 2022. **30**(2): p. 203-205.

393. Hu, Y., et al., *Dissecting the transcriptome landscape of the human fetal neural retina and retinal pigment epithelium by single-cell RNA-seq analysis.* PLoS Biol, 2019. **17**(7): p. e3000365.

394. Parry, D.A., et al., *Loss of the metalloprotease ADAM9 leads to cone-rod dystrophy in humans and retinal degeneration in mice.* Am J Hum Genet, 2009. **84**(5): p. 683-91.

395. Senabouth, A., et al., *Transcriptomic and proteomic retinal pigment epithelium signatures of age-related macular degeneration.* Nat Commun, 2022. **13**(1): p. 4233.

396. Or, C., et al., *Expression of ADAMs (A Disintegrin and Metalloproteinase) 10 and 17 in Human Eyes and in Experimental Models of Age Related Macular Degeneration (AMD).* Investigative Ophthalmology & Visual Science, 2014. **55**(13): p. 3460-3460.

397. Eschenbrenner, E., et al., *TspanC8 tetraspanins differentially regulate ADAM10 endocytosis and half-life.* Life Sci Alliance, 2020. **3**(1).

398. Noy, P.J., et al., *TspanC8 Tetraspanins and A Disintegrin and Metalloprotease 10 (ADAM10) Interact via Their Extracellular Regions: EVIDENCE FOR DISTINCT BINDING MECHANISMS FOR DIFFERENT TspanC8 PROTEINS.* J Biol Chem, 2016. **291**(7): p. 3145-57.

399. Wolkow, N., et al., *Iron upregulates melanogenesis in cultured retinal pigment epithelial cells.* Exp Eye Res, 2014. **128**: p. 92-101.

400. Stroeva, O.G. and V.I. Mitashov, *Retinal pigment epithelium: proliferation and differentiation during development and regeneration.* Int Rev Cytol, 1983. **83**: p. 221-93.

401. Fields, M.A., et al., *Interactions of the choroid, Bruch's membrane, retinal pigment epithelium, and neurosensory retina collaborate to form the outer blood-retinal-barrier.* Prog Retin Eye Res, 2020. **76**: p. 100803.

402. Sinha, D., et al., *Lysosomes: Regulators of autophagy in the retinal pigmented epithelium.* Exp Eye Res, 2016. **144**: p. 46-53.

403. Milner, C.M. and R.D. Campbell, *Structure and expression of the three MHC-linked HSP70 genes.* Immunogenetics, 1990. **32**(4): p. 242-51.

404. Martinez-Vicente, M., G. Sovak, and A.M. Cuervo, *Protein degradation and aging.* Exp Gerontol, 2005. **40**(8-9): p. 622-33.

405. Daugaard, M., et al., *Lens epithelium-derived growth factor is an Hsp70-2 regulated guardian of lysosomal stability in human cancer.* Cancer Res, 2007. **67**(6): p. 2559-67.

406. Rossi, A., et al., *Genetic compensation induced by deleterious mutations but not gene knockdowns.* Nature, 2015. **524**(7564): p. 230-3.

407. El-Brolosy, M.A., et al., *Genetic compensation triggered by mutant mRNA degradation.* Nature, 2019. **568**(7751): p. 193-197.

408. Ma, Z., et al., *PTC-bearing mRNA elicits a genetic compensation response via Upf3a and COMPASS components.* Nature, 2019. **568**(7751): p. 259-263.

409. Arunkumar, R., et al., *What do we know about the macular pigment in AMD: the past, the present, and the future.* Eye (Lond), 2018. **32**(5): p. 992-1004.

410. Shu, D.Y., E. Butcher, and M. Saint-Geniez, *EMT and EndMT: Emerging Roles in Age-Related Macular Degeneration.* Int J Mol Sci, 2020. **21**(12).

411. Jordens, I., et al., *Rab7 and Rab27a control two motor protein activities involved in melanosomal transport.* Pigment Cell Res, 2006. **19**(5): p. 412-23.

412. Gomez, P.F., et al., *Identification of rab7 as a melanosome-associated protein involved in the intracellular transport of tyrosinase-related protein 1.* J Invest Dermatol, 2001. **117**(1): p. 81-90.

413. Hirosaki, K., et al., *Tyrosinase and tyrosinase-related protein 1 require Rab7 for their intracellular transport.* J Invest Dermatol, 2002. **119**(2): p. 475-80.

414. Raposo, G. and M.S. Marks, *Melanosomes--dark organelles enlighten endosomal membrane transport.* Nat Rev Mol Cell Biol, 2007. **8**(10): p. 786-97.

415. Bowman, S.L., et al., *The road to lysosome-related organelles: Insights from Hermansky-Pudlak syndrome and other rare diseases.* Traffic, 2019. **20**(6): p. 404-435.

416. Delevoye, C., M.S. Marks, and G. Raposo, *Lysosome-related organelles as functional adaptations of the endolysosomal system.* Curr Opin Cell Biol, 2019. **59**: p. 147-158.

417. Rozanowska, M., et al., *Free radical scavenging properties of melanin interaction of eu- and pheo-melanin models with reducing and oxidising radicals.* Free Radic Biol Med, 1999. **26**(5-6): p. 518-25.

418. Zareba, M., et al., *The effect of a synthetic neuromelanin on yield of free hydroxyl radicals generated in model systems.* Biochim Biophys Acta, 1995. **1271**(2-3): p. 343-8.

419. Dontsov, A.E., et al., *Understanding the Mechanism of Light-Induced Age-Related Decrease in Melanin Concentration in Retinal Pigment Epithelium Cells.* Int J Mol Sci, 2023. **24**(17).

420. Schallreuter, K.U., J.M. Wood, and J. Berger, *Low catalase levels in the epidermis of patients with vitiligo.* J Invest Dermatol, 1991. **97**(6): p. 1081-5.

421. *Stereoscopic Atlas of Macular Diseases: Diagnosis and Treatment.* Archives of Ophthalmology, 1990. **108**(4): p. 494.

422. Curcio, C.A., *Photoreceptor topography in ageing and age-related maculopathy.* Eye, 2001. **15**(3): p. 376-383.

423. Kim, S.Y., et al., *Morphometric analysis of the macula in eyes with geographic atrophy due to age-related macular degeneration.* Retina, 2002. **22**(4): p. 464-70.

424. Zekavat, S.M., et al., *Photoreceptor Layer Thinning Is an Early Biomarker for Age-Related Macular Degeneration: Epidemiologic and Genetic Evidence from UK Biobank OCT Data.* Ophthalmology, 2022. **129**(6): p. 694-707.

425. Klausner, R.D. and R. Sitia, *Protein degradation in the endoplasmic reticulum.* Cell, 1990. **62**(4): p. 611-4.

426. Berson, J.F., et al., *A common temperature-sensitive allelic form of human tyrosinase is retained in the endoplasmic reticulum at the nonpermissive temperature.* J Biol Chem, 2000. **275**(16): p. 12281-9.

427. Ancans, J., et al., *Melanosomal pH controls rate of melanogenesis, eumelanin/phaeomelanin ratio and melanosome maturation in melanocytes and melanoma cells.* Exp Cell Res, 2001. **268**(1): p. 26-35.

428. Lucien, F., et al., *Simultaneous pH measurement in endocytic and cytosolic compartments in living cells using confocal microscopy.* J Vis Exp, 2014(86).

429. Roth, J., M. Bendayan, and L. Orci, *Ultrastructural localization of intracellular antigens by the use of protein A-gold complex.* J Histochem Cytochem, 1978. **26**(12): p. 1074-81.